Systematically Controlled Decomposition Mechanism in Phosphorus Containing Polymers by Precise Molecular Architecture

Dissertation

zur Erlangung des akademischen Grades eines

“Doctor rerum naturalium (Dr. rer. nat.)“

des Fachbereiches Chemie, Pharmazie und Geowissenschaften (FB 09)

der Johannes Gutenberg-Universität Mainz

vorgelegt von

Jens Christian Markwart

geboren in Frankfurt am Main - Höchst

Mainz, Oktober 2019

MATERIALS IN MAINZ SCIENCE

JOHANNES GUTENBERG UNIVERSITÄT MAINZ

JG|U

MAX-PLANCK-INSTITUT FÜR POLYMERFORSCHUNG

Diese Arbeit wurde im Zeitraum von Oktober 2016 bis Oktober 2019 am Max-Planck-Institut für Polymerforschung im Arbeitskreis von [redacted] unter der Betreuung von [redacted] angefertigt.

Gutachter:

1. Gutachter: [redacted]

2. Gutachter: [redacted]

Erklärung:

Hiermit versichere ich, die vorliegende Arbeit selbstständig und ohne Benutzung anderer als der angegebenen Hilfsmittel angefertigt zu haben. Alle Stellen, die wörtlich oder sinngemäß aus Veröffentlichungen oder anderen Quellen entnommen sind, wurden als solche eindeutig kenntlich gemacht. Diese Arbeit ist in gleicher oder ähnlicher Form noch nicht veröffentlicht und auch keiner anderen Prüfungsbehörde vorgelegt worden.

Jens C. Markwart

Mainz, Oktober 2019

Für meine Familie

„Wenn Sie die Art und Weise ändern, wie Sie die Dinge betrachten, ändern sich die Dinge, die Sie betrachten.“

Max Planck (1858 - 1947)

Table of Contents

Motivation and Objectives

Flame retardants are needed in most polymer products, however their mode of action is determined by their decomposition pathway. Concerning recent restrictions for halogenated flame retardants, organophosphorus flame retardants are promising alternatives as their chemistry allows designing efficient and less-toxic alternatives.[1] The aim of this thesis was to understand the thermal stability and decomposition pathways of a systematic library of novel low molar mass and hyperbranched organophosphorus compounds as flame retardant additives in epoxy resins and matrix for composites during combustion.

Epoxy resins are also used in composites, which are gaining more interest lately.[2] The challenge here is that cross-linked polymer composites currently on the market cannot be recycled. In addition, additives such as flame retardants are still required for these materials if they are to follow safety regulations. A promising solution to this is the development of intrinsic flame-retardant dynamic polymer networks (vitrimers) as matrix for composites, where the influence of the binding sphere (P-O/P-C) was studied. In these materials, vitrimers open the possibility of repairing, a sustainable recycling, including reprocessing, and separation of the fibers from the matrix. This is almost impossible for conventional fiber reinforced polymer composites.

Knowledge about thermal decomposition is important to understand the performance of a flame retardant. With the increasing usage of polymers worldwide, the risk of fires increases, making this knowledge essential. Especially since halogenated alternatives, which are mostly used today as flame retardants, are more and more restricted worldwide due to their environmental persistence and release of corrosive gases like HBr and HCl during combustion.[3] Therefore, health, environment, and sustainability considerations play increasingly important roles in the development of novel flame retardants. Organic phosphorus compounds release less health concerning gases during combustion and are more versatile due to their different flame retardancy mechanisms.[4] Several studies demonstrated already that the combination of phosphorus flame retardants with additional nitrogen-containing additives result in synergistic effects during combustion.[5] However, a systematic study of precisely synthesized phosphorus flame retardants with a variable number of P-O-/P-N- and P-O-/P-C-bonds (such as phosphoramidates, phosphorodiamidates, phosphonates and phosphine oxides) and the influence of sulfur and it's oxidation state has not been performed.

In addition, early leaching of the flame retardant additive from the matrix is undesired and is prevented by increased molar mass. Therefore, this thesis aims to develop an understanding of the thermal decomposition of branched polymers in comparison to their low molar mass counter

parts. The branched structure of such polymers used as flame retardant additives reduces entangling and should allow efficient mixing with the polymer matrix.

Chapter 1: The first chapter gives an introduction into state-of-the-art phosphorus flame retardants and their modes of action. Finally, this chapter will highlight modern trends of phosphorus flame retardants and their potential future application. To that end, representative examples were chosen. However, this is not meant to be a comprehensive summary.

Chapter 2: The influence of the sequential substitution of a P-O bond by a P-N bond (phosphorus binding sphere) on the thermal decomposition and the resulting matrix interaction in flame retardant applications should be studied. Furthermore, the effectiveness of blends of phosphate and phosphoramide in comparison to their synthesized counterparts (phosphoramidate and phosphorodiamidate) on the performance during a simulated fire scenario should be studied.

Chapter 3: Building on chapter two, the effect of hyperbranched phosphorus-based polymeric flame retardants by an A_2+B_3-type approach via thiol-ene polyaddition with varying amounts of P-O and P-N bonds in comparison to their low molar mass counterparts should be studied. It is believed that hyperbranched polymeric flame retardants increase flame retardancy, mitigate negative effects of low molar mass analogs, and can compete with current commercial flame retardants.

Chapter 4: In the previous chapters, only aliphatic flame retardants were studied. The aim of this chapter is to understand the difference in decomposition behavior of aromatic in comparison to aliphatic phosphorus containing flame retardants. The decomposition and vaporizing behavior of a compound is an important factor in its flame-retardant behavior, but also the interaction with pyrolysing matrix has a significant influence. Therefore, the challenge in flame retardancy design is to optimize the flame retardant for exploiting chemical reactions at the right place, time and temperature.

Chapter 5: Building on chapter four, the effect of the matrix (one aliphatic and one aromatic) on the flame retardant behavior of the previous discussed phosphorus flame retardants should be assed. In general, the overlap of decomposition temperature ranges of the flame retardant and matrix determines the efficacy of the system. The chemical structure and the structure-property relationship of both flame retardant and matrix are central to flame retardant performance.

Chapter 6: A library of polymeric phosphorus containing flame retardants was synthesized in chapter three. While key chemical mechanisms and modes of actions were elucidated in chapter three, the role of sulfur in the chemical composition remains an open question. Therefore, the polymers synthesized by thiol-ene polyaddition should be compared with their low molar mass monomer and two sulfur-containing analogues thereof of different oxidation states.

Chapter 7: In this chapter, the phosphorus content should be increased by designing the first phosphorus-based AB_2 monomer for the synthesis of hyperbranched poly phosphoesters. Furthermore, its flame-retardant performance in an epoxy resin compared to a hyperbranched polyphosphoester synthesized in chapter three should be studied. Branched polymers are an important class of polymers with a high number of terminal groups, lower viscosity compared to their linear analogues and higher miscibility, which makes them especially interesting for flame retardant applications, where the flame retardants are blended with another polymer matrix. Hyperbranched poly phosphoesters are gaining more and more interest in the field of flame retardancy, as low molar mass flame retardants often have the disadvantage of blooming out or leaching, which is not desired in consumer products.

Chapter 8: In the previous chapters, epoxy resins with phosphorus flame retardants were studied. A common application for epoxy resins are composites. However, cross-linked polymer composites currently on the market cannot be recycled and often need additive flame retardants. Therefore, in this chapter the first intrinsic flame-retardant dynamic polymer network (vitrimer) based on vinylogous polyurethanes should be synthesized and its flame retardant properties as well as the application in composites assessed.

Chapter 9: During the design of the AB_2 monomer in chapter seven, a protective group for the P-OH functionality was found. Protecting functional groups is often necessary in synthetic chemistry, e.g. due to chemical incompatibility or solubility. Several methods for P-OH protection were proposed, but often with low selectivity or harsh conditions.

Chapter 10: The aim of this chapter was to conduct first studies on anisotropic materials with very high aspect ratios. The crystallization should be controlled by utilizing phosphorus chemistry and simple polycondensation to introduce precisely spaced defects in polyethylene like polymers and by using different temperature profiles for the crystallization. The crystal structure should be analyzed by transmission electron microscopy and solid state NMR to show that the pendant group of the phosphorus is accessible for further chemical reactions. The accessibility should be proven by utilizing the protective group for the P-OH functionality introduced in chapter nine.

[1] M. M. Velencoso, A. Battig, J. C. Markwart, B. Schartel, F. R. Wurm, *Angew. Chem. Int. Ed. Engl.* **2018**, *57*, 10450-10467.

[2] L. Nicolais, M. Meo, E. Milella, *Composite Materials: A Vision for the Future*, Springer London, **2011**.

[3] A. B. Morgan, J. W. Gilman, **2013**, *37*, 259-279.

[4] R. Nazir, S. Gaan, *J. Appl. Polym. Sci.*, *0*, 47910.

[5] S. Gaan, G. Sun, K. Hutches, M. H. Engelhard, *Polym. Degrad. Stab.* **2008**, *93*, 99-108.

Abstract

Polymers are omnipresent in our daily life and with their broad use comes with an increased fire risk, and sustained research into efficient flame retardants is key to ensuring the safety of the populace and material goods from accidental fires. Halogenated flame retardants are still widely used today, but are increasing under review due to concerns regarding health and environment. A promising alternative is phosphorus, a versatile and effective element for use in flame retardants: to solve the task of developing flame-retarding polymeric materials, current formulations employ a variety of modes of action and methods of implementation, as additives or as reactants. During a fire phosphorus-based flame retardants can act in both the gas and condensed phase. The aim of this thesis is to investigate how current phosphorus chemistry can help reducing the flammability of polymers by understanding the decomposition pathways under pyrolytic conditions, and apply this knowledge for the design of various flame-retardant polymers.

Chapter 1: In this chapter, an introduction into phosphorus based flame retardants is given and the challenges of a good flame retardant are discussed. These include the retention of material properties while keeping the price low and being sustainable. Most compounds that contain phosphorus are manufactured from phosphorite, commonly known as “phosphate rock”. At current extraction rates, estimates point to phosphate rock reserves being depleted in the next 370 years, with the exception of the reserves in Morocco. In addition, recent developments in phosphorus-containing reactive and additive flame retardants are discussed while summarizing modern trends and the future of phosphorus flame retardants.

Chapter 2: Flame retardants are inevitable additives to many plastics. Halogenated organics are effective flame retardants but are controversially discussed due to the release of toxic gases during a fire or their persistence if landfilled. Phosphorus-containing compounds are effective alternatives to halogenated flame retardants and have potential lower toxicity and degradability. In addition, nitrogen-containing additives were reported to induce synergistic effects with phosphorus-based flame retardants. However, no systematic study of the gradual variation on a single phosphorus flame retardant containing both P–O and P–N moieties and their comparison to the respective blends of phosphates and phosphoramides was reported. In this study general design principles for P–O- and P–N-based flame retardants were developed and will help to design effective flame retardants for various polymers. A synthesized library of phosphorus flame retardants, which only differ in their P-binding pattern from each other, were studied regarding their decomposition mechanism in epoxy resins. Systematic control over the decomposition pathways of phosphate ($P{=}O(OR)_3$), phosphoramidate ($P{=}O(OR)_2(NHR)$), phosphorodiamidate ($P{=}O(OR)(NHR)_2$), phosphoramide ($P{=}O(NHR)_3$), and their blends was identified, for example, by

reducing *cis*-elimination and the formation of P–N-rich char with increasing nitrogen content in the P-binding sphere. The flame-retardant epoxy resins can compete with commercial flame retardants in most cases, but it was proven that the blending of esters and amides outperformed the single-molecule amidates/diamidates due to distinctively different decomposition mechanisms acting synergistically when blended.

Chapter 3: Multifunctional P-based hyperbranched polymeric flame retardants were successfully synthesized with varying oxygen-to-nitrogen content and characterized via ^{1}H and ^{31}P NMR and GPC. Their miscibility in epoxy resins and impact on glass-transition temperatures were determined via differential scanning calorimetry. Using thermogravimetric and evolved gas analysis, pyrolysis gas chromatography/mass spectrometry, hot stage FTIR, flammability tests UL-94 and LOI, fire testing via cone calorimetry, residue analysis via scanning electron microscopy and elemental analysis, detailed decomposition mechanisms and modes of action are proposed. Hyperbranched polymeric flame retardants have improved miscibility and thermal stability, leading to high flame retardant performance even at low loadings. Polymeric, complex flame retardants increase flame retardancy, mitigate negative effects of low molecular weight variants, and can compete with commercial aromatic flame retardants. The results illustrate the role played by the chemical structure in flame retardancy and highlight the potential of hyperbranched flame retardants as multifunctional additives.

Chapter 4: The current trend for future flame retardants (FRs) goes to novel efficient halogen-free materials, due to the ban of several halogenated flame retardants. Among the most promising alternatives are phosphorus-based flame retardants, and of those, polymeric materials with complex shape has been recently reported. Herein, we present novel aromatic and aliphatic, hyperbranched, halogen-free polyphosphoesters (hbPPEs), which were synthesized by olefin metathesis polymerization and investigated them as a flame retardant in epoxy resins. We compare their efficiency aliphatic vs. aromatic and further assess the differences between the monomeric compounds and the hbPPEs. The decomposition and vaporizing behavior of a compound is an important factor in its flame-retardant behavior, but also the interaction with the pyrolysing matrix has a significant influence on the performance. Therefore, the challenge in designing a FR is to optimize the chemical structure and its decomposition pathway to the matrix, with regards to time and temperature. This behavior becomes obvious in this study and explains the superior gas phase activity of the aliphatic FRs.

Chapter 5: We synthesized a library of phosphorus-based flame retardants (phosphates and phosphoramides of low and high molar mass) and investigated their behavior in two epoxy resins (one aliphatic and one aromatic). The pyrolytic and burning behavior of the two resins (via TGA,

TG-FTIR, Hot stage FTIR, Py-GC/MS, PCFC, DSC, LOI, UL-94, Cone calorimeter) are analyzed and compared to the results of flame retardant (FR)-containing composites. A decomposition pathway incorporating the identified modes of action and known chemical mechanisms is proposed. The overlap of decomposition temperature (T_{dec}) ranges of matrix and FR determines the efficacy of the system. Low molar mass FRs strongly impact material properties like T_g but are very reactive, and high molar mass variants are more thermally stable. Varying P-O and P-N content of the FR affects decomposition, but the chemical structure of the matrix also guides FR behavior. Thus, phosphates afford lower fire load and heat release in aliphatic epoxy resins, and phosphoramides can act as additives in an aromatic matrix or a reactive FRs in aliphatic ones. The chemical structure and the structure-property relationship of both FR and matrix are central to FR performance and must be viewed not as two separate but as one codependent system.

Chapter 6: Hyperbranched polyphosphoesters are promising multifunctional flame retardants for epoxy resins. These polymers were prepared via thiol-ene polyaddition reactions. While key chemical mechanisms and modes of actions were elucidated, the role of sulfur in the chemical composition remains an open question. In this study, we compare the FR-performance of a series of phosphorus-based flame retardant additives with and without sulfur (thio-ethers or sulfones) in their structure. The successful synthesis of the thio-ether or sulfone-containing variants is described and verified by ^{1}H and ^{31}P NMR, also FTIR and MALDI-TOF. A decomposition mechanism is proposed from pyrolytic evolved gas analysis (TG-FTIR, Py-GC/MS), and flame retardancy effect on epoxy resins is investigated in pyrolytic conditions and via fire testing in the cone calorimeter. The presence of sulfur increased thermal stability of the flame retardants and introduced added condensed phase mechanisms. Likely, sulfur radical generation plays a key role in the flame-retardant mode of action, and sulfones released incombustible SO_2. The results highlight the multifunctionality of the hyperbranched polymer, which displays better fire performance than its low molar mass thio-ether analogue due to the presence of vinyl groups and higher stability than its monomer due to the presence of thio-ether groups.

Chapter 7: Branched polymers are an important class of polymers with a high number of terminal groups, lower viscosity compared to their linear analogs and higher miscibility, which makes them especially interesting for flame retardant applications, where the flame retardants (FR) are blended with another polymer matrix. Hyperbranched polyphosphoesters (*hb*PPEs) are gaining more and more interest in the field of flame retardancy, as low molar mass FRs often have the disadvantage of blooming out or leaching, which is not desired in consumer products. Here, we present the first phosphorus-based AB_2 monomer for the synthesis of *hb*PPEs and assess its flame-retardant performance in an epoxy resin compared to a *hb*PPE synthesized by an A_2+B_3 approach.

The *hb*PPE synthesized from an AB_2 monomer exhibited a slightly higher performance compared to a similar *hb*PPE, which was prepared by A_2 + B_3 polyaddition, probably due to its higher phosphorus content.

Chapter 8: Crosslinked-polymer composites currently on the market cannot be recycled. A promising alternative to reach recyclability is the development of dynamic covalent polymer networks. To date, however, additives such as flame retardants are still required for these materials if they are to follow safety regulations. Therefore, herein the first intrinsic flame-retardant dynamic polymer network based on vinylogous polyurethanes is presented and its flame retardant properties, as well as the application in composites, are assessed. In composites, vitrimers open the possibility of recycling, including reprocessing, repairing and separation of the fibers from the matrix. This is almost impossible for conventional fiber-reinforced polymer composites. In addition, the herein presented vitrimer has a similar glass transition temperature to commercially available epoxy resins and the determined values for the bending strength and bending modulus for the phosphorous-containing vitrimer lie within the range of permanently cross-linked epoxy resins reinforced with the same glass fibers.

Chapter 9: Phosphodiesters are bridging elements in nucleic acids. In nature and synthesis, their negative charge protects them from hydrolysis and controls their solubility profile. RNA is a promising material for gene technology but cellular uptake is low due to negative charges. Synthetic oligonucleotides were delivered into cells by a prodrug approach relying on the enzymatic release of the polyphosphodiester oligonucleotides. In synthetic chemistry, a protective group for the P-OH functionality is often necessary, e.g. due to solubility or chemical incompatibility. Several methods for P-OH protection were proposed, but often with low selectivity or harsh conditions. Here, we present the 2-acetylthioethyl group as a versatile protective group for low molecular weight or polymeric phosphodiesters, which can be cleaved under acidic conditions in water or by hydrazine in THF to release the P-OH-functionality, but olefins remain intact. This straightforward use allows designing various synthetic polyphosphodiesters, e.g. for flame-retardant or dispersants.

Chapter 10: Anisotropic materials with very high aspect ratios (“2D materials”), such as platelets are an interesting material class due to their unique properties based on their unilamellar geometry. We utilized phosphorus chemistry and simple polycondensation to introduce precisely spaced defects in polyethylene like polymers. The relatively large size and flexibility of the phosphate groups allows the control of the chain-folding during crystallization. We investigated this behavior by solid state NMR and TEM imaging. Furthermore, we showed that we are able to do chemistry “on surface”. The pendant ester group at the phosphate gives the possibility for the

introduction of functional groups which are accessible for further chemical modification on the crystal surface, which was proven by the introduction of the 2-acetylthioethyl ester group and a later cleavage of the 2-acetylthioethyl ester group to P-OH. In addition we were able to control the lateral crystal size by different temperature profiles.

Zusammenfassung

Polymere sind in unserem täglichen Leben allgegenwärtig und aufgrund ihres breiten Einsatzes mit einem erhöhten Brandrisiko verbunden. Daher ist die kontinuierliche Erforschung effizienter Flammschutzmittel der Schlüssel zur Gewährleistung der Sicherheit von Bevölkerung und materiellen Gütern vor unbeabsichtigten Bränden. Halogenierte Flammschutzmittel sind heute noch weit verbreitet, werden jedoch aufgrund von Bedenken in Bezug auf Gesundheit und Umwelt zunehmend hinterfragt. Eine vielversprechende Alternative ist Phosphor, ein vielseitiges und wirksames Element für den Einsatz in Flammschutzmitteln: Um die Aufgabe der Entwicklung flammhemmender polymerer Werkstoffe zu lösen, setzen aktuelle Formulierungen eine Vielzahl von Wirkmechanismen und Implementierungen, z.B. als Additive oder als Reaktanten, ein. Während eines Brandes können Flammschutzmittel auf Phosphorbasis sowohl in der Gasphase als auch in der kondensierten Phase wirken. Das Ziel dieser Arbeit ist es zu untersuchen, wie die aktuelle Phosphorchemie dazu beitragen kann, die Entflammbarkeit von Polymeren zu verringern, indem die Zersetzungswege unter pyrolytischen Bedingungen verstanden werden, und dieses Wissen für das Design verschiedener flammhemmender Polymere anzuwenden.

Kapitel 1: In diesem Kapitel wird eine Einführung in Flammschutzmittel auf Phosphorbasis gegeben und die Herausforderungen eines guten Flammschutzmittels erörtert. Zu den Herausforderungen gehört z.B. die Beibehaltung der Materialeigenschaften bei gleichzeitig niedrigem Preis und Nachhaltigkeit. Die meisten Verbindungen, die Phosphor enthalten, werden aus Phosphorit hergestellt, das allgemein als "Phosphatgestein" bekannt ist. Schätzungen zufolge werden bei den derzeitigen Förderraten die Phosphatgesteinsreserven in den nächsten 370 Jahren, abgesehen von den Reserven in Marokko, abgebaut sein. Darüber hinaus werden die jüngsten Entwicklungen bei phosphorhaltigen reaktiven und additiven Flammschutzmitteln erörtert, während moderne Trends und die Zukunft von Flammschutzmitteln auf Phosphorbasis zusammengefasst werden.

Kapitel 2: Flammschutzmittel sind für viele Kunststoffe unverzichtbare Additive. Halogenierte organische Stoffe sind wirksame Flammschutzmittel, werden jedoch wegen der Freisetzung giftiger Gase während eines Brandes oder ihrer Persistenz bei der Deponierung kontrovers diskutiert. Phosphorhaltige Verbindungen sind wirksame Alternativen zu halogenierten Flammschutzmitteln und weisen eine möglicherweise geringere Toxizität und eine bessere Abbaubarkeit auf. Darüber hinaus wurde berichtet, dass stickstoffhaltige Additive synergistische Effekte mit Flammschutzmitteln auf Phosphorbasis hervorrufen. Es wurde jedoch noch keine systematische Untersuchung der allmählichen Variation eines einzelnen Phosphorflammschutzmittels, das sowohl P-O- als auch P-N-Einheiten enthält, durchgeführt. Des

Weiteren wurde noch kein Vergleich dieser Flammschutzmittel mit den jeweiligen Mischungen von Phosphat und Phosphoramid berichtet. Daher wurden in dieser Studie allgemeine Entwurfsprinzipien für P-O- und P-N-basierte Flammschutzmittel entwickelt, mit deren Hilfe wirksame Flammschutzmittel für verschiedene Polymere entwickelt werden können. Eine synthetisierte Bibliothek von Flammschutzmitteln aus Phosphorbasis, die sich nur in ihrem P-Bindungsmuster voneinander unterscheiden, wurde hinsichtlich ihres Zersetzungsmechanismus in Epoxidharzen untersucht. Systematische Kontrolle der Abbauwege des Phosphats ($P=O(OR)_3$), Phosphoramidats ($P=O(OR)_2(NHR)$), Phosphordiamidats ($P=O(OR)(NHR)_2$) oder Phosphoramids ($P=O(NHR)_3$) und ihre Mischungen wurden identifiziert, zum Beispiel die Verringerung der *cis*-Eliminierung und die Bildung einer P-N-reichen Kohle mit zunehmendem Stickstoffgehalt in der P-Bindungssphäre. Die flammgeschützten Epoxidharze können in den meisten Fällen mit handelsüblichen flammgeschützten Epoxidharzen konkurrieren. Es wurde jedoch nachgewiesen, dass das Mischen von Phosphat und Phosphoramid die Einzelmoleküle Amidat / Diamidat übertraf, da beim Mischen deutlich unterschiedliche Zersetzungsmechanismen auftreten, die synergistisch wirken.

Kapitel 3: Multifunktionelle hyperverzweigte polymere Flammschutzmittel auf Phosphorbasis wurden erfolgreich mit variierendem Sauerstoff-Stickstoff-Gehalt synthetisiert und über ^{1}H- und ^{31}P-NMR und GPC charakterisiert. Ihre Mischbarkeit in Epoxidharzen und ihr Einfluss auf die Glasübergangstemperaturen wurden mittels Differentialthermoanalyse bestimmt. Unter Verwendung von thermogravimetrischer Analyse und Analyse der entwickelten Gase, Pyrolyse-Gaschromatographie / Massenspektrometrie, hot stage FTIR, Entflammbarkeitstests UL-94 und LOI, Brandtests mittels Cone Calorimeter, Rückstandsanalyse mittels Rasterelektronenmikroskopie und Elementaranalyse, wurden detaillierte Zersetzungsmechanismen und Wirkungsmechanismen vorgeschlagen. Hyperverzweigte polymere Flammschutzmittel haben eine verbesserte Mischbarkeit und Wärmestabilität, was zu einer hohen Flammschutzleistung auch bei bereits geringen Beladungen führt. Komplexe, polymere Flammschutzmittel erhöhen die Flammhemmung, mildern die negativen Auswirkungen von Varianten mit niedrigem Molekulargewicht und können mit kommerziellen aromatischen Flammschutzmitteln konkurrieren. Die Ergebnisse veranschaulichen die Rolle der chemischen Struktur im Flammschutz und verdeutlichen das Potenzial von hyperverzweigten Flammschutzmitteln als multifunktionelle Additive.

Kapitel 4: Der aktuelle Trend für zukünftige Flammschutzmittel geht zu neuartigen, effizienten halogenfreien Materialien, da mehrere halogenierte Flammschutzmittel bereits verboten sind. Zu den vielversprechendsten Alternativen gehören Flammschutzmittel auf Phosphorbasis, und von

diesen wurde kürzlich über Polymermaterialien mit komplexer Form berichtet. Hier präsentieren wir neue aromatische und aliphatische, hyperverzweigte, halogenfreie Polyphosphoester (*hb*PPEs), die durch Olefinmetathesepolymerisation synthetisiert und als Flammschutzmittel in Epoxidharzen untersucht wurden. Wir vergleichen die Effizienz aliphatischer Flammschutzmittel mit aromatischen Flammschutzmitteln und bewerten darüber hinaus die Unterschiede zwischen den monomeren Verbindungen und den *hb*PPEs. Das Zersetzungs- und Verdampfungsverhalten einer Verbindung ist ein wichtiger Faktor für ihr flammhemmendes Verhalten, aber auch die Wechselwirkung mit der pyrolysierenden Matrix hat einen signifikanten Einfluss auf die Leistung. Daher besteht die Herausforderung beim Entwurf eines Flammschutzmittels darin, die chemische Struktur und seinen Zersetzungsweg auf die Matrix in Bezug auf Zeit und Temperatur zu optimieren. Dieses Verhalten wird in dieser Studie deutlich und erklärt die überlegene Gasphasenaktivität der aliphatischen Flammschutzmittel.

Kapitel 5: Wir haben eine Bibliothek von Flammschutzmitteln auf Phosphorbasis (Phosphate und Phosphoramide mit niedriger und hoher Molmasse) synthetisiert und ihr Verhalten in zwei Epoxidharzen (einem aliphatischen und einem aromatischen) untersucht. Das Pyrolyse- und Brennverhalten der beiden Harze (über TGA, TG-FTIR, hot stage FTIR, Py-GC / MS, PCFC, DSC, LOI, UL-94, Cone Calorimeter) wurde analysiert und mit den Ergebnissen der flammgeschützten Harze verglichen. Ein Abbauweg, der die identifizierten Wirkmechanismen und bekannten chemischen Mechanismen beinhaltet, wird vorgeschlagen. Die Überlappung der Zersetzungstemperaturbereiche (T_{dec}) von Matrix und Flammschutzmittel bestimmt die Wirksamkeit des Systems. Flammschutzmittel mit niedriger Molmasse wirken sich stark auf Materialeigenschaften wie T_g aus, sind jedoch sehr reaktiv, und Varianten mit hoher Molmasse sind thermisch stabiler. Unterschiedliche P-O- und P-N-Gehalte im Flammschutzmittel beeinflussen die Zersetzung, aber auch die chemische Struktur der Matrix bestimmt das Flammschutz-Verhalten. So liefern Phosphate in aliphatischen Epoxidharzen eine geringere Brand- und Wärmefreisetzung, und Phosphoramide können als Additive in einer aromatischen Matrix oder als reaktive Flammschutzmittel in einer aliphatischen Matrix wirken. Die chemische Struktur und die Struktur-Eigenschafts-Beziehung von Flammschutzmittel und Matrix sind von zentraler Bedeutung für die Flammschutzleistung-Leistung und müssen nicht als zwei separate, sondern als ein zusammenhängendes System betrachtet werden.

Kapitel 6: Hyperverzweigte Polyphosphoester sind vielversprechende multifunktionelle Flammschutzmittel für Epoxidharze. Diese Polymere wurden über Thiol-En-Polyadditionsreaktionen hergestellt. Während wichtige chemische Mechanismen und Wirkmechanismen aufgeklärt wurden, bleibt die Rolle des Schwefels in der chemischen

Zusammensetzung offen. In dieser Studie vergleichen wir die Flammschutz-Leistung einer Reihe von Flammschutzadditiven auf Phosphorbasis mit und ohne Schwefel (Thioether oder Sulfone) in ihrer Struktur. Die erfolgreiche Synthese der Thioether- oder Sulfon-haltigen Varianten wird durch ^{1}H- und ^{31}P-NMR sowie FTIR und MALDI-TOF beschrieben und verifiziert. Ein Zersetzungsmechanismus aus der pyrolytischen Gasanalyse (TG-FTIR, Py-GC / MS) wird vorgeschlagen, und die Flammschutzwirkung auf Epoxidharze wird unter pyrolytischen Bedingungen und über Brandtests im Cone Calorimeter untersucht. Die Anwesenheit von Schwefel erhöhte dabei die thermische Stabilität der Flammschutzmittel und führte zu zusätzlichen Mechanismen in der kondensierten Phase. Wahrscheinlich spielt die Erzeugung von Schwefelradikalen eine Schlüsselrolle bei der flammhemmenden Wirkungsweise, und Sulfone setzen nicht brennbares SO_2 frei. Die Ergebnisse unterstreichen die Multifunktionalität des hyperverzweigten Polymers, welches aufgrund noch vorhandener Vinylgruppen ein besseres Brandverhalten als sein Thioetheranalog mit niedriger Molmasse aufweist und aufgrund der Anwesenheit von Thioethergruppen eine höhere Stabilität als das Monomer aufweist.

Kapitel 7: Verzweigte Polymere sind eine wichtige Klasse von Polymeren mit einer hohen Anzahl von Endgruppen, einer niedrigeren Viskosität und einer im Vergleich zu ihren linearen Analoga höheren Mischbarkeit, was sie besonders für Flammschutzanwendungen interessant macht, bei denen die Flammschutzmittel (FR) mit einer anderen Polymermatrix gemischt werden. Hyperverzweigte Polyphosphoester (*hb*PPEs) gewinnen im Bereich der Flammhemmung immer mehr an Bedeutung, da niedermolekulare FRs häufig den Nachteil des Ausblühens oder Auswaschens aufweisen, was bei Konsumgütern unerwünscht ist. Hier präsentieren wir das erste auf Phosphor basierende AB_2-Monomer für die Synthese von *hb*PPEs und bewerten dessen Flammschutzleistung in einem Epoxidharz im Vergleich zu einem mit einem A_2 + B_3-Ansatz synthetisierten *hb*PPE. Das aus einem AB_2-Monomer synthetisierte *hb*PPE zeigte eine etwas höhere Leistung im Vergleich zu einem ähnlichen *hb*PPE, das durch A_2 + B_3-Polyaddition hergestellt wurde, wahrscheinlich aufgrund seines höheren Phosphorgehalts.

Kapitel 8: Derzeit auf dem Markt befindliche Verbundwerkstoffe aus vernetzten Polymeren können nicht recycelt werden. Eine vielversprechende Alternative zum Erreichen der Recyclingfähigkeit ist die Entwicklung dynamischer kovalenter Polymernetzwerke. Bisher werden für diese Werkstoffe jedoch noch Additive wie Flammschutzmittel benötigt, um den Sicherheitsbestimmungen zu entsprechen. Daher wird hier das erste intrinsisch flammgeschützte dynamische Polymernetzwerk auf der Basis von vinylogen Polyurethanen vorgestellt und seine flammhemmenden Eigenschaften sowie die Anwendung in Verbundwerkstoffen bewertet. In Verbundwerkstoffen eröffnen Vitrimere die Möglichkeit des Recyclings, einschließlich der

Wiederaufbereitung, Reparatur und Trennung der Fasern von der Matrix. Dies ist bei herkömmlichen faserverstärkten Polymerverbunden nahezu unmöglich. Darüber hinaus hat das hier vorgestellte Vitrimer eine ähnliche Glasübergangstemperatur wie handelsübliche Epoxidharze und die ermittelten Werte für die Biegefestigkeit und das Biegemodul für das phosphorhaltige Vitrimer liegen im Bereich der mit den gleichen Glasfasern verstärkten permanent vernetzten Epoxidharze.

Kapitel 9: Phosphodiester sind Brückenelemente in Nukleinsäuren. In der Natur und in der Synthese schützt ihre negative Ladung sie vor Hydrolyse und bestimmt ihr Löslichkeitsprofil. RNA ist ein vielversprechendes Material für die Gentechnologie, die Zellaufnahme ist jedoch aufgrund negativer Ladungen gering. Synthetische Oligonukleotide wurden durch einen Prodrug-Ansatz in Zellen eingebracht, der auf der enzymatischen Freisetzung der Polyphosphodiester-Oligonukleotide beruhte. In der synthetischen Chemie ist häufig eine Schutzgruppe für die P-OH-Funktionalität erforderlich, z.B. aufgrund von Löslichkeit oder chemischer Unverträglichkeit. Es wurden verschiedene Methoden für den Schutz der P-OH-Funktionalität vorgeschlagen, oft jedoch mit geringer Selektivität oder unter harten Bedingungen. Hier präsentieren wir die 2-Acetylthioethylgruppe als vielseitige Schutzgruppe für niedermolekulare oder polymere Phosphodiester, die unter sauren Bedingungen in Wasser oder durch Hydrazin in THF abgespalten werden kann, um die P-OH-Funktionalität freizusetzen, Olefine bleiben dabei intakt. Diese einfache Verwendung ermöglicht das Entwerfen verschiedener synthetischer Polyphosphodiester, z.B. für Flammschutzmittel oder Dispergiermittel.

Kapitel 10: Anisotrope Materialien mit sehr hohen Seitenverhältnissen („2D-Materialien“) wie Plättchen sind aufgrund ihrer einzigartigen Eigenschaften, welche auf ihrer unilamellaren Geometrie basieren, eine interessante Materialklasse. Wir verwendeten Phosphorchemie und einfache Polykondensation, um in polyethylenähnlichen Polymeren Defekte in genau definierten Abständen einzuführen. Die relativ ausgedehnte Größe und Flexibilität der Phosphatgruppen ermöglicht die Kontrolle der Kettenfaltung während der Kristallisation. Wir untersuchten dieses Verhalten mittels Festkörper-NMR- und TEM. Darüber hinaus haben wir gezeigt, dass wir in der Lage sind, Chemie „an der Oberfläche“ zu betreiben. Die seitenständige Estergruppe am Phosphat gibt die Möglichkeit, funktionelle Gruppen einzuführen, die für eine weitere chemische Modifikation an der Kristalloberfläche zugänglich sind, was durch Einführung der 2-Acetylthioethylestergruppe und eine spätere Spaltung der 2-Acetylthioethylestergruppe zum P-OH bewiesen wurde. Zusätzlich konnten wir die laterale Kristallgröße durch verschiedene Temperaturprofile steuern.

Graphical Abstract

1. **Introduction: Molecular Firefighting - How Modern Phosphorus Chemistry Can Help Solve the Challenge of Flame Retardancy**

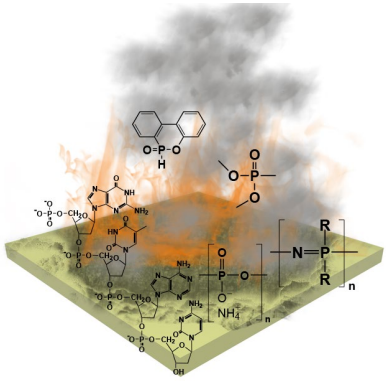

2. **Systematically controlled decomposition mechanism in phosphorus flame retardants by precise molecular architecture: P-O vs. P-N**

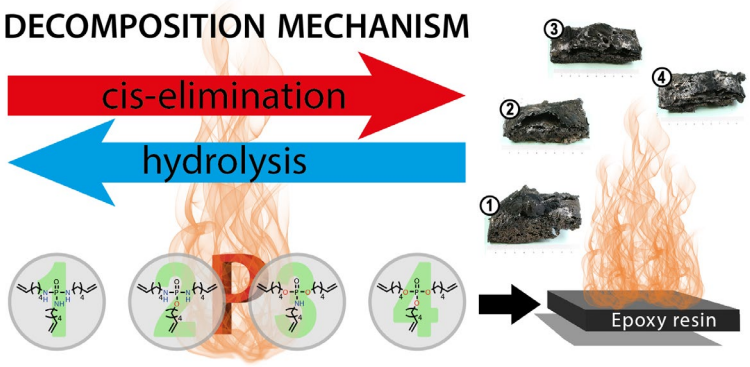

3. **Hyperbranched Phosphorus Flame Retardants: Multifunctional Additives for Epoxy Resins**

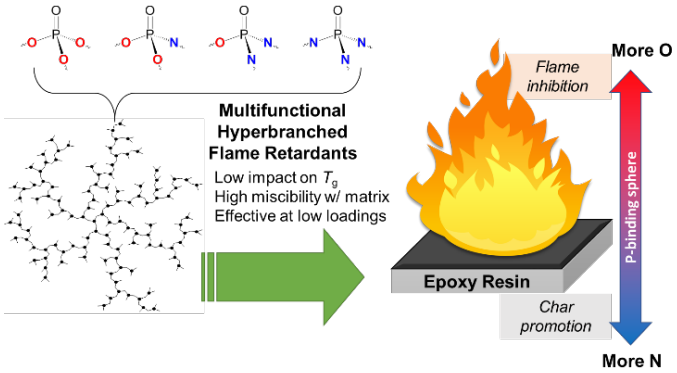

4. **Comparison of novel aromatic and aliphatic hyperbranched poly(phosphoester)s as flame retardants in epoxy resins**

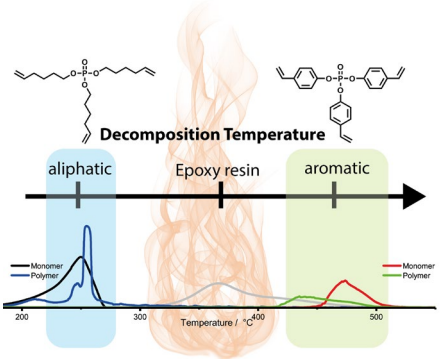

5. **Matrix Matters: Hyperbranched Flame Retardants in Aliphatic and Aromatic Epoxy Resins**

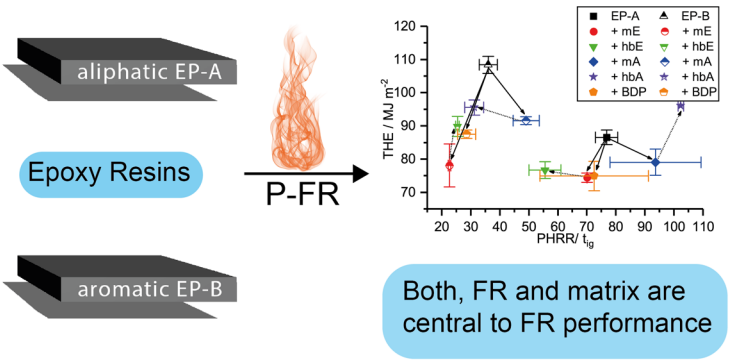

6. **Sulfur's Role in the Flame Retardancy of Thio-Ether–linked Hyperbranched Poly(phosphoesters) in Epoxy Resins**

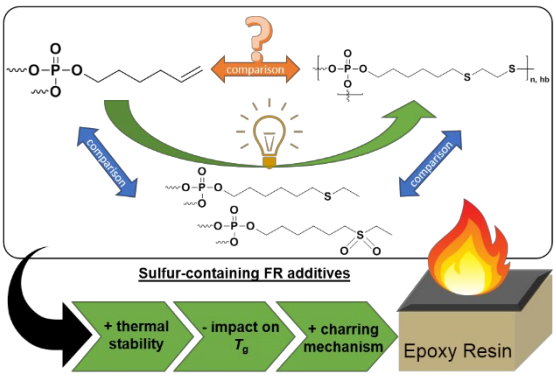

7. **First phosphorus AB_2 monomer for flame-retardant hyperbranched polyphosphoesters: AB_2 vs A_2+B_3**

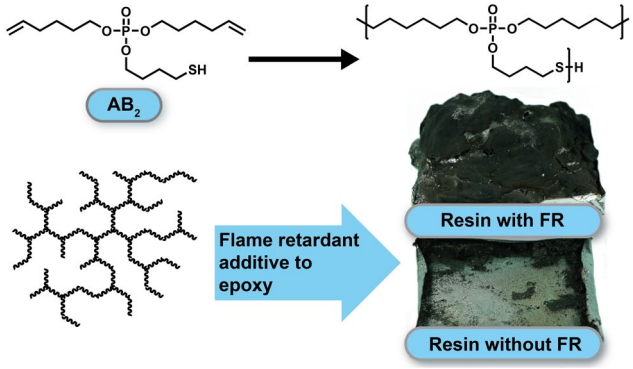

8. **Intrinsic flame retardant vitrimers as a recyclable alternative for epoxy resins in composite materials**

9. **The 2-acetylthioethyl ester group: A versatile protective group for P-OH-groups**

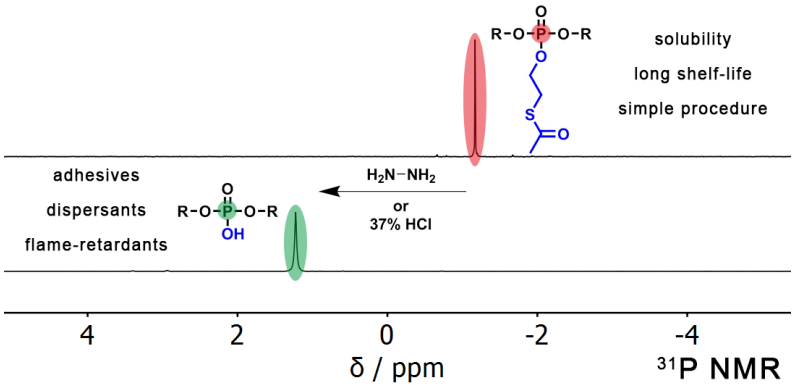

10. Defect engineering of precision polymers: size control and surface chemistry of anisotropic polymer platelets after solution crystallization

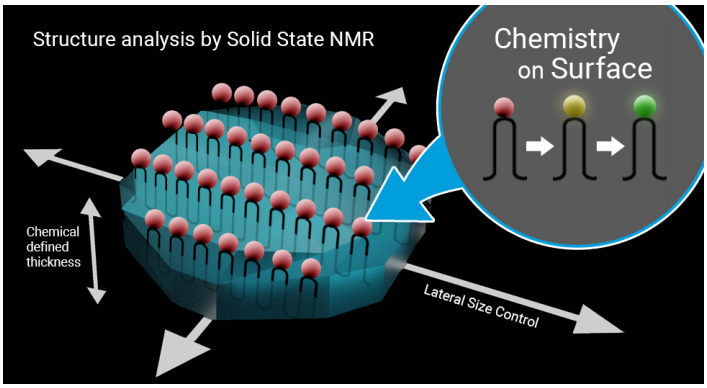

1. Introduction: Molecular Firefighting - How Modern Phosphorus Chemistry Can Help Solve the Challenge of Flame Retardancy

Maria M. Velencoso,[+[a]] Alexander Battig,[+[b]] Jens C. Markwart,[+[a,c]] Bernhard Schartel,[[b]] and Frederik R. Wurm*[[a]]

[a] *Physical Chemistry of Polymers - Max Planck Institute for Polymer Research, Ackermannweg 10, 55128 Mainz, Germany*

[b] *Technical Properties of Polymeric Materials - Bundesanstalt für Materialforschung und -prüfung (BAM), Unter den Eichen 87, 12205 Berlin, Germany*

[c] *Graduate School Materials Science in Mainz, Staudinger Weg 9, 55128 Mainz, Germany*

[+] *These authors contributed equally to this work.*

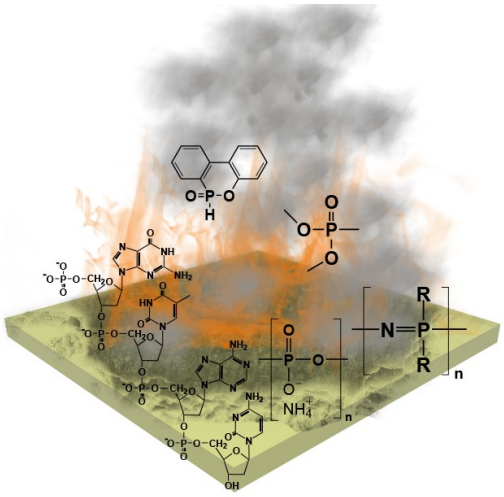

Keywords: biomacromolecules, flame retardants, nanocomposites, phosphorus, polymers

1.1 Notes

Maria M. Velencoso wrote the chapters “Phosphate Rock – A Finite Natural Resource” and “Modern trends and the Future of Phosphorus-based Flame Retardants”, Alexander Battig wrote the chapter “The Challenge of Flame Retardancy – Demands of a Good Flame Retardant” and Jens C. Markwart wrote the chapters “Recent Developments in Reactive Phosphorus Compounds” and “Recent Developments in Additive Phosphorus Compounds”.

1.2 Abstract

The ubiquity of polymeric materials in daily life comes with an increased fire risk, and sustained research into efficient flame retardants is key to ensuring the safety of the populace and material goods from accidental fires. Phosphorus, a versatile and effective element for use in flame retardants, has the potential to supersede the halogenated variants that are still widely used today: current formulations employ a variety of modes of action and methods of implementation, as additives or as reactants, to solve the task of developing flame-retarding polymeric materials. Phosphorus-based flame retardants can act in both the gas and condensed phase during a fire. This Review investigates how current phosphorus chemistry helps in reducing the flammability of polymers, and addresses the future of sustainable, efficient, and safe phosphorus-based flame-retardants from renewable sources.

1.3 The Challenge of Flame Retardancy—Demands of a Good Flame Retardant

Halogenated flame retardants, which were widely applied in the past, have come under increased scrutiny and prompted increased research into halogen-free and phosphorus-based flame retardants (P-FRs) in particular.[1] This development is further attributed to legislation and decisive shifts in market demands, as increased attention has paid to producing more sustainable FRs. P-FRs have now become a prominent alternative to their halogenated counterparts.[2] Phosphorus plays the key role in halogen-free flame retardancy as a result of its chemical versatility, multiple FR mechanisms, and high effectivity already at low loadings. As the demand for safe advanced materials grows, the question for material scientists is: what role can current chemistry play in solving the flame retardancy problem? To more closely understand the task at hand, it is necessary to first outline what constitutes a "good" FR:

1) Material properties must be conserved to the greatest possible extent, with price as the most determining factor.
2) The FR properties must match the polymer processing and pyrolysis characteristics.
3) Health regulations and market direction necessitates that formulations must become increasingly environmentally friendly, recyclable, and sustainable.

In the following sections, these aspects are explored in detail. Then, state-of-the-art P-FRs and their modes of action are discussed and show how these features are embraced. Finally, we highlight modern trends of P-FRs and their potential future application. To that end, representative examples for each section were chosen, but this Review is not meant to be a comprehensive summary. For further reading, we recommend the reviews of Weil and Levchik,[3] Malucelli et al.,[4] and Bourbigot and Duquesne.[5]

1.3.1 Retaining Material Properties: A Question of Price

The chemical composition of the polymer determines the material properties, production routes, application areas, and bulk price (Figure 1.1). Thermoplastic polyolefins (e.g. polyethylene, polypropylene, polyvinyl chloride) are common commodities and mass produced at low costs; $Al(OH)_3$, the most common FR, is both effective and inexpensive to produce, but requires high loadings, which affects the material properties (e.g. coloration, opacity, tensile strength).[6] Commercially available P-FRs (e.g. ammonium polyphosphate, APP) require significantly lower loadings for similar effectivity, and thereby retain the respective material properties.[7] Moreover,

adjuvants and synergists (e.g. metal oxides, charring agents, nanofillers, additional P-FRs) increase the efficacy and further lower the loadings required.[8]

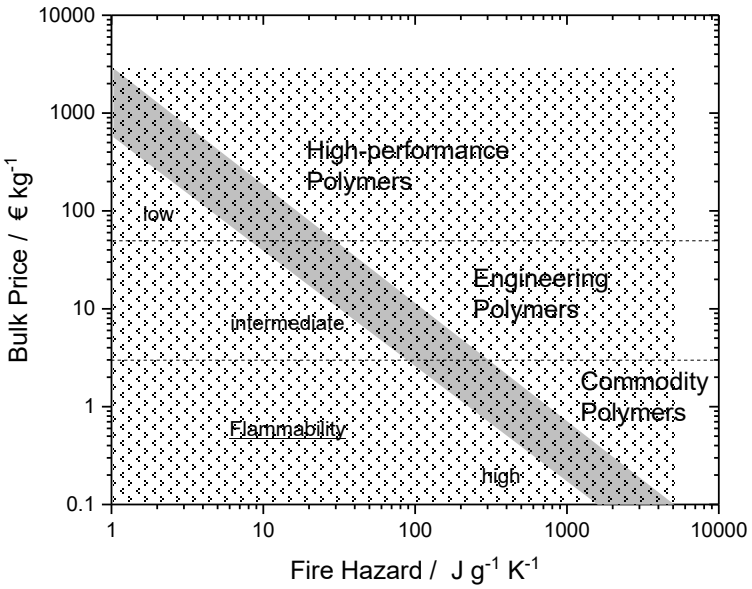

Figure 1.1. Fire hazard versus bulk price of various polymeric material classes.[14]

Engineering polymers (e.g. polyamides, polycarbonates, polyurethanes, polyethylene terephthalates) are applied in more advanced areas (e.g. electronics/electrical engineering, transport, manufacturing). These materials can be synthesized as thermoplasts, elastomers, or thermosets in foams, fibers, or foils, and so a wider array of FRs exist. The use of these FRs depend on the polymer's price, quality grade, and precise application.[9] Notable formulations contain aluminum diethyl phosphinate, melamine polyphosphate, and Zn borate, or melamine cyanurate-microencapsulated red phosphorus.[10]

High-performance polymers (e.g. epoxy/polyester resins, polyetherimides, polysulfones, poly(aryl ether ketones)) are used in specialized fields (e.g. adhesives, coatings, composites) due to their chemical resistance, temperature stability, and high durability.[11] Here, performance outweighs the production costs of the materials and the FRs. Correspondingly, FRs in this material category are the second most important in value terms behind polyolefins: therefore, complex-shaped, multicomponent, and multifunctional FRs are used.[12] Notable formulations include 9,10-dihydro-9-oxa-10-phosphaphenanthrene-10-oxide (DOPO) derivates and variations of P species with synergistic moieties: nitrogen, silicon, sulfur, and boron.[13]

1.3.2 Production Specifics: Finding a Match

The FR's mode of action is key when tailoring suitable formulations for polymer materials. Effective flame retardancy depends strongly on the interaction between the FR and the polymer matrix as well as the structure–property relationship between the two during thermal decomposition. The modes of action can generally be classified into condensed- and gas-phase mechanisms (Figure 1.2), and many successful P-FRs utilize both.[15] In the condensed phase, many P-FRs mediate the formation of char by inducing cyclization, cross-linking, and aromatization/graphitization by dehydration of the polymeric structure. The formation of carbonaceous char reduces the release of volatiles, that is, fuel.[16] Some P-FRs additionally act through intumescence: a multicellular residue acts as a protective layer, slowing down heat transfer to the underlying material.[17] Many FRs alter the melt flow and dripping behavior by promoting either charring combined with a flow limit (non-dripping UL-94 classification) or flame inhibition combined with increased flow, for example, via radical generators (non-flaming dripping UL-94 classification).[18] Some inorganic FRs (e.g. $Al(OH)_3$, $Mg(OH)_2$, Zn borates, boehmite) decompose endothermically and vaporize water, absorbing heat in the condensed phase, and cooling the gas phase.[19] Gas-phase modes of action, usually acting in parallel with condensed-phase mechanisms, crucially increase FR effects: releasing non-combustible gases during decomposition reduces the combustion efficiency (fuel dilution).[20] During the combustion of hydrocarbon fuels, $H^{\cdot}$ and $OH^{\cdot}$ radicals are formed, which propagate the fuel combustion cycle most notably through the strongly exothermic reaction $OH^{\cdot}+CO \rightarrow H^{\cdot}+CO_2$.[21] Many P-FRs decompose to form $P^{\cdot}$ radicals which react with $OH^{\cdot}$ radicals and lower their concentration (flame poisoning).[22]

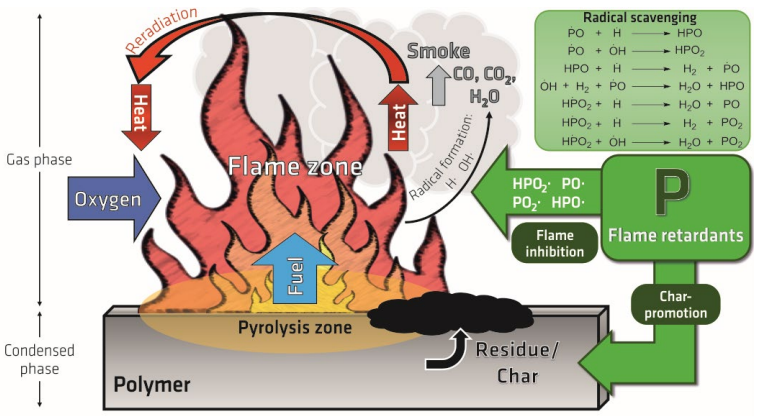

Figure 1.2. Flaming combustion of polymeric material and the role of phosphorus-based flame retardants.[26]

These mechanisms crucially depend on the decomposition temperatures of both the matrix and the FR. Therefore, FRs must be chosen to match explicit polymer processing and pyrolysis specifics. To ensure chemical interaction during pyrolysis but not during processing, premature FR decomposition must be avoided, whereas the overlap of the polymer and FR decomposition temperatures should be maximized.[23] This is key for high-temperature thermoplastic processes (e.g. compounding, extrusion, injection/blow molding), as well as vulcanization for rubbers, or curing for thermosets.[24] For foams, FRs with good foamability are important to maintain mechanical properties, while fiber and textile FRs must undergo spinning, weaving, and washing without loss of material or FR properties.[25]

Today, no single FR can be used for the wide range of polymers available; a FR may work well for one matrix but not for another, as the structure–property relationship is specific to the polymer matrix.[26] This makes the search for novel FRs with improved mechanisms essential for all fields of polymer applications.

1.3.3 Sustainability: A Regulatory and Market Goal

Health, environmental, and sustainability considerations play increasingly important roles in the development of novel FRs. Increased awareness has been paid to the "PBT" (i.e. persistency, bioaccumulation, toxicity) of FRs.[27] Studies on human exposure pathways and ecosystems have highlighted risks of some FRs, thus emphasizing the need for increased control and regulation.[28]

To curtail "PBT material" risks, regulatory bodies have enacted legislature to protect the environment and the general population: within the EU, REACH (Registration, Evaluation, Authorization, and Restriction of Chemicals), which acts upon the RoHS (Restriction of Hazardous Substances) and WEEE (Waste Electrical and Electronic Equipment) Directives, evaluates materials hazards and sets health and safety criteria for chemicals, including FRs.[29] Notably, the use of penta-, octa-, and decabromodiphenyl ethers was restricted under the Stockholm Convention on Persistent Organic Pollutants because of health risks, thus highlighting the need for halogen-free alternatives.[30]

The voluntary ecolabels introduced by ISO help prevent the circulation of PBT material and raise awareness of sustainable, environmentally aware production.[31] The "EU Ecolabel" serves to reduce the environmental impact and health risk of goods, services, and the life cycle of products, much like preexisting labels in Germany and the Nordic countries.[32] The Swedish TCO

Certification specifically credits the sustainability of IT products, a key industry of non-halogenated FRs. Technology companies such as HP and chemical companies such as ICL-IP have implemented methods (GreenScreen, SAFR) to assess the chemical safety of their products.[33]

These trends are in line with consumer desires and the market shift toward more environmentally friendly (and ultimately sustainable) products, thus also prompting the use of bio-based materials and green chemistry in FR formulations.[34] Currently, attention has been placed on recyclable FR materials, further decreasing the environmental impact.[35]

Three key aspects—cost-effective conservation of material properties; matching the thermal stability and mode of action to processing and pyrolysis specifics; increased environmental friendliness with sustainability as a goal—constitute the characteristics of "good" flame retardants. In this respect, novel P-FRs will play a pivotal role in future products: their chemical versatility makes them ideally suited, as will be showcased more closely in the following.

1.4 Phosphate Rock—A Finite Natural Resource

Phosphorus chemistry is one of the oldest areas of chemistry, and involves the continuous development of new methods to improve the safety and sustainability of chemical processes. P-FRs are versatile: 1) the structure of P-FRs can vary from inorganic to organic; 2) the P content in these molecules can vary (e.g. from almost 100% for red P to 14.33% for DOPO); 3) the phosphorus can have different oxidation states, from 0 to +5, thereby resulting in different FR mechanisms (both in the gas and condensed phases). This architectural variation makes phosphorus unique for the design of FRs with tailored property profiles, such as density or glass transition temperatures (T_g), by changing the binding pattern (e.g. from alkyl to phenyl groups).

Most compounds that contain phosphorus are manufactured from phosphorite, commonly known as "phosphate rock". The current industrial pathways for the synthesis of various P-FRs are shown in Scheme 1.1. Phosphate is reduced by an electrothermal process to elemental phosphorus (P_4),[37] which serves as a precursor for the production of the main intermediate compounds in industry such as red phosphorus, phosphoric acid (H_3PO_4), phosphorus trichloride (PCl_3), phosphorus pentachloride (PCl_5), phosphine (PH_3), and hypophosphite ($H_2PO_2^-$). The exploitation of all these pathways for the synthesis of many FRs, such as ammonium polyphosphate,[38] melamine polyphosphate,[39] phosphazenes,[40] diethyl phosphonic metal salts, or DOPO,[13b] validates the versatility of the phosphorus compounds used in FR applications.

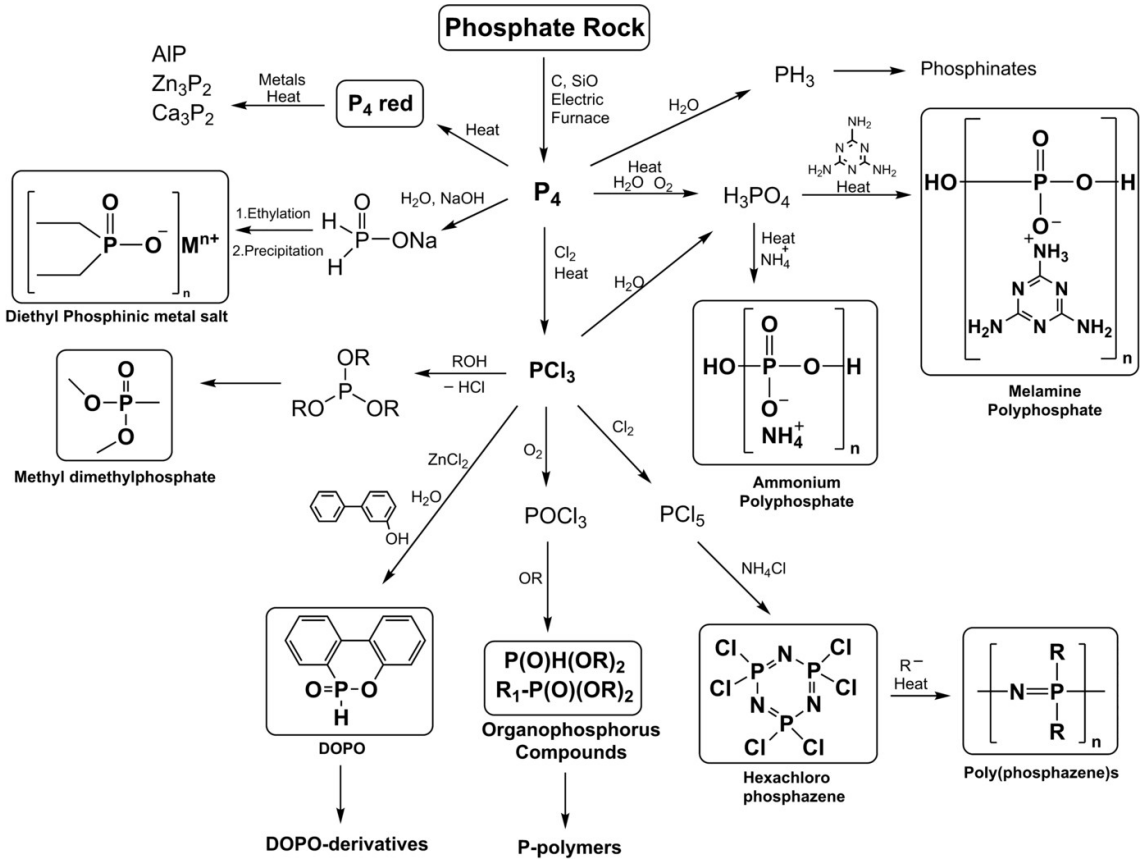

Scheme 1.1. Examples of industrial pathways to various P-based FRs from "phosphate rock". (M is usually zinc or aluminum)

Although a large fraction of the P_4 production is transformed into phosphoric acid, today PCl_3 is the main intermediate for the production of major industrial organophosphorus FRs such as triphenyl phosphate (TPP), resorcinol bis(diphenyl phosphate) (RDP), and bisphenol A bis(diphenyl phosphate) (BADP), as well as for the production of oligomeric or polymeric FRs (Table 1.1). The common pathway for the synthesis of phosphorus-containing polymeric FRs is classical polycondensation (polytransesterification or via phosphoric acid chlorides),[41] but more modern strategies such as olefin metathesis polycondensation[42] or ring-opening polymerization[43] (e.g. of cyclic phosphazene derivatives or cyclic phosphoric acid esters) were also studied more recently.

Table 1.1. Commercial P-FR alternatives to decabromodiphenyl ethers (d-PBDE) according to the United States (US) Environmental Protection Agency (released in January 2014).[a] [36]

Commercial P-FR alternatives to deca-PBDE	Properties	Polymer applications
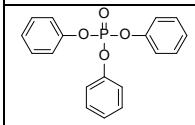 Triphenyl phosphate; TPP	CAS: 115-86-6 M_w: 326.29	PPE-HIPS PC-ABS
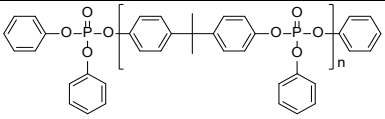 Bisphenol A bis(diphenyl phosphate); BAPP	CAS: 181028-79-5 M_w: 693 (n=1); >1,000 (n=2)	PPE-HIPS PC PC-ABS
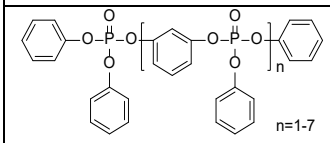 Resorcinol bis(diphenyl phosphate); RDP	CAS: 125997-21-9 M_w: 574.46 (n=1; CASRN 57583-54-7); M_w: 822.64 (n=2; CASRN 98165-92-5	PPE-HIPS PC-ABS
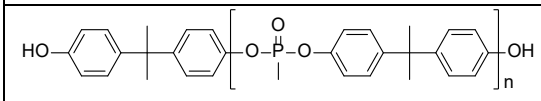 Phosphonate Oligomer	CAS: 68664-06-2 M_w: 1,000-5,000; 25% M_w <1,000	Thermosets
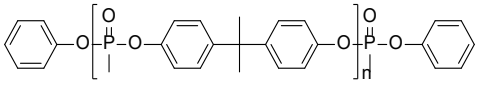 Polyphosphonate	CAS: 68664-06-2 M_w: 10,000 to 50,000; <1% M_w <1,000	Elastomers Engineering Thermoplastic
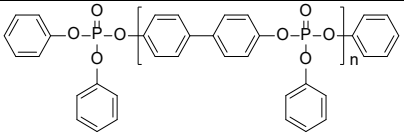 Phosphoric acid, mixed esters with [1,1'-bisphenyl-4,4'-diol] and phenol; BPBP	CAS: 1003300-73-9 M_w: 650.6 (n=1); 974.8 (n=2); >1000 (n≥3)	PPE-HIPS PC-ABS PC
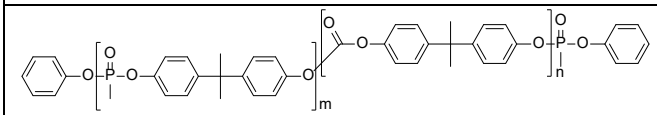 Poly[phosphonate-co-carbonate]	CAS: 77226-90-5 M_w: >1,000; <1% <1,000	Elastomers Engineering Thermoplastic

[a] The mode of action in all cases involves chemical action in the condensed phase and char formation.

However, phosphorus-based chemicals make up less than 3% of all the phosphorus extracted, with most of phosphate (82%) being used as fertilizer or for other purposes, including animal feed additives (7%), detergents, and cleaning products (8%).[44] Phosphate rock is a limited resource that is geographically concentrated in China, the United States, Morocco, Russia, and Jordan (according to the US Geological Survey released in January 2017).[45] At current extraction rates, estimates point to phosphate rock reserves being depleted in the next 370 years, with the exception of the reserves in Morocco.[45]

Currently, there is no alternative for this element; the phosphorus life cycle needs to be considered for agriculture in particular, but also for FRs. Consequently, the EU introduced phosphate rock to the list of critical raw materials in 2014 and elemental phosphorus followed in 2017.[46] Therefore, to ensure that phosphate fertilizers and phosphorus chemicals are preserved for future generations, a sustainable phosphate management, novel methods to better employ feedstock, and recycling strategies are required globally. Possible technologies for phosphorus recovery include a wide range of strategies, such as phytoextraction (optimum annual P removal from Indian mustard seed equal to 114 kg P ha^{-1}), biochar (ca. 10 g P kg^{-1} biochar), or extraction from human urine and feces (recovery of over 80% of total P from urine with approximately 0.5 and 1.3 g $capita^{-1}$ day^{-1}).[47] In addition, it is estimated that the extraction of P from manure in the EU may be near to 1.8 million t a^{-1}, which would satisfy the annual demand of P required for EU fertilizers.[48] On the other hand, as sugars are sometimes referred to as the “new oil” for tomorrow's materials, the extraction of phytic acid or biomacromolecules (deoxyribonucleic acid and caseins) are also strategies to isolate P derivatives for the valorization of by-products from the agro- or food industry (see Section 1.6 and Figure 1.3) and P-FRs can be part of a sustainable phosphorus chemistry.

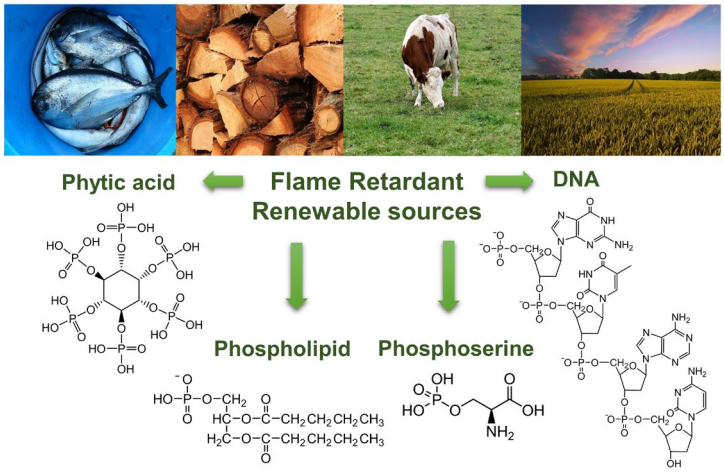

Figure 1.3. Renewable sources of P-FRs.

1.5 Recent Developments in Reactive Phosphorus Compounds

P-FRs can be implemented as either additive or reactive components. The latter allows for the FR to become part of the material's constitution, thereby leading to “inherently” flame-retardant materials.

Reactive FRs are mainly used in thermosets, such as unsaturated polyesters, epoxy resins, or polyurethane foams. They are equipped with functional groups (alcohols, epoxy, amines, halogens, etc.), which allow incorporation into the polymer matrix during curing.[1b,49] In epoxy resins, reactive FRs are preferred since they are covalently attached to the network and thus have a lower impact on the physical properties of the final product. In contrast, additive FRs result in decreased glass transition temperatures (T_g) and are prone to leaching (see Section 1.5). The decreased leaching of reactive FRs also reduces the potential pollution of wastewaters. However, additive FRs dominate the market, as they are easier to use and lower in price. In contrast, reactive FRs are accompanied by the need for a significant reformulation of the curing process. This presents a disadvantage of reactive FRs, that is, each matrix needs a newly designed and formulated FR, while additives may be used for several polymer matrices.[50]

1.5.1 Polyurethanes (PUs)

As a consequence of the wide use of polyurethanes (PUs) in foams, coatings, etc. and their inherent flammability, FRs are necessary. However, not only are the FR properties important, they also have an impact on the environment and physical properties. Biodegradable PUs are commonly synthesized with hydrolyzable soft segments.[51] The use of P-FRs could achieve both, since these materials demonstrate good FR properties and can be both biocompatible and degradable.[52] Chiu et al.[51] synthesized PUs that achieve a V-0 rating in the UL-94 test (classification for the flammability of plastics) and presented efficient FR properties with limited oxygen indices (LOI, minimum oxygen concentration required to sustain combustion) higher than 27.7%. The authors used 4,4-diphenylmethane diisocyanate (MDI) as the hard segment; 5-hydroxy-3-(2-hydroxyethyl)-3-methylpentyl-3-[2-carboxyethylphenylphosphine] propanoate (HMCPP, Figure 1.4) and polycaprolactonediol (PCL) as the soft segments; and 1,4-butanediol (BD) was used as a chain extender. By increasing the HMCPP content (7.5, 15.0, and 22.5 mol% with respect to MDI) in the PUs, the decomposition temperatures and the T_g values were reduced by several degrees.[51]

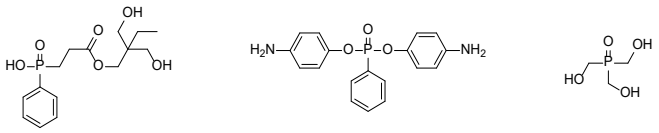

Figure 1.4. Examples of reactive P-FRs: HMCPP (5-hydroxy-3-(2-hydroxyethyl)-3-methylpentyl-3-[2-carboxyethylphenylphosphine]propanoate) used in PU; BAPPO (bis(4-aminophenyl)phenylphosphine oxide) used in PU, PTMA (phosphoryltrimethanol) used in PU.[51,53]

As a water-based example, Çelebi et al.[53a] followed a similar approach to synthesize aqueous dispersions of FR PUs, but instead of incorporating the P-FR as a soft segment, they incorporated it in the chain-extension step. Water-based PUs reduce the use of organic solvents and are, therefore, attractive from an environmental perspective. Bis(4-aminophenyl)phenylphosphine oxide (BAPPO, Figure 1.5) was used for the flame-retardant PU, and ethylenediamine for the non-flame-retardant PU. Poly(propylene-*co*-ethylene)polyol was used as a co-monomer. The physical properties of the two PUs are almost identical, except their gloss properties. This was explained by the difference in the chain conformation of the two PUs. Furthermore, BAPPO increased the crystallinity of the hard segment, through its aromatic groups and longer chain length, which contribute to the higher packing capability of the hard segments.[53a]

The majority of reactive FRs rely on halogens or phosphorus. Halogenated FRs are substituted nowadays because of toxicity and environmental concerns. It was reported that P-containing polyols are mainly the most appropriate reactive FRs for rigid PU foams, but they are rarely used in flexible PU foams (FPUF).[54] Chen et al.[53b] presented FPUFs, which contained phosphoryltrimethanol (PTMA, Figure 1.5) as a cross-linker. They proved that PTMA was mainly active in the condensed phase during a fire scenario. However, PTMA had a negative effect on the cell structure of the foam. With increasing PTMA content, the cell size increased and consequently the number of cell windows decreased. This behavior can be explained by the increased number of closed foam cells arising from the cross-linking nature of the PTMA further influencing the mechanical properties. The FPUF containing 3.2 wt% PTMA showed an increased tensile strength and elongation at break compared to the neat FPUF, because of the change in the foam structure.[53b]

1.5.2 Epoxy Resins

The copolymerization of FRs is not limited to PUs; epoxy resins, often used for their thermomechanical properties and processability, also exhibit high flammability and, therefore, require FRs. The FRs can be introduced to the epoxy- or nitrogen-containing compound.

Zhang et al.[55] proved that it is possible to achieve high T_g values, high thermal stability, and an UL-94 V-0/V-1 rating by the addition reaction of DOPO and epoxy phenol-formaldehyde novolac resin (Scheme 1.2). DOPO was the first efficient halogen-free FR for epoxy resins based on novolac and gained much attention because of its high thermal stability, high reactivity of its P–H bond, and flame-retarding efficiency.[56]

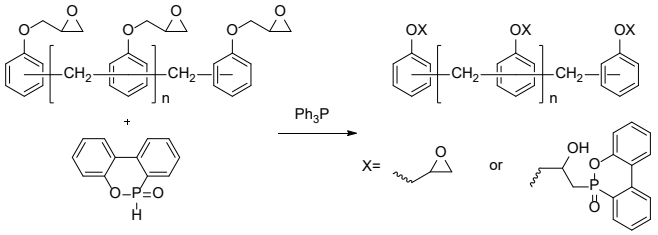

Scheme 1.2. FR-functionalized novolac resin for further use in epoxy resins.[55]

An alternative method to incorporate the FR into the polymer network is to use it in the hardener, a process commonly used for epoxy resins. An example of this approach is the work of Artner et al.,[57] who compared two DOPO derivatives (Figure 1.5): one was modified with amine groups and was used as a FR hardener in epoxy resins, the other had a similar structure, but was an additive FR. The authors revealed that the reactive FR has the potential to be superior over the additive FR.

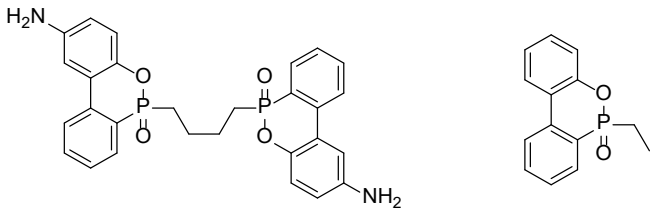

Figure 1.5. DOPO-based hardener (left), nonreactive analogue (right).[57]

By attaching the amine groups directly to DOPO, the solubility of the hardener was increased compared to previous studies. The resin with the DOPO-based diamine hardener presented comparable thermal- and fracture-mechanical properties as the reference epoxy material, namely the diglycidyl ether of bisphenol A with 4,4'-diaminodiphenylsulfone. In contrast to the reactive

FR, the non-reactive additive showed a decrease in the T_g value by about 75 °C and a lower rubber modulus. However, the new hardener revealed a high reactivity, which led to an increase in viscosity during curing, thus posing a problem for application in composite materials because of the reduction in processing time.[57]

In contrast, Ciesielski et al. illustrated that it is not necessary to use reactive FR components to maintain superior mechanical performance. By using the DOPO derivatives (DDM-$(DOP)_2$ and DDM-$(DOP)_2$-S) (Figure 1.6 a,b), their epoxy resins achieved a V-0 rating at 1% P in the resin without significantly lowering the T_g value. It was reported that phosphoramides can ring-open epoxides,[58] so other P-N nucleophiles may also be incorporated into the polymer matrix, depending on the respective reaction kinetics.

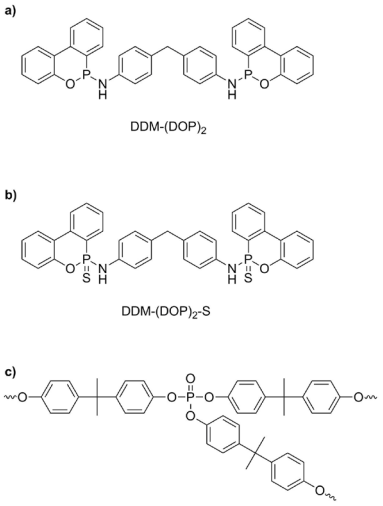

Figure 1.6. a,b) DOPO-based FRs achieving a V-0 rating at 1% P in the epoxy resin; c) *hb*PPE FR for epoxy resins with a lower impact on the T_g value.[58,59]

Reactive phosphate-based FRs can also decrease the T_g value, which may be attributed to the flexibility of the P−O bond. However, Wang and Shi[59] reported that reactive hyperbranched (*hb*) poly(phosphoester)s (PPEs; Figure 1.7 c)—because of their branched structure—reduce the T_g value to a smaller extent. This was attributed to the higher cross-linking density of the *hb*PPE having a greater influence than the P−O flexibility. The *hb*PPE was synthesized in an A_2+B_3 approach by polycondensation of bisphenol A and phosphoryl chloride. This *hb*PPE was used to cure a bisphenol A based epoxy resin by PPh_3 catalysis, which led to a resin with a higher T_g value than the resin cured with only bisphenol A.[59]

1.5.3 Phosphorus Oxidation State

The decrease in the T_g value by the presence of flexible P−O bonds was also reported by Jeng et al.[60c] In addition, they stated that the introduction of sterically demanding groups such as P-O-C_6H_4-O-P can reduce the cross-linking density, thereby resulting in a further lowering of the T_g value. In contrast, the T_g value was reduced less when they used a FR with a more rigid P-Ph group. However, the FR mechanism was also influenced by exchanging a P−O bond by a P−C bond. Most reports indicate that phosphine oxides are rather poor char promoters, but are more active in the gas phase than other P-FRs with higher oxidation numbers such as phosphates.[60] The higher gas-phase activity of phosphine oxides was also reported by Braun et al.[62] who investigated the impact of the P oxidation state on its FR behavior in epoxy resin composites. They reported, in agreement with previous reports,[60b] that the amount of stable residue increased and the release of volatiles containing phosphorus decreased as the oxidation state of P increased (Figure 1.7). However, in previous reports it was concluded that phosphates are the more efficient FRs, because of their higher efficiency as char promoters compared to phosphine oxides.[60b] This conclusion differs from that of Braun et al., who ranked phosphine oxide as the best FR and phosphate as the worst through the observation of an increase in charring and decreased flame inhibition for the phosphates, which significantly accounted for the performance of FR in composites. These conflicting statements can be explained by the fact that Braun et al. investigated composites as a matrix, for which flame inhibition as a main mode of action plus minor charring was a very promising route for flame retardancy.[12d,61] They showed that the key role of the oxidation state was in the type of interaction during the pyrolysis. The authors explained the greater role of the gas-phase activity of composite materials with a high content of carbon fiber through a decrease in the relative impact of the charring.[60b,62]

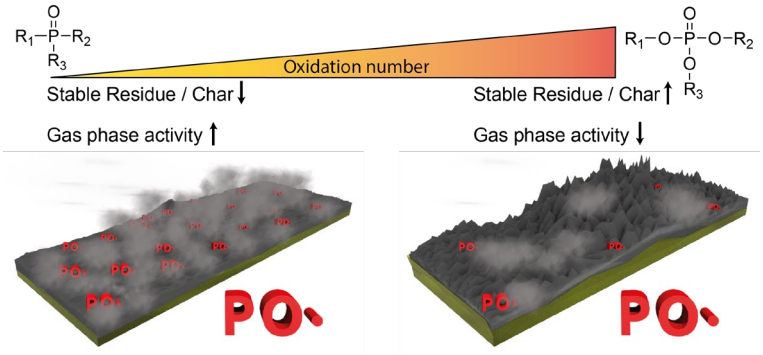

Figure 1.7. The char residue increases and the gas-phase activity decreases as the oxidation state increases.

1.6 Recent Developments in Additive Phosphorus Compounds

Most FRs are added as additives during polymer processing steps instead of being built into the polymer backbone.

The major advantage of additive FRs is their cost-effectivity (i.e. performance value of the material) and ease of application in various matrices, thus they are widely used in industry.[2b,63] Despite these advantages, additive FRs also exhibit several drawbacks, most notably their impact on physical properties such as the T_g value or mechanical stability. Leaching of the FRs over time is a major issue, especially for compounds with a low molecular weight. This may be partly prevented by using polymeric substances; however, phase separation needs to be prevented.[64] The biggest challenge for additive FRs is, therefore, to find the optimal balance between the FR and the mechanical properties.[50a,50b]

1.6.1 Inorganic Phosphorus Flame Retardants

The "classic" example of an inorganic P-FR is red phosphorus, but in practice it is only used as an encapsulated substance to process FR thermoplasts, for example, glass-fiber (GF) reinforced PA 6,6, or in many types of multicomponent FR systems.[9a,65] The main advantages are an unparalleled high P content and efficiency already at small amounts: in GF-reinforced PA 6,6, in combination with metal oxides as synergists, only <7 wt% was necessary to achieve excellent FR performance. While the use of red P alone is declining, it is proposed in combined formulations that include <8 wt% red P, for example, in P + inorganic filler or in P-P mixtures combined with intumescent ammonium polyphosphate (APP) based systems.[10b, 66]

Tan et al. reported a hardener for epoxy resins based on inorganic APP which was modified with piperazine by cation exchange to later act as a hardener. This approach yielded efficient flame retardancy and showed improved mechanical properties compared to the dispersion of APP in the epoxy resin as a result of homogeneous incorporation without aggregation.[67] Duan et al. used APP combined with a *hb*-phosphorus/nitrogen-containing polymer in polypropylene (Scheme 1.3).[68]

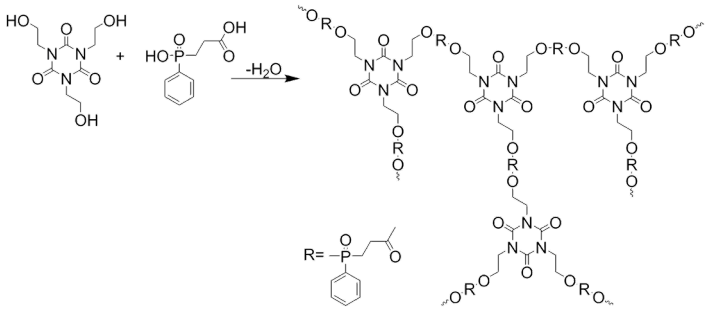

Scheme 1.3. Synthesis of the *hb* FR polymers containing phosphorus/nitrogen.[68]

Formulations using equal parts (10 wt%) of polymer and APP showed high LOI values of up to 30%, compared to LOI values of approximately 20% for 20 wt% of the individual compounds. These results suggested synergism between the *hb* polymer and the APP. Raman spectroscopy revealed that more graphitic char had been formed by the combination of these two compounds. The protective layer effect of the charred layers was also observed in thermogravimetric analysis (TGA) measurements through a higher temperature at maximum weight loss (T_{max}).[68]

Braun et al. showed that the reactivity of the P additive with the polymer matrix (here: GF-reinforced PA 6,6) has a great influence on its interaction with other additives as well as the main activity in the condensed or gas phase. This study illustrated that the main mechanism of melamine polyphosphate (MPP) is dilution of the fuel and the creation of a P-based protective layer. Aluminum phosphinate (AlPi), another FR currently widely applied, on the other hand, acts mainly in the gas phase. The combination of the two additives changes the dominant FR mechanism through the formation of a strong protective layer consisting of aluminum phosphate. The addition of zinc borate led to formation of a boron-aluminum phosphate layer, which showed a better protective layer performance than aluminum phosphate and resulted in the best cone calorimeter (most important instrument in fire testing, measuring heat release rate by the amount of oxygen consumed during combustion) performance of the samples, with hardly any ignition evident.[10a,69]

The use of various salts of dialkylphosphinates, (e.g. aluminum, calcium, and zinc) as effective FRs for GF-reinforced thermoplasts were investigated by Clariant SE. The aluminum salts AlPi are commercially available under several trade names, such as Exolit OP 930, Exolit OP 935, and Exolit OP 1230. The Exolit OP line of products vary in the AlPi modification (e.g. encapsulation, particle size, etc.).[13a]

The synergism between AlPi and nanometric iron oxide or antimony oxide was investigated by Gallo et al., who found different FR behaviors operated: in a redox cycle, Fe_2O_3 oxidized P to inorganic phosphates and was reduced to magnetite, thereby increasing the amount of P in the

condensed phase. However, a catalytic effect on the cross-linking was postulated for Sb_2O_3, a nonreducible oxide, as no hint of the same mechanism was detected. The authors proposed that the surfaces of the metal oxides stabilize the oxygen-containing intermediate structures and thereby promote cross-linking reactions between the polymer chains and also the interaction with P-based intermediates.[70]

Naik et al., and in a recent study Müller et al., compared the influence of the metals in melamine poly(aluminum phosphate), melamine poly(zinc phosphate), and melamine poly(magnesium phosphate) in epoxy resins. Melamine poly(aluminum phosphate) reduced the peak heat release rate (PHRR) by about 50%, whereas the other two melamine poly(metal phosphates) achieved a reduction of PHRR to less than 30% compared to the neat epoxy resin. All three materials reduced the fire load by 21–24% and lowered the CO yield and smoke production. The improved fire behavior is explained by their main activity in the condensed phase, with minor signs of fuel dilution. The fire residue increased and, as a result of intumescence, a protective layer was formed. In addition, synergistic combinations with other flame retardants were also studied: here, melamine poly(zinc phosphate) with melamine polyphosphate showed the best overall FR results as a consequence of strong intumescence, with a low heat release rate (HRR) and the lowest PHRR, maximum average rate of heat emission, and fire growth rate index values.[71]

1.6.2 Organophosphorus Flame Retardants (OPFRs)

Organophosphorus compounds are currently discussed as substitutes for halogenated, mainly brominated, FRs. Most organophosphates are used as additives rather than being chemically bound to the polymer matrix.[72] Besides their use as FRs, they work as plasticizers or antifoaming agents and are used in plastics, furniture, textiles, electronics, construction, vehicles, and the petroleum industry. In the following, some examples of these compounds—selected because of their importance to the field (more than 30 citations)—are discussed.

The influence of the chemical structure on the FR mechanism is not only important to small molecules, but also for organophosphorus polymers. Aromatic polyphosphonates exhibit higher thermal stability than aliphatic polyphosphonates, and, at the same time, they have a higher hydrolytic stability than the aromatic polyphosphates. This was explained by the presence of the stable P−C bond in phosphonates, while phosphates carry an additional hydrolyzable P-O-C linkage that results in lower degradation temperatures.[73]

The influence of the chemical structure of the FR on its mechanism has been intensively studied. While Beach et al. suggested that the major FR mechanism for bromine- and sulfur-containing FR

additives in polystyrene is through enhanced degradation of the polystyrene matrix,[75] the phenomenon of radical generation together with flame inhibition was first investigated by Eichhorn in 1964.[74] The mechanism of the condensed phase is as follows: a hydrogen atom is abstracted from the polystyrene backbone by the flame retardant, followed by β-scission of the polystyrene radical (Scheme 1.4).

$FR \longrightarrow FR\cdot + FR^{*}\cdot$	Homolytic cleavage	(1)
$FR^{*}\cdot + H\text{-}PS \longrightarrow PS\cdot + H\text{-}FR$	FR abstraction of H	(2)
$FR^{*}\cdot + PS\cdot \longrightarrow PS(=) + H\text{-}FR$	Termination	(3)
$PS\cdot \longrightarrow -CH_2C(Ph)=CH_2 + Ph\cdot CHCH_2-$	β scission	(4)

Scheme 1.4. Mechanism for enhanced degradation of polystyrene.[75]

P-FRs show no such enhanced degradation of polystyrene (PS) and, therefore, exhibit lower performance in LOI tests, the reason being the difference in bond dissociation energies. However, combining sulfur with triphenyl phosphate (TPP) resulted in a performance comparable with that of hexabromocyclododecane (HBCD). Loosening of the polymer network by degradation is an important condensed-phase mechanism which allows mass transfer of gas-phase species to the surface and removes fuel and heat away from the pyrolysis zone via melt flow. According to the authors, the synergism between sulfur and TPP was achieved by the sulfur causing enhanced degradation of the PS network (Scheme 1.5), which resulted in an improved mass transfer of TPP to the surface.[75] More recently, Wagner et al. investigated OPFRs with synergists containing disulfide bridges, further identifying the role of radical generators in the enhanced degradation of polystyrene.[76]

As most additive monomeric and oligomeric OPFRs exhibit a plasticizing effect on the polymer matrix and may volatilize or migrate during the processing, alternative FRs are needed. Therefore, academic and industrial studies are increasingly turning to polymeric OPFRs which are designed to be completely miscible with the matrix and, therefore, less likely to migrate over time.[73]

The importance of the FR molecular weight was investigated by comparing the monomeric FR TPP with the oligomeric FRs resorcinol bis(diphenyl phosphate) (RDP) and bisphenol A bis(diphenyl phosphate) (BDP) in polycarbonate/acrylonitrile-butadiene-styrene blends. All three compounds showed activity in the gas phase through flame poisoning, with TPP and RDP revealing a slightly better performance than BDP. However, TPP had almost no condensed-phase activity, while RDP showed some, and BDP demonstrated the highest activity. The behavior was explained by the fact that BDP and RDP catalyzed Fries rearrangements in the PC, while TPP volatized before the

decomposition of PC-ABS because of its low molecular weight, thus preventing chemical interaction.[23c,77]

The phase separation of polymer blends must always be investigated with respect to the desired material properties. In this context, *hb* polymeric FRs are promising materials. Their key properties include many reactive end groups, a relative low intrinsic viscosity compared to linear polymers, and in most cases a high miscibility and solubility with other polymeric materials. In addition, their straightforward synthesis through "hyperbranching", that is, statistical branching polymerization, makes them available on a large production scale. Furthermore, this class of polymers also has the potential to have a lower impact on material characteristics such as mechanical properties and T_g value.[78]

Phosphorus combines chemical versatility and FR effectivity, thus allowing for enormous variety in FR formulations. These examples have shown that P shows different modes of action in FR formulations because of many various criteria: oxidation state, reactive or additive, inorganic or organic, low or high molecular weight, etc.

1.7 Modern Trends and the Future of Phosphorus-Based Flame Retardants

1.7.1 Synergistic Multicomponent Systems

Flame-retardant structures containing heteroatoms such as nitrogen, silicon, sulfur, and boron in combination with phosphorus provide a huge range of specific interactions, compared to the decomposition of phosphorus structures or the decomposition of these with pure hydrocarbons,[26] thereby reducing the overall load of FRs in a material and maximizing effectivity (Figure 1.8).[13d,58,79]

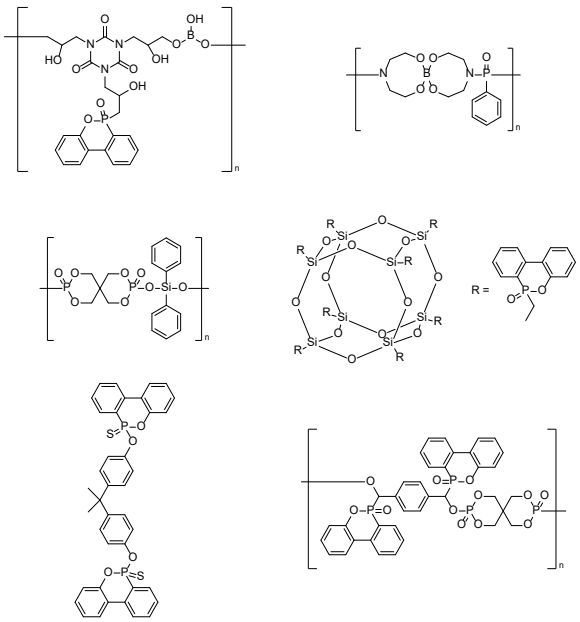

Figure 1.8. Various FR formulations with synergistic moieties. Top row: boron-containing formulations; middle row: silicon-containing formulations; bottom left: P-S-containing formulations; bottom right: formulation containing two types of P.[13a,80]

The combination of phosphorus–nitrogen (P-N) compounds is one of the most promising reported synergisms for halogen-free flame retardants. P-N synergism promotes the formation of cross-linked networks with polymer chains during a fire, thereby encouraging the retention of P in the condensed phase and yielding higher and more thermally stable char formation.[81] Two of the most prominent P-N structures include phosphoramidates[82] and cyclotriphosphazenes.[83]

The main advantages of phosphoramidates over their analogous phosphates are their higher thermal stability,[84] lower volatility,[85] and higher viscosity as a result of hydrogen bonding.[82c] These features can increase the density of the entire system and make them more likely to be retained in the matrix during combustion, thus contributing to a higher condensed-phase activity and affording higher char yields. Neisius et al. suggested the hydrolysis of P−N bonds occurred under acidic conditions to form nonvolatile compounds (Scheme 1.5).[82c] Interestingly, they showed that trisubstituted phosphoramidate displayed poor flame-retardant behavior on flexible polyurethane foams compared to the analogous monosubstituted phosphoramidate (Figure 1.9). The authors suggest that this is because the trisubstituted phosphoramidate decomposes thermally/hydrolytically to form nonvolatile structures that contribute only to condensed-phase activity. However, the monosubstituted phosphoramidate can decompose to form $PO^{\cdot}$ radicals, which might prevent the oxidation of $H^{\cdot}$ and $OH^{\cdot}$ radicals.

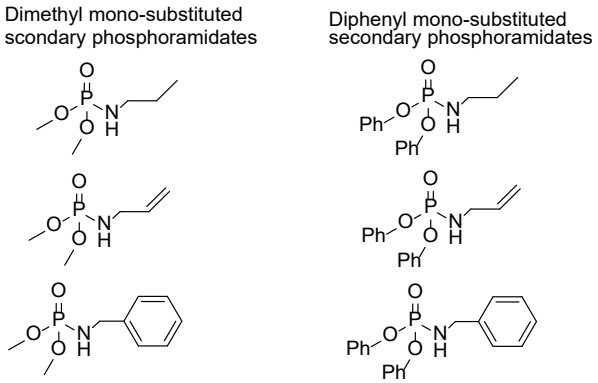

Figure 1.9. Monosubstituted dimethyl/diphenyl phosphoramidates.[82c]

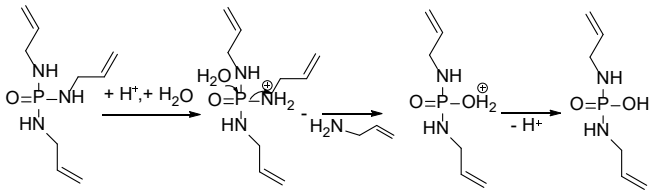

Scheme 1.5. P–N bond hydrolysis under acidic conditions.[82c]

Linear poly(phosphoramidate)s (PPAs) were also studied as FRs.[86] The results indicated an enhanced thermal stability, increased formation of char yields at higher temperatures, and higher glass transition temperatures (T_g) with respect to the analogous poly(phosphate)s. Improvement in the flammability test (30% limiting oxygen index (LOI)) and dripping resistance (V-0 rating in UL-94) was achieved with a loading of about 30 wt% PPA.

In the last decade, a myriad of chemically and thermally stable phosphazene derivatives has been developed (Figure 1.10).[83,86b,87] Cyclophosphazenes are reported to present even higher thermal stabilities than phosphoramidates: the thermal decomposition of the phosphazene-bound piperazine has been reported from 350 °C up to 500 °C (under N_2) with residues between 50 and 70 wt%, depending on the substituents. This large amount of char indicates cross-linking during pyrolysis, for example, through ring-opening polymerization.[83a,88] The hydrolytic lability of P–N bonds limits their application in textiles (washing). Although, recent studies showed self-extinguishing in cotton/polyester blends grafted with allyloxypolyphosphazene.[89]

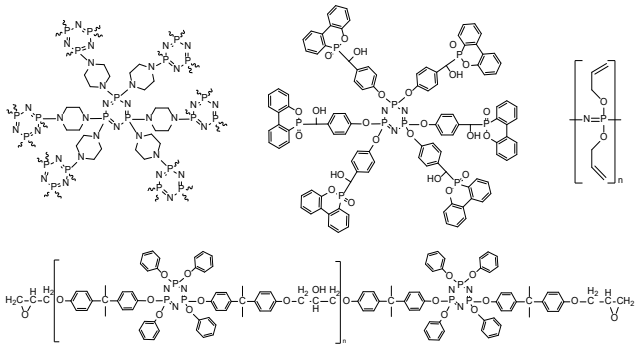

Figure 1.10. Low-molecular-weight and polymeric flame-retardant phosphazenes.[87-90]

Hexachlorophosphazene is the common starting material for polyphosphazenes, as it allows the introduction of various pendant groups after polymerization, for example, the fully inorganic polyaminophosphazene, or functional inorganic-organic hybrid polymers ranging from linear copolymers[90] to branched polymeric structures.[88] The cross-linked or *hb*-poly(phosphazene) structure not only acts as a good carbonization agent, but can also stop dripping and reduce the peak heat release rate (PHRR) by 55%, as reported by Tao et al.[83a]

Polyphosphazenes usually exhibit low T_g values (from −100 °C to above room temperature).[91] Qian et al. synthesized phosphaphenanthrene/cyclotriphosphazene FRs with practically the same T_g value as the neat diglycidyl ether of bisphenol A (DGEBA) epoxy resin.[87] Recently, the Wu research group has been working on the synthesis of several cyclotriphosphazene-linked epoxy resins. T_g values of 160 °C or 145 °C were reached by using them as a matrix[90a] or loading them into DGEBA resins (20 wt%), respectively.[83b,90b] A self-extinguishing UL-94 V-0 rating was achieved with a loading of 30 wt% in the resulting thermosets.

As mentioned in Section 1.5, a current challenge in the development of new FRs is the retention of the mechanical performance of the matrix and effectiveness of the FR. This was achieved to some extent by reactive *hb*PPEs (see Section 1.4.2). Another, very promising approach to meeting this requirement is the combination of P compounds either by blending or covalent linkages to nanometric fillers, such as carbon nanotubes,[92] graphene,[93] polyhedral silsesquioxanes,[94] halloysite nanotubes,[95] montmorillonite, or metal oxide nanoparticles.[96] In some cases, FRs which are covalently grafted onto the nanofillers have higher efficiency than additives at the same concentration.[97] Acceptable grafted amounts of P compounds are between 10 and 30 wt%, which equate to less than 1 wt% phosphorus in the final nanocomposite. A UL-94 V-0 classification (Figure 1.11 a) and an increase in the LOI value have been reported for polypropylene and epoxy resin using DOPO-grafted to SiO_2 nanoparticles,[98] exfoliated graphene,[99] or glass fabric.[97a]

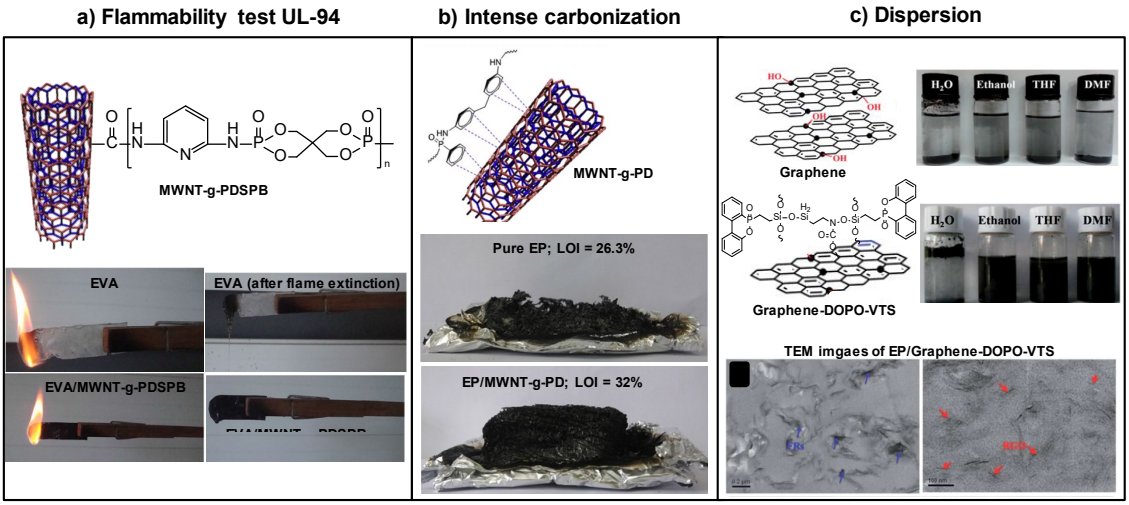

Figure 1.11. Effects of phosphorus-grafted nanofillers in an organic matrix.[100,111] a) UL-94 test of ethylene vinyl acetate (EVA) with 1 wt% multiwalled carbon nanotubes (MWNTs) wrapped on the surface with poly(2,6-diaminopyridine spirocyclic pentaerythritol bisphosphonate) (PDSPB); b) carbonization after the cone calorimeter test of epoxy resin (EP) with 2 wt% of the MWNTs wrapped on the surface with poly(phenylphosphonic-4,4′-diaminodiphenylmethane) (PD); c) photographs of dispersions of graphene and graphene wrapped with 9,10-dihydro-9-oxa-10-phosphaphenanthrene-10-oxide (DOPO) modified vinyl trimethoxysilane (DOPO-VTS) in different solvents and transmission electron microscopy (TEM) images of EP with graphene-DOPO-VTS as a flame retardant.

Typically, the synergistic effect of the nanofillers and P-grafted compounds occurs in the condensed phase. Phosphorus promotes the formation of cross-linked structures, which together with the effect of nanofillers of increasing the melt viscosity promotes intensive carbonization (Figure 1.12 b). However, some studies have suggested that the grafting of chlorinated phosphorus compounds or DOPO-silane derivatives to carbon nanotubes[92b] and graphene[99] also affected the gas phase. The combination of gas- and condensed-phase activity led to a reduction in the PHRR by around 35% and an increase in the LOI values in polyamide 6 and epoxy resin, even achieving the V-0 classification in UL-94 tests.

However, the FR effect of the nanofillers depends not only on the formation of a compact network layer at high temperatures, but also on their ability to be dispersed in the nanocomposite (Figure 1.12). For example, several research groups focused on grafting P compounds such as diphenylphophinic chloride,[92a] hexachlorocyclotriphosphazene,[92b] or an oligomeric diaminobisphosphonate[100] to carbon nanotubes. These polymers cover the surface of the nanotubes with a thin layer, which impedes the formation of π-π interactions and promotes their individual dispersion in polystyrene (PS), polyamide 6 (PA6), or ethylene vinyl acetate (EVA), respectively. Stable dispersions in dimethyl sulfoxide (DMSO), *N*,*N*-dimethylformamide (DMF), or H_2O were achieved after ultrasonication. In addition, Qian et al. also obtained stable colloidal dispersions of graphene grafted with DOPO-silane in ethanol, tetrahydrofuran (THF), and DMF

(Figure 1.12 c).[99] According to the authors, the introduction of compounds with polar groups on the surface of the carbon nanotubes favored their wettability and compatibility with polymer chains.

It is clear that research on synergistic systems is very active. P-N-based compounds have proved to be a robust alternative to the predominantly halogenated FRs in use today. As shown in Section 1.6.1, a condensed-phase mechanism is predominant for P-N compounds as well as for P nanocomposites. In the latter, the key role of P-FRs is to favor the dispersion of the nanofillers, thereby enhancing the formation of a protective char layer and lowering the heat release rate (HRR) during the combustion of the polymer.

1.7.2 Renewable Sources

Fractions of biomass from different industrial sectors (e.g. paper) are utilized to produce bio-based FRs, such as carbohydrate fractions (starch), oil fractions (triglycerides or fatty acids), and phenolic fractions (lignin).[101,102] In some cases, these fractions are modified with P compounds to improve their FR potential.

Since 2006, the group of Cádiz, in particular, have made special efforts in this field.[103] They reported new routes to obtain P-containing triglycerides or fatty acids from vegetable oils by cationic polymerization, by cross-metathesis reaction, or by Michael addition. An increase in the LOI values in the final material was detected. More recently, Howell et al.[104] reported the esterification of isosorbide (from starch) with 10-undecenoic acid (from castor oil) to provide a difunctional ester which can be modified by a thiol-ene reaction to generate a series of phosphate, phosphonate, and phosphinate esters, which were later incorporated into epoxy resins. Howell et al. further synthesized diethyl esters of tartaric acid, a by-product of the wine industry, using diphenylphosphinic chloride, thereby producing an ester which may serve as a base for further FR agents.[105]

Starch, chitin, and chitosan are polysaccharides that carry various chemical functionalities that can undergo reactions such as etherification, esterification, or graft polymerization to produce FRs.[106] Cotton fabric is the matrix par excellence for the application of bio-based FRs and is the most commonly used. Polysaccharide cationic polyelectrolytes deposited through layer-by-layer (LbL) assembly can greatly enhance the char-forming ability of cellulose. 20–40 deposition steps are usually necessary to achieve significant flame-retardant properties, which limits the applicability of this technique. However, Carosio et al.[107] recently achieved self-extinguishing during a flammability test after only two deposited bilayers (less than 5 wt% deposited on cotton) using a

polyphosphoric acid as an anionic polyelectrolyte. The dehydration effect of the polyphosphoric acid promoted the formation of a protective layer from the starch. Xiao et al.[108] reported the synergistic effect of a chitosan/urea compound based on a phosphonic acid melamine salt with melamine pyrophosphate and pentaerythritol in polypropylene, thereby accelerating the decomposition and promoting char formation.

Lignocellulosic materials are aromatic-rich polymers that exhibit high thermal stability and very high char yields. The high number of reactive functional groups in their structure allows their chemical functionalization with P to promote dehydration reactions, and with nitrogen compounds to release NH_3 gas. Liu et al.[109] reported the modification of lignin by grafting polyethylene imine and diethyl phosphite as well as its incorporation in polypropylene/wood composites. Costes et al.[110] modified lignin with $PONH_4$ to improve its FR action in poly(lactic acid). A V-0 classification in UL-94 fire tests was achieved through the incorporation of 20 wt% of the treated lignin.

Interestingly, the authors showed that the thermal stability of lignin is mainly dependent on the nature and the number of monomer units that constitute the plant, which is not only affected by the plant origin but also by the extraction process used. Thus, Organosolv lignin was less thermally stable than Kraft lignin. The thermal degradation of lignin started around 230 °C with the cleavage of the phenylpropanoid side chain and continued with the further cleavage of the main chain (250 °C–450 °C), which produced a large quantity of methane. Above 500 °C, condensation reactions of the aromatic structure occur, promoting the formation of 50 wt% of a stable char up to 650 °C. Lignincellulosic derivatives such us coffee grounds[112] in poly(butylene adipate-*co*-terephtalate) or vanillin[113] in epoxy resins have also been reported as FR additives.

The use of phytic acid from cereal grains, beans, or seed oil (28 wt% P content) has been reported so far as a bio-based P-FR. Phytic acid (PA) decomposes around 200 °C, which ensures the dehydration of a carbon source and makes it a good candidate as an acid source for intumescent systems.[114] Laufer et al. used LbL assembly to develop a fully renewable intumescent system which reduced the flammability of cotton.[114] The combination of 30 bilayers of PA (anionic polyelectrolyte) with chitosan as a cationic polyelectrolyte succeeded in completely extinguishing the flame in a vertical flame test. Recently, Zheng et al.[115] synthesized a melamine phytate (MPA) with a particle size around 1 µm by the reaction of phytic acid with melamine. MPA starts to decompose at around 250 °C, releasing water and producing melamine polyphytate by self-cross-linking. At 400 °C, the *s*-triazine ring from melamine decomposes with generation of inert gases. The addition of a charring agent, dipentaerythritol, was necessary to reach 28.5% in the LOI test

and a V-0 rating in the UL-94 test (the dripping phenomenon of polypropylene needed to be suppressed).

1.7.3 Biopolymers

The groups of Malucelli and Alongi have recently introduced the use of phosphorylated biomacromolecules such as caseins (from milk products) and deoxyribonucleic acid (from the extraction of salmon milt and roe sacs) as inherent FRs; this was part of a strategy for the valorization of by-products from the agro-food industry.[4,116]

α_{S1}-Caseins are phosphorylated proteins containing approximately nine bound phosphate groups per molecule. In cotton fabrics, caseins show thermal degradation profiles analogous to those of ammonium polyphosphate (APP) salts, except that the phosphoric acid is released at lower temperatures compared to the salts, because of the weaker covalent bonds of the phosphate groups in the main chain. The catalytic effect of the phosphoric acid in the dehydration of the cellulose promotes the formation of a thermally stable char at 600 °C. In flammability tests, a significant decrease of 35% in the total burning rate and a reduction of the PHRR by 27% were achieved. In polyester fabrics, the decrease in the burning rate was 67%, but dripping was not suppressed.

The structure of deoxyribonucleic acid (DNA) makes it an ideal intumescent material as it carries 1) phosphates as an acid source, 2) deoxyribose units as a char source, and 3) nitrogen-containing aromatic groups as blowing agents. However, DNA decomposes at lower temperatures (160–200 °C) than the typical intumescent additives (e.g. 300–350 °C).[117] In cotton fabrics, the thermal degradation of DNA was similar to that of APP: the combustion data proved a significant decrease in the PHRR by 50% combined with an intumescent effect.

The application of caseins and DNA to the fabric was carried out by impregnation or by LbL depositions. For significant results, 20 bilayers were necessary to reduce the burning rate and achieve self-extinguishment of the fabric as well as an increase of the final residue after burning. However, the major disadvantage of applying biomacromolecules to fabric is their poor resistance to washing treatments.

Recently, Alongi et al. investigated the potential of DNA coated on different matrices (EVA, PP, PA6) as a “universal” FR.[118] Thicknesses of 3 mm (10 wt% DNA) showed good performances and a reduction in the PHRR of more than 50% in all polymeric matrices (Figure 1.12).

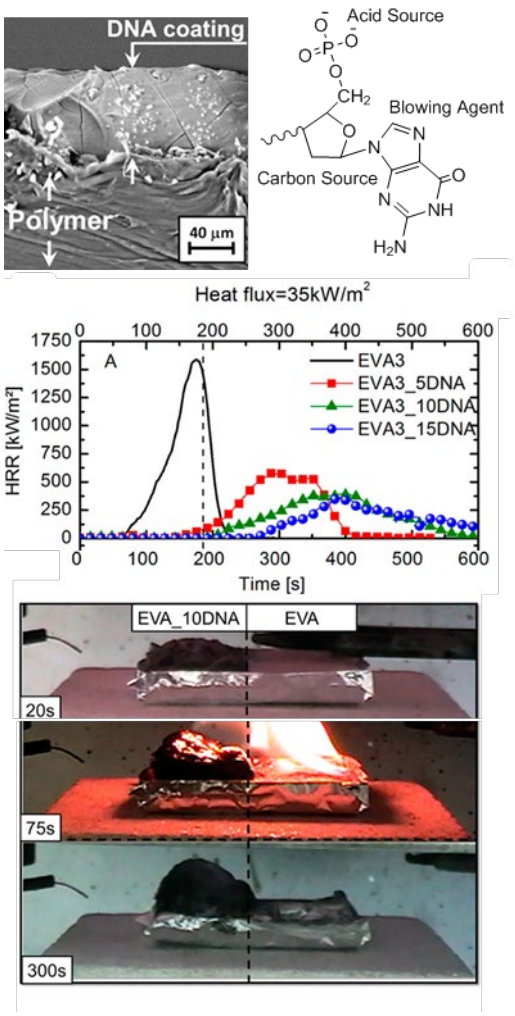

Figure 1.12. Top: DNA-coated polymer surface and chemical structure of a DNA segment and its different compounds acting together to form an intumescent flame retardant. Middle: Heat release rate plots at 35 kW m^{-2} for ethylene vinyl acetate (EVA) and EVA treated with 5, 10, and 15 wt% DNA. Bottom: Snapshots taken at different times during cone calorimetry tests on an EVA sample with only 50% of the surface coated with DNA.[118]

To summarize, the main mechanism of biopolymers in cotton fabrics is the release of phosphoric acid at lower temperatures to catalyze the formation of a thermally stable char. However, two current limitations to their use are their poor resistance to laundering and their expensive production on a large scale.

1.8 Conclusions

Phosphorus is pivotal to the development of novel efficient flame retardants, mainly because of its chemical versatility: it can act in both the condensed and gas phase, as an additive or as a reactive component, in various oxidization states, and in synergy with numerous adjuvant elements. With increased awareness towards nontoxic, recyclable, and bio-based (or even

sustainable) materials, phosphorus has the potential to fulfill all the criteria for future flame retardants. Future FRs will be increasingly tailored to the polymer type and its application, especially for new polymers, including biopolymers. The trend towards high-molecular-weight FRs is apparent, and polymeric, complex, and multifunctional structures will aid in reducing flammability without a loss of valuable properties. Furthermore, investigations into combinations of P with various moieties (P-P, P-Si, P-B, etc.) and multicomponent systems will continue to reduce FR loading and improve FR performance. Finally, the use of renewable resources as effective FRs will ensure a more ecologically aware means of production, thereby increasing the longevity of research into the field of flame retardancy.

"Molecular firefighting" demands the combined efforts of synthetic chemistry, an understanding of FR mechanisms, and knowledge of polymer processing. This interdisciplinary field continues to reveal new insight into the FR mechanisms, which we believe will drive toward a more sustainable P life-cycle for FRs and a new era of polymeric FR materials.

1.9 Acknowledgements

We thank the Deutsche Forschungsgemeinschaft (DFG WU 750/8-1; SCHA 730/15-1) for funding. M. M. V. thanks the Marie Skłodowska-Curie fellowship 705054-NOFLAME. J.C.M. is recipient of a fellowship through funding of the Excellence Initiative in the context of the graduate school of excellence "MAINZ" (Materials Science in Mainz; DFG/GSC 266). F.R.W., M.M.V., and J.C.M. thank Prof. Dr. Katharina Landfester (MPI-P, Germany) for support.

1.10 Conflict of interest

The authors declare no conflict of interest.

1.11 References Chapter 1

[1] a) S. Shaw, *Rev. Environ. Health* **2010**, *25*, 261-306; b) S.-Y. Lu, I. Hamerton, *Prog. Polym. Sci.* **2002**, *27*, 1661-1712; c) S. V. Levchik, E. D. Weil, *Journal of Fire Sciences* **2006**, *24*, 345-364.

[2] a) Lucintel, Irving, TX, USA, **2016**; b) A. B. Morgan, J. W. Gilman, *Fire and Materials* **2013**, *37*, 259-279.

[3] E. D. Weil, S. V. Levchik, *Flame Retardants for Plastics and Textiles: Practical Applications*, 2nd ed., Carl Hanser Verlag GmbH Co KG, **2015**.

[4] G. Malucelli, F. Bosco, J. Alongi, F. Carosio, A. Di Blasio, C. Mollea, F. Cuttica, A. Casale, *Rsc Adv* **2014**, *4*, 46024-46039.

[5] S. Bourbigot, S. Duquesne, *J. Mater. Chem.* **2007**, *17*, 2283-2300.

[6] a) P. R. Hornsby, in *Macromolecular Symposia, Vol. 108*, Wiley Online Library, **1996**, pp. 203-219; b) Lucintel, Irving, TX, USA, **2016**, p. 208.

[7] a) R. W. Nalepa, D. J. Scharf, Hoechst Celanese Corp., **1993**; b) L. J. Chyall, H. A. Hodgen, F. J. Vyverberg, R. W. Chapman, Pabu Services, Inc., **2005**; c) A. Sut, S. Greiser, C. Jäger, B. Schartel, *Polym. Degrad. Stab.* **2015**, *121*, 116-125.

[8] a) E. D. Weil, *Fire retardancy of polymeric materials* **2000**, 115-145; b) M. Lewin, *J. Fire Sci.* **1999**, *17*, 3-19.

[9] a) B. Schartel, R. Kunze, D. Neubert, *J. Appl. Polym. Sci.* **2002**, *83*, 2060-2071; b) S. V. Levchik, G. F. Levchik, A. I. Balabanovich, E. D. Weil, M. Klatt, *Angew. Makromol. Chem.* **1999**, *264*, 48-55; c) P. Catsman, L. C. Govaerts, R. Lucas, C08K 5/521 (2006.01), C08L 69/00 (2006.01) ed. (Ed.: G. E. Company), World Intellectual Property Organization (WIPO), USA, **2000**; d) D. K. Chattopadhyay, D. C. Webster, *Prog. Polym. Sci.* **2009**, *34*, 1068-1133.

[10] a) U. Braun, B. Schartel, M. A. Fichera, C. Jäger, *Polym. Degrad. Stab.* **2007**, *92*, 1528-1545; b) Y. Liu, Q. Wang, *Polym. Degrad. Stab.* **2006**, *91*, 3103-3109.

[11] F. L. Jin, X. Li, S. J. Park, *J Ind Eng Chem* **2015**, *29*, 1-11.

[12] a) *Additives for Polymers* **2017**, *2017*, 10-11; b) S. V. Levchik, E. D. Weil, *Polym. Int.* **2004**, *53*, 1901-1929; c) M. Rakotomalala, S. Wagner, M. Döring, *Materials* **2010**, *3*, 4300-4327; d) B. Schartel, A. I. Balabanovich, U. Braun, U. Knoll, J. Artner, M. Ciesielski, M. Döring, R. Perez, J. K. W. Sandler, V. Altstädt, T. Hoffmann, D. Pospiech, *J. Appl. Polym. Sci.* **2007**, *104*, 2260-2269.

[13] a) M. Ciesielski, B. Burk, C. Heinzmann, M. Döring, in *Novel Fire Retardant Polymers and Composite Materials*, Woodhead Publishing, **2017**, pp. 3-51; b) K. A. Salmeia, S. Gaan, *Polym. Degrad. Stab.* **2015**, *113*, 119-134; c) X. Wang, Y. Hu, L. Song, W. Y. Xing, H. D. A. Lu, P. Lv, G. X. Jie, *Polymer* **2010**, *51*, 2435-2445; d) S. Yang, Q. X. Zhang, Y. F. Hu, *Polym. Degrad. Stab.* **2016**, *133*, 358-366; e) W. C. Zhang, X. M. Li, H. B. Fan, R. J. Yang, *Polym. Degrad. Stab.* **2012**, *97*, 2241-2248.

[14] R. E. Lyon, M. L. Janssens, in *Encyclopedia of Polymer Science and Technology*, John Wiley & Sons, Inc., **2002**.

[15] a) M. Lewin, E. Weil, in *Fire retardant materials* (Eds.: A. R. Horrocks, D. Price), Woodhead Publishing Ltd., **2001**, pp. 31-68; b) S. Rabe, Y. Chuenban, B. Schartel, *Materials* **2017**, *10*, 23.

[16] a) B. Schartel, B. Perret, B. Dittrich, M. Ciesielski, J. Krämer, P. Müller, V. Altstädt, L. Zang, M. Döring, *Macromolecular Materials and Engineering* **2016**, *301*, 9-35; b) M. Lewin, *SPECIAL PUBLICATION-ROYAL SOCIETY OF CHEMISTRY* **1998**, *224*, 3-34; c) S. Levchik, C. A. Wilkie, *Fire retardancy of polymeric materials* **2000**, 171-215.

[17] a) G. Camino, S. Lomakin, in *Fire retardant materials* (Eds.: A. R. Horrocks, D. Price), Woodhead Publishing, Cambridge, UK, **2001**, pp. 318-336; b) J. Alongi, Z. D. Han, S. Bourbigot, *Prog. Polym. Sci.* **2015**, *51*, 28-73; c) S. Bourbigot, M. Le Bras, S. Duquesne, M. Rochery, *Macromolecular Materials and Engineering* **2004**, *289*, 499-511.

[18] a) M. Matzen, B. Kandola, C. Huth, B. Schartel, *Materials* **2015**, *8*, 5621-5646; b) K. Shibuya, H. Hachiya, N. Nanba, (Ed.: J. Asashi Kasei Kabushiki Kaisha), **2002**; c) F. Kempel, B. Schartel, J. M. Marti, K. M. Butler, R. Rossi, S. R. Idelsohn, E. Oñate, A. Hofmann, *Fire Mater* **2015**, *39*, 570-584.

[19] S. Bourbigot, M. Le Bras, R. Leeuwendal, K. K. Shen, D. Schubert, *Polym. Degrad. Stab.* **1999**, *64*, 419-425.

[20] S. Duquesne, M. Le Bras, S. Bourbigot, R. Delobel, F. Poutch, G. Camino, B. Eling, C. Lindsay, T. Roels, *J. Fire Sci.* **2000**, *18*, 456-482.

[21] G. J. Minkoff, *Chemistry of combustion reactions*, Butterworths, **1962**.

[22] J. Green, *J. Fire Sci.* **1996**, *14*, 426-442.

[23] a) S. K. Brauman, *J Fire Retard Chem* **1977**, *4*, 38-58; b) G. Camino, L. Costa, M. P. Luda di Cortemiglia, *Polym. Degrad. Stab.* **1991**, *33*, 131-154; c) B. Perret, K. H. Pawlowski, B. Schartel, *J. Therm. Anal. Calorim.* **2009**, *97*, 949-958.

[24] S. V. Levchik, E. D. Weil, *Polym. Int.* **2005**, *54*, 11-35.

[25] a) M. Modesti, A. Lorenzetti, *Polym. Degrad. Stab.* **2002**, *78*, 167-173; b) K. A. Salmeia, S. Gaan, G. Malucelli, *Polymers* **2016**, *8*; c) A. R. Horrocks, *Polym. Degrad. Stab.* **2011**, *96*, 377-392.

[26] B. Schartel, *Materials* **2010**, *3*, 4710-4745.

[27] a) T. Marzi, A. Beard, in *Flame Retardants, Vol. 12*, INTERSCIENCE, **2006**, p. 21; b) I. van der Veen, J. de Boer, *Chemosphere* **2012**, *88*, 1119-1153.

[28] a) J. D. Meeker, H. M. Stapleton, *Environ. Health Perspect.* **2010**, *118*, 318-323; b) A. M. Sundkvist, U. Olofsson, P. Haglund, *J. Environ. Monit.* **2010**, *12*, 943-951; c) G. L. Wei, D.

Q. Li, M. N. Zhuo, Y. S. Liao, Z. Y. Xie, T. L. Guo, J. J. Li, S. Y. Zhang, Z. Q. Liang, *Environ. Pollut.* **2015**, *196*, 29-46.

[29] A. Beard, T. Marzi, in *Proceedings of Going Green CARE Innovation 2006 Conference. Vienna, Austria*, **2006**.

[30] P. L. Lallas, *American J. International Law* **2001**, *95*, 692-708.

[31] I. ISO, *International Org. for Standardization, Geneve* **2000**.

[32] a) U. Landmann, Freie Universität Berlin **1999**; b) T. B. Bjørner, L. G. Hansen, C. S. Russell, *Journal of Environmental Economics and Management* **2004**, *47*, 411-434.

[33] a) A. Beard, M. Klimes, U. Wietschorke, *2012 Electronics Goes Green 2012+ (Egg)* **2012**; b) H. Wendschlag, H. Holder, C. Robertson, C. Wray, in *2nd International Conference on ICT for Sustainability (ICT4S 2014)*, Atlantis Press, **2014**, pp. 306-310; c) G. Ondrey, *Chem Eng-New York* **2015**, *122*, 19-23.

[34] a) G. Marosi, B. Szolnoki, K. Bocs, A. Toldy, in *Polymer Green Flame Retardants*, 1st Edition ed. (Eds.: C. Papaspyrides, P. Kiliaris), Elsevier Inc., Amsterdam; Oxford; Waltham, **2014**, pp. 181-220; b) A. Sakharov, P. Sakharov, S. Lomakin, G. Zaikov, in *AIP Conf. Proc., Vol. 1459*, AIP, **2012**, pp. 316-318; c) M. Zammarano, D. M. Fox, S. Matko, T. Kashiwagi, J. W. Gilman, R. D. Davis, *Fire Mater.* **2011**, 337-342.

[35] a) P. F. Sommerhuber, J. L. Wenker, S. Ruter, A. Krause, *Resour Conserv Recy* **2017**, *117*, 235-248; b) D. Hoang, T. Nguyen, H. An, J. Kim, *Macromol Res* **2016**, *24*, 537-546; c) M. Schlummer, A. Maurer, T. Leitner, W. Spruzina, *Waste Management & Research* **2006**, *24*, 573-583.

[36] EPA, in *An Alternatives Assessment for the Flame Retardant Decabromodiphenyl ether (DecaBDE)*, https://www.epa.gov/sites/production/files/2014-05/documents/decabde_final.pdf, **2014**.

[37] J.-L. Montchamp, *Acc. Chem. Res.* **2014**, *47*, 77-87.

[38] K. T. Carter*, Vol. US3464808 A* (Ed.: S. Co), **1969**.

[39] J. D. Leman, A. J. Robertson*, Vol. US4117200* (Ed.: A. C. Company), **1978**.

[40] N. Fukuoka, H. Yasuda, M. Nishimatsu, Y. Ohmae*, Vol. EP1403273 A1* (Ed.: L. Chemipro Kasei Kaisha), **2004**.

[41] L. K. Muller, T. Steinbach, F. R. Wurm, *Rsc Adv* **2015**, *5*, 42881-42888.

[42] a) F. Marsico, A. Turshatov, R. Peköz, Y. Avlasevich, M. Wagner, K. Weber, D. Donadio, K. Landfester, S. Baluschev, F. R. Wurm, *J. Am. Chem. Soc.* **2014**, *136*, 11057-11064; b) M. Steinmann, J. Markwart, F. R. Wurm, *Macromolecules* **2014**, *47*, 8506-8513; c) G. Becker,

L. Vlaminck, M. M. Velencoso, F. E. Du Prez, F. R. Wurm, *Polymer Chemistry* **2017**, *8*, 4074-4078.

[43] a) T. Wolf, T. Steinbach, F. R. Wurm, *Macromolecules* **2015**, 48, 3853-3863; b) T. Steinbach, S. Ritz, F. R. Wurm, *ACS Macro Letters* **2014**, *3*, 244-248.

[44] R. W. Scholz, A. H. Roy, F. S. Brand, D. T. Hellums, A. E. Ulrich, *Sustainable Phosphorus Management: A Global Transdisciplinary Roadmap*, Springer Netherlands, **2014**.

[45] J. Cooper, R. Lombardi, D. Boardman, C. Carliell-Marquet, *Resources, Conservation and Recycling* **2011**, *57*, 78-86.

[46] EU, http://ec.europa.eu/growth/sectors/raw-materials/specific-interest/critical_es, **2017**.

[47] E. D. Roy, *Ecol. Eng.* **2017**, *98*, 213-227.

[48] A. Ehmann, I.-M. Bach, S. Laopeamthong, J. Bilbao, I. Lewandowski, *Agriculture* **2017**, *7*, 1.

[49] A. H. Landrock, *Handbook of Plastic Foams: Types, Properties, Manufacture and Applications*, Elsevier Science, **1995**.

[50] a) G. Marosi, B. Szolnoki, K. Bocz, A. Toldy, in *Polymer Green Flame Retardants*, Elsevier, Amsterdam, **2014**, pp. 181-220; b) B. Szolnoki, A. Toldy, P. Konrád, G. Szebényi, G. Marosi, *Periodica Polytechnica Chemical Engineering; Vol 57 No 1-2 (2013)* **2013**; c) S. V. Levchik, *J. Fire Sci.* **2006**, *24*, 345-364.

[51] S.-H. Chiu, C.-L. Wu, H.-T. Lee, J.-H. Gu, M.-C. Suen, *Journal of Polymer Research* **2016**, *23*, 205.

[52] M. Steinmann, M. Wagner, F. R. Wurm, *Chemistry – A European Journal* **2016**, *22*, 17329-17338.

[53] a) F. Çelebi, O. Polat, L. Aras, G. Gündüz, I. M. Akhmedov, *J. Appl. Polym. Sci.* **2004**, *91*, 1314-1321; b) M.-J. Chen, C.-R. Chen, Y. Tan, J.-Q. Huang, X.-L. Wang, L. Chen, Y.-Z. Wang, *Ind. Eng. Chem. Res.* **2014**, *53*, 1160-1171.

[54] L. Chen, C. Ruan, R. Yang, Y.-Z. Wang, *Polymer Chemistry* **2014**, *5*, 3737-3749.

[55] X.-H. Zhang, F. Liu, S. Chen, G.-R. Qi, *J. Appl. Polym. Sci.* **2007**, *106*, 2391-2397.

[56] a) C. Klinkowski, L. Zang, M. Döring, *Materials China* **2013**, *32*, 144-158; b) M. Rakotomalala, S. Wagner, M. Döring, *Materials* **2010**, *3*, 4300.

[57] J. Artner, M. Ciesielski, O. Walter, M. Döring, R. M. Perez, J. K. W. Sandler, V. Altstädt, B. Schartel, *Macromol. Mater. Eng.* **2008**, *293*, 503-514.

[58] M. Ciesielski, A. Schäfer, M. Döring, *Polym. Adv. Technol.* **2008**, *19*, 507-515.

[59] Q. F. Wang, W. F. Shi, *Polym. Degrad. Stab.* **2006**, *91*, 1289-1294.

[60] a) P. M. Hergenrother, C. M. Thompson, J. G. Smith, J. W. Connell, J. A. Hinkley, R. E. Lyon, R. Moulton, *Polymer* **2005**, *46*, 5012-5024; b) S. Monge, G. David, B. Z. Tang, A. S. Abd-El-Aziz, S. Craig, J. Dong, T. Masuda, C. Weder, *Phosphorus-Based Polymers: From Synthesis to Applications*, Royal Society of Chemistry, **2014**; c) R.-J. Jeng, J.-R. Wang, J.-J. Lin, Y.-L. Liu, Y.-S. Chiu, W.-C. Su, *J. Appl. Polym. Sci.* **2001**, *82*, 3526-3538.

[61] a) U. Braun, B. Schartel, *Macromol. Mater. Eng.* **2008**, *293*, 206-217; b) B. Perret, B. Schartel, K. Stoss, M. Ciesielski, J. Diederichs, M. Döring, J. Krämer, V. Altstädt, *Macromol. Mater. Eng.* **2011**, *296*, 14-30.

[62] U. Braun, A. I. Balabanovich, B. Schartel, U. Knoll, J. Artner, M. Ciesielski, M. Döring, R. Perez, J. K. W. Sandler, V. Altstädt, T. Hoffmann, D. Pospiech, *Polymer* **2006**, *47*, 8495-8508.

[63] J. H. Song, *Journal of Vinyl and Additive Technology* **1995**, *1*, 46-50.

[64] C. Vasile, *Handbook of Polyolefins, Second Edition*, CRC Press, **2000**.

[65] U. Braun, B. Schartel, *Macromol. Chem. Phys.* **2004**, *205*, 2185-2196.

[66] H. Q. Yin, D. D. Yuan, X. F. Cai, *J. Therm. Anal. Calorim.* **2013**, *111*, 499-506.

[67] Y. Tan, Z.-B. Shao, L.-X. Yu, J.-W. Long, M. Qi, L. Chen, Y.-Z. Wang, *Polymer Chemistry* **2016**, *7*, 3003-3012.

[68] L. J. Duan, H. Y. Yang, L. Song, Y. B. Hou, W. Wang, Z. Gui, Y. Hu, *Polym. Degrad. Stab.* **2016**, *134*, 179-185.

[69] E. Gallo, U. Braun, B. Schartel, P. Russo, D. Acierno, *Polym. Degrad. Stab.* **2009**, *94*, 1245-1253.

[70] E. Gallo, B. Schartel, D. Acierno, P. Russo, *Eur. Polym. J.* **2011**, *47*, 1390-1401.

[71] a) A. D. Naik, G. Fontaine, F. Samyn, X. Delva, Y. Bourgeois, S. Bourbigot, *Polym. Degrad. Stab.* **2013**, *98*, 2653-2662; b) A. D. Naik, G. Fontaine, F. Samyn, X. Delva, J. Louisy, S. Bellayer, Y. Bourgeois, S. Bourbigot, *Fire Safety J* **2014**, *70*, 46-60; c) A. D. Naik, G. Fontaine, F. Samyn, X. Delva, J. Louisy, S. Bellayer, Y. Bourgeois, S. Bourbigot, *Rsc Adv* **2014**, *4*, 18406-18418; d) P. Müller, B. Schartel, *J. Appl. Polym. Sci.* **2016**, *133*; e) P. Müller, M. Morys, A. Sut, C. Jäger, B. Illerhaus, B. Schartel, *Polym. Degrad. Stab.* **2016**, *130*, 307-319.

[72] G.-L. Wei, D.-Q. Li, M.-N. Zhuo, Y.-S. Liao, Z.-Y. Xie, T.-L. Guo, J.-J. Li, S.-Y. Zhang, Z.-Q. Liang, *Environ. Pollut.* **2015**, *196*, 29-46.

[73] L. Chen, Y.-Z. Wang, *Materials* **2010**, *3*, 4746-4760.

[74] J. Eichhorn, *J. Appl. Polym. Sci.* **1964**, *8*, 2497-2524.

[75] M. W. Beach, N. G. Rondan, R. D. Froese, B. B. Gerhart, J. G. Green, B. G. Stobby, A. G. Shmakov, V. M. Shvartsberg, O. P. Korobeinichev, *Polym. Degrad. Stab.* **2008**, *93*, 1664-1673.

[76] J. Wagner, P. Deglmann, S. Fuchs, M. Ciesielski, C. A. Fleckenstein, M. Doring, *Polym. Degrad. Stab.* **2016**,*129*,63-76.

[77] K. H. Pawlowski, B. Schartel, *Polym. Int.* **2007**, *56*, 1404-1414.

[78] K. Tauber, F. Marsico, F. R. Wurm, B. Schartel, *Polymer Chemistry* **2014**, *5*, 7042-7053.

[79] a) B. Liang, X. D. Hong, M. Zhu, C. J. Gao, C. S. Wang, N. Tsubaki, *Polym. Bull.* **2015**, *72*, 2967-2978; b) S. Q. Song, J. J. Ma, K. Cao, G. J. Chang, Y. W. Huang, J. X. Yang, *Polym. Degrad. Stab.* **2014**, *99*, 43-52; c) W. C. Zhang, X. M. Li, R. J. Yang, *Polym. Degrad. Stab.* **2011**, *96*, 2167-2173; d) X. Wang, Y. Hu, L. Song, H. Y. Yang, W. Y. Xing, H. D. Lu, *Prog. Org. Coat.* **2011**, *71*, 72-82.

[80] S. Hörold, in *Polymer Green Flame Retardants*, 1st Edition ed. (Eds.: C. Papaspyrides, P. Kiliaris), Elsevier Inc., Amsterdam; Oxford; Waltham, **2014**, pp. 221-254.

[81] F. Laoutid, L. Bonnaud, M. Alexandre, J. M. Lopez-Cuesta, P. Dubois, *Materials Science and Engineering: R: Reports* **2009**, *63*, 100-125.

[82] a) A. Toldy, B. Szolnoki, I. Csontos, G. Marosi, *J. Appl. Polym. Sci.* **2014**, *131*, n/a-n/a; b) B. Edwards, S. Rudolf, P. Hauser, A. El-Shafei, *Industrial & Engineering Chemistry Research* **2015**, *54*, 577-584; c) M. Neisius, S. Liang, H. Mispreuve, S. Gaan, *Industrial & Engineering Chemistry Research* **2013**, *52*, 9752-9762; d) X. Zhao, F. R. Guerrero, J. Llorca, D.-Y. Wang, *ACS Sustainable Chemistry & Engineering* **2016**, *4*, 202-209.

[83] a) K. Tao, J. Li, L. Xu, X. Zhao, L. Xue, X. Fan, Q. Yan, *Polym. Degrad. Stab.* **2011**, *96*, 1248-1254; b) H. Liu, X. Wang, D. Wu, *Polym. Degrad. Stab.* **2014**, *103*, 96-112.

[84] K. N. Bauer, H. T. Tee, M. M. Velencoso, F. R. Wurm, *Prog. Polym. Sci.* **2017**, *73*, 61-122.

[85] S. Gaan, G. Sun, K. Hutches, M. H. Engelhard, *Polym. Degrad. Stab.* **2008**, *93*, 99-108.

[86] a) B. Li, Z. Zhan, H. Zhang, C. Sun, *Journal of Vinyl & Additive Technology* **2014**, *20*, 10-15; b) D. Freitag, P. Go, Y. JEONG, L. Kagumba, Google Patents, **2013**; c) W. Zhao, J. Liu, H. Peng, J. Liao, X. Wang, *Polym. Degrad. Stab.* **2015**, *118*, 120-129.

[87] L. J. Qian, L. J. Ye, G. Z. Xu, J. Liu, J. Q. Guo, *Polym. Degrad. Stab.* **2011**, *96*, 1118-1124.

[88] P. Wen, Q. Tai, Y. Hu, R. K. K. Yuen, *Ind. Eng. Chem. Res.* **2016**, *55*, 8018-8024.

[89] T. Mayer-Gall, D. Knittel, J. S. Gutmann, K. Opwis, *ACS Appl. Mater. Interfaces.* **2015**, *7*, 9349-9363.

[90] a) Y. Bai, X. Wang, D. Wu, *Ind. Eng. Chem. Res.* **2012**, *51*, 15064-15074; b) H. Liu, X. Wang, D. Wu, *Polym. Degrad. Stab.* **2015**, *118*, 45-58.

[91] S. Rothemund, I. Teasdale, *Chem. Soc. Rev.* **2016**, *45*, 5200-5215.

[92] a) W. Xing, W. Yang, W. Yang, Q. Hu, J. Si, H. Lu, B. Yang, L. Song, Y. Hu, R. K. K. Yuen, *ACS Appl. Mater. Interfaces.* **2016**, *8*, 26266-26274; b) J. Sun, X. Gu, S. Zhang, M. Coquelle, S. Bourbigot, S. Duquesne, M. Casetta, *Polym. Adv. Technol.* **2014**, *25*, 1099-1107; c) S. Qiu, X. Wang, B. Yu, X. Feng, X. Mu, R. K. K. Yuen, Y. Hu, *J. Hazard. Mater.* **2017**, *325*, 327-339.

[93] B. Yu, Y. Shi, B. Yuan, S. Qiu, W. Xing, W. Hu, L. Song, S. Lo, Y. Hu, *J. Mater. Chem.* **2015**, *3*, 8034-8044.

[94] a) M. Raimondo, S. Russo, L. Guadagno, P. Longo, S. Chirico, A. Mariconda, L. Bonnaud, O. Murariu, P. Dubois, *Rsc Adv* **2015**, *5*, 10974-10986; b) A. Lorenzetti, S. Besco, D. Hrelja, M. Roso, E. Gallo, B. Schartel, M. Modesti, *Polym. Degrad. Stab.* **2013**, *98*, 2366-2374.

[95] D. C. O. Marney, W. Yang, L. J. Russell, S. Z. Shen, T. Nguyen, Q. Yuan, R. Varley, S. Li, *Polym. Adv. Technol.* **2012**, *23*, 1564-1571.

[96] E. Gallo, B. Schartel, U. Braun, P. Russo, D. Acierno, *Polym. Adv. Technol.* **2011**, *22*, 2382-2391.

[97] a) J. Jiang, Y. Cheng, Y. Liu, Q. Wang, Y. He, B. Wang, *J. Mater. Chem.* **2015**, *3*, 4284-4290; b) S. Pappalardo, P. Russo, D. Acierno, S. Rabe, B. Schartel, *Eur. Polym. J.* **2016**, *76*, 196-207.

[98] Q. Dong, M. Liu, Y. Ding, F. Wang, C. Gao, P. Liu, B. Wen, S. Zhang, M. Yang, *Polym. Adv. Technol.* **2013**, *24*, 732-739.

[99] X. Qian, L. Song, B. Yu, B. Wang, B. Yuan, Y. Shi, Y. Hu, R. K. K. Yuen, *J. Mater. Chem.* **2013**, *1*, 6822-6830.

[100] G. Xu, J. Cheng, H. Wu, Z. Lin, Y. Zhang, H. Wang, *Polym. Compos.* **2013**, *34*, 109-121.

[101] R. Menard, C. Negrell, M. Fache, L. Ferry, R. Sonnier, G. David, *Rsc Adv* **2015**, *5*, 70856-70867.

[102] P. Jia, L. Hu, M. Zhang, G. Feng, Y. Zhou, *Eur. Polym. J.* **2017**, *87*, 209-220.

[103] a) M. Sacristán, J. C. Ronda, M. Galià, V. Cádiz, *J. Appl. Polym. Sci.* **2011**, *122*, 1649-1658; b) M. Moreno, G. Lligadas, J. C. Ronda, M. Galià, V. Cádiz, *J. Polym. Sci., Part A: Polym. Chem.* **2012**, *50*, 3206-3213.

[104] B. A. Howell, Y. G. Daniel, *J. Therm. Anal. Calorim.* **2015**, *121*, 411-419.

[105] B. A. Howell, K. E. Carter, *J. Therm. Anal. Calorim.* **2010**, *102*, 493-498.

[106] H. Pan, W. Wang, Y. Pan, L. Song, Y. Hu, K. M. Liew, *Carbohydr. Polym.* **2015**, *115*, 516-524.

[107] F. Carosio, G. Fontaine, J. Alongi, S. Bourbigot, *ACS Appl. Mater. Interfaces.* **2015**, *7*, 12158-12167.

[108] Y. Xiao, Y. Zheng, X. Wang, Z. Chen, Z. Xu, *J. Appl. Polym. Sci.* **2014**, *131*.

[109] L. Liu, M. Qian, P. a. Song, G. Huang, Y. Yu, S. Fu, *ACS Sustain. Chem. Eng.* **2016**, *4*, 2422-2431.

[110] L. Costes, F. Laoutid, M. Aguedo, A. Richel, S. Brohez, C. Delvosalle, P. Dubois, *Eur. Polym. J.* **2016**, *84*, 652-667.

[111] a) C. Bao, Y. Guo, B. Yuan, Y. Hu, L. Song, *J. Mater. Chem.* **2012**, *22*, 23057-23063; b) S. Wang, F. Xin, Y. Chen, L. Qian, Y. Chen, *Polym. Degrad. Stab.* **2016**, *129*, 133-141.

[112] H. Moustafa, C. Guizani, A. Dufresne, *J. Appl. Polym. Sci.* **2017**, *134*, n/a-n/a.

[113] S. Wang, S. Ma, C. Xu, Y. Liu, J. Dai, Z. Wang, X. Liu, J. Chen, X. Shen, J. Wei, J. Zhu, *Macromolecules* **2017**, *50*, 1892-1901.

[114] G. Laufer, C. Kirkland, A. B. Morgan, J. C. Grunlan, *Biomacromolecules* **2012**, *13*, 2843-2848.

[115] Z. Zheng, B. W. T. Y. S. Liu, X. Cui, H. Wang, *Polym. Compos.* **2015**, *36*, 1606-1619.

[116] J. Alongi, F. Carosio, G. Malucelli, *Polym. Degrad. Stab.* **2014**, *106*, 138-149.

[117] J. Alongi, A. Di Blasio, J. Milnes, G. Malucelli, S. Bourbigot, B. Kandola, G. Camino, *Polym. Degrad. Stab.* **2015**, *113*, 110-118.

[118] J. Alongi, F. Cuttica, F. Carosio, *ACS Sustain. Chem. Eng.* **2016**, *4*, 3544-3551.

2. Systematically controlled decomposition mechanism in phosphorus flame retardants by precise molecular architecture: P-O vs. P-N

Jens C. Markwart[+[a, c]], Alexander Battig[+[b]], Lisa Zimmermann[[d]], Martin Wagner[[e]], Jochen Fischer[[f]], Bernhard Schartel*[[b]], Frederik R. Wurm*[[a]]

[a] *Physical Chemistry of Polymers - Max Planck Institute for Polymer Research, Ackermannweg 10, 55128 Mainz, Germany*

[b] *Technical Properties of Polymeric Materials - Bundesanstalt für Materialforschung und -prüfung (BAM), Unter den Eichen 87, 12205 Berlin, Germany*

[c] *Graduate School Materials Science in Mainz, Staudinger Weg 9, 55128 Mainz, Germany*

[d] *Department of Aquatic Ecotoxicology, Goethe University Frankfurt, Max-von-Laue-Str. 13, 60438 Frankfurt/Main, Germany*

[e] *Department of Biology, Norwegian University of Science and Technology, 7491 Trondheim, Norway*

[f] *Institute for Biotechnology and Drug Research gGmbH (IBWF), Erwin-Schrödinger-Str. 56, 67663 Kaiserslautern, Germany*

[+] *These authors contributed equally to this work.*

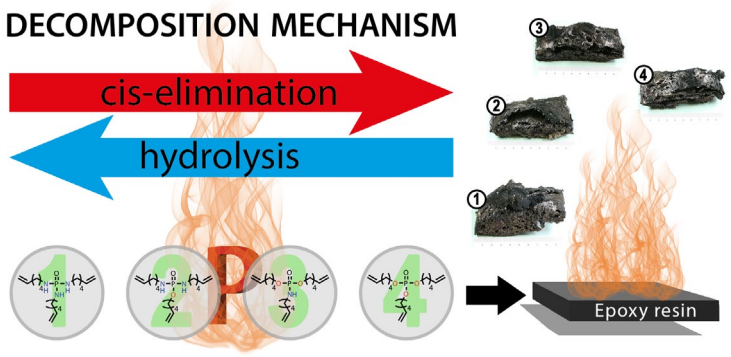

Keywords: epoxies, flame retardants, mechanistic study, phosphorus, toxicity

2.1 Notes

Alexander Battig performed the flame-retardancy measurements. Lisa Zimmermann and Jochen Fischer performed the toxicity experiments.

2.2 Abstract

Flame retardants (FR) are inevitable additives to many plastics. Halogenated organics are effective FRs but are controversially discussed due to the release of toxic gases during a fire or their persistence if landfilled. Phosphorus-containing compounds are effective alternatives to halogenated FRs and have potential lower toxicity and degradability. In addition, nitrogen-containing additives were reported to induce synergistic effects with phosphorus-based FRs. However, no systematic study of the gradual variation on a single phosphorus FR containing both P–O and P–N moieties and their comparison to the respective blends of phosphates and phosphoramides was reported. This study developed general design principles for P–O- and P–N-based FRs and will help to design effective FRs for various polymers. We synthesized a library of phosphorus FRs that only differ in their P-binding pattern from each other and studied their decomposition mechanism in epoxy resins. Systematic control over the decomposition pathways of phosphate ($P{=}O(OR)_3$), phosphoramidate ($P{=}O(OR)_2(NHR)$), phosphorodiamidate ($P{=}O(OR)(NHR)_2$), phosphoramide ($P{=}O(NHR)_3$), and their blends was identified, for example, by reducing *cis*-elimination and the formation of P–N-rich char with increasing nitrogen content in the P-binding sphere. Our FR epoxy resins can compete with commercial FRs in most cases, but we proved that the blending of esters and amides outperformed the single-molecule amidates/diamidates due to distinctively different decomposition mechanisms acting synergistically when blended.

2.3 Introduction

Polymers are omnipresent in our everyday life. However, their inherent risk of fire makes the use of flame retardants (FRs) inevitable. For this purpose, halogenated organics were used as effective FRs, but today these are controversially debated due to the release of toxic gases during a fire or their persistence if discarded. Currently, organophosphates are discussed as promising alternatives to halogenated FRs due to their effective flame-retardant properties and potential to design nontoxic and biodegradable FRs.[1]

The combination of phosphorus FRs (P-FRs) with additional nitrogen-containing additives resulted in synergistic effects during a fire by forming phosphorus–nitrogen intermediates or an increased charring.[2] However, a systematic study of precisely synthesized P-FRs with a variable number of P–N bonds (such as phosphoramidates and phosphorodiamidates, Figure 2.1) has not been performed. We prepared a series of aliphatic organophosphates/-amides (**1**–**4**) with a precise binding pattern around the central phosphorus and used them as a FR additive in epoxy resins. Their *in vitro* toxicity was also assessed and compared to commercial halogenated or other organophosphate-based FRs. Importantly, the effects of the P-binding pattern (**1**–**4**) have been studied during a fire scene to understand their decomposition pathway and compared to blends of phosphate and phosphoramide (these are **1** and **4**) on the performance during a simulated fire scenario.

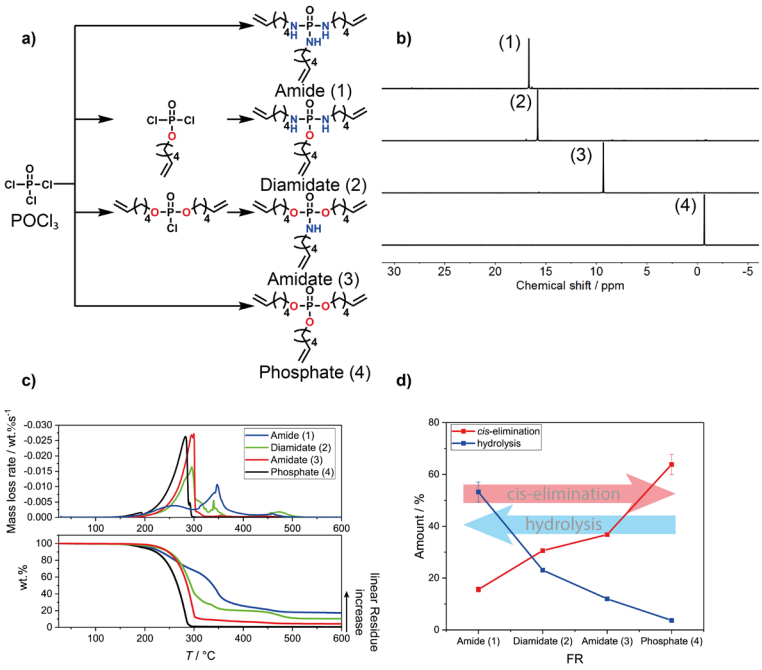

Figure 2.1. Characterization of flame retardants: amide (**1**), diamidate (**2**), amidate (**3**), and phosphate (**4**) (a) Schematic representation of the synthesis: the amide (**1**) and phosphate (**4**) are a one-step synthesis and the diamidate (**2**) and amidate (**3**) are a two-step synthesis. (b) $^{31}P–\{^{1}H\}$ NMR of the flame retardants in $CDCl_3$. (c) Mass loss of the flame retardants in thermogravimetric tests; char yield increase with increasing nitrogen content. (d) Correlation of relative amount of *cis*-elimination and hydrolysis in the released gases during pyrolysis GC-MS (connection between the data points are only to guide the eye).

These P-FRs mainly differ in their main mode of action, which are gas and condensed phase activity. In the condensed phase, phosphorus-containing materials exhibit FR properties due to the enhanced formation and stabilization of carbonaceous char, which retains fuel in the condensed phase. Additionally, an intumescent multicellular char may protect the underlying polymer from heat, acting as a heat shield.[3-5] The increased charring is explained by dehydration of the polymer and the formation of phosphoric acid derivatives, leading to cross-linking and aromatization.[6] Activity in the gas phase is mainly due to the formation of PO radicals, slowing down the exothermic radical process in the combustion zone, leading to a reduced combustion efficiency and therefore reducing the heat release.[4,7,8]

The phosphorus–nitrogen synergism accelerates the polymer phosphorylation by increasing the *in situ* production of phosphoric acid due to catalyzing *cis*-elimination.[9] The same is true for P–N bonds, which are more reactive than P–O bonds regarding the phosphorylation process. This retains phosphorus in the condensed phase and therefore promotes char formation and stabilization.[10] Furthermore, P and N react to form thermally stable polymeric compounds in the condensed phase.[9] While studies have shown the impact of nitrogen- and phosphorus-containing

FRs,[11,12] systematic studies on the gradual variation of the phosphorus binding pattern and its impact on the FR mechanism are rare.[6] In addition, the comparison of phosphoramidates and phosphorodiamidates produced via chemical synthesis against blending the respective phosphate and phosphoramide, hitherto uninvestigated, is presented herein. The P-FRs are synthesized and characterized in detail on the molecular level; for example, degradation temperature and pathway are assessed. They are used as additive FRs in epoxy resins and are investigated in a simulated fire scenario with state-of-the-art techniques (LOI, UL-94, and cone calorimeter).

The knowledge about the varying decomposition mechanisms for combined P–O- and P–N-based FRs will help the future preparation of biofriendly and effective FRs for various polymer materials since there is no universal FR design. FRs are optimized for a special application and matrix. For this task, it is important to know how the FR degrades to estimate possible interactions between matrix and FRs during a fire scenario.[13]

2.4 Results and Discussion

2.4.1 Synthesis and Design of Materials

To investigate the influence of the P–O vs P–N ratio on FR efficiency, a systematic library of organophosphates/-amidates is necessary. Four P-FRs with a central phosphorus atom and three ω-hexenyl chains were synthesized. The organic side chains ensure miscibility with the epoxy matrix, and the double bonds were introduced to increase the charring performance.[14,15] Tri(hex-5-en-1-yl)phosphoramide (**1**), tri(hex-5-en-1-yl)phosphorodiamidate (**2**), tri(hex-5-en-1-yl)phosphoramidate (**3**), and tri(hex-5-en-1-yl)phosphate (**4**) were synthesized starting from $POCl_3$ via esterification with 5-hexen-1-ol or amidation with hex-5-en-1-amine (Figure 2.1a). The phosphoramide (**1**) and the phosphate (**4**) were prepared in a single step. In contrast, the phosphorodiamidate (**2**) and the phosphoramidate (**3**) were synthesized in two steps to guarantee the correct binding pattern, first by esterification followed by the amidation (the amidation as the first step may result in multiple amidations). All P-FRs were of sufficient purity after the synthesis without the need for additional purification steps as proven by ^{1}H and ^{31}P NMR spectra (Figures S2.2–S2.13 and Figure 2.1b). ^{31}P NMR spectroscopy is a precise technique to control the correct binding pattern and purity of the compounds: the phosphate exhibited a single resonance at −0.67 ppm, whereas the signal shifted downfield with increasing nitrogen content (Figure 2.1b). By these procedures, all P-FRs were easily available up to at least 50 g with standard university lab equipment.

Organophosphorus compounds are currently considered as alternatives for halogenated FRs[16,17] due to their potentially lower toxicity.[18-20] To evaluate their toxicity, we tested **1**–**4** in fungi and plant cells. Additionally, we used reporter gene assays based on yeast and human cells to assess their baseline toxicity and endocrine activities (estrogenic and antiandrogenic). Compounds **1**, **2**, and **4** induced baseline toxicity increasing in the following order (**4** < **2** < **1**) but were less toxic than the halogenated commercial tetrabromo bisphenol A (see the Supporting Information for details). While none of the compounds were estrogenic, **3** and **4** induced some antiandrogenic activity (**4** < **3**). Although the compounds partly induced toxicity, the actual concentrations of FRs leaching from finished products still need to be determined.

2.4.2 Decomposition Studies

Phosphoramides exhibit higher thermal stability, lower volatility, and higher viscosity due to additional hydrogen bonding compared to their analogue phosphates.[21] These properties may increase the overlap of the decomposition temperatures of both matrix and flame retardant. This overlap leads to higher reactivity during the pyrolysis and an increased residue amount as a higher phosphorus content is maintained in the condensed phase due to interactions of the FR with the matrix and their respective decomposition products.[22,23]

The combination of TGA, FTIR, and pyrolysis GC-MS gave a deeper insight into how the FRs decompose under pyrolytic conditions.

For the pure FRs (**1**–**4**) mass loss under pyrolysis, measured by thermogravimetric analysis (TGA, Figure 2.1c), proved the gradual change of the decomposition behavior according to the structure variation from **1** to **4**; this already suggests a possible effect on the FR mechanism during a fire. The phosphoramide (**1**) proved the highest decomposition temperature (T_{max}) at 317 °C, which decreased with increasing O content of the FR to 274 °C for **2**, 269 °C for **3**, and 250 °C for **4**. In addition, the char yield (measured at 600 °C) decreased from **1** with 17 wt% to <1 wt% for **4**, indicating a different activity of the pure compounds in the gas and/or condensed phase. The phosphate decomposition curve followed a typical behavior of a vaporizing material with a clear boiling point while with increasing nitrogen content the degradation occurs via multiple decomposition steps over a broader temperature range. As P–N bonds are present in the FR, they can form more stable intermediates through a polymerization process that require higher amounts of thermal energy to vaporize, if at all, as is noticeable by the subsequent increase in T_{max} and higher amount of residue for each additional nitrogen introduced.

The FTIR spectra from the evolved gases (measured at T_{max}, Figure S2.18) proved the presence of several decomposition products, among them those that correspond to hydrolysis products, i.e., 5-hexen-1-ol and hex-5-en-1-amine (after scission of the P–O or P–N bond, respectively). The spectra also indicated the presence of derivatives containing P═O and P–O moieties at 1299 and 1030 cm^{-1} for the phosphate (**4**), while we detected additional vibrations for the (NH_2)–P═O band at 1159 cm^{-1} during the decomposition of **2** and **3**. In addition, all nitrogen-containing P-FRs exhibited C–N bands at 1075 cm^{-1}, P–N–C or P–N–P bands at 980 cm^{-1}, and N–H bands at 769 cm^{-1}. For all nitrogen-containing FRs at higher temperatures ($T > T_{max}$) P–N bands between 1330 and 1300 cm^{-1} and two characteristic bands for ammonia at 965 and 930 cm^{-1} were detected, albeit shifted or overlapped with other signals, pointing to the formation of incombustible gas resulting in flame dilution.

Pyrolysis GC-MS supports these results and further proves the presence of the major decomposition products. Compound **4** decomposed mainly by a *cis*-elimination during pyrolysis as indicated by the high amount of 1,5-hexadiene which was detected at a retention time of 2.6 min (Figure S2.29). Also, the other P–O-containing FRs (**2** and **3**) released 1,5-hexadiene during decomposition, but the amount of *cis*-elimination decreased with increasing P–N content (Figure 2.1d). Additionally, 5-hexen-1-amine and 5-hexen-1-ol were detected for **2** and **3** (retention at 6.1 and 6.7 min in Figure S2.29). Additionally, for **2**–**4**, phosphoric acid derivatives at retention times of 23.7, 24.6, and 25.8 min were identified, corresponding to the gas-phase activity of such compounds. Because of transesterifications during the decomposition, in the GC elugrams of **3**, also compound **4** was detected, while in the elugram of the pyrolysis GC-MS of **2**, transesterification leads to the formation of **3** and **4**. In stark contrast, during the decomposition of **1**, almost no *cis*-elimination occurred, and only little amounts of phosphoric acid derivatives were observed, indicating the formation of nonvolatiles and thus underlining the condensed phase activity of the phosphoramide. This was further supported by solid-state ^{31}P NMR of the char residues, which exhibited distinct signals for P–N compounds (Figure S2.46).

2.4.3 Flame-Retardant Behavior in Epoxies

The FR performances of **1**–**4** and blends of **1** and **4** were studied in an epoxy resin based on bisphenol A diglycidyl ether (DGEBA) and 2,2'-dimethyl-4,4'-methylenebis(cyclohexylamine) (DMC). The epoxy plates were prepared by mixing DGEBA with DMC in the presence of 10 wt% of each FR in an aluminum mold and curing for 3 h at 150 °C (Figure 2.2a). As the P–NHR bond may also act as a curing agent under certain conditions, we performed a control experiment with **1** and

phenyl glycidyl ether at the curing conditions for the epoxy. Under the cross-linking conditions, no ring-opening of the epoxide occurred from the P-NHR bond (cf. Figures S2.14–S2.16), proving that **1**–**3** act as additive, and not reactive, FRs. As a benchmark, the commercially available and industrially used FR bisphenol A diphenyl phosphate (BDP) was chosen, as it was already used successfully in epoxy resins.[24,25]

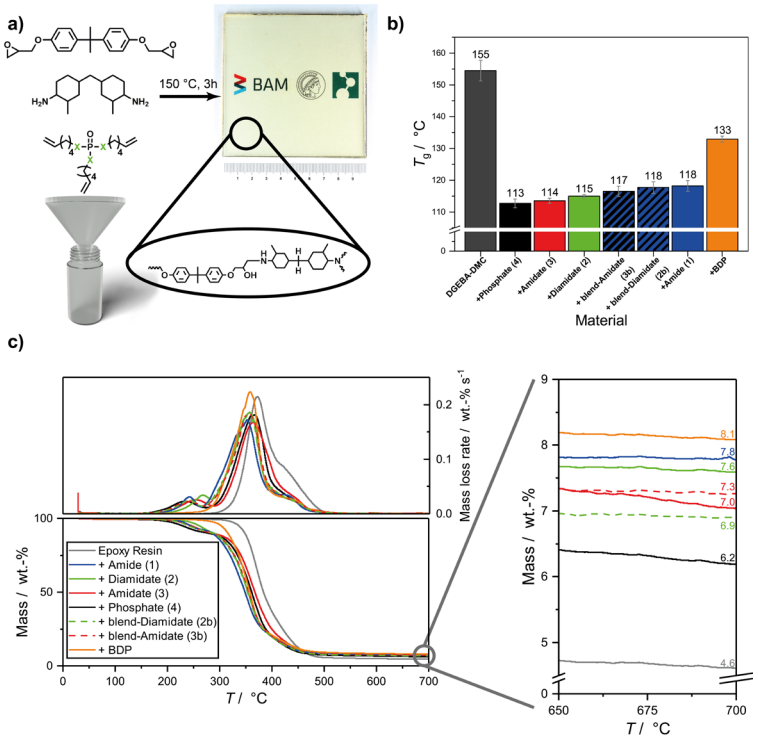

Figure 2.2. Characterization of flame-retarded epoxy resins. (a) Schematic representation of the epoxy resin synthesis. (b) Glass transition temperature of epoxy resin and flame-retarded composites. (c) Thermogravimetry (10 K min^{-1}; N_2) of the epoxy resins with FRs; increase of char yield with increasing nitrogen content of the flame retardant.

Typically, additive FRs act as plasticizers of the epoxy resin and reduce the glass transition temperature (T_g). All flame-retarded epoxy resins with 10 wt% **1**, **2**, **3**, or **4** also exhibited lower T_gs by 36–42 °C compared to the neat epoxy resin. **4** shows the highest decrease of T_g (to 113 °C), while with increasing amount of NH bonds an increase of the T_gs was detected, probably due to hydrogen-bonding effects (Figure 2.2b). Blending of **1** and **4** in a 1:2 or 2:1 molar ratio to "simulate" the elemental composition of a phosphoramidate (**3b**) and phosphorodiamidate (**2b**) resulted in a slightly higher T_g compared to the pure **2** and **3** was detected. For BDP, the T_g of the neat epoxy (155 °C) was reduced to 133 °C. In all cases, the aliphatic FRs **1**–**4** result in a higher decrease of T_g compared to the stiff aromatic BDP.[26]

To understand the differences of **1**–**4** (and **2b** and **3b**) on the behavior of the loaded epoxies during combustion, we elucidated the FR mode of actions and mechanisms. A crucial step toward

understanding the FR mechanisms is analyzing the pyrolysis of the epoxy resins with FRs by TGA. The burning with a stable flame is dominated by an anaerobe pyrolysis, producing volatile fuel that is combusted in the flame. This model suits most polymeric materials in most fire scenarios such as ignition and developing fires and thus for all the important fire tests for polymeric materials, such as UL 94, LOI, and flaming combustion in the cone calorimeter. Although the heating rate is relatively slow, thermogravimetry under nitrogen is the best common analytical method to investigate the pyrolysis controlling the burning of polymeric materials.[27] A lower onset temperature of the degradation for the FR epoxies was detected compared to the neat epoxy. This was attributed to volatilization of the FRs and is indicated by an additional decomposition step equal to ~10 wt%. Notably, however, the main decomposition step shifts to higher temperatures with increasing amount of P–O bonds in the additive. Importantly, for all FR epoxy resins, an increased char yield was detected, which further increased slightly with increasing P–N bonds in the FRs (Figure 2.2c).

While microscale experiments aid in understanding certain aspects of a material's fire-retardant properties, they do not fully evaluate fire behavior on a macroscopic scale. Two reaction-to-small-flame tests were conducted, namely limiting oxygen index (LOI) and the Underwriter's 94 (UL-94) test, as well as forced-flaming conditions via cone calorimetry. LOI measures the lowest oxygen concentration necessary to sustain combustion in a candle-like setup, while UL-94 measures dripping and flame-spread behavior in vertical and horizontal positions.

The pure epoxy resin exhibited an oxygen index (OI) of OI = 18.7 vol%, proving the inherent flammability of these materials. When a FR was incorporated, the OI increased to approximately OI = 23–24 vol%, corresponding to a relative increase of ca. 22–28%. The addition of any of the tested FRs increased the OI and slowed down the flame spread and thereby reduced the fire hazard. However, the differences between all tested materials are minimal, mostly due to the relatively low FR loading (10 wt%) and low P content of a sample (~1% P in each resin). The P-FRs performed on an equal level to the benchmark epoxy resin with BDP, indicating that the burning behavior in OI tests can only be altered with higher loading/higher P content in order attain OI > 27–29 vol%. This is needed to fulfill the demands of diverse flame-retardancy requirements.[14] A similar behavior was obtained from UL-94 tests, where the benchmark BDP-loaded epoxy resin failed vertical tests and only achieved an HB rating in horizontal tests (lowest rating before not passing) due to the high flammability of epoxy resins. The herein-prepared resins with P-FRs achieved the same rating, although not all FRs managed to reduce the horizontal burn speed; most noticeably, the resin with phosphoramide (**1**) was barely within the margin of error of passing HB classification. In all UL-94 tests, the strong formation of char was visible for the prepared resins

with P-FRs, yet the increase of viscosity of the epoxy resin resulted in the protective char dripping away from the sample. These results illustrate that at 10 wt% loading the FRs cannot stop vertical flame spread due to melt dripping although a strong char formation is visible. Similar to LOI, better classification can be achieved with higher FR loading or higher P content of the sample.

Cone calorimetry measurements proved a significant effect of all P-FRs on epoxy resins during a simulated fire scenario. The epoxy plates (10 × 10 × 0.4 cm^3) were irradiated with a heat flux of 50 kW m^{-2} at a distance of 35 mm, simulating a developing fire.[28] The results of the forced-flaming condition experiments underlined that the epoxy resin burned with a high heat release rate (HRR) and lost 99.3 wt% of its mass, presenting nearly no residue (Figure 2.3d). All flame-retarded resins exhibited a clear reduction of peak or heat release rate (PHRR), an increase in residue yield, a lowering of the total heat evolved (THE = total heat released (THR) at flame out), and a reduction of fire growth rate (FIGRA = maximum (HRR/t)) (Figure 2.3b,c and Table S2.4). The epoxy resin loaded with the phosphate (**4**) demonstrated the lowest PHRR (855 kW m^{-2}, reduced by 48%) and THE (78.1 MJ m^{-2}, reduced by 28%) and displayed a HRR curve corresponding to a charring material with a protective layer. This behavior was clearly visible during the experiments as well as in the cross sections of the residues, as the decomposition of the resin with **4** and the volatilization of its products acted as blowing agents, creating a voluminous intumescent char that shielded the underlying material from the heat source. With increasing P–N content of the FR, a lower reduction of PHRR and THE was detected. **1**, **2**, and **3** showed a small plateau at *t* = 60 s, but the lack of blowing agent created a char layer, which was unable to shield the underlying material, leading to additional decomposition of the epoxy and thus a higher PHRR. Epoxy resins with **1** as the additive even had a higher PHRR (1832 kW m^{-2}) than the neat epoxy resin (1696 kW m^{-2}). However, the residue yields of epoxy resins loaded with **1** (8.4 wt%) was in a similar range as the best performing epoxy loaded with **4** (9.2 wt%).

a)

Material composition	DGEBA-DMC	+ Amide (1)	+ Diamidate (2)	+ Amidate (3)	+ Phosphate (4)	+ BDP
LOI						
[c(O2)] / %	18.7 ± 0.3	22.9 ± 0.2	23.3 ± 0.2	22.8 ± 0.2	23.2 ± 0.3	24.0 ± 0.2
UL-94						
Classification	HB	HB	HB	HB	HB	HB
Burn speed / mm s^{-1}	31.7 ± 3.6	38.3 ± 2.9	29.5 ± 1.9	34.0 ± 1.8	30.0 ± 1.6	19.6 ± 3.6

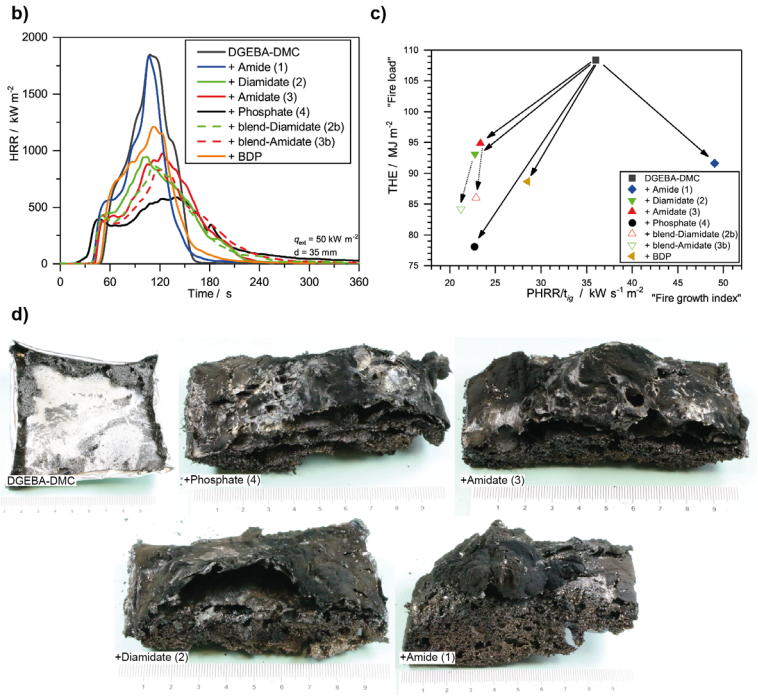

Figure 2.3. Cone calorimeter, UL-94, and limiting oxygen index (LOI) tests of the epoxy resins. (a) Summarized results of LOI and UL-94 tests, with all flame retardants increasing the OI and achieving HB classification in the UL-94 test. (b) Heat release rate over time of epoxy resins, with the phosphate (**4**) presenting the lowest peak heat release and the amide (**1**) the highest. (c) Petrella plot of the different epoxy resins with all flame retardants having a positive effect (lowering THE), especially the phosphate (**4**) lowering both fire load and fire growth index and the amide (**1**) only lowering the former. (d) Photos of char residue after cone calorimeter test: the epoxy resin has almost no residue; pore size decreases from phosphate (**4**) to amide (**1**) along with an increase in char residue.

All flame-retarded epoxy resins revealed an increase in residue yield compared to the epoxy resin without FRs. In pyrolysis investigations, TGA experiments of the pure FRs demonstrated that **1** presented a large amount of residue while **4** hardly left any. The increase in residue was proportional to the increase in P–N bonds, i.e., **4** < **3** < **2** < **1**. In forced flaming conditions, this trend was not clearly visible. However, as has been proven in previous experiments,[29] the residue yields of pure FRs in TGA experiments do not necessarily correlate with the residue yields of flame-retarded resins. Specifically, the interactions between FR and matrix govern the residue yield. For the flame-retarded epoxy resins, although residue yields were in the order **4** > **2** > **1** > **3**, the increased residue amount for resins with **4** can be explained by the formation of a protective layer which reduces the mass transfer of combustible material into the flame zone and shields

underlying material from thermal radiation. For the nitrogen-containing compounds, the previously noted trend was also seen, especially given the margin of error for resins with **2**, illustrating that residue yields increase with increasing nitrogen content in the binding sphere of phosphorus.

The effective heat of combustion (EHC) is the quotient of the total heat evolved and the total mass loss; therefore, it is a ratio between these two values. In cone calorimetry experiments, the EHC relates to flame dilution and flame inhibition, and a reduction in EHC is a parameter for the gas phase activity of a FR.[23] The phosphate (**4**) displayed a reduction in EHC of ∼20%, from 29.6 MJ kg^{-1} for the epoxy resin to 21.6 MJ kg^{-1} for the resin with **4**, which points to gas phase activity of the FR (Figure 2.4b). Noticeably, this effect is minimized if P–N bonds were installed into the FR, as **1**, **2**, and **3** reduced the EHC only by ca. 4–5%, indicating that the gas phase activity of the synthesized P-FRs decreased with the presence of nitrogen in the chemical structure. Although residue yields of resins with **1**, **2**, **3**, and **4** are within the same range (ca. 8–10 wt% mass loss), the ratios between the THEs and total mass loss changed. This change resulted from flame dilution and flame inhibition effects which affect THE. The blended FRs (**2b** and **3b**) were also tested in epoxy resins, and the results were compared to resins with **2** and **3**. The results show that the blended FRs achieved higher residue yields a lower PHRR, decreased THE, and a lower EHC than resins with only **2** or **3**. In fact, the PHRR of the resins with **2b** or **3b** are comparable to the resins loaded with **4** which showed the strongest reduction of this value compared to the epoxy resin. Resins with **3b** had a 15% lower PHRR than resins with **3**, while resins with **2b** or **3b** demonstrated 8% or 11% lower THE values and residue yields 47% or 49% higher than resins with only **2** or **3**, respectively. Consequently, the EHCs of resins with **2b** or **3b** are 4% or 7% lower than resins with **2** or **3**, respectively. Noticeably, the fire growth rate (FIGRA) of resins with **2b** are 20% lower than resins with **2**. These results clearly demonstrate that the presence of two types of P-FRs in epoxy resins increases FR efficacy compared to a single P-FR with the same O:N ratio. In the case of **2** and **3**, the P–N linkages retain the phosphorus in the condensed phase, forming char during decomposition (Scheme 2.1, right pathway). This retention of P in the char reduces flame inhibition as P retention in the condensed phase competes with P release in the gas phase.[23]

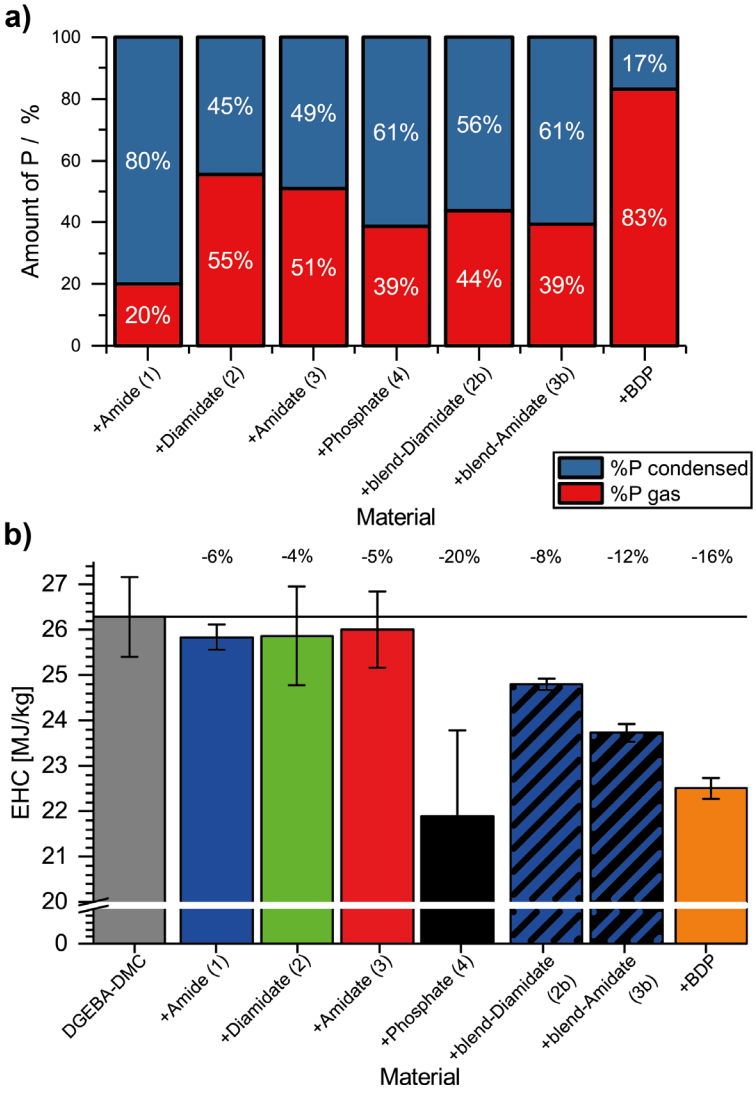

Figure 2.4. (a) Phosphorus content determined by elemental analysis from the residues after cone calorimeter tests (blue bars). Calculated amount of phosphorus in the gas phase (red bars). (b) Comparison of effective heat of combustion (EHC) of epoxy resins with and without FRs. The numbers above the bars represent the relative change to the non-flame-retarded epoxy resin.

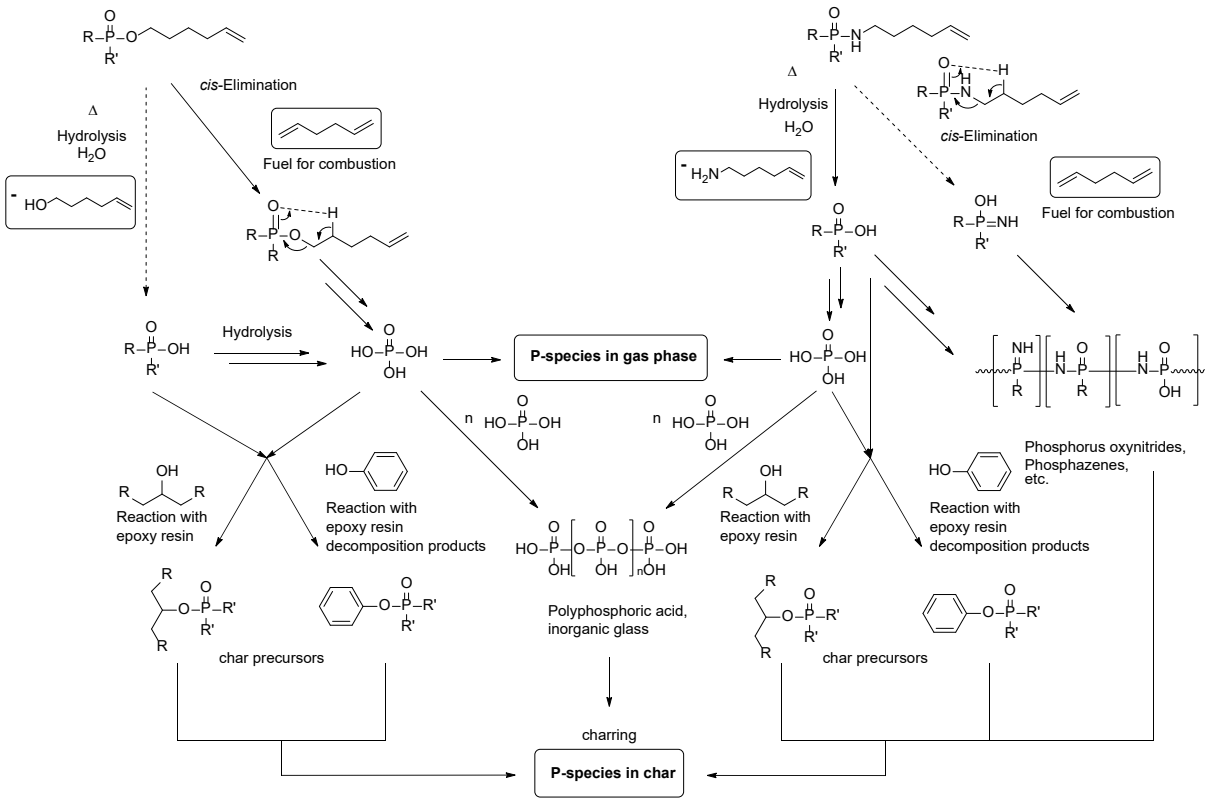

Scheme 2.1. Scheme of Proposed Decomposition and Reaction Pathways of P–O- and P–N-Containing Phosphorus Flame Retardants[a]

[a] P–O containing P-FRs are more prone to *cis*-elimination, resulting in the formation of phosphoric acid and enabling transesterification reactions. P–N-containing P-FRs are more to hydrolysis, resulting in the formation of phosphorus oxynitrides and phosphazenes. Products in squares were identified via TG-FTIR and pyrolysis GC-MS.

The residues after cone calorimeter tests were analyzed for their phosphorus content via elemental analysis, indicating the largest amount of P (80%) in the condensed phase for resins loaded with **1** (Figure 2.4a). The difference in gas and condensed phase activity is explained by the different decomposition mechanisms as discussed previously.

In epoxy resins, the phosphate (**4**) readily forms phosphoric acid via *cis*-elimination and creates networks with aromatic char in the condensed phase and is present at the main decomposition step due to incorporation into the decomposing matrix via esterification (Scheme 2.1). In contrast, the phosphoramide (**1**) was hydrolyzed under these conditions. However, **1** also generated polymeric compounds containing phosphazene or phosphorus oxynitride components in the condensed phase, as indicated by solid-state NMR (Figure S2.46), leading to an increased residue and high P content in the char. The phosphoramidate (**3**) and phosphorodiamidate (**2**), containing both P–O and P–N bonds, exhibit both decomposition mechanisms with decreasing *cis*-elimination when the P–N content increases and transesterification (compare the pyrolysis GC-MS data).

The effect of combining phosphate and amide led to synergistic flame-retardant effects, which were not observed for the combination of P–O and P–N in a single FR additive. The exchange of P–O bonds with P–N bonds reduced the effectiveness of one mechanism but did not sufficiently promote the other. This conclusion was exemplified in the amount of residue in cone calorimeter tests as well as the P content of the residue (Figure 2.4a): the residue amounts in epoxy resins were ordered **4** ≥ **2** > **1** > **3** (i.e., 9.2% ≥ 5.0% > 8.4% > 7.6%) and **2b** > **3b** > **4** > **1** (i.e., 13.4% > 11.3% > 9.2% > 8.4%) for the blended materials, showing an increase in residue for the blended FRs. As for P content in the condensed phase, the amidate (**3**) and diamidate (**2**) showed lower amounts of P in their residues (49% and 45%, respectively) than the blended FRs **3b** and **2b** (61% and 56%, respectively).

The FTIR spectra of the evolved gases during the first decomposition step (Figure 2.5) showed that the FRs decompose above 200 °C, and some decomposition products enter the gas phase, which is a typical behavior for low molecular weight FRs.[22] Looking at the main decomposition step at around 360 °C (Figure S2.21), TG-FTIR showed the DGEBA-DMC decomposition pattern,[30] pointing to the degradation of the resin matrix. An exception was the epoxy resin with **4**, where the phosphate still displayed characteristic bands during the main decomposition step, implying the presence of phosphate beyond the FR's boiling point. This phenomenon was caused by the reaction between matrix and phosphate (Scheme 2.1), as the phosphate was more likely to produce phosphoric acid than the nitrogen-containing counterparts due to the difference in bond dissociation energies, leading to incorporation of phosphates into the polymer matrix by transesterification.

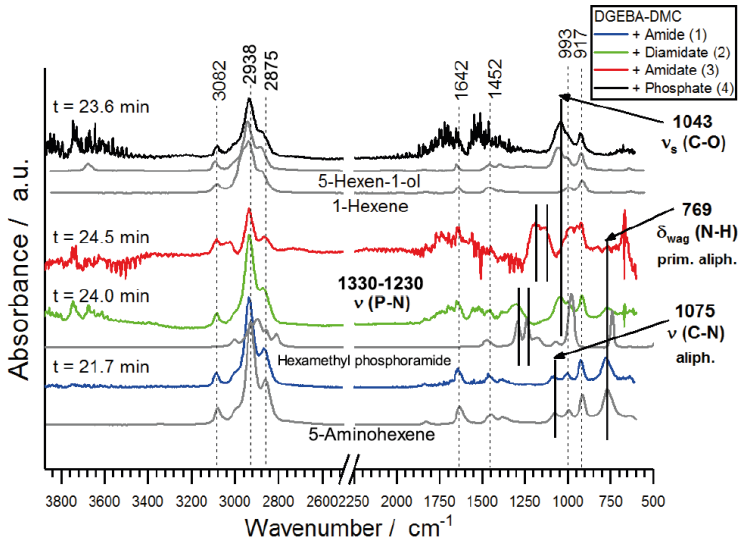

Figure 2.5. TG-FTIR spectra of the first decomposition step of flame-retarded epoxy resins.

Hot stage FTIR spectra (Figure S2.27) of the condensed phase at various temperatures implied the presence of phosphorus species in the residue (Table S2.3). All resins containing FRs exhibited bands corresponding to various phosphorus species at 600 °C, i.e., at end of the test. These bands were not detected in the epoxy resin, indicating condensed phase activity for all tested FRs. For **4**, the presence of medium intensity bands at 1181 cm^{-1}, corresponding to C–O stretching vibration of phenols, and at 828 cm^{-1}, corresponding to C–H bonds of aromatic rings, point to the formation of substituted aromatic compounds in the condensed phase. The band was strongest for **4**, which points to the ability of the phosphate to bind hydroxyl-functionalized aromatic rings during the decomposition of the matrix into the condensed phase. In contrast, all nitrogen-containing FRs (**1**–**3**) demonstrated a medium intensity band at 1398 cm^{-1}, which corresponds to P═N–P or P–N–Ph vibrations, which are probably attributed to polyphosphazenes or phosphor oxynitride in the condensed phase, as underlined by a higher amount of residue after the TGA experiments for N-containing FRs.

2.5 Conclusion

A systematic library of phosphorus-containing flame-retardant (FR) additives (**1**–**4**) with precisely adjusted P/N/O ratio were synthesized. Compounds **1**–**4** were less toxic than their halogenated counterpart for most end points, and compounds **2** and **4** represented the best alternatives. With this library, the decomposition pathway of the FRs in an epoxy resin during combustion was controlled.

By a combination of different techniques, we were able to elucidate the degradation mechanism of the different P-FRs and proved a gradual change of the decomposition depending on the chemical structure. In a simulated fire scenario, the phosphate (**4**) exhibited the highest efficiency in epoxy resins and was active in both the gas and the condensed phase effectively. The gas phase activity was explained by the predominant *cis*-elimination mechanism during the combustion (from pyrolysis GC-MS). With an exchange of P–O bonds with P–N bonds, the amount of *cis*-elimination decreased and hydrolysis increased as a decomposition pathway. The amide (**1**) with three P–N bonds proved the highest condensed phase activity of the investigated structures due to cleavage of the P–N bonds during the combustion. This also resulted in the lowest FR performance of **1**. Notably, the blends of phosphate and phosphoramide (**2b** and **3b**) outperformed the pure **2** and **3**. We believe this is an effect of combining different decomposition mechanisms, which leads to synergistic flame retardancy. These findings will further contribute to the development of systematic libraries of P-based FRs with low toxicity and high efficiency.

2.6 Experimental Section

2.6.1 Tri(hex-5-en-1-yl)phosphate (4)

To a dried three-necked, 2 L round-bottom flask fitted with a dropping funnel, 5-hexen-1-ol (274.2 mL, 2.28 mol, 3.5 equiv) and triethylamine (318.6 mL, 2.28 mol, 3.5 equiv) were added under an argon atmosphere in dry dichloromethane (500 mL). Then phosphoryl chloride (60.6 mL, 0.65 mol, 1.0 equiv) dissolved in dry dichloromethane (50 mL) was added dropwise to the solution, keeping the temperature at 0 °C. The reaction was allowed to stir overnight at room temperature and was then filtered. Afterward, the crude mixture was concentrated at reduced pressure, dissolved in toluene and then filtered to remove most of the ammonium salt byproduct. Then, the crude product was washed with 10% aqueous hydrochloric acid solution, a saturated solution of calcium carbonate, and brine. The organic layer was dried over anhydrous sodium sulfate, filtered, and dried *in vacuo*.

For the biological tests the compound **4** was purified by chromatography over neutral alumina oxide using diethyl ether as eluent to give a clear, slight yellow oil (yield: 95%). The purity and chemical structure were determined by ^{1}H NMR, ^{13}C {H} NMR, and ^{31}P {H} NMR spectroscopy as well as electrospray ionization mass spectrometry (ESI-MS).

^{1}H NMR (300 MHz, chloroform-*d*, δ): 5.83–5.70 (m, 3H, e), 5.02–4.93 (m, 6H, f), 4.02 (q, 6H, a), 2.10–2.03 (td, 6H, d), 1.68 (tt, 6H, b), 1.46 (tt, 6H, c). ^{31}P {H} NMR (121 MHz, chloroform-*d*, δ): −0.67 (s, 1P, 1). ^{13}C {H} NMR (75 MHz, chloroform-*d*, δ): 138.17 (s, 3C, e), 114.85 (s, 3C, f), 67.38 (d, 3C, a), 33.11 (s, 3C, d), 29.60 (d, 3C, b), 24.67 (s, 3C, c). ESI-MS: 345.21 $[M + H]^{+}$ (calculated M+: 344.21).

2.6.2 Tri(hex-5-en-1-yl)phosphoramide (1)

To a dried three-necked, 2 L round-bottom flask fitted with a dropping funnel, hex-5-en-1-amine (286.2 mL, 2.28 mol, 3.5 equiv) and triethylamine (318.6 mL, 2.28 mol, 3.5 equiv) were added under an argon atmosphere in dry dichloromethane (500 mL). Then, phosphoryl chloride (60.6 mL, 0.65 mol, 1.0 equiv) dissolved in dry dichloromethane (50 mL) was added dropwise to the solution, keeping the temperature at 0 °C. The reaction was allowed to stir overnight at room temperature and was then filtered. Afterward, the crude mixture was concentrated at reduced pressure and then filtered for the second time. The crude product was redissolved in diethyl ether (200 mL) and stored overnight at −20 °C. The solution was filtered again to remove the triethylamine hydrochloride completely. The crude product was washed with 10% aqueous

hydrochloric acid solution, a saturated solution of calcium carbonate, and brine. The organic layer was dried over anhydrous sodium sulfate, filtered, and dried *in vacuo*.

For the biological tests the compound **1** was purified by chromatography over silica using DCM and methanol (9:1) as eluent to give a clear, slight yellow oil (yield: 92%). The purity and chemical structure were determined by ^{1}H NMR, ^{13}C {H} NMR, and ^{31}P {H} NMR spectroscopy as well as electrospray ionization mass spectrometry (ESI-MS).

^{1}H NMR (300 MHz, chloroform-*d*, δ): 5.81–5.68 (m, 3H, e), 4.98–4.89 (m, 6H, f), 2.85 (quint, 6H, a), 2.36–2.29 (q, 3H, g), 2.05–1.98 (td, 6H, d), 1.48–1.34 (m, 12H, b, c). ^{31}P {H} NMR (121 MHz, chloroform-*d*, δ): 16.67 (s, 1P, 1). ^{13}C {H} NMR (75 MHz, chloroform-*d*, δ): 138.50 (s, 3C, e), 114.67 (s, 3C, f), 41.09 (s, 3C, a), 33.39 (s, 3C, d), 31.69 (d, 3C, b), 26.09 (s, 3C, c). ESI-MS: 342.24 $[M + H]^{+}$, 683.44 $[2M + H]^{+}$) (calculated: 341.26).

2.6.3 Hex-5-en-1-yl Phosphorodichloridate

To a dried three-necked, 250 mL round-bottom flask fitted with a dropping funnel, phosphoryl chloride (18.7 mL, 205.00 mmol, 10.0 equiv) was added under an argon atmosphere in dry toluene (50 mL). Then triethylamine (2.8 mL, 20.50 mmol, 1.0 equiv) and 5-hexen-1-ol (2.5 mL, 20.50 mmol, 1.0 equiv) dissolved in dry toluene (5 mL) were added dropwise to the solution, keeping the temperature at 0 °C. The reaction was stirred 1 h at room temperature. Afterward, the crude product was concentrated at reduced pressure and filtered to remove the triethylammonium chloride. Then, all byproducts and starting material were removed under reduced pressure (RT, 5×10^{-2} mbar). The product was used without any further purification.

2.6.4 Di(hex-5-en-1-yl)phosphorochloridate

To a dried three-necked 250 mL round-bottom flask fitted with a dropping funnel, phosphoryl chloride (8.1 mL, 88.89 mmol, 1.0 equiv) was added under an argon atmosphere in dry toluene (80 mL). Then triethylamine (22.2 mL, 160.00 mmol, 1.8 equiv) and 5-hexen-1-ol (19.2 mL, 160.00 mmol, 1.8 equiv) dissolved in dry toluene (20 mL) were dropwise to the solution, keeping the temperature at 0 °C. The reaction was allowed to stir overnight at room temperature and was then filtered. Afterward, the crude mixture was concentrated at reduced pressure.

The compound was purified by distillation (90 °C, $<10^{-1}$ mbar 30 min; 110 °C, $<10^{-1}$ mbar 15–20 min) to give a clear, slight yellow oil (yield: 82%). The purity and chemical structure were determined by ^{1}H NMR and ^{31}P {H} NMR spectroscopy.

^{1}H NMR (300 MHz, chloroform-*d*, δ): 5.78–5.65 (m, 2H, e), 4.98–4.89 (m, 4H, f), 4.21–1.09 (m, 4H, a), 2.02 (td, 4H, d), 1.69 (tt, 4H, b), 1.45 (tt, 4H, c). ^{31}P {H} NMR (121 MHz, chloroform-*d*, δ): 4.73 (s, 1P, 1).

2.6.5 Tri(hex-5-en-1-yl)phosphorodiamidate (2)

To a dried three-necked 250 mL round-bottom flask fitted with a dropping funnel, hex-5-en-1-yl phosphorodichloridate (4.5 g, 20.50 mmol, 1.0 equiv) was added under an argon atmosphere in dry toluene (50 mL). Then hex-5-en-1-amine (5.4 mL, 43.05 mmol, 2.1 equiv) and triethylamine (6.0 mL, 43.05 mmol, 2.1 equiv) were added dropwise to the solution, keeping the temperature at 0 °C. The reaction was allowed to stir overnight at room temperature and was then filtered. The crude mixture was concentrated at reduced pressure, and the crude product was dissolved in diethyl ether to wash it with 10% aqueous hydrochloric acid solution, a saturated solution of calcium carbonate, and brine. The organic layer was dried over anhydrous sodium sulfate, filtered, and concentrated on the rotary evaporator.

For the biological tests the compound **2** was purified by chromatography over silica using ethyl acetate, petroleum ether, and methanol (9:1:0.1) as eluent to give a clear, slight yellow oil (yield: 95%). The purity and chemical structure were determined by ^{1}H NMR, ^{13}C {H} NMR, and ^{31}P {H} NMR spectroscopy as well as electrospray ionization mass spectrometry (ESI-MS).

^{1}H NMR (300 MHz, chloroform-*d*, δ): 5.76–5.63 (m, 3H, f, l), 4.94–4.84 (m, 6H, g, m), 3.83 (q, 2H, h), 2.78 (q, 4H, b), 2.61 (br, 2H, a), 1.98 (m, 6H, e, k), 1.57 (m, 2H, (i), 1.44–1.29 (m, 6H, c, d, j). ^{31}P {H} NMR (121 MHz, chloroform-*d*, δ): 15.81 (s, 1P, 1). ^{13}C {H} NMR (75 MHz, chloroform-*d*, δ): 138.44 (s, 2C, f), 138.36 (s, C, l), 114.73 (s, C, m), 114.65 (s, 2C, g), 64.61 (d, C, h), 41.01 (s, 2C, b), 33.32 (s, 2C, e), 33.25 (s, C, k), 31.43 (d, 2C, c), 29.99 (d, C, (i), 25.96 (s, 2C, d), 24.97 (s, C, j). ESI-MS *m*/*z*: 343.24 $[M + H]^+$, 685.42 $[2M + H]^+$ (calculated: 342.24).

2.6.6 Tri(hex-5-en-1-yl)phosphoramidate (3)

To a dried three-necked 250 mL round-bottom flask fitted with a dropping funnel, di(hex-5-en-1-yl)phosphorochloridate (25.0 g, 88.9 mmol, 1.0 equiv) was added under an argon atmosphere in dry toluene (80 mL). Then triethylamine (13.6 mL, 97.78 mmol, 1.1 equiv) and 1-hexene-5-amine (12.3 mL, 97.78 mmol, 1.1 equiv) were added dropwise to the solution at room temperature. The reaction was stirred overnight and filtered. The crude mixture was concentrated at reduced pressure, and the crude product was dissolved in diethyl ether to wash it with 10% aqueous

hydrochloric acid solution, a saturated solution of calcium carbonate, and brine. The organic layer was dried over anhydrous sodium sulfate, filtered, and dried *in vacuo*.

For the biological tests the compound was purified by chromatography over silica using ethyl acetate and petroleum ether (6:4) as an eluent to give a clear, slight yellow oil (yield: 63%). The purity and chemical structure were determined by ^{1}H NMR, ^{13}C {H} NMR, and ^{31}P {H} NMR spectroscopy.

^{1}H NMR (300 MHz, chloroform-*d*, δ): 5.83–5.69 (m, 3H, e, l), 5.01–4.91 (m, 6H, f, m), 3.95 (m, 4H, a), 2.70 (br, H, g), 2.85 (br, 2H, h), 2.04 (td, 6H, d, k), 1.66 (m, 4H, b), 1.50–1.35 (m, 8H, c, i, j). ^{31}P {H} NMR (121 MHz, chloroform-*d*, δ): 9.48 (s, 1P, 1). ^{13}C {H} NMR (75 MHz, chloroform-*d*, δ): 138.47 (s, C, l), 138.41 (s, 2C, e), 114.87 (s, 2C, f), 114.81 (s, C, m), 66.06 (d, 2C, a), 41.33 (s, C, h), 33.37 (s, C, k), 33.29 (s, 2C, d), 31.21 (d, C, (i), 29.90 (d, 2C, b), 25.92 (s, C, j), 24.95 (s, 2C; c). ASAP-MS *m*/*z*: 689.2 (2M + H) (calculated: 344.21).

2.7 Acknowledgments

The authors thank the Deutsche Forschungsgemeinschaft (DFG WU 750/8-1; SCHA 730/15-1) for funding. J.C.M. is the recipient of a fellowship through funding of the Excellence Initiative (DFG/GSC 266) in the context of the graduate school of excellence “MAINZ” (Materials Science in Mainz). F.R.W. and J.C.M. thank Prof. Dr. Katharina Landfester (MPI-P, Germany) for support. We thank Robert Graf (MPI-P, Germany) for the solid-state NMR measurements. A.B. thanks William Harris and Letícia Lima for their assistance in measuring and preparing samples. L.Z. and F.R.W. thank the German Federal Ministry for Education and Research (BMBF) for their support of the program “Research for sustainable development (FONA)”, “PlastX-Plastics as a systemic risk for social-ecological supply systems” (Grant 01UU1603A).

2.8 References Chapter 2

[1] M. M. Velencoso, A. Battig, J. C. Markwart, B. Schartel, F. R. Wurm, *Angew. Chem. Int. Ed. Engl.* **2018**, *57*, 10450-10467.

[2] H. Nishihara, S. Tanji, R. Kanatani, *Polym. J.* **1998**, *30*, 163.

[3] C. I. Lindsay, S. B. Hill, M. Hearn, G. Manton, N. Everall, A. Bunn, J. Heron, I. Fletcher, *Polym. Int.* **2000**, *49*, 1183-1192.

[4] B. Schartel, *Materials* **2010**, *3*, 4710-4745.

[5] J. Green, *J. Fire Sci.* **1992**, *10*, 470-487.

[6] U. Braun, A. I. Balabanovich, B. Schartel, U. Knoll, J. Artner, M. Ciesielski, M. Döring, R. Perez, J. K. W. Sandler, V. Altstädt, T. Hoffmann, D. Pospiech, *Polymer* **2006**, *47*, 8495-8508.

[7] K. Täuber, F. Marsico, F. R. Wurm, B. Schartel, *Polymer Chemistry* **2014**, *5*, 7042-7053.

[8] G. J. Minkoff, C. F. H. Tipper, *Chemistry of Combustion Reactions*, Butterworths, **1962**.

[9] S. Gaan, G. Sun, K. Hutches, M. H. Engelhard, *Polym. Degrad. Stab.* **2008**, *93*, 99-108.

[10] F. Laoutid, L. Bonnaud, M. Alexandre, J. M. Lopez-Cuesta, P. Dubois, *Materials Science and Engineering: R: Reports* **2009**, *63*, 100-125.

[11] F. Gao, L. Tong, Z. Fang, *Polym. Degrad. Stab.* **2006**, *91*, 1295-1299.

[12] S. Gaan, G. Sun, *J. Anal. Appl. Pyrolysis* **2007**, *78*, 371-377.

[13] A. B. Morgan, J. W. Gilman, **2013**, *37*, 259-279.

[14] A. F. Grand, C. A. Wilkie, *Fire Retardancy of Polymeric Materials*, CRC Press, **2000**.

[15] Y.-H. Cho, K. Kim, S. Ahn, H. K. Liu, *J. Power Sources* **2011**, *196*, 1483-1487.

[16] S.-Y. Lu, I. Hamerton, *Prog. Polym. Sci.* **2002**, *27*, 1661-1712.

[17] S. V. Levchik, E. D. Weil, *J. Fire Sci.* **2006**, *24*, 345-364.

[18] X.-B. Zheng, J.-P. Wu, X.-J. Luo, Y.-H. Zeng, Y.-Z. She, B.-X. Mai, *Environment International* **2012**, *45*, 122-128.

[19] H. Xiao, L. Shen, Y. Su, E. Barresi, M. DeJong, H. Hung, Y.-D. Lei, F. Wania, E. J. Reiner, E. Sverko, S.-C. Kang, *Environ. Pollut.* **2012**, *161*, 154-161.

[20] G. C. Windham, S. M. Pinney, A. Sjodin, R. Lum, R. S. Jones, L. L. Needham, F. M. Biro, R. A. Hiatt, L. H. Kushi, *Environ. Res.* **2010**, *110*, 251-257.

[21] T.-M. Nguyen, S. Chang, B. Condon, R. Slopek, E. Graves, M. Yoshioka-Tarver, *Industrial & Engineering Chemistry Research* **2013**, *52*, 4715-4724.

[22] B. Perret, K. H. Pawlowski, B. Schartel, *J. Therm. Anal. Calorim.* **2009**, *97*, 949.

[23] B. Schartel, B. Perret, B. Dittrich, M. Ciesielski, J. Krämer, P. Müller, V. Altstädt, L. Zang, M. Döring, *Macromolecular Materials and Engineering* **2016**, *301*, 9-35.

[24] M. Rakotomalala, S. Wagner, M. Döring, *Materials* **2010**, *3*, 4300.

[25] M. Ciesielski, A. Schäfer, M. Döring, *Polym. Adv. Technol.* **2008**, *19*, 507-515.

[26] J. M. G. Cowie, V. Arrighi, *Polymers: Chemistry and Physics of Modern Materials, Third Edition*, CRC Press, **2007**.

[27] B. Schartel, C. A. Wilkie, G. Camino, *J. Fire Sci.* **2016**, *34*, 447-467.

[28] B. Schartel, T. R. Hull, *Fire and Materials* **2007**, *31*, 327-354.

[29] E. Wawrzyn, B. Schartel, M. Ciesielski, B. Kretzschmar, U. Braun, M. Döring, *Eur. Polym. J.* **2012**, *48*, 1561-1574.

[30] B. Schartel, B. Perret, B. Dittrich, M. Ciesielski, J. Krämer, P. Müller, V. Altstädt, L. Zang, M. Döring, *Macromolecular Materials and Engineering* **2015**, *301*, 9-35.

2.9 Supporting Information

2.9.1 Experimental Procedures

2.9.1.1 Materials

All chemicals were purchased from commercial suppliers as reagent grade and used without further purification.

2.9.1.2 DSC

Differential scanning calorimetry measurements were performed using a Netzsch 204 F1 "Phoenix" differential scanning calorimeter (DSC) (Netzsch Instruments, Selb, Germany), using 5 mg sample and three heating and two cooling runs at 10 K min^{-1} from -80 to 180 °C. The data was evaluated as an average of the 2nd and 3rd heating run, if $p < 5\%$.

For Differential Scanning Calorimetry (DSC), a Mettler Toledo DSC 823^e was used. With a heating and cooling rate of 10 K min^{-1} three measurements of heating, cooling and heating were performed. The measurements were done in a nitrogen atmosphere with a flow rate of 30 mL min^{-1}.

2.9.1.3 TGA

For the thermogravimetric analysis (TGA) of the neat flame retardants, a Mettler Toledo TGA/DSC 3+ in a nitrogen atmosphere was used. Using 10 mg of the sample, the measurements were performed in a range from 25 °C to 600 °C with a heating rate of 10 K min^{-1}.

2.9.1.4 ESI-MS

Electrospray ionization mass spectrometry (ESI-MS) was performed on a Q-Tof Ultima 3 from Waters Micromass, Milford, Massachusetts. 1 mg of the sample was dissolved in 1 ml of THF. The prepared solution was injected into the ionization chamber of the ESI-MS instrument at 120 °C.

2.9.1.5 TG-FTIR

Both decomposition and evolved gases were investigated under pyrolytic and thermo-oxidative conditions via Fourier transform infrared (FTIR) spectroscopy coupled with thermogravimetric analysis. For epoxy resins with and without FRs, 10 mg of powder attained from cryomilling were used for measurements, while 5 mg samples were measured for pure FRs. Using a TG 209 F1 Iris

(Netzsch Instruments, Selb, Germany), samples were heated at a rate of 10 K min^{-1} from 30 to 900 °C under a nitrogen or synthetic air (80:20) gas flow of 30 ml min^{-1}. The evolved gases were analyzed using a Tensor27 infrared spectrometer (Bruker Optics, Ettlingen, Germany), which was coupled to the TG via a transfer line heated to 270 °C.

2.9.1.6 Pyrolysis–Gas Chromatography-Mass Spectrometry (Py-GC-MS)

Py-GC-MS measurements were conducted as follows: a micro-furnace double-shot pyrolyzer (PY3030iD, Frontier Laboratories, Japan) was connected via a split-/splitless inlet port to a gas chromatograph (7890B, Agilent Technologies, USA) combined with a mass selective detector (5977B, Agilent Technologies, USA). The EI ionization energy of the MSD was 70 eV, the scan range was 15–550 amu. 300 µg samples were inserted by gravimetric fall into the pyrolysis zone at 500 °C and pyrolyzed in a helium atmosphere. The evolved pyrolysis products were separated with an Ultra Alloy +-5 capillary column (l = 30 m, iD = 0.25 mm, film thickness = 0.25 µm) with a helium flow of 1 ml min^{-1}. The column temperature was kept at 40 °C for 2 min and increased at a rate of 10 °C min^{-1} to 300 °C where it was held for 10 min. The temperature of the GC injector was 300 °C and it was operated in a split mode of 1:300. Peak assignments were made with the help of the NIST14 MS library.

2.9.1.7 Gas Chromatography-Mass Spectrometry (GC-MS)

GC-MS measurement was conducted on Shimadzu GC-2010 plus gas chromatography and QP2010 ultra mass spectrometer with fused silica column (122-5532, DB-5MS) and flame ionization detector.

2.9.1.8 PCFC

The heat release capacity, total heat released, and heat of combustion of the volatiles were determined using pyrolysis combustion flow calorimetry (PCFC) using a microscale combustion calorimeter (MCC) (Fire Testing Technologies Ltd., East Grinstead, UK). 5 mg powdered samples were pyrolyzed from 150 to 750°C and combusted at 900°C at a heating rate of 1 K s^{-1} under a total gas flow of 100 ml min^{-1} (80 ml min^{-1} nitrogen, 20 ml min^{-1} oxygen).

2.9.1.9 Hot Stage FTIR

The condensed phase activity was monitored using hot-stage FT-infrared spectroscopy using a Vertex70 FTIR spectrometer (Bruker Optics, Ettlingen, Germany), equipped with an FTIR600 Linkam hot-stage cell (Linkam Scientific Instruments Ltd., Chilworth, UK). The samples were pressed into a KBr plate, loaded into the Linkam cell, and heated at a rate of 10 K min^{-1} from 30 to 600 °C under a nitrogen gas flow of 300 ml min^{-1}.

2.9.1.10 UL-94, LOI

Two separate tests, namely Underwriter's Laboratory 94 (UL-94) and limiting oxygen index (LOI), were performed to determine and characterize the flammability in terms of the flame retarded resins' reaction-to-small-flames. UL-94 was performed in accordance with the standard DIN EN 60695-11-10 in horizontal and vertical orientation. LOI was performed according to DIN EN ISO 4589-2. All samples were conditioned at 23°C and 50% relative humidity for at least 80 hours.

2.9.1.11 Cone Calorimeter

All epoxy resin samples were subjected to bench-scale forced flaming combustion using a cone calorimeter (Fire Testing Technology Ltd., East Grinstead, UK) at a distance of 35 mm between specimen and cone heater and a heat flux of 50 kW m^{-2} and in accordance with ISO 5660. Specimens sized 100 x 100 x 4 mm^3 were conditioned at 23°C and 50% relative humidity for at least 48 hours and then subjected to irradiation.

2.9.1.12 Residue morphology

The fire residue surfaces and core interiors were examined via scanning electron microscopy (SEM) using a Zeiss EVO MA10 (Zeiss, Oberkochen, Germany) with an acceleration voltage of 10 kV. Prior to the investigation, the residues were sputtered with gold to reduce the degradation of the images due to sample charging.

2.9.1.13 NMR

Nuclear magnetic resonance (NMR) analysis, ^{1}H, ^{31}P {Hb and ^{13}C {H} NMR spectra were recorded with Bruker Avance spectrometers operating with 250, 300, 500 and 700 MHz frequencies in deuterated chloroform, deuterated dimethyl sulfoxide or deuterated *N,N*-dimethylformamide as

a solvent. The calibration of the spectra was done against the solvent signal. The spectra were analyzed using MestReNova 9 from Mestrelab Research S.L.

2.9.1.14 Solid-state NMR

^{31}P CP/MAS NMR measurements were performed with a standard 4 mm magic angle spinning MAS double resonance probe head at 121.5 MHz Larmor frequency.

2.9.1.15 Sample preparation

All epoxy resins were prepared using bisphenol A diglycidylether (DGEBA) (Araldite MY740, Bodo Möller Chemie GmbH, Offenbach am Main, Germany) as the epoxide agent and 2,2'-dimethyl-4,4'-methylene-bis-(cyclohexylamine) (DMC) (Sigma Aldrich Co. LLC/ Merck KgaA, Darmstadt, Germany) as the amine hardener. The materials were mixed, poured into aluminum molds of desired dimensions, then hardened at 150°C for 3h. The flame retarded epoxy resins were produced in the same manner, except 10 wt.-% of the mixture was replaced with the respective flame retardant.

2.9.1.16 Baseline toxicity – microtox assay

In the Microtox assay, the potential of compounds to inhibit the bioluminescence of *Aliivibrio fischeri* is determined by observations of e.g. the bacteria's metabolism or growth. The assay was performed according to the International Organization for Standardization (ISO 11348-3, 2007)(ISO 2017) modified to a 96-well plate format as previously described by Escher et al. and Völker et al.[1,2] Stock solutions were prepared in dimethyl sulfoxide (DMSO) and further diluted in the assay to concentrations ranging from 0.02 to 3.00 mM (<1% DMSO v/v). All compounds were tested in five independent experiments with two technical replicates each. We used GraphPad Prism 5.0 (GraphPad Software, San Diego, CA) for nonlinear regressions (four-parameter logistic function) to calculate the concentration inducing 20% luminescence inhibition (EC_{20}).

2.9.1.17 Endocrine activity – yeast-based reporter-gene assays

In order to investigate whether compounds influence the endocrine system, we tested their relative agonistic activity at the human estrogen receptor α[3] and antagonistic activity at the human androgen receptor[4] as previously described with minor modifications regarding the measurement of the reporter gene activity.[5,6] In brief, we determined the reporter gene activity

at 540 nm 40 min after adding 50 µl *lacZ* buffer (supplemented with 50% w/v 4-methylumbelliferyl-beta-D-glucuronide and 15.4% *w/v* dithiothreitol) to 30 µl sample solution. Depending on the compound's cytotoxicity, concentrations ranging from 0.8 nm to 3 mM were tested. Each assay was repeated three to six times resulting in 24 to 48 replicates. Data analysis was performed using GraphPad Prism 5.0. Estrogenic and antiandrogenic activities were normalized to the pooled negative and solvent controls (0%) and the maximal assay response induced by the references compounds 17β-estradiol and flutamide, respectively. Relative activities at highest noncytotoxic concentrations are given. If possible, dose-response relationships and respective EC_{20} values were calculated using a four-parameter logistic function, constrained to a bottom level of zero.

2.9.1.18 Bacterial and fungal strains

The strains of *Bacillus subtilis* subsp. *spizizenii* (ATCC 6633) and *Staphylococcus aureus* (ATCC 11632) were cultivated at NB (Difco™ Nutrition Broth, BD, France) at 37°C. All fungal strains (*Candida albicans*, ATCC 90028; *Rhizomucor miehei*, Tü 284; *Penicillium notatum*, IBWF gGmbH and *Paecilomyces variotii*, ETH 114646) were cultured on YMG (4 g/L yeast extract, 10 g/L malt extract, 4 g/L glucose, pH 5.5) at 27°C or 37°C, respectively.

Pyricularia oryzae[7] and *Botrytis cinereal*[8] were cultured on CM[9] and malt medium (20 g/L malt extract, pH 5.5) at 27°C for 3 to 4 weeks, respectively.

HeLa-S3 (DSMZ ACC 161) were grown as described previously by Schüffler et al. [10]

2.9.1.19 Antibacterial and Antifungal Assays

The disk diffusion method was performed to determine the antibacterial and antifungal properties of the chemical compounds. It was mainly based on published methods. [11-13] All agar plates were prepared in 90 mm sterile Petri dishes (PS Sarstedt, 82.1472 Germany) with 20 mL of agar (Difco™ Nutrition Broth, BD, France for bacteria and Difco™ potato dextrose Broth, BD, France for fungi). The bacterial inoculum suspension was diluted in the liquid agar media at 45°C. The inoculated medium was poured into the Petri dishes. For fungi, a spore solution was added to the liquid agar medium at 45°C. The mixture was also poured into Petri dishes. The plates were stored at 4°C until further use. Sterilized assay paper disks (MN 827, #484000; 6.0 mm in diameter, Macherey-Nagel, Germany) were soaked with 10 and 50 µg of the compound solved in DMSO and placed on inoculated plates. The plates were incubated at 37°C overnight for bacteria and at 27°C for 48 h for fungi, respectively. Afterward, the diameters of inhibition zones were measured. As a control,

standard antibiotics (50 µg streptomycin for bacteria or 50 µg hygromycin B for fungi), as well as pure DMSO, were included. Each assay was performed thrice. *Pyricularia oryzae* was used for the spore germination test as previously published by Kettering et al. (2005). [14] The method was slightly adapted for the spore germination assay of *Botrytis cinerea*.[8] The cytotoxicity was analyzed as described previously.[15] Phytotoxicity was tested with *Setaria italic* and *Lepidium sativum* with minor alterations.[16] The tested compounds were prepared in aliquots of 10, 20 and 50 µg per 48-well solved in DMSO. The plates were freeze-dried afterward to remove the solvent. To each well 12 seeds and 200 µL H_2O were added. Afterward, the plates were incubated in a plant humidity chamber for 5 to 7 days. As a control 5% H_3PO_4 was added to the water poured onto the seeds. All tests were prepared as triplicates.

2.9.2 Additional: Results and Discussion

2.9.2.1 *In vitro* bioassays

We compared the *in vitro* toxicity of the compound **1**-**4** with tributyl phosphate (TBP) and halogenated tetrabromo bisphenol A (TBBPA). We investigated the compounds' baseline toxicity as well as their estrogenic and antiandrogenic activities. In concentrations of up to 3 mM, FRs 1-4 showed baseline toxicity in a concentration-dependent manner (Figure S2.20). However, TBBPA was the most potent in inhibiting bacteria luminescence followed by **1**, **2** and TBP (Table S2.1). Compared to that, **4** and **3** were less toxic. We observed an interesting structure-toxicity relationship: The luminescence inhibition induced by the phosphoramides increases with the number of P-N bonds.

Three of the alternative FRs showed a relative antiandrogenic activity of up to 40.59% (**4**). Here, we observed the opposite pattern as for the baseline toxicity: **4** and **3** induced a higher effect (Table S2.1) as the FRs with more P-N bonds, TBP was the most potent antiandrogen. None of the alternative FRs activated the estrogen receptor in the tested concentrations. TBBPA induced a slight estrogenic activity of 6.01% at 3.1 µM, the highest noncytotoxic concentration.

In conclusion, the alternative FRs induced both a certain baseline toxicity and antiandrogenic effects at the investigated concentrations but 2 and 4 represent a good alternative for their halogenated counterparts.

2.9.2.2 Biological activities in fungi, bacteria, hela, and plant cells

In the agar diffusion assay, only TBBPA and **3** inhibited the germination of *P. oryzae* at 5 µg/mL and 50 µg/mL when dissolved in DMSO. **3**, when dissolved in water also inhibited the rice blast

pathogen at 10 µg/mL. Furthermore, we were able to detect a cytotoxic activity of TBBPA, **1**, **3** and **4** of 50%, 25%, 75% and 100% cell death when 50 µg/mL of the compounds were added, respectively. The cytotoxicity effects were interestingly not detectable when the compounds were solved in DMSO. No phytotoxic effect of all tested compounds (50 µg per disc) was observed against *Setaria italica* and *Lepidium sativum*, regardless of the used solvent.

The toxic effects of TBBPA were already discussed and investigated during the last decade.[17-19] The degradation of brominated flame retardants by microorganisms was assayed in recent years.[20,21] In our study, we determined whether brominated flame retardants show a higher toxicity on a wide range of microorganisms and plants as well as a cytotoxic effect than the herein developed phosphorus flame retardants. Especially the fungicidal effect on *Pyricularia oryzae* was perspicuously lower for **1**, **2** and **4** than for TBBPA.

2.9.3 Additional data

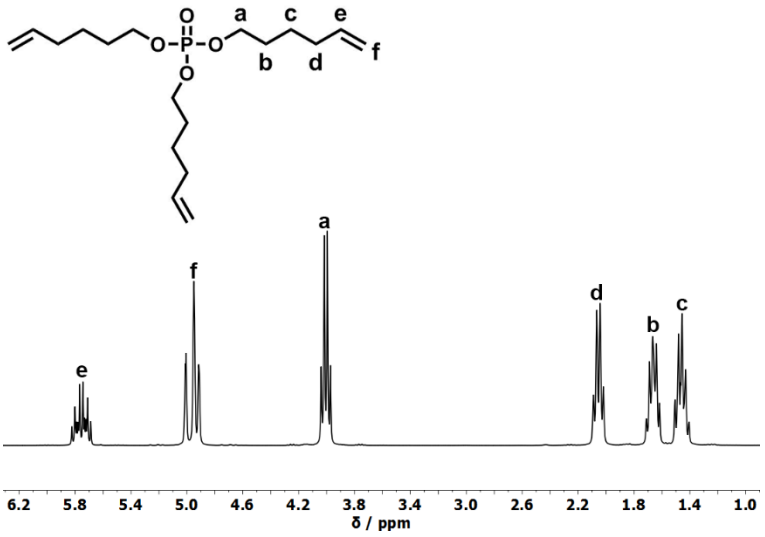

Figure S2.1. ^{1}H-NMR (300 MHz in $CDCl_3$ at 298 K) of **4**.

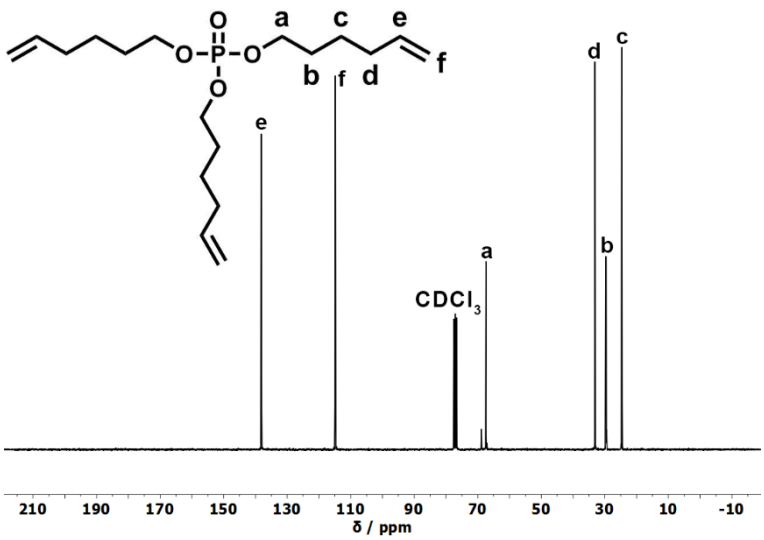

Figure S2.2 ^{13}C {H}-NMR (75 MHz in $CDCl_3$ at 298 K) of **4**.

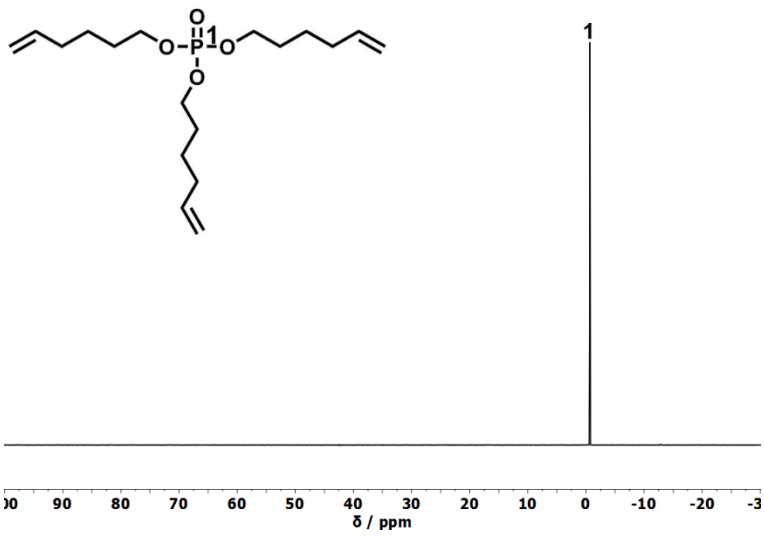

Figure S2.3. ^{31}P {H}-NMR (121 MHz in $CDCl_3$ at 298 K) of **4**.

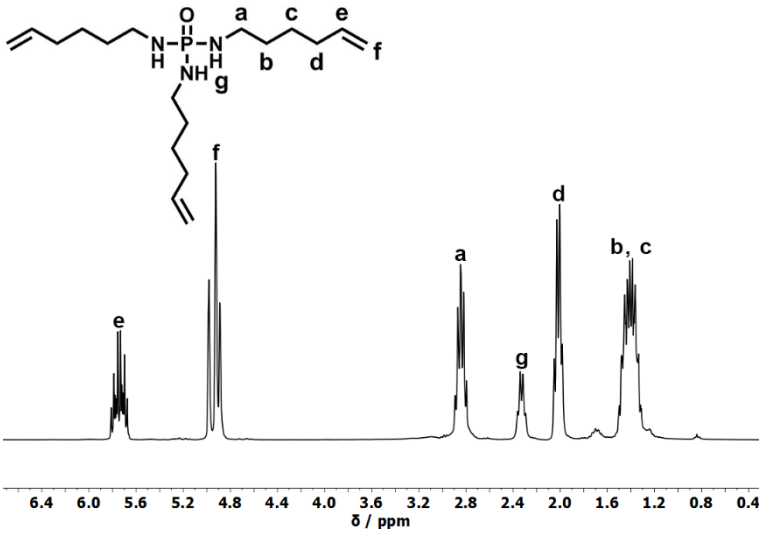

Figure S2.4. ^{1}H-NMR (300 MHz in $CDCl_3$ at 298 K) of **1**.

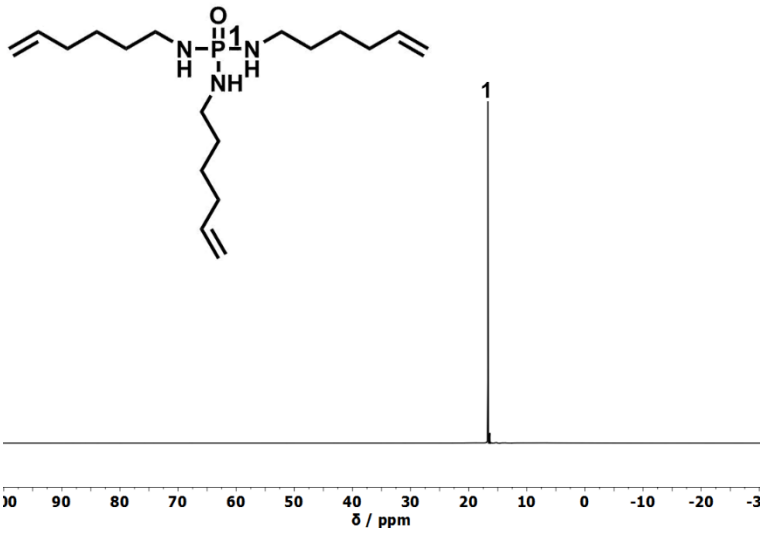

Figure S2.5. ^{31}P {H}-NMR (121 MHz in $CDCl_3$ at 298 K) of **1**.

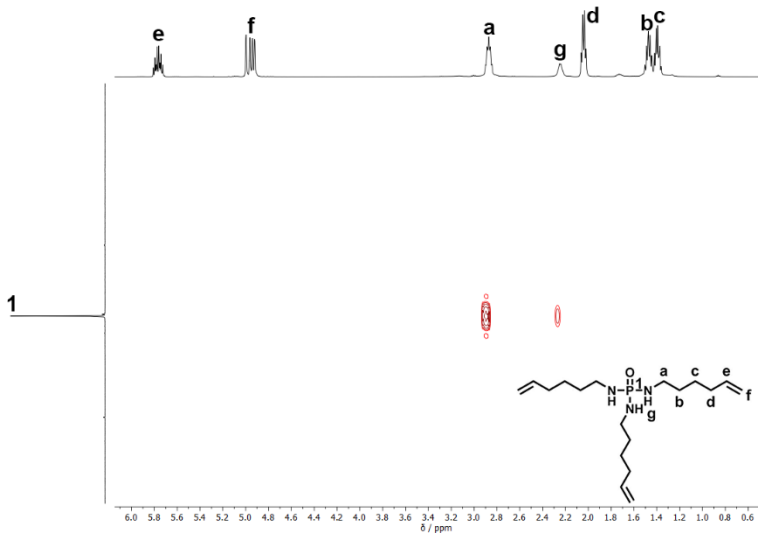

Figure S2.6. ^{31}P {H}-^{1}H-HMBC (200/500 MHz in $CDCl_3$ at 298 K) of **1**.

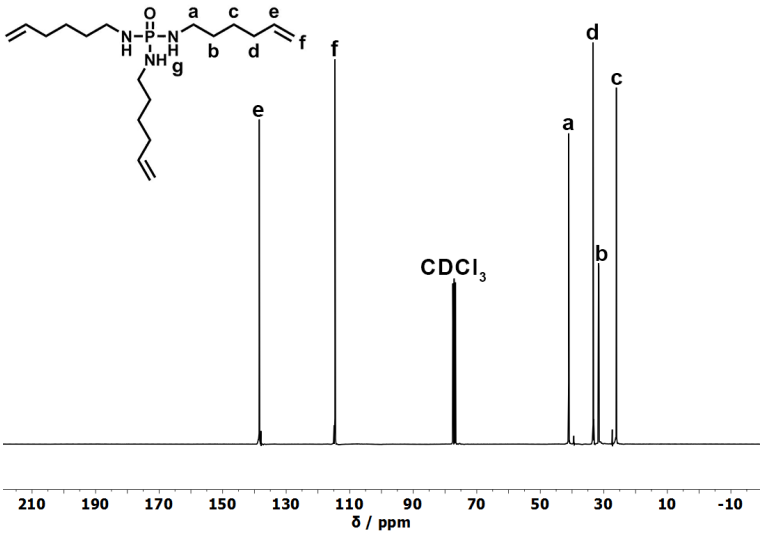

Figure S2.7. ^{13}C {H}-NMR (75 MHz in $CDCl_3$ at 298 K) of **1**.

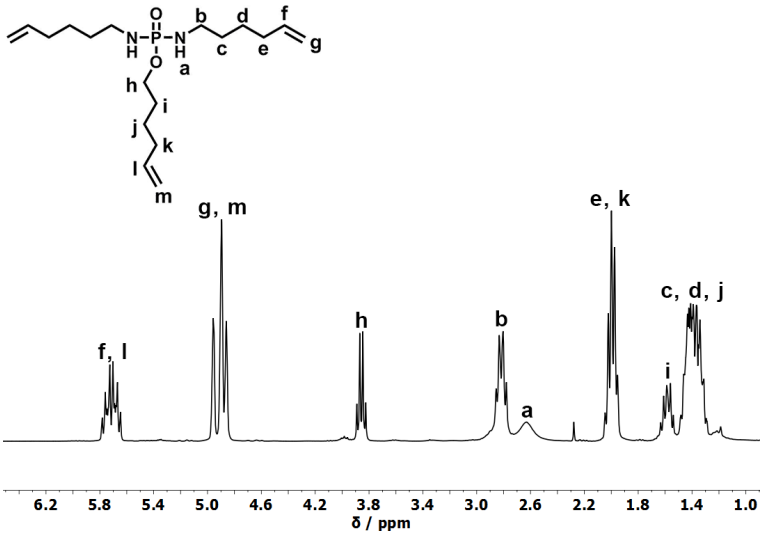

Figure S2.8. ^{1}H-NMR (300 MHz in $CDCl_3$ at 298 K) of **2**.

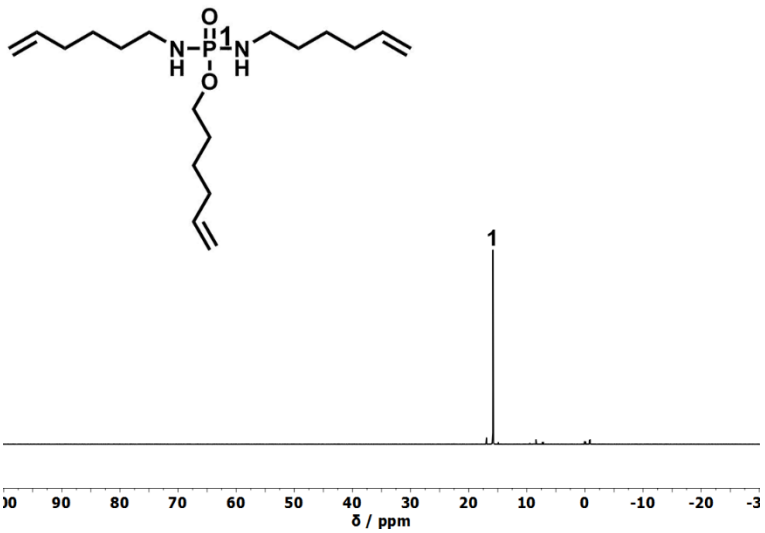

Figure S2.9 ^{31}P {H}-NMR (121 MHz in $CDCl_3$ at 298 K) of **2**.

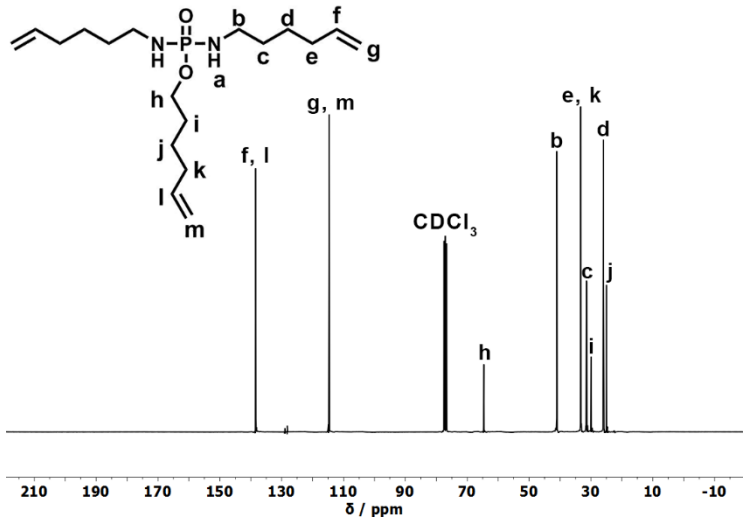

Figure S2.10. ^{13}C {H}-NMR (75 MHz in $CDCl_3$ at 298 K) of **2**.

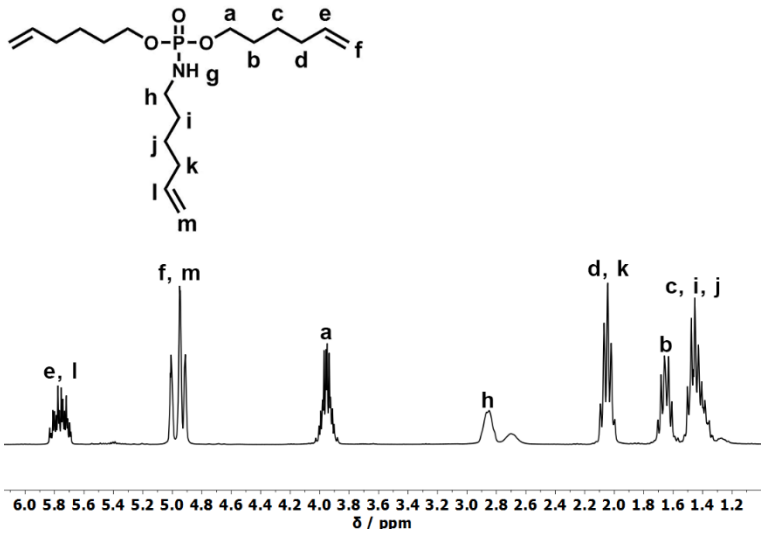

Figure S2.11. ^{1}H-NMR (300 MHz in $CDCl_3$ at 298 K) of **3**.

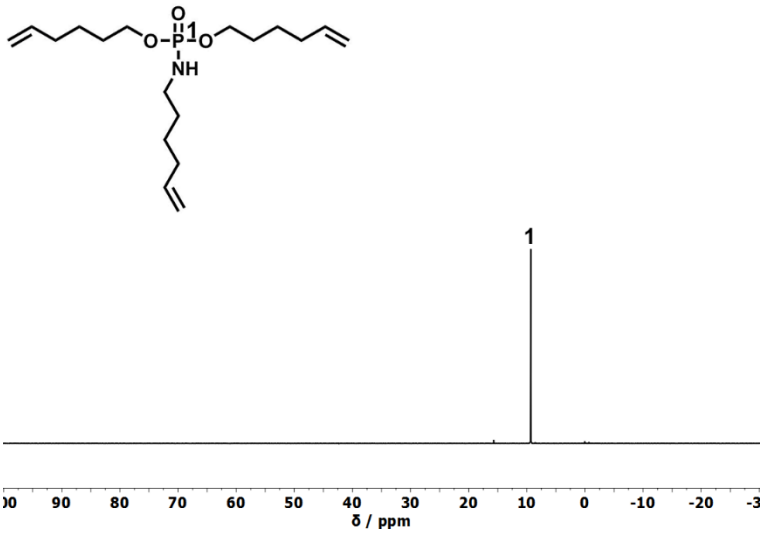

Figure S2.12. ^{31}P {H}-NMR (121 MHz in $CDCl_3$ at 298 K) of **3**.

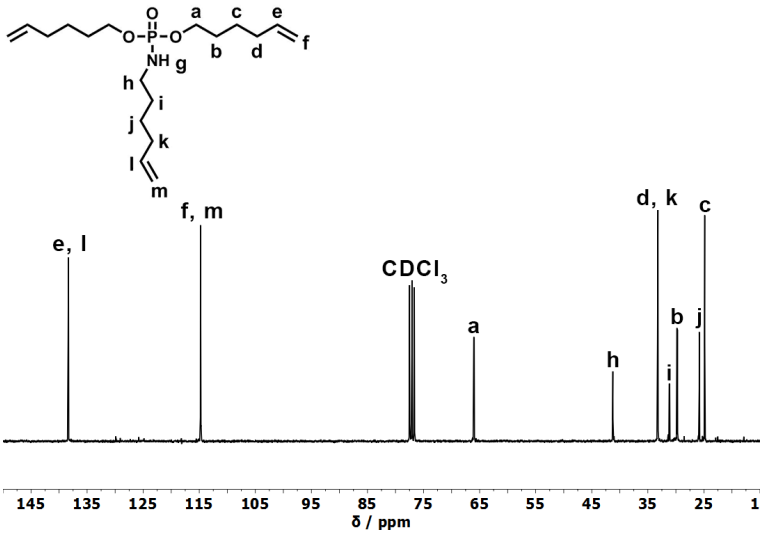

Figure S2.13. ^{13}C {H}-NMR (75 MHz in $CDCl_3$ at 298 K) of **3**.

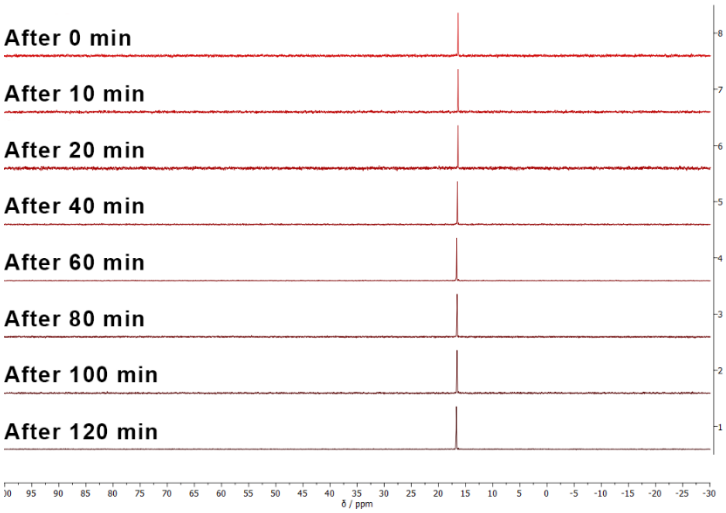

Figure S2.14. ^{31}P {H}-NMR (121 MHz in $CDCl_3$ at 298 K): No reaction of **1** with PGE and DMC under the used epoxy curing conditions.

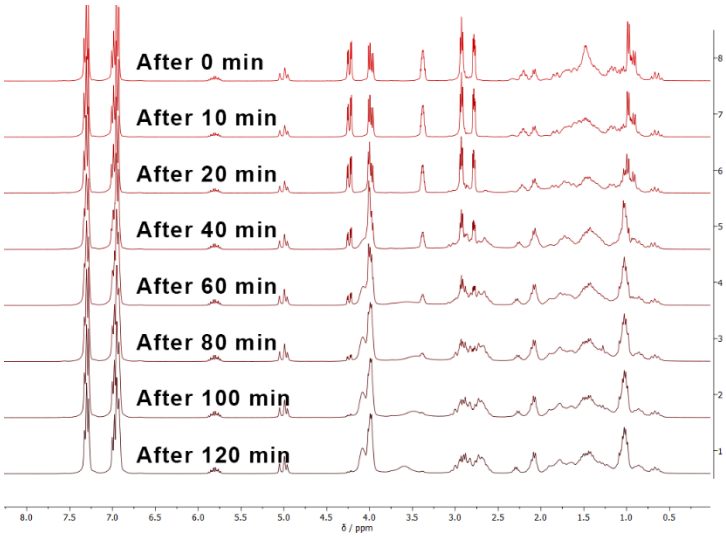

Figure S2.15 ^{1}H-NMR (300 MHz in $CDCl_3$ at 298 K): No reaction of **1** with PGE and DMC under the used epoxy curing conditions.

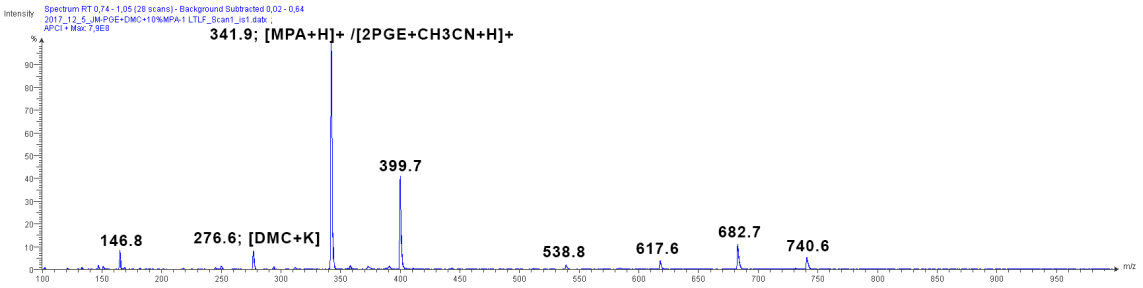

Figure S2.16. After the reaction of **1**, PGE and DMC under the used epoxy curing condition MS still shows the unreacted **1**.

Table S2.1. Baseline toxicity (EC20, of five experiments run in duplicates), relative antiandrogenic and estrogenic activity (EC20 and/or relative activity at highest non-cytotoxic concentration (in brackets), n=24-48) of conventional and alternative flame retardants.

	4	3	2	1	TBP	TBBPA
Baseline toxicity, EC_{20} [mM]	2.07	> 3.00	0.59	0.25	1.17	0.09
Relative antiandrogenic activity, EC_{20} [mM]	1.43	0.31	> 3.00	> 3.00	0.04	> 3.00
Relative antiandrogenic activity [%]	40.59 ± 3.33 (3 mM)	35.02 ± 2.92 (3 mM)	7.41 ± 2.03 (3 mM)	-	45.32 ± 2.31 (100 µM)	-
Relative estrogenic activity [%]	-	-	-	-	-	6.01 ± 0.38 (3.13 µM)

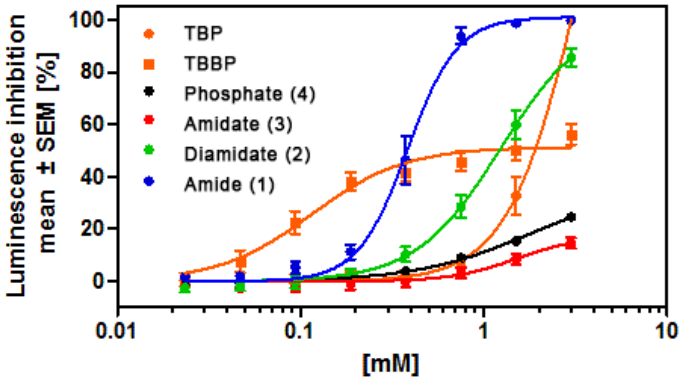

Figure S2.17 Baseline toxicity of conventional and alternative flame retardants (0.02 – 3 mM) as mean luminescence inhibition ± SEM in the Microtox assay. Data were pooled from five independent experiments run in duplicates.

Table S2.2. Summarized raw data of the biological assays.

samble name	solvent	Pyricularia oryzae in H_2O				Pyricularia oryzae in CM				Botrytis cinerea in H_2O	Hela S3		Setaria italica	Lepidium sativum	B. brevis		S. aureus		C. albicans		R. miehei		P. notatum		P. variotii	
		5 µg/ml	10 µg/ml	25 µg/ml	50 µg/ml	5 µg/ml	10 µg/ml	25 µg/ml	50 µg/ml	50 µg/ml	5 µg/ml	50 µg/ml	50 µg/R	50 µg/R	10 µg/R	50 µg/R	10 µg/R	50 µg/R	10 µg/R	50 µg/R	10 µg/R	50 µg/R	10 µg/R	50 µg/R	10 µg/R	50 µg/R
TBBPA	DMSO	+++	+++	+++	+++	+++	+++	+++	+++	-	-	50%	-	-	-	-	-	-	-	-	-	-	-	-	-	-
	H_2O	-	-	-	-	-	-	-	-	-	+	-	+	-	-	-	+	-	-	-	-	+	-	-	-	-
4	DMSO	-	-	-	-	-	-	-	-	-	+	-	+	-	-	-	+	-	-	-	-	+	-	-	-	-
	H_2O	-	-	-	-	-	-	-	-	-	-	100%	-	-	-	-	-	-	-	-	-	-	-	-	-	-
1	DMSO	-	-	-	-	-	-	-	-	-	-	-	-	-	-	-	-	-	-	-	-	-	-	-	-	-
	H_2O	-	-	-	-	-	-	-	-	-	-	25%	-	-	-	-	-	-	-	-	-	-	-	-	-	-
2	DMSO	-	-	-	-	-	-	-	-	-	+	-	+	-	-	-	+	-	-	-	-	-	-	-	-	-
	H_2O	-	-	+	-	-	-	-	-	-	+	-	+	-	-	-	+	-	-	-	-	-	-	-	-	-
3	DMSO	-	-	-	+	-	-	-	++	-	+	-	+	-	-	-	+	-	-	-	+	-	-	-	-	-
	H_2O	-	+	+++	+++	-	-	+++	+++	-	-	75%	+/-	-	-	-	-	-	-	-	-	-	-	-	-	-

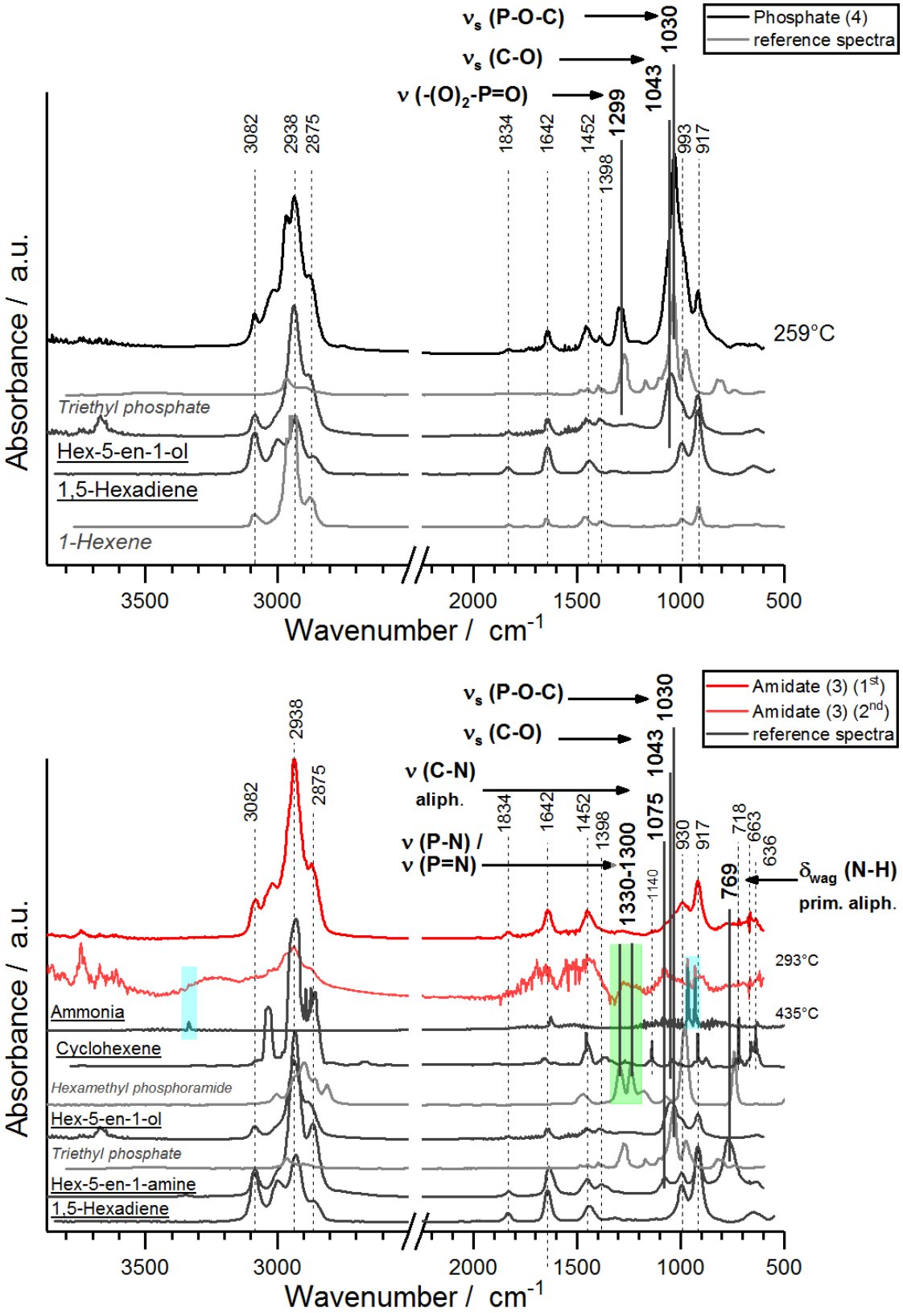
ν_s (P-O-C)
ν_s (C-O)
ν (-(O)$_2$-P=O)
1030
1043
1299
Phosphate (4)
reference spectra
3082
2938
2875
1834
1642
1452
1398
993
917
259°C
Triethyl phosphate
Hex-5-en-1-ol
1,5-Hexadiene
1-Hexene
Absorbance / a.u.
3500
3000
2000
1500
1000
500
Wavenumber / cm^{-1}
ν_s (P-O-C)
ν_s (C-O)
ν (C-N)
aliph.
ν (P-N) /
ν (P=N)
Amidate (3) (1st)
Amidate (3) (2nd)
reference spectra
1030
1043
1075
1330-1300
1140
930
917
769
718
663
636
δ_{wag} (N-H)
prim. aliph.
293°C
435°C
Ammonia
Cyclohexene
Hexamethyl phosphoramide
Hex-5-en-1-ol
Triethyl phosphate
Hex-5-en-1-amine
1,5-Hexadiene

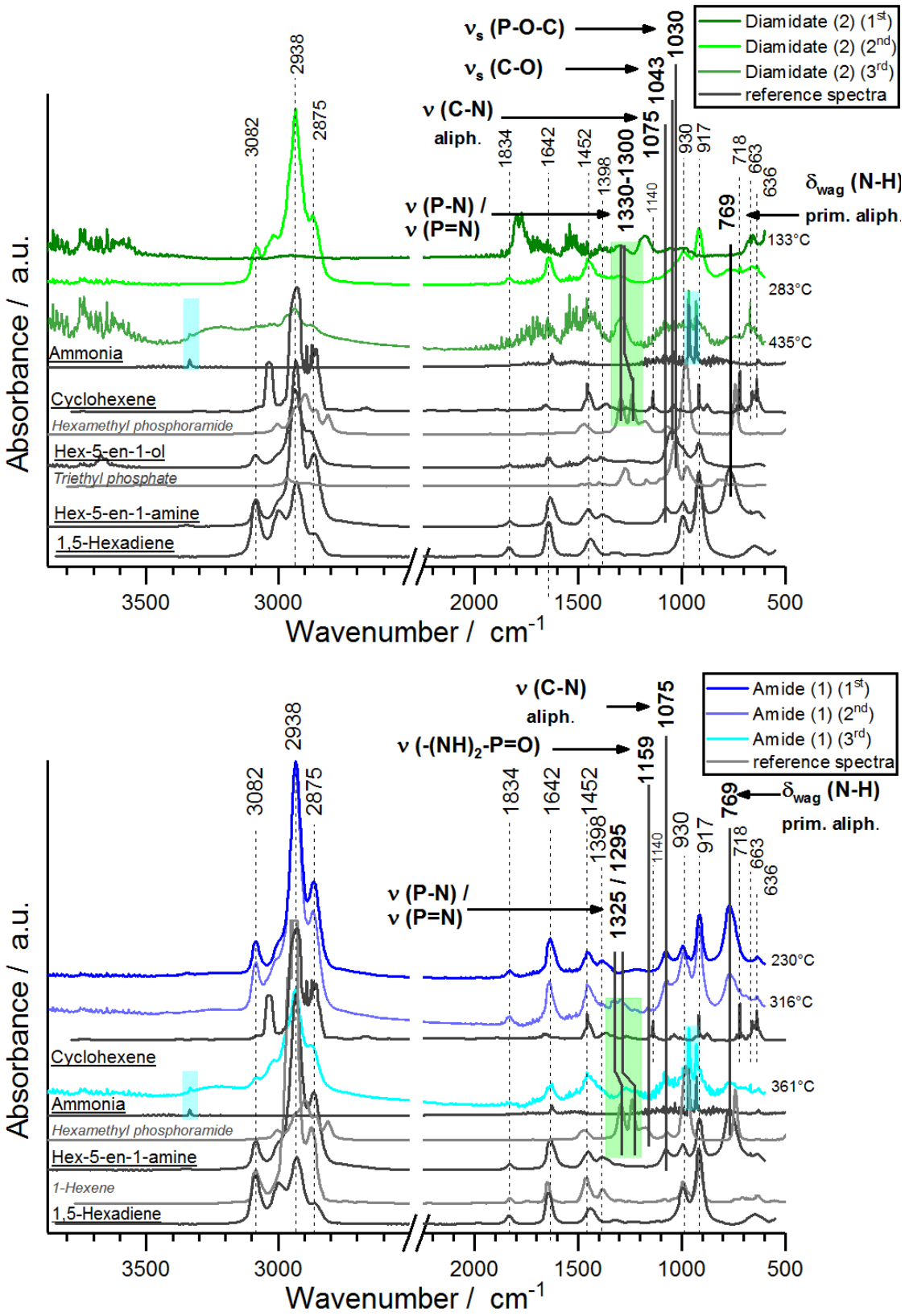

Figure S2.18 Pyrolysis products at T_{max} of raw flame retardants and comparative spectra in N_2 via TG-FTIR. Heating rate: 10 K min^{-1}.

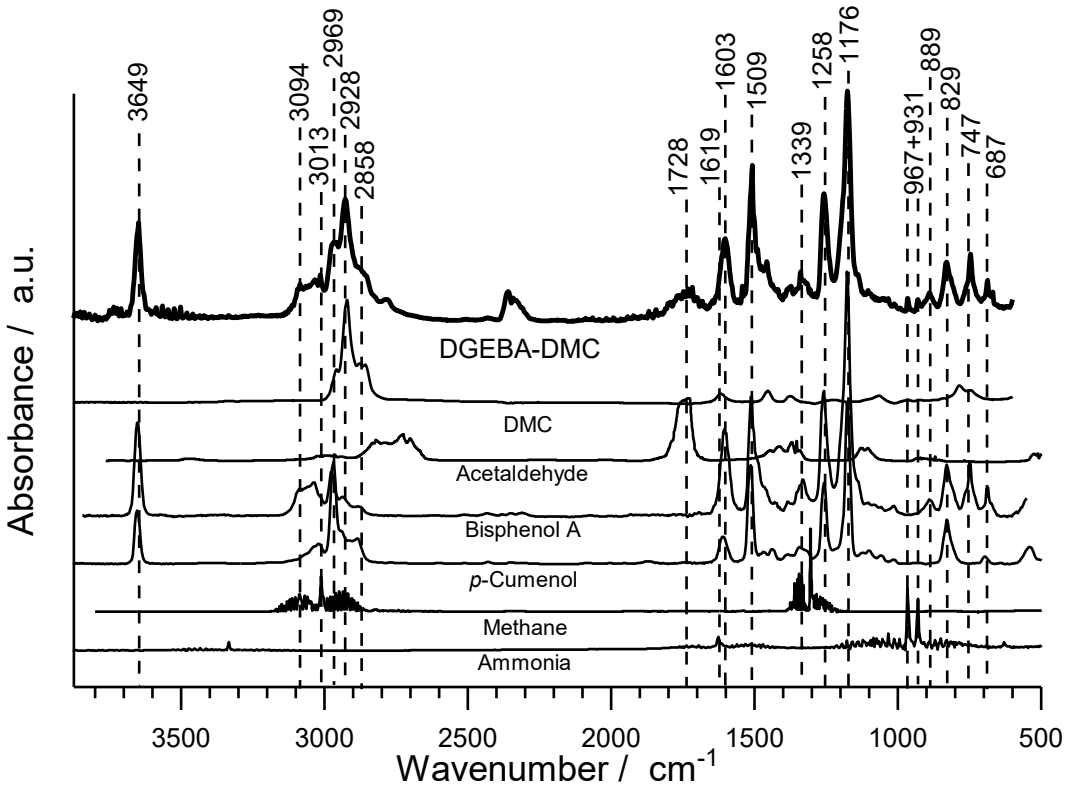

Figure S2.19. FTIR spectrum of pyrolysis products of EPR DGEBA-DMC at T_{max} (*T* = 372°C, *t* = 34.4 min). Below: comparative spectra, taken from NIST.

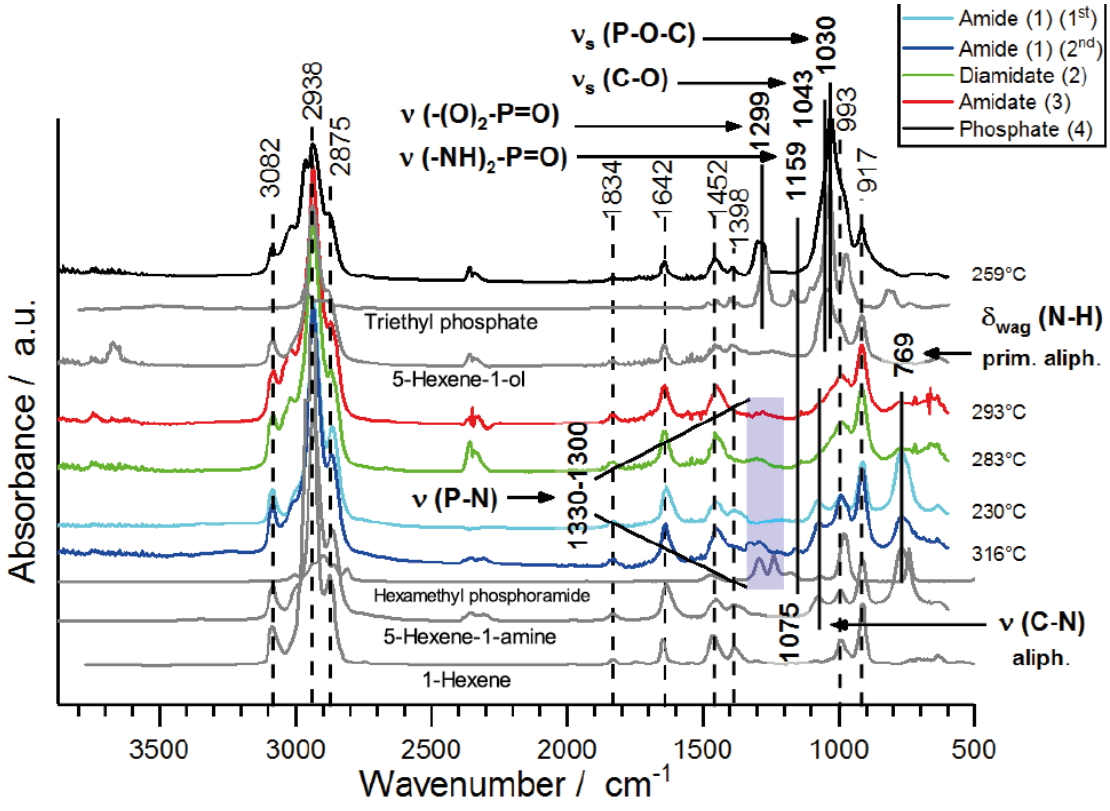

Figure S2.20. TG-FTIR spectra of the first decomposition step of flame retardants.

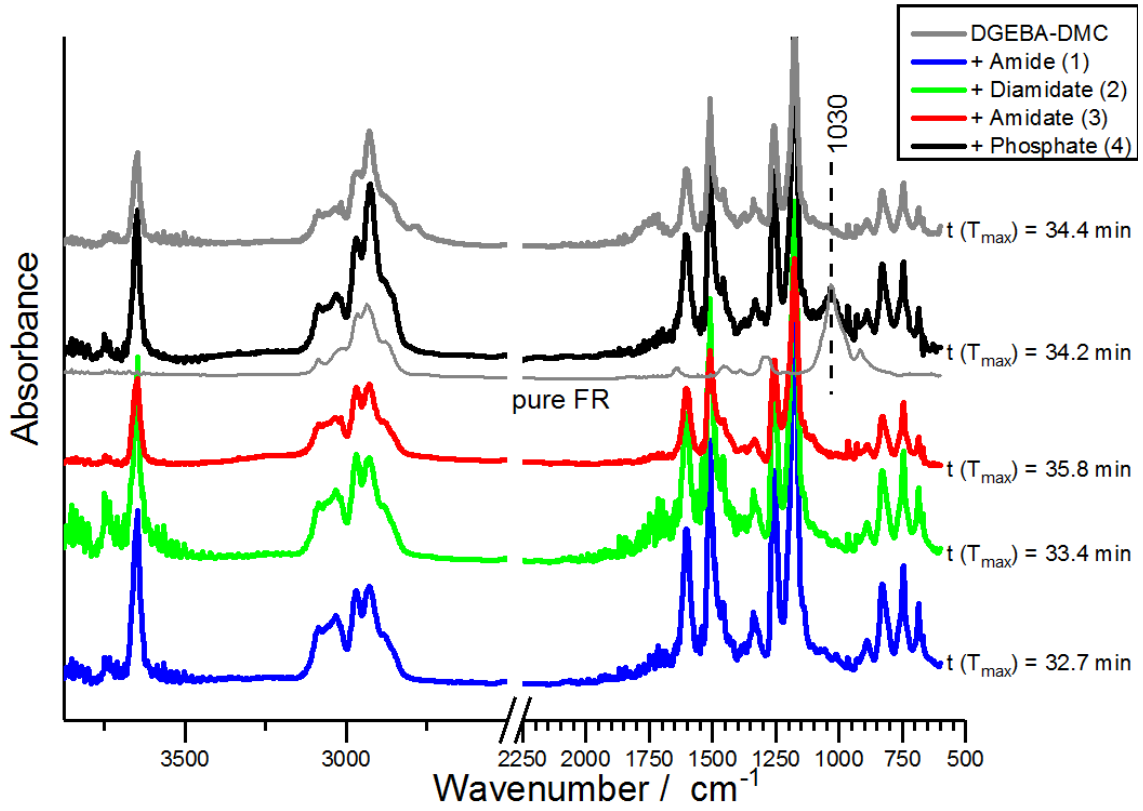

Figure S2.21 Main decomposition step of DGEBA-DMC + FRs.

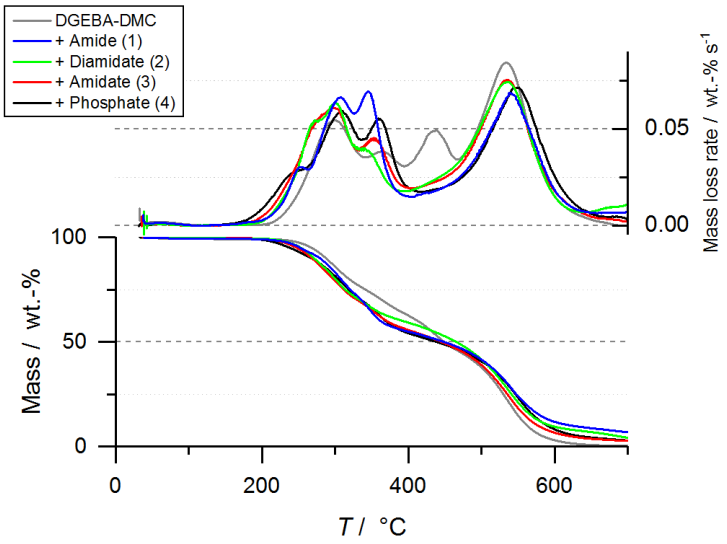

Figure S2.22. Mass loss (bottom) and mass loss rate (top) curves of neat and flame retarded DGEBA-DMC epoxy resins in synthetic air (80:20) via TGA. Heating rate: 10 K min^{-1}.

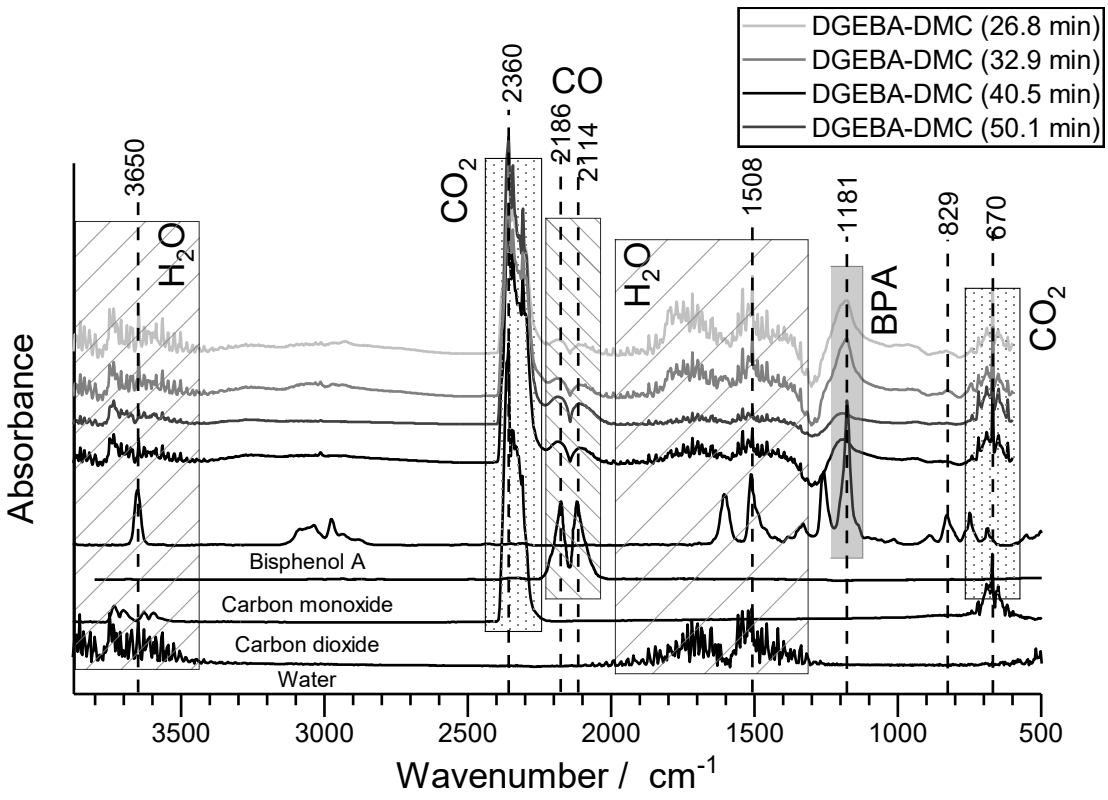

Figure S2.23. Decomposition products at decomposition steps of neat DGEBA-DMC epoxy resin and comparative spectra in synthetic air via TG-FTIR. Heating rate: 10 K min^{-1}.

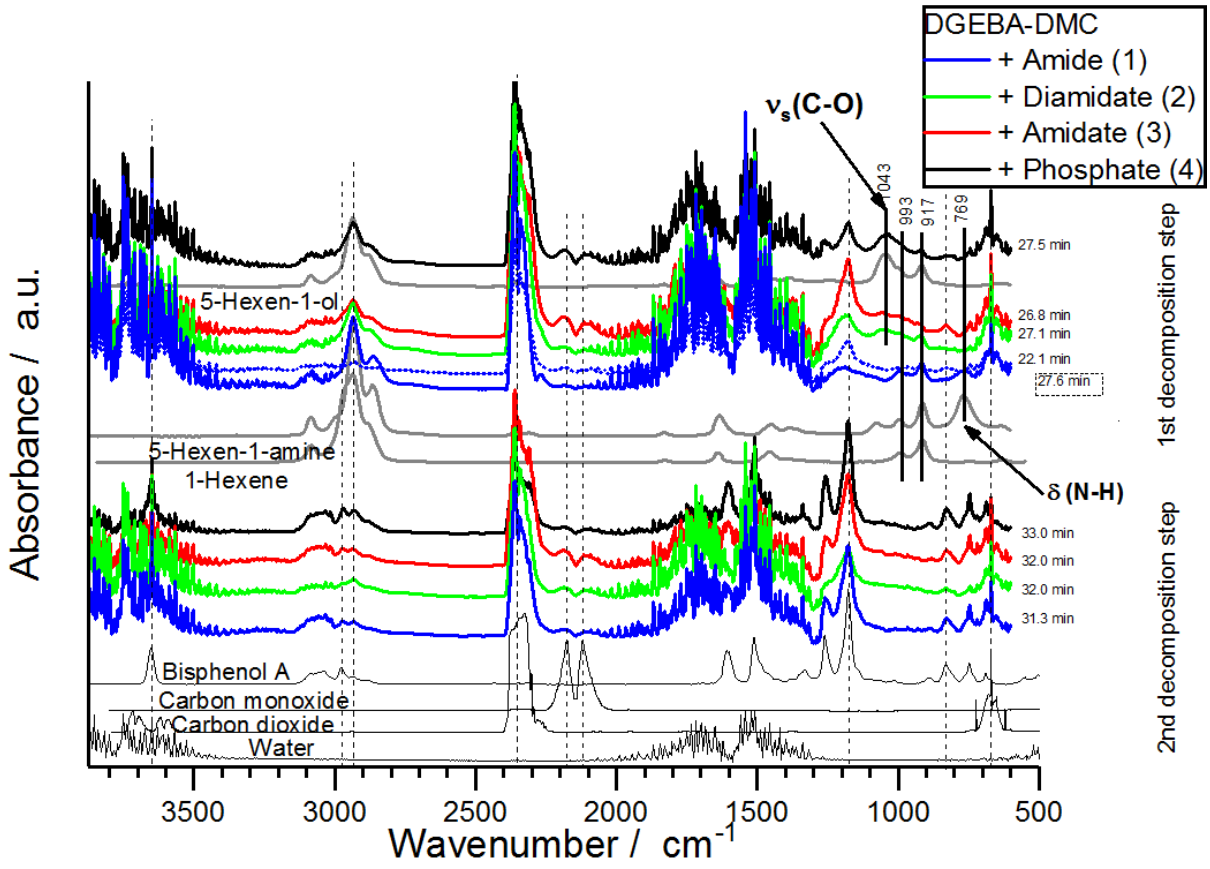

Figure S2.24. Decomposition products at decomposition steps of flame retarded DGEBA-DMC epoxy resin and comparative spectra in synthetic air via TG-FTIR. Heating rate: 10 K min^{-1}.

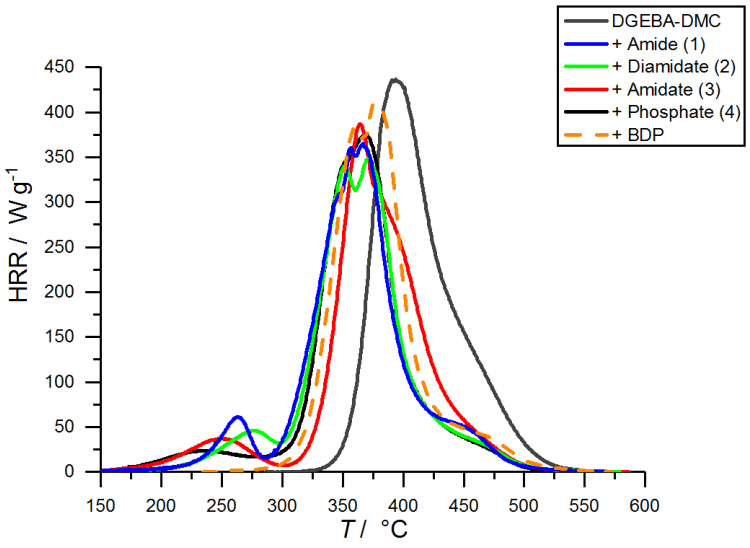

Figure S2.25. Heat release rate curves of neat and flame retarded DGEBA-DMC epoxy resins in N_2 via PCFC. Heating rate: 1 K s^{-1}.

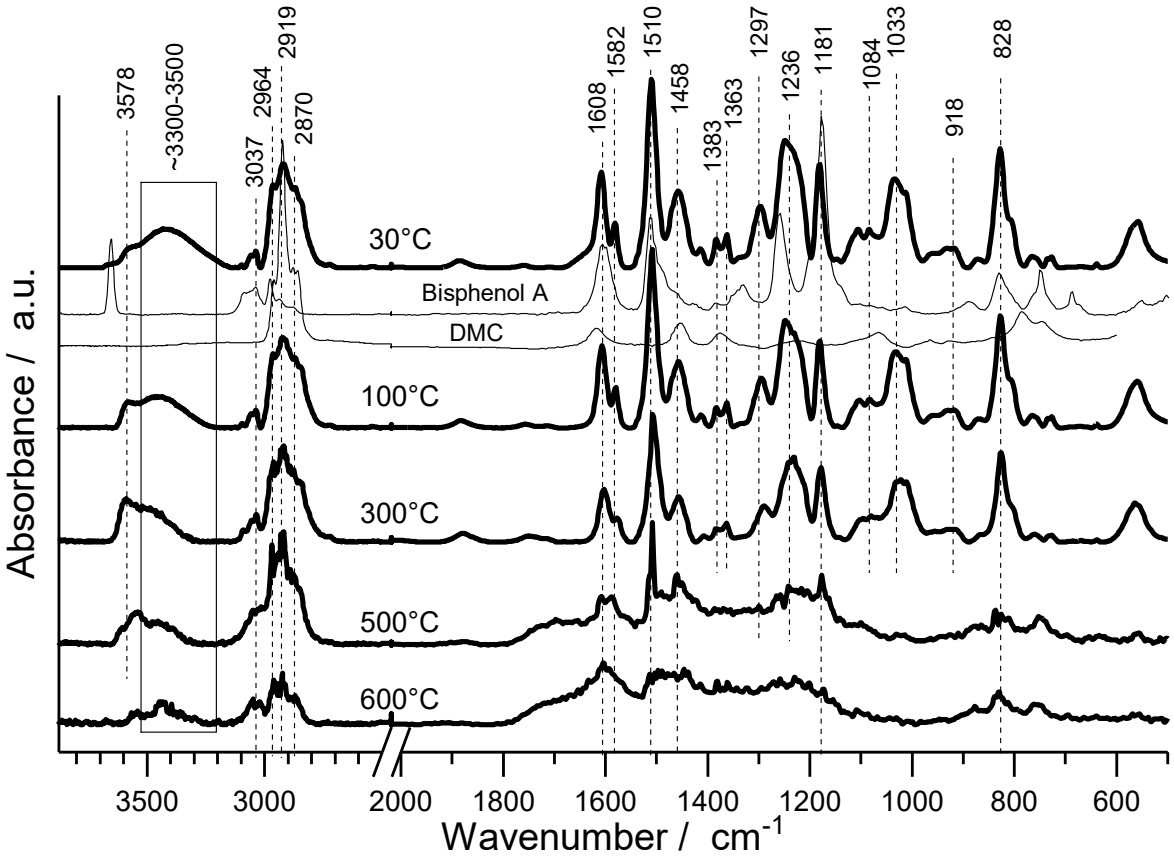

Figure S2.26. Hot stage FTIR spectra of condensed phase of DGEBA-DMC at 30-600 °C.

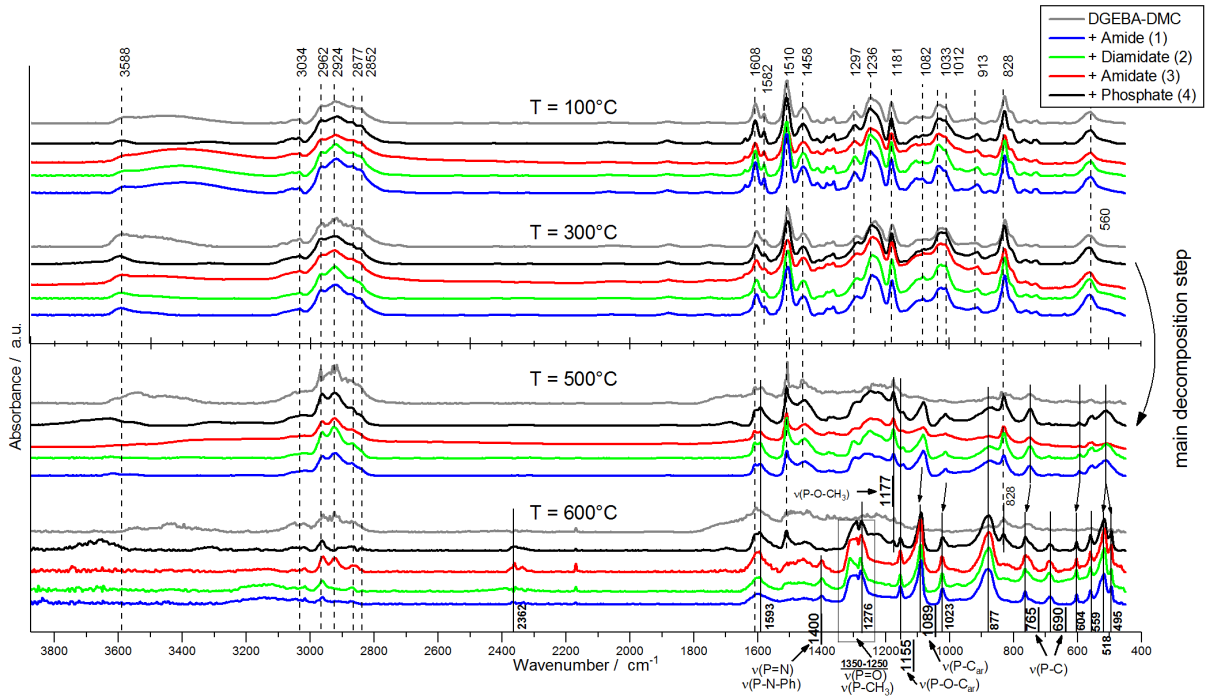

Figure S2.27. Linkam Hot stage FTIR shows clear P-based signals in all FR epoxy resins, but not in pure polymer.

Table S2.3. Assignment of characteristic P bands observed in S29.

Group	Range Literature [cm^{-1}]	Measured [cm^{-1}]
P-H	2400 – 2350 [a]	2362
P-CH_3 (asym)	1450 – 1395 [b]	1400
P-CH_2-R	1440 – 1400 [b]	1400
P-Phenyl	1440 (s) [a]	(1400)
P=O	1300 – 1250 [a]	1276
P-CH_3 (sym)	1346 – 1255 [b]	1276
	1240 – 1180 (P=O) [a]	(1276), (1177), (1155)
P-O-Aryl	1240 – 1190 [a]	(1177)
P-Phenyl	1130 – 1090 [b]	1089
Phosphate (inorganic)	1100 – 1000 [a]	1089, 1023
	1 OH: 1040 – 909 (P=O) [b] 2 OH: 1030 – 972 950 – 917	1023
P-O-Alkyl	1050 – 1030 [a]	1089, (1023)
P-O-P	970 – 910 (wide) [a]	(~877)
P-H (wag)	990 – 885 interacts with C-O-P [b]	~877
P-CH_3	977 – 842 [b]	~877
P-C	754 – 634 [b]	(765), 690
C-C skeletal vibr. (Branched alkanes)	540 – 485 [c]	518, 495

a) M. Hesse, H. Meier, B. Zeeh; Spektroskopische Methoden in der organischen Chemie; 4. überarbeitete Auflage; Georg-Thiem Verlag Stuttgart- New York b) https://faculty.missouri.edu/~glaserr/8160f10/A03_Silver.pdf, c) George Socrates "Infrared and Raman Characterisitc Group frequencies" John Wiley & Sons, 18.06.2004

Table S2.4. Summary of the data gained via cone calorimetry.

Material composition	DGEBA-DMC	+ Phosphate (4)	+ Amidate (3)	+ Diamidate (2)	+ Amide (1)	+ BDP
THR / MJ m^{-2}	108.4 ± 2.6	78.1 ± 6.5	94.9 ± 2.7	93.1 ± 2.5	91.6 ± 1.2	87.5 ± 1.2
PHRR / kW m^{-2}	1696 ± 180	885 ± 16	982 ± 14	889 ± 70	1832 ± 96	1180 ± 41
t_{ig} / s	47 ± 1	39 ± 0	42 ± 1	39 ± 0	38 ± 2	42 ± 6
ML / wt.-%	99.3 ± 0.1	90.9 ± 0.1	92.4 ± 0.4	90.9 ± 2.5	91.6 ± 0.2	96.9 ± 0.2
Residue / wt.-%	0.7 ± 0.1	9.2 ± 0.1	7.6 ± 0.4	9.1 ± 2.6	8.4 ± 0.2	3.1 ± 0.2
EHC / MJ kg^{-1}	26.9 ± 1.0	21.6 ± 1.8	25.6 ± 0.6	25.9 ± 1.1	25.3 ± 1.0	22.7 ± 0.2
χ / -	0.82 ± 0.02	0.65 ± 0.06	0.80 ± 0.02	0.82 ± 0.04	0.75 ± 0.03	0.69 ± 0.01
MARHE / kW m^{-2}	732 ± 24	404 ± 20	481 ± 4	477 ± 1	630 ± 27	546 ± 12
FIGRA / kW m^{-2} s^{-1}	15.5 ± 2.3	9.0 ± 0.2	8.2 ± 0.6	8.0 ± 0.4	9.8 ± 0.7	11.0 ± 0.7
TSP / m^{-3}	28.5 ± 1.1	24.4 ± 6.1	24.1 ± 1.5	29.8 ± 1.9	23.8 ± 0.1	23.8 ± 0.1

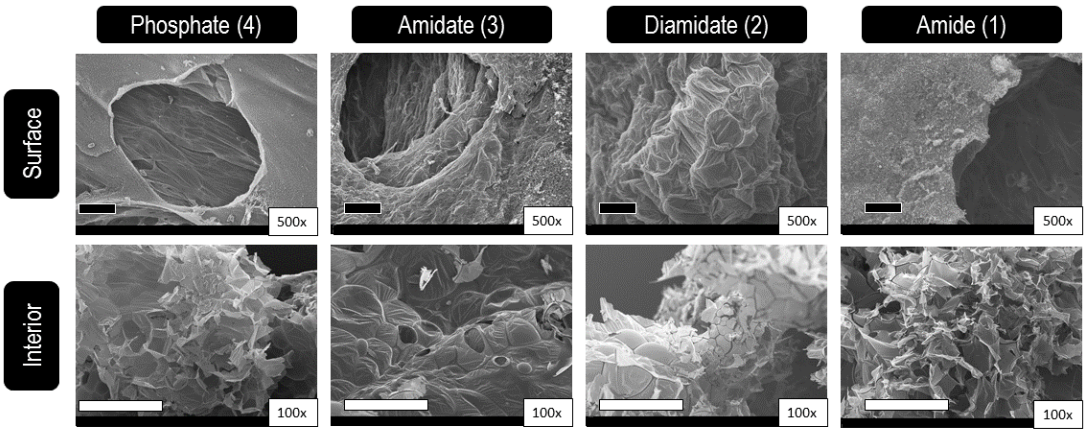

Figure S2.28. Morphology (top row: surface; bottom row: interior) of flame retarded DGEBA-DMC epoxy resin residues via SEM; black bar is equal to 100 µm, white bar is equal to 1 mm.

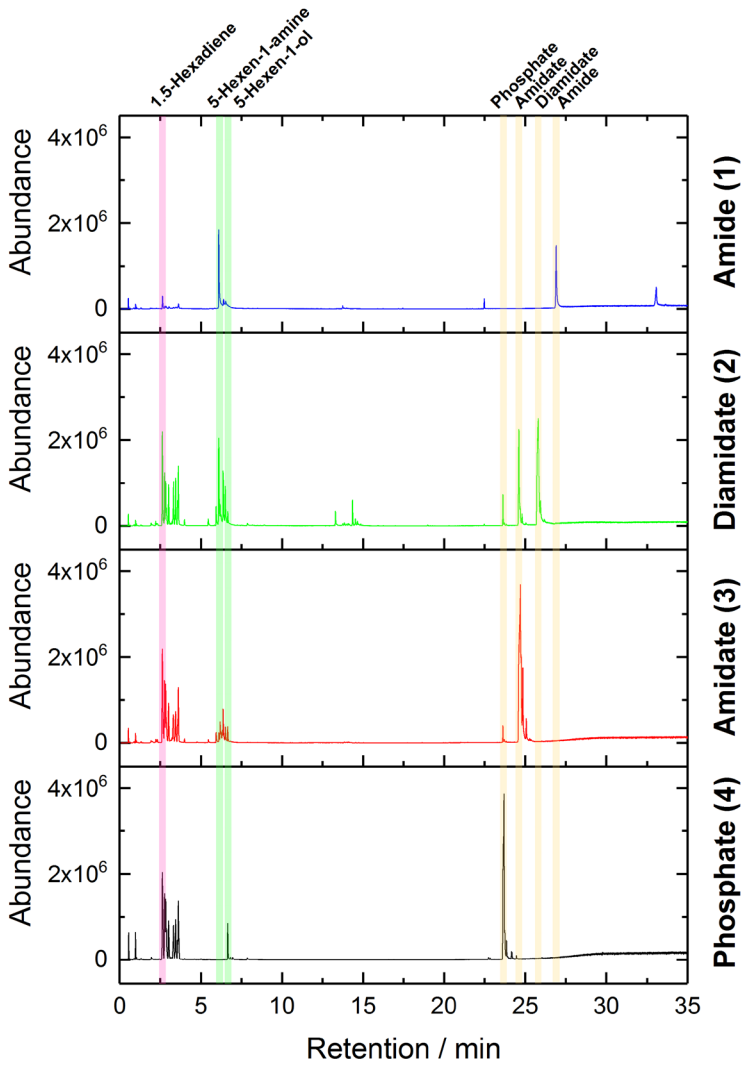

Figure S2.29. Total ion chromatogram of pyrolysis GC MS of the monomeric FRs. Relevant compounds are highlighted and were assigned using NIST14 MS library and GC MS reference spectra of the neat FRs.

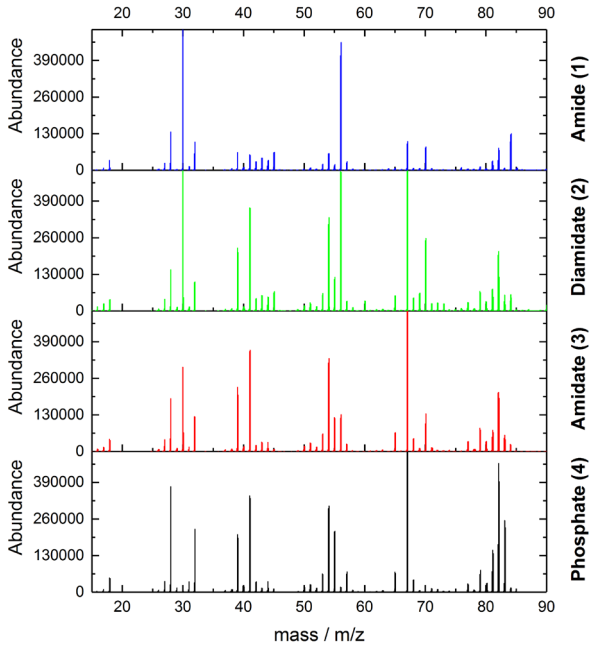

Figure S2.30 Section 1 (red) at 2.63 min in the pyrolysis GC MS total ion chromatogram was assigned to 1,5-hexadiene.

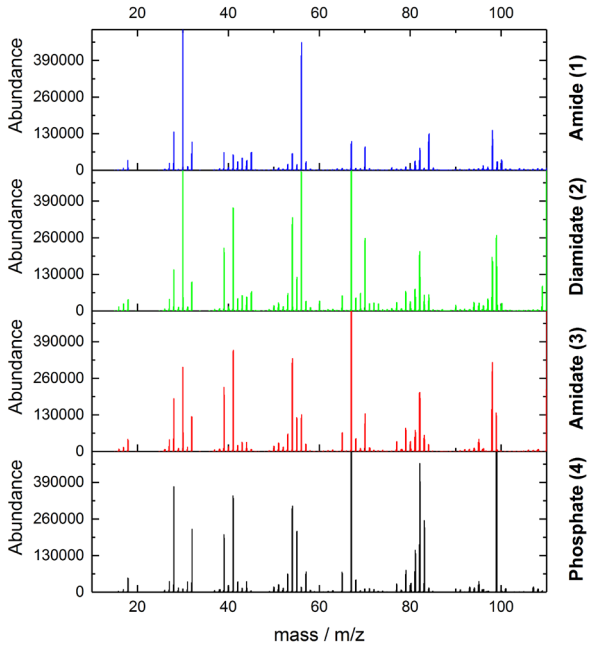

Figure S2.31. Section 2 (green) at 6.1 min in the pyrolysis GC MS total ion chromatogram was assigned to 5-hexen-1-amine.

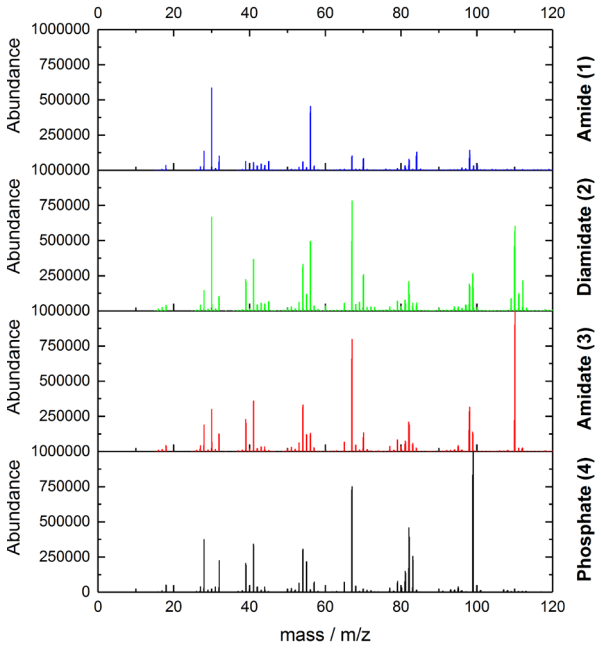

Figure S2.32. Section 3 (green) at 6.7 min in the pyrolysis GC MS total ion chromatogram was assigned to 5-hexen-1-ol.

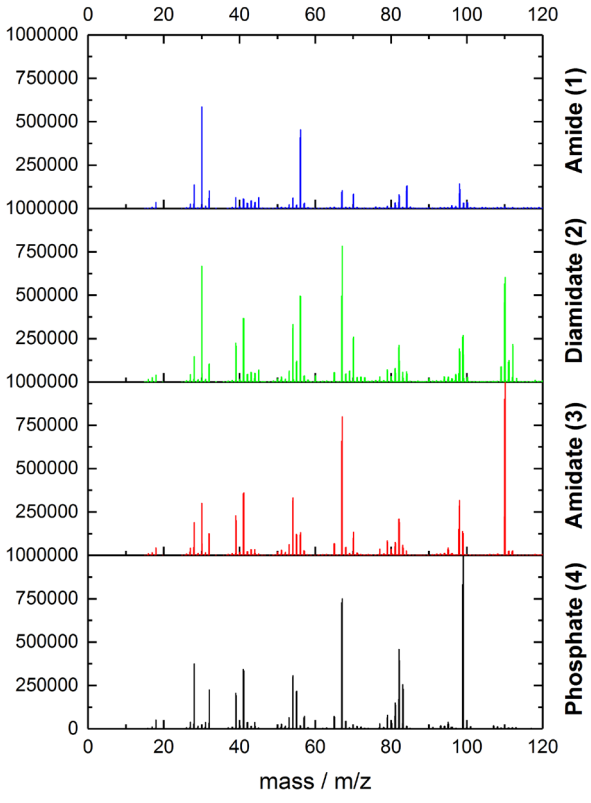

Figure S2.33. Section 4 (orange) at 23.7 min in the pyrolysis GC MS total ion chromatogram was assigned to **4**.

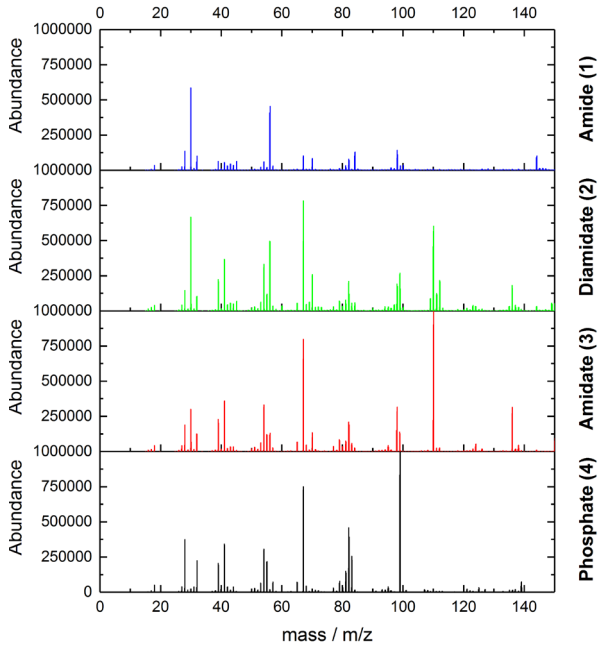

Figure S2.34. Section 5 (orange) at 24.6 min in the pyrolysis GC MS total ion chromatogram was assigned to **3**.

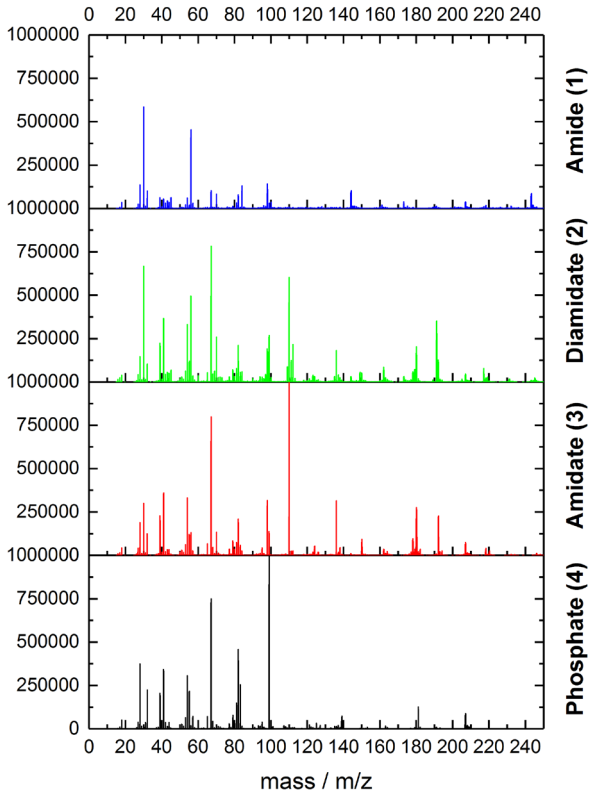

Figure S2.35. Section 6 (orange) at 25.8 min in the pyrolysis GC MS total ion chromatogram was assigned to **2**.

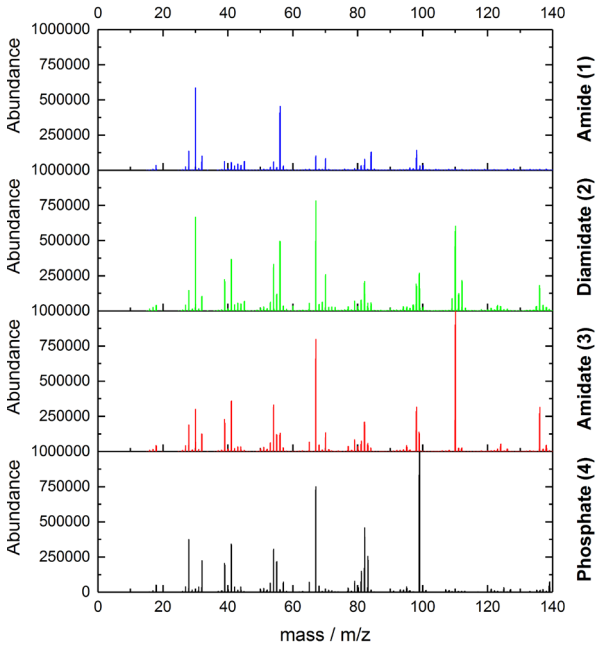

Figure S2.36. Section 7 (orange) at 26.9 min in the pyrolysis GC MS total ion chromatogram was assigned to **1**.

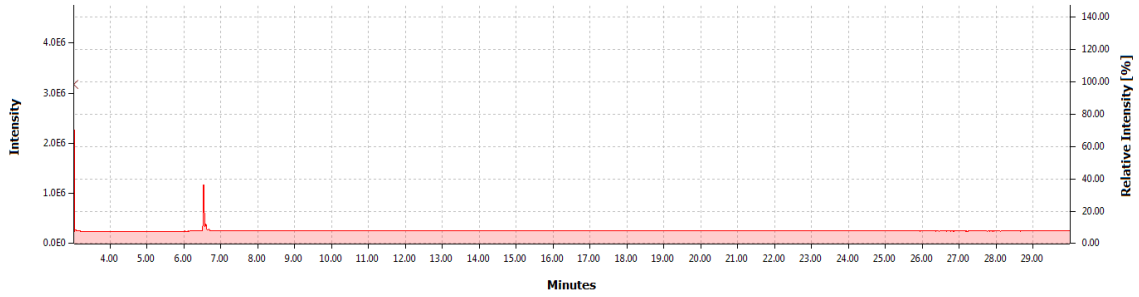

Figure S2.37. Total ion chromatogram of GC MS of **4**.

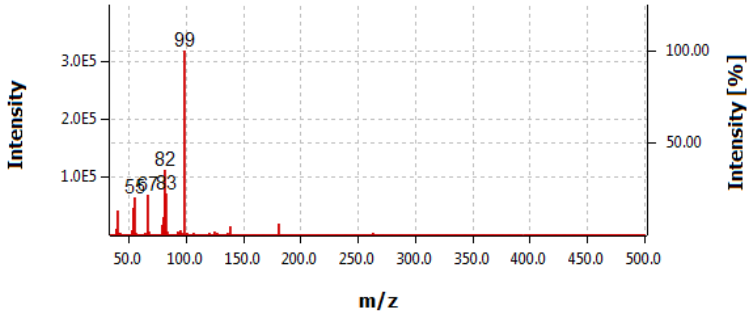

Figure S2.38. Mass spectrum of **4** at 6.53 min.

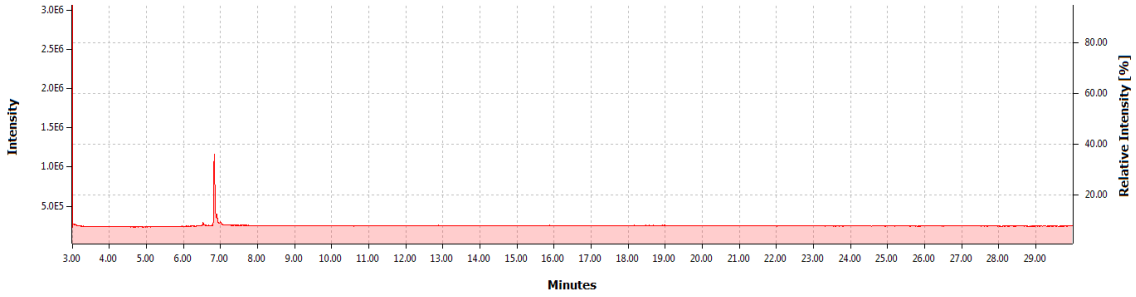

Figure S2.39 Total ion chromatogram of GC MS of **3**.

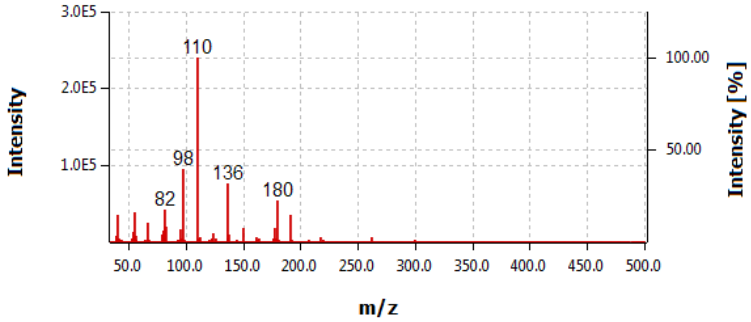

Figure S2.40. Mass spectrum of **3** at 6.83 min.

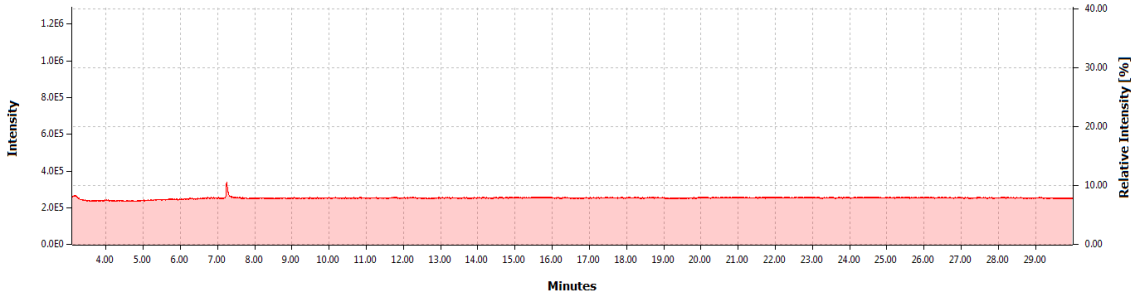

Figure S2.41. Total ion chromatogram of GC MS of **2**.

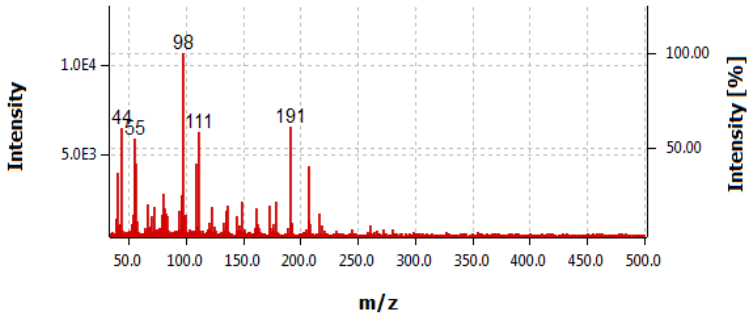

Figure S2.42. Mass spectrum of **2** at 7.25 min.

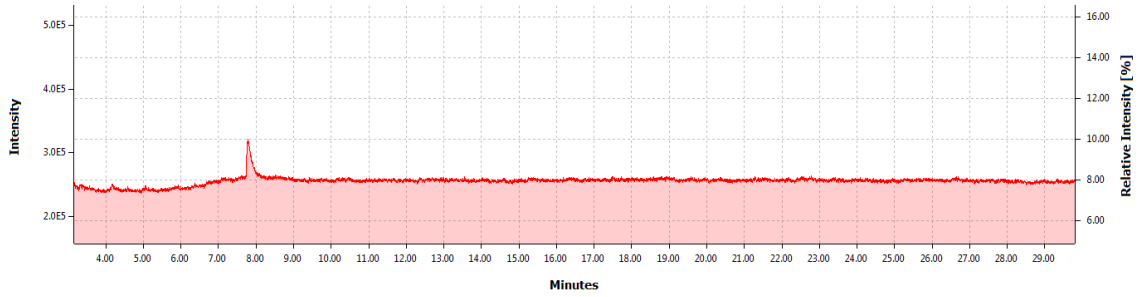

Figure S2.43 Total ion chromatogram of GC MS of **1**.

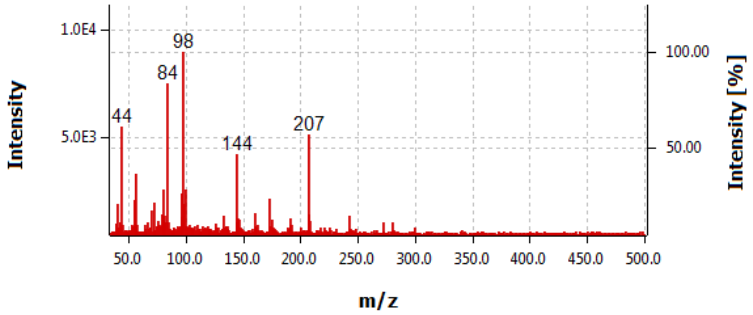

Figure S2.44. Mass spectrum of **1** at 7.78 min.

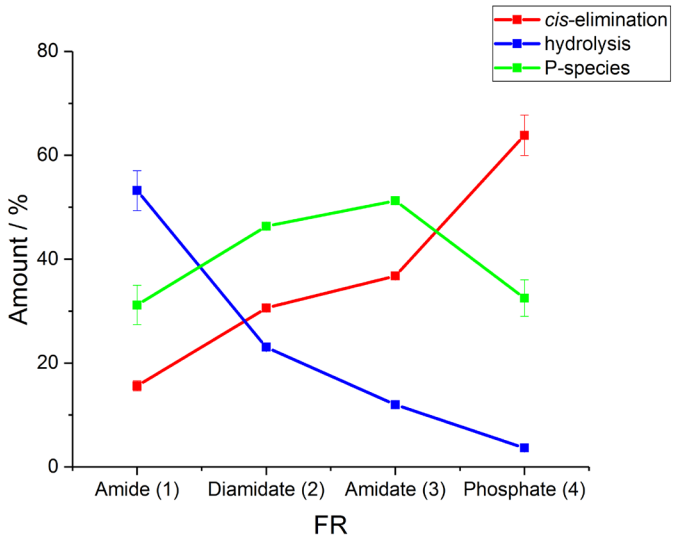

Figure S2.45 Relative amount of *cis*-elimination, hydrolysis and P-species in the released gases during pyrolysis GC-MS.

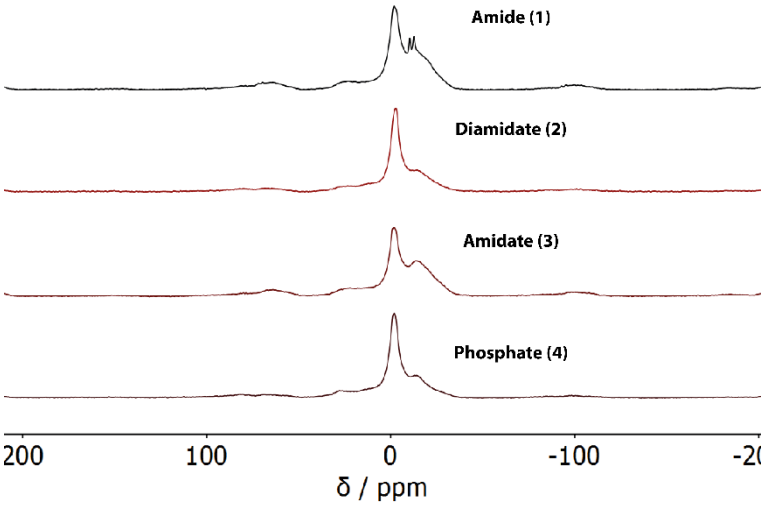

Figure S2.46. ^{31}P CP/MAS solid state NMR (10 kHz) of the char residue after cone calorimeter test.

2.9.4 References SI Chapter 2

[1] B. I. Escher, N. Bramaz, J. F. Mueller, P. Quayle, S. Rutishauser, E. L. M. Vermeirssen, *J. Environ. Monit.* **2008**, *10*, 612-621.

[2] J. Völker, T. Vogt, S. Castronovo, A. Wick, T. A. Ternes, A. Joss, J. Oehlmann, M. Wagner, *Water Res.* **2017**, *116*, 220-230.

[3] E. J. Routledge, J. P. Sumpter, **1996**, *15*, 241-248.

[4] P. Sohoni, J. P. J. T. J. o. e. Sumpter, **1998**, *158 3*, 327-339.

[5] M. Wagner, J. J. E. S. Oehlmann, P. Research, **2009**, *16*, 278-286.

[6] J. Völker, S. Castronovo, A. Wick, T. A. Ternes, A. Joss, J. Oehlmann, M. Wagner, *Environmental Science & Technology* **2016**, *50*, 10606-10615.

[7] D. Odenbach, B. Breth, E. Thines, R. W. S. Weber, H. Anke, A. J. Foster, **2007**, *64*, 293-307.

[8] A. Schüffler, D. Kautz, J. C. Liermann, T. Opatz, T. Anke, *The Journal Of Antibiotics* **2009**, *62*, 119.

[9] N. J. Talbot, D. J. Ebbole, J. E. Hamer, **1993**, *5*, 1575-1590.

[10] A. Schüffler, J. C. Liermann, H. Kolshorn, T. Opatz, H. Anke, *Tetrahedron Lett.* **2009**, *50*, 4813-4815.

[11] H. Anke, O. Bergendorff, O. Sterner, *Food Chem. Toxicol.* **1989**, *27*, 393-397.

[12] F. M. Talontsi, P. Facey, M. D. K. Tatong, M. Tofazzal Islam, H. Frauendorf, S. Draeger, A. v. Tiedemann, H. Laatsch, *Phytochemistry* **2012**, *83*, 87-94.

[13] G. Li, S. Kusari, M. Lamshöft, A. Schüffler, H. Laatsch, M. Spiteller, *J. Nat. Prod.* **2014**, *77*, 2335-2341.

[14] M. Kettering, C. Valdivia, O. Sterner, H. Anke, E. Thines, *The Journal Of Antibiotics* **2005**, *58*, 390.

[15] S. Schoettler, M. Bascope, O. Sterner, T. Anke, in *Zeitschrift für Naturforschung C, Vol. 61*, **2006**, p. 309.

[16] A. Stärk, T. Anke, in *Zeitschrift für Naturforschung C, Vol. 46*, **1991**, p. 989.

[17] L. T. M. Van der Ven, T. Van de Kuil, A. Verhoef, C. M. Verwer, H. Lilienthal, P. E. G. Leonards, U. M. D. Schauer, R. F. Cantón, S. Litens, F. H. De Jong, T. J. Visser, W. Dekant, N. Stern, H. Håkansson, W. Slob, M. Van den Berg, J. G. Vos, A. H. Piersma, *Toxicology* **2008**, *245*, 76-89.

[18] K. K. Kefeni, J. O. Okonkwo, O. I. Olukunle, B. M. Botha, *Environmental Reviews* **2011**, *19*, 238-253.

[19] J. Yang, K. M. Chan, *Aquat. Toxicol.* **2015**, *159*, 138-147.

[20] E. Eljarrat, D. Barceló, *Brominated Flame Retardants*, Springer Berlin Heidelberg, **2011**.

[21] F. Sun, B. A. Kolvenbach, P. Nastold, B. Jiang, R. Ji, P. F.-X. Corvini, *Environmental Science & Technology* **2014**, *48*, 14291-14299.

3. Hyperbranched Phosphorus Flame Retardants: Multifunctional Additives for Epoxy Resins

Alexander Battig,[a]+ Jens C. Markwart,[b,c]+ Frederik R. Wurm,[b]* and Bernhard Schartel[a]*

[a] *Technical Properties of Polymeric Materials - Bundesanstalt für Materialforschung und -prüfung (BAM), Unter den Eichen 87, 12205 Berlin, Germany*

[b] *Physical Chemistry of Polymers - Max Planck Institute for Polymer Research, Ackermannweg 10, 55128 Mainz, Germany*

[c] *Graduate School Materials Science in Mainz, Staudinger Weg 9, 55128 Mainz, Germany*

+ *These authors contributed equally to this work.*

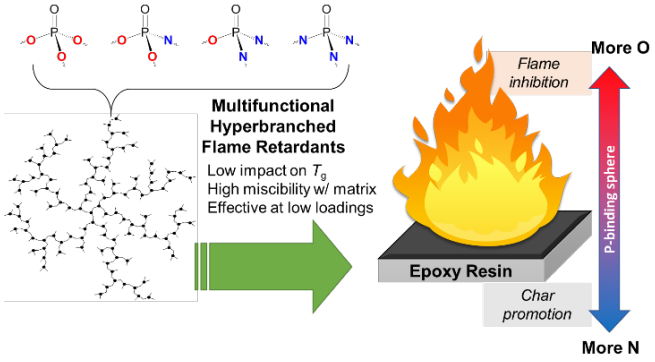

Keywords: Hyperbranched, phosphorus, flame retardancy, multifunctional, phosphates, phosphoramidate, phosphoramide, epoxy resin

3.1 Notes

Alexander Battig performed the flame-retardancy measurements.

3.2 Abstract

We successfully synthesized multifunctional P-based hyperbranched polymeric flame retardants (*hb*-FRs) with varying oxygen-to-nitrogen (O : N) content and characterized them *via* ^{1}H and ^{31}P NMR and GPC. Their miscibility in epoxy resins (EP) and impact on glass-transition temperatures (T_g) were determined *via* differential scanning calorimetry (DSC). Using thermogravimetric and evolved gas analysis (TGA, TG-FTIR), pyrolysis gas chromatography/mass spectrometry (Py-GC-MS), hot stage FTIR, flammability tests UL-94 and LOI, fire testing *via* cone calorimetry, residue analysis *via* scanning electron microscopy (SEM) and elemental analysis, detailed decomposition mechanisms and modes of action are proposed. *hb*-polymeric FRs have improved miscibility and thermal stability, leading to high FR performance even at low loadings. Polymeric, complex FRs increase flame retardancy, mitigate negative effects of low molecular weight variants, and can compete with commercial aromatic FRs. The results illustrate the role played by the chemical structure in flame retardancy and highlight the potential of *hb*-FRs as multifunctional additives.

3.3 Introduction

Polymeric materials are pervasive throughout almost all aspects of modern life. Their tunable properties promote a wide range of applications, from packaging, transport, and construction to consumer electronics, automotive, and aeronautics. In particular, high-performance polymers are increasingly used to reduce weight and improve fuel efficiency in aviation and automobiles, and their material properties are paramount to their effective use. However, plastics are intrinsically flammable and carry a large fire load, consequently prompting the use and continued research into flame retardants (FRs). Due to environmental and toxicological concerns,[1] efforts into developing halogen-free alternatives to improve safety and reduce risks have led to the formulation of effective phosphorus-based FRs (P-FRs).[2-5]

Moreover, there exists a trend towards polymeric FRs, as the blooming out or leaching of low molar mass FRs is undesirable in consumer products.[6] Low molar mass FRs usually possess low thermal stability, thus limiting their processability. Furthermore, the overlap between the decomposition temperatures of the FR and matrix is crucial to achieving good performance.[7,8] In comparison, oligomeric or polymeric FRs are more effective due to their increased thermal stability which leads to improved chemical interactions during decomposition, yielding higher char yields and better overall flame retardancy.[9,10] In addition, FRs with novel architectures have been investigated, highlighting the impact of the complex chemical structure on the mechanical properties and glass-transition temperature (T_g) of the polymer matrix.

One group of polymers which has the potential to merge the approaches of utilizing high molar mass and complex molecular architecture is hyperbranched (*hb*) polymers. *hb* polymers are a group of specialized macromolecules that exhibit a high branching density and are more easily synthesized *via* a one-pot synthesis than other complex polymers.[11,12] A wide array of synthesis routes and applications has been extensively investigated.[13-15]

Due to their unique characteristics, these complex macromolecules have found use in the biomedical field,[16-18] and recently, they have been proposed as FRs for polymers.[19-21] *hb* flame retardants (*hb*-FRs) combine the potential of polymeric FRs with the advantages of complex geometries.[22,23] Their high molar mass and complex architecture lead to high solubility and miscibility with other materials.[24] Chiefly among *hb*-FRs, *hb*-polyphosphoesters have been recently proposed as effective FRs,[25] also in epoxy resins (EP).[26] Additionally, phosphorus (P) and nitrogen (N) containing *hb*-FRs have been investigated,[27,28] as the synergistic qualities of P–N compounds have been widely discussed.[29,30]

In a recent study, we have investigated the flame retardancy effect of P-FRs by systematically varying the structure, namely phosphates, phosphoramidates, phosphorodiamidates, and

phosphoramides, and have proven the differences in the decomposition mechanism and mode of action.[31]

In this article, we synthesized *hb*-FRs from the previously investigated corresponding monomeric FRs by a radical $A_2 + B_3$ thiol–ene polyaddition (Scheme 3.1) and investigated their decomposition mechanism. The aim is to compare the FR potential of *hb*-FRs with varying P–O and P–N contents, and the high molar mass variants are compared to their monomers in terms of flame retardancy mechanisms, mode of action, and efficacy in epoxy resins. The $A_2 + B_3$ strategy was chosen due to its ease of synthesis and potential for up-scaling.[32,33] As P–O and P–N-bonds possess different stabilities and degradation pathways, an optimized FR performance can be obtained by a precise synthesis of P-FRs.[31]

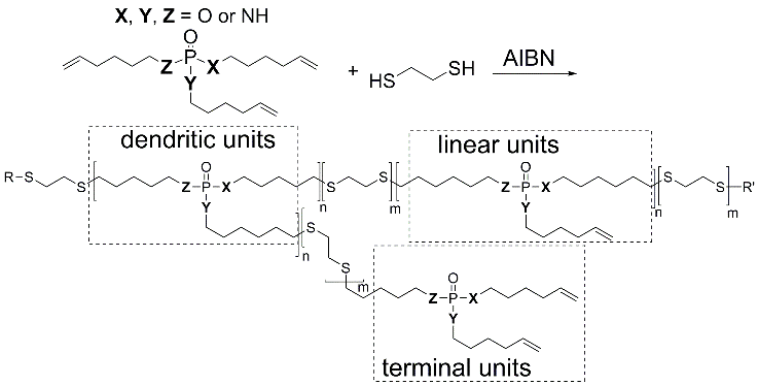

Scheme 3.1. Synthesis of *hb*-FRs *via* an $A_2 + B_3$ thiol–ene polyaddition, and schematic representation of dendritic, linear, and terminal units of the *hb*-structure.

However, the polymerization process alters the end-group functionality and may affect gas-phase activity. It is unclear which flame-retardant affects the *hb* polymeric variants of previously investigated P-FRs. Moreover, the role of complex molecular architecture in the FR's chemical mechanism remains unclear. With this study, investigating the decomposition pathway of distinctively different *hb*-FRs and their mode of action in EP becomes possible, allowing for a deeper understanding of these multifunctional additives as effective FRs for high-performance polymers. Crucially, the material properties of epoxy resins must be conserved, and by comparing these aliphatic *hb*-FRs to a state-of-the-art, commercially available benchmark FR, their performance can be more accurately estimated. While there have been many reports on P-FR formulations for epoxy resins,[34] of which some studied one type of *hb*-FR,[35,36] this study aims at investigating four high-molar mass *hb* P-FRs with systematically varying P–O and P–N contents which are able to retain the material properties of DGEBA-based EP. The results of material and flame retardancy studies aid in optimizing future design of P-FRs.

3.4 Results and discussion

3.4.1 Hyperbranched flame retardants (*hb*-FRs)

3.4.1.1 Chemical synthesis and structure identification

The influence of the P–O *vs.* P–N ratio on the FR efficiency of low molecular weight P-FRs has been studied recently.[38] To explore the influence of polymeric materials in comparison with monomeric materials, we extended this systematic library with the respective *hb*-polymers. *hb*-Polyphosphoramide (**1**), *hb*-polyphosphorodiamidate (**2**), *hb*-polyphosphoramidate (**3**), and *hb*-polyphosphate (**4**) were synthesized starting from the respective B_3-monomers in a radical thiol–ene polyaddition using 1,2-ethanedithiol as an A_2-comonomer and AIBN followed by precipitation into *n*-hexane or toluene (Scheme 3.1). The successful $A_2 + B_3$ polymerization was indicated by a reduction in the double-bond resonances in the ^{1}H NMR spectra and the detection of a new singlet at 2.71 ppm and a triplet at 2.55 ppm (see the ESI†). By these procedures, all P-FRs were easily available up to at least 80 g with standard university lab equipment. Fig. S3.1–S3.3† show the ^{1}H NMR spectra of the *hb*-polymers with varying oxygen-to-nitrogen (O : N) ratios. The spectrum of the monomeric phosphate in Fig. 3.1a highlights the change from the monomeric to polymeric structure. Here, the appearance of a CH_2 group (triplet) at 2.55 ppm signified a successful polymerization, as it corresponds to the methylene group adjacent to the thioether. The singlet at 2.71 ppm belongs to the two methylene groups between the two thioether linkages. The signals from 1.70 to 1.38 ppm were attributed to the methylene groups of the alkyl chain. Fig. S3.4–S3.7† show the ^{31}P {H} NMR spectra of the hyperbranched polymers with varying O : N ratios. The resonance of the P-atom shifted depending on its chemical surroundings to lower field with increasing nitrogen content surrounding P (from 17.13 ppm for **1** to −0.66 ppm for **4**).

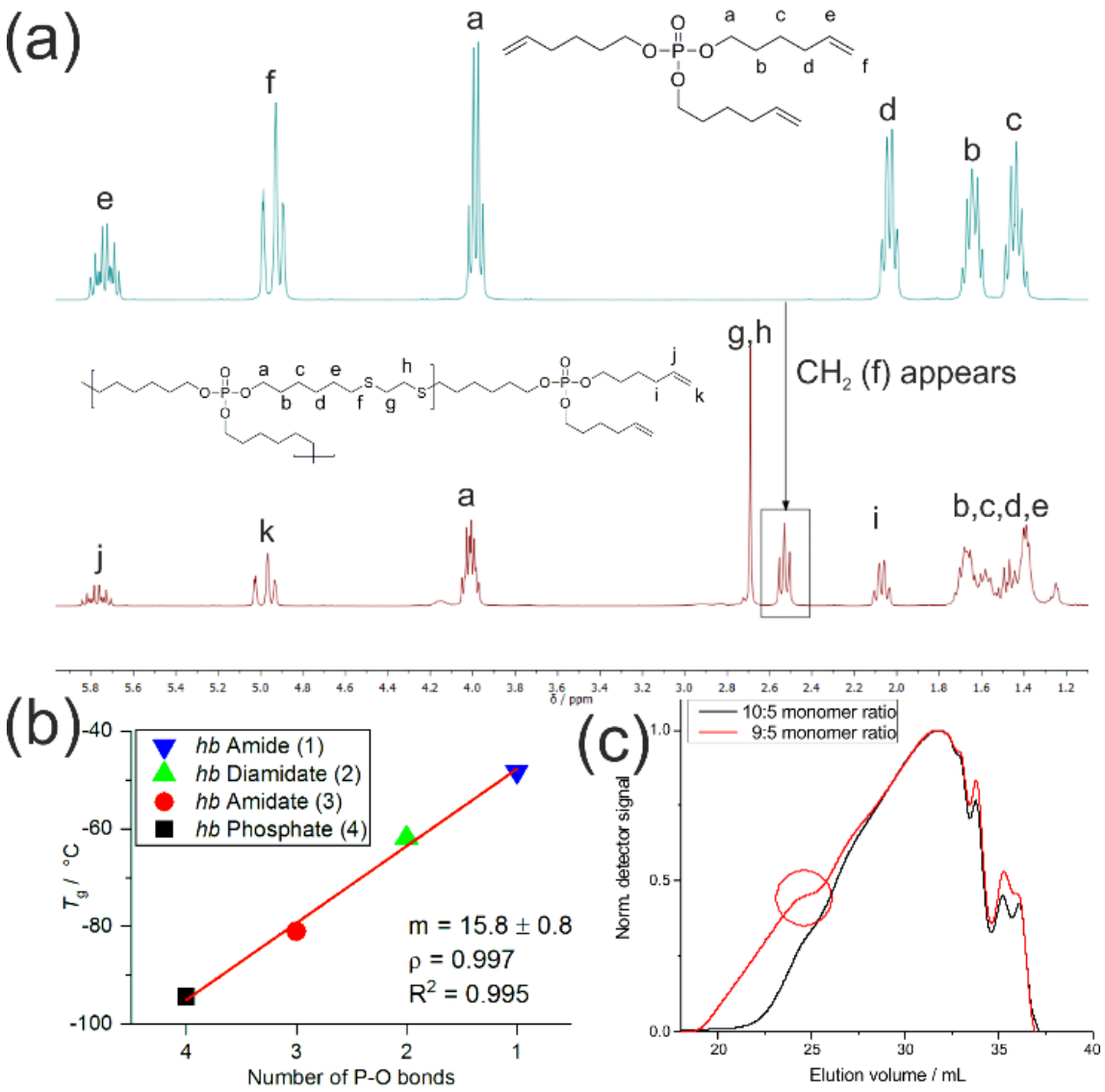

Figure 3.1. (a) ^{1}H NMR (300 MHz in $CDCl_3$ at 298 K) of tri(hex-5-en-1-yl)phosphate (top) and *hb*-polyphosphate (**4**) (bottom). The appearance of the singlet (g and h) and the triplet (f) signifies successful thiol–ene reactions. (b) Relationship between the number of P–O bonds in *hb*-FRs and their glass transition temperature (T_g) *via* differential scanning calorimetry (DSC). Linear fit (red line) with a slope (*m*), Pearson's correlation coefficient (ρ) and its square (R^2). (c) GPC-elugrams (RI detection) of A_2 + B_3 polymerization to **4** at different monomer feed ratios. The red circle indicates the beginning of gelation.

As an A_2 + B_3 polymerization can produce both cross-linked and soluble *hb*-polymers,[24] depending on the polymerization conditions and monomer feed ratios, we optimized the polymerization conditions using **4** as an example. Table S3.1† summarizes the conditions which were varied to produce soluble polymers compared to cross-linking, yield and molecular weights for different monomer feed ratios. For all molar feed ratios up to 8 : 5 (thiols of the A_2 *vs.* double bonds of the B_3), cross-linking was observed. For molar ratios 5 : 9, 5 : 10 and 5 : 11, no gelation occurred, and soluble polymers were obtained. The molecular weights decreased with increasing excess of the

B_3-monomer. Also, the 5 : 9 ratio did not always prevent cross-linking, most probably due to variations in the mixing process by the mechanical stirrer. GPC elugrams also sometimes exhibited shoulders to lower elution volumes, indicating an onset of gelation under these conditions (Fig. 3.1c). Although the 5 : 9 ratio provided the highest molecular weights after 24 h of polymerization, the broadest molar mass dispersity with *ca.* M_w/M_n = 12 was obtained. The 5 : 11 and 5 : 10 ratios both prevented gelation and resulted in lower molar masses. We chose the 5 : 10 ratio for the following studies as it prevented gelation effectively and resulted in higher molar masses than the 5 : 11 ratio. All polymers were obtained in yields of 76–89% as off-white and viscous oils.

3.4.1.2 Material properties

The glass-transition temperatures (T_g) of the *hb*-polymers were investigated *via* differential scanning calorimetry (DSC), indicating the fully amorphous behavior of all synthesized polymers (Fig. S3.17 and Table S3.2†). The glass-transition temperature increased linearly with the reduction of P–O bonds, *i.e.* an increase of P–N bonds, in the *hb*-polymer structure (Fig. 3.1b). The T_g of the *hb*-polyphosphate was detected at −94 °C and increased by approx. 16 °C for each subsequent N bound to P to *ca.* −48 °C for **1**.

3.4.1.3 Pyrolysis

The decomposition behaviors of the *hb*-FRs under pyrolytic conditions were investigated using TGA (Fig. 3.2a and Table S3.3†). The mass loss curve of the *hb*-phosphate (**4**) exhibited a main single decomposition step at 274 °C (81 wt% mass loss) with a gradual decomposition thereafter. The *hb*-amidate (**3**) displayed a mass loss curve similar to **4**: its onset temperature ($T_{5\%}$) and temperature of maximum mass loss rate (T_{max}) were in a similar range (242 °C and 281 °C, respectively); however, the main decomposition step presented an additional shoulder that extended over a range of approx. 40 °C and peaked at 335 °C. Additionally, a small decomposition step (approx. 8 wt%) appeared at 481 °C. The *hb*-diamidate (**2**) exhibited a decomposition step which extended over a large temperature range from $T_{5\%}$ at 194 °C to just before T_{max} at 359 °C. Similarly, the *hb*-amide (**1**) also showed a steady decomposition between $T_{5\%}$ at 190 °C until shortly before T_{max} at 361 °C. For both **1** and **2**, a small decomposition step (approx. 10 wt%) occurred at 463 °C and 428 °C, respectively. The amount of residue increased from 11.2 wt% for **4** to 17.6 wt% for **1**.

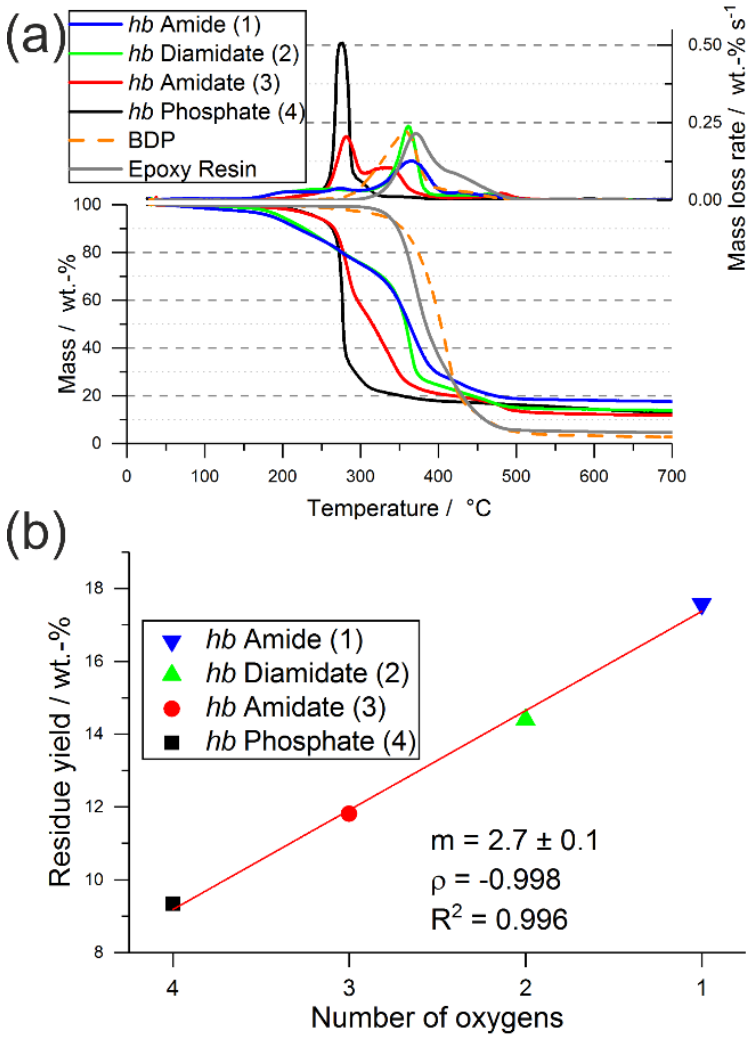

Figure 3.2. Pyrolysis investigations *via* thermogravimetric analysis (TGA) of hb-FRs: (a) mass loss (bottom) and mass loss rate (top) over *T* of *hb*-FRs; (b) linear relationship between the number of oxygen atoms in the P-binding sphere of *hb*-FRs and their residue yield at 700 °C (red line: linear fit; *m*: slope; *ρ*: Pearson's correlation coefficient or PCC; R^2: PCC squared).

Interestingly, the residue amount after pyrolytic decomposition increased with increasing N content by approx. 2.7 wt%, and Fig. 3.2b illustrates the linear increase between the number of O in the P-binding sphere and the residue yield. The increase in residue yield with increasing P–N bonds in the *hb*-FRs results from the formation of thermally stable intermediates that decompose over a broad temperature range. When comparing **3** and **4**, the replacement of a P–O bond with a P–N bond increased residue yield and introduced an additional decomposition step at elevated temperatures. When comparing **1** and **2** to **3** and **4**, the mass loss behavior changed drastically from a single-step decomposition with a shoulder to a multi-step decomposition over a large temperature range, pointing to a crucial influence of the number of P–N bonds in the polymer on its decomposition pathway.

To better understand the decomposition mechanisms of the FRs under pyrolytic conditions, the materials were investigated *via* evolved gas analysis using TGA-FTIR (Fig. 3.3a–d) and pyrolysis gas chromatography/mass spectrometry (Py-GC/MS) (Fig. 3.4). The evolved gas FTIR spectra of decomposition products correspond to specific decomposition steps during pyrolysis of *hb*-FRs. For *hb*-FRs, either 5-hexene-1-ol and/or 5-hexene-1-amine was detected during the decomposition, depending on the O : N ratio, which correlates well with previous investigations for low molar mass P-FRs.[31] 5-Hexene-1-ol was identified *via* the vibration band at 1054 cm^{-1} from the stretching vibration of (C–O). 5-Hexene-1-amine was identified *via* the stretching vibration band at 1068 cm^{-1} from (C–N) and the wagging deformation band at 769 cm^{-1} from (N–H). Additionally, 1,5-hexadiene was identified as a decomposition product (*via* a β-elimination) for all *hb*-FRs *via* the bands at 3082 cm^{-1} from unsaturated hydrocarbons and those at 1642 cm^{-1}, 1452 cm^{-1}, 998 cm^{-1} and 917 cm^{-1} belonging to various C–H vibrations of the hexene moiety, which were also observed in 5-hexene-1-amine and 5-hexene-1-ol. Interestingly, at T > 330 °C, all spectra showed few if any bands for unsaturated hydrocarbons (bands > 3000 cm^{-1}). Furthermore, **2**, **3**, and **4** exhibited the production of a P-species at T = 260–280 °C: for **2** and **3**, the bands at 1330–1300 cm^{-1} from the overlapping stretching vibrations of P═O or P–N, and for **4**, the bands at 1299 cm^{-1} from the stretching vibration R_2–(P═O)–OH, and 1034 cm^{-1} from R_2–(P–OH)═O or the stretching vibration of (P–O–C). During the decomposition of the *hb*-FRs with P–N bonds, the evolution of ammonia at T = 330–360 °C and temperatures above 440 °C was identified by the bands at 3334 cm^{-1}, 1642 cm^{-1}, 966 cm^{-1}, 931 cm^{-1}, and 629 cm^{-1}.

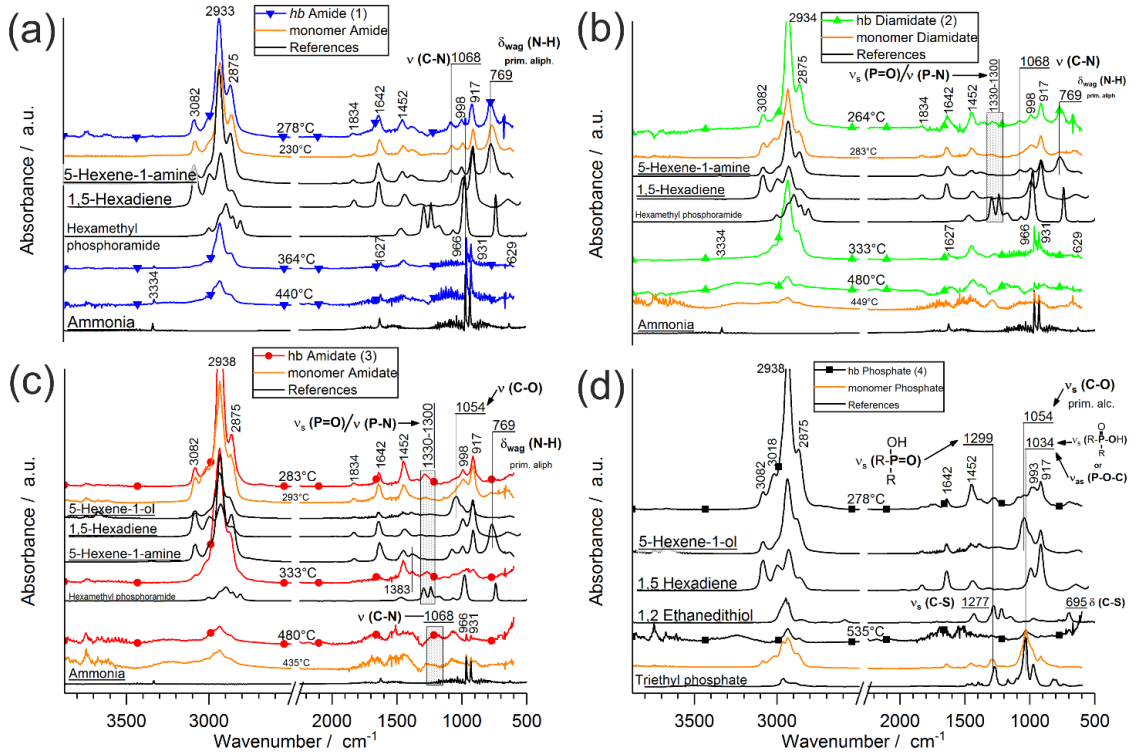

Figure 3.3. Evolved gas analysis *via* FTIR (TG-FTIR) of *hb*-FRs: (a–d) FTIR spectra of *hb*-FRs at specific decomposition steps, their monomeric variants (orange) and comparative spectra.

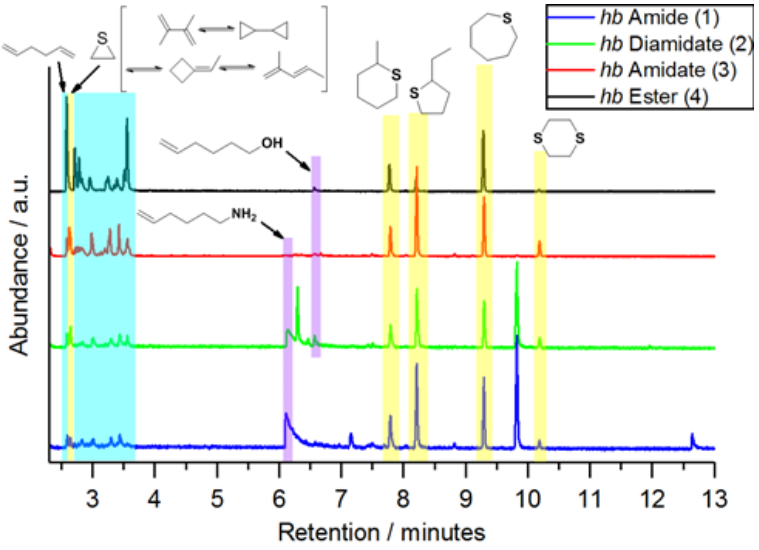

Figure 3.4. Ion chromatograms of *hb*-FRs from pyrolysis gas chromatography/mass spectrometry (Py-GC-MS) measurements. Highlighted areas correspond to relevant compounds identified *via* the NIST14 MS library.

The FTIR spectra, TGA mass loss curves, and residue amounts after pyrolysis point toward a certain behavior during pyrolysis: all units of the *hb*-FR undergo several types of decomposition reactions, and several mechanisms occur simultaneously or in tandem with one another. A general decomposition pathway is described in Scheme 3.2, and hydrolysis (Scheme S3.1†), elimination

(Scheme S3.2†), and intra- or intermolecular reactions (Scheme S3.3†) are described more in depth in the ESI.†

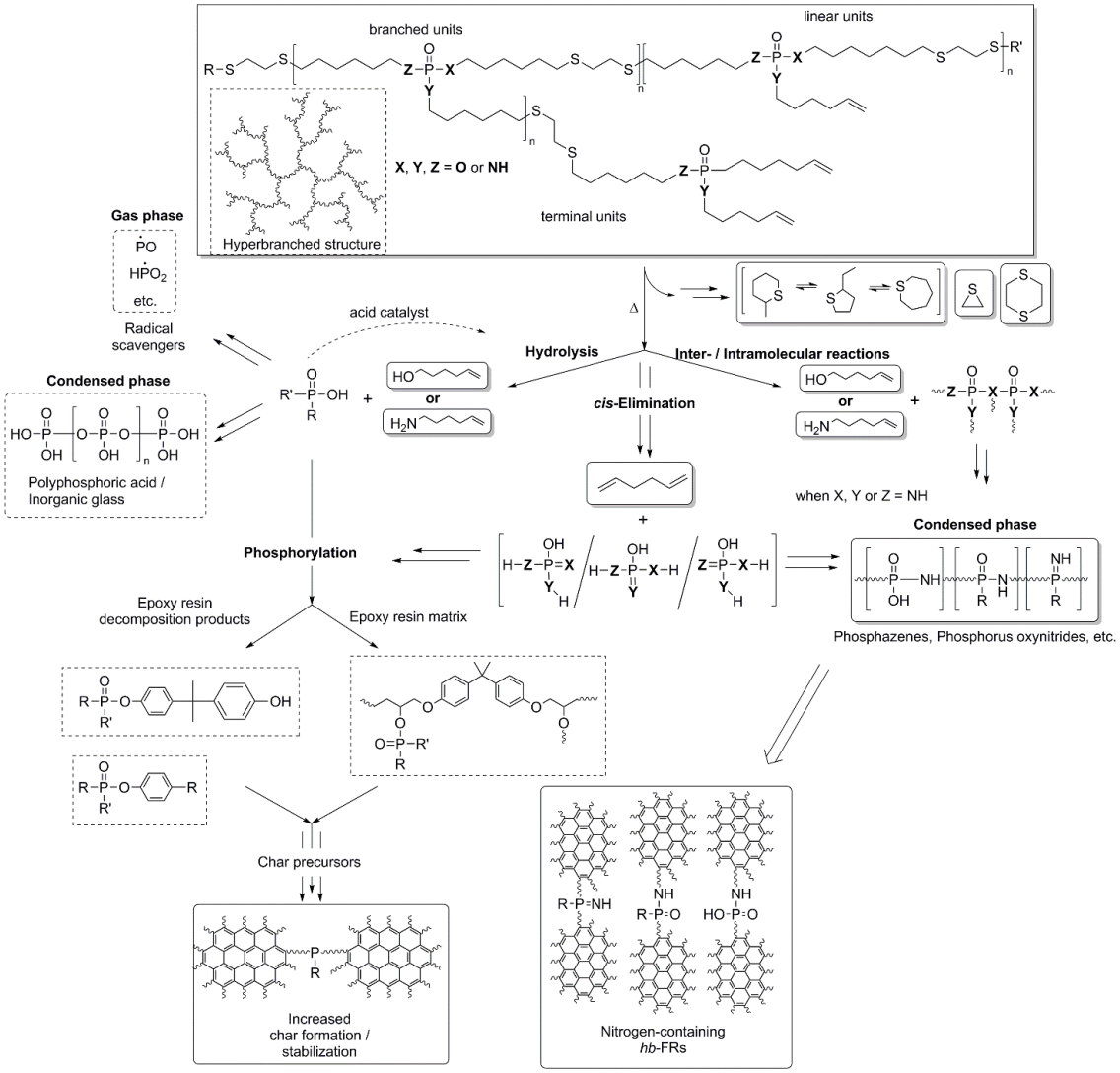

Scheme 3.2. Proposed decomposition mechanism of *hb*-FRs and FR interaction with EP during thermal decomposition of EP-*hb*-FRs. Solid squares: identified products (TG-FTIR, hot stage FTIR, *etc.*).

For Py-GC/MS, µg samples were pyrolyzed at a specific temperature and the evolved gases passed through a GC separation column and an MS detector. Measurements at 500 °C (Fig. 3.4) revealed additional information on the decomposition mechanism of *hb*-FRs: the production of 1,5-hexadiene was identified by the mass spectrum at 2.6 min (Fig. S3.8†) and the signals at retention times of 2.7–3.7 min (areas highlighted in blue) were assigned to various C_6H_{10}-species formed by the high-temperature rearrangement of 1,5-hexadiene. Moreover, 5-hexene-1-amine and 5-hexene-1-ol (areas highlighted in purple) were observed at retention times of 6.1 min (Fig. S3.10†) and 6.6 min (Fig. S3.11†), respectively. Additionally, all *hb*-FRs formed cyclic sulfur-containing

compounds (areas highlighted in yellow). The mass spectra of all *hb*-FRs at retention times of 2.63 min (corresponding to thiirane), 7.8 min (corresponding to 4-methylthiane), 8.2 min (corresponding to 2-ethylthiophane), 9.3 min (corresponding to thiepane), and 10.2 min (corresponding to 1,4-dithiane) are summarized in Fig. S3.9, S3.12, S3.13, S3.14 and S3.15,† respectively. A mechanism leading to the production of these products is proposed in Scheme S3.4.†

3.4.2 Flame retardant epoxy resins (EP-FRs)

3.4.2.1 Material properties

The miscibility of **1** and **4** with EP was studied from 0 up to 40 wt%: all samples were translucent and showed no sign of macro-phase separation (Fig. 3.5a). The miscibility of **4** with EP is further supported by SEM and TEM images (Fig. S3.21†). A homogeneous surface of a section of EP with 10 wt% of **1** is shown in Fig. S3.16a.† There is no obvious indication of phase separation. Fig. S3.16b† displays the surface of EP fractured under cryogenic conditions and etched in dichloromethane according to the method of Meng *et al.*,[37] who studied the phase separation within EP by fracturing the sample under cryogenic conditions and etching it in dichloromethane for thirty minutes. The filler used by Meng *et al.* was soluble in dichloromethane like **4** used in this experiment. The cut block surface which was etched in dichloromethane is illustrated in Fig. S3.16c† and showed no signs of phase separation as indicated by the absence of grooves on the surface. These results are supported by a sample stained with ruthenium tetroxide and analyzed by TEM (Fig. S3.16d†), in which a homogeneous surface is visible, indicating no sign of phase separation. Differential scanning calorimetry (DSC) measurements (Fig. S3.17†) presented only one glass-transition temperature (T_g), further supporting the absence of macro phase separation.

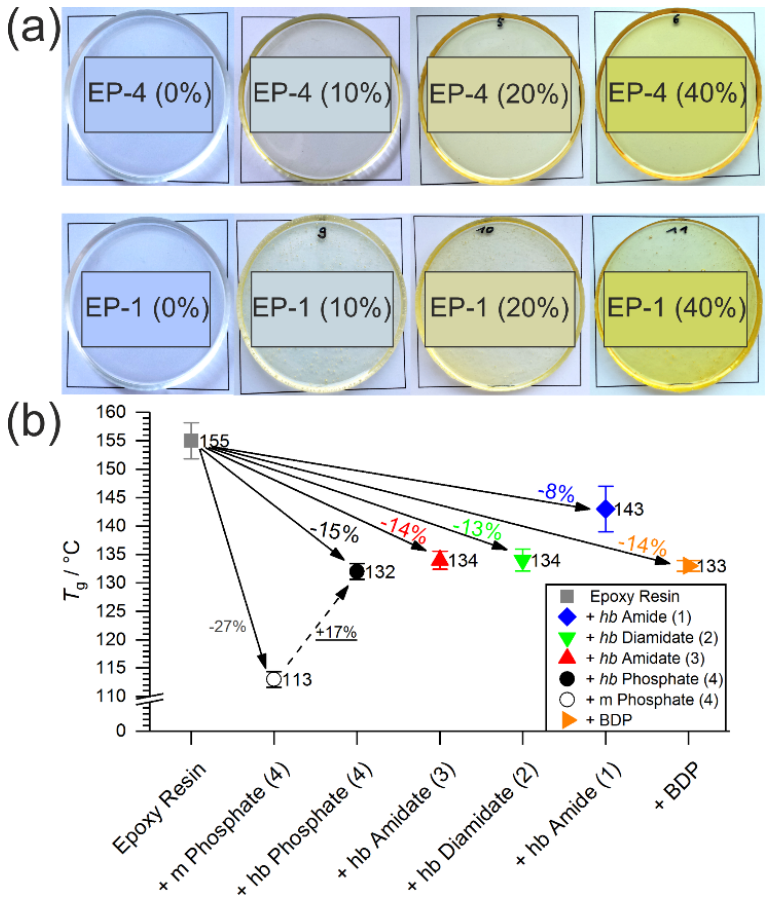

Figure 3.5. (a) EPs with increasing FR loadings (top row: EP-**4**; bottom row: EP-**1**; left to right: 0, 10, 20, 40 wt%), phase separation not visible regardless of loading; (b) T_g values of EP and EP-FRs and change in T_g relative to EP (in %), (dotted line: relative change in T_g from EP with the monomer of **4** to EP-**4**).

All *hb*-FRs were used as additive flame retardants and under the curing conditions no side-reactions of the phosphoramide-bond with the epoxy were reported.[31] The impact of *hb*-FRs on the T_g of EP (Fig. S3.18†) is presented in Fig. 3.5b, and the change of T_g relative to EP is noted. When comparing the T_g of EP with the monomer of **4** with the T_g of EP-**4**, the *hb*-FR exhibited a relative increase of 17%, which showcases the decreased effect of *hb*-FRs over their low molecular weight P-FR counterparts. All *hb*-FRs except **1** lowered T_g of EP at a similar level to the benchmark material BDP, *i.e.* by 14%. **1** had the lowest impact on T_g compared to the other FRs, lowering T_g by only 8% to 142.5 °C. The T_g values are ordered **4** < **3** < **2** < **1**, following the trend visible in the T_g of pure *hb*-FRs. It should be noted that *hb*-FRs are composed of aliphatic hydrocarbons as opposed to BDP, which contains aromatic rings. The reduced effect on T_g that these aliphatic FRs exhibit is comparable to that by aromatic compounds, which speaks for the ability of *hb*-FRs to mitigate the plasticizing effect of conventional aliphatic FRs. The *hb*-polymers present significantly higher T_g values in EP than their monomeric analogues (16–21% increase),[31] highlighting their character as multifunctional FRs.

3.4.2.2 Pyrolysis – mass loss and evolved gas analysis

To understand the decomposition behavior of EP-*hb*-FRs, the mass loss and evolved gas analysis of the pyrolytic decomposition was investigated *via* TGA coupled with gas FTIR. The results are summarized in Table S3.4.† The mass loss and mass loss rate curves of EP and EP-FRs (Fig. 3.6a) and the change in residue yields at 700 °C (Fig. 3.6b) signify a significant change in the decomposition of EP when *hb*-FRs are added, providing evidence for their interaction during pyrolysis. EP began to decompose at $T_{5\%}$ = 338 °C and reached T_{max} at 372 °C. The material decomposed in a single main step equal to a mass loss of 62 wt%, with a shoulder beginning at 424 °C equal to a mass loss of 33 wt%. The residue at 700 °C was 4.5 wt%. The mass loss and evolved gas analysis of the resin DGEBA-DMC has been previously reported and will not be discussed in further detail here.[38,39] The resin with the benchmark material BDP (EP-BDP) decomposed in a single step with a shoulder, analogously to EP. However, $T_{5\%}$ was 33 °C and T_{max} was 15 °C lower than that of EP, which is attributed to a reduction in cross-linking density of the flame retardant EP system. The shoulder starting at 423 °C showed a lower decomposition rate compared to EP. The mass loss at T_{max} increased to 75 wt% and decreased to 16 wt% at the shoulder. This results from the interaction of BDP with the decomposing matrix, more closely the binding of phenol-derivatives and cycloalkanes which exhibit a maximum in the production rate in this temperature range.[9] This interaction also explains the increased residue yield of EP-BDP, which nearly doubled to 8.2 wt%.

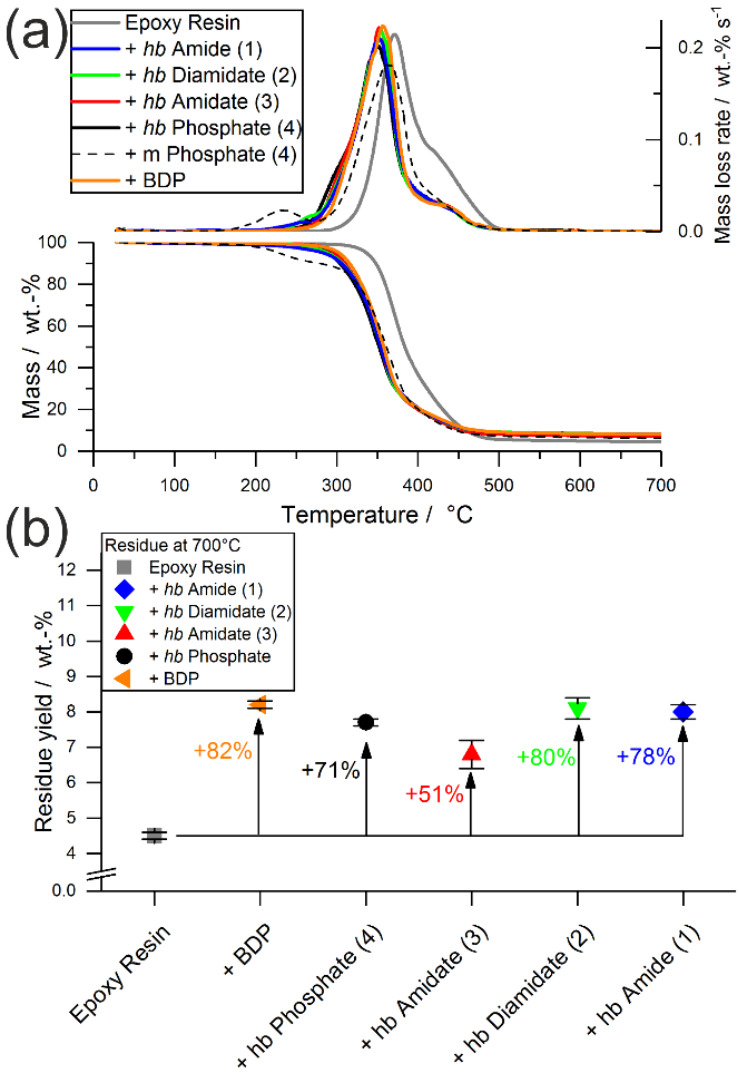

Figure 3.6. (a) Mass loss (bottom) and mass loss rate (top) over *T* of EP-FRs from TGA measurements (dotted line: EP with the monomer of **4**); (b) residue yields at 700 °C from TGA measurements of EP and EP-FRs and change relative to EP (in %).

All EP-*hb*-FRs exhibited a similar decomposition behavior to EP-BDP: $T_{5\%}$ was lower than EP by an average of approx. 47 °C, while T_{max} was lowered by an average of approx. 21 °C. The residue yields of the EP-*hb*-FRs varied depending on the O : N ratio of the *hb*-FRs (Fig. 3.6b): EP with *hb*-phosphate (EP-**4**) and EP with *hb*-amidate (EP-**3**) showed a similar residue yield (7.7 and 6.8 wt%, respectively), while EP with *hb*-diamidate (EP-**2**) and *hb*-amide (EP-**1**) exhibited residue yields similar to EP-BDP (8.1 wt% and 8.0 wt%, respectively). Although EP-**3** exhibited a lower residue yield, all *hb*-FRs increased residue yields by the same margin as the benchmark FR, signifying their ability to interact with the decomposing matrix, forming thermally stable residues. The mass loss of *hb*-FRs in EP was strikingly different from their monomeric FR variants: whereas the latter exhibited a mass loss equal to approx. 10 wt% near 220 °C (Fig. 3.3b, dotted line), all *hb*-FRs are

significantly more thermally stable than their low molar mass counterparts in this temperature range and exhibited only minor decomposition.[31] This higher decomposition temperature increased the overlap of FRs and matrix decomposition, leading to higher reactivity and interaction during pyrolysis,[9,40] further illustrating the multifunctional capabilities of *hb*-FRs and the ability of polymeric FRs to overcome the impediments of their monomeric FR variants as well as perform equally to aromatic compounds.

When comparing the FTIR spectra of evolved gases near $T_{5\%}$ for EP-*hb*-FRs with monomeric FR variants in EP (Fig. 3.7a), the distinct similarities in the spectra indicate analogous decomposition products, namely 5-hexene-1-ol, 5-hexene-1-amine, cyclohexene, 1,5-hexadiene, and acetaldehyde. The spectra of EP-**2**, EP-**3**, and EP-**4** exhibited the (C–O) stretching vibration band at 1054 cm^{-1} assigned to 5-hexene-1-ol. EP-**2** and EP-**3** produced cyclohexene as identified *via* the C–H bending vibration at 1140 cm^{-1}. The spectra of EP-**1** showed the (C–N) vibration band of aliphatic hydrocarbons at 1068 cm^{-1} and the (N–H) wagging deformation of primary amines of aliphatic molecules at 769 cm^{-1}, pointing to the production of 5-hexene-1-amine. Moreover, the (C=O) stretching vibration at 1730 cm^{-1}, corresponding to acetaldehyde, was visible for EP-**1**, EP-**3**, and EP-**4**, while it was concealed under noise for EP-**2**. Acetaldehyde is a product of the decomposition of unreacted epoxide groups from EP.[39] The band at 3082 cm^{-1} belonging to the (C=C) stretching vibration was visible in all EP-*hb*-FR spectra at $T_{5\%}$ and indicated that the decomposition products are unsaturated. When investigating the evolved gas spectra of EP, EP-*hb*-FRs, and EP-BDP at T_{max} (Fig. 3.7b), all spectra were identical to the spectrum of EP, signifying that EP-*hb*-FRs did not exhibit gas evolvement at this point. This correlates well with the mass loss curves of the *hb*-FRs under pyrolytic conditions (Fig. 3.2a), as the *hb*-FRs have nearly completely decomposed at the T_{max} of EP. These FTIR spectra provide further evidence that terminal and linear units of the *hb* structure decomposed near $T_{5\%}$ as evidenced by the presence of unsaturated hydrocarbons present solely on these units and 5-hexene-1-ol and/or 5-hexene-1-amine, respectively. As previously mentioned, this can be rationalized by the lower thermal stability of the ω-hexenyl side chains compared to the thiol-linked main chain.

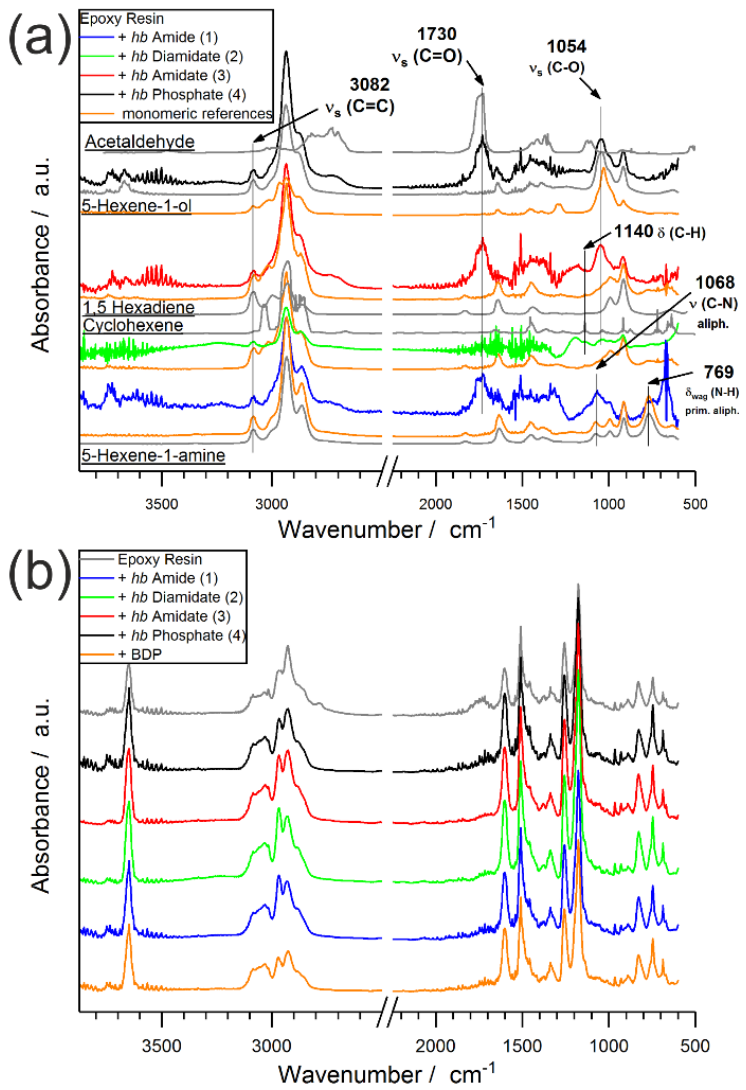

Figure 3.7. Evolved gas spectra of EP-*hb*-FRs *via* TG-FTIR at $T_{5\%}$; (orange: monomeric FR spectra at T_{max}; gray: comparative spectra) (b) evolved gas spectra of EP and EP-*hb*-FRs *via* TG-FTIR at T_{max}.

The decomposition pathway is a complex interaction of the FR, the matrix and the decomposition species thereof.[40] The detection of various P-species in the condensed phase (Fig. S3.19†) confirms that *hb*-FRs interact with the decomposing matrix. The incorporation of P into the residue increases charring *via* enhanced cyclization of the hydrocarbon chains and stabilizes the carbonaceous char by acting as cross-linking points between the polyaromatic hydrocarbons.[41] The proposed mechanism is presented in Scheme 3.2: the decomposition of *hb*-FRs leads to the formation of O═(P–OH) groups *via* hydrolysis of the (P–N) or (P–O) bond, respectively, resulting in the production of phosphoric acid and acid derivatives. These P-based acids interact with EP in three ways: acting as acid catalysts for further hydrolysis,[42] aiding in the phosphorylation process of the EP matrix *via* esterification and dehydration,[43] and forming an inorganic glass *via* polyphosphoric acid, thus affording thermal stability to the residue.[7,44] For N-containing *hb*-FRs,

the formation of phosphazenes, phosphorus oxynitrides, and other $P_xN_yO_z$ species further increased cross-linking of the aromatic char, and the presence of N can accelerate phosphorylation through synergy.[45-47]

3.4.2.3 Fire behavior

EP and all EP-FRs were investigated for their reaction-to-small-flame behavior *via* UL-94 and LOI (Table S3.6†) and under forced-flaming conditions in a cone calorimeter to determine their fire load, residue yields, smoke and gas production, and heat release rate (HRR). The HRR of a "steady state" burning polymer is described by the following equations:[48]

Equation 1:

$$HRR = \chi \cdot \theta(t) \cdot (1-\mu) \cdot (h^0_c/h_g) \cdot \dot{q}''_{eff}$$

Equation 2:

$$\dot{q}''_{eff} = (\dot{q}''_{ex} + \dot{q}''_{flame} - \dot{q}''_{rerad} - \dot{q}''_{loss})$$

where χ is the combustion efficiency, $\vartheta(t)$ is the time-dependent protective layer effect, μ is the residue yield, h^0_c is the heat of complete combustion, h_g is the heat of gasification, $\dot{q}''_{eff}$ is the effective heat flux, $\dot{q}''_{ex}$ is the external heat flux, $\dot{q}''_{flame}$ is the heat flux due to thermal feedback, $\dot{q}''_{rerad}$ is the heat flux from reradiation, and $\dot{q}''_{loss}$ is the loss of heat flux out of the flame.

The results of the cone calorimeter experiments are summarized in Table 3.1 and Fig. 3.8 plots the HRR and total heat released (THR) as functions of time. The shape of the HRR-curves gives insight into the behavior of the material during flaming combustion and highlights the modes of action of the FRs.[49] For EP, the shape was typical of non-charring, thermally intermediately thick samples: after ignition, the material began to decompose with a strong initial increase in the HRR. The quasi-static HRR corresponding to the steady state HRR is marked only by a shoulder and disappears near the peak of heat release rate (PHRR). The peak results from a reduction of $\dot{q}''_{loss}$ caused by the glass wool under the sample preventing heat transfer to the sample holder as the pyrolysis zone approaches. EP had a PHRR of 1696 kW m^{-2} and a total heat evolved (THE = THR at flame-out) of 108.4 MJ m^{-2}. It exhibited an effective heat of combustion (EHC = total heat evolved/total mass loss) of 26.9 MJ kg^{-1} and a residue yield of 0.7 wt%. For EP-BDP, the HRR-curve resembled a mixture of thermally thick charring materials and thermally intermediately thick non-charring materials: while it retained the characteristic shape of EP, the addition of a charring mode of action was visible, resulting in a 30% reduction of the PHRR (1180 kW m^{-2}). THE and EHC were

also 19% and 16% lower than EP (THE = 87.5 MJ m^{-2}; EHC = 22.7 MJ kg^{-1}), respectively. The residue yield was 3.1 wt%.

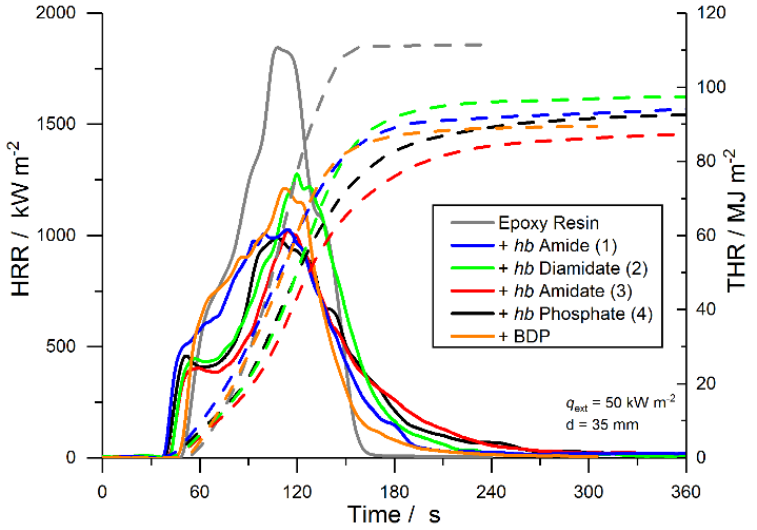

Figure 3.8. Heat release rate (HRR, full line) and total heat released (THR, dotted line) over *t* of EP and EP-FRs.

Table 3.1. Results from cone calorimeter experiments of EP and EP-FRs

	EP	EP-**1**	EP-**2**	EP-**3**	EP-**4**	EP-BDP
THE [MJm^{-2}]	108.4 ±2.6	95.5 ±2.3	99.1 ±2.7	86.6 ±0.1	89.8 ±3.0	87.5 ±1.2
PHRR [kWm^{-2}]	1696 ±180	1189 ±155	1325 ±10	1019 ±17	953 ±41	1180 ±41
Residue [wt.-%]	0.7 ±0.1	12.1 ±2.7	7.0 ±0.1	13.6 ±0.5	7.5 ±0.6	3.1 ±0.2
EHC [$MJkg^{-1}$]	26.9 ±1.0	25.5 ±0.5	26.8 ±0.8	25.1 ±0.1	24.3 ±0.6	22.7 ±0.2

All EP-*hb*-FRs reduced the fire load of EP by 9–20% and the PHRR by 22–44% and increased residue yields in the order EP-**2** < EP-**4** < EP-**1** < EP-**3**. EP-**2** showed the lowest residue amount (7.0 wt%) and EP-**3** exhibited the highest amount (13.6 wt%). EP-**3** and EP-**4** displayed the greatest reduction in PHRR and THE, while EP-**1** and EP-**2** did not achieve the same reduction in these indices. Nearly all *hb*-FRs exhibited a plateau-like shape approx. 20–30 s after ignition, which was caused by the formation of a protective char layer on the sample surface, shielding the underlying material from irradiation and reducing the PHRR. Additionally, the release of P-containing volatiles, observed in pyrolysis investigations (Fig. 3.2), acted in the gas phase as radical scavengers or fuel diluters, thus reducing THE. As combustion continued, the protective layer effect rescinded, and the decomposition of the underlying material increased towards the PHRR. After flame-out, the char layer underwent thermo-oxidation as evidenced by the slow increase of THR over time in the plateau-state at t > 240 s.

Petrella-plots are a way to assess fire behavior and flame retardancy:[50] the fire load (THE) is plotted over the fire growth index (PHRR/t_{ig}), as THE quantitatively describes heat released but

lacks a description of release rate, while PHRR/t_{ig} describes the flashover potential (severity of a fire, or peak heat release potential) but is not quantitative. The Petrella-plot of EP and EP-FRs (Fig. 3.9) displays that, while the PHRR/t_{ig} of EP was 36 kW m^{-2} s^{-1} and the THE was 109.6 MJ m^{-2}, all EP-FRs exhibited a lower PHRR/t_{ig} and THE, as indicated by the shift to the lower left corner of the coordinate system. **2** displayed the lowest flame retardancy, lowering THE by only 10% to 99.1 kW m^{-2} s^{-1} and PHRR/t_{ig} by only 7% to 33.6 MJ m^{-2}, while **3** showed the greatest reduction in both THE (21% reduction to 86.6 MJ m^{-2}) and PHRR/t_{ig} (31% reduction to 24.9 kW m^{-2} s^{-1}). The plot visualizes the ability of **3** and **4** to act more effectively in forced-flaming conditions than **1** and **2**, providing further evidence that a critical O : N ratio determines decomposition behavior due to changes in the flame-retardancy mechanism and mode of action. Moreover, **3** and **4** outperform BDP, providing further evidence that *hb*-FRs can compete with aromatic compounds.

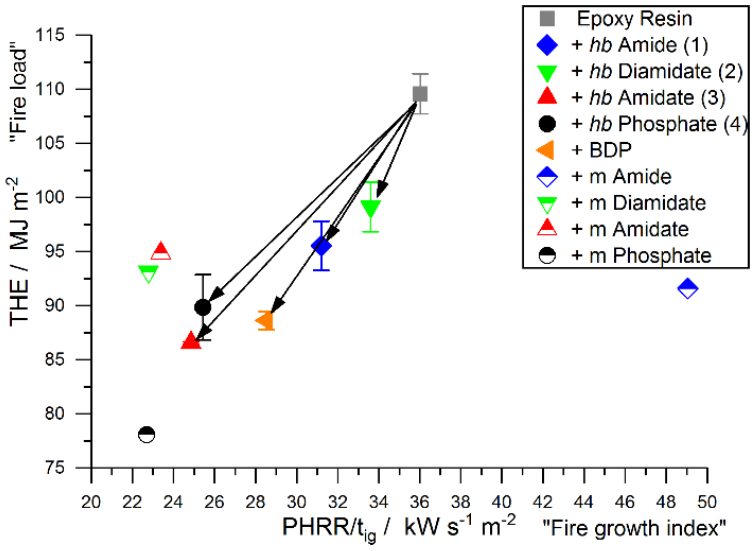

Figure 3.9. Petrella-plot of EP and EP-FRs, assessing fire load (THE) *versus* fire growth (PHRR/t_{ig}).

Furthermore, Fig. 3.9 also visualizes the change in fire behavior from the monomer to polymer: the low molar mass variants exhibited very scattered results, where the monomer of **4** had a very different impact compared to the monomer of **1** in terms of lowering the fire load and fire growth index of EP. Although the *hb*-FRs presented varied results based on their O : N ratio, in general they displayed significantly less disperse values for fire growth and fire load, the result of a more pronounced chemical interaction between the FR and matrix during decomposition.

3.5 Experimental

3.5.1 Materials

3.5.1.1 Chemicals

All chemicals were purchased from commercial suppliers as reagent grade and used without further purification. The monomers were prepared according to the literature.[31]

3.5.2 Methods

3.5.2.1 NMR

Nuclear magnetic resonance measurements (^{1}H, ^{31}P-{H} and ^{13}C-{H} NMR) were performed on a Bruker Avance (Bruker, Ettlingen, Germany) spectrometer at 250, 300, 500, and 700 MHz on samples solved in deuterated chloroform, deuterated dimethyl sulfoxide or deuterated *N*,*N*-dimethylformamide. Calibration spectra were measured against the solvent signal. All spectra were analyzed using MestReNova 9 (Mestrelab Research S.L., Santiago de Compostela, Spain).

3.5.2.2 GPC-MALS

For gel permeation chromatography with multi-angle laser light scattering online detection (GPC-MALS), a light scattering detector combined with a suitable concentration detector was connected to the output of the GPC columns for the direct determination of the molecular weight. The refractive index increment (d*n*/d*c*) was determined online under the assumption that 100% of the sample mass is injected and elutes from the column. For the P–N containing polymers, DMAc as the mobile phase with 2 g L^{-1} LiBr and 2 g L^{-1} TRIS was used. As the stationary phase, a GRAM linear M column with a particle size of 10 µm from PSS Polymer Standards Service GmbH was used. The operation temperature was 60 °C. For the phosphate, the mobile phase was THF. As the stationary phase, three SDV columns with a porosity of 10^{6}, 10^{4} and 500 Å and a particle size of 10 µm from PSS Polymer Standards Service GmbH were used. The operation temperature was 30 °C.

3.5.2.3 DSC

For *hb*-FRs, a Mettler Toledo DSC 823e (Mettler Toledo, Columbus OH, USA) was used at a heating and cooling rate of 10 K min^{-1} under a nitrogen atmosphere with a flow rate of 30 ml min^{-1}. Three

measurements of a heating–cooling–heating cycle were performed. Measurements of the flame retardant epoxy resins were performed on a Netzsch 204 F1 “Phoenix” (Netzsch Instruments, Selb, Germany) using a 5 mg solid sample. Three heating and two cooling runs were performed at a rate of 10 K min^{-1} in the temperature range from −80 to 180 °C for epoxy resins. The T_g of a material was taken as an average of the 2nd and 3rd heating run.

3.5.2.4 TGA/TG-FTIR

Thermogravimetric analysis and evolved gas analysis *via* FTIR measurements were performed on a TG 209 F1 Iris (Netzsch Instruments, Selb, Germany) coupled to a Tensor27 Infrared Spectrometer (Bruker Optics, Ettlingen, Germany) *via* a heated (T = 270 °C) transfer-line. Samples sized 5 mg (*hb*-FR) or 10 mg (epoxy resins, powdered) were heated at a rate of 10 K min^{-1} from 30 to 900 °C under a nitrogen atmosphere *via* gas flow at 30 ml min^{-1}. The epoxy resins were powdered using a CryoMill (RETSCH, Germany) under liquid nitrogen.

3.5.2.5 Hot-stage-FTIR

FTIR spectra of the condensed phase during pyrolysis were recorded on a hot-stage FTIR using a Vertex70 FTIR spectrometer (Bruker Optics, Ettlingen, Germany) fitted with an FTIR600 Linkam hot stage cell (Linkam Scientific Instruments Ltd, Chilworth, UK). Powdered samples were pressed into a platelet with potassium bromide as the carrying agent and heated at a rate of 10 K min^{-1} from 30 to 600 °C under a nitrogen purge at 300 ml min^{-1}. The scan resolution was 0.4 cm^{-1} and samples were measured between 4000 and 400 cm^{-1}.

3.5.2.6 LOI

Limiting oxygen index measurements were performed in accordance with ISO 4589-2. The samples corresponded to type IV of the standard (dimensions: 130 mm × 6.5 mm × 3 mm). All samples were stored at 23 °C and 50% relative humidity for at least 80 hours before measurements.

3.5.2.7 UL-94

Underwriter's Laboratory 94 measurements were performed on samples stored at 23 °C and 50% relative humidity for at least 80 hours in vertical and horizontal orientation according to EN 60695-11-10. The samples were sized 125 mm × 13 mm × 3 mm.

3.5.2.8 Cone calorimetry

All forced-flaming measurements were performed on a cone calorimeter (Fire Testing Technology Ltd, East Grinstead, UK) using a heat flux of 50 kW m^{-2} on samples sized 100 mm × 100 mm × 4 mm, conditioned for at least 48 hours at 23 °C and 50% relative humidity, in accordance with ISO 5660 thus simulating a developing fire.[49] As the standard distance of 25 mm caused the sample residues to touch the heating coil due to intumescence, thus interfering with the measurement results, a distance to the cone heater of 35 mm was chosen.[51] The measurements were conducted in duplicate, and a third measurement was performed if the margin of error was greater than 10%.

3.5.2.9 Elemental analysis

All cone calorimetry residue samples were ground into powder with a mortar and pestle for homogenization purposes and approx. 5 g of material was collected. All elemental analysis measurements were performed by Mikroanalytisches Labor Kolbe (c/o Fraunhofer Institut UMSICHT, Oberhausen, Germany). Phosphorus-contents were determined chromatographically *via* a UV/VIS Specord 90 (Analytik Jena AG, Jena, Germany). For statistical purposes, all measurements were repeated twice.

3.5.2.10 SEM

Scanning electron microscopy measurements were performed on a Zeiss EVO MA10 (Card Zeiss AG, Oberkochen, Germany) using an acceleration voltage of 10 kV. The samples were glued to the sample holder, and then sputtered with gold prior to measurements to avoid charging effects.

3.5.2.11 Py-GC-MS

Pyrolysis gas chromatography/mass spectrometry measurements were conducted using a micro-furnace double-shot pyrolyzer (PY3030iD, Frontier Laboratories, Japan) connected *via* a split/splitless inlet port to a gas chromatograph (7890B, Agilent Technologies, USA) combined with a mass selective detector (5977B, Agilent Technologies, USA). The scan range was 15–550 amu and the EI ionization energy of the MSD was 70 eV. *Via* gravimetric fall into the pyrolysis zone (T = 500 C), 300 µg samples were pyrolyzed under a helium atmosphere. Using an Ultra Alloy±5 capillary column (l = 30 m, iD = 0.25 mm, film thickness = 0.25 µm), all evolved pyrolysis products were separated under a helium flow of 1 ml min^{-1}. The column temperature was held at T = 40 °C for 120 s, then increased at a rate of 10 K min^{-1} to T = 300 °C and held there for 10 min. The GC

injector temperature was *T* = 300 °C and it was operated in a split mode of 1 : 300. Peak assignments were made using the NIST14 MS library as a reference.

3.5.2.12 Synthesis of *hb*-polyphosphoramide (1), *hb*-polyphosphorodiamidate (2), *hb*-polyphosphoramidate (3), and *hb*-polyphosphate (4)

1, **2**, **3** and **4** were prepared by a radical thiol–ene polyaddition (Scheme 3.1). For **1**, **2**, and **3**, 234 mmol of the previously synthesized monomer[31] (1 eq.) and 16.7 g of 1,2-ethanedithiol (177 mmol; 0.76 eq.) were dissolved in 240 ml *N*,*N*-dimethylformamide and added to a reactor fitted with a mechanical stirrer under an argon atmosphere. As a radical initiator, 690.5 mg azobisisobutyronitrile (AIBN) (4.1 mmol; 0.02 eq.) was used. For **4**, 80.00 g of **4** (232 mmol; 1 eq.) and 16.57 g of 1,2-ethanedithiol (176 mmol; 0.75 eq.) were dissolved in 240 ml toluene and added to a reactor fitted with a mechanical stirrer under an argon atmosphere. For **2**, **3**, and **4**, 686.5 mg of AIBN (4.18 mmol; 0.02 eq.) was used as a radical initiator, and for **1**, 686.5 mg of AIBN (4.18 mmol; 0.02 eq.) was used. The solution was heated at 100 °C for 24 hours. The crude mixture was then concentrated at reduced pressure. **3** and **4** were precipitated twice into toluene. **1** and **2** were precipitated twice into *n*-hexane. Finally, the polymers were dried at reduced pressure until constant weight (yield **2**, **3**, **4**: 73 g, 76%; yield **1**: 86 g, 89%). The purity and chemical structure were determined by ^{1}H NMR and ^{31}P {H} NMR spectroscopy.

3.5.3 Structure characterization

3.5.3.1 *hb*-Polyphosphoramide (1)

^{1}H NMR (300 MHz, chloroform-d): δ [ppm] = 5.84–5.71 (m); 5.02–4.94 (m); 4.02 (m); 2.70 (s); 2.54 (t); 2.06 (td); 1.69 (m); 1.59 (m); 1.40 (m); 1.39 (m); (Fig. 3.1a).

^{31}P {H} NMR (121 MHz, chloroform-d1): δ [ppm] = −0.66 (s) (Fig. S3.4†).

3.5.3.2 *hb*-Polyphosphorodiamidate (2)

^{1}H NMR (300 MHz, chloroform-d): δ [ppm] = 5.85–5.72 (m); 5.03–4.93 (m); 3.98 (m); 2.87 (br); 2.70 (s); 2.64 (br); 2.54 (t); 2.06 (td); 1.70–1.36 (m); (Fig. S3.1†).

^{31}P {H} NMR (121 MHz, chloroform-d): δ [ppm] = 9.24 (s) (Fig. S3.5†).

3.5.3.3 *hb*-Polyphosphoramidate (3)

^{1}H NMR (300 MHz, chloroform-d): δ [ppm] = 5.84–5.71 (m); 5.04–4.93 (m); 3.93 (m); 2.87 (br); 2.70 (s); 2.54 (t); 2.07 (td); 1.64–1.25 (m); (Fig. S3.2†).

^{31}P {H} NMR (121 MHz, chloroform-d): δ [ppm] = 15.49 (s) (Fig. S3.6†).

3.5.3.4 *hb*-Polyphosphate (4)

^{1}H NMR (300 MHz, chloroform-d): δ [ppm] = 5.85–5.72 (m); 5.03–4.93 (m); 2.88 (br); 2.70 (s); 2.54 (t); 2.07 (td); 1.58–1.24 (m); (Fig. S3.3†).

^{31}P {H} NMR (121 MHz, chloroform-d): δ [ppm] = 17.13 (s) (Fig. S3.7†).

3.5.3.5 Preparation of FR thermosets

The polymer resin was based on diglycidyl ether of bisphenol A (DGEBA) (Araldite MY740, Bodo Müller Chemie GmbH, Offenbach am Main, Germany) and the amine component 2,2'-dimethyl-4,4'-methylene-bis-(cyclohexylamine) (DMC) (Sigma Aldrich Co. LLC/Merck KgaA, Darmstadt, Germany). The needed ratios of DGEBA and DMC (see Table 3.2) were calculated using epoxy equivalent weights (ratio 100 : 35), and 10 wt% of the total batch size was replaced with *hb*-FRs or the benchmark FR bisphenol A bis(diphenyl phosphate) (BDP) (ICL-IP, Tel-Aviv, Israel). All samples needed for measurements were prepared in one batch in the following manner: the respective *hb*-FR was placed in a 1 L polypropylene cup, then DGEBA was added and the chemicals were blended with a wooden spatula until they became homogeneous. DMC was added, and the mixture was thoroughly mixed. Any resulting bubbles were removed *in vacuo*. The compounds were poured into prepared aluminum molds, and then cured in an oven at 90 °C for 30 minutes, at 120 °C for 30 minutes, and at 150 °C for 1 hour. UL-94 and LOI samples were cut into specified dimensions and stored under climate control prior to testing for at least 48 hours according to the respective standards.

Table 3.2. Composition of FR thermosets

Material	Content [g]				
	EP	EP-1	EP-2	EP-3	EP-4
DGEBA	222.2	200	200	200	200
DMC	77.8	70	70	70	70
1	-	30	-	-	-
2	-	-	30	-	-
3	-	-	-	30	-
4	-	-	-		30

3.6 Conclusions

Phosphorus-containing hyperbranched polymers for use as multifunctional flame-retardant additives for epoxy resins were synthesized *via* A_2 + B_3 thiol–ene polymerization. A systematic library of P–O and P–N containing polymers allowed the adjustment of the decomposition mechanism. Results from DSC and TGA experiments showed that T_g and residue yield after pyrolysis increased linearly with the N-content of the *hb*-FRs, and those FRs with a higher N-content were thermally more stable than those with a higher O-content. This was determined to result from a change in the decomposition mechanism which was proposed herein, and that a crucial O : N-ratio determined the pathway. Investigations of flame-retardant epoxy resins provided further evidence of the shift in the chemical decomposition mechanism and ultimately mode of action: all materials exhibited a condensed phase mechanism, as exemplified by the appearance of P-signals in hot stage FTIR measurements, the increase in residue yields in cone calorimeter measurements, and the high amount of the P-content in these residues as determined by elemental analysis. However, *hb*-FRs with a higher O-content exhibited a stronger reduction in the effective heat of combustion, signifying a more pronounced gas phase mechanism. This was supported by CO-yield comparison (see the ESI†) which showed that *hb*-FRs with a higher N-content more strongly affected the combustion efficiency. SEM and residue analysis also illustrated the intumescent characteristic of these FR additives. All *hb*-FRs were compared to the benchmark FR BDP and the results from all measurements demonstrated the ability of these aliphatic FRs to perform at a similar or superior level to an aromatic compound, even at low loadings (P-content in EP < 1%). The *hb*-FRs' ability to mitigate some of the drawbacks of low molecular weight aliphatic FR additives, such as high volatility, low miscibility, poor cohesion in the matrix (leaching or blooming), or strong impact on T_g, speaks for their practical use as multifunctional flame retardant additives and showcases the enormous potential hyperbranched polymers can have in developing future materials in the field of flame retardancy.

3.7 Conflicts of interest

There are no conflicts to declare.

3.8 Acknowledgements

The authors thank the Deutsche Forschungsgemeinschaft (DFG) for funding (DFG SCHA 730/15-1; WU 750/8-1).Alexander Battig thanks Patrick Klack for his assistance with the cone calorimeter

measurements, Martin Günther, and Michael Morys for their help with SEM images, Dr Katharina Kebelmann for her help with Py-GC-MS measurements, and Letícia V. Lima for her aid in sample preparation and measurements. Jens C. Markwart is the recipient of a fellowship through funding of the Excellence Initiative (DFG/GSC 266) in the context of the graduate school of excellence "MAINZ" (Materials Science in Mainz"). Frederik R. Wurm and Jens C. Markwart thank Prof. Dr Katharina Landfester (MPI-P, Germany). Open Access funding provided by the Max Planck Society.

3.9 Notes and References Chapter 3

Supplemental Information contains:

NMR spectra (Figures S3.1–S3.7); Polymerization study (Table S3.1); DSC results (Table S3.2); TGA results of *hb*-FRs (Table S3.3); Hydrolysis decomposition (Scheme S3.1); Elimination decomposition (Scheme S3.2); Inter- and intramolecular decomposition (Scheme S3.3); Sulfur decomposition (Scheme S3.4); Mass spectra of Py-GC-MS (Figures S3.8-15); Surface etching (Figure S3.16); TGA results of EP-*hb*-FRs (Table S3.4); Condensed phase FTIR (Figure S3.17, Table S3.5); LOI & UL-94 measurements (Table S3.6); MARHE & FIGRA of cone calorimeter (Table S3.7); CO-yields (Figure S3.18, Table S3.8); Residue analysis (Figure S3.19).

[1] S. Shaw, *Reviews on environmental health* **2010**, *25*, 261-306.

[2] M. M. Velencoso, A. Battig, J. C. Markwart, B. Schartel, F. R. Wurm, *Angew Chem Int Edit* **2018**, *57*, 10450-10467.

[3] X. Wang, W. Xing, X. Feng, B. Yu, L. Song, Y. Hu, *Polym Chem-Uk* **2014**, *5*, 1145-1154.

[4] S. V. Levchik, E. D. Weil, *Journal of Fire Sciences* **2006**, *24*, 345-364.

[5] B. Perret, B. Schartel, K. Stöß, M. Ciesielski, J. Diederichs, M. Döring, J. Krämer, V. Altstädt, *European Polymer Journal* **2011**, *47*, 1081-1089.

[6] M. Rakotomalala, S. Wagner, M. Döring, *Materials* **2010**, *3*, 4300-4327.

[7] G. Camino, L. Costa, M. P. Luda di Cortemiglia, *Polymer Degradation and Stability* **1991**, *33*, 131-154.

[8] S. K. Brauman, *J Fire Retard Chem* **1977**, *4*, 38-58.

[9] B. Perret, K. H. Pawlowski, B. Schartel, *Journal of Thermal Analysis and Calorimetry* **2009**, *97*, 949-958.

[10] K. H. Pawlowski, B. Schartel, *Polymer International* **2007**, *56*, 1404-1414.

[11] B. I. Voit, A. Lederer, *Chemical Reviews* **2009**, *109*, 5924-5973.

[12] C. J. Hawker, R. Lee, J. M. J. Frechet, *Journal of the American Chemical Society* **1991**, *113*, 4583-4588.

[13] A. Sunder, R. Hanselmann, H. Frey, R. Mulhaupt, *Macromolecules* **1999**, *32*, 4240-4246.

[14] C. Chen, G. Liu, X. Liu, S. Pang, C. Zhu, L. Lv, J. Ji, *Polym Chem-Uk* **2011**, *2*, 1389-1397.

[15] R. Hu, J. W. Y. Lam, J. Liu, H. H. Y. Sung, I. D. Williams, Z. Yue, K. S. Wong, M. M. F. Yuen, B. Z. Tang, *Polym Chem-Uk* **2012**, *3*, 1481-1489.

[16] S. E. Stiriba, H. Frey, R. Haag, *Angew Chem Int Edit* **2002**, *41*, 1329-1334.

[17] M. Calderon, M. A. Quadir, S. K. Sharma, R. Haag, *Adv Mater* **2010**, *22*, 190-218.

[18] K. Y. Pu, K. Li, J. B. Shi, B. Liu, *Chemistry of Materials* **2009**, *21*, 3816-3822.

[19] P. Y. Wen, X. F. Wang, W. Y. Xing, X. M. Peng, B. Yu, Y. Q. Shi, G. Tang, L. Song, Y. Hu, R. K. K. Yuen, *Industrial & Engineering Chemistry Research* **2013**, *52*, 17015-17022.

[20] J. Li, C. H. Ke, L. Xu, Y. Z. Wang, *Polymer Degradation and Stability* **2012**, *97*, 1107-1113.

[21] K. C. Cheng, C. C. Wang, J. L. Ruan, C. H. Wu, C. W. Li, *Polymers for Advanced Technologies* **2018**, *29*, 2529-2536.

[22] L. Zang, S. Wagner, M. Ciesielski, P. Müller, M. Döring, *Polymers for Advanced Technologies* **2011**, *22*, 1182-1191.

[23] B. Schartel, J. H. Wendorff, *Polym Eng Sci* **1999**, *39*, 128-151.

[24] F. Wurm, H. Frey, in *Polymer Science: A Comprehensive Reference, Vol. 6* (Eds.: K. Matyjaszewski, M. Möller), Elsevier, Amsterdam, **2012**, pp. 177-198.

[25] D. H. Zhang, H. Y. Wu, T. C. Li, A. Q. Zhang, Y. L. Peng, F. X. Jing, *Polymer Composites* **2011**, *32*, 36-43.

[26] X. L. Chen, C. M. Jiao, S. X. Li, J. Sun, *Journal of Polymer Research* **2011**, *18*, 2229-2237.

[27] L. J. Duan, H. Y. Yang, L. Song, Y. B. Hou, W. Wang, Z. Gui, Y. Hu, *Polymer Degradation and Stability* **2016**, *134*, 179-185.

[28] Z. Li, P. Wei, Y. Yang, Y. G. Yan, D. A. Shi, *Polymer Degradation and Stability* **2014**, *110*, 104-112.

[29] S. Gaan, G. Sun, K. Hutches, M. H. Engelhard, *Polymer Degradation and Stability* **2008**, *93*, 99-108.

[30] G. F. Levchik, Y. V. Grigoriev, A. I. Balabanovich, S. V. Levchik, M. Klatt, *Polymer International* **2000**, *49*, 1095-1100.

[31] J. C. Markwart, A. Battig, L. Zimmermann, M. Wagner, J. Fischer, B. Schartel, F. R. Wurm, *ACS Applied Polymer Materials* **2019**, *1*, 1118-1128.

[32] H. Chen, J. Kong, *Polym Chem-Uk* **2016**, *7*, 3643-3663.

[33] T. Emrick, H. T. Chang, J. M. J. Frechet, *Macromolecules* **1999**, *32*, 6380-6382.

[34] M. Ciesielski, B. Burk, C. Heinzmann, M. Döring, in *Novel Fire Retardant Polymers and Composite Materials* (Ed.: D.-Y. Wang), Woodhead Publishing, **2017**, pp. 3-51.

[35] J. Deng, W. F. Shi, *Eur. Polym. J.* **2004**, *40*, 1137-1143.

[36] K. Täuber, F. Marsico, F. R. Wurm, B. Schartel, *Polymer Chemistry* **2014**, *5*, 7042-7053.

[37] F. L. Meng, S. X. Zheng, T. X. Liu, *Polymer* **2006**, *47*, 7590-7600.

[38] L.-H. Lee, *Journal of Polymer Science Part A: General Papers* **1965**, *3*, 859-882.

[39] D. P. Bishop, D. A. Smith, *Journal of Applied Polymer Science* **1970**, *14*, 205-223.

[40] B. Schartel, B. Perret, B. Dittrich, M. Ciesielski, J. Krämer, P. Müller, V. Altstädt, L. Zang, M. Döring, *Macromolecular Materials and Engineering* **2016**, *301*, 9-35.

[41] U. Braun, A. I. Balabanovich, B. Schartel, U. Knoll, J. Artner, M. Ciesielski, M. Döring, R. Perez, J. K. W. Sandler, V. Altstädt, T. Hoffmann, D. Pospiech, *Polymer* **2006**, *47*, 8495-8508.

[42] M. Steinmann, M. Wagner, F. R. Wurm, *Chemistry – A European Journal* **2016**, *22*, 17329-17338.

[43] J. W. Lyons, *Journal of Fire & Flammability* **1970**, *1*, 302-311.

[44] B. Schartel, *Materials* **2010**, *3*, 4710-4745.

[45] S. V. Levchik, in *Flame Retardant Polymer Nanocomposites* (Eds.: A. B. Morgan, C. A. Wilkie), John Wiley & Sons, Inc., **2006**, pp. 1-29.

[46] E. D. Weil, *Fire retardancy of polymeric materials* **2000**, 115-145.

[47] S. V. Levchik, G. F. Levchik, A. I. Balabanovich, E. D. Weil, M. Klatt, *Angew Makromol Chem* **1999**, *264*, 48-55.

[48] R. Lyon, in *Handbook of Building Materials for Fire Protection* (Ed.: C. Harper), McGraw-Hill, New York, New York, **2004**, pp. 3.1-3.51.

[49] B. Schartel, T. R. Hull, *Fire and Materials* **2007**, *31*, 327-354.

[50] R. Petrella, *Journal of fire sciences* **1994**, *12*, 14-43.

[51] B. Schartel, M. Bartholmai, U. Knoll, *Polymer Degradation and Stability* **2005**, *88*, 540-547.

3.10 Footnotes

† Electronic supplementary information (ESI) available: NMR spectra (Fig. S3.1–S3.7); polymerization study (Table S3.1); DSC results (Table S3.2); TGA results of *hb*-FRs (Table S3.3); hydrolysis decomposition (Scheme S3.1); elimination decomposition (Scheme S3.2); inter- and intramolecular decomposition (Scheme S3.3); sulfur decomposition (Scheme S3.4); mass spectra of Py-GC-MS (Fig. S3.8–3.15); surface etching (Fig. S3.16); DSC (Fig. S3.17 and 3.18); TGA results of

EP-*hb*-FRs (Table S3.4); condensed phase FTIR (Fig. S3.19 and Table S3.5); LOI & UL-94 measurements (Table S3.6); MARHE & FIGRA of cone calorimeter (Table S3.7); CO-yields (Fig. S3.20 and Table S3.8); residue analysis (Fig. S3.21).

‡ These authors contributed equally.

3.11 Supporting Information

3.11.1 Structure Characterization: ^{1}H and ^{31}P NMR

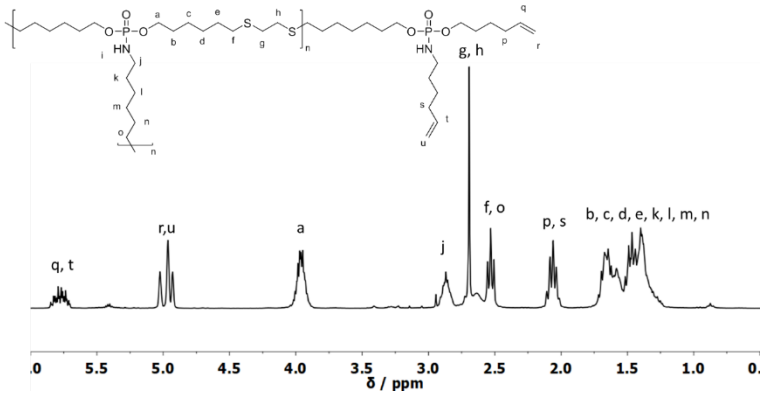

Figure S3.1. ^{1}H NMR (300 MHz in $CDCl_3$ at 298 K) of *hb*-polyphosphoramidate (**3**).

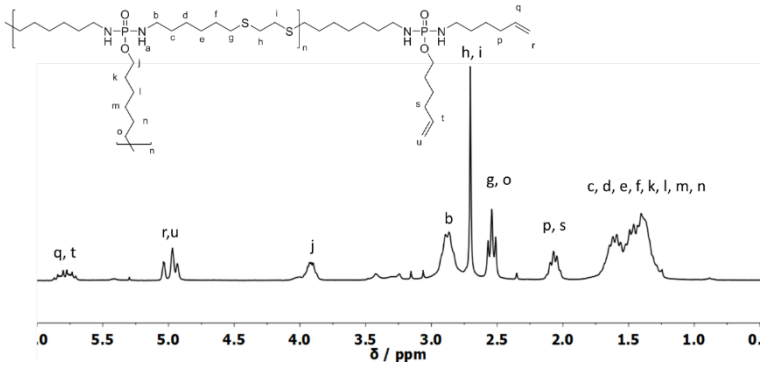

Figure S3.2. ^{1}H NMR (300 MHz in $CDCl_3$ at 298 K) of *hb*-polyphosphorodiamidate (**2**).

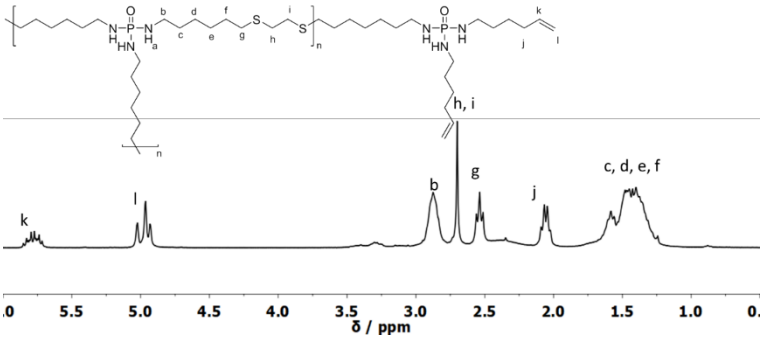

Figure S3.3. ^{1}H NMR (300 MHz in $CDCl_3$ at 298 K) of *hb*-polyphosphoramide (**1**).

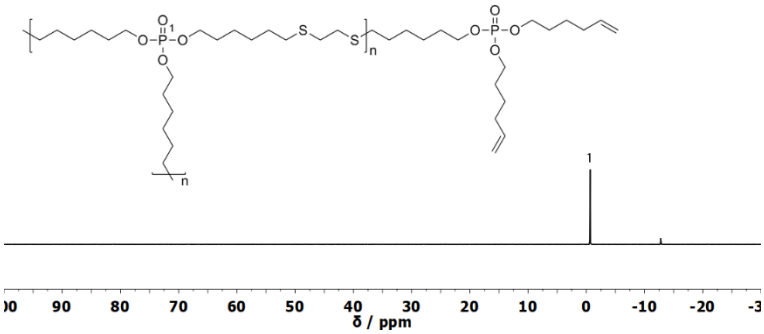

Figure S3.4. ^{31}P {H} NMR (121 MHz in $CDCl_3$ at 298 K) of *hb*-polyphosphate (**4**).

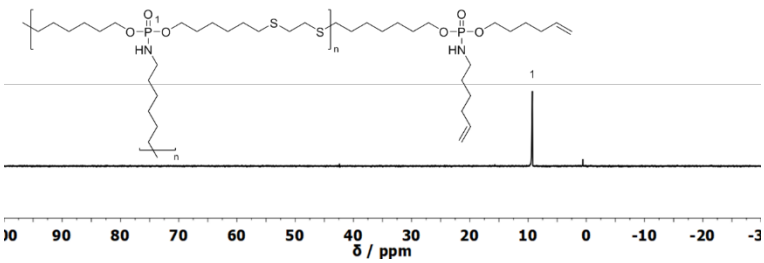

Figure S3.5. ^{31}P {H} NMR (121 MHz in $CDCl_3$ at 298 K) of *hb*-polyphosphoramidate (**3**).

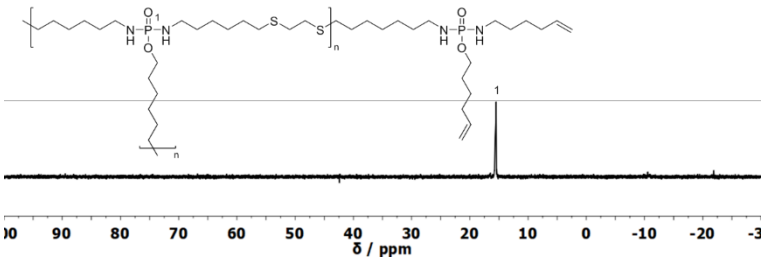

Figure S3.6. ^{31}P {H} NMR (121 MHz in $CDCl_3$ at 298 K) of *hb*-polyphosphorodiamidate (**2**).

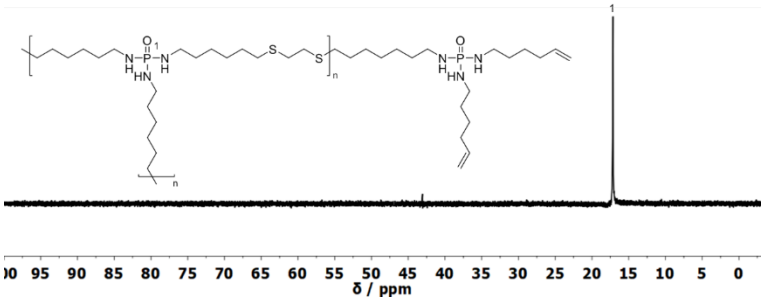

Figure S3.7. ^{31}P {H} NMR (121 MHz in $CDCl_3$ at 298 K) of *hb*-polyphosphoramide (**1**).

3.11.2 Polymerization study

Table S3.1. Variation of polymerization conditions at different A_2:B_3 ratios. A_2 is 1,2-ethanedithiol and B_3 is tri(hex-5-en-1-yl)phosphate.

Ratio*	CL	time until CL / min	M_n / g mol^{-1}	M_w / g mol^{-1}	PDI	Yield / %
10:5	Yes	180	-	-	-	-
5:6	Yes	24	-	-	-	-
5:7	Yes	103	-	-	-	-
5:8	Yes	120	-	-	-	-
5:9	No	-	4,300	53,400	12.44	87
5:10	No	-	3,400	11,300	3.29	82
5:11	No	-	3,000	7,900	2.66	79

* molar feed ratio of functional groups, i.e. thiols : double bonds.

3.11.3 Material Properties: Differential Scanning Calorimetry

Table S3.2. Glass-transition temperatures (T_g) of *hb*-FRs determined *via* differential scanning calorimetry (DSC).

	hb phosphate (**4**)	*hb* amidate (**3**)	*hb* diamidate (**2**)	*hb* amide (**1**)
T_g / °C	-94	-81	-62	-48

3.11.4 Pyrolysis: Thermogravimetric Analysis of *hb*-FRs

Table S3.3. Results from thermogravimetric analysis (TGA) of *hb*-FRs under pyrolytic conditions (N_2 flow = 30 ml min^{-1}, heating rate = 10 K min^{-1}).

Material	hb Phosphate (**4**)	hb Amidate (**3**)	hb Diamidate (**2**)	hb Amide (**1**)
$T_{5\%}$ / °C	241 ± 2	245 ± 3	194 ± 5	190 ± 3
T_1 / °C (preceeding main decomposition step)	-	-	257 ± 5	273 ± 3
T_{max} / °C (main decomposition step)	274 ± 3	281 ± 0	359 ± 2	361 ± 4
T_2 / °C (1st subsequent decomposition step)	-	335 ± 4	-	-
T_3 / °C (2nd subsequent decomposition step)	-	481 ± 0	461 ±3	428 ± 3
Residue / wt.-% (at 700 °C)	11 ± 1	12 ± 0	14 ± 1	18 ± 0

3.11.5 Proposed decomposition mechanisms: Hydrolysis

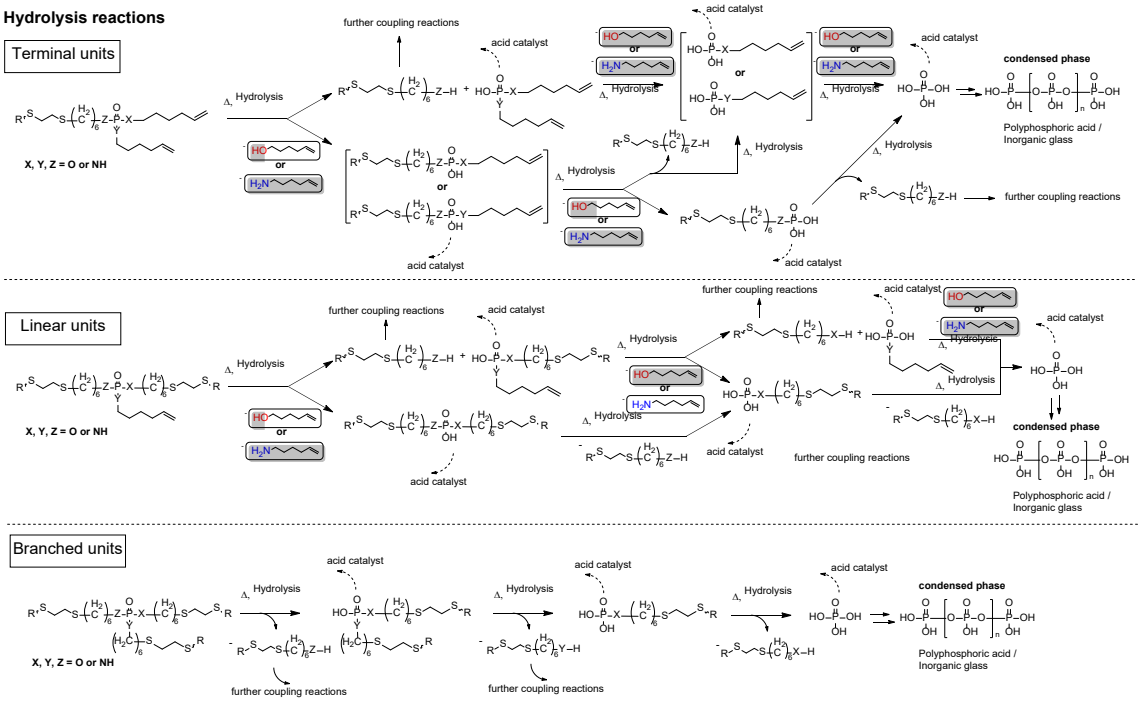

Scheme S3.1. Proposed decomposition mechanism of hydrolysis reactions during pyrolysis.

Hydrolysis reactions of phosphates/-amides (Scheme S3.2) produce phosphates that act as acid catalysts, thereby promoting further hydrolysis reactions.[1] For terminal units and linear units in our P-FRs, two hydrolysis pathways could occur: either the P-(O-C_6H_{11}) or P-(NH-C_6H_{11}) bond can be hydrolyzed, leading to the production of 5-hexene-1-ol or 5-hexene-1-amine, respectively (side chain reaction in linear and terminal units), or alternatively, the P-(O-R) or P-(NH-R) bond connecting the unit to the polymer backbone is hydrolyzed (main chain reaction). Main chain reactions yield new functional groups which could undergo further coupling reactions, e.g. transesterification.[2] Sufficient hydrolysis reactions lead to the cleavage of the phosphorus-containing moiety from the main chain. Complete hydrolysis leads to the formation of phosphoric acid,[3] which typically polymerizes under these conditions to polyphosphoric acid or inorganic glasses in the condensed phase.[4]

3.11.6 Proposed decomposition mechanisms: *cis*-Elimination

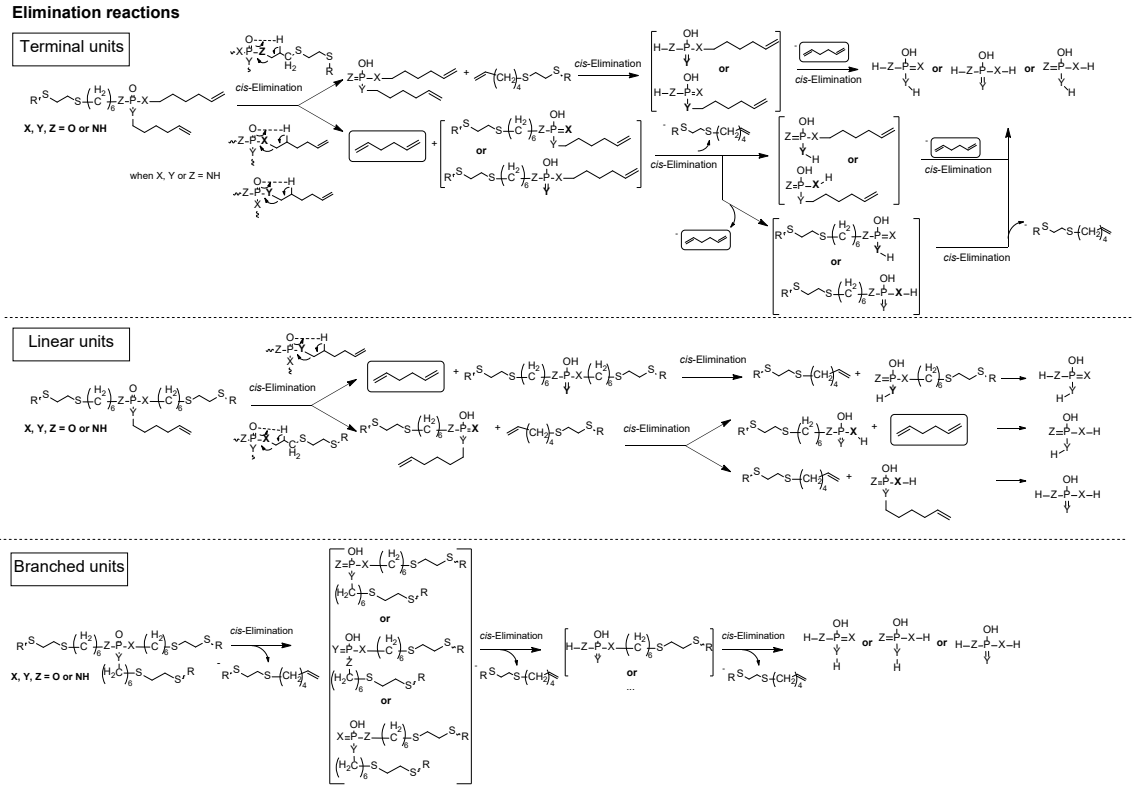

Scheme S3.2. Proposed decomposition mechanism of elimination reactions during pyrolysis.

Besides hydrolysis, elimination reactions (Scheme S3) involve the hydrogen atom in the *cis*-position (relative to the P=O bond) of the β-CH_2 moiety of the hydrocarbon chain.[5-7] Here, hydrogen bonding facilitates the cleavage of the (O-C) or (N-C) bond, generating either 1,5-hexadiene (side chain reaction) or a terminal allyl group (main chain reaction), the latter forming new vinyl groups that undergo cross-linking reactions during decomposition, e.g. *via* radical initiation or cyclization. For N-containing *hb*-FRs, elimination reactions could produce P=N bond, which could further lead to the formation of phosphazenes, phosphorus oxynitrides, or other $(P\text{-}O\text{-}N)_x$ compounds in the condensed phase through rearrangement and polymerization processes during thermal decomposition.[8-9]

3.11.7 Proposed decomposition mechanisms: Inter-/intramolecular reactions

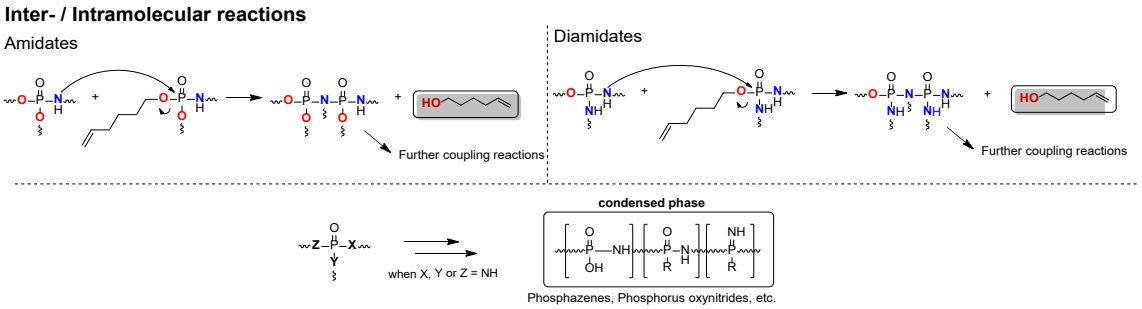

Scheme S3.3. Proposed decomposition mechanism of inter- and intramolecular reactions during pyrolysis.

Additionally, inter- and intramolecular reactions (Scheme S3.4) can occur between two separate molecules, two moieties of the same hyperbranched polymer, or between the FR and matrix. These reactions occur in nitrogen-containing compounds like phosphoramidates, -diamidates, and amides. While the secondary amine acts as a base, the amine hydrogen attacks the pentavalent P of a P-N bond in the vicinity.[10] As a result, 5-hexene-1-ol is produced in an addition-elimination-type reaction. For nitrogen-containing compounds, inter- and intramolecular reactions, as well as rearrangements, may also lead to the formation of thermally stable phosphazenes, phosphorus-oxynitrides, and other $(P\text{-}O\text{-}N)_x$ species.[11-12]

3.11.8 Proposed decomposition mechanisms: Sulfur components

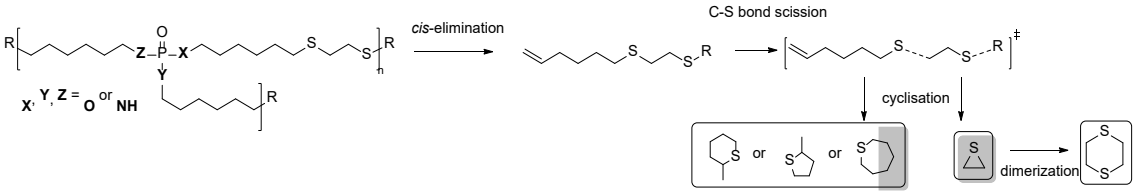

Scheme S3.4. Proposed decomposition mechanism leading to the formation of cyclic sulfur-components.

The scission of C-S-bonds of *cis*-elimination products (see Scheme S3.2) could lead to $C_6H_{12}S$ and C_2H_4S fragments. Cyclisation of the former leads to 4-methylthiane, 2-ethylthiophane, or thiepane, and cyclisation of the latter yields thiirane, which may dimerize to form 1,4-dithiane.

3.11.9 Mass spectra from Py–GC-MS

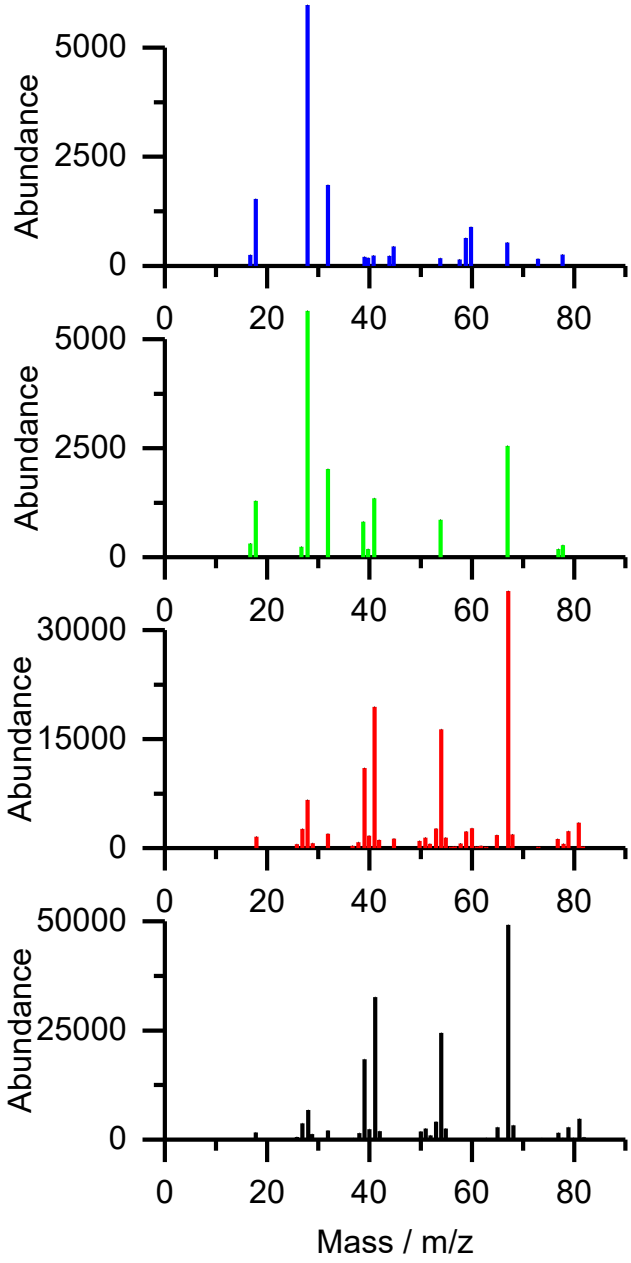

Figure S3.8. Mass spectra from Py-GC-MS measurements at a retention time of 2.6 min (blue region in Figure 3.4), assigned to 1,5-hexadiene.

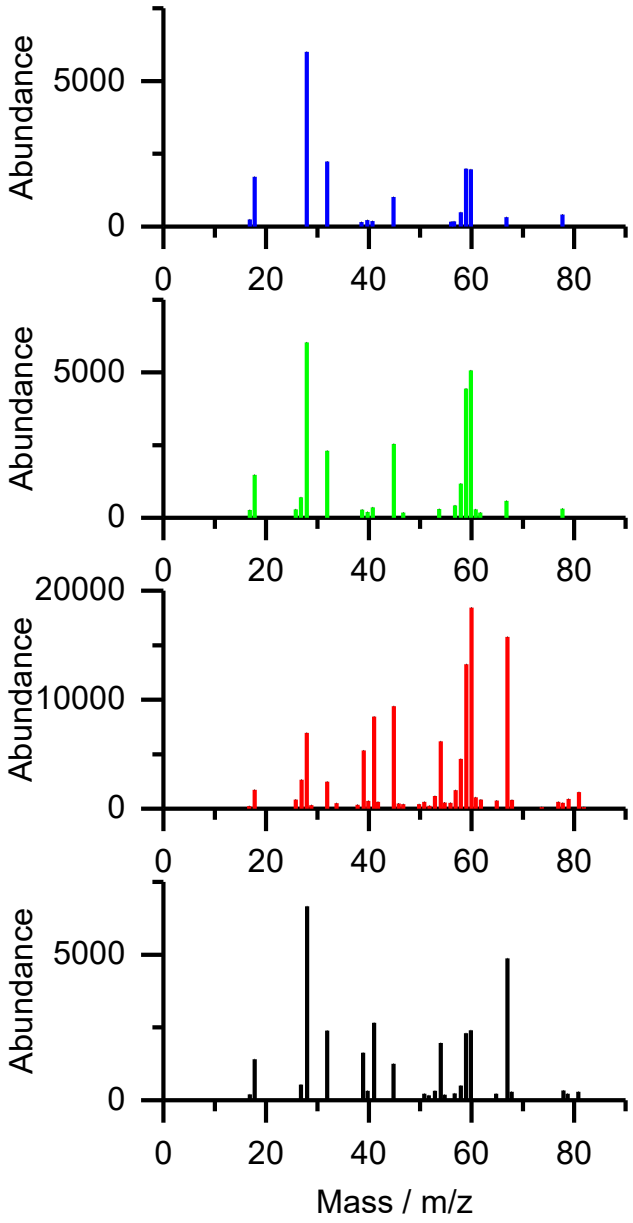

Figure S3.9. Mass spectra from Py-GC-MS measurements at a retention time of 2.63 min (yellow region in Figure 3.4), assigned to thiirane.

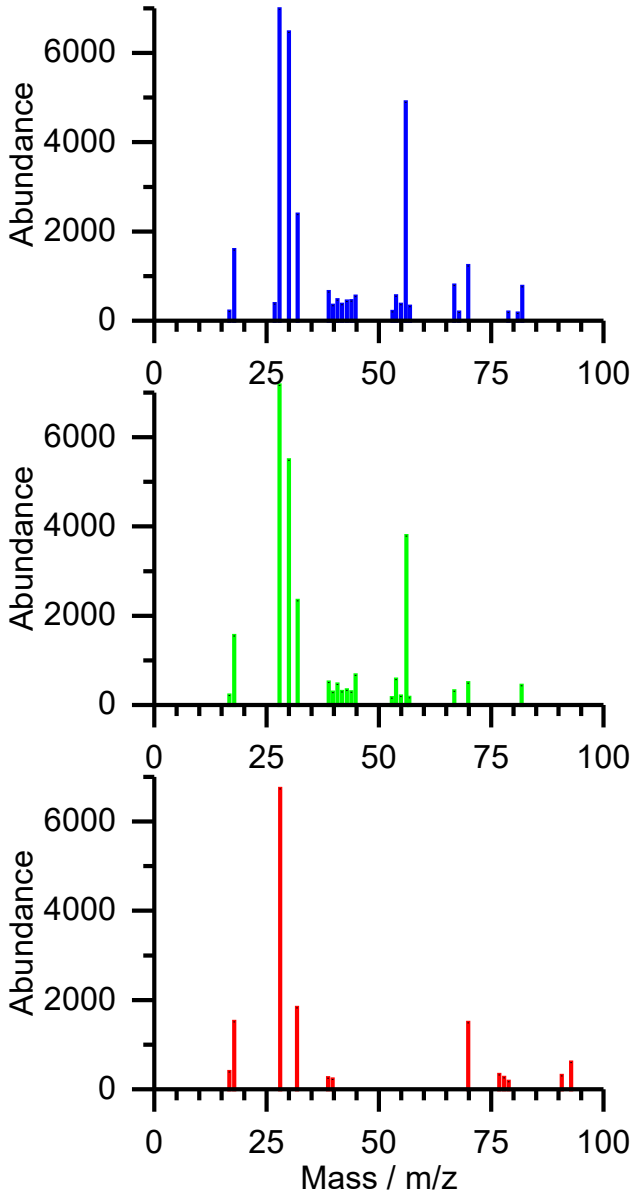

Figure S3.10. Mass spectra from Py-GC-MS measurements at a retention time of 6.1 min (purple region in Figure 3.4), assigned to 5-hexene-1-amine.

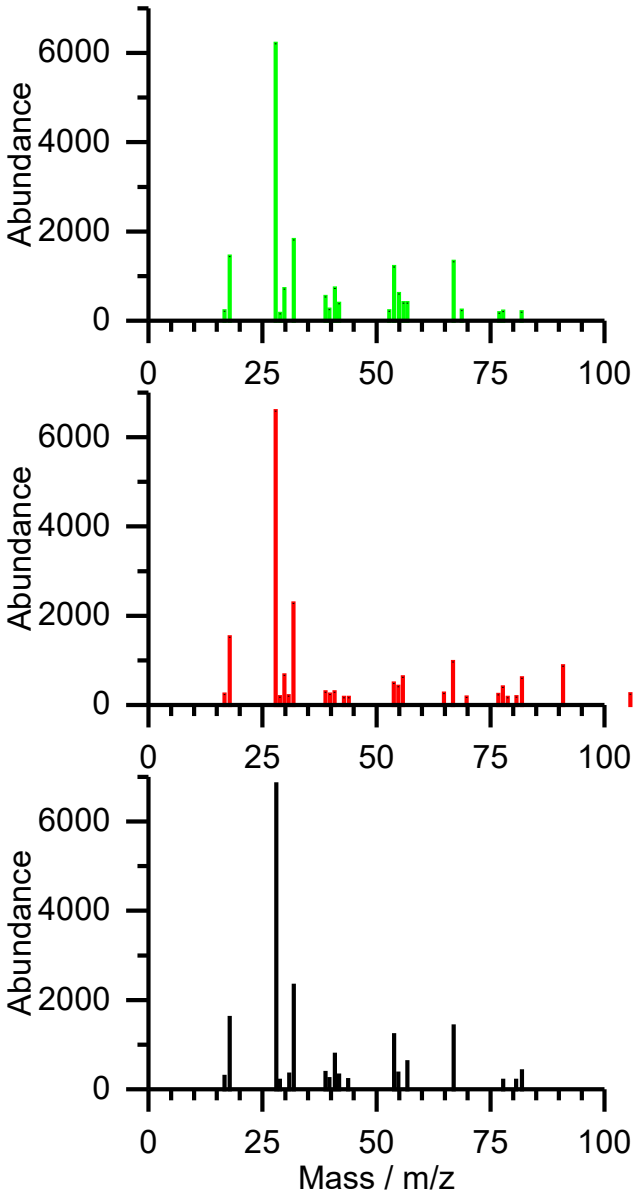

Figure S3.11. Mass spectra from Py-GC-MS measurements at a retention time of 6.6 min (purple region in Figure 3.4), assigned to 5-hexene-1-ol.

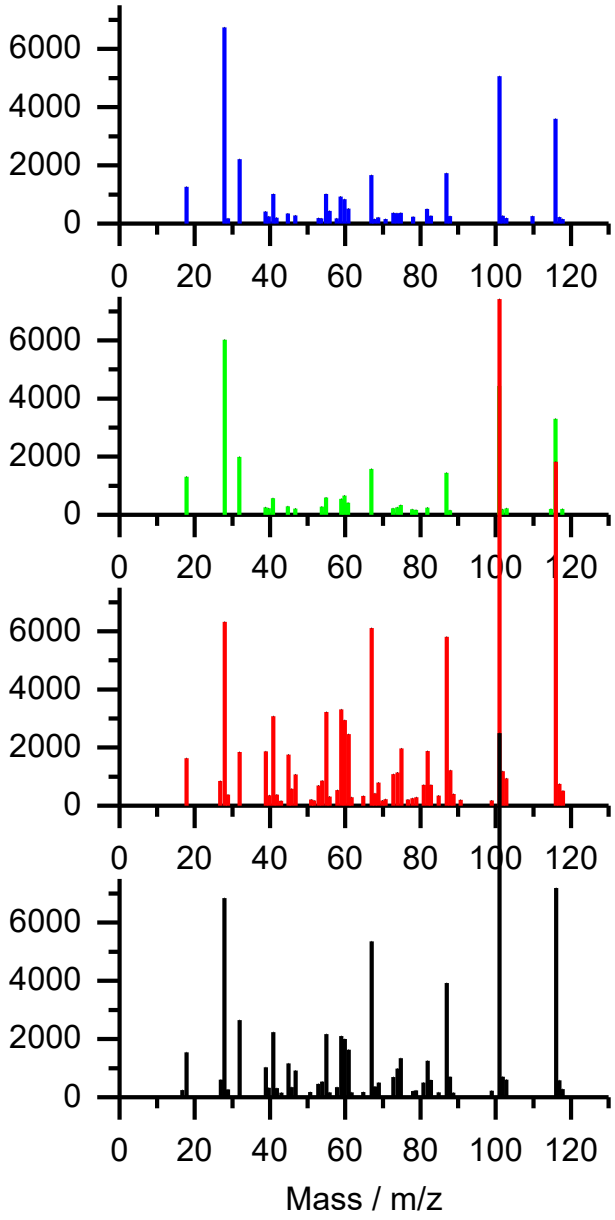

Figure S3.12. Mass spectra from Py-GC-MS measurements at a retention time of 7.8 min (yellow region in Figure 3.4), assigned to 4-methylthiane.

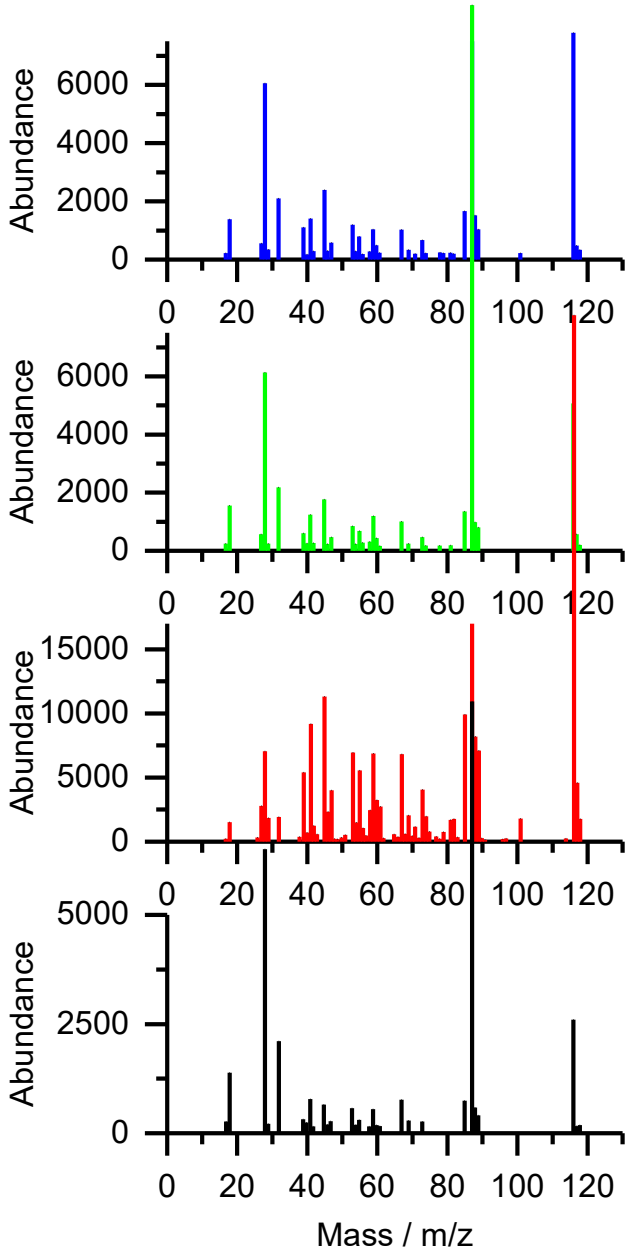

Figure S3.13. Mass spectra from Py-GC-MS measurements at a retention time of 8.2 min (yellow region in Figure 3.4), assigned to 2-ethylthiophane.

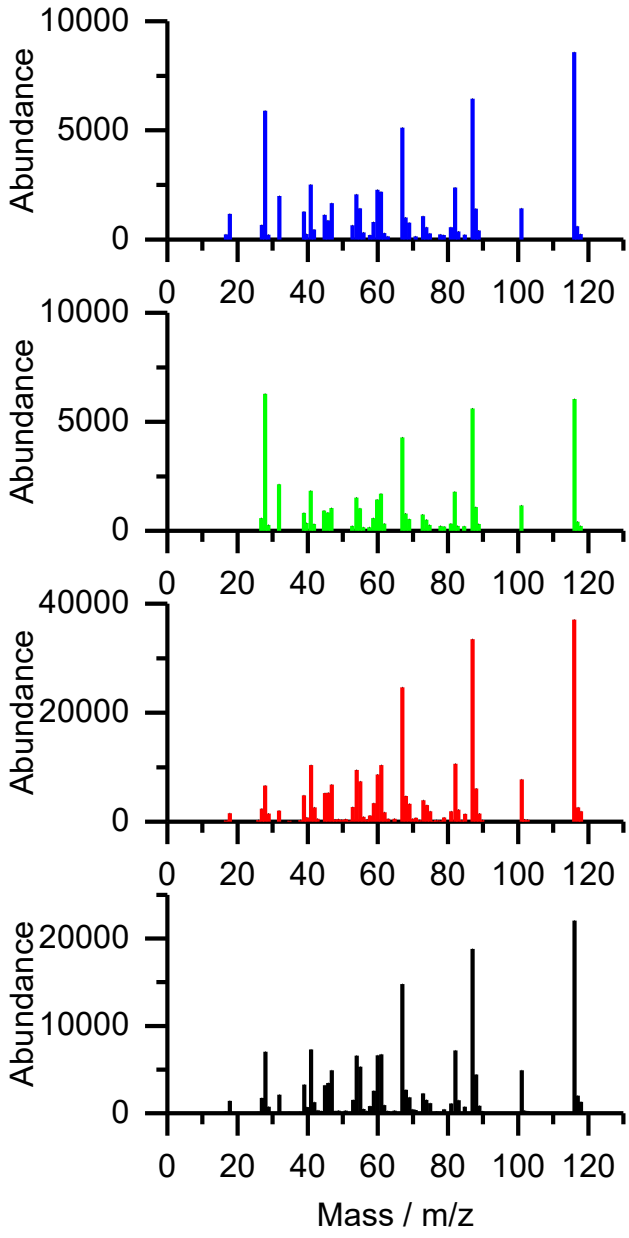

Figure S3.14. Mass spectra from Py-GC-MS measurements at a retention time of 9.3 min (yellow region in Figure 3.4), assigned to thiepane.

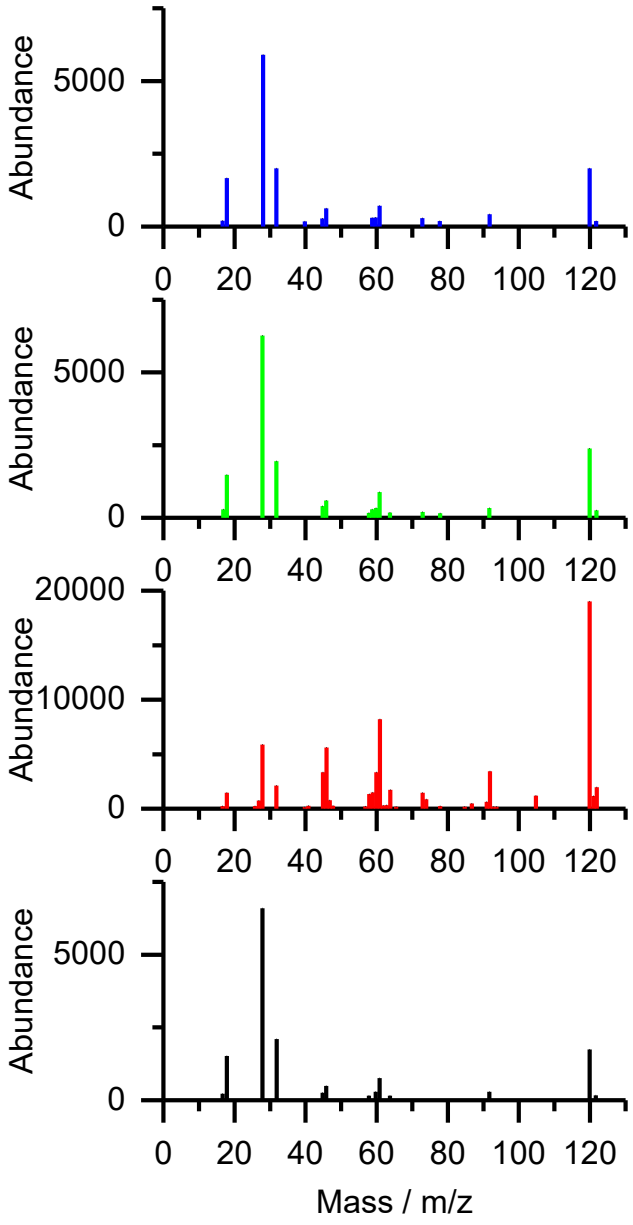

Figure S3.15. Mass spectra from Py-GC-MS measurements at a retention time of 10.2 min (yellow region in Figure 3.4), assigned to 1,4-dithiane.

3.11.10 Surface Etching

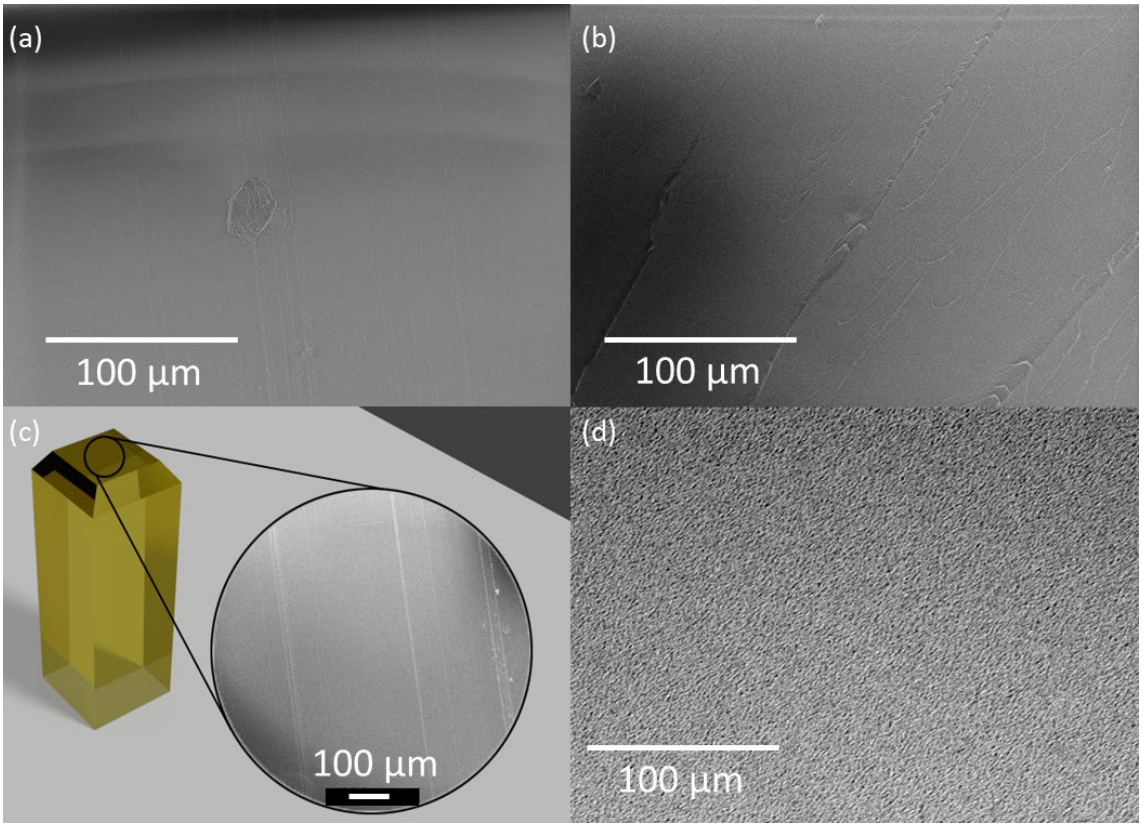

Figure S3.16. Electron microscopy images of EP-**4**: (a) SEM image of surface; (b) SEM image of surface after etching in dichloromethane under cryogenic conditions; (c) illustrated cut block used in etching experiments; (d) TEM image of surface stained with ruthenium tetroxide, showing no phase separation.

3.11.11 Glass-transition temperature from Differential Scanning Calorimetry

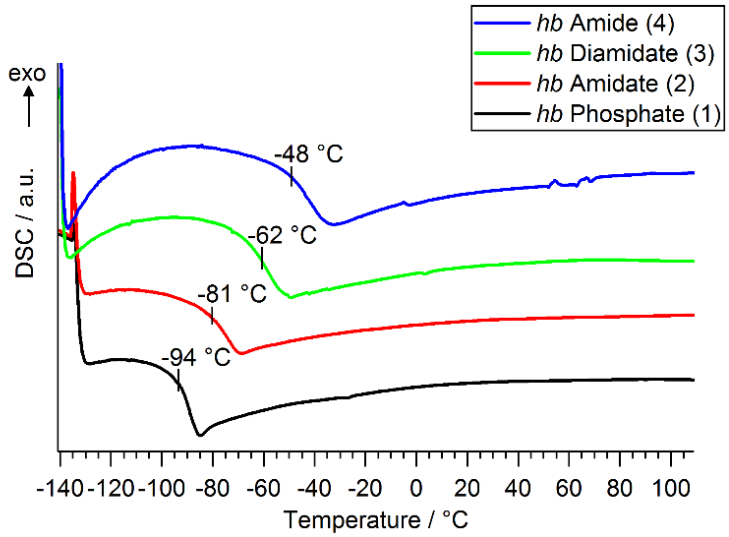

Figure S3.17. DSC curves of *hb*-FRs and noted glass-transition temperature (T_g).

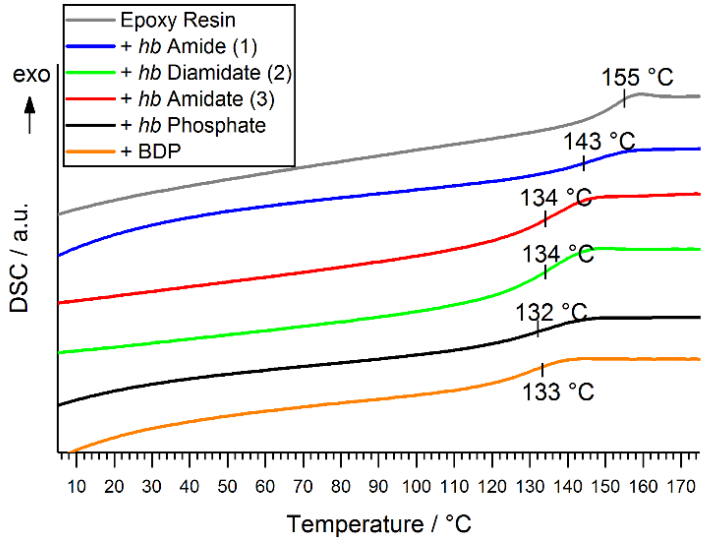

Figure S3.18. DSC curves of EP-*hb*-FRs and noted glass transition temperature (T_g).

3.11.12 Pyrolysis: Thermogravimetric Analysis of EP-*hb*-FRs

Table S3.4. Summary of TGA mass loss experiments of epoxy resins and flame retarded variants.

Material	$T_{5\%}$ / °C	T_{max} / °C	$T_{shoulder}$ / °C	*Mass loss / wt.-% (pre-main step)*	*Mass loss / wt.-% (main step)*	*Mass loss / wt.-% (shoulder)*	Residue / wt.-% (700 °C)
DGEBA-DMC	337.6 ± 0.9	372.4 ± 1.0	424.0 ± 5.0	-	62.0 ± 0.8	33.2 ± 0.3	4.5 ± 0.1
+ BDP	304.1 ± 1.2	357.3 ± 0.3	423.2 ± 0.1	-	74.6 ± 0.2	16.1 ± 0.3	8.2 ± 0.1
+ *hb* Phosphate (4)	288.6 ± 1.4	350.8 ± 1.2	423.8 ± 5.8	19.9 ± 0.1	54.6 ± 0.1	23.2 ± 0.7	7.7 ± 0.1
+ *hb* Amidate (3)	293.8 ± 3.2	351.8 ± 0.3	421.3 ± 3.9	-	77.8 ± 0.4	15.0 ± 0.2	6.8 ± 0.4
+ *hb* Diamidate (2)	286.6 ± 2.3	351.9 ± 2.0	423.2 ± 0.1	4.4 ± 0.2	69.8 ± 0.1	16.8 ± 0.2	8.1 ± 0.3
+ *hb* Amide (1)	282.6 ± 0.9	350.7 ± 1.2	420.5 ± 0.5	3.0 ± 0.1	74.7 ± 0.3	12.9 ± 0.2	8.0 ± 0.2

3.11.13 Pyrolysis: Condensed Phase Analysis

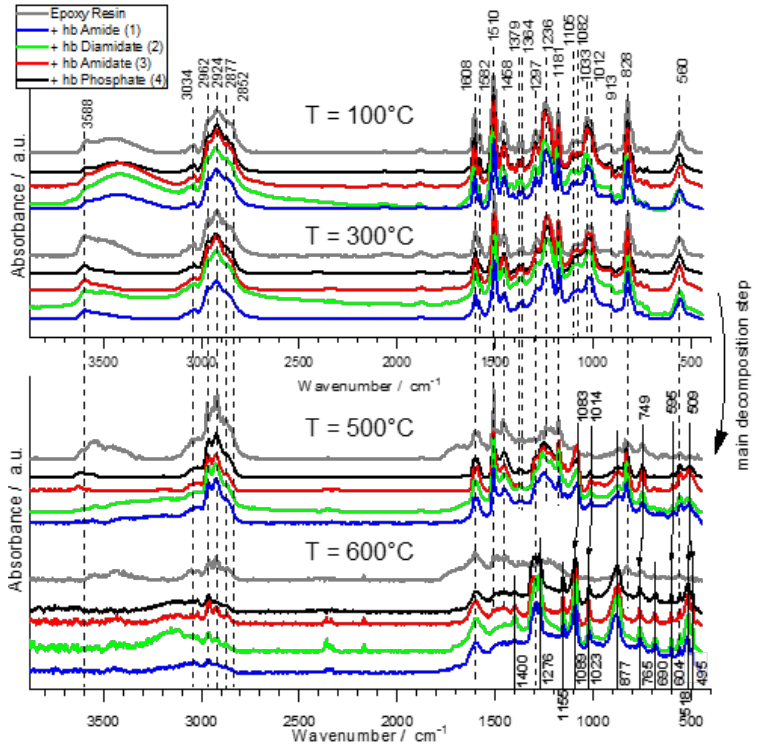

Figure S3.19. Condensed phase FTIR spectra of EP and EP-FRs at specific *T via* hot stage FTIR measurements. Dotted lines: EP signals; solid lines: P signals.

Table S3.5. Various phosphorus FTIR signals from literature compared to measured signals.

Measured [cm^{-1}]	Literature [cm^{-1}]	Group
2362	2200–2360[13]	R_2-(P=S)=O
	2600–2540[13]	R-(S-H)
1400	1100–1400 (cyclic compound)[14]	ν(P=N)
	1230–1500 (acyclic compound)[14]	
1400	1380–1425[15]	(P-N-Ph)
1297–1276	1300–1250[15]	ν(P=O);
1297–1276	1346–1255[13]	ν_{sym}(P-CH_3)
1155	1240–1180[15]	R_2-(P=O)-OH
	1240–1190[15]	P-O-(Aryl-C)
1089	1130–1090[13]	ν(P-Ph)
	1050–1030[15]	P-O-(Alkyl-C)
1023	1130–1090[15]	Phosphate (inorganic)
	1040–909[13]	ν(P-OH)=O
877 (wide)	990–885[15]	P-O-P
	977–842 (interacts with P-O-C)[13]	δ_{wag}(P-H)
765, 690	754–634[13]	ν(P-C)
604, 518, 495	540–485[14]	ν_{skel}(C-C)

Hot Stage FTIR analysis was used to determine the changes in chemical structure of EP-*hb*-FRs in the condensed phase; spectra are from 100 °C, 300 °C (between $T_{5\%}$ and T_{max}), 500 °C (after T_{max}), and 600 °C (Figure S3.19). At $T > T_{max}$, i.e. the spectra at 500 and 600 °C, the disappearance of characteristic DGEBA-DMC bands of the EP was detected, due to thermal decomposition of the matrix as previously reported.[16] At T = 600 °C, there were only very few characteristic bands visible and the spectrum was very noisy due to complete decomposition. Especially bands at 1510 cm^{-1} (bisphenol A) and at 1224 and 1028 cm^{-1} (2-hydroxytrimethylene) showed a strong decrease in absorption due to volatilization of bisphenol A units. The EP-*hb*-FR spectra revealed the appearance of bands which were assigned to various phosphorus-containing species at T = 500 °C and especially at T = 600 °C (Table S3.5). Crucially, the band at 1400 cm^{-1} corresponding to (P=N) or (P-N-Ph) stretching vibrations and is visible for the resins with N-containing FRs, which correlates with previous investigations of the monomeric FR variants. This band was visible for EP-**4** as well, indicating that **4** interacts with the decomposing EP's amine component. The broad band between 1350–1250 cm^{-1} was assigned to the (P=O) or (P-CH_3) stretching vibration. The bands at 1155 cm^{-1} and the strong signal at 1089 cm^{-1} belong to (P=O) or aromatic hydrocarbons bound to phosphorus. The absorption band at 1089 cm^{-1} has also been noted in (-P-O-P-O) containing structures.[17] The broad band at 877 cm^{-1} was identified as those from di-substituted aromatic rings,[18-19] but may also indicate the presence of (P-O-P) bonds.[20] The two bands at 765 and 690 cm^{-1} indicated the formation of (P-C) bonds.

3.11.14 Flammability: Reaction to Small Flames

EP and all EP-FRs were tested *via* UL-94 and limiting oxygen index (LOI) experiments to ascertain their flammability characteristics and reaction-to-small-flame behavior. The results of these experiments are summarized in Table S3.6. EP exhibited an oxygen index (OI) of 18.7 vol.-% in LOI experiments and the addition of FRs increased OI above 22 vol.-%. The benchmark FR BDP increased OI to the highest value of all tested materials (24.0 vol.-%). For *hb*-FRs, EP-**4** displayed the lowest OI of all tested materials (22.1 vol.-%), and the OI increased with increasing N-content in the P-binding sphere, with EP-**1** presenting the highest OI of all *hb*-FRs (23.3 vol.-%). Although the change in OI is not very pronounced, it is explained by the decomposition mechanism described in Scheme 3.2: *hb*-FRs with more (P-N) bonds form thermally stable char and suppress flammability more effectively than those materials with higher amounts of (P-O) bonds.

Table S3.6. Results of reaction-to-small-flame tests LOI and UL-94 for EP and EP-FRs.

	EP	EP-**1**	EP-**2**	EP-**3**	EP-**4**	EP-BDP
LOI						
O_2 / vol.-%	18.7 ± 0.3	23.3 ± 0.2	22.6 ± 0.2	22.5 ± 0.2	22.1 ± 0.2	24.0 ± 0.2
UL-94						
Classification	HB	HB	HB	HB75	HB	HB
Burn speed / mm s^{-1}	31.7 ± 3.6	22.0 ± 0.7	27.0 ± 0.1	41.8 ± 1.5	27.7 ± 4.4	19.6 ± 3.6

The UL-94 test results highlighted that all materials fail to attain a V-classification due mainly to the intense burning and the flaming dripping of the EP matrix. In horizontal tests, all materials achieved an HB classification, except EP-**3**. EP showed a burn speed of 31.7 mm s^{-1}, and EP-BDP attained the lowest burning speed at 19.6 mm s^{-1}. EP-*hb*-FRs exhibited lower burning speed than EP, and EP-**1** had the lowest value (22.0 mm s^{-1}). The reduction in burning speed in UL-94 tests also point to a reduction of flammability with increasing P-N bonds of the *hb*-system for the same reason. The reaction-to-small-flames experiments highlight that higher loadings than the chosen FR load (10 wt.-%) are necessary to attain OI-values and V-classification required for high-performance materials.[21] However, it must be stated that the results exemplify that a reduction of burning speed and a relative increase in OI of approx. 18–26% was possible already at relatively low loadings, signifying the efficacy of *hb*-FRs in EP.

3.11.15 Fire Behavior

Table S3.7. Maximum average rate of heat emission (MARHE) and fire growth rate (FIGRA) of EP and EP-FRs via cone calorimeter measurements.

	EP	EP-**1**	EP-**2**	EP-**3**	EP-**4**	EP-BDP
MARHE / kWm^{-2}	732 ±24	571 ±25	560 ±16	439 ±3	466 ±14	546 ±12
FIGRA / $kWm^{-2}\,s^{-1}$	15.5 ±2.3	10.0 ±0.1	8.1 ±0.1	7.5 ±0.6	9.0 ±0.2	11.0 ±0.7

The maximum average rate of heat emission (MARHE, from DIN CEN/TS 45545) and fire growth rate (FIGRA, from EN 13823) are used to assess fire protection behavior and help to quantify combustion and flame inhibition into tangible values (Table S3.7). For EP, the MARHE was 732 kW m^{-2} and the FIGRA was 15.5 kW m^{-2} s^{-1}. EP-BDP displayed a 25% lower MARHE (546 kW m^{-2}) and a 29% lower FIGRA (11.0 kW m^{-2} s^{-1}). Furthermore, all EP-*hb*-FRs exhibited a 22–36% reduction in MARHE and a 35–48% lower FIGRA. All *hb*-FRs reduced FIGRA more strongly than BDP, while only **3** and **4** lowered the MARHE more strongly than BDP. Although there are differences among the respective *hb*-FRs in terms of lowering PHRR, THE, MARHE, and FIGRA, the results speak for the ability of the chemical superstructure of the *hb*-FRs to perform on equal terms to an aromatic benchmark FR under forced flaming conditions, further illustrating their multifunctional abilities.

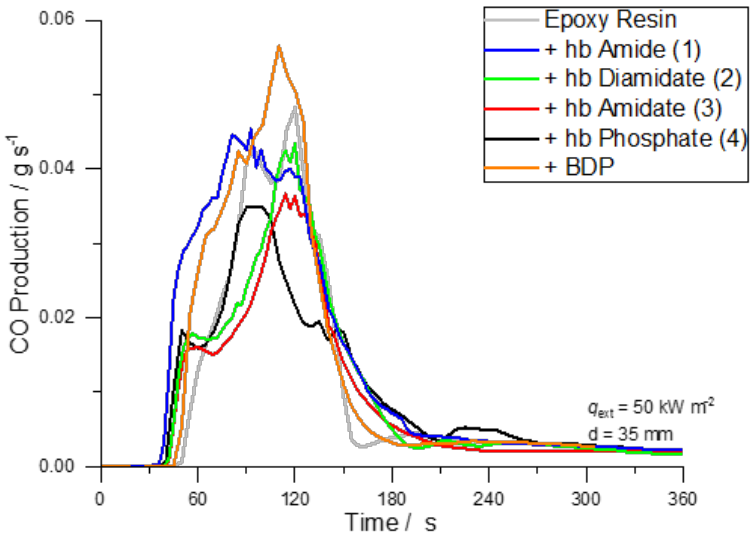

Figure S3.20. Carbon monoxide (CO) production over *t* of EP and EP-FRs during cone calorimeter measurements.

Table S3.8. CO yields (COY).

	EP	EP-**1**	EP-**2**	EP-**3**	EP-**4**	EP-BDP
COY / 10^{-2} g g^{-1}	9.0 ±1.0	12.9 ±0.5	9.8 ±0.2	9.4 ±0.1	9.9 ±0.1	11.3 ±0.7

Figure S3.20 shows the carbon monoxide (CO) production during cone calorimeter measurements, and CO yields (COY) are displayed in Table S3.8. The CO production during combustion is crucial to understanding the FR effect: a reduction in χ (combustion efficiency) is accompanied by an increase in CO and smoke production, as they are byproducts of an incomplete combustion. Consequently, efficient flame inhibition is intrinsically accompanied by an increase in COY.[22] EP showed a CO yield of $9.0 \cdot 10^{-2}$ g g^{-1}, while EP-BDP exhibited a 26% increase in COY. The *hb*-FRs increased COY by 4–43%: EP-**1** showed the largest COY increase (43%), indicating the most incomplete combustion for this material, while EP-**3** displayed the lowest relative COY increase at 4%. Table 3.1 also compares the material's EHC, which is a parameter for gas phase activity, and a reduction in EHC signifies effective flame inhibition.[23] BDP, **3**, and **4** lowered EHC in EP by 16, 6 and 10%, respectively, while **2** had no effect on EHC of EP, and **1** actually increased EHC by 5%. These results provide further evidence that *hb*-FRs with higher O-content in the binding sphere of P show a stronger gas phase mechanism resulting in lower EHC, while those with higher N-content present a more pronounced condensed phase mechanism that leads to a decreased combustion efficiency and higher CO yield. These findings correlate well with the mass loss behavior of *hb*-FRs under pyrolysis, where a critical O:N ratio governed the decomposition behavior.

3.11.16 Residue analysis

The residues from cone calorimeter tests were investigated *via* scanning electron microscopy (SEM) and elemental analysis to understand the micro- and macroscopic effects of *hb*-FRs on EP. The residues in Figure S3.21 exemplify the condensed phase effect of *hb*-FRs: Figure S3.21a shows an EP specimen before and Figure S3.21b displays the residue after cone calorimeter measurements. EP combusted almost completely with only a very small residue amount (0.7 wt.-%). For EP-*hb*-FRs (Figure S3.21d,e,h,i), the formation of char fixed fuel into the condensed phase leading to increased residue yields (7–12 wt.-%). The residues had a puffy, foam-like structure. The voluminous structure pointed to an intumescent system, as evidenced by the swollen characteristic of the char-structure averaging at 4 cm in height (Figure S3.21e,i). Cross-sections of the residues revealed a multicellular structures, and SEM images from the residue surfaces (Figure S3.21f,j) and cores (Figure S3.21g,k) provided further evidence of an intumescent system.[24-25] The morphology of the residue cores consisted of a 3-D network of bubble-like surfaces with an open cell structure.[26] The bubbles' diameter ranged from <300 µm for EP-**1** to roughly 500 µm for EP-**4**. The surface images exemplify that the protective layer of the intumescent char relied on the formation of bubbles insulating the underlying material from irradiation. The bubbles near the top

of the sample were exposed to radiation and thermo-oxidation after flame-out, leading to a fusing of the cells and the formation of a rough carbonaceous surface topography. This explains the phenomenon seen in cone calorimeter measurements, where a decline in HRR and a small plateau-like shape of the HRR(*t*) curve roughly 20–30 s after the ignition was observed. The decomposing material formed an intumescent foam and when the top layer decomposed, its insulating properties diminished, resulting in renewed decomposition of the underlying material. Notably, the bubble-size for EP-**4** were larger than those in EP-**1**. This phenomenon results from increased partial pressure inside the material caused by the higher gas production of EP-**4** during decomposition, which led to better thermal insulation and lower PHRR.

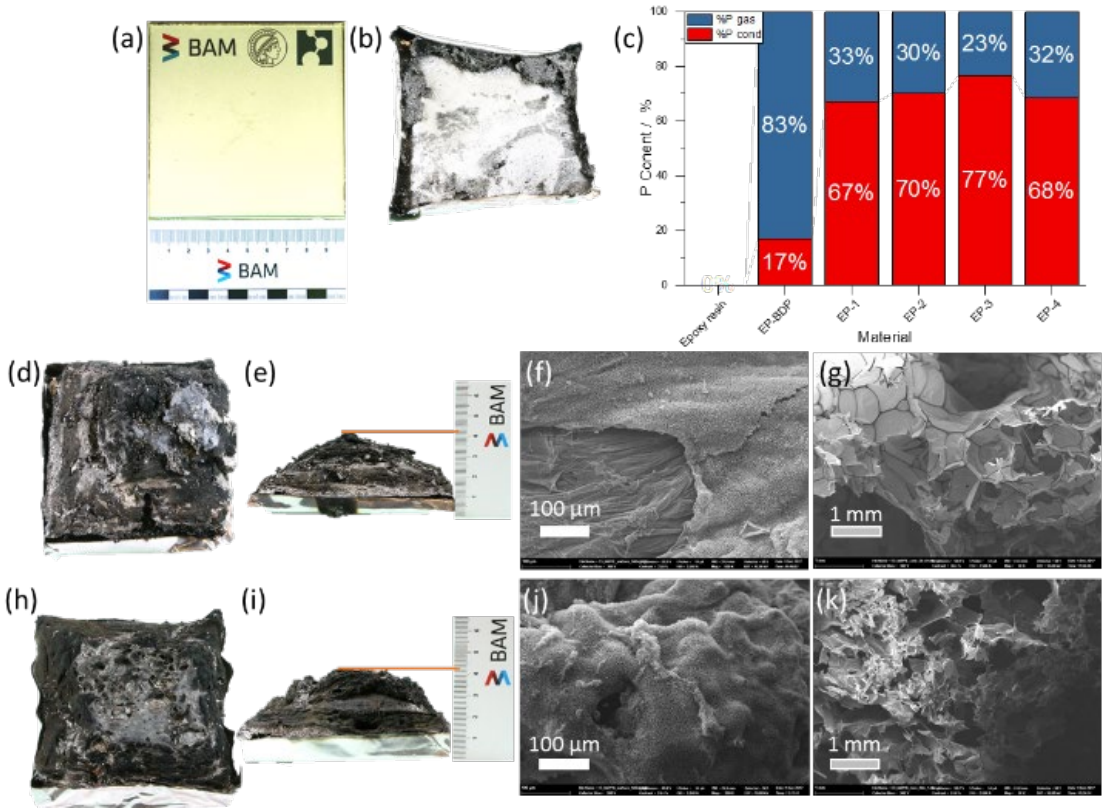

Figure S3.21. Residue analysis of samples after cone calorimeter experiments; (a) Image of EP specimen before measurement; (b) EP specimen after measurement, exhibiting little residue; (c) P-content in gas (blue) and condensed (red) phase, calculated *via* elemental analysis of residues; (d,h) Residue image (top view) of EP-**4** and EP-**1**; (e,i) Residue image (profile view) of EP-4 and EP-1; (f,j) SEM images of EP-**4** and EP-**1** residue surface; (g,k) SEM image of EP-**4** and EP-**1** residue core.

Figure S3.21c portrays the P-content in the condensed phase (red) of residues after cone calorimeter measurements *via* elemental analysis. The amount of P present in the gas phase (blue)

was calculated by subtracting the measured mass of P in the residue from the calculated mass of P in the initial EP-FR. As Figure S3.21c shows, BDP had 17% P-content in the condensed phase, meaning 83% of P went into the gas phase, which is in accordance with previous findings.[8, 27] Figure S3.21c also displays that, while there are differences in the P-content among them, all *hb*-FRs exhibited between 67–77% P-content in the condensed and 23–33% in the gas-phase. This corresponds well with the increase in residue yields of EP-*hb*-FRs in forced-flaming tests and showcases the ability of *hb*-FRs to retain fuel *via* specific reactions of P in the condensed phase. It should be noted that the elemental analysis was performed on residue samples taken after cone calorimeter measurements (end of test) and not specifically at flame-out, meaning there is substantial thermo-oxidation of the sample. As many (P-N)-containing species are not thermally stable, their decomposition during thermo-oxidation explains the lower P-content of EP-**1** and EP-**2** samples.

However, when comparing *hb*-FRs to their low molar mass monomers, the results from elemental analysis point to a shift in mode of action. In previous findings, the monomer of **1** exhibited an 80% P-content in the condensed phase, while the monomer of **2** displayed 55% P-content in the gas phase.[28] This change in condensed phase activity can be rationalized by the increase in chemical interaction between EP and FR during combustion due to the higher thermal stability of *hb*-FR, further highlighting the multifunctional capabilities of P-FRs with complex molecular architectures.

3.11.17 References SI Chapter 3

[1] D. Marsh, Chemical Defence Experimental Establishment Porton Down (United Kingdom), **1954**.

[2] K. N. Bauer, L. Liu, D. Andrienko, M. Wagner, E. K. Macdonald, M. P. Shaver, F. R. Wurm, *Macromolecules* **2018**, *51*, 1272-1279.

[3] P. A. Glaude, C. Melius, W. J. Pitz, C. K. Westbrook, *P Combust Inst* **2002**, *29*, 2469-2476.

[4] S. Hörold, *Polymer Degradation and Stability* **1999**, *64*, 427-431.

[5] W. Gerrard, *J Chem Soc* **1944**, 85-90.

[6] R. W. Baier, S. W. Weller, *Ind Eng Chem Proc Dd* **1967**, *6*, 380-385.

[7] S. Gaan, G. Sun, K. Hutches, M. H. Engelhard, *Polymer Degradation and Stability* **2008**, *93*, 99-108.

[8] S. V. Levchik, E. D. Weil, *Journal of Fire Sciences* **2006**, *24*, 345-364.

[9] S. V. Levchik, G. F. Levchik, A. I. Balabanovich, E. D. Weil, M. Klatt, *Angew Makromol Chem* **1999**, *264*, 48-55.

[10] C. Nguyen, J. Kim, *Polymer Degradation and Stability* **2008**, *93*, 1037-1043.

[11] S. V. Levchik, in *Flame Retardant Polymer Nanocomposites* (Eds.: A. B. Morgan, C. A. Wilkie), John Wiley & Sons, Inc., **2006**, pp. 1-29.

[12] E. D. Weil, *Fire retardancy of polymeric materials* **2000**, 115-145.

[13] C. Hampton, D. Demoin, R. E. J. O. S. Glaser, **2010**.

[14] G. Socrates, *Infrared and Raman characteristic group frequencies: tables and charts*, John Wiley & Sons, **2004**.

[15] M. Hesse, H. Meier, B. Zeeh, *Spektroskopische Methoden in der organischen Chemie*, Georg Thieme Verlag, **2005**.

[16] B. Perret, B. Schartel, K. Stöß, M. Ciesielski, J. Diederichs, M. Döring, J. Krämer, V. Altstädt, *European Polymer Journal* **2011**, *47*, 1081-1089.

[17] L. C. Thomas, *Interpretation of the infrared spectra of organophosphorus compounds*, Heyden London, **1974**.

[18] A. S. Politou, C. Morterra, M. J. D. Low, *Carbon* **1990**, *28*, 529-538.

[19] M. C. Despinasse, B. Schartel, *Thermochimica Acta* **2013**, *563*, 51-61.

[20] U. Braun, A. I. Balabanovich, B. Schartel, U. Knoll, J. Artner, M. Ciesielski, M. Döring, R. Perez, J. K. W. Sandler, V. Altstädt, T. Hoffmann, D. Pospiech, *Polymer* **2006**, *47*, 8495-8508.

[21] A. F. Grand, C. A. Wilkie, *Fire retardancy of polymeric materials*, CRC Press, **2000**.

[22] B. Schartel, *Materials* **2010**, *3*, 4710-4745.

[23] B. Schartel, B. Perret, B. Dittrich, M. Ciesielski, J. Krämer, P. Müller, V. Altstädt, L. Zang, M. Döring, *Macromolecular Materials and Engineering* **2016**, *301*, 9-35.

[24] J. Alongi, Z. D. Han, S. Bourbigot, *Progress in Polymer Science* **2015**, *51*, 28-73.

[25] P. Müller, M. Morys, A. Sut, C. Jäger, B. Illerhaus, B. Schartel, *Polymer Degradation and Stability* **2016**, *130*, 307-319.

[26] S. Bourbigot, M. Le Bras, in *Plastics Flammability Handbook* (Ed.: J. Troitzsch), Carl Hanser Verlag GmbH & Co. KG, Munich, **2004**, pp. 133-172.

[27] S. Rabe, Y. Chuenban, B. Schartel, *Materials* **2017**, *10*, 23.

[28] J. C. Markwart, A. Battig, L. Zimmermann, M. Wagner, J. Fischer, B. Schartel, F. R. Wurm, *ACS Applied Polymer Materials* **2019**, *1*, 1118-1128.

4. Comparison of novel aromatic and aliphatic hyperbranched poly(phosphoester)s as flame retardants in epoxy resins

Jens C. Markwart[a,b]+, Alexander Battig[c]+, Maria M. Velencoso[a], Dennis Pollok[a], Bernhard Schartel[c], Frederik R. Wurm[a]*

[a] *Physical Chemistry of Polymers - Max Planck Institute for Polymer Research, Ackermannweg 10, 55128 Mainz, Germany*

[b] *Technical Properties of Polymeric Materials - Bundesanstalt für Materialforschung und -prüfung (BAM), Unter den Eichen 87, 12205 Berlin, Germany*

[c] *Graduate School Materials Science in Mainz, Staudinger Weg 9, 55128 Mainz, Germany*

+ *These authors contributed equally to this work.*

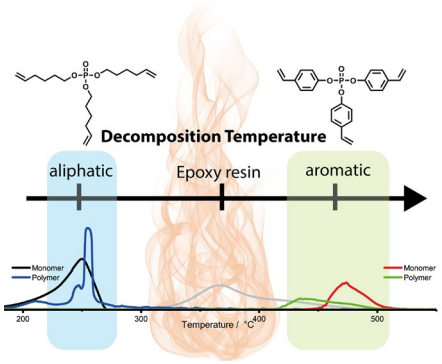

Keywords: phosphorus, flame retardants, epoxies, mechanistic study, toxicity

4.1 Notes

To be submitted in this or altered form.

Alexander Battig performed the flame-retardancy measurements. Maria M. Velencoso and Dennis Pollok performed parts of the syntheses.

4.2 Abstract

The current trend for future flame retardants (FRs) goes to novel efficient halogen-free materials, due to the ban of several halogenated flame retardants. Among the most promising alternatives are phosphorus-based flame retardants, and of those, polymeric materials with complex shape has been recently reported. Herein, we present novel aromatic and aliphatic, hyperbranched, halogen-free polyphosphoesters (hbPPEs), which were synthesized by olefin metathesis polymerization and investigated them as a flame retardant in epoxy resins. We compare their efficiency aliphatic vs. aromatic and further assess the differences between the monomeric compounds and the hbPPEs. The decomposition and vaporizing behavior of a compound is an important factor in its flame-retardant behavior, but also the interaction with the pyrolysing matrix has a significant influence on the performance. Therefore, the challenge in designing a FR is to optimize the chemical structure and its decomposition pathway to the matrix, with regards to time and temperature. This behavior becomes obvious in this study and explains the superior gas phase activity of the aliphatic FRs.

4.3 Introduction

The overlap of the decomposition temperatures of a flame retardant (FR) and its polymer matrix is essential for its effectiveness in the case of fire.[1-3] Aromatic polymers typically have a higher thermal stability than aliphatic polymers. In the case of a FR, this higher thermal stability influences at which temperatures the active species are available in the gas phase. An important example for this behavior was reported for brominated aromatic and aliphatic flame retardants in polypropylene. The thermal decomposition of aliphatic flame retardants starts below the thermal decomposition of polypropylene, which leads to a good performance in this matrix. Aromatic flame retardants decompose after polypropylene and therefore, at the decomposition temperature of polypropylene, no optimal debromination is achieved, resulting in mediocre performance.[4]

Here, we compared an aromatic with an aliphatic hyperbranched polyphosphoester (hbPPE) prepared via acyclic triene metathesis (ATMET) polymerization as additive FRs in epoxy resins. We discuss the structure-property relationship and utilize thermal analysis to understand the flame-retardant mechanism and investigate the influence of the higher thermal stability of the aromatic compounds and the resulting availability of phosphorus in the gas phase.[4]

In spite of their high flammability, the excellent mechanical and insulating properties of epoxy resins have led to their widespread application as lightweight material products for construction or electrical equipment. In 2016, the market for epoxy resins had a volume of US$ 21.5 billion.[5] Typically, epoxy resins are treated with flame retardants in many applications.

For several decades, halogenated flame retardants were used as effective flame retardants. However, in recent years, due to their potential harm to health and environment, their use has been legislatively restricted around the world, promoting a growing demand for halogen-free alternatives, of which phosphorus is an attractive alternative.[6] Phosphorus in the gas phase is reported to be similar or even superior to hydrogen halides like HBr,[7] has attractive plasticizing properties,[8] adjustable hydrophilicity[9] and potential degradability[10] and biocompatibility.[11]

Versatility of polymer chemistry was used to address problems of low molar mass flame retardants, such as poor matrix compatibility, leaching or migration out of the polymer matrix. In literature, polyphosphoesters are gaining increased attention as a promising class of polymeric flame retardants because of the aforementioned reasons and their versatile chemistry that allows tuning their chemical structure to control degradation behavior and matrix compatibility. Branched polymers with their high number of reactive or end-groups, lower intrinsic viscosities and higher matrix compatibility compared to linear polymers are interesting candidates for flame retardant additives.[12-15] Also PPEs can be prepared as branched polymers, typically relying on the

pentavalency of phosphorus.[16] However, the majority of hbPPEs reported in literature are aliphatic materials, only a few publications have reported on aromatic hbPPEs.[17-21] The field is dominated mostly by classical linear aromatic phosphates, such as resorcinol bis(diphenyl phosphate) or bisphenol A bis(diphenyl phosphate) due to their good flame retardant performance, but typically with relatively low molar mass and definition.[22-24] To further understand the flame retardant mechanism and improve performance, additional research in the field of hbPPEs is necessary and this work contributes to this development.

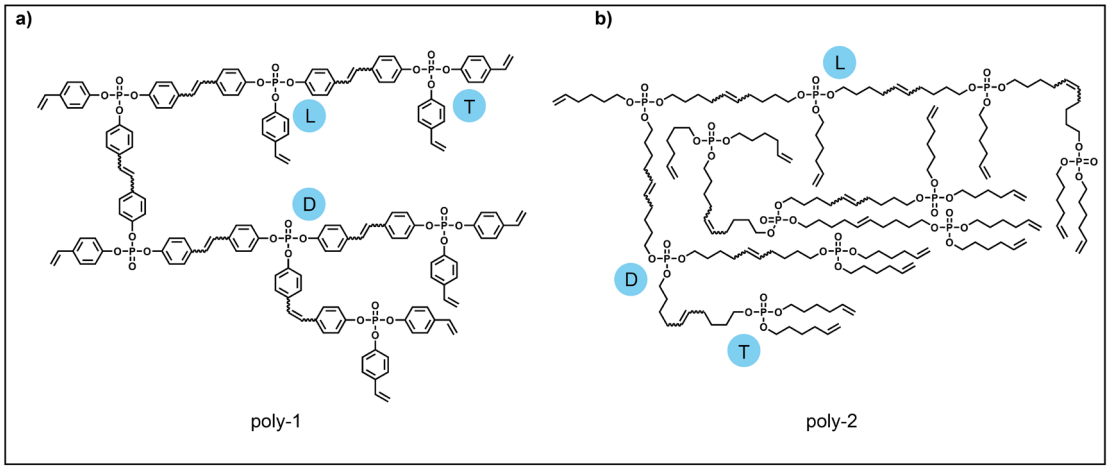

Scheme 4.1. Chemical structures of the investigated polymers: a) the aromatic poly-1 and b) the aliphatic poly-2.

4.4 Results

Acyclic diene metathesis polymerization (ADMET) is a versatile technique to prepare a broad range of linear functional polymers.[25-29] Olefin metathesis is also able to polymerize an A_3 monomer without any complementary B_2 monomer needed to give a hyperbranched structure.[14] For the synthesis of aromatic hbPPEs via acyclic triene metathesis (ATMET) polymerization, an aromatic phosphoester with vinyl groups is mandatory. In this study, the synthesis of tris(p-vinylphenyl)phosphate (1) was performed in a single reaction step from $POCl_3$ and 4-vinylphenol without further purification such as distillation or chromatography, thus obtaining the A_3-monomer in high purity and yield (Figure 4.1 a). The resulting monomer is a liquid at room temperature and has a phosphorus content of 7.66 wt.%. 1 is soluble in aromatic solvents (e.g. toluene) and halogenated solvents (e.g. dichloromethane and chloroform), and insoluble in water. 1 proved a thermal stability until a temperature of 127 °C (measured by TGA), at which the vinyl groups undergo radical cross-linking, due mainly to the electron-withdrawing resonance effect of

the adjacent phosphate at the ring. The cross-linking-reaction was proven by heating 1 to 300 °C in a silicon form for 2 h producing a hard, cross-linked PPE (Figure S4.23).

1 was used as a novel A_3 monomer for the ATMET polymerization to produce poly-1. The protocol of the ATMET polymerization of the 1 monomer is described in Figure 4.1 a and in detail in the Experimental Part. The monomer was dissolved together with the respective Grubbs catalyst in a 37 wt.% solution of 1-chloronaphthalene at 40 °C and the polymerization was conducted for 5 min in vacuo. Poly-1 was used as a flame-retardant additive in epoxy resins after precipitation into cold hexane. No polymerization in the bulk conditions at 60 °C was observed, probably due to the high viscosity of the monomer. We carried out polymerizations with Grubbs 1st generation catalyst at 40 ºC and 60 ºC, but almost only oligomers were observed (M_n < 1200 g mol^{-1} from size exclusion chromatography (SEC), Figure S4.1). When Grubbs Hoveyda 2nd generation catalyst was used, a broad range of molecular weights was obtained, depending on the reaction conditions (Table S4.1 and Figure 4.1 g). SEC showed a molar mass of ca. M_n 3000 g mol^{-1} with dispersities $M_w/M_n \approx 3$ after 120 min of reaction. However, when the addition of the catalyst was carried out in two phases, higher apparent molar masses of ca. M_n 4800 g mol^{-1} with broad molar mass distribution ($M_w/M_n \approx 11$) were obtained. Longer reaction times led to cross-linking of the material. To prevent crosslinking, the reaction can be terminated by the addition of ethyl vinyl ether or methyl acrylate. The resulting polymer was partially soluble in aromatic solvents (e.g. toluene) but proved high solubility in halogenated solvents (e.g. dichloromethane and chloroform). Extraction of the crude polymer with toluene resulted in the precipitation of the high molecular weight fractions, providing a poly-1 sample with a molar mass of ca. M_n 11500 g mol^{-1} and M_w/M_n = 1.7 from SEC (Figure 4.1 g).

The polymerization of 1 was followed by ^{1}H NMR spectroscopy (Figure 4.1 b and 4.1 c). After the polycondensation, the resonances of the terminal double bonds at 5.16 ppm, 5.61 ppm and 6.59 ppm decreased and a new signal at 6.92 ppm for the internal double bonds was detected. The ^{31}P NMR spectrum revealed a distinct signal at the same chemical environment (-17.73 ppm) of the monomer (Figure 4.1 d and 4.1 e).

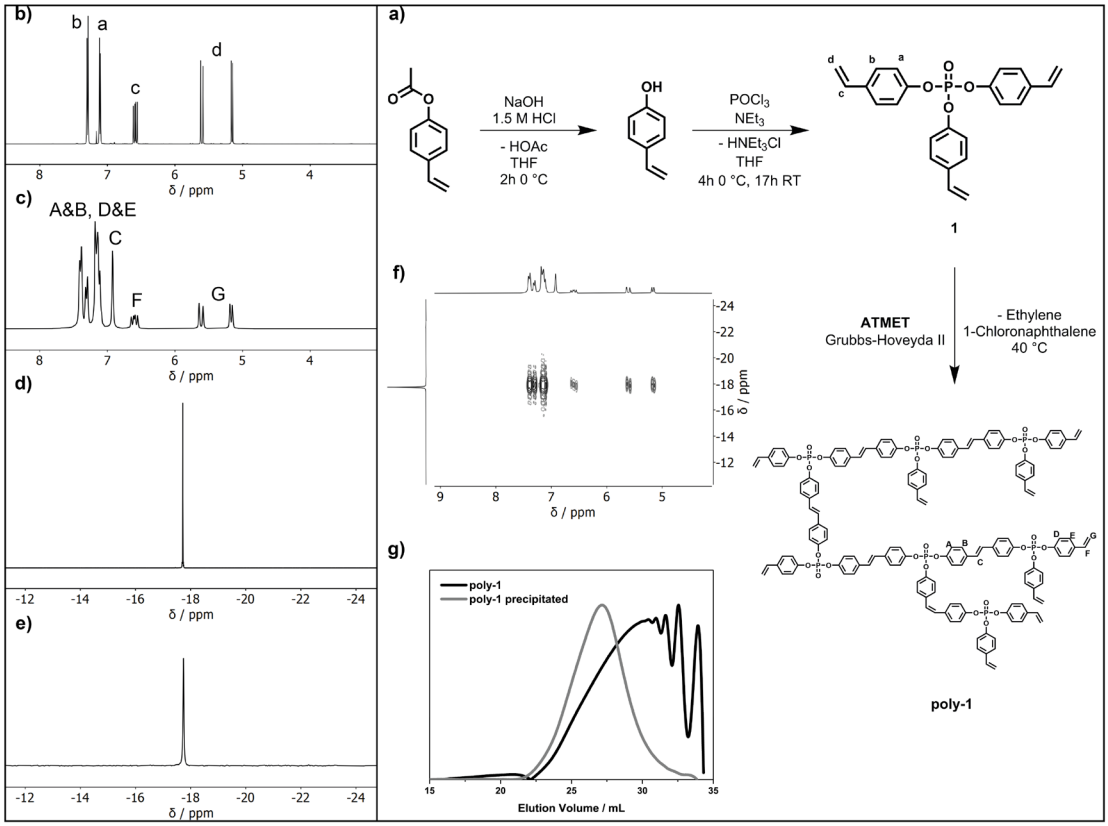

Figure 4.1. a) Synthesis scheme of tris(p-vinylphenyl)phosphate (1) and poly(tris(p-vinylphenyl)phosphate) (hbPPE); b) ^{1}H NMR spectra of 1; c) ^{1}H NMR spectra of poly-1; d) ^{31}P NMR spectra of 1; e) ^{31}P NMR spectra of poly-1; f) ^{1}H^{31}P HMBC spectra of poly-1; g) SEC curves of poly-1 before and after precipitation in Toluene.

In addition to the aromatic poly-1, we also synthesized the aliphatic analogue from tri(hex-5-en-1-yl)phosphate (2) by ATMET polymerization (cf. Figure 4.2 a and Experimental Part). Grubbs 1st generation catalyst was used for the polymerization which was terminated after ca. 15 min by the addition of ethyl vinyl ether, before cross-linking occurred and precipitated into hexane. The reaction was performed at 1 g and several polymer batches were combined to conduct the flame retardancy tests (after combining the different batches, SEC of the mixture showed a molar mass of ca. M_n 4400 g mol^{-1} (Figure S4.24)).

The successful polymerization of 2 was followed by ^{1}H NMR spectroscopy. The signals of the terminal double bonds at 5.81 ppm and 5.15 ppm decreased, whereas an additional signal for the internal double bonds at 5.40 ppm was detected (Figure 4.2 b and c). No shift in the phosphorus signal was observed, as the distance between the reactive olefins and the phosphorus is separated by the long alkyl chain (Figure 4.2 d and e). The increase in thermal stability of poly-2 compared to 2 was marginal ($T_{on,\ 10\%;\ poly\text{-}2}$ = 206 °C and $T_{on,\ 10\%;\ poly\text{-}2}$ 215 °C).

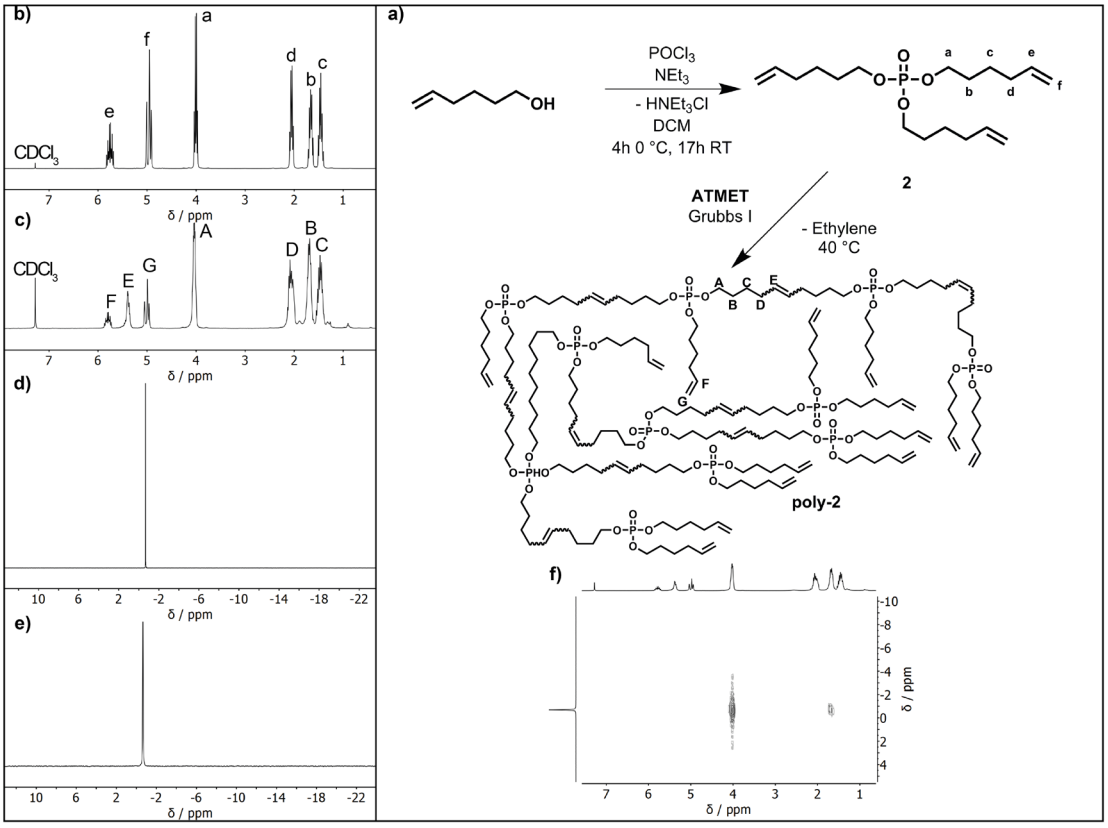

Figure 4.2. a) Synthesis scheme of tri(hex-5-en-1-yl)phosphate (2) and poly(tri(hex-5-en-1-yl)phosphate) (poly-2); b) ^{1}H NMR spectra of 2; c) ^{1}H NMR spectra of poly-2; d) ^{31}P NMR spectra of 2; e) ^{31}P NMR spectra of poly-2; f) ^{1}H^{31}P HMBC spectra of poly-2.

4.4.1 Thermal characterization of FRs

The analysis of both polymers by differential scanning calorimetry (DSC) revealed a large difference in the glass transition temperatures (T_g):poly-2 with its long and flexible aliphatic chains between the phosphate groups exhibited a low T_g of -66 °C. In contrast, poly-1 exhibited a T_g, which was 126 °C higher ($T_{g,\ poly\text{-}1}$ = 60 °C) due to the rigid aromatic groups.[30] This difference in T_g also impacts the T_g of the final FR-containing epoxy resins and therefore must be considered. If a plasticizing-effect on the final FR epoxy resin is desired, the aliphatic FR may eliminate the need for additional plasticizer.

4.4.2 Pyrolysis: Thermal decomposition via thermogravimetric analysis

The decomposition of the FRs under pyrolytic conditions were investigated using thermogravimetric analysis (TGA) (Figure 4.3). During a fire, the burning is dominated by an anaerobic pyrolysis producing volatile fuel, which is then combusted in the flame. This model is

accurate for most polymeric materials in fire scenarios such as developing fires.[31] Therefore, it is also applicable for fire tests of polymeric materials like flaming combustion in the cone calorimeter. Moreover, the model applies to reaction to small flame tests such as limited oxygen index (LOI) and UL 94, where the extinguishment of a flame is monitored. TGA under nitrogen is the most common analytical method to investigate the pyrolysis controlling the burning of polymeric materials.[31] The mass loss curve of 1 has two distinct decomposition steps: the first mass loss step of 1 at T_{dec} = 143 °C is likely due to the cleavage of PO-Ar or P-OAr bonds. This behavior is indicated by the release of aromatic compounds, which were identified by TGA coupled with FTIR spectroscopy (Figure S4.11). The resulting radicals of the bond cleavage initiate a radical polymerization reaction of the vinyl groups, resulting in a cross-linked polymer. This increase in molar mass prevents any further release into the gas phase. In contrast, poly-1 has a steady decrease of mass; it has only few free double bonds available, which allow for further cross-linking. Consequently, end-groups are continually eliminated. The second decomposition step is the main decomposing step of the material, which is at the maximum degradation temperature T_{max} = 470 °C for 1 and at T_{max} = 435 °C for poly-1. The slight reduction in T_{max} for poly-1 is explained with the fact that poly-1 has only few vinyl groups for post cross-linking available; therefore, 1 is more efficient in its cross-linking reaction during the first mass loss step, resulting in a high molecular mass, cross-linked network. The aliphatic compounds only experience one decomposition step, which is at much lower temperatures compared to the aromatic compounds. The difference between 2 and poly-2 is only marginal with 19 °C ($T_{max, 2}$ = 250 °C, $T_{max, poly\text{-}2}$ = 269 °C).

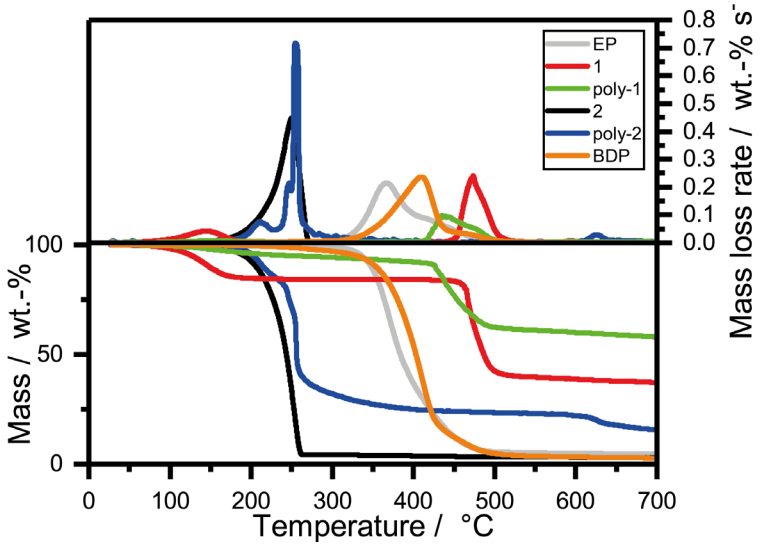

Figure 4.3. *Top*: Mass loss rate over temperature of pure flame retardants and the pure epoxy resin. *Bottom*: Pyrolysis investigations via thermogravimetric analysis (TGA; 10 K min-1; N_2); increase of residue yield from aliphatic to aromatic and from monomeric to polymeric.

Considering the decomposition temperature of the epoxy resin (EP, based on bisphenol A diglycidylether (DGEBA) and 2,2'-dimethyl-4,4'-methylene-bis-(cyclohexylamine) (DMC), ($T_{max, epoxy}$ = 366 °C)), another important observation was made: The aliphatic FRs decomposed at lower temperatures than the matrix, whereas the aromatic compounds decomposed at a higher temperatures than the matrix, resulting in potentially less interaction between matrix and FR (Figure 4.3). As a benchmark, the commercially available and industrially used FR bisphenol-A diphenyl phosphate (BDP) was chosen, as it was already used successfully in epoxy resins.[32-33] BDP has a decomposition temperature which is similar to the one of the epoxy resin ($T_{max, BDP}$ = 409 °C).

There is also a clear difference in residue amounts between the aliphatic and the aromatic materials: the residue increases from aliphatic to aromatic and from monomer to polymer. Residues increased from 3 wt.-% (2) to 37 wt.-% for 1 and from 24 wt.-% (poly-2) to 60 wt.-% for poly-1. The large difference in residues between aliphatic and aromatic compounds is explained by the interaction of phosphorus species with aromatic components, resulting in polyaromatic residue.[34]

4.4.3 Pyrolysis: Evolved gas analysis via TGA-FTIR

During TGA, the evolved gases were analyzed via FTIR (TGA-FTIR), giving insight into the decomposition products, and therefore the process as a whole (Figure S4.9-S4.12). 2 decomposed in a single step at 259 °C and its main decomposition products were 5-hexen-1-ol, 1,5-hexadiene, and a phosphate-species, as has been previously reported (Figure S4.9).[35] poly-2 exhibited disparate products during decomposition: at 216 °C, the spectrum shares most similarities to 1,3-hexadiene (c,t), especially by the bands at 999 and 905 cm^{-1}, but also those at 1806, 1605, 1460, 1316, and 1174 cm^{-1} (Figure S4.10).[36] At 259 °C, 2-octene (c,t) and *trans*-1,4-hexadiene were identified, the former by those bands at 1460, 1405, and 692 cm^{-1}, and the latter by the bands at 971 and 919 cm^{-1}. The FTIR spectra of monounsaturated hydrocarbons share many similarities, and the spectra are likely caused by the overlap of several species. For 1, the spectrum at 143 °C revealed the production of aromatic products including *p*-Cresol, 4-ethylphenol, and *p*-tolyl acetate, the latter a product of rearrangement reactions, and identified by the bands at 1786 (C=O) [37-38], 1372, 1011, and 908 cm^{-1} (Figure S4.11).[36] At 470 °C, the spectrum revealed the presence of bisphenol A, characteristically seen in the decomposition of epoxy resins,[39-42] providing evidence for cross-linking reactions occurring at elevated temperatures. For poly-1, two distinct decomposition products were identified at T_{max}: at 447 °C, the main product was phenol,

while at 487 °C, the production of benzene was clearly visible by the band at 672 cm^{-1} (Figure S4.12).

4.4.4 Thermal characterization of FRs in Epoxy resins

The FR-performance of the aliphatic and aromatic FRs was studied in an epoxy resin (EP) based on DGEBA and DMC. The epoxy plates were prepared by mixing DGEBA with DMC in the presence of 10 wt.-% of each FR, pouring the mixture into aluminum molds of desired dimensions, followed by curing for 3 h at 150 °C. The T_g of the epoxy resin was 155 °C. Typically, additive FRs act as plasticizers of the epoxy resin and reduce the glass transition temperature (T_g).[43] All flame-retarded epoxy resins with 10 wt.-% 1, poly-1, 2 and poly-2 exhibited lower T_gs by 6 – 28 °C compared to the epoxy resin. 1 had almost no influence on the T_g of EP due to its ridged aromatic structure (T_g of EP-1: 149 °C), poly-1 reduced the T_g to 127 °C and EP-BDP lies in between with a T_g of 133 °C. In all cases, the addition of aliphatic FRs 2 and poly-2 resulted in a higher or equivalent decrease in T_g compared to the aromatic FRs ($T_{g,\,2}$ = 127 °C, $T_{g,\,poly\text{-}2}$ = 149 °C). This difference in influence on the T_g was already expected due to the large difference in T_g of the pure FRs.

4.4.5 Pyrolysis: Evolved gas analysis via TGA/TGA-FTIR

A crucial step towards understanding the FR mechanisms is analyzing the pyrolysis of the epoxy resins with FRs by TGA. The epoxy resin had a main decomposition step at 366 °C and therefore no overlap with the aliphatic or aromatic FRs (except the reference BDP). This behavior is not ideal since it reduces the interaction between matrix and FR. The mass loss curves of EP-2 and EP-poly-1 have two distinct signals. In the case of EP-2, the low molecular weight compound already boils from the matrix before the matrix decomposes. This is indicated by the mass loss of approx. 10 wt.-%, which is equal to the amount of FR in the epoxy resin. For EP-poly-1, the first mass loss step is explained with the loss of terminal groups. The temperatures of highest decomposition rate (T_{max}) of EP-2 (T_{max} = 367 °C), EP-1 (T_{max} = 359 °C), EP-poly-1 (T_{max} = 361 °C) and EP-BDP (T_{max} = 357 °C) are very close to the T_{max} of the neat epoxy resin. However, poly-2 reduced T_{max} of EP to 334 °C. The broad range of decomposition is caused by the broad poly dispersity and the high number of low molecular weight fractions, which leave the matrix earlier compared to the higher molecular fragments.

The residue at 700 °C increased for all tested FR containing EPs. EP-2 had a low increase to 5.1 wt.-% compared to 4.5 wt.-% of EP. EP-BDP had a residue of 8.2 wt.-%, which was notably higher. EP-

1 had a residue of 9.1 wt.-%, while EP-poly-2 and EP-poly-1 were in a similar range with 13.3 wt.-% and 14.7 wt.-%, respectively, the latter presenting the greatest increase in residue yield.

The evolved gas analysis of FR-containing resins during pyrolysis (Figure S4.13-S4.16) revealed the development of decomposition products unique to the individual FRs. All materials exhibited the spectrum of DGEBA-DMC at 371 – 375 °C, except EP-poly-2 where this spectrum appeared at 349 °C. The EP-spectrum contained signals from bisphenol A (e.g. 1603, 1510, 1255, 1176 cm^{-1}) and ammonia (965, 930 cm^{-1}). Only EP-2 contained a phosphate signal (1033 cm^{-1})[44] at 373 °C (Figure S4.13). Both EP-2 and EP-poly-2 exhibited gas production at $T < T_{max}$ (266 and 287 °C, respectively): while for EP-2, the spectrum contained signals from 5-hexen-1-ol (3082, 2936, 1043, 918 cm^{-1}) and a phosphate species (1033 cm^{-1}) (Figure S4.13), the spectrum of EP-poly-2 displayed overlapped signals from 5-hexen-1-ol as well as longer-chained monounsaturated alcohols, as exemplified by the spectrum of oct-2-en-4-ol which contains the band at 967 cm^{-1} (Figure S4.14). These species resulted from the scission of the aliphatic chain between phosphate-moieties and then rearrangement reactions. For EP-1, the spectrum at 203 °C revealed the evolution of alkyl-substituted phenols such as *p*-*n*-propyl phenol, as identified by the bands at 1255, 1176 and 830 cm^{-1} which are prevalent throughout substituted aromatic molecules (Figure S4.15).[37-38] Moreover, the spectrum at 437 °C displayed other substituted phenols that are unlike bisphenol A, providing further support that 1 forms thermally stable polyaromatic compounds at elevated temperatures. EP-poly-1 also displayed similar polyaromatic molecules not stemming from bisphenol A such as 4-(3-hydroxyisoamyl) phenol at 482 °C (Figure S4.16), as identified by the lack of signals at 1332, 747, and 686 cm^{-1}.[36]

4.4.6 Pyrolysis: Condensed phase analysis via Hot-stage FTIR

Investigations via hot-stage FTIR into the condensed phase activity of the FRs in EP revealed many similarities and some subtle differences between the individual FRs (Figure S4.17-S4.10). At 100 °C (Figure S4.17), the spectrum of EP is clearly visible in all materials, yet some additional bands are visible: for EP-2 and EP-poly-2, the band at 1025 cm^{-1} was pronounced and may correspond to (P-O) signals which are strong for the aliphatic FRs.[44] The bands at 1639 and 914 cm^{-1} were present in EP-2 and EP-1, as these corresponds to ν_s(C=C) and δ_{oop}(C-H) of the vinyl groups, respectively.[37-38] EP-poly-2, EP-1, and EP-poly-1 contained a distinctly strong band at 961 cm^{-1} from δ_{oop}(C-H) of vinylene groups. The band at 734 cm^{-1} in EP-poly-1 may belong to δ_{oop}(C-H) of *cis*-vinylene groups; these may show higher absorbance in aromatic systems.[37-38] At 300 °C (Figure S4.18), the spectrum of EP-poly-2 exhibited the most changes due to advanced decomposition ($T_{5\%}$ = 249 °C)

compared to the other materials. Here, the band at 1083 cm^{-1} became pronounced; it may correspond to δ_{as}(P-O-C) or ν(P=O) of Ar_2-(P=O)-OH, especially because this band was prominent for EP-1 at 300 °C, but also all FR-containing spectra at 500 °C, thus implying the formation of aromatic P-compounds.[37-38, 44] For EP-poly-2, the appearance of the strong band at 521 cm^{-1} may signify the evolution of monounsaturated hydrocarbons, as *cis*- and *trans*-alkenes as well as alkyl-substituted vinylenes exhibit strong signals from skeletal vibrations here. At 500 °C (Figure S4.19), the band at 1293 cm^{-1} appeared for all materials other than EP, and most prominently for EP-poly-2. This band may belong to ν(P=O) of $(ArO)_3$-P=O, providing more evidence for the binding of aromatic rings by P-species of the FRs. Moreover, this band was clearly visible at 600 °C for all materials except EP, as the aromatic species are not stabilized by phosphorus. At 600 °C (Figure S4.20), many absorption bands were visible which were not present in EP, implicating a strong condensed phase mechanism of all tested FRs. Many of these bands have been characterized previously (Markwart et al., Battig et al.).[35, 45] Furthermore, the presence of several DGEBA-DMC typical bands (underlined in Figure S4.20) at 1593, 880, 823, 764, and 688 cm^{-1} suggest that the aromatic structures of DGEBA and its decomposition products were held intact through the formation of stable P-species.

4.4.7 Fire behavior: Cone calorimeter

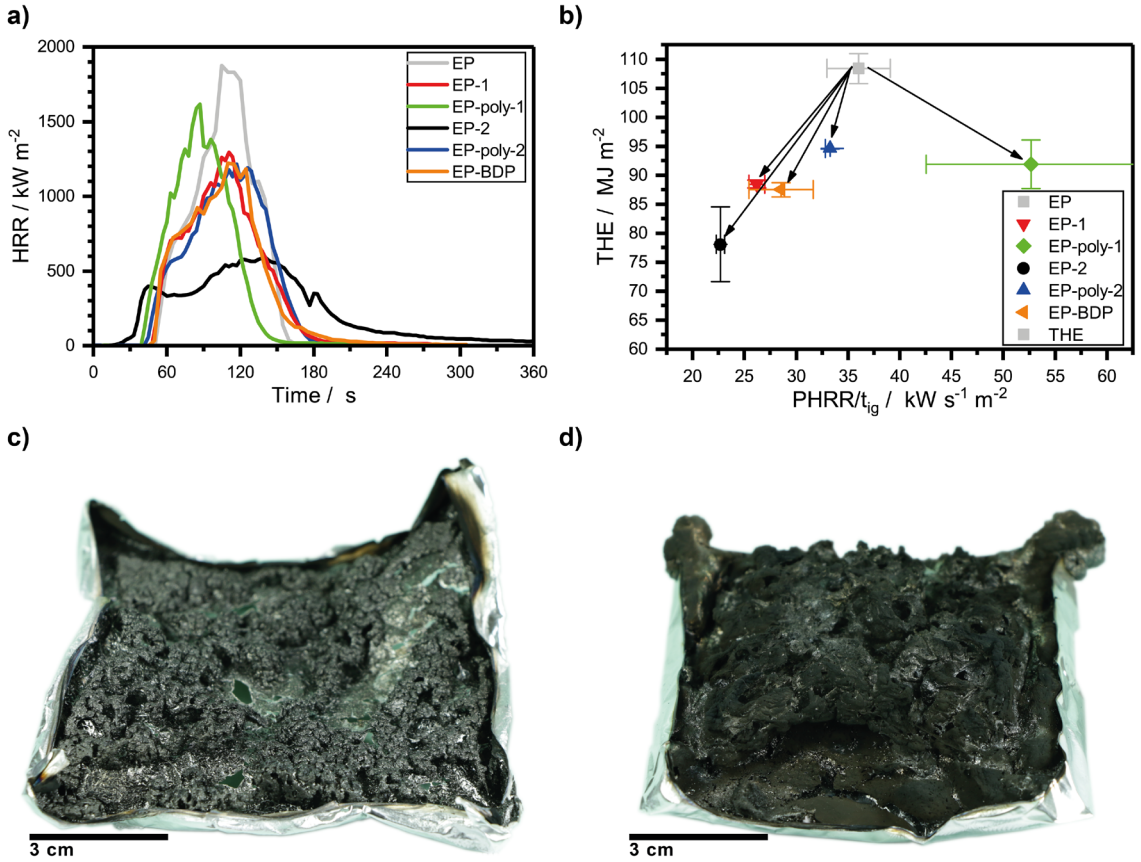

Figure 4.4. a) Heat release rate (HRR) of epoxy resin and epoxy resin with FRs measured by cone calorimeter. b) Petrella plot of the different epoxy resins with all FRs having a positive effect (lowering total heat evolved (THE)), especially 2. c) Residue of EP-poly-1 after cone calorimeter measurement, presenting a high graphitic residue yield but poor protective layer. d) Residue of EP-poly-2 after cone calorimeter measurements, presenting a good protective layer by the production of voluminous, multicellular char.

Investigations with the cone calorimeter proved a significant effect of all FRs on epoxy resins. The epoxy plates (100 x 100 x 4 mm^3) were irradiated with a heat flux of 50 kW m^{-2}, simulating a developing fire.[46] The results of the forced-flaming condition experiments underlined that the epoxy resin burned with a high heat release rate (HRR) and lost 99.3 wt.-% of its mass, presenting nearly no residue (Table S4.4). The aliphatic FRs in resins exhibited a reduction of peak or heat release rate (PHRR), as well as reduction of fire growth rate (FIGRA = max. (HRR/t)). Especially 2 reduced the PHRR of EP significantly (885 vs. 1696 kW m^{-2}) due to the formation of a voluminous char layer that insulated the underlying polymer. This behavior was clearly visible during the experiments as well as in the cross-sections of the residues, as the decomposition of the resin with 2 and the volatilization of its products acted as blowing agents, creating a voluminous intumescent char that shielded the underlying material from the heat source. Moreover, it was very active in

the gas phase, as evidenced by a reduction in the effective heat of combustion (EHC = total heat evolved / total mass loss), which is a parameter for gas phase activity.[3] The polymeric poly-2 did not exhibit the same type of FR efficacy due to a lower reactivity with the matrix. Notably, it only slightly lowered PHRR (1248 kW m^{-2}) and was less active in the gas phase (EHC = 24.9 MJ kg^{-1}). The aromatic FRs in resins did not exhibit a clear reduction in PHRR and FIGRA like 2. On the contrary, PHRR increased for EP-poly-1, and FIGRA was only slightly lowered. The epoxy resins loaded with 1 had a PHRR of 1194 kW m^{-2} and a FIGRA of 11.2 kW m^{-2} s^{-1} (pure epoxy: 1696 kW m^{-2} (PHRR) 15.5 kW m^{-2} s^{-1} (FIGRA)). Both values are on par to those of EP with the commercial FR BDP. Moreover, EP-1 exhibited a moderate 13% reduction of EHC (23.3 MJ kg^{-1}) EP-poly-1 showed a PHRR of 1969 kW m^{-2} and a FIGRA of 15.0 kW m^{-2} s^{-1}. The high PHRR is caused by the high decomposition temperature of the FR compared to the matrix, as seen in TGA measurements (Figure 4.3). All flame-retarded resins exhibited an increase in residue yield and a lowering of the total heat evolved (THE = total heat released (THR) at flame out) (Figure S4.22 and Table S4.4). The THE for the epoxy resins containing hb polymers were all comparable to EP-BDP (87.5 MJ m^{-2}- 94.6 MJ m^{-2}). The THE of EP-1 (88.4 MJ m^{-2}) was comparable to that of EP-2 (78.1 MJ m^{-2}). The epoxy resin loaded with the 2 demonstrated the lowest PHRR (885 kW m^{-2}, reduced by 48%) and THE (78.1 MJ m^{-2}, reduced by 28%) and displayed a HRR curve corresponding to a charring material with a protective layer. For EP-poly-2 and EP-1, the HRR curves were nearly identical to EP-BDP: The shape of the HRR curves suggest a quasi-static HRR above ca. 60 s after ignition, indicating the formation of an insulating char layer. However, the insulating properties were soon overcome and additional fuel was transported into the flame, coming to a head shortly thereafter at PHRR. The HRR curve of EP-poly-1 illustrates that the sample ignited earlier than the pure EP, due to a reduced cross-linking density caused by the presence of FRs. Thereafter, fuel was continually fed into the flame before the FR could interact with EP, leading to a poor char layer production. For the polymers and especially for EP-poly-1, a lower reduction of PHRR and THE was detected, most probably due to the lower reactivity. The residue yields of epoxy resins loaded with 1 (5.3 ± 0.0 wt%) were higher than the neat epoxy (0.7 ± 0.1 wt%), yet much lower compared to the aliphatic monomeric phosphate (9.2 ± 0.1 wt.%), most likely due to the high reactivity of 2. The resin with poly-1 had an increase in char residue (7.0 ± 1.5 wt.%) compared to EP-1 (5.3 ± 0.0 wt.-%). Although the aromatic FRs were less effective in lowering PHRR and FIGRA in cone calorimeter measurements than the aliphatic counterparts, their efficacy in creating high residue yields in pyrolysis measurements should not go unnoted.

4.5 Materials and Methods

4.5.1 Materials

All chemicals were purchased from commercial suppliers as reagent grade and used without further purification. The monomer 2 was prepared according to literature.[35]

4.5.2 Instrumentation and Characterization Techniques

4.5.2.1 Size exclusion chromatography (SEC)

Size exclusion chromatography (SEC) measurements were performed in DMF at 60 ºC with a PSS SecCurity system (Agilent Technologies 1260 Infinity). Sample injection was performed by a 1260-ALS autosampler (Waters) at 60 °C. GRAM columns (PSS) with dimensions of 300 × 80 mm, 10 µm particle size, and pore sizes of 100, 1000, and 10000 Å were employed. The DRI Shodex RI-101 detector (ERC) and UV−vis 1260-VWD detector (Agilent) were used for detection. Calibration was achieved using PS standards provided by Polymer Standards Service.

4.5.2.2 Nuclear magnetic resonance (NMR)

Nuclear magnetic resonance (NMR) was performed in a Bruker Avance III 300 MHz and 500 MHz spectrometer. All spectra were measured in either d_6-DMSO or $CDCl_3$ at 298 K. The spectra were calibrated against the solvent signal ($CDCl_3$ (7.26 ppm) or d_6-DMSO (2.50 ppm)) and analyzed using MestReNova 11 from Mestrelab Research S.L and Bruker Topspin 3.0 software.

4.5.2.3 Electron spray ionization mass (ESI-MS)

Electron spray ionization mass (ESI-MS) was performed by A Q-Tof Ultima 3 from Waters Micromass Milford Massachusetts spectrometer. 1 mg of the sample was dissolved in 1 mL of solvent (THF or DCM) and injected into ionization chamber at 120 °C which operated with a stream of 100 L h^{-1} and a reference voltage of 35 V.

4.5.2.4 Differential scanning calorimetry (DSC)

Differential scanning calorimetry (DSC) measurements were performed using a Mettler Toledo instrument 1/700 or DSC823 under nitrogen atmosphere at a heating rate of 10 °C min^{-1} starting from -140 °C.

4.5.2.5 TGA-FTIR

Both decomposition and evolved gases were investigated under pyrolytic and thermo-oxidative conditions via Fourier transform infrared (FTIR) spectroscopy coupled with thermogravimetric analysis. For epoxy resins with and without FRs, 10 mg of powder attained from cryomilling were used for measurements, while 5 mg samples were measured for pure FRs. Using a TG 209 F1 Iris (Netzsch Instruments, Selb, Germany), samples were heated at a rate of 10 K min^{-1} from 30 to 900 °C under a nitrogen or synthetic air (80:20) gas flow of 30 ml min^{-1}. The evolved gases were analyzed using a Tensor27 infrared spectrometer (Bruker Optics, Ettlingen, Germany), which was coupled to the TGA via a transfer line heated to 270 °C.

4.5.2.6 Hot Stage FTIR

The condensed phase activity was monitored using hot-stage FT-infrared spectroscopy using a Vertex70 FTIR spectrometer (Bruker Optics, Ettlingen, Germany), equipped with an FTIR600 Linkam hot-stage cell (Linkam Scientific Instruments Ltd., Chilworth, UK). The samples were pressed into a KBr plate, loaded into the Linkam cell, and heated at a rate of 10 K min^{-1} from 30 to 600 °C under a nitrogen gas flow of 300 ml min^{-1}.

4.5.2.7 Cone Calorimeter

All epoxy resin samples were subjected to bench-scale forced flaming combustion using a cone calorimeter (Fire Testing Technology Ltd., East Grinstead, UK) at a distance of 35 mm between specimen and cone heater and a heat flux of 50 kW m^{-2} and in accordance with ISO 5660. Specimens sized 100 x 100 x 4 mm^3 were conditioned at 23°C and 50% relative humidity for at least 48 hours and then subjected to irradiation.

4.5.3 Synthetic Procedures

4.5.3.1 Synthesis of the 4-vinylphenol

Preparation of 4-vinylphenol was realized according to the method of Ricks-Laskoski et al.[47] To a dried three-necked, 2 L round bottom flask fitted with a dropping funnel and an mechanical stirrer 4-acetoxystyrene (53.36 g, 0.33 mol, 1 eq.) and tetrahydrofuran (200 mL) were added under an argon atmosphere and ice-cooling. Ice-cooling was continued throughout the process. 5 M solution of aqueous sodium hydroxide (100 mL, 0.8 mol, 2.4 eq.) was added dropwise to this solution. The yellow solution was stirred for 2 h under ice-cooling until the reaction was

completed as indicated by TLC (SiO_2: R_f = 0.75, 30 vol.% ethyl acetate / hexane). Then 1.5 M hydrochloric acid (340 mL) was added slowly to the crude reaction mixture until a pH of 7-5 was reached. The product was extracted with cold ethyl acetate (5 × 50 mL), washed with distilled water (3 × 50 mL), dried over magnesium sulfate and filtered. The product was distilled at reduced pressure while cooling with an ice bath to yield a crystalline solid (30.9 g, 78%). The product was stored at -20 °C under argon atmosphere and light exclusion to suppress self-initiated polymerization.

^{1}H NMR (300 MHz, 298 K, DMSO-d6): δ/ppm = 9.53 (s, 1H), 7.28 (d, 2H, J = 9 Hz), 6.74 (d, 2H, J = 9 Hz), 6.61 (dd, 1H, J = 12 Hz/18 Hz), 5.68 (d, 1H, J = 18 Hz), 5.04 (d, 1H, J = 12 Hz).

^{13}C{H} NMR (75.48 MHz, 298 K, DMSO-d6): δ/ppm = 157.3, 136.4, 128.2, 127.4, 115.3, 110.6.

4.5.3.2 Synthesis of the tris(p-vinylphenyl)phosphate (1)

To a dried three-necked, 1 L round bottom flask fitted with a dropping funnel and an mechanical stirrer, 4-vinylphenol (15 g, 0.125 mol, 4 eq.) dissolved in THF (300 mL) and triethylamine (12.63 g, 0.125 mol, 4 eq.) in THF (10 mL) at 0 °C and under an argon atmosphere. Then phosphoryl chloride (4.79 g, 0.031 mol, 1 eq.) in THF (30 mL) was added to the solution dropwise at 0 °C. Then the reaction was allowed to warm up to room temperature and stirred overnight at room temperature. The mixture was filtered and concentrated at reduced pressure while cooling in an ice-bath. The product was dissolved in DCM (100 mL) and extracted with water and a 1 M potassium hydroxide solution. The organic layer was dried over MgSO4, filtered and concentrated at reduced pressure yield a colorless viscous liquid (8.4 g, 67%). The product was stored at -20 °C under argon atmosphere and light exclusion to suppress self-initiated polymerization.

^{1}H NMR (500 MHz, 298 K, $CDCl_3$): δ/ppm = 7.29 (d, 2 H, J = 10 Hz), 7.11 (d, 2 H, J = 10 Hz), 6.58 (dd, 1 H, J = 10 Hz/ 15 Hz), 5.60 (d, 1 H, J = 15 Hz), 5.16 (d, 1 H, J = 10 Hz).

^{13}C{H} NMR (75.48 MHz, 298 K, $CDCl_3$): δ/ppm = 149.9 (d, J = 30 Hz), 135.6 (s), 135.2 (s), 127.6 (d, J = 6 Hz), 120.2 (d, J = 21 Hz), 114.3 (s).

^{31}P{H} NMR (121.5 MHz, 298 K, $CDCl_3$): δ/ppm = -17.72 (s). ESI MS: 405.14.

4.5.3.3 ATMET polymerization to poly(1)

In a Schlenk tube fitted with a magnetic stirring bar, tris(p-vinylphenyl)phosphate (1) (1 g, 2.47 mmol) dissolved in 1-chloronaphthalene (1.67 g) was placed under an argon atmosphere at 40 °C. Then, the Grubbs-Hoveyda catalyst 2nd gen. (4.65 mg, 0.007 mmol, 0.3 mol%) was added.

The polymerization was carried out at a controlled vacuum of 5×10^{-2} mbar to remove the evolving ethylene. When the viscosity increased (typically after ca 5 min), the flask was filled with argon and the reaction was terminated by adding ethyl vinyl ether or methyl acrylate (5 mL). The brown solution was stirred for 1 h at 40 °C and then the mixture was concentrated at reduced pressure. The product was precipitated twice into hexane and dried at reduced pressure to give an off-white powder (yields 50-90%).

^{1}H NMR (500 MHz, 298 K, $CDCl_3$): δ /ppm = 7.57 (d, J = 16 Hz), 7.39 (m), 7.30 (d, J = 5 Hz), 7.16 (m), 6.92 (s), 6.59 (dd, J = 10 Hz/17 Hz), 5.61 (d, J = 17 Hz), 5.16 (d, J = 10 Hz).
^{13}C{H} NMR (75.48 MHz, 298 K, $CDCl_3$): δ/ppm = 149.8, 135.6, 134.8, 129.7, 127.9, 120.4, 118.3, 114.4.
^{31}P{H} NMR (202.46 MHz, 298 K, $CDCl_3$): δ/ppm = -17.73.

4.5.3.4 Tri(hex-5-en-1-yl)phosphate (2)

Tri(hex-5-en-1-yl)phosphate was synthesized as described elsewhere.[35]

4.5.3.5 Poly(tri(hex-5-en-1-yl)phosphate) (poly-2) by ATMET polymerization

In a Schlenk tube fitted with a magnetic stirring bar, tri(hex-5-en-1-yl)phosphate (2) (2 g, 5.81 mmol) was placed under an argon atmosphere at 60 ºC. Then, Grubbs catalyst 1st gen. (33.45 mg, 40.65 µmol, 0.7 mol%) was added. The polymerization was carried out at a controlled vacuum of 5×10^{-2} mbar to remove the evolving ethylene. When the viscosity increased, the flask was filled with argon and the reaction was terminated by adding ethyl vinyl ether (0.4 mL). The product was precipitated twice into hexane and dried at reduced pressure to give a viscous off-white polymer (yields 85-96%.).

^{1}H NMR (300 MHz, 298 K, $CDCl_3$): δ /ppm = 5.81 (ddt, J = 16.9, 10.2, 6.6 Hz), 5.40 (m, J = 5.5, 5.1 Hz), 4.99 (t, J = 13.9 Hz), 4.03 (m, 6H), 2.08 (qd, J = 14.8, 12.0, 8.3 Hz, 6H), 1.68 (h, J = 6.9 Hz, 6H), 1.47 (dp, J = 15.1, 7.5 Hz, 6H).
^{31}P{H} NMR (121.5 MHz, 298 K, $CDCl_3$): δ/ppm = -0.66.

4.5.3.6 Epoxy resins

All epoxy resins were prepared using bisphenol A diglycidylether (DGEBA) (Araldite MY740, Bodo Möller Chemie GmbH, Offenbach am Main, Germany) as the epoxide agent and 2,2'-dimethyl-

4,4'-methylene-bis-(cyclohexylamine) (DMC) (Sigma Aldrich Co. LLC/ Merck KgaA, Darmstadt, Germany) as the amine hardener. The materials were mixed, poured into aluminum molds of desired dimensions, then hardened at 150°C for 3h. The flame retarded epoxy resins were produced in the same manner, except 10 wt.-% of the mixture was replaced with the respective flame retardant.

4.6 Conclusion

The herein presented aromatic and aliphatic, hyperbranched, halogen-free polyphosphoesters (hbPPEs) were synthesized by olefin metathesis polymerization and investigated as a flame retardant in epoxy resins. The impact on the T_g of the matrix was different for all tested materials. However, in all cases, the addition of aliphatic FRs 2 and poly-2 resulted in a higher or equivalent decrease of T_g compared to the aromatic FRs.

Regarding their flame retardant properties, the aromatic FRs proved a significant increase in residue yield and thermal stability in pyrolysis investigations compared to their aliphatic counterparts: the aromatic moieties acted as char precursors, thereby retaining significant residue yields. Moreover, condensed phase analysis concluded the formation of P-species for all tested resins with FRs.

Investigations with the cone calorimetry proved a significant effect of all FRs on epoxy resins during a developing fire. The aliphatic FRs were more effective on the tested matrix due to their greater overlap in decomposition temperature and thus better matrix interaction. The greater interaction, resulted in a stronger reduction of peak of heat release rate (PHRR) and fire growth rate (FIGRA = max. (HRR/t)) than those resins with aromatic FRs. Especially 2 reduced the PHRR of EP significantly due to the formation of a voluminous char layer that insulated the underlying polymer. Moreover, 2 was very active in the gas phase, as evidenced by a reduction in the effective heat of combustion. While pyrolytic investigations proved high residue yields and interaction with the matrix for poly-2, it did not exhibit the same type of FR efficacy as 2 in cone calorimeter tests due to a less pronounced reactivity with the matrix in form of phosphorylation. The aromatic FRs were less effective in lowering PHRR and FIGRA in cone calorimeter measurements than the aliphatic counterparts, however, their efficacy in creating high residue yields in pyrolysis measurements should not go unnoted. The aromatic FRs might be more suited for materials with higher decomposition temperatures to increase the matrix-FR interaction. Moreover, the addition of a synergist may promote chemical interaction.

4.7 Supplementary Materials

The following are available online at www.mdpi.com/xxx/s1, Table S4.1: Polymerization conditions of **1** with Grubbs Hoveyda 2nd in 1-chlornaphthaline generation catalyst at 40 °C in solution., Figure S4.1: SEC curves (VWD-Signal 270 nm) of **poly-1** in DMF polymerized with Grubbs 1st generation catalyst and Grubbs Hoveyda 2nd generation catalyst at 40 ºC., Figure S4.2: ^{1}H NMR (300 MHz in $CDCl_3$ at 298 K) spectra of 4-vinylphenol., Figure S4.3: ^{1}H-NMR (500 MHz in $CDCl_3$ at 298 K) spectra of 1., Figure S4.4: ^{31}P {H}-NMR (121 MHz in CDCl3 at 298 K) spectra of 1., Figure S4.5: ^{1}H-MR (300 MHz in CDCl3 at 298 K) spectra of poly-1., Figure S4.6: ^{31}P {H}-NMR (121 MHz in CDCl3 at 298 K) spectra poly-1 ., Figure S4.7: ^{1}H-MR (300 MHz in CDCl3 at 298 K) spectra of poly-2., Figure S4.8: ^{31}P {H}-NMR (121 MHz in CDCl3 at 298 K) spectra of poly-2., Figure S4.9: TGA-FTIR spectrum of **2** (top, black), identifying the main decomposition products (1,5-hexadiene; 5-hexen-1-ol and phosphate species, comparison shown in gray below) at specific decomposition temperature (259 °C) using references from NIST library., Figure S4.10: TGA-FTIR spectrum of **poly-2** (top, blue), identifying the main decomposition products (1,3-hexadiene (c,t) and 2-octene (c,t) and trans-1,4-hexadiene, comparison shown in gray below) at specific decomposition temperature (216 °C, 259 °C) using references from NIST library, Figure S4.11: TGA-FTIR spectrum of **1** (top, red), identifying the main decomposition products (p-tolyl acetate; p-cresol; 4-ethylphenol and bisphenol A, comparison shown in gray below) at specific decomposition temperature (143 °C, 470 °C) using references from NIST library., Figure S4.12: TGA-FTIR spectrum of **poly-1** (top, green), identifying the main decomposition products (phenol and benzene, comparison shown in gray below) at specific decomposition temperature (447 °C and 487 °C) using references from NIST library., Figure S4.13: TGA-FTIR spectrum of **EP-2** (top, black), identifying the main decomposition products (5-hexen-1-ol; phosphate species and decomposition products of the matrix, a comparison is shown in gray below) at specific decomposition temperature (266 °C, 373 °C) using references from NIST library., Figure S4.14: TGA-FTIR spectrum of **EP-poly-2** (top, blue), identifying the main decomposition products (5-hexen-1-ol; oct-2-en-4ol and decomposition products of the matrix, a comparison is shown in gray below) at specific decomposition temperature (287 °C, 349 °C) using references from NIST library., Figure S4.15: TGA-FTIR spectrum of **EP-1** (top, red), identifying the main decomposition products (p-n-propylphenol and decomposition products of the matrix, a comparison is shown in gray below) at specific decomposition temperature (203 °C, 371 °C, 437 °C) using references from NIST library., Figure S4.16: TGA-FTIR spectrum of **EP-poly-1** (top, green), identifying the main decomposition products (4-(3-hydroxyisoamyl)phenol and decomposition products of the matrix, a comparison is shown in gray below) at specific decomposition temperature (375 °C, 482 °C)

using references from NIST library., Figure S4.17: Results from hot-stage FTIR measurements, comparing the condensed phase spectra of EP-FRs at 100 °C., Figure S4.18: Results from hot-stage FTIR measurements, comparing the condensed phase spectra of EP-FRs at 300 °C., Figure S4.19: Results from hot-stage FTIR measurements, comparing the condensed phase spectra of EP-FRs at 500 °C., Figure S4.20: Results from hot-stage FTIR measurements, comparing the condensed phase spectra of **EP-FRs** at 600 °C, underlined bands are typical to DGEBA-DMC., Table S4.2: Glass transition temperatures (T_g) of the flame retardant containing epoxy resins (measured by DSC), Figure S4.21: Mass loss (bottom) and mass loss rate (top) over *T* of neat epoxy resin and flame retardant containing epoxy resins from TGA measurements (10 K min^{-1}; N_2)., Table S4.3: TGA data of the flame retardant containing epoxy resins. $T_{5\%}$: Temperature at which 5% mass-loss happened; T_{max}: Temperature of maximum degradation; Residue: Residue at 700 °C., Figure S4.22: Total heat released (THR) of epoxy resin and epoxy resin with flame retardant measured by cone calorimeter., Table S4.4: Results from cone calorimeter measurements of the flame retardant containing epoxy resins., Figure S4.23: Cross-linking of **1** at 300 °C in a silicon form for 2 h, producing a hard, cross-linked PPE resin., Figure S4.24: Chemical structure of Diglycidyl ether of bisphenol A (DGEBA) and 2,2'-Dimethyl-4,4'-methylene-bis(cyclohexylamine) (DMC).

4.8 Author Contributions

conceptualization, J.C.M., A.B., M.M.V., B.S. and F.R.W.; methodology, J.C.M., A.B. and M.M.V.; validation, J.C.M, A.B., M.M.V., B.S. and F.R.W.; formal analysis, J.C.M and A.B..; investigation, J.C.M., A.B., M.M.V. and D.P.; resources, B.S. and F.R.W.; data curation, J.C.M, A.B., M.M.V. and D.P.; writing—original draft preparation, J.C.M. and A.B..; writing—review and editing, J.C.M., A.B., B.S. and F.R.W.; visualization, J.C.M. and A.B.; supervision, B.S. and F.R.W.; project administration, J.C.M., A.B., M.M.V., B.S. and F.R.W.; funding acquisition, B.S. and F.R.W.

4.9 Funding

This research was funded by the Deutsche Forschungsgemeinschaft, grant number DFG WU 750/ 8-1 and SCHA 730/ 15-1, and the Excellence Initiative in the context of the graduate school of excellence "MAINZ" (Materials Science in Mainz), grant number DFG/GSC 266.

4.10 Acknowledgments

The authors thank Angelika Manhart (MPIP, Germany) for synthetic assistance. Frederik R. Wurm and Jens C. Markwart thank Prof. Dr. Katharina Landfester (MPI-P, Germany).

4.11 Conflicts of Interest

The authors declare no conflict of interest.

4.12 References Chapter 4

[1] B. Perret, K. Pawlowski, B. Schartel, *J. Therm. Anal. Calorim.* **2009**, *97*, 949-958.

[2] M.-C. Despinasse, B. Schartel, *Polym. Degrad. Stab.* **2012**, *97*, 2571-2580.

[3] B. Schartel, B. Perret, B. Dittrich, M. Ciesielski, J. Krämer, P. Müller, V. Altstädt, L. Zang, M. Döring, *Macromolecular Materials and Engineering* **2016**, *301*, 9-35.

[4] A. B. Morgan, C. A. Wilkie, *Flame Retardant Polymer Nanocomposites*, Wiley, **2007**.

[5] P. Müller, B. Schartel, *J. Appl. Polym. Sci.* **2016**, 133.

[6] M. M. Velencoso, A. Battig, J. C. Markwart, B. Schartel, F. R. Wurm, *Angew. Chem. Int. Ed. Engl.* **2018**, *57*, 10450-10467

[7] B. Schartel, *Materials* **2010**, *3*, 4710-4745.

[8] S.-Y. Lu, I. Hamerton, *Prog. Polym. Sci.* **2002**, *27*, 1661-1712.

[9] K. N. Bauer, L. Liu, D. Andrienko, M. Wagner, E. K. Macdonald, M. P. Shaver, F. R. Wurm, *Macromolecules* **2018**, *51*, 1272-1279.

[10] T. Steinbach, F. R. Wurm, *Angew. Chem. Int. Ed.* **2015**, *54*, 6098-6108.

[11] S. Monge, B. Canniccioni, A. Graillot, J.-J. Robin, *Biomacromolecules* **2011**, *12*, 1973-1982.

[12] J. Ye, G. Liang, A. Gu, Z. Zhang, J. Han, L. Yuan, *Polym. Degrad. Stab.* **2013**, *98*, 597-608.

[13] Y. H. Kim, *J. Polym. Sci., Part A: Polym. Chem.* **1998**, *36*, 1685-1698.

[14] K. Täuber, F. Marsico, F. R. Wurm, B. Schartel, *Polymer Chemistry* **2014**, *5*, 7042-7053.

[15] C. Gao, D. Yan, *Prog. Polym. Sci.* **2004**, *29*, 183-275.

[16] H. Henke, O. Brüggemann, I. Teasdale, *Macromol. Rapid Commun.* **2017**, *38*, 1600644.

[17] Q. F. Wang, W. F. Shi, *Polym. Degrad. Stab.* **2006**, *91*, 1289-1294.

[18] J. Deng, S. W. Zhu, W. F. Shi, *J. Appl. Polym. Sci.* **2004**, *94*, 2065-2070.

[19] J. Deng, W. F. Shi, *Eur. Polym. J.* **2004**, *40*, 1137-1143.

[20] X. Chen, C. Jiao, S. Li, J. Sun, *Journal of Polymer Research* **2011**, *18*, 2229-2237.

[21] X. Chen, J. Zhuo, C. Jiao, *Polym. Degrad. Stab.* **2012**, *97*, 2143-2147.

[22] K. H. Pawlowski, B. Schartel, *Polym. Int.* **2007**, *56*, 1404-1414.

[23] E. D. Weil, *J. Fire Sci.* **2011**, *29*, 259-296.

[24] E. D. Weil, S. V. Levchik, in *Flame Retardants for Plastics and Textiles*, Carl Hanser Verlag GmbH & Co. KG, **2015**, pp. I-XX.

[25] F. Marsico, M. Wagner, K. Landfester, F. R. Wurm, *Macromolecules* **2012**, *45*, 8511-8518.

[26] T. Steinbach, E. M. Alexandrino, C. Wahlen, K. Landfester, F. R. Wurm, *Macromolecules* **2014**, *47*, 4884-4893.

[27] T. Steinbach, E. M. Alexandrino, F. R. Wurm, *Polymer Chemistry* **2013**, *4*, 3800-3806.

[28] M. Steinmann, J. Markwart, F. R. Wurm, *Macromolecules* **2014**, *47*, 8506-8513.

[29] H. Mutlu, L. M. de Espinosa, M. A. R. Meier, *Chem. Soc. Rev.* **2011**, *40*, 1404-1445.

[30] J. M. G. Cowie, V. Arrighi, *Polymers: Chemistry and Physics of Modern Materials, Third Edition*, CRC Press, **2007**.

[31] B. Schartel, C. A. Wilkie, G. Camino, *J. Fire Sci.* **2016**, *34*, 447-467.

[32] M. Rakotomalala, S. Wagner, M. Döring, *Materials* **2010**, *3*, 4300.

[33] M. Ciesielski, A. Schäfer, M. Döring, *Polym. Adv. Technol.* **2008**, *19*, 507-515.

[34] U. Braun, A. I. Balabanovich, B. Schartel, U. Knoll, J. Artner, M. Ciesielski, M. Döring, R. Perez, J. K. W. Sandler, V. Altstädt, T. Hoffmann, D. Pospiech, *Polymer* **2006**, *47*, 8495-8508.

[35] J. C. Markwart, A. Battig, L. Zimmermann, M. Wagner, J. Fischer, B. Schartel, F. R. Wurm, *ACS Applied Polymer Materials* **2019**, *1*, 1118-1128.

[36] P. J. Linstrom, W. G. Mallard*, Vol. 2019*, Institute of Standards and Technology, Gaithersburg MD, **2018**.

[37] G. Socrates, *Infrared and Raman Characteristic Group Frequencies: Tables and Charts*, Wiley, **2004**.

[38] M. Hesse, H. Meier, B. Zeeh, *Spektroskopische Methoden in der organischen Chemie*, Thieme, **2005**.

[39] S. V. Levchik, E. D. Weil, *Polym. Int.* **2004**, *53*, 1901-1929.

[40] S. V. Levchik, G. Camino, M. P. Luda, L. Costa, G. Muller, B. Costes, *Polym. Degrad. Stab.* **1998**, *60*, 169-183.

[41] D. P. Bishop, D. A. Smith, *J. Appl. Polym. Sci.* **1970**, *14*, 205-223.

[42] L.-H. Lee, *Journal of Polymer Science Part A: General Papers* **1965**, *3*, 859-882.

[43] M. Ciesielski, B. Burk, C. Heinzmann, M. Döring, in *Novel Fire Retardant Polymers and Composite Materials* (Ed.: D.-Y. Wang), Woodhead Publishing, **2017**, pp. 3-51.

[44] L. C. Thomas, *Interpretation of the infrared spectra of organophosphorus compounds*, Heyden, London; New York, **1974**.

[45] A. Battig, J. C. Markwart, F. R. Wurm, B. Schartel, *Polymer Chemistry* **2019**, 10, 4346-4358.

[46] B. Schartel, T. R. Hull, *Fire and Materials* **2007**, *31*, 327-354.

[47] H. L. Ricks-Laskoski, B. L. Chaloux, S. M. Deese, M. Laskoski, J. B. Miller, M. A. Buckley, J. W. Baldwin, M. A. Hickner, K. M. Saunders, C. M. Christensen, *Macromolecules* **2014**, *47*, 4243-4250.

4.13 Supporting Information

Table S4.1. Polymerization conditions of **1** with Grubbs Hoveyda 2nd in 1-chlornaphthaline generation catalyst at 40 °C in solution.

1st addition					
Polymer	%mol Catalyst	Time (min)	Mn (g/mol)	Mw (g/mol)	D
1.2	0.32	60	1300	1400	1.1
1.3[i]	0.65	60	1700	2400	1.4
1.5[ii]	0.65	45	-	-	-
1.15	0.81	120	3000	8700	2.9
2nd addition (after sampling of 1st addition)					
Polymer	%mol Catalyst	Time (min)	Mn (g/mol)	Mw (g/mol)	D
1.2	0.32	60	1756	2390	1.36
1.3	0.65	30	4185	56306	13.45
1.5	0.32	25	4875	55333	11.35

[i] in bulk. [ii] cross-linked.

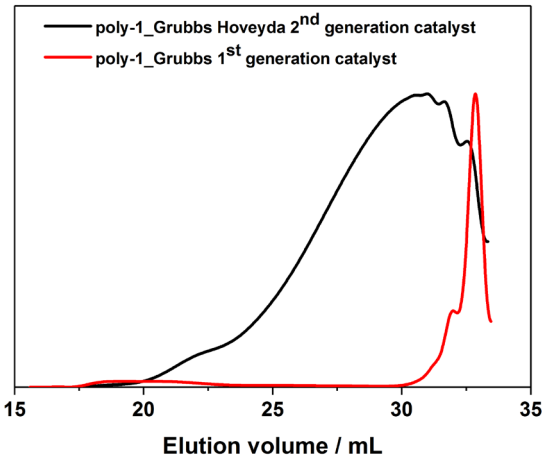

Figure S4.1. SEC curves (VWD-Signal 270 nm) of **poly-1** in DMF polymerized with Grubbs 1st generation catalyst and Grubbs Hoveyda 2nd generation catalyst at 40 °C.

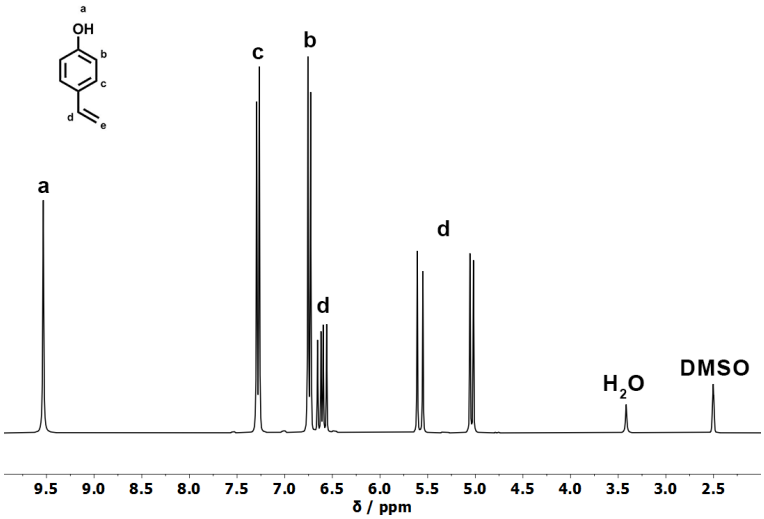

Figure S4.2. ^{1}H NMR (300 MHz in $CDCl_3$ at 298 K) spectra of 4-vinylphenol.

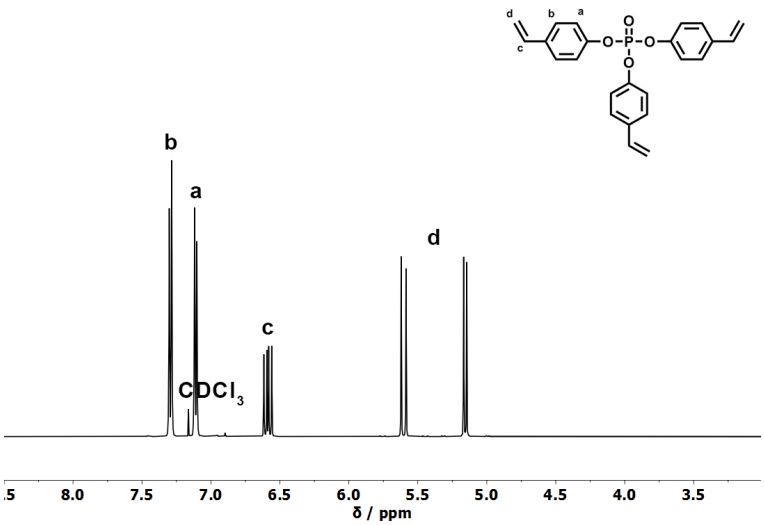

Figure S4.3. ^{1}H-NMR (500 MHz in $CDCl_3$ at 298 K) spectra of **1**.

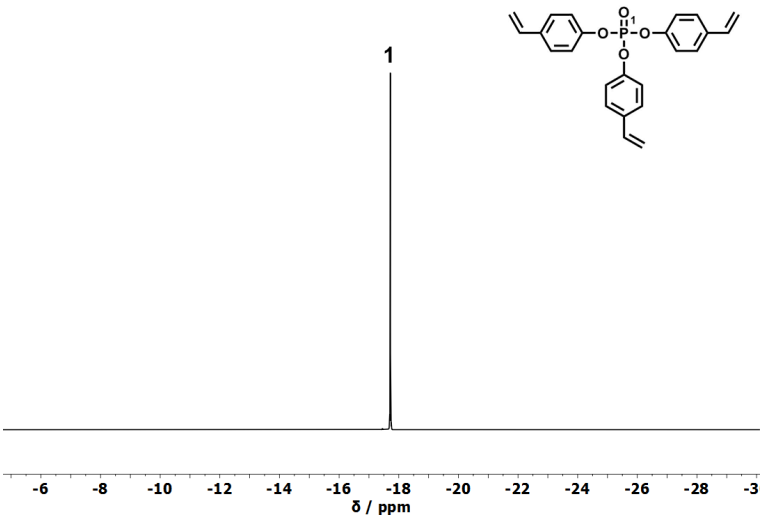

Figure S4.4. ^{31}P {H}-NMR (121 MHz in $CDCl_3$ at 298 K) spectra of **1**.

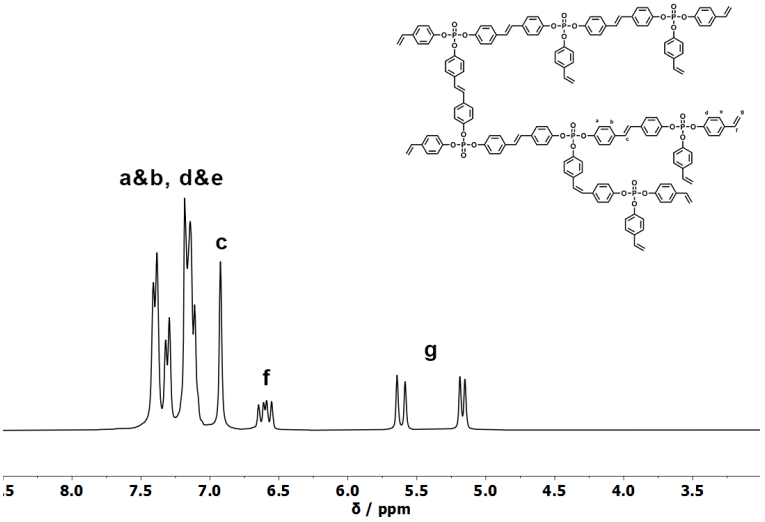

Figure S4.5. ^{1}H-MR (300 MHz in $CDCl_3$ at 298 K) spectra of **poly-1**.

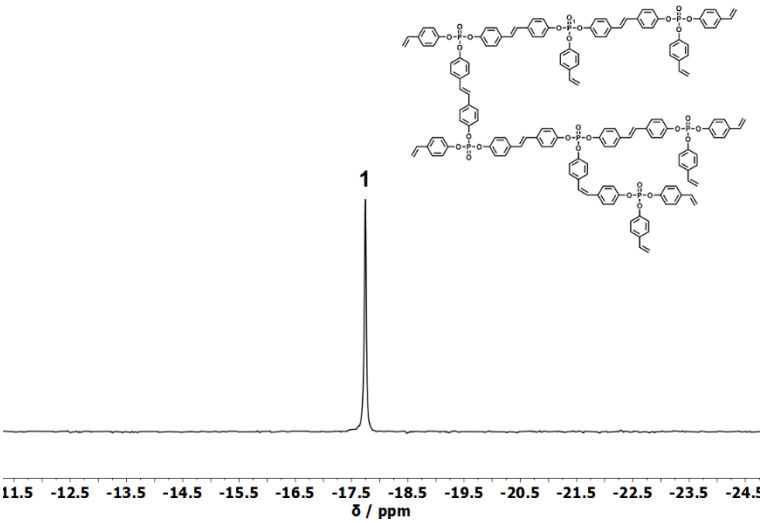

Figure S4.6. ^{31}P {H}-NMR (121 MHz in $CDCl_3$ at 298 K) spectra of **poly-1**.

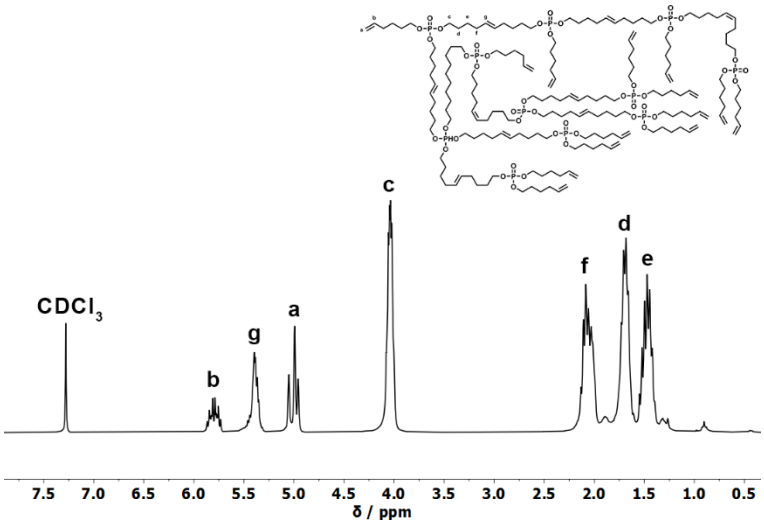

Figure S4.7. ^{1}H-MR (300 MHz in $CDCl_3$ at 298 K) spectra of **poly-2**.

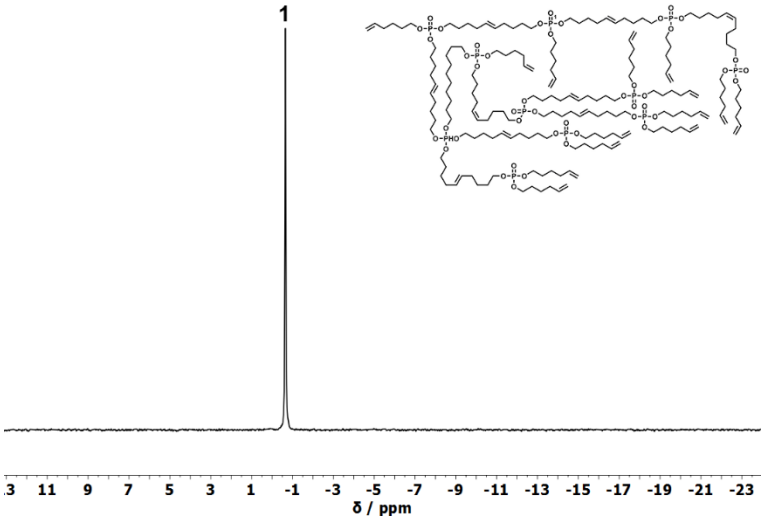

Figure S4.8. ^{31}P {H}-NMR (121 MHz in $CDCl_3$ at 298 K) spectra of **poly-2**.

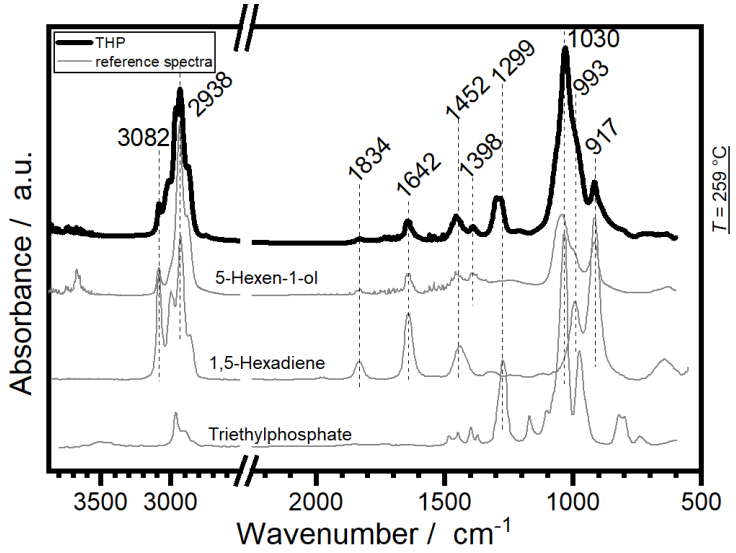

Figure S4.9. TGA-FTIR spectrum of **2** (top, black), identifying the main decomposition products (1,5-hexadiene; 5-hexen-1-ol and phosphate species, comparison shown in gray below) at specific decomposition temperature (259 °C) using references from NIST library.[1]

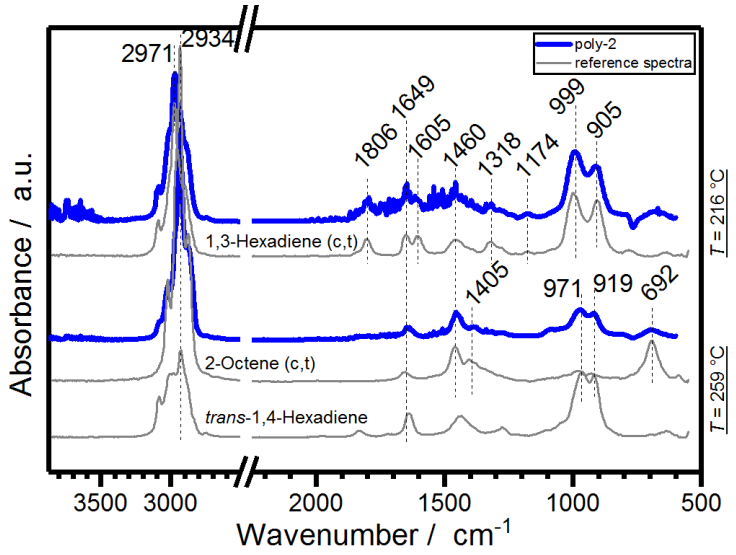

Figure S4.10. TGA-FTIR spectrum of **poly-2** (top, blue), identifying the main decomposition products (1,3-hexadiene (c,t) and 2-octene (c,t) and trans-1,4-hexadiene, comparison shown in gray below) at specific decomposition temperature (216 °C, 259 °C) using references from NIST library.[1]

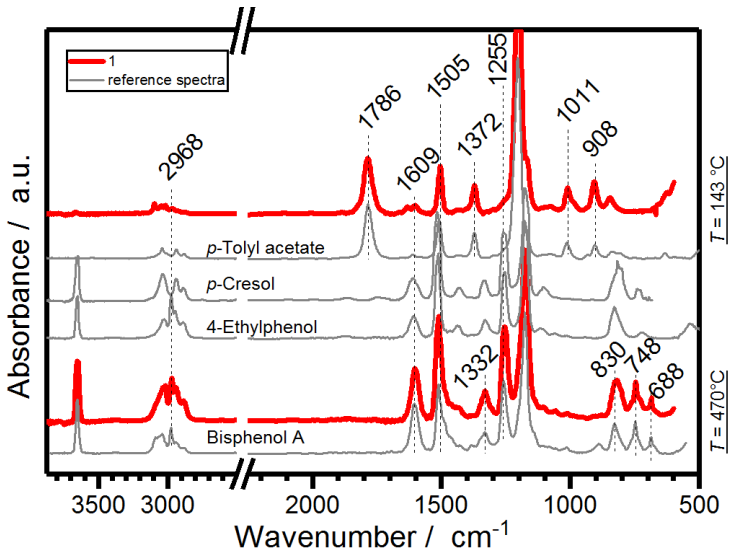

Figure S4.11. TGA-FTIR spectrum of **1** (top, red), identifying the main decomposition products (p-tolyl acetate; p-cresol; 4-ethylphenol and bisphenol A, comparison shown in gray below) at specific decomposition temperature (143 °C, 470 °C) using references from NIST library.[1]

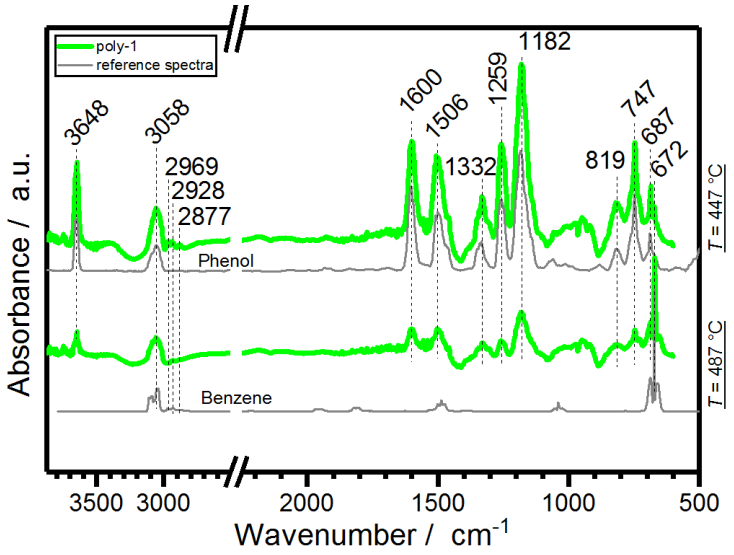

Figure S4.12. TGA-FTIR spectrum of **poly-1** (top, green), identifying the main decomposition products (phenol and benzene, comparison shown in gray below) at specific decomposition temperature (447 °C and 487 °C) using references from NIST library.[1]

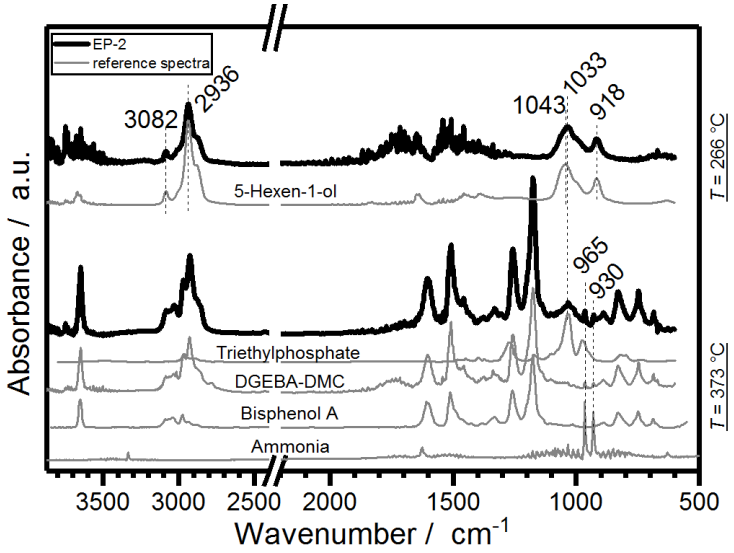

Figure S4.13. TGA-FTIR spectrum of **EP-2** (top, black), identifying the main decomposition products (5-hexen-1-ol; phosphate species and decomposition products of the matrix, a comparison is shown in gray below) at specific decomposition temperature (266 °C, 373 °C) using references from NIST library.[1]

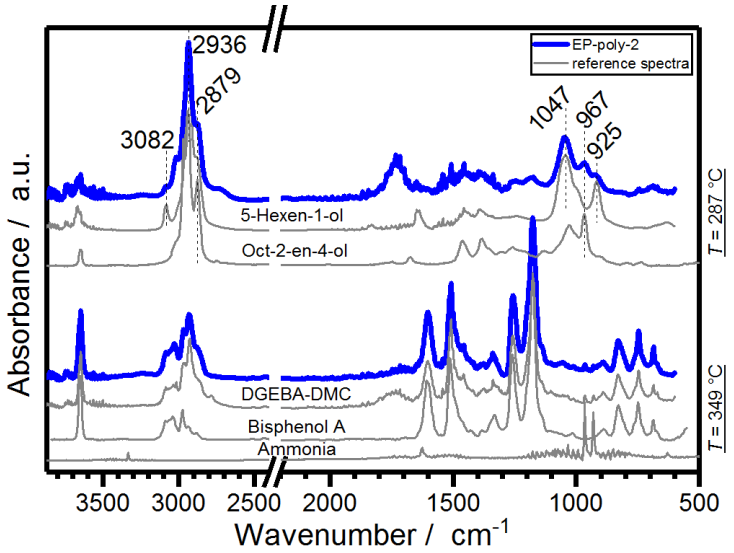

Figure S4.14. TGA-FTIR spectrum of **EP-poly-2** (top, blue), identifying the main decomposition products (5-hexen-1-ol; oct-2-en-4ol and decomposition products of the matrix, a comparison is shown in gray below) at specific decomposition temperature (287 °C, 349 °C) using references from NIST library.[1]

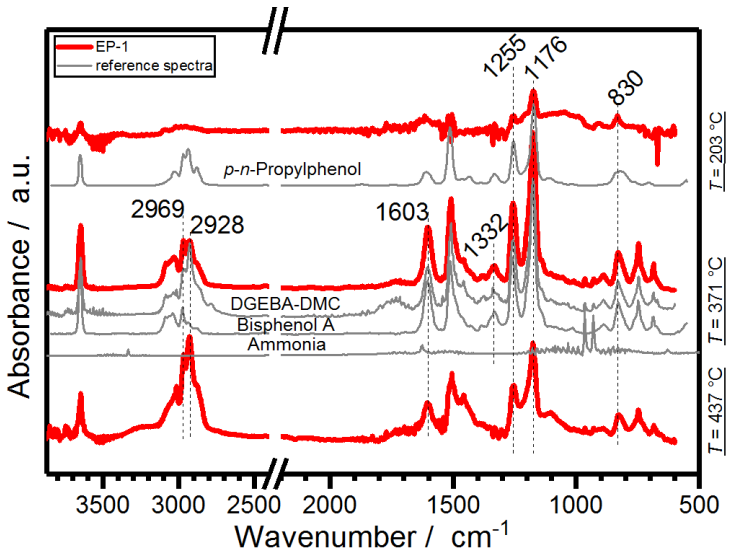

Figure S4.15. TGA-FTIR spectrum of **EP-1** (top, red), identifying the main decomposition products (p-n-propylphenol and decomposition products of the matrix, a comparison is shown in gray below) at specific decomposition temperature (203 °C, 371 °C, 437 °C) using references from NIST library.[1]

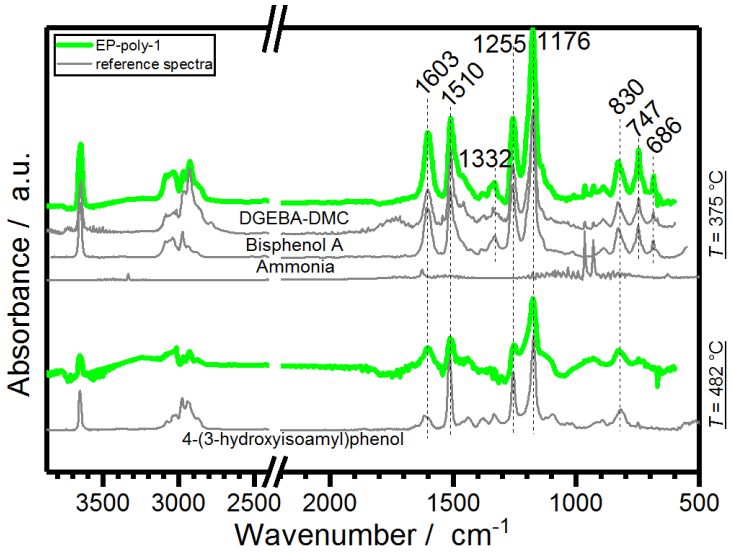

Figure S4.16. TGA-FTIR spectrum of **EP-poly-1** (top, green), identifying the main decomposition products (4-(3-hydroxyisoamyl)phenol and decomposition products of the matrix, a comparison is shown in gray below) at specific decomposition temperature (375 °C, 482 °C) using references from NIST library.[1]

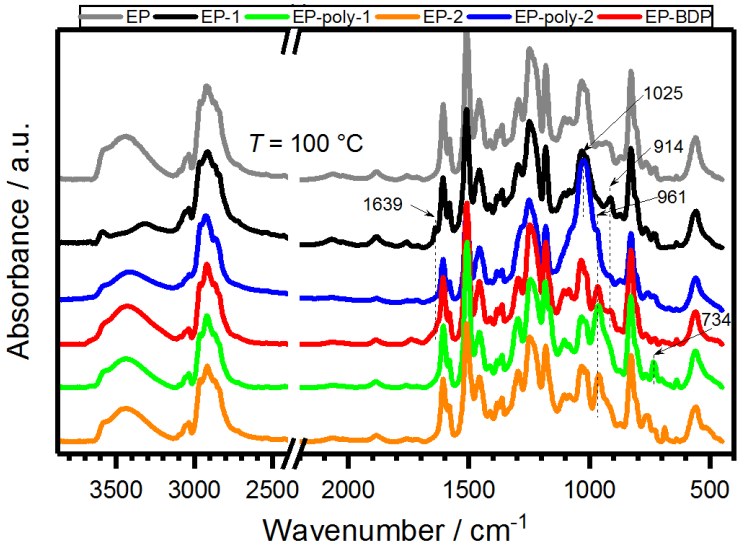

Figure S4.17. Results from hot-stage FTIR measurements, comparing the condensed phase spectra of EP-FRs at 100 °C.

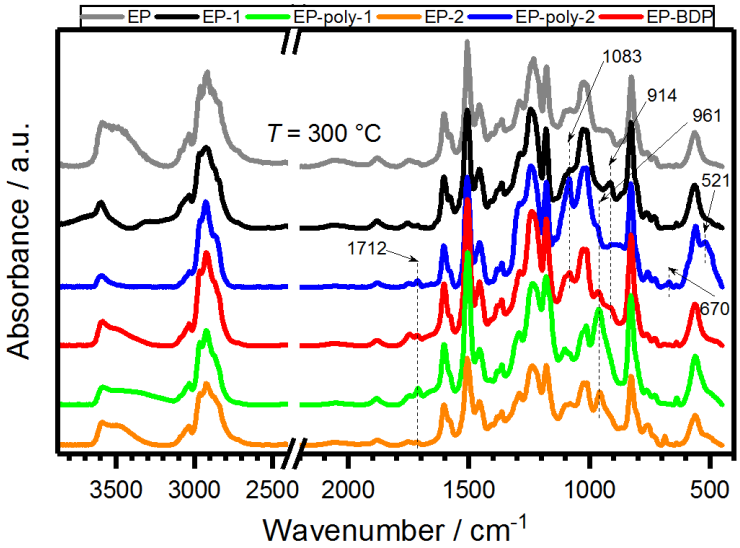

Figure S4.18. Results from hot-stage FTIR measurements, comparing the condensed phase spectra of EP-FRs at 300 °C.

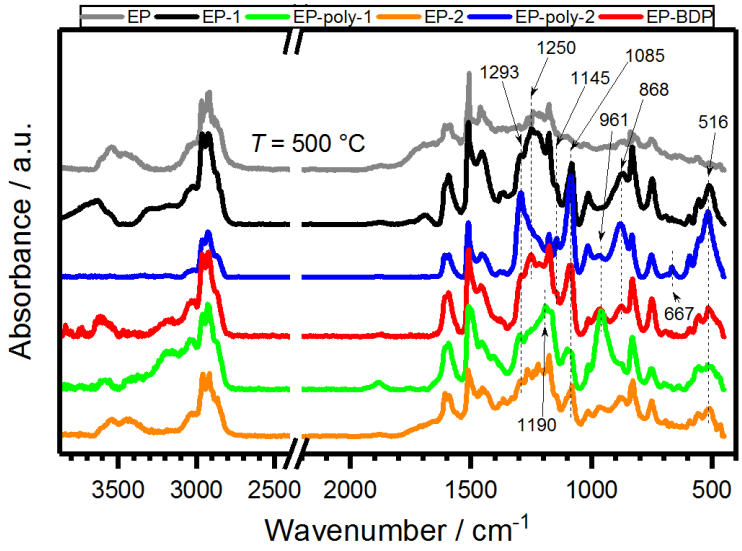

Figure S4.19. Results from hot-stage FTIR measurements, comparing the condensed phase spectra of EP-FRs at 500 °C.

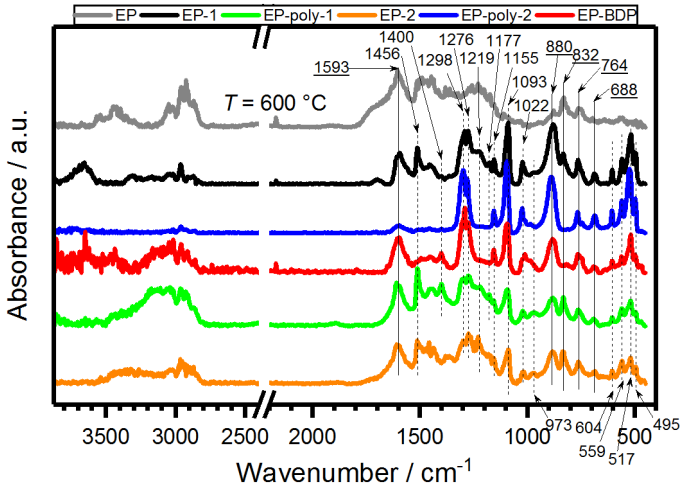

Figure S4.20. Results from hot-stage FTIR measurements, comparing the condensed phase spectra of **EP-FRs** at 600 °C, underlined bands are typical to DGEBA-DMC.

Table S4.2. Glass transition temperatures (T_g) of the flame retardant containing epoxy resins (measured by DSC).

Material	T_g
EP-1	149 ± 1
EP-poly-2	127 ± 3
EP- 2	113 ± 1
EP-poly-2	154 ± 2

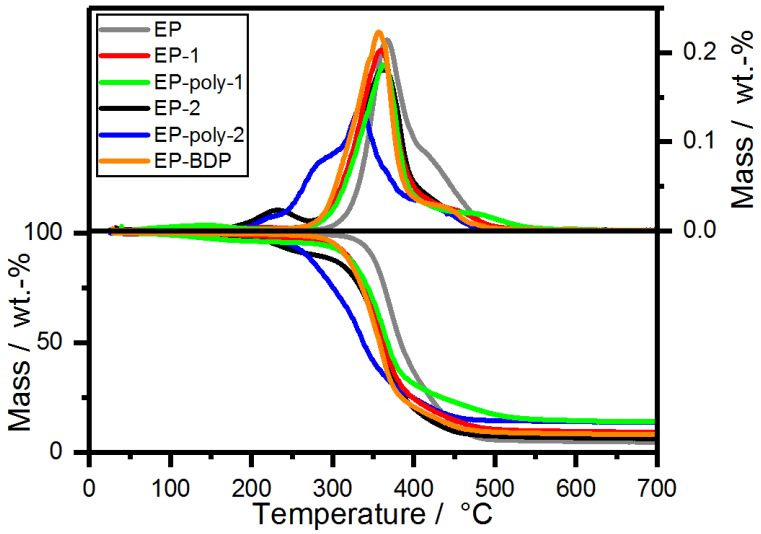

Figure S4.21. Mass loss (bottom) and mass loss rate (top) over *T* of neat epoxy resin and flame retardant containing epoxy resins from TGA measurements (10 K min^{-1}; N_2).

Table S4.3. TGA data of the flame retardant containing epoxy resins. $T_{5\%}$: Temperature at which 5% mass-loss happened; T_{max}: Temperature of maximum degradation; Residue: Residue at 700 °C.

Material	$T_{5\%}$ / °C	T_{max} / °C	Residue / wt.-%
DGEBA-DMC (EP)	338 ± 1	372 ± 1	4.5 ± 0.1
EP-1	279 ± 1	359 ± 1	9.1 ± 0.2
EP-poly-1	299 ± 3	361 ± 1	14.7 ± 0.5
EP-2	231 ± 1	367 ± 0	5.1 ± 0.1
EP-poly-2	249 ± 3	337 ± 2	13.3 ± 0.2
EP-BDP	304 ± 1	357 ± 0	8.2 ± 0.1

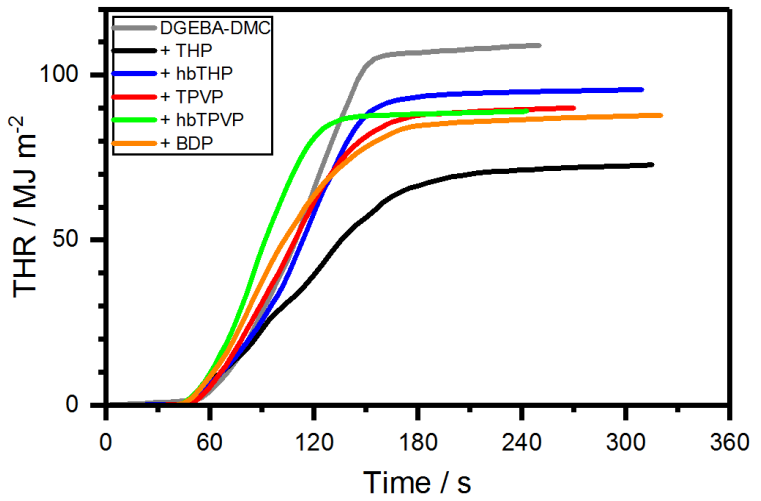

Figure S4.22. Total heat released (THR) of epoxy resin and epoxy resin with flame retardant measured by cone calorimeter.

Table S4.4. Results from cone calorimeter measurements of the flame retardant containing epoxy resins.

Material	THE / MJ m^{-2}	PHRR / kW m^{-2}	Residue / wt.-%	EHC / MJ kg^{-1}	FIGRA / kW m^{-2} s
DGEBA-DMC (EP)	108 ± 3	1696 ± 180	0.7 ± 0.1	26.9 ± 1.0	15.5 ± 2.3
EP-1	88 ± 1	1194 ± 100	5.3 ± 0.0	23.3 ± 0.2	11.2 ± 0.0
EP-poly-1	92 ± 4	1969 ± 353	7.0 ± 1.5	25.0 ± 1.5	15.0 ± 0.7
EP-2	78 ± 6	885 ± 16	9.2 ± 0.1	21.7 ± 1.8	9.0 ± 0.2
EP-poly-2	95 ± 0	1248 ± 32	5.1 ± 0.7	24.9 ± 0.2	9.0 ± 0.0
EP-BDP	87 ± 1	1180 ± 41	3.1 ± 0.2	22.7 ± 0.2	11.0 ± 0.7

Figure S4.23. Cross-linking of **1** at 300 °C in a silicon form for 2 h, producing a hard, cross-linked PPE resin.

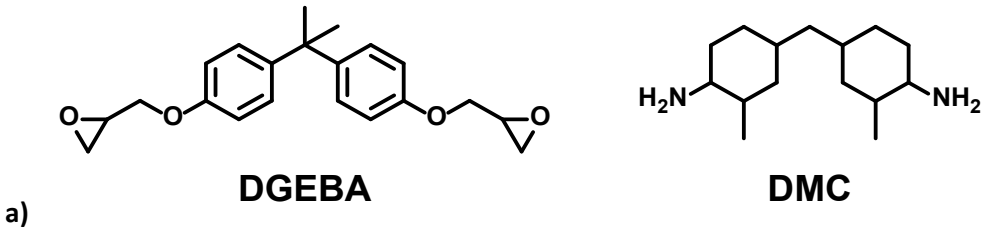

a)

Figure S4.24. Chemical structure of Diglycidyl ether of bisphenol A (DGEBA) and 2,2'-Dimethyl-4,4'-methylene-bis(cyclohexylamine) (DMC).

Figure S4.25. Residue of **EP-1** after cone calorimeter measurement, exhibiting a moderate protective layer effect from the formation of a rigid char layer.

Figure S4.26. Residue of **EP-2** after cone calorimeter measurements, exhibiting a strong protective layer from the large voluminous, multicellular char.

4.13.1 References SI Chapter 4

[1] P. J. Linstrom, W. G. Mallard*, Vol. 2019*, Institute of Standards and Technology, Gaithersburg MD, **2018**.

5. Matrix Matters: Hyperbranched Flame Retardants in Aliphatic and Aromatic Epoxy Resins

Alexander Battig,[a]+ Jens C. Markwart,[b,c]+ Frederik R. Wurm,*[b] and Bernhard Schartel[a]*

[a] *Technical Properties of Polymeric Materials - Bundesanstalt für Materialforschung und -prüfung (BAM), Unter den Eichen 87, 12205 Berlin, Germany*

[b] *Physical Chemistry of Polymers - Max Planck Institute for Polymer Research, Ackermannweg 10, 55128 Mainz, Germany*

[c] *Graduate School Materials Science in Mainz, Staudinger Weg 9, 55128 Mainz, Germany*

+ *These authors contributed equally to this work.*

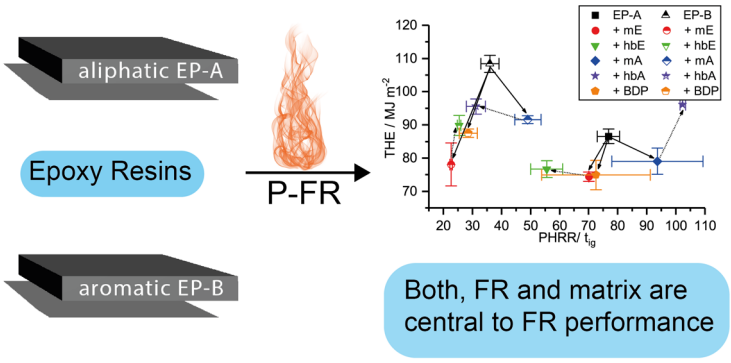

Keywords: flame retardant; phosphate; phosphorus; phosphoramide; epoxy resin; hyperbranched polymer

5.1 Notes

Alexander Battig performed the flame-retardancy measurements.

5.2 Abstract

We synthesized a library of phosphorus-based flame retardants (phosphates and phosphoramides of low and high molar mass) and investigated their behavior in two epoxy resins (one aliphatic and one aromatic). The pyrolytic and burning behavior of the two resins (via TGA, TG-FTIR, Hot stage FTIR, Py-GC/MS, PCFC, DSC, LOI, UL-94, Cone calorimeter) are analyzed and compared to the results of flame retardant (FR)-containing composites. A decomposition pathway incorporating the identified modes of action and known chemical mechanisms is proposed. The overlap of decomposition temperature (T_{dec}) ranges of matrix and FR determines the efficacy of the system. Low molar mass FRs strongly impact material properties like T_g but are very reactive, and high molar mass variants are more thermally stable. Varying P-O and P-N content of the FR affects decomposition, but the chemical structure of the matrix also guides FR behavior. Thus, phosphates afford lower fire load and heat release in aliphatic epoxy resins, and phosphoramides can act as additives in an aromatic matrix or a reactive FRs in aliphatic ones. The chemical structure and the structure-property relationship of both FR and matrix are central to FR performance and must be viewed not as two separate but as one codependent system.

5.3 Introduction

Phosphorus-based FRs (P-FRs) have gained added attention as suitable alternatives to halogenated FRs. Primarily, this is due to heightened health and environmental concerns over halogen-containing formulations. P-FRs offer a broad range of application for many polymer types, as reactive or additive components, mainly due to the chemical versatility of phosphorus.[1-4] Moreover, their mode of action can be adjusted to suit a specific application by altering the P-FR composition: Recently, a study conducted on the ratio of P-O to P-N bonds highlighted the change in mode of action and decomposition mechanism of low molar mass P-FRs in epoxy resins.[5] Additionally, by polymerizing these low molar mass P-FRs into hyperbranched (hb) polymers, the effect of complex architecture on the flame retardancy of epoxy resins was investigated, and the effectiveness of hb polymers as multifunctional FRs was elucidated.[6]

The interaction between decomposition compounds of FR and matrix affect the combustion efficiency, peak of heat release rate, and effective heat of combustion in fire scenarios.[7-8] Previous works have shown that one underlying mode of action is the formation of aromatic char precursors and the stabilizing role of phosphorus in them.[9] Critically, this effect is maximized when the overlap of decomposition temperature (T_{dec}) ranges of matrix and FR is greatest.[10-12] Investigation of the previously synthesized low molar mass monomeric FRs (mFRs) and the polymeric hyperbranched FRs (hbFRs) in an epoxy resins (EP) concluded that the FR's mode of action is alterable by the presence of nitrogen in the P-binding sphere (P-N vs. P-O).[5] Moreover, its chemical interaction capabilities are increased by polymerization, mainly due to the shift to higher T_{dec}. Furthermore, the role of sulfur in the flame retardancy of hbFRs is the subject of another investigation. These changes in the chemical composition and architecture led to higher residue yields and more effective flame retardancy of a bisphenol A based epoxy resin (EP-B).[6]

The structure-property relationship of the FR and matrix are crucial to effective flame retardancy. As it stands, the modes of action and chemical FR mechanisms previously proposed for mFRs and hbFRs are based on their performance in an aromatic, bisphenol A-based polymer resin. However, a fuller understanding of the FRs' capabilities may be gained from examining their performance in an aliphatic epoxy resin (EP-A) and comparing the results to the previously examined EP-B, which is precisely the approach proposed in the following manuscript.

The aliphatic epoxy resin EP-A (Scheme 5.1) has been previously investigated in use as fiber-reinforced composites and as a basis for reactive phosphorus-based FR-crosslinking agents.[13-14] Its epoxide agent is based on pentaerythritol, a main component (carbon-source) in intumescent systems.[15-16] Pentaerythritol glycidyl ether has further been investigated as a chain extender and plasticizing agent for bisphenol A systems,[17] as well as a starting material for polyurethanes.[18]

We have investigated the flame retardancy effects of previously synthesized and characterized monomeric and hb polymeric FRs in aliphatic and aromatic epoxy resins. As a means to compare the efficacy of these FRs in the respective matrices, an industrially available FR, previously proven effective in epoxy resins, namely bisphenol A bis(diphenyl phosphate) (BDP), was used as a benchmark. This work aims at understanding the fundamental chemical interactions at play of phosphates and phosphoramides – as low molar mass and hyperbranched polymeric variants – in two distinct epoxy resin systems. By comparing the results, greater insight into the mode of action and chemical mechanisms surrounding these P-FRs may be gained. More significantly, investigating these FRs in different matrices expands the understanding of the FR-matrix system and the codependence of the two on effective flame retardancy. This work is not aimed at optimizing the performance of the materials, but rather at observing their behavior in divergent matrices and extrapolating their function by means of multi-method pyrolysis and fire behavior investigations.

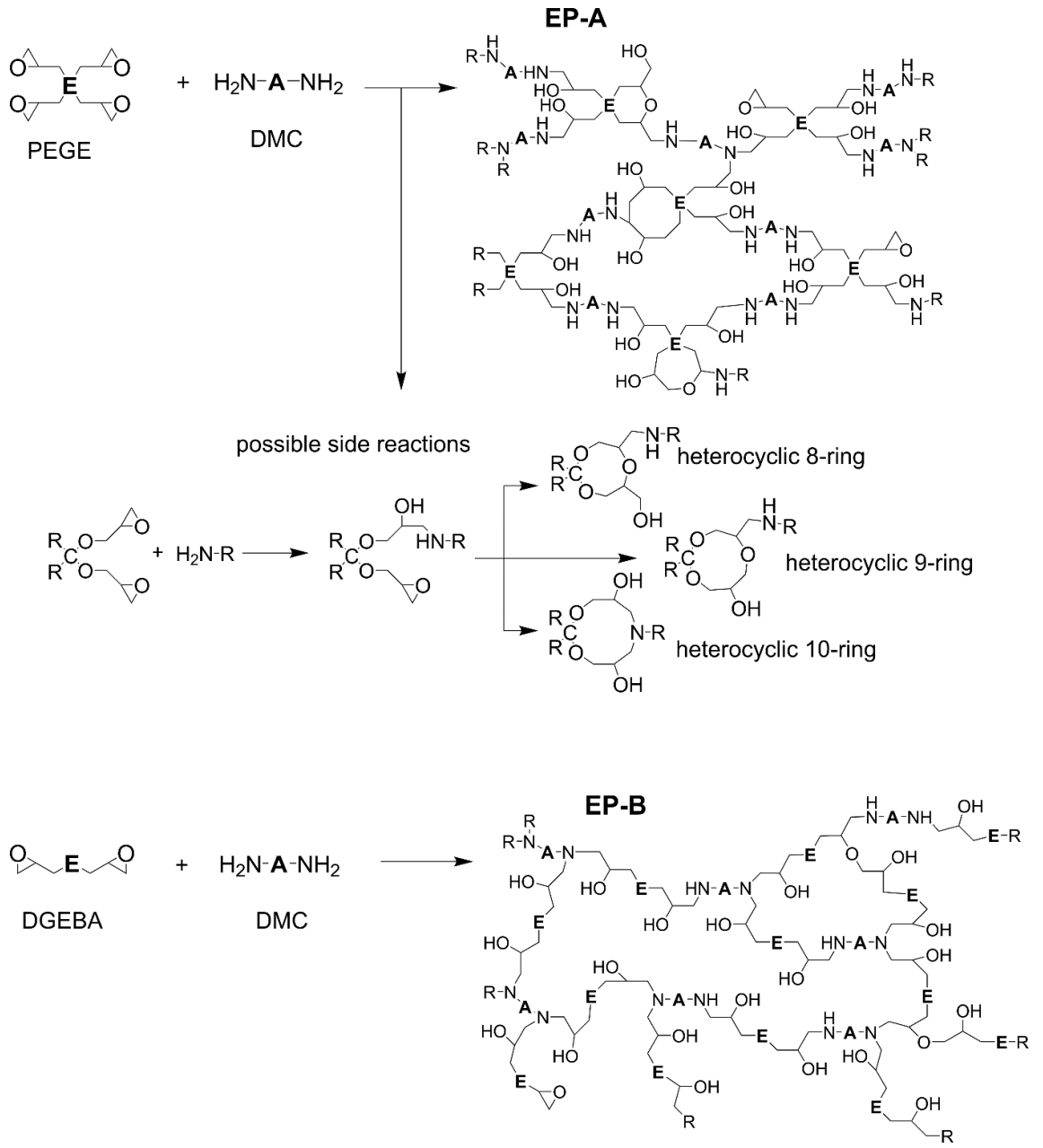

Scheme 5.1. General synthesis scheme of EP-A (top) and EP-B (bottom) and schematic representation of matrices (E: epoxy component PEGE; A: amine component DMC).

5.4 Materials and Methods

Table 5.1. Material names, abbreviations, and chemical structures.

Name	Short name	Chemical structure	P content (calc) [%]
Pentaerythritol tetraglycidyl ether	PEGE	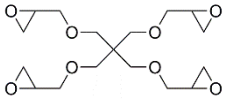	-
Digylcidyl ether of bisphenol A	DGEBA	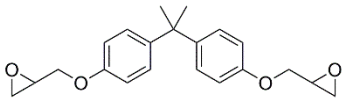	-
2,2'-Dimethyl-4,4'-methylene-bis-(cyclohexylamine)	DMC	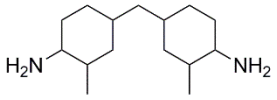	-
Tri(hex-5-en-1-yl) phosphate	mE	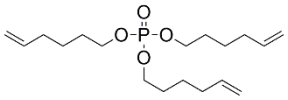	9.0
hb-Phosphoester	hbE	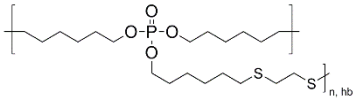	7.1
Tri(hex-5-en-1-yl) phosphoramide	mA	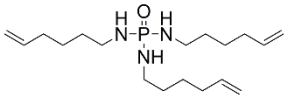	9.1
hb-Phosphoramide	hbA	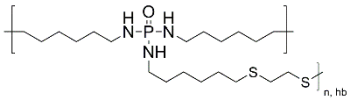	7.1
Bisphenol A diphenyl phosphate	BDP	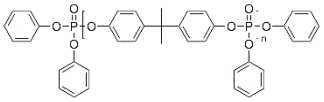	8.1

All materials (Table 5.1) were used without further purification.

The aliphatic epoxide agent pentaerythritol tetraglycidyl ether (PEGE, ipox CL 16) was supplied by ipox chemicals GmbH (Laupheim, Germany). The aromatic epoxide agent diglydyl ether of bisphenol A (DGEBA, Araldite MY740) was supplied by Bodo Müller Chemie GmbH (Offenbach am Main, Germany). The amine component 2,2'-dimethyl-4,4'-methylene-bis-(cyclohexylamine) (DMC) was purchased from Sigma Aldrich Co. LLC / Merck KgaA (Darmstadt, Germany). The benchmark FR bisphenol A bis(diphenyl phosphate) (BDP) was supplied by Albemarle (Louvain-la-Neuve, Belgium). The mFRs and hbFRs were previously synthesized and characterized:[5-6] starting from $POCl_3$, mE was produced via esterification with hex-5-en-1-ol, and mA was prepared via amidation with hex-5-en-1-amine. hbE and hbA were produced via a radical thiol-ene polyaddition, combining mE or mA as monomers, respectively, with 1,2-ethanethiol as comonomer and azoisobutyronitrile (AIBN) as a radical initiator. Purities and chemical structures were identified via ^{1}H and ^{31}P {H} NMR.

All epoxy resin samples (with or without FR) were prepared as follows (Table 5.2): the epoxide agent (PEGE or DGEBA) was poured into in a 1 L polypropylene cup. For FR-containing composites, 10 wt.-% of the total batch was replaced with the FR. The amount of FR, and therefore P-content regarding weight equivalents, was identical in both systems. The FR was mixed with the epoxide agent with a wooden spatula. Once the components were fully mixed, the amine component DMC was added, and the mixture was again stirred until homogenous. The contents were poured into prepared aluminum molds sized 100 mm x 100 mm x 4 mm (for cone calorimeter specimens) or 130 mm x 130 mm x 3 mm (for LOI or UL-94 specimens). UL-94 and LOI samples were cut from the mold into appropriate specimen sizes according to their respective standards.

Table 5.2. Composition of tested epoxy resin and composite specimen.

Material	Composition [g] (exemplary 500 g batch)											
	EP-A	+ mE	+ hbE	+ mA	+ hbA	+ BDP	EP-B	+ mE	+ hbE	+ mA	+ hbA	+ BDP
PEGE	301	271	271	271	271	271	-	-	-	-	-	-
DGEBA	-	-	-	-	-	-	370	333	333	333	333	333
DMC	199	179	179	179	179	179	130	117	117	117	117	117
mE	-	50	-	-	-	-	-	50	-	-	-	-
hbE	-	-	50	-	-	-	-	-	50	-	-	-
mA	-	-	-	50	-	-	-	-	-	50	-	-
hbA	-	-	-	-	50	-	-	-	-	-	50	-
BDP	-	-	-	-	-	50	-	-	-	-	-	50

5.4.1 NMR

Nuclear magnetic resonance (NMR) analysis, ^{1}H, ^{31}P {H}, ^{1}H,^{1}H-COSY and ^{1}H,^{31}P-HMBC NMR spectra were recorded with Bruker Avance spectrometers operating with 300 or 500 MHz frequencies in deuterated chloroform or deuterated N,N-dimethylformamide as a solvent. The calibration of the spectra was done against the solvent signal. The spectra were analyzed using MestReNova 9 from Mestrelab Research S.L.

5.4.2 TGA, TG-FTIR and Hot Stage FTIR

Powdered samples for TGA-FTIR, PCFC and hot stage FTIR measurements were obtained using a CryoMill (RETSCH, Germany) under liquid nitrogen cooling.

Thermogravimetric analysis (TGA) measurements were performed on a TG 209 F1 Iris (Netzsch Instruments, Selb, Germany). 10 mg powdered samples were used for EPs and EPs with FRs, and 5 mg samples for pure FRs. Samples were heated from 30 to 900 °C at a rate of 10 K min^{-1} under a 30 ml min^{-1} nitrogen flow.

Evolved gas analysis of TGA samples was conducted using a Fourier transform infrared spectrometer Tensor27 (Bruker Optics, Ettlingen, Germany) (TG-FTIR). The machines were coupled by a 1.0 m transfer line heated to 270 °C.

Condensed phase FTIR spectra during pyrolysis were gathered using a FTIR600 hot-stage cell (Linkam Scientific Instruments Ltd., Chilworth, UK) fitted to a Vertex70 FTIR spectrometer (Bruker Optics, Ettlingen, Germany). The measuring range was 4000 to 40 cm^{-1} at a resolution of 0.4 cm^{-1}. Approx. 5 mg of powdered material was pressed into a potassium bromide platelet (d = 1 cm; w = 0.1 cm) and placed into the hot-stage cell. Under a nitrogen flow of 300 ml min^{-1}, the samples were heated from 30 to 600 °C at a rate of 10 K min^{-1}.

5.4.3 Pyrolysis Gas Chromatography - Mass Spectrometry (Py-GC/MS)

Pyrolysis Gas Chromatography - Mass Spectrometry (Py-GC/MS) measurements were performed using a PY3030iD micro-furnace double-shot pyrolyzer (Frontier Laboratories, Japan) coupled via a split/ splitless inlet port to a 7890B gas chromatograph (Agilent Technologies, USA) and combined with a 5977B mass selective detector (Agilent Technologies, USA). The EI ionization energy of the MSD was 70 eV and the scan range was 15 to 50 amu. 150 µg samples were pyrolyzed at 500 °C in a helium atmosphere by a gravimetric fall into the pyrolysis zone. All evolved pyrolysis products were separated under a helium flow of 1 ml min^{-1} using an Ultra Alloy +-5 capillary column of a length of 30 m, and inner diameter of 0.25 mm, and a film thickness of 0.25 µm. The temperature of the column was held for 2 min at 40 °C, then increased to 300 °C at a rate of 10 K min^{-1} and held for 10 min. The temperature of the gas chromatograph injector was 300 °C, and it was operated in a split mode of 1:300. The NIST 14 MS library was used for peak assignment.

5.4.4 PCFC

Pyrolysis flow combustion calorimetry (PCFC) measurements were conducted on a microscale combustion calorimeter (Fire Testing Technologies Ltd., East Grinstead, UK). 5 mg powdered samples were pyrolyzed at a heating rate of 1 K s^{-1} from 150 to 750 °C. The combustor temperature was set to 900 °C. The gas flow of nitrogen was 80 ml min^{-1} and 20 ml min^{-1} for oxygen.

5.4.5 DSC

Differential scanning calorimetry (DSC) measurements were conducted on a Netzsch 204 FR "Phoenix" (Netzsch Instruments, Selb, Germany). 5 mg samples were taken from the bulk material. In the range of -80 to 180 °C, three heating and two cooling runs were conducted at a rate of 10 K min^{-1} under a 30 ml min^{-1} nitrogen flow. The second and third heating run was used to determine T_g.

5.4.6 UL-94

Underwriter's Laboratory 94 (UL-94) testing was performed in vertical and then in horizontal orientation in accordance with EN 60695-11-10. Samples sized approx. 125 mm x 12 mm x 3 mm were stored at 50% relative humidity and 23 °C for at least 80 hours prior to testing.

5.4.7 LOI

Limiting oxygen index (LOI) testing was conducted in accordance with ISO 4589-2. Type IV samples sized 125 mm x 6 mm x 3 mm were used after storage at 50% relative humidity and 23 °C for at least 80 hours.

5.4.8 Cone Calorimeter

Forced-flaming measurements were conducted using a cone calorimeter (Fire Testing Technology Ltd., East Grinstead, UK) in accordance with ISO 5660. Samples sized 100 mm x 100 mm x 4 mm were stored at 50% relative humidity and 23 °C for at least 48 hours prior to testing. Samples were irradiated with a heat flux of 50 kW m^{-2} at a distance of 35 mm between specimen and cone heater, thus simulating a developing fire.[19-20] Measurements were conducted in duplicate, unless the margin of error was greater than 10%, whereupon a third specimen was measured.

5.5 Results and Discussion

5.5.1 Pyrolysis – Decomposition Temperature and Mass Loss

The pyrolytic decomposition temperature (T_{dec}) and mass loss of the epoxy resin matrices EP-A and EP-B, as well as the flame retardants mE, hbE, mA, hbA, and BDP, were investigated via TGA (Figure 5.1a & Table 5.1)

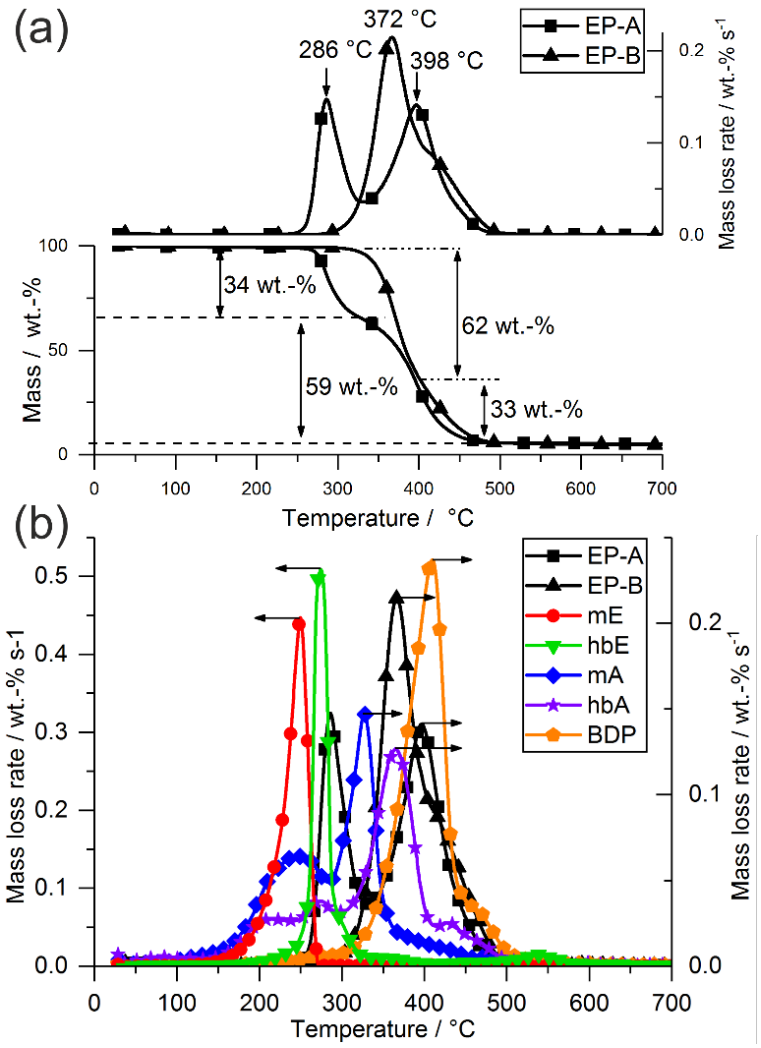

Figure 5.1. Results from TGA measurements. a) Mass loss (bottom) and mass loss rate (top) of epoxy resins EP-A and EP-B; b) Mass loss rates of FRs and EPs, indicating decomposition temperature ranges.

The mass loss and mass loss rate curves of EP-A and EP-B (Figure 5.1a) outline the difference in thermal stability of the two materials. The onset temperature $T_{5\%}$ (the temperature at 5% mass loss) of EP-A was 276 °C, and that of EP-B was 338 °C. Noticeably, EP-A exhibited two distinct decomposition steps, while EP-B's mass loss occurred in one step with a slight shoulder. The first decomposition step of EP-A, identified by the temperature at peak mass loss rate, occurred at

286 °C and corresponded to about 34 wt.-% mass loss, while the second step at 398 °C amounted to a 59 wt.-% mass loss. For EP-B, the main decomposition step (T_{max}) at 372 °C amounted to a 62 wt.-% mass loss, while the shoulder at about 424 °C constituted a loss of about 33 wt.-%. Both materials retained similar residues at 700 °C (4.6 wt.-% for EP-A and 4.5 wt.-% for EP-B).

The pure FRs have been previously characterized in detail,[5-6] and Figure 5.1b summarizes the mass loss rates of these materials during pyrolysis. Additionally, Table 5.3 summarizes the results from TGA measurements for all materials. mE decomposed in a single step ($T_{5\%}$ = 195 °C, T_{max} = 250 °C). For the hyperbranched polymeric variant hbE, $T_{5\%}$ (242 °C) and T_{max} (280 °C) were shifted to higher temperatures due to increased thermal stability of the hb-structure.[6] Notably, the residue yield at 700 °C of hbE (11.2 wt.-%) was four times higher than that of mE (2.8 wt.-%). mA decomposed in two steps, the first at 236 °C (36 wt.-% mass loss) and the second at 317 °C (46 wt.-% mass loss), retaining a residue of 15.6 wt.-% at 700 °C. The hyperbranched polymeric phosphoramide hbA exhibited a higher T_{max} compared to mA, comparable to the shift seen from mE to hbE. While $T_{5\%}$ was only slightly higher than mA, hbA decomposed in multiple steps over a large temperature range, exhibiting four peak mass loss rates at 212 °C (11 wt.-% mass loss), 273 °C (14 wt.-% mass loss), T_{max} at 361 °C (47 wt.-% mass loss), and 430 °C (8 wt.-% mass loss). The residue yield at 700 °C was 18 wt.-%, an increase of 14% compared to mA.

The benchmark FR BDP decomposed in a single decomposition step with a shoulder. Its $T_{5\%}$ was at 331 °C and T_{max} at 415 °C, accounting for an 85 wt.-% mass loss. Thus, BDP was the most thermally stable FR used in this study. The shoulder at approx. 467 °C presented a mass loss of 12 wt.-%, preserving a residue of only about 2 wt.-% at 700 °C.

Table 5.3. Results from TGA measurements of pure FRs and the epoxy resin matrices EP-A and EP-B.

	$T_{5\%}$ / °C	T_1 / °C	ML_1 / wt.-%	T_2 / °C	ML_2 / wt.-%	T_{max} / °C	ML_{max} / wt.-%	T_3 / °C	ML_3 / wt.-%	Residue (700°C)
EP-A	276 ±2	-	-	286 ±2	34.8 ±0.3	398 ±1	58.8 ±1.2	-	-	4.6 ±0.3
EP-B	338 ±1	-	-	-	-	372 ±1	62.0 ±0.8	424 ±5	33.2 ±0.3	4.5 ±0.1
mE	195 ±3	-	-	-	-	250 ±2	95.7 ±1.4	-	-	2.8 ±0.8
hbE	242 ±2	-	-	-	-	280 ±1	83.3 ±0.2	-	-	11.2 ±1.4
mA	181 ±2	236 ±10	36.1 ±0.5	-	-	317 ±10	46.4 ±0.3	-	-	15.6 ±0.8
hbA	190 ±3	212 ±2	11.1 ±1.2	273 ±3	14.2 ±2.3	361 ±3	47.1 ±0.5	430 ±4	7.9 ±0.8	17.8 ±0.4
BDP	331 ±1	-	-	-	-	415 ±6	85.5 ±2.2	467 ±3	11.8 ±1.3	1.8 ±0.9

5.5.2 Pyrolysis – Evolved gas analysis of EP

There have been several in-depth investigations into the thermal decomposition of EP-B.[21-23] Although flame retardancy of EP-A has been investigated previously,[13, 24] less is known about the pyrolytic evolved gases corresponding to the mass loss steps of EP-A. To understand the flame retardancy effects of the FRs on the polymer, the decomposition steps of the matrix must be more closely identified. To this end, pyrolysis – gas chromatography / mass spectrometry (Py-GC/MS) enables a more in-depth analysis of the evolved gases during pyrolysis. Two single-shot measurements were measured at specific temperatures: T = 325 °C (Figure 5.2a) and 500 °C (Figure 5.2b). They represent the end of a mass loss step, as indicated by a minimum of the mass loss rate curve of EP-A in TGA experiments. Thus, products from the decomposition step at T = 286 °C can be observed separately from the step at T = 398 °C. Notably, the spectra at 500 °C contain information of decomposition products of both steps and not only the second. By analyzing the difference in spectra, a clearer image of the decomposition mechanism is presented.

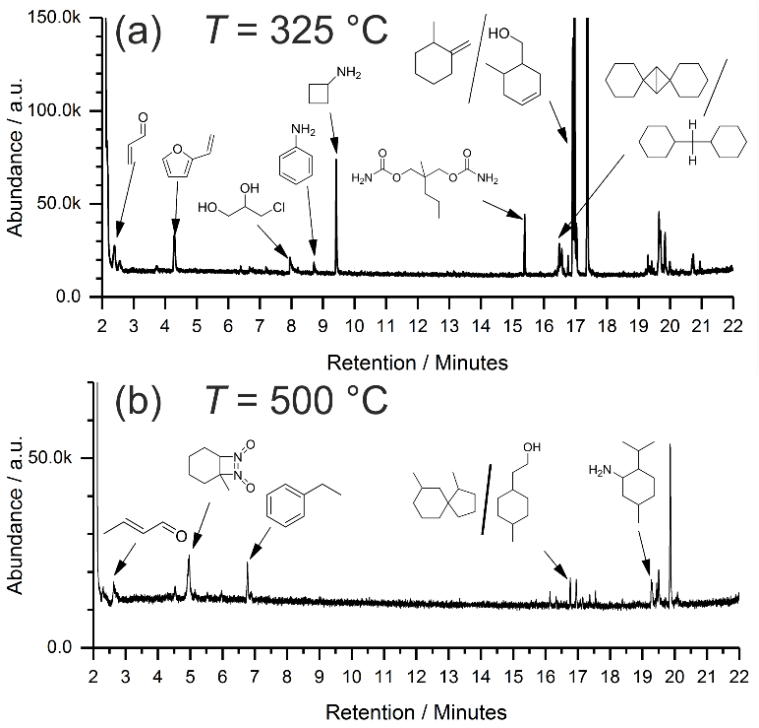

Figure 5.2. Gas chromatograph of EP-A taken at (a) 325°C and (b) 500 °C (B) via Py-GC/MS. Molecules matching MS spectra at specific retention times are noted with arrows.

The chromatograph in Figure 5.2a reveals the production of several specific decomposition products from the EP-A matrix at 325 °C: At low retention times (2 –10 min), low molar mass molecules were identified via comparative mass spectra, such as acrolein at 2.39 min (Figure S5.1), 2-vinylfuran at 4.29 min (Figure S5.2), 3-chloro-1,2-propanediol at 7.95 min (Figure S5.3), aniline at 8.72 min (Figure S5.4), and cyclobutylamine at 9.42 min (Figure S5.5). At higher retention times, the mass spectra resembled meprobamate at 15.39 min (Figure S5.6) and dispiro[cyclohexane-1,2'-bicyclo(1.1.0)butane-4',1"-cyclohexane] at 16.48 – 16.57 min (Figure S5.7). Additionally, 1-methyl-2-methylenecyclohexane and 6-methyl-3-cyclohexane-1-methanol at 16.97 min (Figure S5.8) were among the products identified as decomposition products from their mass spectra.

Figure 5.2b exhibits those products pyrolyzed at 500 °C. Notably, the spectrum is significantly different to Figure 5.2a. At low retention times (2 – 8 min), the mass spectral data saw similarities with 2-butenal at 2.66 min (Figure S5.9), 1,2-dinitroso-2-methyl-cyclohexane at 4.54 min (Figure S5.10), and ethylbenzene at 6.77 min (Figure S5.11). At higher retention times, the mass spectra resembled 2-(4-methylcyclohexyl) ethanol or 1,7-dimethylspiro[4.5]decane at 16.76 min (Figure S5.12), as well as neomenthylamine at 19.30 min (Figure S5.13).

It should be noted that the NIST 14 library was utilized for structure identification purposes. Several fragmentations in the mass spectra do not fully correspond to the fragmentation pattern of the molecules mentioned above. However, their fragmentation pattern closely resembles these

products, and they provide clues to the decomposition mechanism of EP-A. By using TGA-FTIR, corroborating evidence to the presence of these decomposition products may be gained.

By coupling the TGA to a Fourier transform infrared spectrometer (FTIR) via a transfer line, FTIR-spectra from the evolved gases at specific decomposition steps were captured. The gas spectra at the two main decomposition steps of EP-A are plotted in Figure 5.3, along with reference spectra of decomposition products.

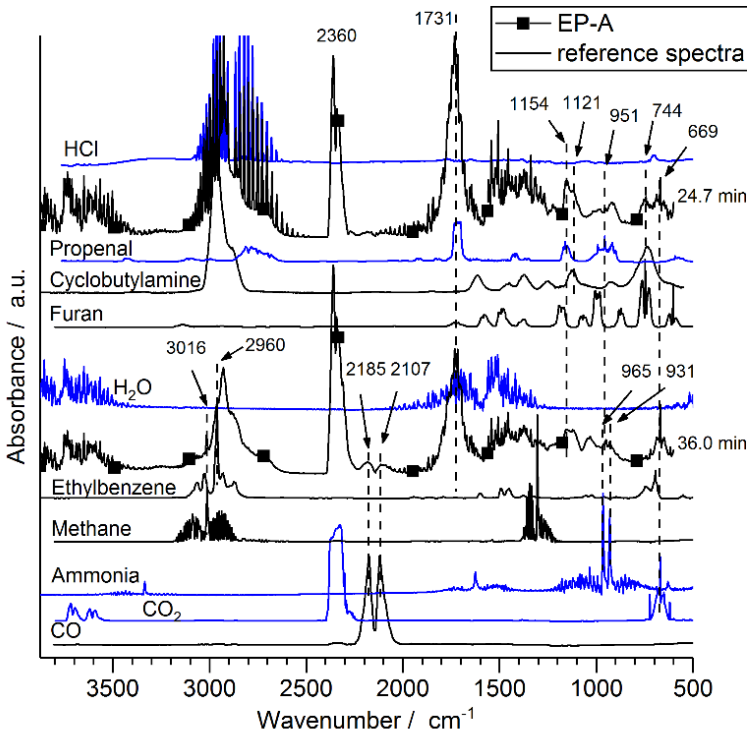

Figure 5.3. Evolved gas FTIR spectra of EP-A at the main decomposition steps (t = 24.7 and 36.0 min) and comparative spectra (blue lines: main decomposition products).

Notable decomposition products in the spectrum at 24.7 min were water (approx. 4000 – 3475 cm^{-1} and 2100 – 1275 cm^{-1}), carbon dioxide (2360 and 669 cm^{-1}), carbon monoxide (2185 and 2107 cm^{-1}), and hydrochloric acid (approx. 3100 – 2550 cm^{-1}), the latter resulting from epichlorohydrin, an educt in the production of pentaerythritol tetraglycidol ether. The decomposition of epichlorohydrin also yielded acrolein from the epoxy group, as identified via the large (C=O) band at 1731 cm^{-1} as well as 1154 cm^{-1}, and especially the sharp band at 951 cm^{-1}. The presence of cyclobutylamine was identified by 1121 cm^{-1} and the broad (N-H) band around 750 cm^{-1}, while the sharp band at 744 cm^{-1} corresponded to furan.

At 36.0 min, notable decomposition products include water, methane (3016 cm^{-1}), carbon dioxide, carbon monoxide, and ammonia (965 and 931 cm^{-1}). Notably, HCl is not present in the spectrum

at 36.0 min. The carbonyl (C=O) band at 1731 is predominantly visible, providing evidence for the evolution of aldehydes such as propenal at 2.66 min. The band at 2960 cm^{-1} signaled the production of ethylbenzene, which correlates with its presence at 6.77 min.

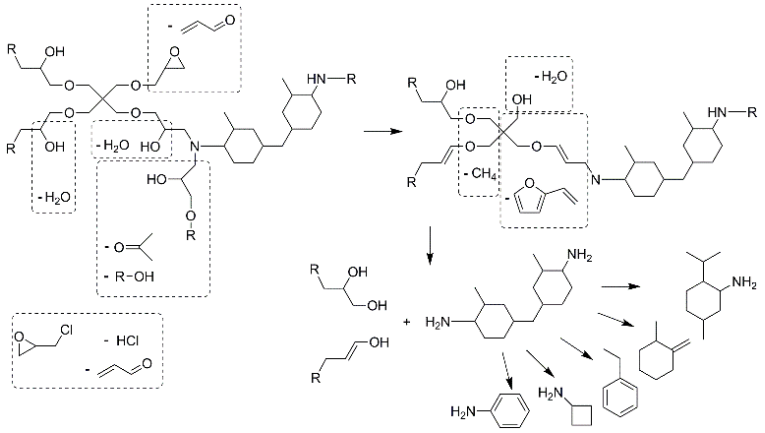

Scheme 5.2. Proposed decomposition mechanism of EP-A.

From the data gathered from Py-GC/MS and TG-FTIR, a decomposition mechanism of EP-A (Scheme 5.2) is proposed. The two decomposition steps (see Figure 5.1a) correspond to specific mechanisms: At 286 °C, unreacted epoxide moieties decomposed to form acrolein, and (unreacted) amine components produced cyclobutylamine, aniline, etc. Unreacted epichlorohydrin provided the hydrochloric acid seen in Figure 5.3 at 24.7 min. Water and ketones were released from secondary hydroxyls. Additionally, some rearrangements and dehydration of the cyclic hydrocarbons from the amine component formed aromatic moieties. These decomposed at higher temperatures, along with more densely cross-linked moieties, resulting in the second decomposition step which peaked at 398 °C. Here, the decomposition of aromatic moieties resulted in the production of ethylbenzene, and hydrolysis of amines led to the evolution of ammonia. The decomposition of aromatic structures at this temperature correlated with the decomposition step of EP-B, which is based on the aromatic bisphenol A structure. EP-B displayed a maximum mass loss at 372 °C and has a shoulder in the same temperature range as EP-A's second mass loss step, indicating that aromatic decomposition occurs in this temperature range.
The characterization of EP-A is crucial to understanding the flame retardancy effects of the FRs, as the interaction between FR and matrix during decomposition determines the efficacy of the FR system.

5.5.3 Material properties of EPs and EP-FRs

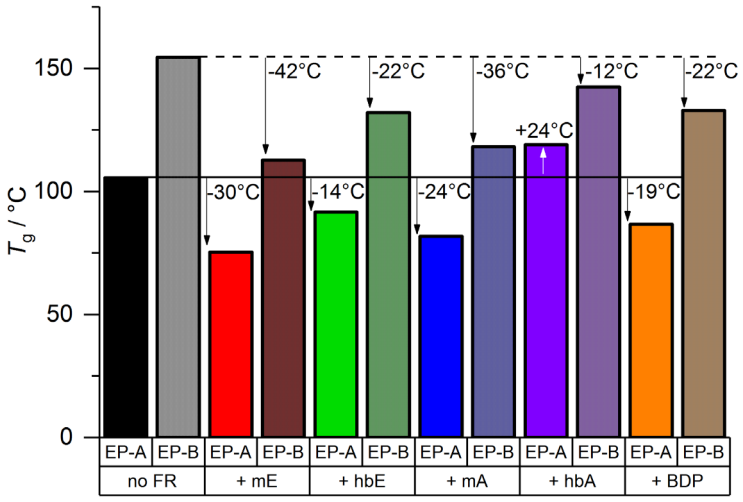

Figure 5.4. Glass-transition temperatures (T_g) of EP-A and EP-B, and FR composites thereof via DSC measurements. Change in T_g of the FR-containing composites to the respective epoxy resin is noted.

One of the principal properties of polymeric materials is the glass-transition temperature (T_g). It determines the functional temperature range of the material. In the T_g plots of the matrices EP-A and EP-B (Figure 5.4), there is a noticeable difference of approx. 50 °C between them: the T_g of EP-A was 105 °C, while EP-B's T_g was 155 °C. As EP-B contains aromatic rings, it's T_g is inherently higher due to increased stiffness of the polymer chains.[25] The incorporation of a FR additive into a polymer resin has the potential to change the material properties of the matrix. Most additives act as plasticizers and reduce T_g of the material due to a reduction in the cross-linking density,[26] and this phenomenon was observable in the T_gs of EP-A and EP-B with FRs. More specifically, the low molar mass FRs mE and mA decreased T_g more strongly than the polymeric hbFRs. The relatively low impact of the hbFRs on T_g has been previously studied and is linked to the higher molar mass compared to mFRs.[6] Notably, the addition of BDP decreased T_g between 19 – 22 °C, which is in the same range as the hbE, but not hbA, as its presence increased the T_g of EP-A.This behavior highlights the versatility of hbFRs in different epoxy resin matrices, especially given that hbFRs are aliphatic and BDP is aromatic. mE lowered T_g of the matrices by 30 – 42 °C, while hbE only lowered T_g by 14 – 22 °C. Similarly, mA lowered T_g by 24 – 36 °C. hbA exhibited very different behavior in EP-A than in EP-B: in the aromatic matrix, T_g was lowered by 12 °C, while in the aliphatic matrix, T_g was increased by 24 °C. This behavior is explained by the varied reactivity of the epoxy resin matrix: Previous investigations proved that phosphoramides act as additives in EP-B, as ^{31}P and ^{1}H-NMR showed no reaction with phenyl glycidyl ether.[5] However, the glycidol groups in EP-A possess a different reactivity. To assess whether phosphoramides compete with

the amine component DMC during the curing process, mA was mixed with glycidol and left to react under the same curing conditions, and a ^{1}H-NMR was measured afterward (Figure S5.14). The highlighted areas in Figure S5.14 signify that mA reacted with glycidol, as the mixture of the two at curing conditions contained different signals than the two individual components. From the ^{1}H-NMR spectra, the signals of the amide protons (highlighted blue, Figure S5.14) and the epoxy methylene and methine groups (highlighted gray) disappear. Moreover, Figure S5.15 (^{1}H^{1}H-COSY) highlights the correlation between the methylene groups obtained from the gylcidol and the methylene groups of the hexenyl sidechain, proving the successful reaction of the phosphoramide with glycidol. This is further supported by Figure S5.16, which shows a correlation of the two methylene groups with the phosphorus and the disappearance of the amide proton. It follows that phosphoramides compete with DMC in EP-A, but not in EP-B formulations. Therefore, the increase in T_g is the result of hbA acting as a reactive FR instead of an additive. The effect is stronger for hbA than for mA due to the presence of many net-points in hbA not present in mA. Thus, the macromolecular structure of hbA helped promote cross-linking in EP-A, yielding a higher T_g. This toughening effect of the epoxy resin has been previously described,[27,28] yet the results herein point to the ability of a single hbFR to act either as an additive or a reactive FR based on the chemical structure of the epoxide-component.

5.5.4 Pyrolysis – Decomposition Temperature and Mass Loss of EP-FRs

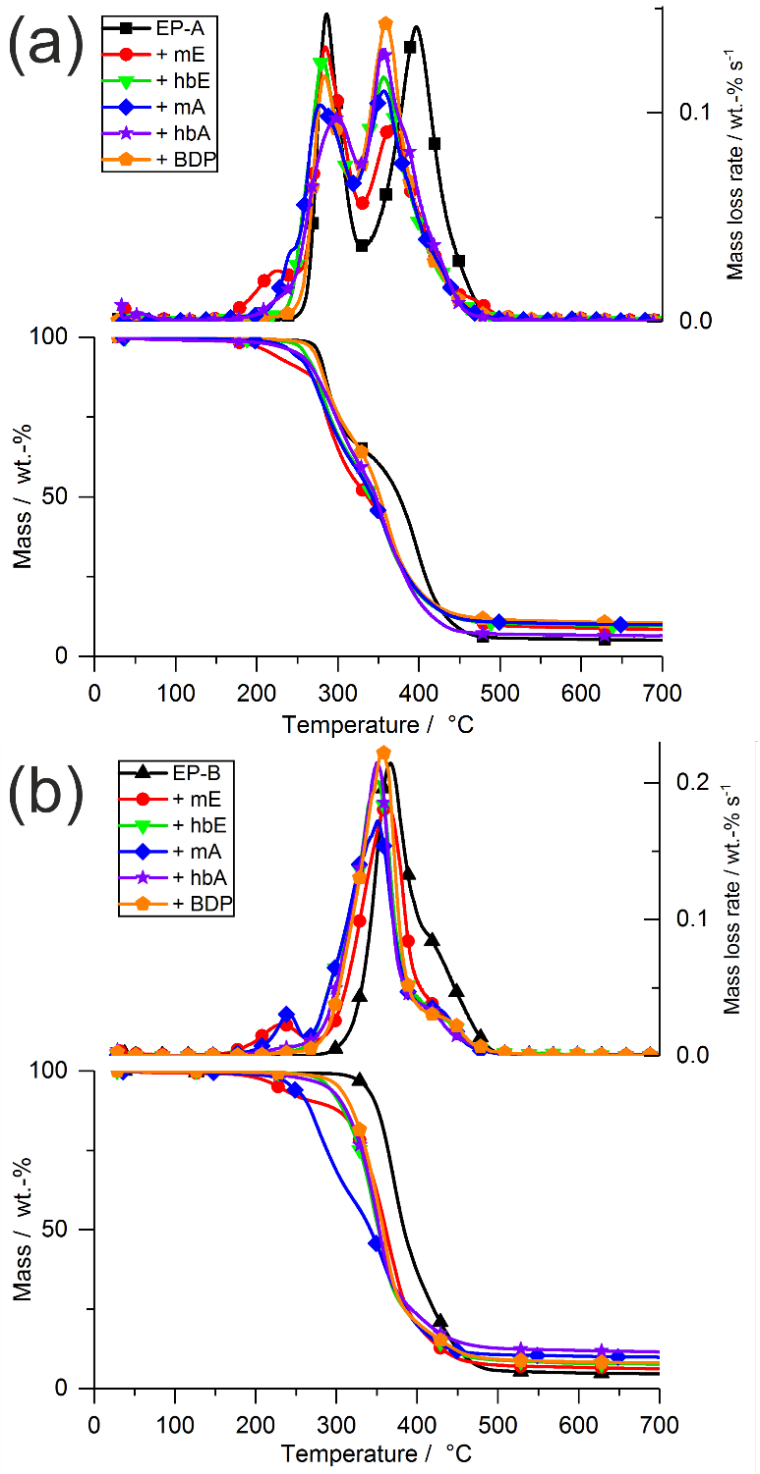

Figure 5.5. (a) Mass loss (bottom) and mass loss rate (top) of EP-A and FR-containing resins, and (b) mass loss (bottom) and mass loss rate (top) of EP-B and FR-containing resins.

The addition of FRs to a polymer matrix typically alters its decomposition behavior. In Figure 5.5a, the mass loss and mass loss rate of EP-A is presented along with its FR containing variants, and

Figure 5.5b shows the same for EP-B. The results of TGA measurements of all FR-containig materials are summarized in Table 5.4.

During thermal decomposition, specific reactions ultimately control the decomposition mechanism, e.g. hydrolysis, rearrangements, etc. For FR-containing polymers, the decomposition pathway of the matrix is influenced by the decomposing FR: as the matrix and FR decompose, their respective decomposition products react with another, ideally forming thermally stable residues. This interaction between FR and matrix presupposes that the partially decomposed matrix may interact freely with the partially decomposed FR, yet this interaction is greatest if both materials decompose in the same temperature range, i.e. at the same "time". It follows then that the interaction between matrix and FR is greatest if the overlap of T_{dec} is also greatest, as has been previously shown to be the case.[10-12]

Table 5.4. Results from TGA measurements of the epoxy matrices EP-A and EP-B and the FR-containing resins.

Material	$T_{5\%}$ / °C	T_1 / °C	ML_1 / wt.-%	T_{max1} / °C	ML_{max1} / wt.-%	T_{max2} / °C	ML_{max2} / wt.-%	μ (700°C) / wt.-%	μ (calc) / wt.-%
EP-A	276 ±2	-	-	286 ±2	34.8 ±0.3	398 ±1	58.8 ±1.2	4.6 ±0.3	–
+ mE	218 ±1	226 ±1	13.0 ±0.1	285 ±1	33.4 ±0.5	368 ±3	45.5 ±1.2	8.2 ±0.7	4.4
+ hbE	257 ±2	-	-	280 ±1	37.8 ±0.1	356 ±1	52.4 ±0.4	9.3 ±0.2	5.3
+ mA	244 ±1	241 ±1	6.8 ±0.2	281 ±1	32.6 ±0.1	357 ±1	50.9 ±0.1	9.2 ±0.3	5.7
+ hbA	253 ±1	-	-	299 ±1	39.2 ±0.2	356 ±1	51.9 ±0.1	7.5 ±0.1	5.9
+ BDP	271 ±1	-	-	282 ±1	31.8 ±0.5	358 ±1	57.8 ±0.6	9.8 ±0.3	4.2
EP-B	338 ±1	-	-	372 ±1	62.0 ±0.8	424 ±5	33.2 ±0.3	4.5 ±0.1	–
+ mE	231 ±1	233 ±1	8.9 ±0.1	337 ±1	77.8 ±0.1	422 ±1	7.4 ±0.2	5.1 ±0.6	4.3
+ hbE	289 ±1	-	-	351 ±1	54.6 ±0.1	424 ±6	23.2 ±0.7	7.7 ±0.1	5.2
+ mA	245 ±2	243 ±1	7.1 ±0.4	352 ±1	74.1 ±0.3	415 ±1	10.7 ±0.1	7.6 ±0.2	5.6
+ hbA	283 ±1	-	-	351 ±1	74.7 ±0.3	421 ±1	12.9 ±0.2	8.0 ±0.2	5.8
+ BDP	304 ±1	-	-	357 ±1	74.6 ±0.2	423 ±1	16.1 ±0.3	8.2 ±0.1	4.2

μ = residue

Resins with the low molar mass FRs mE and mA exhibited low $T_{5\%}$ due to the additional mass loss steps below 300°C, a result of the FRs vaporizing in this temperature range. The polymeric FRs hbE and hbA also lowered $T_{5\%}$ in both EP-A and EP-B, but the effect was less pronounced and is supposed to be related to a decrease in cross-linking density leading to a decreased thermal

stability.[26] Those resins containing BDP exhibited the weakest impact on $T_{5\%}$ due to BDP's high thermal stability (T_{max} = 415 °C).

In the range of the second decomposition step (T_{max2}), the changes of the corresponding mass loss (ML_{max2}) of EP-A with FRs were caused by the reaction of the FRs with the decomposing polymer matrix, either prior to or in this temperature range. Notably, T_{dec} of the pure FRs closely match the T_{dec} ranges of EP-A: mE (T_{max} = 250 °C) and hbE (T_{max} = 280 °C) decompose close to T_{max1} of EP-A at 286 °C, while mA (T_{max} = 317 °C) decomposes between the two maxima, and hbA (T_{max} = 361 °C) decomposes close to T_{max2} at 398 °C. For EP-B, the main decomposition step at T_{max1} = 372 °C is more closely aligned to mA and hbA, than mE or hbE; as a result, the increase in residue yields reflect this behavior. As previously described, the first decomposition step is tied to dehydration and cyclisation, while the second decomposition step is related to the breakdown of aromatic moieties. Those FRs that decompose closely to T_{max1} may phosphorylate the matrix, which ultimately leads to cross-linking at higher temperatures. Moreover, the change in T_{max2} as well as the reduction in mass loss results from the interaction of P-species with aromatic components forming polyaromatic residue. This correlates well with the increase in residue at 700 °C for all FRs. Therefore, the increased overlap between FR and matrix T_{dec}-ranges led to improved chemical interaction, resulting in higher residue yields.

Calculated residue yields were obtained by adding the residue of each individual component at their respective content, simulating a decomposition of the products without interaction. The measured residue yields are significantly higher than the calculated values, meaning that chemical interaction between the components during pyrolysis must cause this increase. All FRs increased residue yields of EP-A at 700°C: mE and mA increased residue yields by a factor of 1.8 and 2.0, respectively, while hbE and hbA increased residues by a factor of 2.0 and 1.6, respectively. BDP increased residues by a factor of 2.1. For EP-B, mE and mA increased residues by a factor of 1.1 and 1.7, respecively, while hbE and hbA increased residues by a factor of 1.7 and 1.8, respectively. BDP had the greatest impact on EP-B, increasing residues by a factor of 1.8.

5.5.5 Pyrolysis – Evolved gas analysis of EP-FRs

The evolved gases from TGA measurements were analyzed via FTIR, and the spectra of EP-A at T_{max1} and T_{max2} are displayed in Figures 5.6a and 5.6c, respectively; these spectra are rescaled to highlight the fingerprint region in Figures 5.6b and 5.6d, respectively. Figure 5.7a shows the spectra of EP-B with FRs at $T_{5\%}$, while the spectra at T_{max} are compiled in Figure 5.7b, and a rescaled version is plotted in Figure 5.7c.

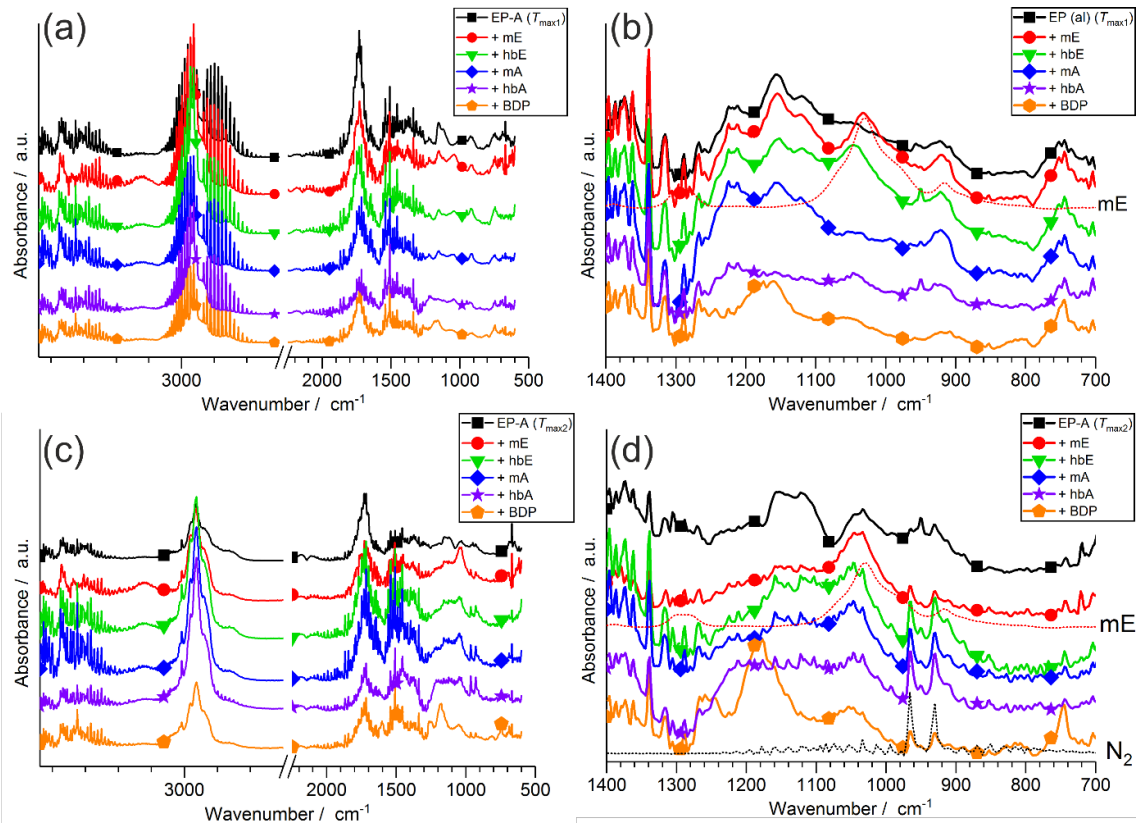

Figure 5.6. Evolved gas spectra of pyrolysis products of EP-A at specific decomposition temperatures via TG-FTIR. (a) Spectra at T_{max1}, and (b) rescaled spectra between 1400—700 cm^{-1}. (c) Spectra at T_{max2}, and (d) rescaled spectra between 1400–700 cm^{-1}.

The spectra of EP-A with FRs in Figures 5.6a and 5.6c demonstrate that all materials produce many of the same gases during decomposition, namely water, carbon dioxide, and carbon monoxide, as well as hydrochloric acid at T_{max1} (Figure 5.6a) and methane at T_{max2} (Figure 5.6c). More closely, the evolution of P-containing species was identified via the band near 1030 cm^{-1} in Figures 5.6b and 6d for EP-A/mE, as indicated by the comparative spectra of pure mE. Moreover, while the evolution of ammonia was prevalent in all spectra at T_{max2} (Figures 5.6c and 5.6d), as indicated by the two bands at 960 and 930 cm^{-1}.

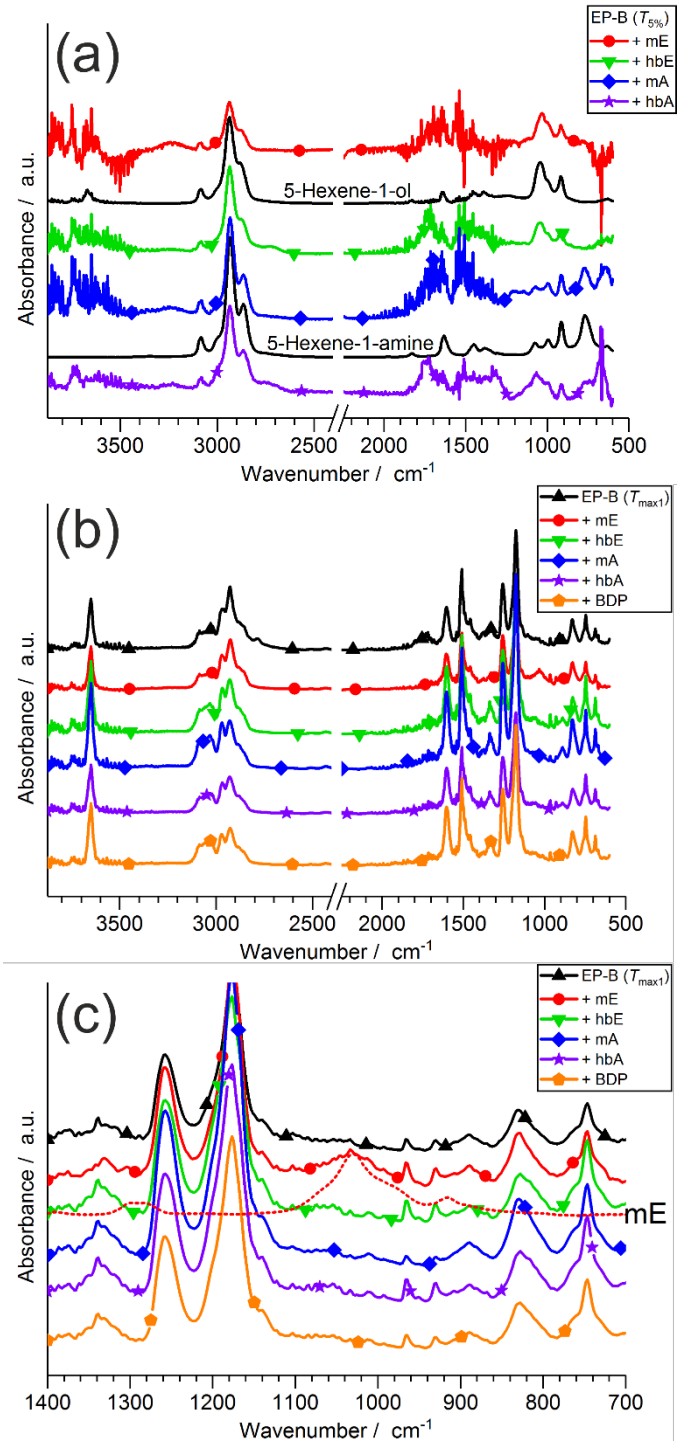

Figure 5.7. Evolved gas spectra of pyrolysis products of EP-B at specific decomposition temperatures via TG-FTIR. (a) Spectra at $T_{5\%}$;(b) Spectra at T_{max}, and (c) rescaled spectra between 1400–700 cm^{-1}.

The spectra in Figure 5.7a correspond to evolved gases at $T_{5\%}$ from resins with mE, hbE, mA, and hbA, respectively. For EP-B/mE and EP-B/mA, TGA measurements indicated a mass loss of approx. 10 wt.-% at about 240 °C, prior to the main decomposition step. Although such a mass loss step was missing for the resins with hbE and hbA, similar products to those from EP-B with mFRs were identified in the spectra at $T_{5\%}$. The reason lies in the production of hex-5-ene-1-ol for the

phosphate-containing mE and hbE, or hex-5-ene-1-amine for the phosphoramide-containing mA and hbA. These products may result from hydrolysis of P-O or P-N, respectively, as has been previously described,[5] and the process may provide further P-species than can interact with the decomposing matrix. Figure 5.7b illustrates that all materials exhibited mostly identical decomposition products at T_{max} for EP-B, predominately bisphenol A, as well as carbon monoxide and water, as previously described.[5,6] An additional absorption band appeared in the spectra of EP-B/mE, which was highlighted in Figure 5.7c: the band at 1030 cm^{-1} was among the main signals in the TG-FTIR spectrum of pure mE at its T_{max}. The appearance of this band corresponds to a P-based signal, as many P-signals overlap in this region, e.g. ν_{as} (P-O-C) or ν_{s} (P-OH).

5.5.6 Pyrolysis – Condensed phase activity of EP-FRs via TG-FTIR

During thermal decomposition, the condensed phase interaction of FR and matrix may lead to the formation of polyaromatic compounds, and P-species play a significant role as networking points. Condensed phase FTIR spectra via hot-stage FTIR provide insight into the change in chemical surrounding during pyrolysis of the materials, and offer clues to the interaction of the matrix and FR.

The FRs investigated herein have been previously shown to act in the condensed phase with EP-B, either through phosphorylation of the matrix, the formation of polyphosphates as inorganic glasses, or as (poly)phosphazenes, phosphorus oxynitrides, etc.[29-31] Therefore, the effect of FRs on EP-B in the condensed phase are not discussed further.

Figure 5.8 displays the condensed phase FTIR spectra of EP-A with FRs at key temperatures corresponding to various stages of decomposition: before the first decomposition step (100 °C; top), between two decomposition steps (325 °C; 2nd from top), end of the second decomposition step (500 °C , 2nd from bottom), and final residues at the end of the experiment (600 °C; bottom).

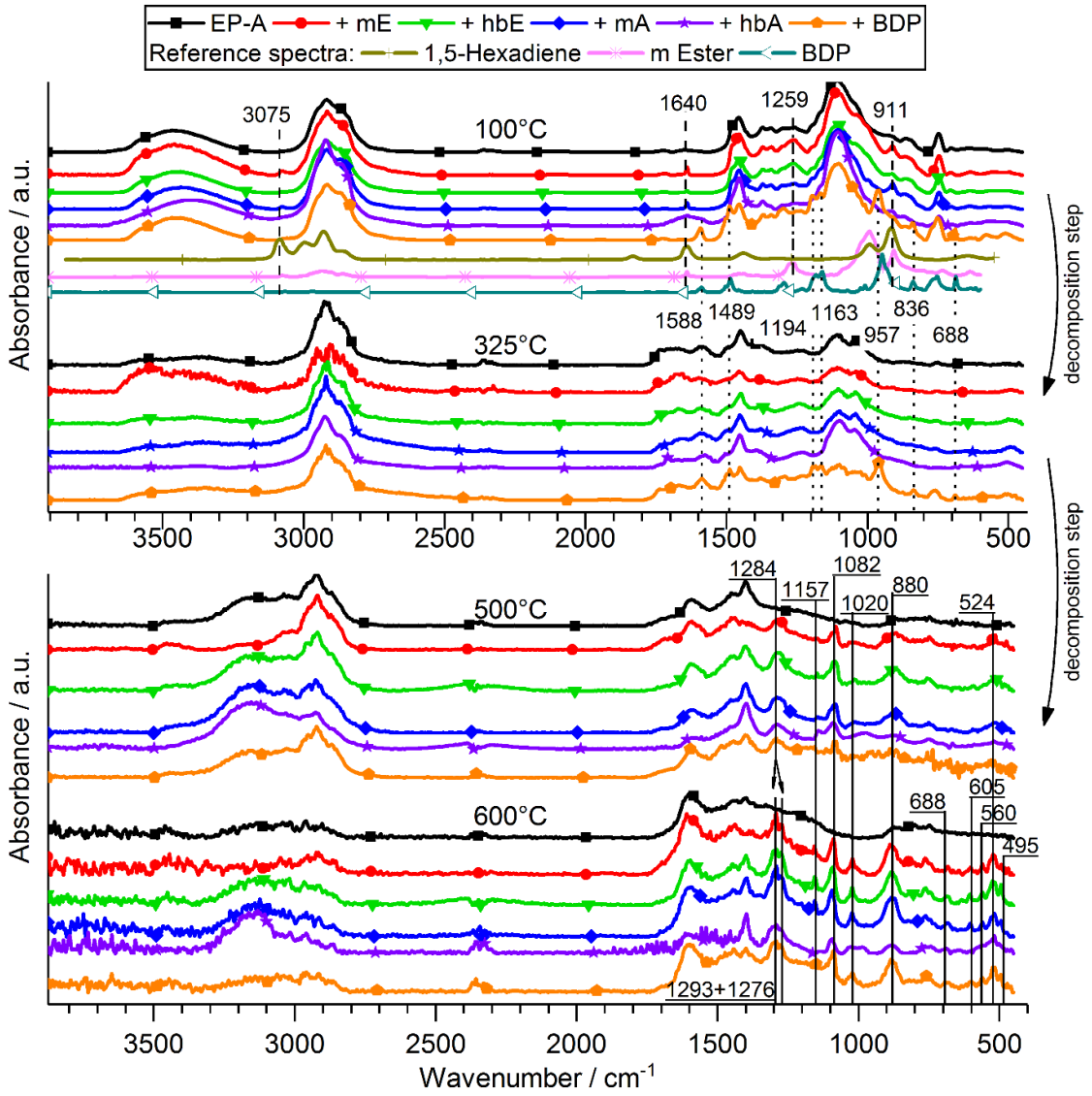

Figure 5.8. Condensed phase FTIR spectra taken at specific temperatures via hot-stage FTIR. Vertical dashed line: bands from 1,5-hexadiene; vertical dash-dotted line: signal from pure mE (comparative); vertical dotted line: bands from BDP; full lines: phosphorus signals.

For the pure resin EP-A, the first decomposition step entailed the decrease of water signals above 3200 cm^{-1} (ether or secondary alcohol bonds) and decreased absorption of characteristic fingerprint signals near 1100 and 750 cm^{-1} (either saturated hydrocarbons or possibly (C-Cl) bonds from epichlorohydrin). At 325 °C, the increased absorption around 1750–1650 cm^{-1} pointed to dehydration of saturated hydrocarbons, as this region is common for stretching vibrations of (C=C) bonds. Additionally, amides, ketones, aldehydes, and esters show characteristic signals in this region, therefore implying hydrolysis of ether bonds. The decrease of the ether absorption band at 1100 cm^{-1} provides further evidence of this process, further supporting the proposed mechanism in Scheme 5.2. The disappearance of the signal at 750 cm^{-1} (possibly epichlorohydrin)

may explain the appearance of hydrochloric acid in the FTIR spectra of this decomposition step (see Figure 5.6a). The comparison of the spectra before and after the second decomposition step of EP-A (325 °C and 500 °C) revealed that the ether bands at 1100 cm^{-1} disappeared in the pure EP-A spectrum, and the broad absorption around 1750–1650 cm^{-1} reduced to only containing a signal at 1600 cm^{-1}, which corresponds to secondary amides, or phenol-based signals. The broad absorption band >3000 cm^{-1} at 500 °C pointed to the formation of unsaturated hydrocarbons, but it is also a common range for (N-H) hydrogen bonding. At 600 °C, the main signals from hydrocarbons at around 3000 cm^{-1} disappeared and only the signal at 1600 cm^{-1} remained prominent.

With the addition of FRs, the condensed phase spectra of EP-A were altered: At 100 °C, the spectra of EP-A/mE and EP-A/mA exhibited sharp bands at 3075, 1640, and 911 cm^{-1}, which correspond to signals present in 1,5-hexadiene. Moreover, those resins with phosphate-containing FRs mE and hbE displayed a band at 1259 cm^{-1} that was also present in the ATR spectrum of pure mE, belonging to the stretching vibration of phosphate (P=O).[8,32] The spectra of EP-A with BDP at 100 °C further contained characteristic bands pertaining to pure BDP, namely at 1588, 1489, 1194, 1163, 957, 836, and 688 cm^{-1}.

When comparing the spectra at 100 °C to that of 325 °C, the bands at 3075, 1640, and 911 cm^{-1} from 1,5-hexadiene disappeared for both EP-A/mE and EP-A/mA, which correlated with the decomposition mechanisms described previously. The signals from BDP persisted, as this material only decomposed at higher temperatures (compare Figure 5.1b), as visible in the spectra at 500 °C. At 500 °C, several specific bands appeared in all spectra of EP-A with FRs, namely 1284 cm^{-1} [ν(P=O)], 1157 cm^{-1} [R2-(P=O)-OH or P-O-C_{aryl}], 1082 cm^{-1} [ν(P-Ph) or P-O-C_{alkyl}], 1020 cm^{-1} [ν(P-OH)=O, or PO_4^-], 880 cm^{-1} [P-O-P or δ_{wag}(P-H)], and 524 cm^{-1} [ν_{skel}(C-C)].[8,32] These signals gained in intensity and sharpness at 600 °C, and the signal at 1284 cm^{-1} split in two: 1293 cm^{-1} [ν(P=O)] and 1276 cm^{-1} [ν_{sym}(P-CH_3)]. Additionally, new signals at 688, 605, 560, and 495 cm^{-1}, belonging to phenols and P-species, appeared. These bands, which are also present in residues of these FRs in EP-B,[5,6] points towards the chemical integration of P-species into the residue, and this condensed phase mechanism was responsible for the residue increase in TGA and PCFC measurements. For EP-A/mA and EP-A/hbA, the band at 1339 cm^{-1} corresponded to ν(P=N-Ar)[33] or P=N-P compounds as their vibration occurs in this wavenumber range;[34] their appearance pointed to the presence of phosphazenes.

5.5.7 Fire testing of EP-FRs via Cone Calorimeter

An effective method to ascertain the flame-retardancy potential is by comparing the forced-flaming combustion of pure and FR-containing polymer matrices by cone calorimeter. The method yields crucial information on heat release rate (HRR), peak of HRR (PHHR), fire load (= total heat release, THE), mass loss, and heat release per mass loss (= effective heat of combustion, EHC). The results of cone calorimeter measurements of EP-A (Figure 5.9a) and EP-B (Figure 5.9b), with and without FRs, help illustrate the FR effect on the two distinct matrices. Table 5.5 summarizes the main results for EP-A and EP-B.

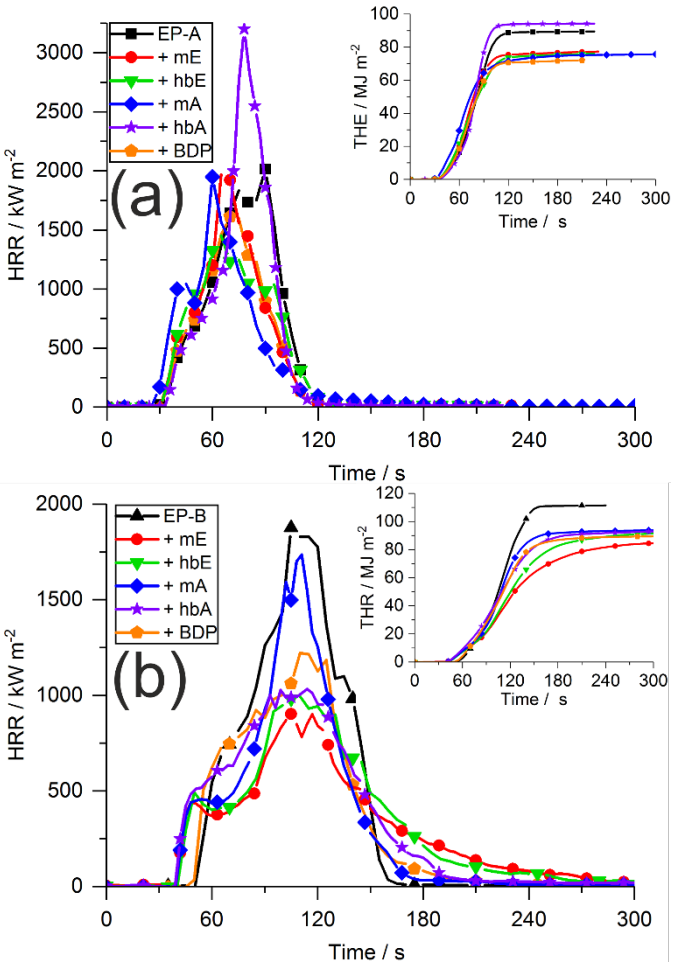

Figure 5.9. Heat release rate (HRR) and total heat release (THR) over time of (a) EP-A and FR-containing composites, and (b) EP-B and FR-containing composites, respectively, from cone calorimeter measurements.

In Figure 5.9a, the addition of FRs altered the shape of the HRR curve, most notably for EP-A/hbA. All FRs increased PHRR of EP-A (1881 kW m^{-2}) apart from hbE (reduction of 11%). hbA had the largest impact on PHRR (3172 kW m^{-2}), increasing it by a factor of 1.7. As changes in the PHRR correlate strongly with the protection layer effect,[8,35] the addition of hbA led to a decreased

protection layer, thus increasing the flux of fuel into the fire. This was made evident by THR at flame-out (= THE): hbA in EP-A increased THE by 10%, while the other FRs decreased THE by 12% on average. The addition of FRs into EP-A increased residue yields up to 6.3 wt.-% for mA and 5.5 wt.-% for hbA, while the phosphate FRs mE and hbE only increased char yield to 3.6 and 3.5 wt.-%, respectively. Notably, there is a slightly higher P-content in the resins with mE and mA compared to hbE and hbA, yet both phosphates in EP-A produce similar residue yields, and mA's increase in residue compared to hbA in EP-A cannot only be explained by the different P-contents. While residue yields give insight into the mass converted into fuel during combustion, the relationship between fire load per mass loss, i.e. EHC, provides better insight into the FR-effect. EP-A had an EHC of 22.0 MJ kg^{-1} and the addition of most FRs reduced this value by about 10%, from 19.2 MJ kg^{-1} for BDP up to 21.2 MJ kg^{-1} for mA. However, hbA increased EHC of EP-A to 25.3 MJ kg^{-1}, an increase of 15%. Moreover, the reduction of EHC is strong evidence for the gas-phase activity of P-FRs.[8] Therefore, mE and hbE are more effective FRs in EP-A than mA and hbA: they lowered fire load, showed some protective layer effects, increased residue yield, and lowered EHC by exhibiting an effective gas-phase mode of action. The phosphoramide-containing FRs proved less effective in EP-A, as both mA and hbA increased PHRR and had little influence on EHC. When taking the heat of combustion of the volatiles into account (cf. Figure S5.17, Table S5.1), the poor flame retardancy of EP-A/hbA is attributed to the strong contribution of the FR to the heat, as well as the lack of protective layer effects. The latter were caused by a low interaction between matrix and FR, resulting from the FR interacting with itself rather than with the matrix during decomposition, similarly to phosphorus-FRs in PC/ABS blends.[36]

Figure 5.9b exhibits HRR and THR curves over time from EP-B as a pure resin and with FR additives. The results highlight the change in interaction between FR and polymer matrix: For EP-B, all FRs lowered fire loads and increased char yields. The phosphate-containing FRs mE, hbE, and BDP lowered THE and PHRR more strongly than the amide-containing FRs mA and hbA. Phosphates incurred higher mass loss, but lower EHCs. Phosphoramide-containing FRs in EP-B led to significantly higher residue yields compared to the pure resin, but both mA and hbA had subdued effects on PHRR and EHC: hbA exhibited lower PHRR but higher EHC, and mA showed the opposite effect. However, the relative changes in PHRR and EHC of phosphoramide-containing FRs were much lower in EP-B than in EP-A: hbA decreased PHRR in EP-B (although it increased it in EP-A) and the increase in EHC was only 5% (versus 15% in EP-A).

For both matrices, the benchmark material BDP effectively lowered THE of the matrices EP-A and EP-B. BDP exhibited predominantly a gas phase mechanism and a minor condensed phase mechanism, as evidenced by the reduction in EHC and small increase in residue, respectively.

The residues after fire testing (Figure S5.18) further illustrated the efficacy of phosphates in EP-A and EP-B to produce voluminous, multicellular residues with more effective protection layer effects than phosphoramidates, which created a dense, brittle char. The difference in char formation was further illustrated in reaction to small flames tests, i.e. limiting oxygen index (LOI) and Underwriter's Laboratory 94 (UL-94) tests (Table S5.2). All FRs generally increased the oxygen index of EP-A and EP-B, phosphoramidates in EP-A burned with a reduced horizontal burn speed compared to phosphates, as their dense char was more successful at preventing horizontal flame spread. In EP-B, hbFRs lowered burn speeds by forming stable chars, compared to the more voluminous but fragile char that mFRs formed due to their high volatility.

Table 5.5. Results of cone calorimeter measurements at a heat flux of 50 kW m^{-2}.

	THE / MJ m^{-2}	PHRR / kW m^{-2}	Residue / wt.-%	EHC / MJ kg^{-1}
EP-A	86.5 ±2.1	1881 ±133	1.7 ±0.1	22.0 ±0.6
+ mE	74.4 ±1.4	1933 ±35	3.6 ±0.1	19.4 ±0.4
+ hbE	76.7 ±2.5	1672 ±220	3.5 ±0.1	20.0 ±0.7
+ mA	79.0 ±2.6	2287 ±337	6.3 ±0.7	21.2 ±1.2
+ hbA	96.0 ±2.3	3172 ±29	5.5 ±1.6	25.3 ±0.2
+ BDP	74.9 ±4.4	1992 ±379	2.6 ±0.1	19.2 ±1.1
EP-B	108.4 ±2.6	1696 ±180	0.7 ±0.1	26.9 ±1.0
+ mE	78.1 ±6.5	885 ±16	9.2 ±0.1	21.6 ±1.8
+ hbE	89.8 ±3.0	953 ±41	7.5 ±0.6	24.3 ±0.6
+ mA	91.6 ±1.2	1833 ±96	8.4 ±0.2	25.3 ±1.0
+ hbA	95.5 ±2.3	1189 ±155	12.1 ±2.7	28.2 ±2.4
+ BDP	87.5 ±1.2	1180 ±41	3.1 ±0.2	22.7 ±0.2

An effective method to visualize flame retardancy is by Petrella plot, which graphs fire load (= THE) over fire growth rate (= PHRR / t_{ig}).[37] Ideally, the addition of FRs leads to a reduction of both (i.e. shift to lower left corner of graph). Figure 5.10 depicts the Petrella-plot of EP-A and EP-B resin formulations. For EP-A, phosphate-containing FRs improved both fire growth rate and fire load. When comparing mE to hbE, the polymeric FR slightly increased THE but decreased PHRR / t_{ig}. For phosphoramide-containing FRs, mA decreased fire load, but increased the fire growth rate, and hbA increased both. The behavior is different for EP-B: the phosphate-containing FRs improved flame retardancy by the greatest amount, yet both phosphoramide-containing FRs lowered THE, with hbA lowering both fire load and fire growth rate.

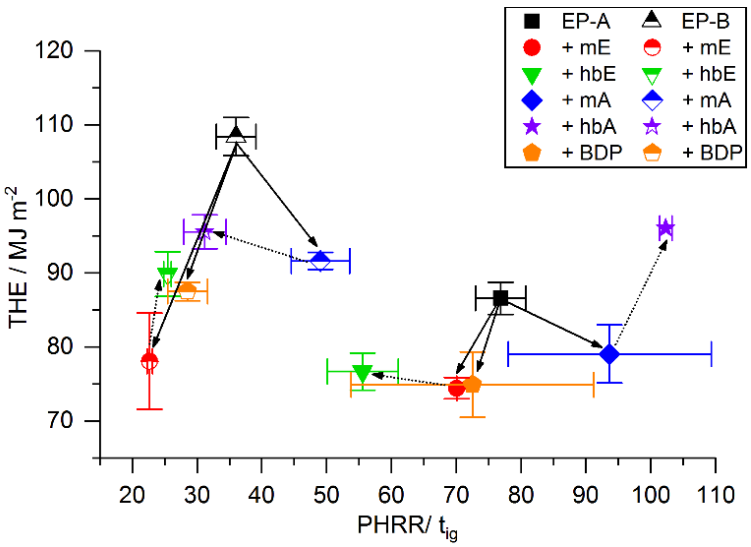

Figure 5.10. Petrella-plot of EP-A and EP-B with FRs, assessing fire load versus fire growth rate. Solid lines: monomeric / polymeric FR; dashed lines: difference between monomeric and hb polymeric FR.

5.5.8 Modes of Action and Molecular Mechanism

As previously investigated,[5,6] the addition of mE, mA, hbE, or hbA to EP-B increased residue yields in both pyrolysis and flaming investigations: the FRs or their decomposition products interact either directly with the matrix or its decomposition products via phosphorylation, thus catalyzing the formation of polyaromatic char and acting as a char stabilizer.[9] Moreover, EP-B contains aromatic rings which can act as char precursors, further enhancing the charring potential in the presence of P-FRs. mA and hbA were shown to be more active in the condensed phase, especially through the formation of (poly-)phosphazenes / phosphorus oxynitrides.[5,6] For mE and hbE, the phosphate-moiety is susceptible to *cis*-elimination,[5,38] leading to more active phosphate-species, which acted in the condensed and, via radical scavenging, in the gas phase. As previous investigations showed, phosphates were more likely to undergo *cis*-eliminations, while phosphoramides were more likely to undergo hydrolysis reactions.[5]

EP-A, on the other hand, is aliphatic and contains four epoxide groups per epoxy moiety; bisphenol A in EP-B only contains two. Therefore, the polymer network of EP-A has a different network density, and more importantly, a higher polarity. As investigated, the polymer matrix of EP-A decomposes in two steps under pyrolysis, and some of those steps yield aromatic components via rearrangement or dehydrogenation, which can act as char precursors. Moreover, the incorporation of FRs led to residue yields that were higher than the calculated sum of the individual components, signalizing the interaction of matrix and FR. Additionally, T_{max} of mE and hbE were closer to T_{max1} of EP-A, while T_{max} mA and hbA were closer to T_{max} of EP-B. The chemical

interaction was more pronounced for these specific FRs with a specific matrix, because the T_{dec}-ranges of matrix and FR more closely matched, meaning that decomposition products of both materials were more likely to react with another.

In flaming conditions, the difference between phosphoramide- and phosphate-containing FRs became more apparent in EP-A: The addition of mE and hbE increased residue yields and led to a substantial reduction in EHC (mE: -12%; hbE: -9%) and THE (mE: -14%; hbE: -11%). These results are explained by the effective fuel fixation caused by increased interaction of matrix and FR, as well as the proven gas-phase activity / flame poisoning of the phosphate-containing FRs. The addition of mA and hbA to EP-A did not improve the fire performance in the same way that it did for EP-B. The reason for this may be a less pronounced chemical interaction and the resulting change in condensed phase activity. mA and hbA more greatly promoted char formation in EP-B due to the interaction with bisphenol A-derived aromatic char precursors. Lacking those precursors in EP-A, these phosphoramide-containing FRs formed P-N compounds that, although retaining fuel in the form of residue, did not offer a good protection layer effect. Poor protective layers cause increased mass flux into the flame, resulting in higher PHRR. Furthermore, hbA itself decomposes via hydrolysis and produces hex-5-ene-1-amine,[6] which additionally increases the fire load of the sample. Moreover, EP-A is more polar than EP-B, which may further impede the phosphoramide-containing FRs from interacting with the decomposing matrix.

Scheme 5.3 illustrates the proposed decomposition mechanism of the FRs and their interaction with the decomposing matrices EP-A or EP-B. While hbFRs have a decomposition pathway distinct from the mFRs, they share general decomposition mechanisms. More importantly, hbFRs contain thiol-ether bonds, which propagate cross-linking reactions. Phosphate-based FRs undergo *cis*-eliminations, while phosphoramide-based FRs undergo hydrolysis.[5] Both steps lead to a P-hydroxyl-group, which may interact with the epoxy resin matrix or decomposition products thereof via phosphorylation. The higher epoxide-group content in EP-A leads to a higher content of secondary hydroxyl groups; therefore, phosphorylation of EP-A is more likely than in EP-B. As the phosphate-based FRs have a lower T_{dec}, they are more likely to phosphorylate these hydroxyls before key functional groups of EP-A are lost due to advanced decomposition. Hence, they have a stronger interaction in the condensed phase, which explains the reduction in fire load of EP-A, as increased phosphorylation leads to higher fuel storage. Furthermore, the phosphate-based FRs more readily form P-based radicals, thus acting strongly in the gas phase in both EP-A and EP-B. This radical scavenging mechanism is strong for phosphate-based FRs and explains the strong decrease in EHC of all matrices. The phosphoramide-based FRs are less likely to interact with the decomposing aliphatic matrix, in part because these FRs may undergo inter- / intramolecular

reactions with themselves, leading to the production of phosphorus oxynitrides or (poly-)phosphazenes, as seen in condensed phase FTIR via the presence of P=N compounds. A similar auto-reaction was shown for aryl phosphates in PC/ABS blends, where an FR was shown to crosslink with itself rather than enhance charring.[39] Phosphoramide-based FRs proved effective in the condensed phase in EP-B due to interaction with aromatic moieties, especially given that mA and hbA decompose in similar temperature ranges as EP-B. For EP-A, these aromatic moieties form only after rearrangements or dehydrogenation and are not readily available reaction partners; therefore, the interaction between phosphoramide-based FRs and EP-A is weak in the condensed phase. Lacking reaction partners, phosphorus oxynitrides or (poly-)phosphazenes offer little protective layer effects, and contribute to increasing fire loads; this increased THE in fire tests of mA and hbA in both resins. Although the phosphoramide-based FRs produced a substantial residue yield, previous investigations have shown that not quantity but residue morphology and properties thereof are paramount in flame retardancy.[8]

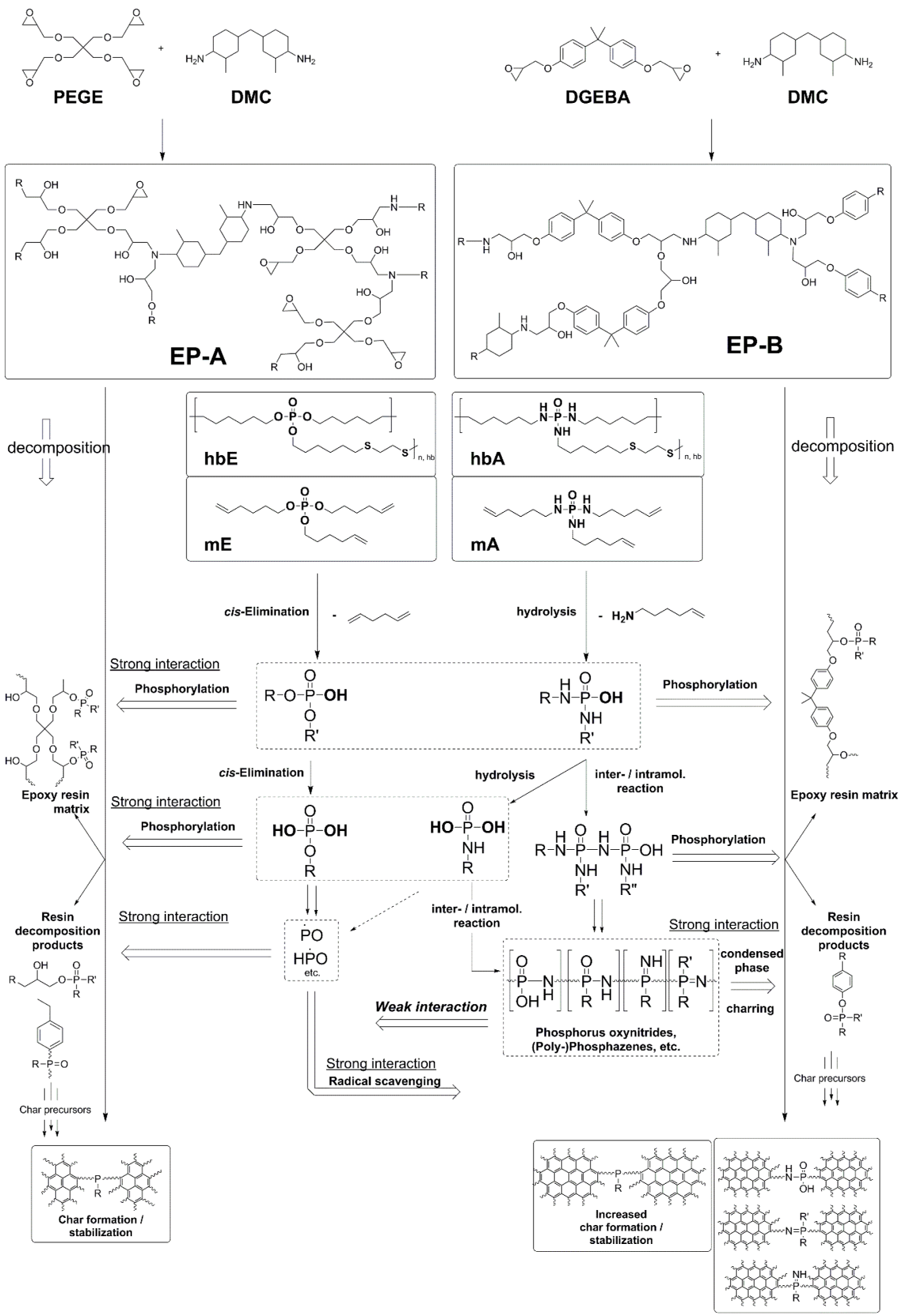

Scheme 5.3. Proposed main decomposition pathways of epoxy resin matrices with FRs, and interaction between the two.

5.6 Conclusion

A systematic library of phosphorus-based FRs (phosphate and phosphoramide as low and high molar masses) was prepared and investigated in two chemically different epoxy resins, one aliphatic and one aromatic. Investigations of the pyrolytic decomposition via TGA-FTIR, pyrolysis-GC/MS, hot stage FTIR, and PCFC, as well as fire behavior of the pure matrices provided a background into understanding how the FR-containing composites behaved under pyrolysis and fire testing conditions.

The chemical decomposition mechanisms of the FRs are essential to understand their mode of action. However, also the chemical structure of the polymer matrix strongly influences the possible reactions during fire. The reaction between decomposition products of both matrix and FR are crucial to achieve efficient flame retardancy. Moreover, the importance of T_{dec} overlap between FR and polymer matrix cannot be understated. When this overlap of FR and matrix is highest, the chemical interaction is greatest, leading to effective flame retardancy in the form of higher char yield, reduced PHRR and lower THE. The presented results provide some crucial tools to potentially optimize matrix-FR-systems:

hbFRs exhibited a slightly less pronounced reactivity but a higher thermal stability than mFRs. This means that T_{dec} is tunable via molecular weight. Especially for the multifunctional hbFRs, this may prove useful for processing, especially given their decreased impact on T_g. The overlap in temperature range between FR and matrix can thus be increased if the molar mass of the FR is adjusted.

Phosphoramides typically possess a higher T_{dec} compared to structurally analogous phosphates, but phosphates exhibit a stronger gas phase mode of action. Crucially, altering the P-O and P-N content results in varying degrees of chemical interaction between matrix and FR. Depending on the properties of the matrix, the FR can be shifted from additive to reactive FR for epoxy resins, thus acting as a toughening agent, further highlighting the chemical versatility of these materials as FRs.

It must be carefully considered how the efficacy or mechanisms of FRs are evaluated, as these may change depending on the polymer's chemical composition. Even within the realm of epoxy resins, alterations to the chemical structure of the material affect flame retardancy. The results of this study help underline that the chemical structure-property relationship of the flame retardant and the matrix matters when investigating the FR-efficacy and mode of action of these synthesized FRs.

5.7 Acknowledgement

The authors thank the Deutsche Forschungsgemeinschaft (DFG) for funding (DFG SCHA 730/15-1; WU 750/8-1).

Alexander Battig thanks Patrick Klack for his assistance with the cone calorimeter, and Dr. Katharina Kebelmann for her assistance with the Py-GC/MS.

Jens C. Markwart is the recipient of a fellowship through funding of the Excellence Initiative (DFG/ GSC 266) in the context of the graduate school of excellence "MAINZ" (Materials Science in Mainz).

Jens C. Markwart and Frederik R. Wurm thank Prof. Dr. Katharina Landfester (MPI-P, Germany).

5.8 References Chapter 5

[1] M. M. Velencoso, A. Battig, J. C. Markwart, B. Schartel, F. R. Wurm, *Angew Chem Int Edit* **2018**, *57*, 10450-10467.

[2] F. Marsico, M. Wagner, K. Landfester, F. R. Wurm, *Macromolecules* **2012**, *45*, 8511-8518.

[3] M. Steinmann, J. Markwart, F. R. Wurm, *Macromolecules* **2014**, *47*, 8506-8513.

[4] T. Steinbach, F. R. Wurm, *Angew Chem Int Edit* **2015**, *54*, 6098-6108.

[5] J. C. Markwart, A. Battig, L. Zimmermann, M. Wagner, J. Fischer, B. Schartel, F. R. Wurm, *ACS Applied Polymer Materials* **2019**, *1*, 1118-1128.

[6] A. Battig, J. C. Markwart, F. R. Wurm, B. Schartel, *Polymer Chemistry* **2019**, 10, 4346-4358.

[7] A. F. Grand, C. A. Wilkie, *Fire retardancy of polymeric materials*, CRC Press, **2000**.

[8] B. Schartel, B. Perret, B. Dittrich, M. Ciesielski, J. Krämer, P. Müller, V. Altstädt, L. Zang, M. Döring, *Macromolecular Materials and Engineering* **2016**, *301*, 9-35.

[9] U. Braun, A. I. Balabanovich, B. Schartel, U. Knoll, J. Artner, M. Ciesielski, M. Döring, R. Perez, J. K. W. Sandler, V. Altstädt, T. Hoffmann, D. Pospiech, *Polymer* **2006**, *47*, 8495-8508.

[10] K. H. Pawlowski, B. Schartel, *Polymer International* **2007**, *56*, 1404-1414.

[11] M. C. Despinasse, B. Schartel, *Polymer Degradation and Stability* **2012**, *97*, 2571-2580.

[12] B. Perret, K. H. Pawlowski, B. Schartel, *Journal of Thermal Analysis and Calorimetry* **2009**, *97*, 949-958.

[13] A. Toldy, B. Szolnoki, G. Marosi, *Polymer Degradation and Stability* **2011**, *96*, 371-376.

[14] A. Toldy, B. Szolnoki, I. Csontos, G. Marosi, *Journal of Applied Polymer Science* **2014**, *131*.

[15] M. Jimenez, S. Duquesne, S. Bourbigot, *Surface & Coatings Technology* **2006**, *201*, 979-987.

[16] J. Alongi, Z. D. Han, S. Bourbigot, *Progress in Polymer Science* **2015**, *51*, 28-73.

[17] T. Misaki, T. Hirohata, M. Yoshii, T. Hamasaki, *Journal of Applied Polymer Science* **1989**, *37*, 2617-2625.

[18] M. Fleischer, H. Blattmann, R. J. G. C. Mülhaupt, *Green Chem*. **2013**, *15*, 934-942.

[19] B. Schartel, T. R. Hull, *Fire and Materials* **2007**, *31*, 327-354.

[20] B. Schartel, M. Bartholmai, U. Knoll, *Polymers for Advanced Technologies* **2006**, *17*, 772-777.

[21] J. Artner, M. Ciesielski, O. Walter, M. Döring, R. M. Perez, J. K. W. Sandler, V. Altstädt, B. Schartel, *Macromolecular Materials and Engineering* **2008**, *293*, 503-514.

[22] L.-H. Lee, *Journal of Polymer Science Part A: General Papers* **1965**, *3*, 859-882.

[23] D. P. Bishop, D. A. Smith, *J. Appl. Polym. Sci.* **1970**, *14*, 205-223.

[24] A. Toldy, N. Toth, P. Anna, G. Marosi, *Polymer Degradation and Stability* **2006**, *91*, 585-592.

[25] J. M. G. Cowie, V. Arrighi, *Polymers: chemistry and physics of modern materials*, CRC press, **2007**.

[26] M. Ciesielski, B. Burk, C. Heinzmann, M. Döring, in *Novel Fire Retardant Polymers and Composite Materials* (Ed.: D.-Y. Wang), Woodhead Publishing, **2017**, pp. 3-51.

[27] L. Boogh, B. Pettersson, J. A. E. Manson, *Polymer* **1999**, *40*, 2249-2261.

[28] R. Mezzenga, L. Boogh, J. A. E. Manson, *Composites Science and Technology* **2001**, *61*, 787-795.

[29] S. V. Levchik, in *Flame Retardant Polymer Nanocomposites* (Eds.: A. B. Morgan, C. A. Wilkie), John Wiley & Sons, Inc., **2006**, pp. 1-29.

[30] E. D. Weil, *Fire retardancy of polymeric materials* **2000**, 115-145.

[31] S. V. Levchik, G. F. Levchik, A. I. Balabanovich, E. D. Weil, M. Klatt, *Angew Makromol Chem* **1999**, *264*, 48-55.

[32] M. Hesse, H. Meier, B. Zeeh, *Spektroskopische Methoden in der organischen Chemie*, Georg Thieme Verlag, **2005**.

[33] L. C. Thomas, Interpretation of the infrared spectra of organophosphorus compounds, Heyden, London; New York, **1974**.

[34] I. Zhmurova, A. Kisilenko, A. Kirsanov, *JOURNAL OF GENERAL CHEMISTRY USSR* **1962**, *32*, 2544.

[35] S. Brehme, B. Schartel, J. Goebbels, O. Fischer, D. Pospiech, Y. Bykov, M. Döring, *Polym. Degrad. Stab.* **2011**, *96*, 875-884.

[36] E. Wawrzyn, B. Schartel, M. Ciesielski, B. Kretzschmar, U. Braun, M. Döring, *Eur. Polym. J.* **2012**, *48*, 1561-1574.

[37] R. Petrella, *Journal of fire sciences* **1994**, *12*, 14-43.

[38] S. Gaan, P. Rupper, V. Salimova, M. Heuberger, S. Rabe, F. Vogel, *Polymer Degradation and Stability* **2009**, *94*, 1125-1134.

[39] E. Wawrzyn, B. Schartel, M. Ciesielski, B. Kretzschmar, U. Braun, M. Doring, *European Polymer Journal* **2012**, *48*, 1561-1574.

5.9 Supporting Information

5.9.1 Pyrolysis-Gas Chromatography/Mass Spectrometry spectra

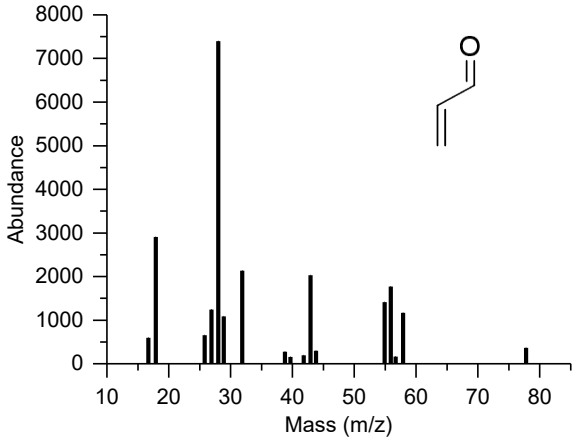

Figure S5.1. Mass spectrum of pyrolysis products of EP-A at 325 °C at 2.39 min, corresponding to acrolein.

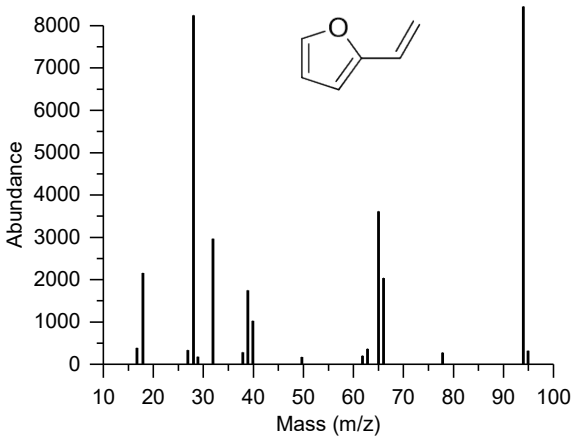

Figure S5.2. Mass spectrum of pyrolysis products of EP-A at 325 °C at 4.28 min, corresponding to 2-ethenylfuran.

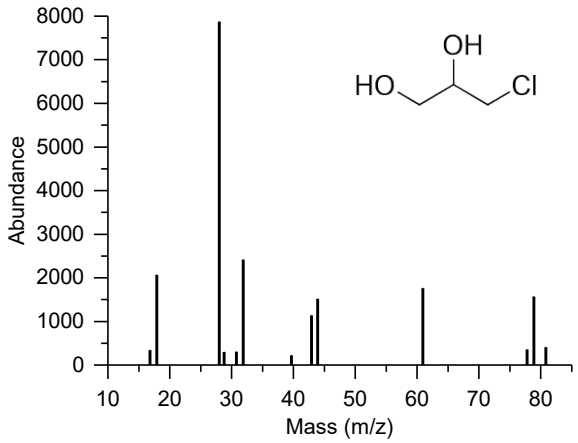

Figure S5.3. Mass spectrum of pyrolysis products of EP-A at 325 °C at 7.96 min, corresponding to 3-chloro-1,2-propanediol.

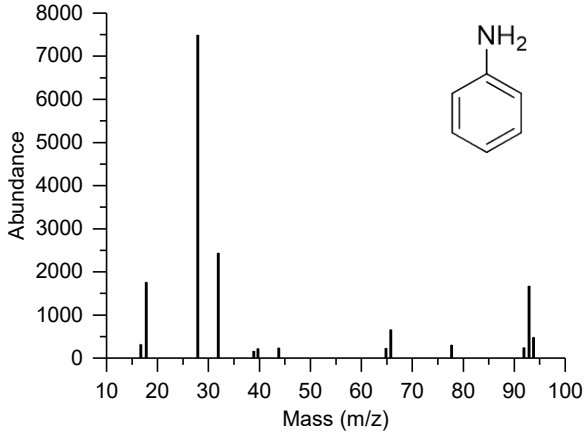

Figure S5.4. Mass spectrum of pyrolysis products of EP-A at 325 °C at 8.73 min, corresponding to aniline.

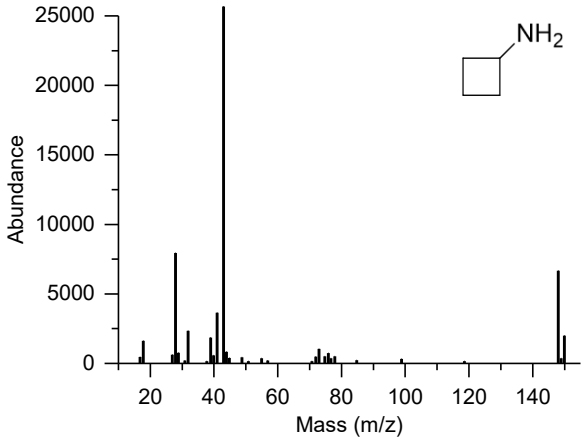

Figure S5.5. Mass spectrum of pyrolysis products of EP-A at 325 °C at 9.41 min, corresponding to cyclobutylamine.

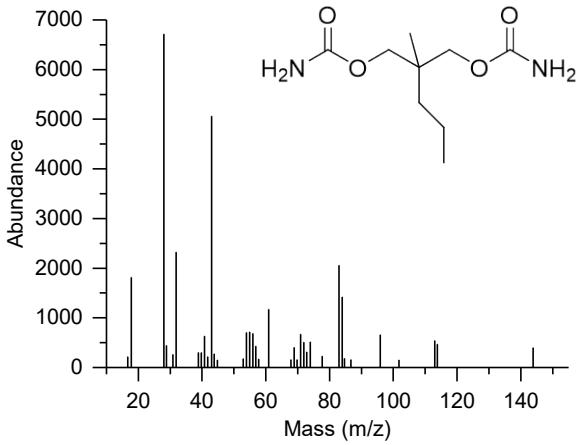

Figure S5.6. Mass spectrum of pyrolysis products of EP-A at 325 °C at 15.40 min, corresponding to mebrobamate.

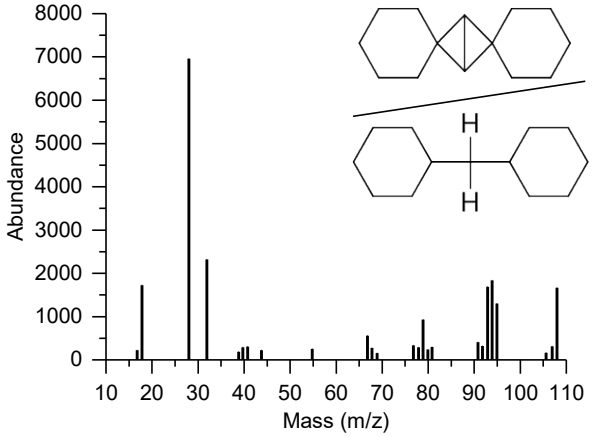

Figure S5.7. Mass spectrum of pyrolysis products of EP-A at 325 °C at 16.49 min, identified as dispiro[cyclohexane-1,2'-bicyclo(1.1.0)butane-4',1''-cyclohexane], which may correspond to 4,4'-methylene-bis(cyclohexane).

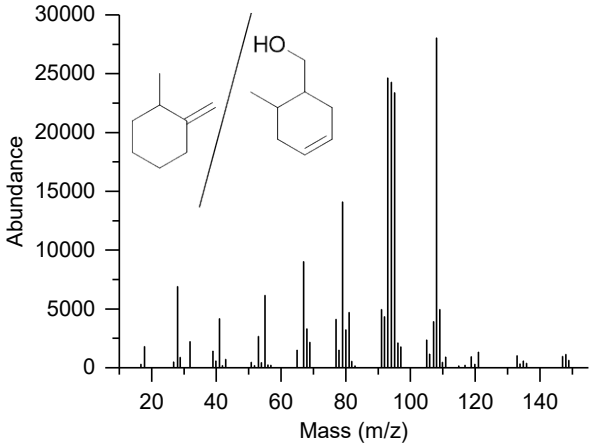

Figure S5.8. Mass spectrum of pyrolysis products of EP-A at 325 °C at 16.97 min, corresponding to 1-methyl-2-methylenecyclohexane and/or 6-methyl-3-cyclohexane-1-methanol.

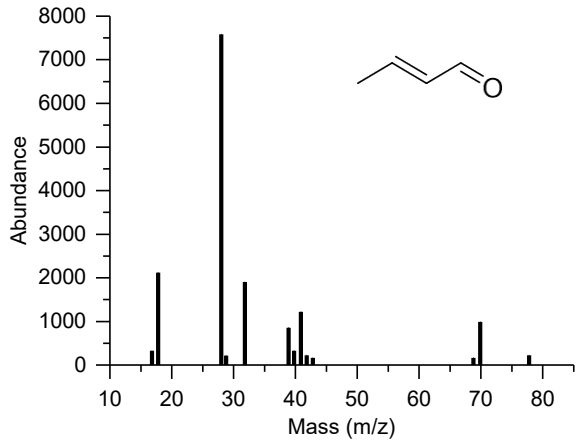

Figure S5.9. Mass spectrum of pyrolysis products of EP-A at 500 °C at 2.66 min, corresponding to 2-butenal.

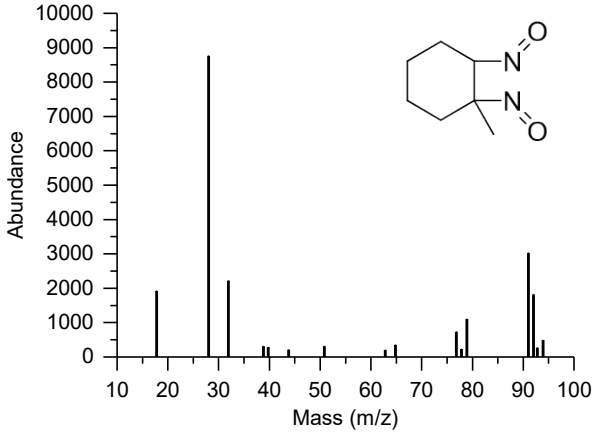

Figure S5.10. Mass spectrum of pyrolysis products of EP-A at 500 °C at 4.54 min, corresponding to 1,2-dinitroso-2-methyl-cyclohexane.

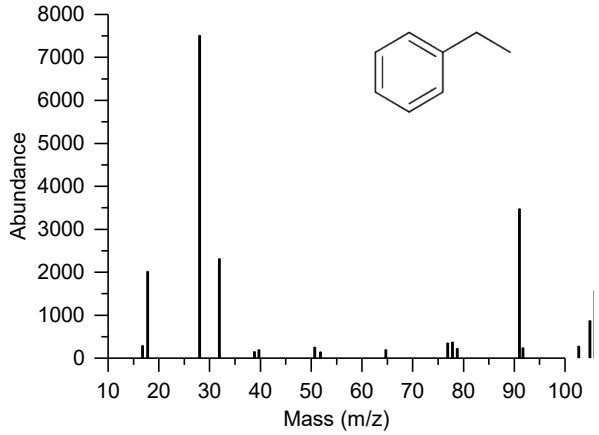

Figure S5.11. Mass spectrum of pyrolysis products of EP-A at 500 °C at 6.77 min, corresponding to ethylbenzene.

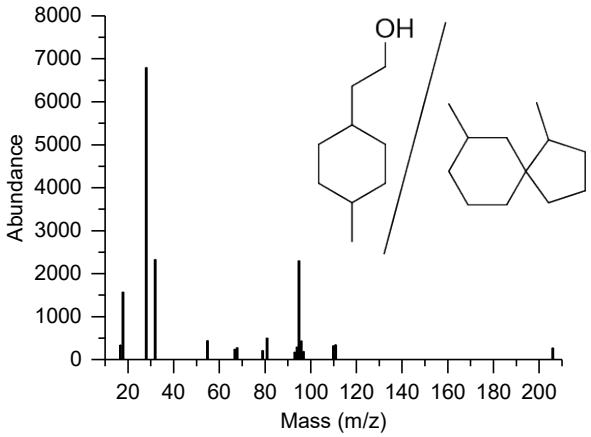

Figure S5.12. Mass spectrum of pyrolysis products of EP-A at 500 °C at 16.77 min, corresponding to 2-(4-methylcyclohexyl) ethanol, or 1,7-dimethylspiro[4.5]decane.

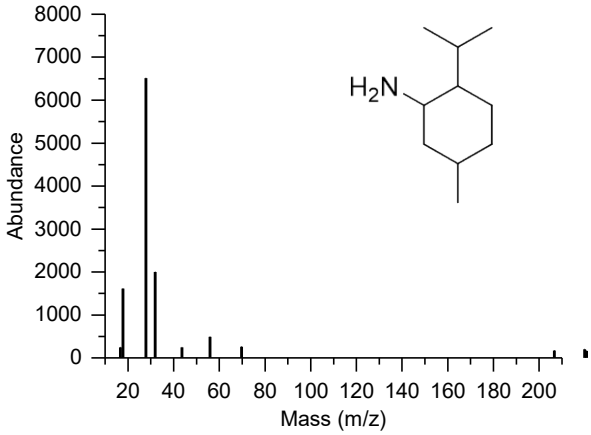

Figure S5.13. Mass spectrum of pyrolysis products of EP-A at 500 °C at 19.30 min, corresponding to neomenthylamine.

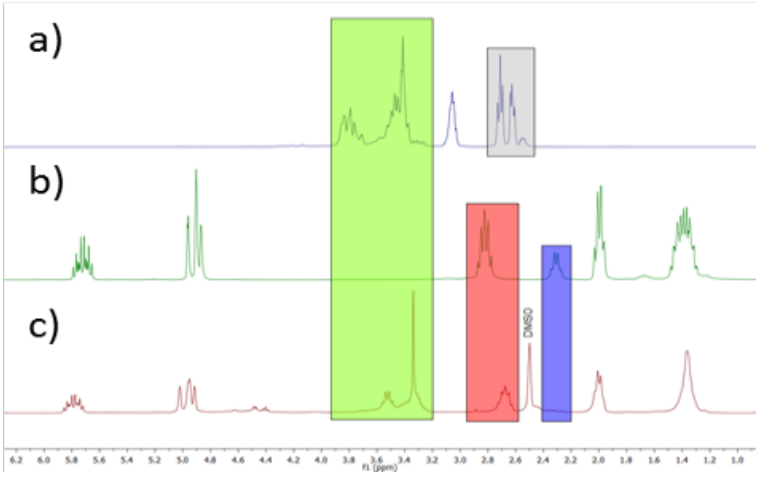

Figure S5.14. a) ^{1}H-NMR (250 MHz in $CDCl_3$ at R.T.) of glycidol; b) ^{1}H-NMR (300 MHz in $CDCl_3$ at R.T.) of mA; c) ^{1}H-NMR (300 MHz in d-DMSO at R.T.) of mA reacted with glycidol.

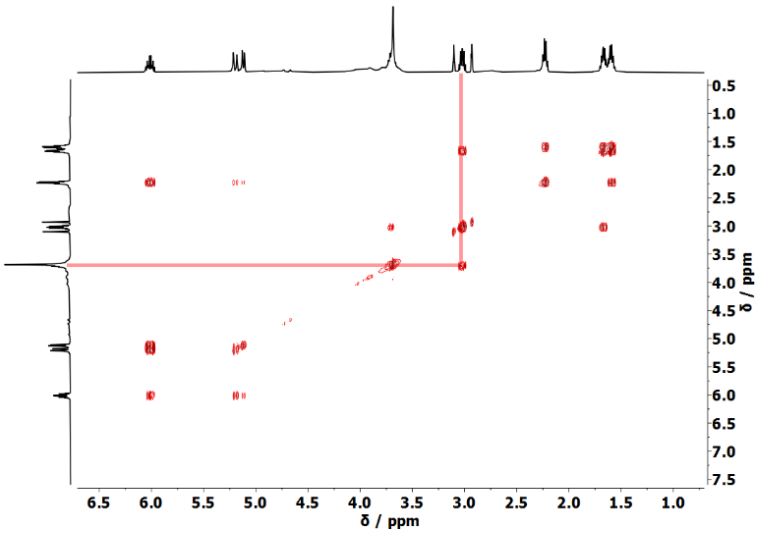

Figure S5.15. ^{1}H-^{1}H COSY (250 MHz in DMF-*d* at R.T.) of mA reacted with glycidol.

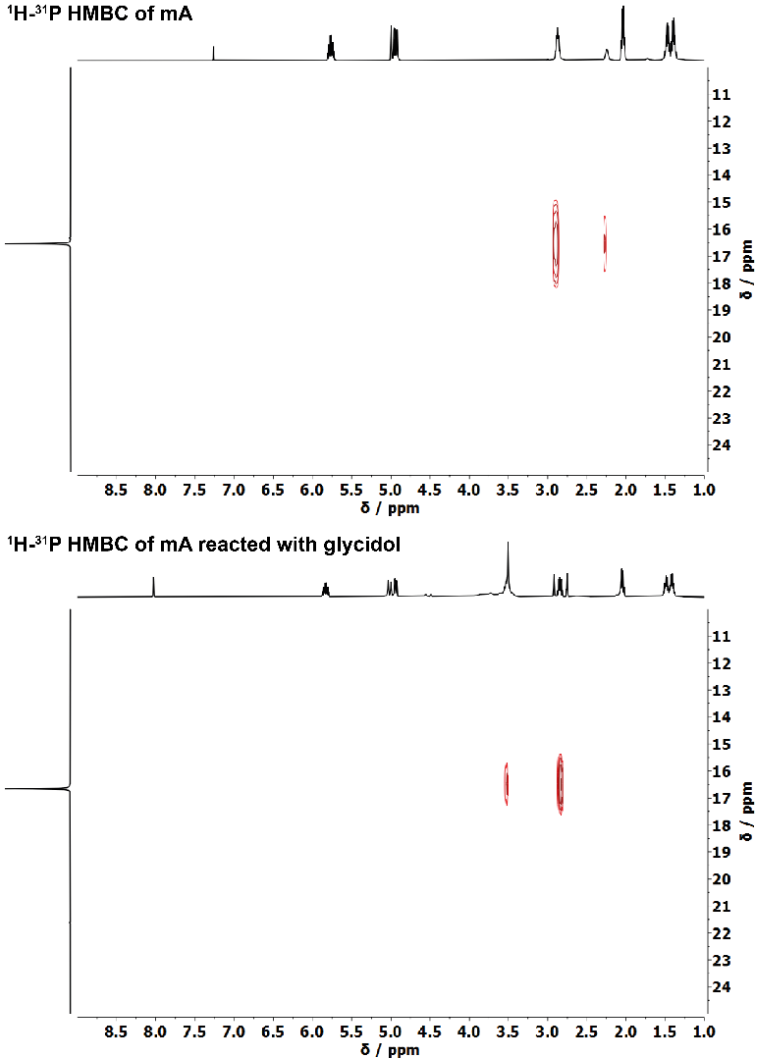

Figure S5.16. ^{1}H-^{31}P HMBC of mA (top) (250 MHz in $CDCl_3$ at R.T.) and ^{1}H-^{31}P HMBC of mA reacted with glycidol (bottom) (250 MHz in DMF-*d* at R.T.), indicating the reaction of mA with glycidol.

5.9.2 Heat of combustion of EP-FRs

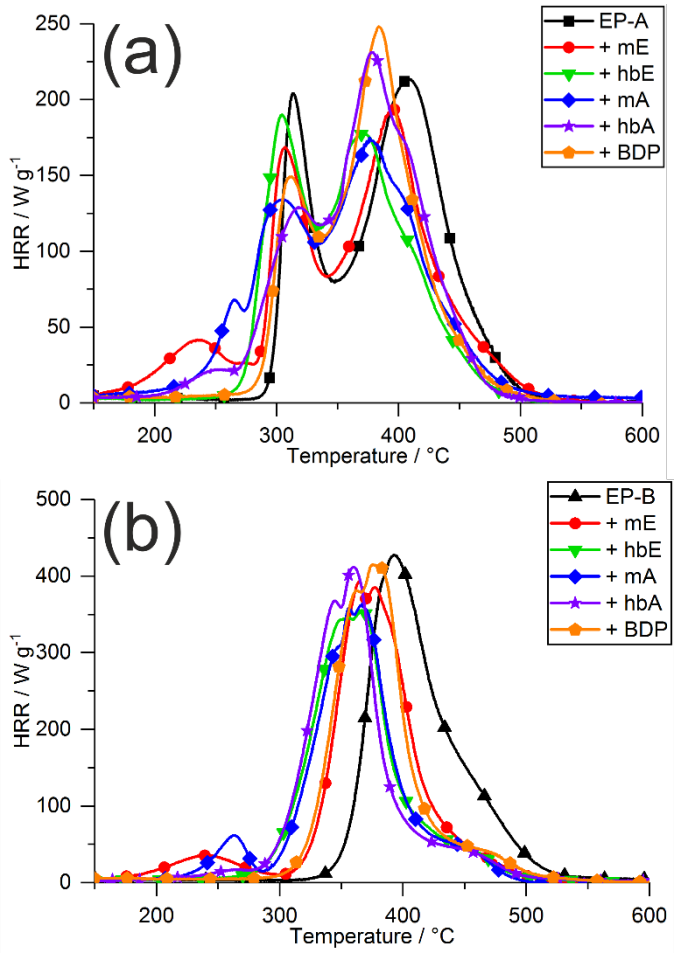

Figure S5.17. Heat release rate curves of (a) EP-A with FRs, and (b) EP-B with FRs via PCFC measurements.

In a fire, the gaseous products from pyrolytic decomposition at the gas / condensed phase interface feed the diffusion flame. Determining the heat of complete combustion via PCFC is useful in assessing the heat release of volatiles and provides an insight into the combustibles and possible flame-retardant modes of action such as flame dilution. It should be noted that the results from PCFC cannot be compared to forced-flaming conditions via cone calorimetry, as flame poisoning, a crucial mode of action for P-FRs, is not detectable in PCFC. The heat release curves from PCFC measurements of EP-A with FRs are plotted in Figure S5.17a, Figure S5.17b depicts those curves from EP-B with FRs, and Table S5.1 summarizes the results.

When mE and mA were present in resins, a small increase in heat release appeared at approx. 250 °C. Notably, the hbFRs exhibited a less pronounced increase in heat release in the same temperature range as the low molar mass FRs. This small increase in heat release coincides with the mass loss step near 250 °C in TGA measurements (Figures 5.5a and 5.5b). Thus, the volatiles

from this decomposition step contribute to the heat release; moreover, FTIR analysis pointed to the production of hex-5-ene-1-ol or hex-5-ene-1-amine in Figure 5.7a.

The addition of FRs increased the residue yields of both EP-A and EP-B similarly: mE increased residue yield by a factor of 2.1 in EP-A and by 1.2 in EP-B, while the increase factor for hbE was 2.1 in EP-A and 2.7 in EP-B. The addition of mA into EP-A increased residues by a factor of 3.7, but it only increased residues by a factor of 2.9 in EP-B. In contrast, hbA's residue increase factor was 2.8 in EP-A and 3.0 for EP-B. Phosphoramide-containing FRs caused higher residue yields than those containing phosphates due to greater overlap in T_{dec}-range (compare Figure 5.1b). BDP attained higher residue yields in EP-B (factor: 3.0) than in EP-A (factor: 1.5), which correlates well with previous TGA measurements.

The heat of complete combustion (h^0_c), which is the ratio of total heat release and mass loss, may change for flame-retarded materials if incombustible gases such as water, CO_2, or ammonia are released. The h^0_c of EP-A and EP-B was altered by the addition of FRs in different ways: both mE and mA increased h^0_c by 1% in EP-A and by 2% in EP-B, respectively. On the other hand, hbE decreased h^0_c by 3% in EP-A and by 1% in EP-B, while hbA increased h^0_c in EP-A and decreased it in EP-B. The polymeric FR hbA may have a higher affinity to the aromatic matrix EP-B during decomposition, causing the release of more incombustible gases during pyrolysis.

Table S5.1. Results from pyrolysis and complete combustion of the volatiles of EP-A and EP-B resins with FRs via PCFC measurements.

	HRC / J g^{-1} K^{-1}	THE / kJ g^{-1}	Residue / wt.-%	h^0_c / kJ g^{-1}
EP-A	223 ±8	24.3 ±0.1	1.7 ±0.1	25.1 ±0.1
+ mE	202 ±3	24.5 ±0.2	3.6 ±0.1	25.3 ±0.2
+ hbE	194 ±3	22.7 ±0.1	3.5 ±0.1	24.4 ±0.1
+ mA	186 ±6	23.5 ±0.1	6.3 ±0.7	25.3 ±0.1
+ hbA	232 ±2	24.9 ±0.2	4.8 ±0.2	26.1 ±0.1
+ BDP	255 ±7	23.0 ±0.2	2.6 ±0.1	24.6 ±0.3
EP-B	434 ±7	32.0 ±0.3	2.1 ±0.1	32.7 ±0.1
+ mE	432 ±9	32.7 ±0.3	2.5 ±0.5	33.5 ±0.4
+ hbE	447 ±1	30.5 ±0.3	5.7 ±0.1	32.3 ±0.4
+ mA	386 ±4	31.1 ±0.4	6.1 ±0.1	33.5 ±0.1
+ hbA	398 ±31	30.0 ±0.3	6.4 ±0.2	32.0 ±0.2
+ BDP	255 ±7	30.1 ±0.4	6.2 ±0.1	32.1 ±0.4

5.9.3 Reaction to small flames via LOI and UL-94

Reaction-to-small-flame tests, i.e. limiting oxygen index (LOI) and Underwriter's Laboratory 94 (UL-94), help to determine the behavior of a given material in the incipient fire stage. Vertical and horizontal flame-spread give insight into the flammability of the material: flame-retarded materials often reach higher oxygen indices (OI) or better UL-94 ratings (e.g. V-0) than their base matrix due to gas or condensed phase activity such as flame poisoning or char formation, or alternatively through enhanced dripping.

Table S5.2 summarizes the results from LOI and UL-94 measurements and highlights the change in behavior compared to the base material. The addition of FRs increased charring, which was able to snuff downward flame spread and led to increased OI. The addition of FRs led to an OI increase between 2 – 5 vol.-% in EP-A, and an average increase of 4.4 vol-% in EP-B. Notably, mE and hbE attained slightly higher OI values in EP-A than in EP-B, while mA and hbA, and especially BDP, raised OI more strongly in EP-B than in EP-A. The addition of BDP led to the highest OI in EP-B (24.0 vol.-%), yet it presented the lowest OI in EP-A (21.6 vol.-%). The change in behavior resulted from the lack of chemical interaction during combustion, as indicated from TGA results.

Table S5.2. Results from reaction to small flame tests LOI and UL-94 of EP-A and EP-B with FRs.

	OI / vol.-%	ΔOI / vol.-%	UL-94 class	Burn speed / mm min^{-1}	rel. Δ(Burn speed)
EP-A	19.7 ±0.3	–	HB40	43.0 ±0.8	–
+ mE	24.5 ±0.2	+ 4.8	HB	31.1 ±0.3	- 28%
+ hbE	24.4 ±0.3	+ 4.7	HB	35.1 ±0.2	- 18%
+ mA	23.3 ±0.2	+ 3.6	HB	30.1 ±6.5	- 30%
+ hbA	22.1 ±0.2	+ 2.4	HB	25.2 ±6.5	-41%
+ BDP	21.6 ±0.2	+ 1.9	HB	27.7 ±1.5	- 36%
EP-B	18.7 ±0.3	–	HB	31.7 ±3.6	–
+ mE	23.2 ±0.3	+ 4.5	HB	30.0 ±1.6	- 5%
+ hbE	22.1 ±0.2	+ 3.4	HB	27.7 ±4.4	- 13%
+ mA	22.9 ±0.2	+ 4.2	HB	38.3 ±2.9	+ 21%
+ hbA	23.3 ±0.2	+ 4.6	HB	22.0 ±0.7	- 31%
+ BDP	24.0 ±0.2	+ 5.3	HB	19.6 ±3.6	- 38%

All tested materials burned intensely in UL-94 vertical tests, owing to the high fire load of the epoxy resins; thus, all materials required horizonal tests. EP-A burned with an average burn speed of 43.0 mm s-1, reaching only an HB40 classification. The addition of FRs decreased the horizonal burn speed by 18–41%, the lowest value belonging to EP-A/hbA. Similarly, the addition of FRs to EP-B altered the horizontal burning speed. Notably, while the addition of mA increased burn speed in EP-B, it lowered the horizontal burn speed in EP-A. This is attributed to the increased heat of

combustion of mA in EP-B, but not in EP-A. Moreover, hbA decreased the burning speed in both matrices, but impacted EP-A most strongly, a result of its reactive FR properties in this matrix. However, while the materials gained some improvement through the addition of FRs, the high fire load of the epoxy resins could not be overcome by the FRs. While OI and burning speed generally improved with FR addition, higher FR loadings may be necessary to attain higher OI and V-classification of high-performance materials.

5.9.4 Residue Analysis

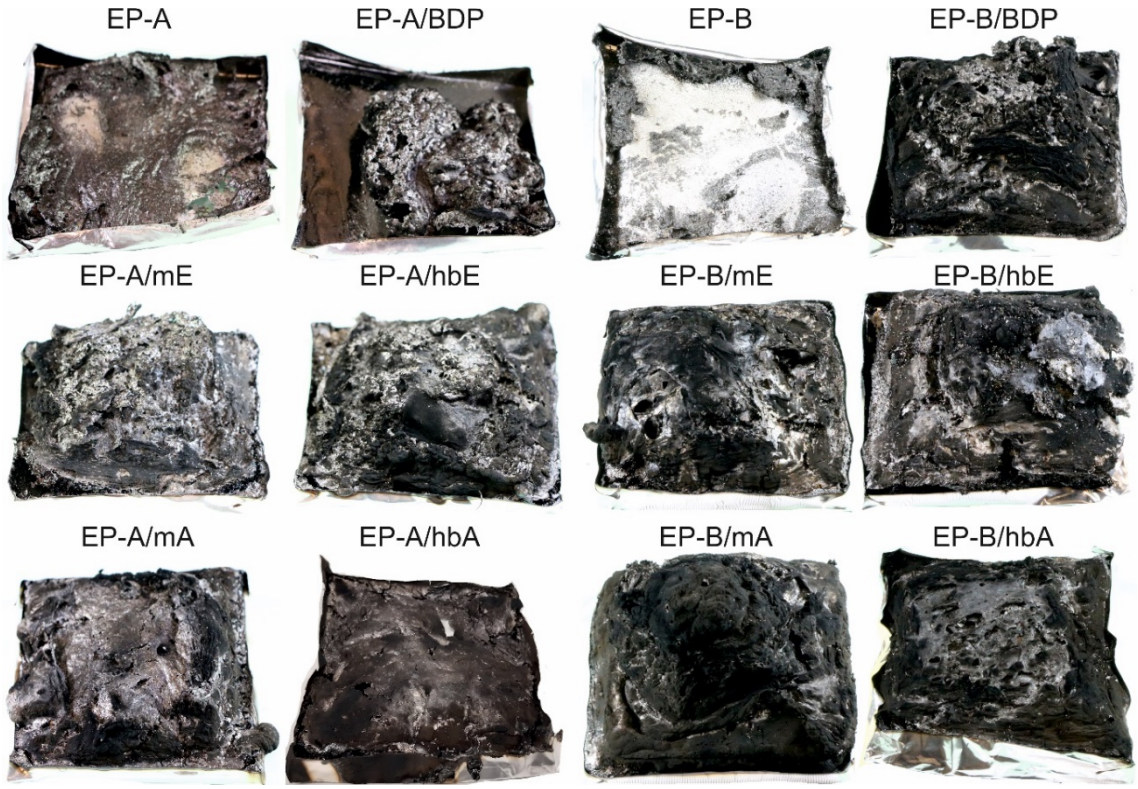

Figure S5.18. Residues from cone calorimeter measurements of EP-A and EP-B resins and FR containing composites.

The specimen residues after cone calorimeter measurements provide a valuable insight into the mode of action of the tested FRs. Figure S5.18 presents the residues of EP-A and EP-B resins and their FR containing composites. Notably, EP-A and EP-B burned almost completely with little residue remaining. The addition of BDP to the matrices increased the residue amount, yet the morphology of EP-B/BDP was different than that of EP-A/BDP: although the difference in residue amount is only about 0.5 wt.-%, EP-B/BDP was more voluminous and resembled a multicellular char layer. Consequently, BDP formed a more effective protective layer, thus explaining the strong reduction of PHRR for EP-B but not EP-A. The phosphate FRs mE and hbE more strongly reduced PHHR in EP-B than in EP-A for the same reason, as the residue surface of EP-A/mE and EP-A/hbE

were frayed and less voluminous than that of EP-B/mE and EP-B/hbE. For the phosphoramide FRs mA and hbA, the lack of a strong multicellular char acting as a protective layer resulted in the increased PHRR compared to EP-A and EP-B. Instead, the residues were dense and brittle and offered scant protective layer effects. The incorporation of mA into the matrices generally increased PHRR because the dense char acted as a thermal conductor to the underlying material, thereby increasing the release of volatiles. Notably, EP-A/mA had the shortest burning time (Figure 5.9a). For hbA, the difference in PHRR between EP-A and EP-B is due to the difference in volume and the multicellular structure of EP-B/hbA.

6. Sulfur's Role in the Flame Retardancy of Thio-Ether–linked Hyperbranched Poly(phosphoesters) in Epoxy Resins

Alexander Battig,[a]+ Jens C. Markwart,[b,c]+ Frederik R. Wurm,[b]* and Bernhard Schartel[a]*

[a] *Technical Properties of Polymeric Materials - Bundesanstalt für Materialforschung und -prüfung (BAM), Unter den Eichen 87, 12205 Berlin, Germany*

[b] *Physical Chemistry of Polymers - Max Planck Institute for Polymer Research, Ackermannweg 10, 55128 Mainz, Germany*

[c] *Graduate School Materials Science in Mainz, Staudinger Weg 9, 55128 Mainz, Germany*

+ *These authors contributed equally to this work.*

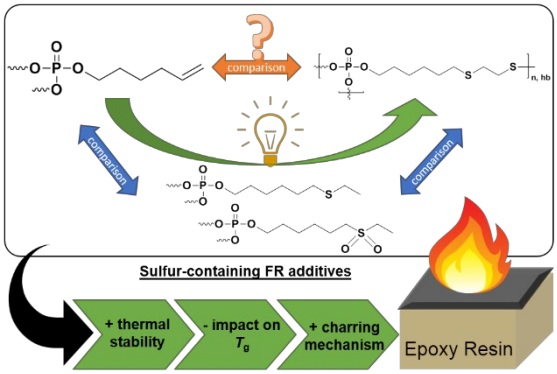

Keywords: Phosphoester, Hyperbranched, Sulfur, Thio-Ether, Flame Retardant, Epoxy Resin

6.1 Notes

To be submitted in this or altered form.

Alexander Battig performed the flame-retardancy measurements.

6.2 Abstract

Hyperbranched poly(phosphoesters) are promising multifunctional flame retardants for epoxy resins. These polymers were prepared via thiol-ene polyaddition reactions. While key chemical mechanisms and modes of actions were elucidated, the role of sulfur in the chemical composition remains an open question. In this study, we compare the FR-performance of a series of phosphorus-based flame retardant additives with and without sulfur (thio-ethers or sulfones) in their structure. The successful synthesis of the thio-ether or sulfone-containing variants is described and verified by ^{1}H and ^{31}P NMR, also FTIR and MALDI-TOF. A decomposition mechanism is proposed from pyrolytic evolved gas analysis (TG-FTIR, Py-GC/MS), and flame retardancy effect on epoxy resins is investigated in pyrolytic conditions and via fire testing in the cone calorimeter. The presence of sulfur increased thermal stability of the flame retardants and introduced added condensed phase mechanisms. Likely, sulfur radical generation plays a key role in the flame-retardant mode of action, and sulfones released incombustible SO_2. The results highlight the multifunctionality of the hyperbranched polymer, which displays better fire performance than its low molar mass thio-ether analogue due to the presence of vinyl groups and higher stability than its monomer due to the presence of thio-ether groups.

6.3 Introduction

Polymeric flame retardants (FRs) based on phosphorus (P) are gaining increased attention,[1] not only because they more closely adhere to REACH, but particularly due to their ability to mitigate some of the drawbacks of low molar mass variants, e.g. leaching or blooming out of the matrix, which diminish material properties such as glass-transition temperature (T_g). Especially hyperbranched (hb) polymers have been recently investigated, as these materials act as multifunctional FRs in polymer resins, thereby exhibiting good miscibility, low impact on T_g, and effective flame retardancy already at low loadings.[2] Hyperbranched polymers may be produced in a one-pot synthesis, as opposed to the highly symmetrical dendrimers;[3] this ease of synthesis is a major contributor to the use of these complex-shaped polymers in a wide array of fields.[4-5] The choice of reaction type is highly relevant to the material properties and application, and a wide range of synthetic approaches have been described.[6-7] Previously, P-based A_3-type hb-polymers were synthesized,[8] and their efficacy as FRs for bisphenol A-based epoxy resins (EPs) was proven.[9] Another approach to attain P-based hb-polymers is via an A_2+B_3-type reaction: in previous works, we synthesized P-based polymeric hyperbranched FRs (hb-FRs) and proved their efficacy as additive FRs in bisphenol A-based epoxy resins (EPs).[10] The hb-FRs were synthesized via thiol-ene polyaddition using ethanedithiol as an A_2-unit and low molar mass P-based FRs with systematically varied P-O and P-N contents as B_3-units. These low molar mass FRs were previously synthesized and investigated as additives in EP.[11] Research into the low molar mass FRs and their hb-polymeric variants proved that polymerization generally improved thermal stability and decreased impacts on T_g. However, the comparison between hb-polymers and their monomers did not fully consider the role of the sulfur (S)-containing A_2-component and how its presence may affect flame retardancy.

In this work, we aim to investigate the role of S-containing compounds, i.e. thio-ethers and sulfones, in the flame retardancy of P-based FRs and thereby gain a better understanding of the impact of the A_2-linker of hb-FRs. Two S-containing low molar mass P-FRs are synthesized and their performance as additives in bisphenol-A-based EPs are compared to the previously synthesized hb-FR (**hbPPE**) and its non-S-containing monomer (**mPE**). To better compare low molar mass FRs to **hbPPE**, we prepared a thio-ether-containing compound (**mPE-S**) via thiol-ene reaction of **mPE** with ethanethiol. Additionally, **mPE-S** was oxidized to form a sulfone-containing compound (**mPE-S-ox**).

The use of sulfur in flame retardancy has been investigated for a wide array of flame retardants and polymers. The role of sulfur oxidation was investigated for P-esters in bisphenol A, where it was found that flame retardancy increased with increasing levels of oxidation state.[12] Several S-

containing FRs have been previously investigated in polycarbonates (PC), many of them as aromatic sulfonate salts.[13] Although the flame-retardant mechanisms and modes of action are not completely clear, one investigation stipulated that Fries-rearragement was accelerated by aromatic sulfonates in PC, causing higher cross-linking but a faster decomposition.[14] Moreover, extensive investigations into the flame-retardant mechanism of elemental sulfur, sulfides, and disulfides were performed, highlighting that these compounds decompose to form sulfur radicals, which may promote cross-linking reactions.[15-16] Sulfone-containing FRs were shown to release sulfur dioxide into the gas-phase,[17] which acts not only as a fuel-diluent thus reducing the combustion efficiency, but was shown to act as a radical-scavenger.[18-19] Additionally, P-containing sulfones have been investigated as a toughening agent and flame retardant for epoxy resins.[20] Other S-based FRs include sulfamic acid-based salts, i.e. ammonium sulfamate, or diammonium imidobisulfonate, which proved as effective FRs for cotton and wool,[21] polyamide 6,[22-23] and polymethyl methacrylate or polystyrene.[24] Furthermore, P and S-containing FRs have also been investigated in PC[25] and in thermoplastic polyurethanes.[26]

By analyzing the difference between S- and non-S-containing low molar mass FRs, new light may be shed on the role that S plays in effective flame retardancy of hb-FRs. Furthermore, by assessing the flame-retardant mechanism of S-containing low molar mass FRs (S-FRs), additional information on the mode of action and chemical mechanism of hb-FRs may be gained, thus potentially helping improve future formulations.

6.4 Materials and Methods

Table 6.1. Material abbreviation, names, chemical structures, and calculated phosphorus content.

Abbreviation	Name	Chemical structure	P-content (calc.)
mPE	Tri(hex-5-en-1-yl)phoshate	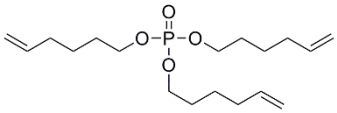	9.0 wt.-%
mPE-S	Tris[6-(ethyl thio)hexyl]phoshate	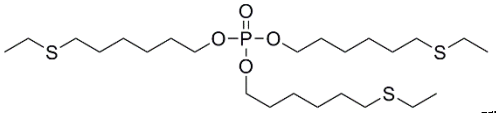	5.8 wt.-%
mPE-S-ox	Tris[6-(ethyl sulfonyl)hexyl]phoshate	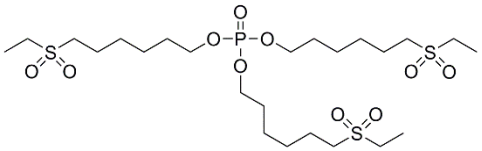	4.9 wt.-%
hbPPE	*hb*-Poly(phosphate)	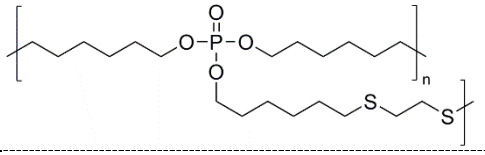	7.0 wt.-%
BDP	Bisphenol A bis(diphenyl phosphate)	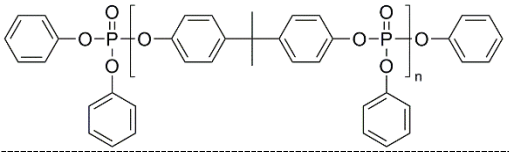	8.5 wt.-%
DGEBA	Diglycidyl ether of bisphenol A	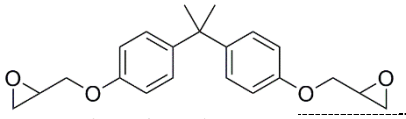	-
DMC	2,2'-dimethyl-4,4'-methylene-bis-(cyclohexylamine)	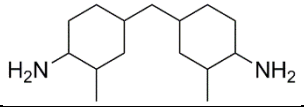	-

All chemicals were purchased from commercial suppliers as reagent grade and used without further purification. Bisphenol A bis(diphenyl phosphate) (BDP) was supplied by Albemarle (Louvain-la-Neuve, Belgium). Diglydyl ether of bisphenol A (DGEBA, Araldite MY740) was supplied by Bodo Müller Chemie GmbH (Offenbach am Main, Germany). 2,2'-dimethyl-4,4'-methylene-bis-(cyclohexylamine) (DMC) was purchased from Merck KgaA (Darmstadt, Germany).

6.4.1 Syntheses

6.4.1.1 mPE, hbPPE

mPE was prepared as previously described,[11] by the reaction of phosphoryl chloride with 5-hexene-1-ol. hbPPE was prepared as previously described,[10] where **mPE** reacted with 1,2-ethanedithiol using azobisisobutyronitrile (AIBN) as an initiator.

6.4.1.2 mPE-S

mPE (56.5 g; 164.0 mmol; 1.0 eq.) was added to a dried 250 mL round bottom flask under an argon atmosphere. Then, ethanethiol (48.5 mL; 656.2 mmol; 4.0 eq.) was slowly added while stirring and cooling the flask with a water bath at room temperature. After a few minutes AIBN (808.1 mg; 4.9 mmol; 0.03 eq.) was added and the reaction was stirred overnight at 40 °C. The crude mixture was concentrated at reduced pressure to give a yellowish oil in quantitative yields.

^{1}H NMR (300 MHz, Chloroform-*d,* δ): 4.01 (q, *J* = 6.7 Hz, 6H), 2.51 (q, *J* = 7.3 Hz, 12H), 1.68 (dd, *J* = 12.9, 6.2 Hz, 6H), 1.63 – 1.51 (m, 6H), 1.39 (s, 12H), 1.24 (t, *J* = 7.4 Hz, 9H). (Figure S6.1)

^{31}P {H} NMR (121 MHz, Chloroform-*d,* δ): -0.67 (s, 1P). (Figure S6.2)

6.4.1.3 mPE-S-ox

mPE-S (33.0 g; 62.2 mmol; 1.0 eq.), dissolved in *N,N*-dimethylformamide (DMF) (125 mL), was added to a 250 mL round bottom flask. Then, $B(OH)_3$ (82.9 mg; 1.2 mmol; 0.02 eq.) and 35% H_2O_2 (55 mL; 621.7 mmol; 10.0 eq.) were added while stirring and cooling the flask with a water bath. The reaction was allowed to continue over night at 75 °C. The crude mixture was transferred to a separation funnel, where dichloromethane (DCM) and water was added. The water phase was washed two more times with DCM and the combined organic layers were washed with NaHCO3 solution, 10% aqueous hydrochloric acid solution and brine. The organic layer was dried over magnesium sulfate, filtered and concentrated at reduced pressure to give a white wax in quantitative yields.

^{1}H NMR (300 MHz, Chloroform-*d,* δ): 4.00 (q, J = 6.6 Hz, 6H), 2.95 (q, J = 7.4 Hz, 12H), 1.82 (dd, J = 6.4, 5.7 Hz, 6H), 1.68 (dd, J = 6.6 Hz, 6H), 1.43 (m, 12H), 1.37 (t, J = 7.5 Hz, 9H). (Figure S6.3)

^{31}P {H} NMR (121 MHz, Chloroform-*d,* δ): -0.71 (s, 1P). (Figure S6.4)

MALDI-TOF: 627.25 $[M+H]^+$, 649.24 $[M+Na]^+$, 665,21 $[M+K]^+$ (Calculated M^+ : 626.24).

6.4.1.4 Sample preparation

Epoxy resin samples were prepared in the following manner: DGEBA was placed into in a 1 L polypropylene cup and, where applicable, the FR (10 wt.-% loading) was added. With a wooden spatula, the mixture was mixed until homogenous. DMC was then added next, then all components were stirred until fully mixed. Finally, the contents were poured into prepared aluminum molds. For cone calorimeter measurements, aluminum molds sized 100 mm x 100 mm x 4 mm were used. For LOI or UL-94 specimens, molds sized 130 mm x 130 mm x 4 mm were used, and appropriately sized sample specimen (according to respective standards) were cut from these.

6.4.2 Methods

6.4.2.1 NMR

^{1}H, ^{31}P {H} and ^{13}C {H} nuclear magnetic resonance (NMR) spectra were recorded with Bruker Avance spectrometers operating with 250, 300, 500, and 700 MHz frequencies in deuterated chloroform or deuterated dimethyl sulfoxide as a solvent. The calibration of the spectra was done against the solvent signal. The spectra were analyzed using MestReNova 9 from Mestrelab Research S.L.

6.4.2.2 Matrix-assisted laser desorption/ ionization – time of flight

Matrix-assisted laser desorption/ ionization – time of flight (MALDI–TOF) measurements were carried out with a Reflex I mass spectrometer (Bruker, Bremen, Germany), equipped with a 337 nm nitrogen laser. The spectra were recorded in the linear mode with the Bruker HIMAS detector at an acceleration voltage of 30 kV. 2-[(2*E*)-3-(4-*tert*-butylphenyl)-2-methylprop-2-enylidene]malononitrile (DCTB) was used as matrix. To avoid fragmentation in MALDI–TOF mass spectrum (MS) measurements, the laser power required for the desorption/ionization process was carefully adjusted slightly above threshold.

6.4.2.3 TGA

A TG 209 F1 Iris (Netzsch Instruments, Selb, Germany) was used for thermographic analysis (TGA) measurements. A CryoMill (RETSCH, Germany) was used to powder epoxy resin-based samples under liquid nitrogen. Pure FR samples (5 mg) or powdered polymer samples (10 mg) were heated at a constant heating rate (10 K min^{-1}) from 30 – 900 °C under a nitrogen flow (30 mL min^{-1}). A Fourier transform infrared spectrometer Tensor27 (Bruker Optics, Ettlingen, Germany) was used for evolved gas analysis of TGA samples (TG-FTIR). A heated (270 °C) transfer line connected TGA with FTIR. A Vertex70 FTIR spectrometer (Bruker Optics, Ettlingen, Germany) with an attached FTIR600 hot-stage cell (Linkam Scientific Instruments Ltd., Chilworth, UK) was used to measure condensed phase FTIR (range: 4000 – 40 cm^{-1}; resolution 0.4 cm^{-1}). Samples (5 mg) were mixed with potassium bromide (150 mg) and pressed into a platelet (pressure: 7 t). Under a constant heating rate (10 K min^{-1}) and constant nitrogen flow (300 ml min^{-1}), the platelets were heated from 30 – 600 °C.

6.4.2.4 Pyrolysis–Gas Chromatography-Mass Spectrometry (Py-GC/MS)

A PY3030iD micro-furnace single-shot pyrolyzer (Frontier Laboratories, Japan) coupled via a split/ splitless inlet port to a 7890B gas chromatograph (Agilent Technologies, USA) and combined with a 5977B mass selective detector (Agilent Technologies, USA) was used to measure pyrolysis gas chromatography – mass spectrometry (Py-GC/MS). The mass spectrometer detector (ionization energy = 70 eV) had a scan range of 15 – 50 amu. Samples (150 µg) were pyrolyzed (500 °C) via gravimetric fall into the pyrolysis zone under helium atmosphere. Using an Ultra Alloy +-5 capillary column (length = 30 m; inner diameter = 0.25 mm; film thickness = 0.25 µm), evolved pyrolysis products were separated under a constant flow of helium (1 mL min^{-1}). The column temperature ran for 2 min at 40 °C, then heated (10 K min^{-1}) to 300 °C and held for 10 min. The gas chromatograph injector (*T* = 300 °C) ran a split of 1:300. Peak assignments and product identification were done with the NIST 14 MS library.

6.4.2.5 PCFC

A microscale combustion calorimeter (Fire Testing Technologies Ltd., East Grinstead, UK) was used for pyrolysis flow combustion calorimetry (PCFC) measurements. At a constant heating rate (1 K s^{-1}) and constant gas flow (nitrogen: 80 mL min^{-1}; oxygen: 20 mLl min^{-1}), powdered samples (5 mg) were pyrolyzed from 150 – 750 °C, and the evolved gases were combusted at 900 °C.

6.4.2.6 DSC

A Netzsch 204 FR "Phoenix" (Netzsch Instruments, Selb, Germany) was used to measure differential scanning calorimetry (DSC). Samples from the bulk material (5 mg) were measured at a constant heating / cooling rate (10 K min^{-1}) from -80 – 180 °C. Three heating and two cooling runs were measured, and data was collected from the second and third heating run to determine the glass transition temperature.

6.4.2.7 Cone Calorimeter

A cone calorimeter (Fire Testing Technology Ltd., East Grinstead, UK) was used for forced-flaming combustion experiments according to ISO 5660. Samples (100 mm x 100 mm x 4 mm) were stored in a climate control (*T* = 23 °C; RH = 50%) for at least 48 h before testing. To simulate a developing fire, [27-28] a distance between sample and heater of 35 mm and a heat flux of 50 kW m^{-2} was chosen. Tests were conducted in duplicate, unless the margin of error was greater than 10%, whereupon a third measurement was conducted.

6.5 Results and Discussion

6.5.1 Synthesis of FRs

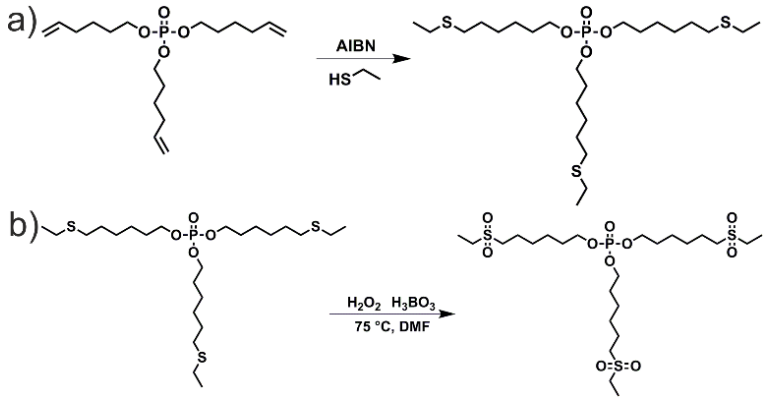

Scheme 6.1. Synthesis schemes of thio-ether and sulfone-containing FRs: a) mPE and ethanethiol reacted via thiol-ene-reaction with AIBN as initiator to form mPE-S; b) mPE-S was oxidized with hydrogen peroxide with boronic acid as a catalyst to form mPE-S-ox.

mPE was synthesized by reacting 5-hexen-1-ol with phosphoryl chloride as previously described.[11]

The synthesis of **mPE-S** was performed in a single reaction step from **mPE** and ethanethiol by a thiol-ene-reaction (Scheme 6.1 a). Further purification such as distillation or chromatography was not necessary. The resulting compound was a liquid at room temperature and had a calculated P-content of 5.84 wt.-%. It was soluble in aromatic solvents (e.g. toluene) and halogenated solvents (e.g. dichloromethane and chloroform), and insoluble in water. Successful synthesis of **mPE-S** was followed by ^{1}H NMR spectroscopy (Figure 6.1 a). After the thiol-ene-reaction, the resonances of the double bonds at 8.83 – 5.70 ppm and 5.02 – 4.93 ppm vanished, and a new resonance signal at 2.51 ppm for the methylene groups next to the thio-ether was detected. The ^{31}P NMR spectrum (Figure 6.1 b) revealed a single signal at -0.67 ppm, which is typical for phosphates.

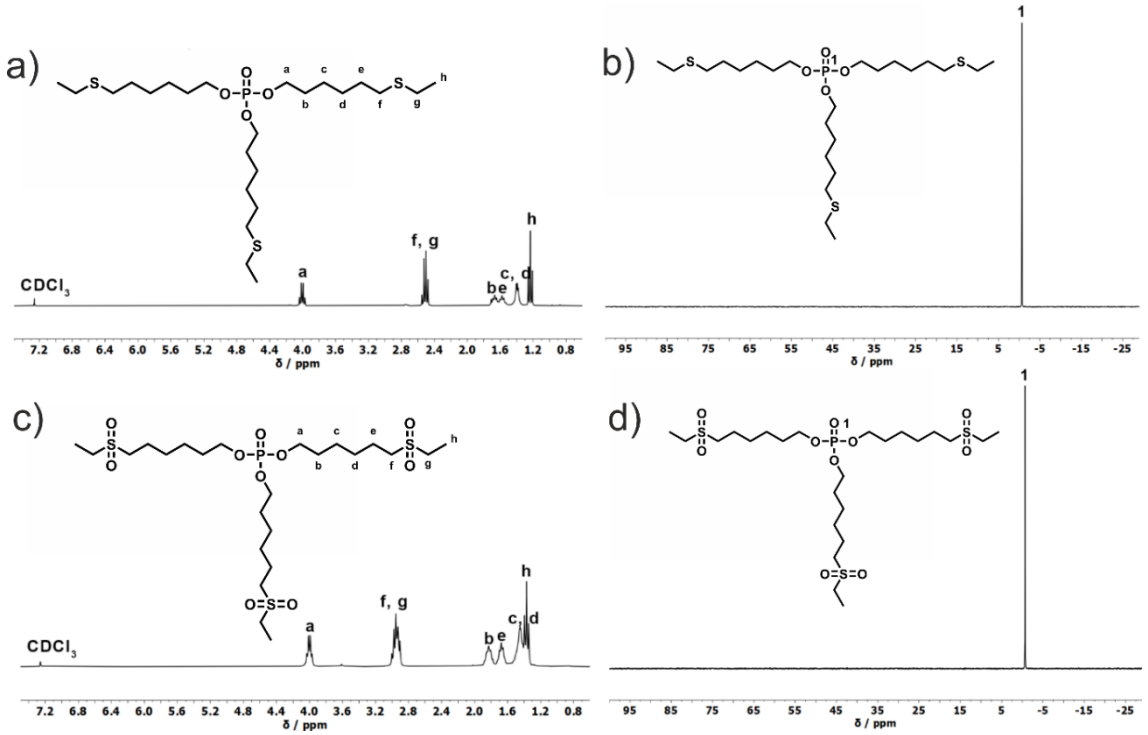

Fiugre 6.1. a) ^{1}H NMR (300 MHz in $CDCl_3$ at 298 K) of **mPE-S**; b) ^{31}P {H} NMR (121 MHz in $CDCl_3$ at 298 K) of **mPE-S**; c) ^{1}H NMR (300 MHz in $CDCl_3$ at 298 K) of **mPE-S-ox**; ^{31}P {H} NMR (121 MHz in $CDCl_3$ at 298 K) of **mPE-S-ox**.

In a second reaction, **mPE-S** was oxidized to **mPE-S-ox** by hydrogen peroxide using boronic acid as a catalyst (Scheme 6.1 b) at 75 °C overnight. After oxidation to the sulfone, the resonance of the methylene groups next to the sulfone group shifted downfield to 2.95 ppm in ^{1}H NMR (Figure 6.1 c), which is characteristic and had been reported for similar compounds earlier.[29] In addition, the successful oxidation to the sulfone and not to the sulfoxide was supported by IR spectroscopy as shown by the characteristic frequencies at 1299 cm^{-1} and 1124 cm^{-1} (Figure 6.2 a) [30] and MALDI-TOF mass spectrometry (Figure 6.2 b).

The polymeric FR **hbPPE** was prepared via a thiol-ene reaction of **mPE** with ethanedithiol. Its synthesis has been previously described and will not be further illustrated here.[10]

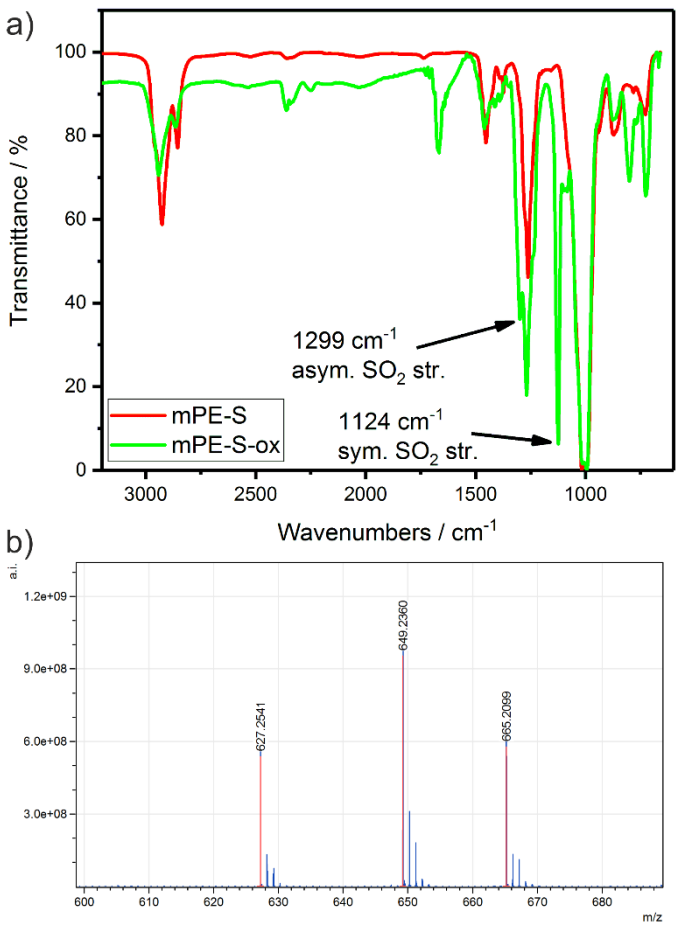

Figure 6.2. a) FTIR of mPE-S and mPE-S-ox, highlighting the asymmetrical and symmetrical SO_2 stretching frequencies; b) MALDI of mPE-S-ox with DCBT as matrix (left to right: $[M+H]^+$, $[M+Na]^+$, and $[M+K]^+$).

6.5.2 Pyrolysis – Decomposition Temperature and Mass Loss of FRs

Table 6.2. Results from thermogravimetric analysis (TGA) of FRs and EP.

Material	$T_{5\%}$ / °C	T_{max} / °C	ML_{max} / wt.-%	$T_{shoulder}$ / °C	$ML_{shoulder}$ / wt.-%	Residue (700°C) / wt.-%
mPE	195 ±3	250 ±2	95.7 ±1.4	–	–	2.8 ±0.8
mPE-S	228 ±4	277 ±0	90.2 ±1.6	–	–	7.5 ±0.2
mPE-S-ox	252 ±4	286 ±2	83.4 ±0.0	–	–	11.8 ±0.5
hbPPE	242 ±2	280 ±1	83.3 ±0.2	–	–	11.2 ±1.4
DGEBA-DMC	338 ±1	372 ±1	62.0 ±0.8	424 ±5	33.2 ±0.3	4.5 ±0.1
BDP	331 ±1	415 ±6	85.5 ±2.2	467 ±3	11.8 ±1.3	1.8 ±0.9

Onset temperatures ($T_{5\%}$); temperature of maximum decomposition rate (T_{max}); mass loss of decomposition step at T_{max} (ML_{max}); temperature of additional decomposition step, i.e. "shoulder" ($T_{shoulder}$); mass loss of decomposition step at shoulder ($ML_{shoulder}$).

All FRs were characterized by their mass loss under pyrolytic conditions via thermogravimetric analysis (TGA) (Table 6.2). The mass loss and mass loss rate curves of **mPE-S** and **mPE-S-ox** (Figure 6.3 a) highlight that both S-FRs are more thermally stable than **mPE**. The beginning of decomposition, i.e. the temperature at 5 wt.-% mass loss ($T_{5\%}$), of **mPE-S** was approx. 30 °C higher than **mPE**, and $T_{5\%}$ of **mPE-S-ox** was approx. 10 °C higher than **hbPPE**. The temperature of maximum decomposition rate (T_{max}) of **mPE-S** was in the same temperature region as **hbPPE**, and **mPE-S-ox** decomposed at slightly higher temperatures (T_{max} = 286 °C). The increased thermal stability stems from the thio-ether or sulfone groups, which are more thermally stable than allyl-groups. By "end-capping" the vinyl groups of **mPE**, added thermal stability is afforded to **mPE-S**. Furthermore, sulfone groups are more thermally stable than the thio-ether groups, as **mPE-S-ox** degrades at elevated temperatures compared to **mPE-S**. When comparing the residues at 700 °C, the residue of **mPE-S** was higher than that of **mPE** by a factor of 2.7. Moreover, the residue of **mPE-S-ox** was in the same range as that of **hbPPE**. The presence of thio-ethers altered the decomposition mechanism of **mPE** by replacing the highly reactive vinyl group; moreover, the thio-ether bond decomposed to form sulfur radicals. As it has been shown that free-radical formation plays a significant role in flame retardancy,[31] the higher residue yield is explained by sulfur radicals undergoing cross-linking reaction with the decomposing FR.

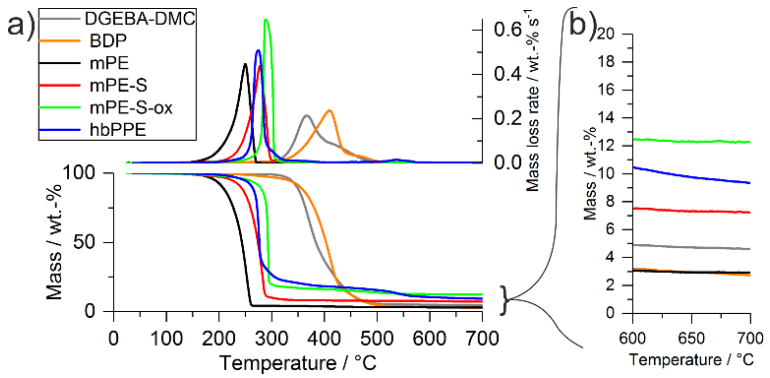

Figure 6.3. a) Mass loss (bottom) and mass loss rate (top) of pyrolytic decomposition of pure FRs and EP via TGA; b) Comparison of residue remaining between 600 – 700 °C of pure FRs and EP.

6.5.3 Pyrolysis – Evolved gas analysis of FRs

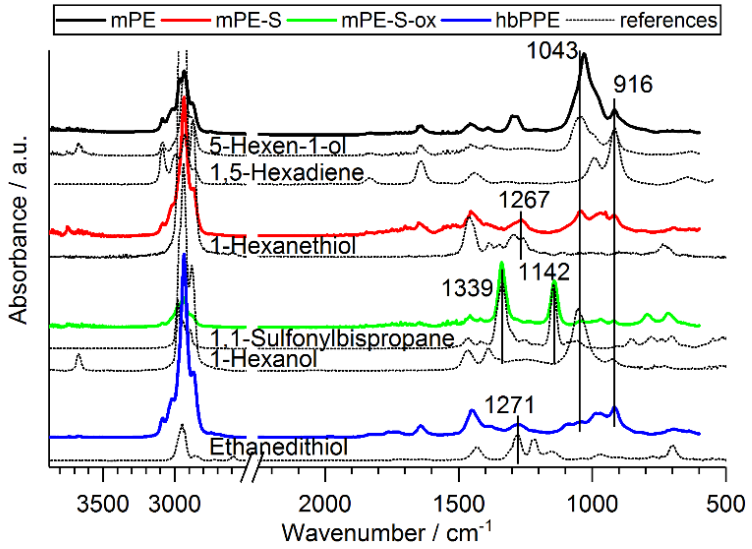

Figure 6.4. FTIR spectra of pyrolytic decomposition products of FRs at T_{max} via thermogravimetric analysis coupled with Fourier transform infrared spectroscopy (TG-FTIR).

The evolved gases during pyrolytic decomposition were analyzed via thermogravimetric analysis coupled with Fourier transform infrared spectroscopy (FTIR) (Figure 6.4) and pyrolysis coupled with gas chromatography and subsequent mass spectrometry (Py-GC/MS) (Figure 6.5). The decomposition products of **mPE** and **hbPPE** were previously investigated: the main products correspond to 5-hexen-1-ol, where the ω-OH group was identified by the band at 1043 cm^{-1}, and 1,5-hexadiene, where the vinyl group exhibited a strong band at 916 cm^{-1}.[32] The vinyl function, which was visible for all tested FRs, resulted from *cis*-eliminations, where the scission of the (PO)-C bond results in an vinyl group.[11] **hbPPE** exhibited an additional absorption band at 1271 cm^{-1} which matched a signal from ethanedithiol,[33] indicating the presence of S in the decomposition spectrum. For **mPE-S**, the spectrum exhibited an absorption band at 1267 cm^{-1} which was nearly

identical to the band seen in **hbPPE** and comparatively 1-hexanethiol.[33] Thus, this band relates to thio-ether or thiol groups. Moreover, the spectrum showed similarities to 5-hexen-1-ol via the band at 1043 cm^{-1}, implying that the decomposition product contained signals of both ω-OH and thio-ether groups, caused by the hydrolytic scission of the P-O bond, resulting in the production of 6-(ethylsulfanyl)-1-hexanol. For **mPE-S-ox**, the decomposition spectrum displayed strong absorption at 1339 and 1142 cm^{-1} belonging to characteristic sulfone groups,[32] as evidenced by the comparative spectrum of 1,1-sulfonylbispropane.[33] Furthermore, the development of 1-hexanol was underlined by the absorption at 1043 cm^{-1} and confirmed by Py-GC/MS.

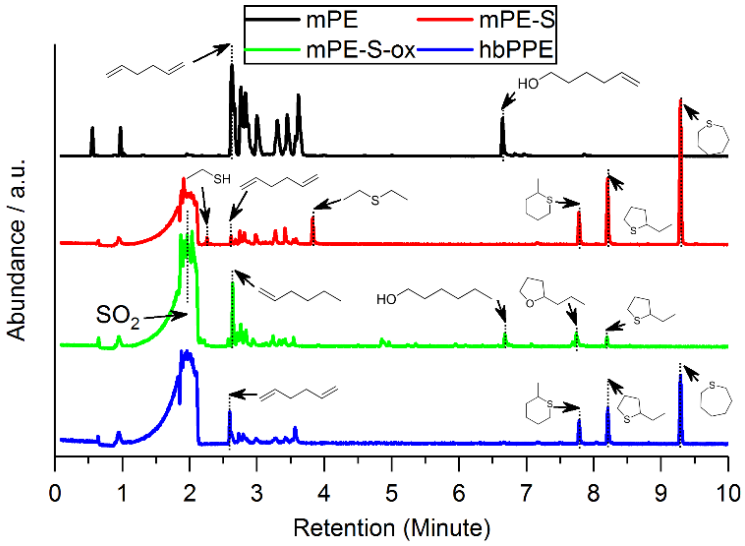

Figure 6.5. Gas chromatograms of FRs from Pyrolysis-Gas Chromatography/ Mass Spectrometry (Py-GC/MS) measurements.

Py-GC/MS measurements of the FRs (Figure 6.5) provided further evidence of the evolution of specific decomposition gases identified in FTIR spectra of the evolved gases (Figure 6.4). The presence of 5-hexene-1-ol in the spectrum of **mPE** was verified at a retention time of 6.63 min (Figure S6.6). For **mPE-S**, the production of ethanethiol at 2.26 min (Figure S6.2) and diethyl sulfide at 3.38 min (Figure S6.5) were observed. Identical to **hbPPE**, **mPE-S** decomposed to form tetrahydro-2-methyl-2H-thiopyran (7.79 min, Figure S6.9), 2-ethyltetrahydro thiophene (8.21 min, Figure S6.10), and thiepane (9.29 min, Figure S6.11). Notably, **mPE-S-ox** formed SO_2, as implied by the spectrum at 1.92 min (Figure S6.1), as well as 1-hexanol at 6.68 min (Figure S6.7). The formation of SO_2 for sulfones has been noted in literature.[17] **mPE-S-ox** decomposed to form a tetrahydrofuran-like material; the spectrum of 2-propyl-tetrahydrofuran showed similarities to the mass spec at 7.75 min (Figure S6.8), yet 2-ethyl-tetrahydrofuran is more reasonably formed when considering the C-atom amount. Notably, the mass spectrum at 8.21 min of **mPE-S-ox**

shared similarities with 2-ethyltetrahydro thiophene, possibly stemming from unreacted thio-ether groups. The production of 1,5-hexadiene was present in the spectra of **mPE**, **mPE-S**, and **hbPPE** at 2.63 min (Figure S6.3). However, for mPE-S-ox the evolution of 1-hexene was observed at 2.64 min (Figure S6.4).

The decomposition mechanisms for **mPE**[11] and **hbPPE**[10] have been described previously, and generally involved *cis*-eliminations and hydrolysis reactions. From the evolved gas analyses from FTIR and Py-GC/MS measurements, a decomposition mechanism for the S-FRs is proposed (Scheme 6.2):

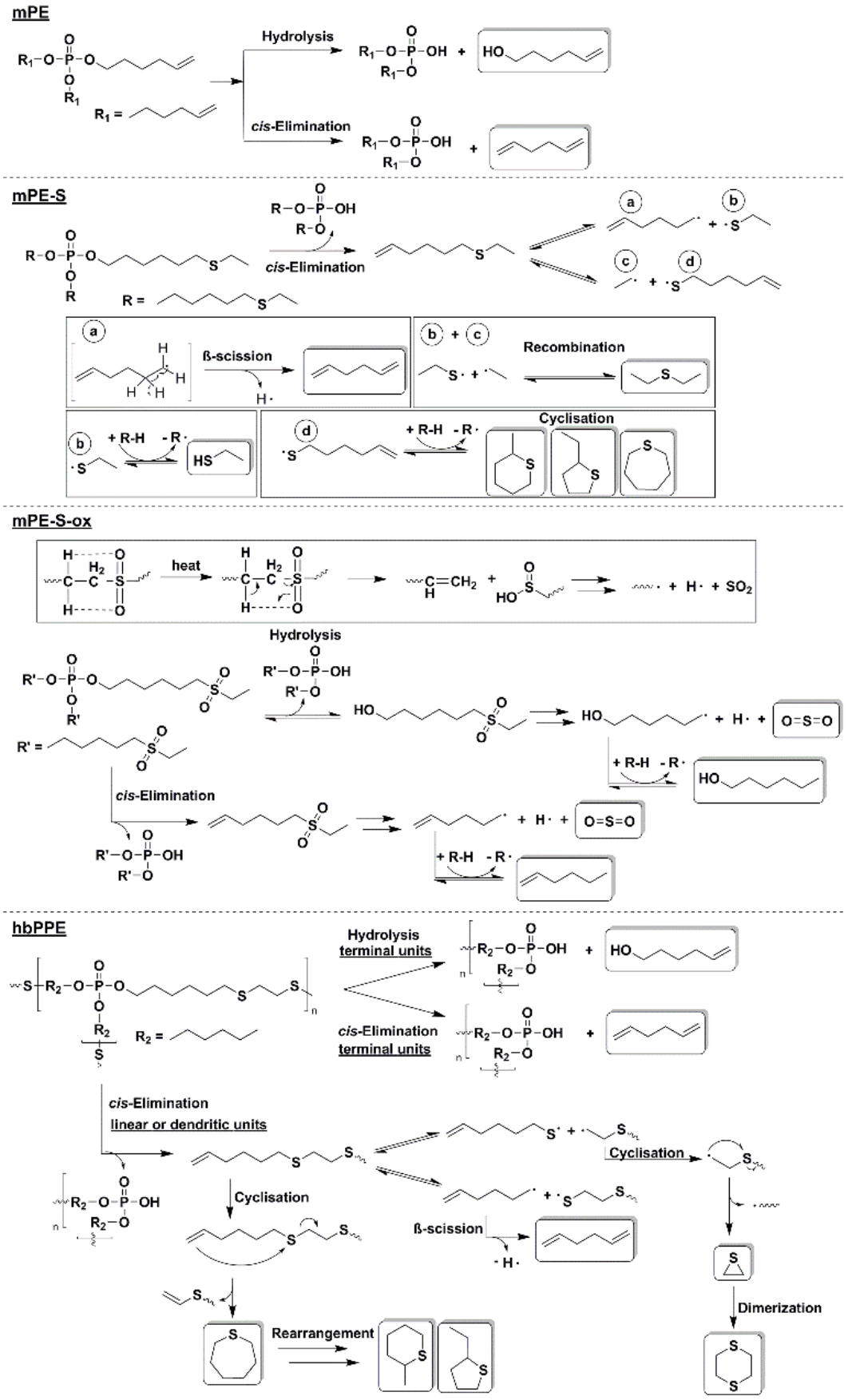

Scheme 6.2. Proposed decomposition scheme of **mPE**, **mPE-S**, **mPE-S-ox**, and **hbPPE**. Substances in solid boxes were identified in FTIR or Py-GC/MS and comparative spectra.

The decomposition of several thio-ether[34] and sulfone[35-36] containing compounds has been described in literature and involves the production of S-radicals. For **mPE-S**, *cis*-elimination leads to the production of 6-(ethylsulfanyl)-1-hexene, which further decomposes via the homolytic cleavage of the C-S bond, thus producing the products (a), (b), (c), and (d) (Scheme 6.2), depending on which C-S bond is cleaved. The ß-scission of (a) leads to the formation of 1,5-hexadiene, which was identified in Py-GC/MS, and the recombination reaction of (b) and (c) leads to the formation of diethyl sulfide, which was also detected. Hydrogen atom abstraction of (b) leads to ethanethiol, which was observed at 2.26 min, and hydrogen transfer of (d) and cyclisation reactions lead to the formation of tetrahydro-2-methyl-2H-thiopyran, 2-ethyltetrahydro thiophene, and thiepane. For **mPE-S-ox**, the driving force of decomposition is the release of SO_2: sulfone-containing olefins undergo a transfer of the ß-hydrogen atom to the sulfone-group and subsequent elimination of a vinyl functionalized olefin and sulfinic acid, the latter rapidly decomposing to form SO_2 and alkyl radicals.[37] Hydrolysis or *cis*-elimination reactions of **mPE-S-ox** form 1-(ethylsulfonyl) hexanol or 1-(ethylsulfonyl)-hex-5-en, respectively. Both products decompose via the aforementioned mechanism, and via hydrogen atom transfer reactions 1-hexanol or 1-hexene are produced; both compounds were identified in Py-GC/MS. The decomposition of **hbPPE** is expanded (Scheme 6.2) to more precisely describe the production of several measured compounds: while hydrolysis or *cis*-elimination reactions of terminal groups lead to the production of 5-hexene-1-ol or 1,5-hexadiene, respectively, *cis*-elimination of linear or dendritic units yields thio-ether-containing compounds. These thio-ethers undergo cyclisation and elimination reactions to form cyclic thio-ethers, but they also undergo homolytic C-S bond cleavage to form free radical compounds: the vinyl-functionalized alkyl radical undergoes ß-scission to yield 1,5-hexadiene, and previously reported[10] thiirane and 1,4-dithiane are formed from elimination reactions and subsequent dimerization, respectively.

6.5.4 Material properties – Resin Composites

In most cases, additives act as plasticizers in polymer resins: additives affect the cross-linking density of the material, altering its mechanical properties and affecting the glass-transition temperature (T_g).[38] The impact of the FRs on the T_g of EP was determined via differential scanning calorimetry (DSC) (Figure 6.6 a) DGEBA-DMC had a T_g of 155 °C, and the addition of FRs lowered it between 21 – 38 °C (Figure 6.6 b). EP with BDP (**EP/BDP**) had a T_g of ca. 134 °C; EP with **hbPPE** (**EP/hbPPE**) and EP with **mPE-S-ox** (**EP/mPE-s-ox**) displayed T_gs in a similar temperature range, i.e. 132 and 129 °C, respectively. Resins with **mPE** (**EP/mPE**) and **mPE-S** (**EP/mPE-S**) exhibited the

lowest T_gs at 117 and 118 °C, respectively. DSC measurements pointed out that the thio-ether-containing **mPE-S** affected the T_g of EP similarly to the allyl-functionalized **mPE**, indicating that "end-capping" did not improve the impact on T_g. Furthermore, the sulfone-containing **mPE-S-ox** had a reduced impact on T_g of EP, comparable to that of **hbPPE**. This phenomenon can be explained by the bulky sulfone groups that affect the free-volume of the matrix, thus altering the energy needed to attain a flowing process of the polymer chain, resulting in increased T_g.[39]

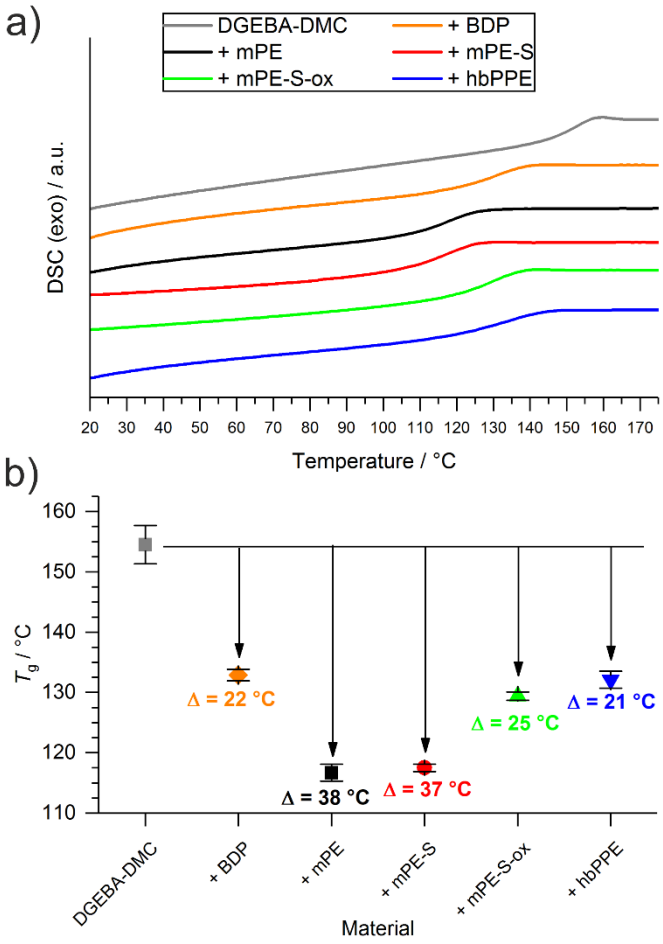

Figure 6.6. a) Differential scanning calorimetry (DSC) measurements of the second heating run of EP and EP-FRs; b) Relative change in glass-transition temperature (T_g) of EP-FRs compared to EP.

6.5.5 Pyrolysis – Decomposition Temperature and Mass Loss of Resin Composites

The pyrolytic decomposition of EP and EP-FRs was investigated via TGA (Figure 6.7 a): the mass loss of EPs with S-FRs illustrated that the low $T_{5\%}$ and approx. 10 wt.-% mass loss near 230 °C exhibited by **EP/mPE** was not shared by **EP/mPE-S** or **EP/mPE-S-ox** (Table 6.2), implying that "end-capping" the vinyl-groups increased the thermal stability of the FRs. This is further exemplified by the low T_{max} of **EP/mPE** compared to the S-FR-containing EPs; T_{max} of **EP/mPE-S** and **EP/mPE-S-ox** were both in the same range as **EP/BDP** and **EP/hbPPE**, i.e. about 15 – 20 °C lower than T_{max} of EP. Moreover, the residue yields at 700 °C of S-FR-containing FRs were higher than **EP/mPE** (Figure 6.7 b). The addition of **mPE** to resins increased residue yields after pyrolysis by about 13%, which is the lowest among the tested FRs. However, **mPE-S-ox** and **mPE-S** had a greater impact on residue, increasing yields by 41% compared to pure EP (residue = 4.5 wt.-%). When comparing **EP/mPE** to the S-FRs, the thio-ether "end-capping" led to an increase in residue yield by 24% (Table S6.1). The sulfone-containing FR did not additionally yield higher residues compared to the thio-ether. The presence of sulfur increased the thermal stability of **mPE**, leading to increased interaction with the decomposing matrix, thus producing higher char yields. Moreover, the presence of sulfu in FRs may promote cross-linking reactions by generating sulfur-radicals, as noted in the decomposition of the pure FRs. The oxidation state of sulfur did not play a role in the increase of residue. EP with **hbPPE** exhibited higher pyrolytic residues than those EPs with low molar mass S-FRs, even though pure **mPE-S-ox** had similar residue yields as pure **hbPPE**. The presence of sulfur in FRs improved the residue yields of EP in pyrolysis, thus helping to explain the high residue yields of **EP/hbPPE**. Additionally, the presence of certain S-species may act as a synergist for P-based flame retardants; previous investigations into halogenated flame retardants for polystyrene proved some synergistic effects of disulfides and sulfonamides.[40]

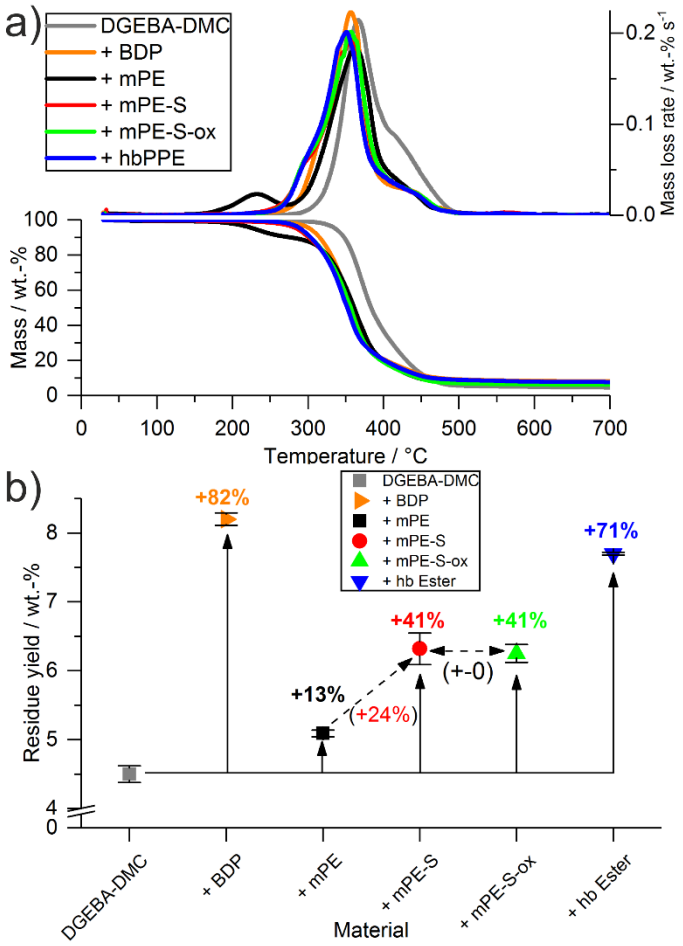

Figure 6.7. a) Mass loss (bottom) and mass loss rate (top) versus temperature via thermogravimetric analysis (TGA); b) Change in residue yields of EP-FR compared to EP.

6.5.6 Pyrolysis – Evolved gas analysis of Resin Composites

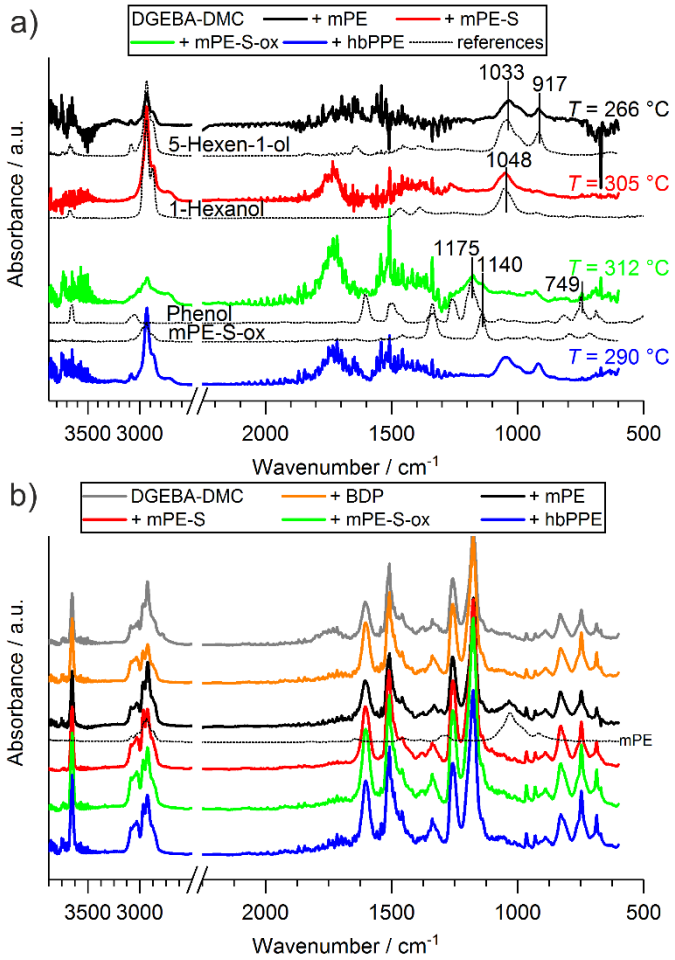

Figure 6.8. TG-FTIR spectra of pyrolytic decomposition products at a) decomposition step prior to main step, and at b) main decomposition step.

The evolved gas analysis of the resin composites further illustrated the FR mechanisms: FTIR analysis of the pyrolytic decomposition products (Figure 6.8) highlighted the evolution of specific products prior to the main decomposition step (Figure 6.8 a), namely 5-hexen-1-ol for **EP/mPE** and **EP/hbPPE**. For **EP/mPE-S**, the spectrum shared similarities with 1-hexanol, especially via the absorption band at 1048 cm^{-1} and the lack of absorption at 917 cm^{-1} which corresponds to δ_{oop}(C-H) of the vinyl groups. The spectrum of **EP/mPE-S-ox** at 312 °C exhibited decomposition products from the epoxy matrix, especially from phenol products, identified by the absorption bands at 1175 and 749 cm^{-1}. Moreover, the spectrum shares similarities with the evolved gas of pure **mPE-S-ox**, as identified by the band at 1140 cm^{-1} belonging to $\nu_s(SO_2)$, thus implying that some SO_2-species progressed into the gas phase. The spectra at the main decomposition step (Figure 6.8 b) showed the decomposition of the epoxy matrix, as evidenced by the similarities of all spectra with that of EP. As previously reported, [11] the spectrum of **EP/mPE** exhibited **mPE** signals even at the

main decomposition step, most probably due to phosphorylation of the resin caused by the strong reactivity of **mPE**.

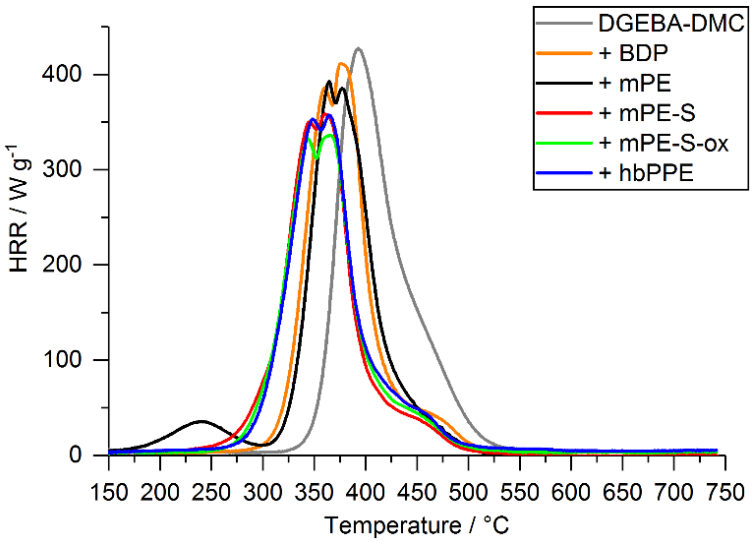

Figure 6.9. Heat release rates over time of EP and EP-FRs from pyrolysis combustion flow calorimetry (PCFC).

The resin composites were analyzed by means of pyrolysis combustion flow calorimetry (PCFC) to further understand how the evolved gas affects the gas phase. Although some FRs are known to act in the gas phase via radical scavenging, this mode of action cannot be detected in PCFC due to the complete oxidation of the pyrolysis products in the combustion zone. However, PCFC (otherwise known as micro cone calorimetry, i.e. MCC) may be used to measure fuel dilution effects, as the evolution of incombustible gases do not contribute to oxygen consumption, i.e. heat release. The production of incombustible gases can be quantified by changes in the the heat of complete combustion (h_c^0). The plot of HRR vs. time (Figure 6.9) of PCFC measurements pointed to a decrease in PHRR for most flame retardant-containing EPs, with **mPE-S-ox** lowering the PHRR of EP by 21% (340 W g^{-1}, as opposed to 429 W g^{-1} of EP). **EP/mPE-S-ox** also displayed the lowest heat release capacity (HRC), THE, and h_c^0, followed by **EP/mPE-S** (Table S6.2). The low molar mass S-FRs proved effective in producing incombustible products during pyrolytic decomposition. For **mPE-S-ox**, SO_2-release was identified in Py-GC/MS measurements, and PCFC results of **EP/mPE-S-ox** further prove that its release is a gas-phase mechanism of this FR. Moreover, **mPE-S** also produced a S-containing compound during pyrolysis, namely 1-hexanethiol or a derivative thereof. As this product further decomposes, it produced incombustible gases, as indicated by the reduction in h_c^0. Notably, **hbPPE** does not have the same effect in lowering h_c^0 as **mPE-S** or **mPE-S-ox** in **EP**; this is mainly due to the presence of linear and terminal units in the structure of **hbPPE**, which decomposed to form 1,5-hexadiene, analogous to **mPE**. The release of this compound

contributed to the combustion heat, thus explaining the increase in h_c^0 for **EP/mPE** compared to EP. Thus, the thio-ether groups competed with the vinyl-groups in **hbPPE**, leading to only moderate reduction in h_c^0.

6.5.7 Pyrolysis – Condensed Phase Activity of Resin Composites

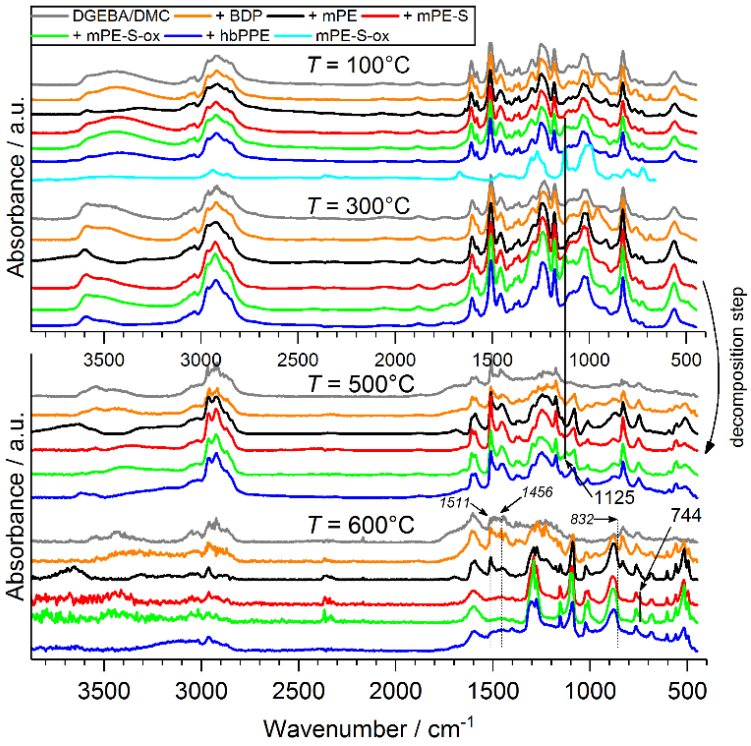

Figure 6.10. Condensed phase FTIR spectra from hot stage FTIR measurements of EP and EP-FRs at specific temperatures (100, 300, 500, 600 °C). Dotted lines/ italic numbers: bands not present in S-FRs.

The condensed phase spectra from hot-stage FTIR measurements (Figure 6.10) portrayed the change in specific absorption bands for all FR-containing EP composites. For **EP/mPE-S-ox**, the band of asymmetrical $\nu(SO_2)$ was visible at 1125 cm^{-1} between 100 – 500 °C, indicating its presence even after the main decomposition step of EP. Moreover, both **EP/mPE-S** and **EP/mPE-S-ox** exhibited an absorption band at 744 cm^{-1} at 600 °C, which correspond to S-containing species, such as ν(C-S) of O=CH-S-Ar, ν_s(S-O-C) of S-O-CH_2-R, or ν_s(P=S) of various P and S-containing compounds.[30, 32] The spectra of the S-containing EP-FRs and **EP/hbPPE** do not exhibit absorption bands at 1511, 1456 and 832 cm^{-1}, where EP, **EP/mPE**, and **EP/BDP** show signals. These bands originate from Bisphenol A-based compounds; their disappearance for **EP/mPE-S**, **EP/mPE-S-ox**, and **EP/hbPPE** indicates that S-FRs have a different decomposition mechanism.

The volatility of the low molar mass FRs was significantly reduced after thiol-ene reaction and oxidation (cf. TGA measurements in Figure 6.3), but the additional thio-ethers or sulfons affected the FR's reactivity. Phosphorylation is a major contributor to the condensed phase mechanism of P-FRs: the interaction between hydroxyl groups in the resin matrix and P-species leads to increased charring.[41] However, this mechanism changes when polar groups such as thio-ether or sulfone are present. Thus, although all FR are active in the condensed phase and S-containing FRs exhibited higher residue amounts in EP in pyrolysis measurements (Table 6.3), the type of residue is notably different from sulfur-free to S-containing FRs. It has been reported that the production of sulfonic acid further promotes char formation.[42-43] The presence of S-containing species may point to such a process for the tested FRs.

6.5.8 Fire Testing of Resin Composites

Fire testing via cone calorimeter measurements proved effective in examining the mode of action of the various FRs and especially the S-FRs. From the results (Table 6.3), a reduction of the total heat evolved (THE = total heat release [THR] at flame-out) of all FRs occurred, although the degree of reduction was distinct for each FR. **mPE** had the strongest impact on reducing the fire load of EP, lowering THE by 28% (Figure 6.11 b). The S-FRs **mPE-S-ox** and **mPE-S** exhibited a less pronounced fire load reduction, only lowering THE by 8 and 11%, respectively, whereas the benchmark FR **BDP** and the hyperbranched polymeric FR **hbPPE** both lowered THE by 17 and 19%, respectively. The HRR curves (Figure 6.11 a) shed some light on the mode of action of the low molar mass S-FRs: About 30 s after ignition, the curves of **EP/mPE** and **EP/hbPPE** exhibited a reduction in HRR and displayed a plateau-like area resultant from the formation of a protective char layer. This plateau is also visible for **EP/mPE-S** and **EP/mPE-S-ox**, but the reduction in HRR is less pronounced; furthermore, the peak of heat release rate (PHRR) of **EP/mPE-S-ox** was higher than that of **EP/mPE-S**, indicating that the protective layer effect was stronger for the thio-ether-containing FR than for the sulfone-containing one. This point is strengthened by the fact that **EP/mPE-S** and **EP/hbPPE** had similar PHRR values; both contain thio-ether groups. The changes to THE and PHRR can be visualized via Petrella-plot, where the fire load, i.e. THE, is plotted versus the fire growth index, i.e. PHRR/ time to ignition (t_{ig}) (Figure 6.11 c).[44] Both low molar mass S-FRs were able to lower fire load and fire growth index of EP in a similar manner, with **mPE-S** lowering THE more strongly. However, **mPE** and **hbPPE** were more effective in lowering fire load and fire growth rate of EP, illustrating that these materials were more able to bind fuel or create a strong protective layer than the S-FRs. This is further exemplified by the residue yields: while all FRs

increased char yields (Figure 6.11 d), **EP/mPE-S-ox** had the second lowest char yield of all tested materials, the lowest exhibited by **EP/BDP**. Moreover, the char yield of **EP/mPE-S** was in a similar range to **EP/hbPPE**, further highlighting that thio-ether-containing FRs were more effective in storing fuel in the form of carbonaceous char than sulfone-containing FRs. The S-FRs were able to create higher residue amounts in pyrolytic investigations of EP than during fire tests, and the low char yield also helps explain the higher fire loads of **EP/mPE-S** and **EP/mPE-S-ox** compared to the other EP-FRs. The low char yield in fire tests resulted from a reduced phosphorylation of the matrix, i.e. a low reactivity of the FR's decomposition products with the decomposing matrix. Moreover, mPE-S and mPE-S-ox have a lower P-content than mPE or hbPPE (Table 6.1), thus explaining the lower residue yields and higher fire load resulting from a reduced P-based condensed and gas phase activity. Fire tests proved that the high volatility and reactivity of **mPE**, as well as its higher P-content, was more effective in binding fuel compared to the thio-ether and sulfone-containing FRs. As evolved gas analysis proved the production of SO_2 for the sulfone-containing FR, it's gas diluting effect may be the main mode of action; however, it is plausible that the release of SO_2 inhibited the FR to effectively bind fuel in the condensed phase. Furthermore, the reduced P-content of **mPE-S-ox** further explains the lower residue yield and protective layer effect in EP, as well as a higher fire load.

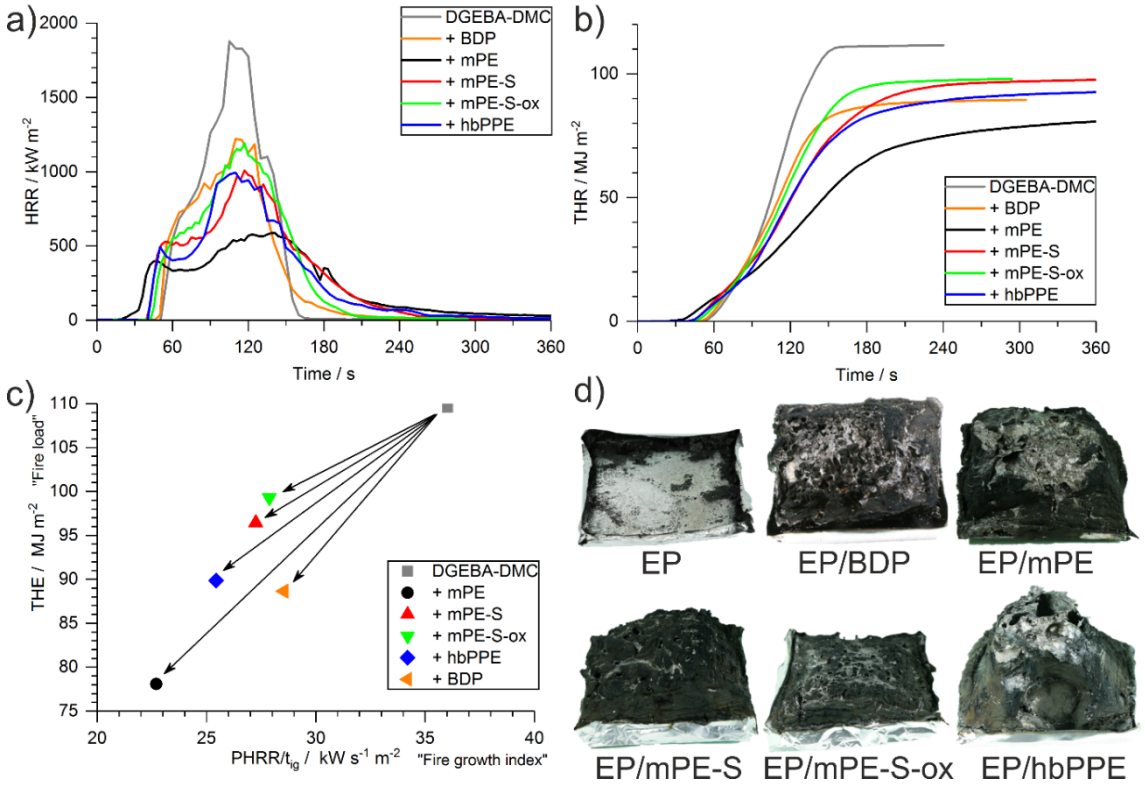

Figure 6.11. a) Heat release rate (HRR) versus time of EP and EP-FRs; b) Total heat release (THR) versus time of EP and EP-FRs; c) Petrella-plot of EP and EP-FRs; d) Residue photographs (10 cm x 10 cm aluminum tray base) of EP and EP-FRs after cone calorimeter measurements.

Table 6.3. Results from cone calorimeter measurements.

	THE / MJ m^{-2}	PHRR / kW m^{-2}	μ / wt.-%	EHC / MJ kg^{-1}
EP	108.4 ±2.6	1696 ±180	0.7 ±0.1	26.9 ±1.0
EP/BDP	87.5 ±1.2	1180 ±41	3.1 ±0.2	22.7 ±0.2
EP/mPE	78.1 ±6.5	885 ±16	9.2 ±0.1	21.6 ±1.8
EP/mPE-S	96.5 ±0.7	958 ±51	7.7 ±0.0	25.2 ±0.6
EP/mPE-S-ox	99.3 ±5.0	1219 ±26	4.7 ±0.5	27.5 ±0.4
EP/hbPPE	89.8 ±3.0	953 ±41	7.5 ±0.6	24.3 ±0.6

Total heat evolved (THE = total heat released at flame-out); peak of heat release rate (PHRR); char yield (μ); effective heat of combustion (EHC).

6.6 Conclusion

To gain further insight into the flame-retardant effect of polymeric hyperbranched poly(phosphoesters) **hbPPE**, the material was compared to two sulfur-containing low molar mass variants of the monomeric phosphoester **mPE**.

Pyrolytic decomposition investigations of the FRs illustrated that the increased thermal stability and higher residue yield of **hbPPE** compared to its monomer **mPE** stemmed not only from its higher molecular mass, but also from the thio-ether groups present in **hbPPE**: the thio-ether-containing **mPE-S** displayed a higher T_{dec} and residue yield than to **mPE**, and the sulfone-containing **mPE-S-ox** proved even more thermally stable and retained higher residues than **mPE-S**. The presence of sulfur altered the decomposition mechanism of the P-FRs: thio-ethers promoted the production of S-radicals which cross-linked to promote residue yield, while sulfonates decomposed to release incombustible SO_2.

In epoxy resins, the sulfur-containing FRs affected the glass-transition temperature of the resin less strongly than the sulfur-free **mPE**. Moreover, the presence of sulfur decreased the volatility of the P-FRs and encouraged an overlap of decomposition temperatures of FR and matrix, thus improving chemical reactivity. Moreover, the presence of sulfur increased condensed phase activity, and several sulfur species were identified in the residues via FTIR. Fire tests of FR-containing epoxy resins exemplified that **hbPPE**'s effectiveness as an FR was not rooted solely in the presence thio-ether groups, but the occurrence of both vinyl and thio-ether groups.

The results of this study highlight that the presence of sulfur in **hbPPE** played a significant role to the multifunctional qualities of the hyperbranched P-FR, mainly by improving thermal stability, reducing the impact on T_g of epoxy resins, and adding additional chemical decomposition mechanisms in the condensed phase and thus improving residue yields.

6.7 Acknowledgements

Funding: This work was supported by the Deutsche Forschungsgemeinschaft [DFG SCHA 730/15-1; DFG WU 750/8-1].

Alexander Battig thanks Dr. Katharina Kebelmann (BAM) for help with Py-GC/MS measurements and Patrick Klack (BAM) for support with the cone calorimeter. Jens C. Markwart is the recipient of a fellowship through funding of the Excellence Initiative (DFG/ GSC 266) in the context of the graduate school of excellence "MAINZ" (Materials Science in Mainz). Frederik R. Wurm and Jens C. Markwart thank Prof. Dr. Katharina Landfester (MPIP) for support.

6.8 References Chapter 6

[1] M. M. Velencoso, A. Battig, J. C. Markwart, B. Schartel, F. R. Wurm, *Angew Chem Int Edit* **2018**, *57*, 10450-10467.

[2] Q. F. Wang, W. F. Shi, *Polymer Degradation and Stability* **2006**, *91*, 1747-1754.

[3] C. J. Hawker, J. M. J. Frechet, *Journal of the American Chemical Society* **1990**, *112*, 7638-7647.

[4] Q. Cao, P. S. Liu, *European Polymer Journal* **2006**, *42*, 2931-2939.

[5] A. Asif, W. F. Shi, *European Polymer Journal* **2003**, *39*, 933-938.

[6] B. I. Voit, A. Lederer, *Chemical Reviews* **2009**, *109*, 5924-5973.

[7] C. R. Yates, W. Hayes, *Eur. Polym. J.* **2004**, *40*, 1257-1281.

[8] F. Marsico, A. Turshatov, R. Pekoz, Y. Avlasevich, M. Wagner, K. Weber, D. Donadio, K. Landfester, S. Baluschev, F. R. Wurm, *Journal of the American Chemical Society* **2014**, *136*, 11057-11064.

[9] K. Täuber, F. Marsico, F. R. Wurm, B. Schartel, *Polym Chem-Uk* **2014**, *5*, 7042-7053.

[10] A. Battig, J. Markwart, F. R. Wurm, B. Schartel, *Polym Chem-Uk* **2019**, *10*, 4346-4358.

[11] J. C. Markwart, A. Battig, L. Zimmermann, M. Wagner, J. Fischer, B. Schartel, F. R. Wurm, *ACS Applied Polymer Materials* **2019**, *1*, 1118-1128.

[12] B. A. Howell, Y. G. Daniel, *Journal of Fire Sciences* **2018**, *36*, 518-534.

[13] S. V. Levchik, E. D. Weil, *Polymer International* **2005**, *54*, 981-998.

[14] J. Green, *Journal of Fire Sciences* **1996**, *14*, 426-442.

[15] W. Pawelec, A. Holappa, T. Tirri, M. Aubert, H. Hoppe, R. Pfaendner, C. E. Wilen, *Polymer Degradation and Stability* **2014**, *110*, 447-456.

[16] J. Wagner, P. Deglmann, S. Fuchs, M. Ciesielski, C. A. Fleckenstein, M. Döring, *Polymer Degradation and Stability* **2016**, *129*, 63-76.

[17] U. Braun, U. Knoll, B. Schartel, T. Hoffmann, D. Pospiech, J. Artner, M. Ciesielski, M. Döring, R. Perez-Gratero, J. K. W. Sandler, V. Altstädt, *Macromolecular Chemistry and Physics* **2006**, *207*, 1501-1514.

[18] C. L. Rasmussen, P. Glarborg, P. Marshall, *P Combust Inst* **2007**, *31*, 339-347.

[19] M. R. Zachariah, O. I. Smith, *Combustion and Flame* **1987**, *69*, 125-139.

[20] R. M. Perez, J. K. W. Sandler, V. Altstädt, T. Hoffmann, D. Pospiech, M. Ciesielski, M. Döring, U. Braun, A. I. Balabanovich, B. Schartel, *Polymer* **2007**, *48*, 778-790.

[21] M. Lewin, *Journal of Fire Sciences* **1997**, *15*, 263-276.

[22] M. Lewin, J. Brozek, M. M. Martens, *Polymers for Advanced Technologies* **2002**, *13*, 1091-1102.

[23] M. Lewin, J. Zhang, E. Pearce, J. Gilman, *Polymers for Advanced Technologies* **2007**, *18*, 737-745.

[24] J. Y. He, G. Cai, C. A. Wilkie, *Polymers for Advanced Technologies* **2014**, *25*, 160-167.

[25] W. Zhao, B. Li, M. J. Xu, L. L. Zhang, F. M. Liu, L. M. Guan, *Polym Eng Sci* **2012**, *52*, 2327-2335.

[26] Y. H. Chen, H. Q. Peng, J. H. Li, Z. X. Xia, H. Tan, *Journal of Thermal Analysis and Calorimetry* **2014**, *115*, 1639-1649.

[27] B. Schartel, T. R. Hull, *Fire and Materials* **2007**, *31*, 327-354.

[28] B. Schartel, M. Bartholmai, U. Knoll, *Polymers for Advanced Technologies* **2006**, *17*, 772-777.

[29] M. S. F. Lie Ken Jie, O. Bakare, *Chem. Phys. Lipids* **1992**, *61*, 139-147.

[30] G. Socrates, *Infrared and Raman characteristic group frequencies: tables and charts*, John Wiley & Sons, **2004**.

[31] G. Camino, L. Costa, *Polymer Degradation and Stability* **1988**, *20*, 271-294.

[32] M. Hesse, H. Meier, B. Zeeh, *Spektroskopische Methoden in der organischen Chemie*, Georg Thieme Verlag, **2005**.

[33] P. J. Linstrom, W. G. Mallard, *Vol. 2018*, Institute of Standards and Technology, Gaithersburg MD, **2018**.

[34] J. P. Machon, A. Nicco, *European Polymer Journal* **1971**, *7*, 1693-1707.

[35] F. Vögtle, L. Rossa, *Angewandte Chemie-International Edition in English* **1979**, *18*, 515-529.

[36] E. Wellisch, E. Gipstein, O. J. Sweeting, *Journal of Applied Polymer Science* **1964**, *8*, 1623-1631.

[37] E. Wellisch, O. J. Sweeting, E. Gipstein, *J Org Chem* **1962**, *27*, 1810-&.

[38] M. Ciesielski, B. Burk, C. Heinzmann, M. Döring, in *Novel Fire Retardant Polymers and Composite Materials* (Ed.: D.-Y. Wang), Woodhead Publishing, **2017**, pp. 3-51.

[39] J. M. G. Cowie, V. Arrighi, *Polymers: chemistry and physics of modern materials*, CRC press, **2007**.

[40] J. Eichhorn, *Journal of Applied Polymer Science* **1964**, *8*, 2497-2524.

[41] B. Schartel, B. Perret, B. Dittrich, M. Ciesielski, J. Krämer, P. Müller, V. Altstädt, L. Zang, M. Döring, *Macromolecular Materials and Engineering* **2016**, *301*, 9-35.

[42] A. Ballistreri, G. Montaudo, E. Scamporrino, C. Puglisi, D. Vitalini, S. Cucinella, *J Polym Sci Pol Chem* **1988**, *26*, 2113-2127.

[43] A. Nodera, T. Kanai, *Journal of Applied Polymer Science* **2004**, *94*, 2131-2139.

[44] R. Petrella, *Journal of fire sciences* **1994**, *12*, 14-43.

6.9 Supporting Information

6.9.1 Pyrolysis–Gas Chromatography/ Mass Spectrometry

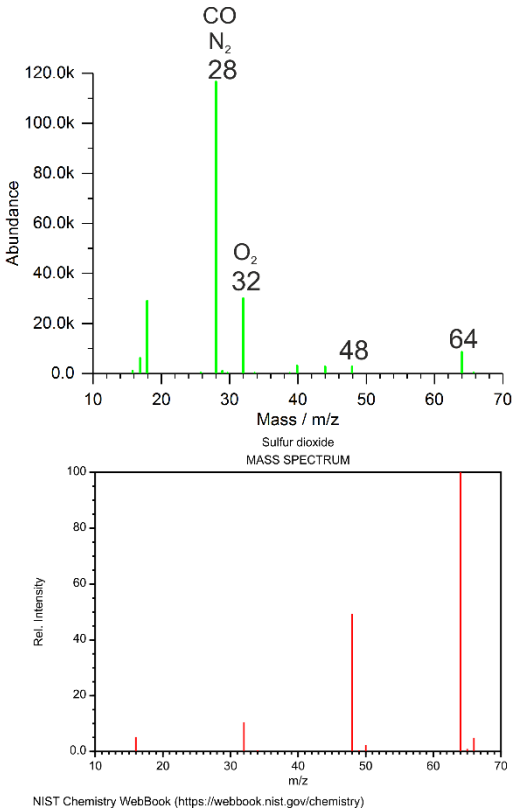

Figure S6.1. Mass spectrum of mPE-S-ox at 1.92 min, and a comparative spectrum of sulfur dioxide from the NIST database.[1]

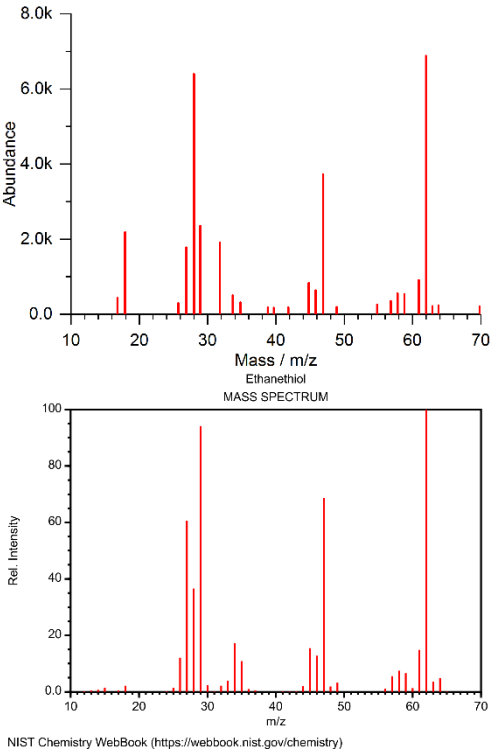

Figure S6.2. Mass spectrum of mPE-S at 2.26 min, and a comparative spectrum of ethanethiol from the NIST database.[1]

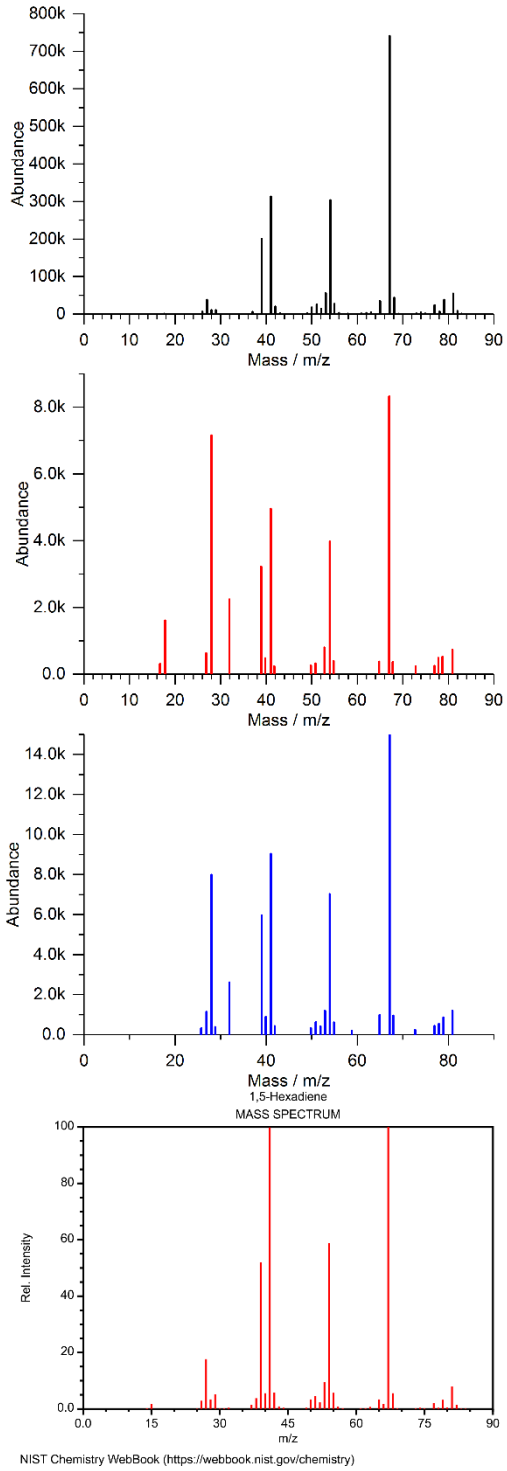

Figure S6.3. Mass spectra of mPE, mPE-S, and hbPPE at 2.63 min, and a comparative spectrum of 1,5-hexadiene from the NIST database.[1]

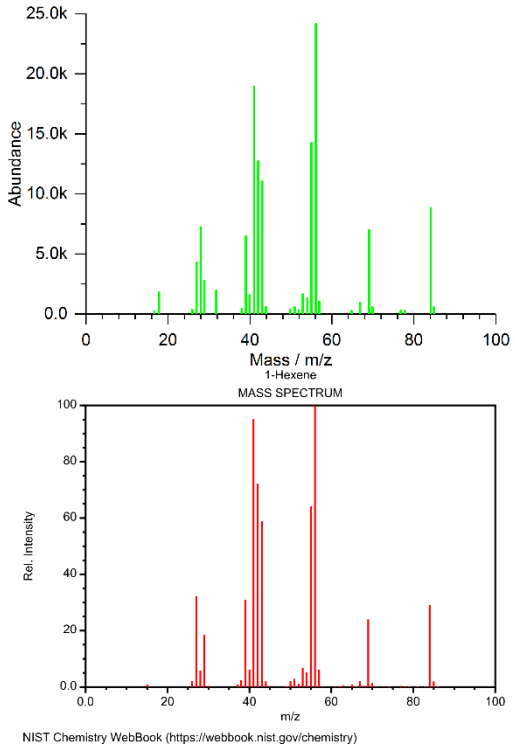

Figure S6.4. Mass spectrum of mPE-S-ox at 2.64 min, and a comparative spectrum of 1-hexene from the NIST database.[1]

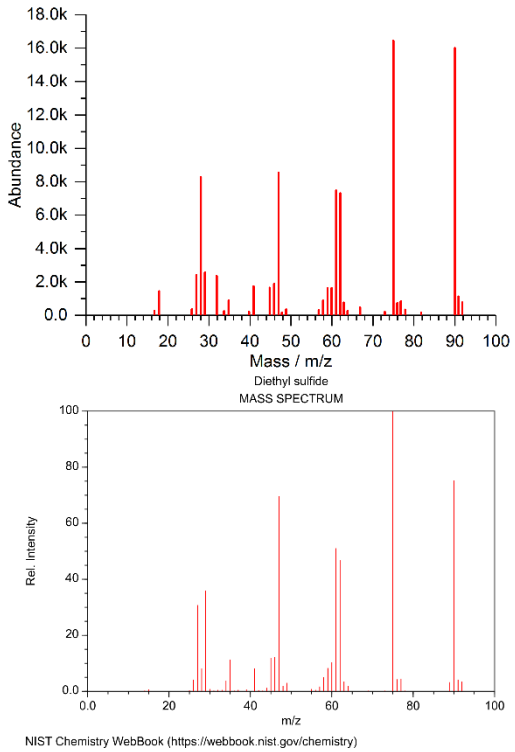

Figure S6.5. Mass spectrum of mPE-S at 3.38 min, and a comparative spectrum of diethyl sulfide from the NIST database.[1]

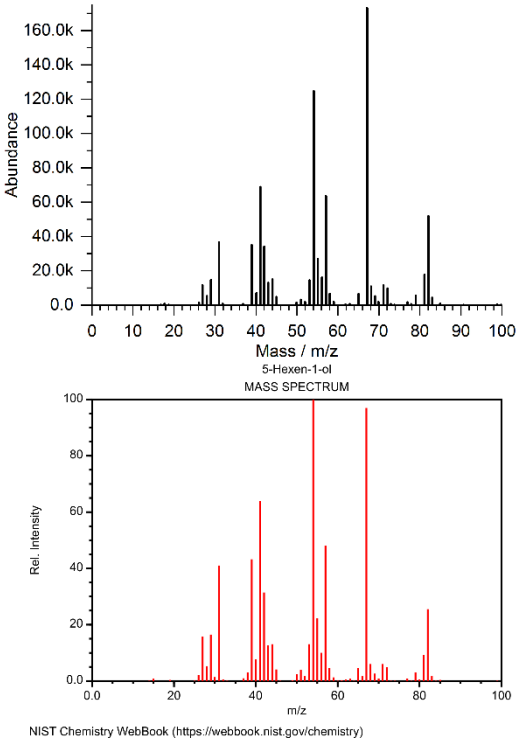

Figure S6.6. Mass spectrum of mPE at 6.63 min, and a comparative spectrum of 5-hexene-1-ol from the NIST database.[1]

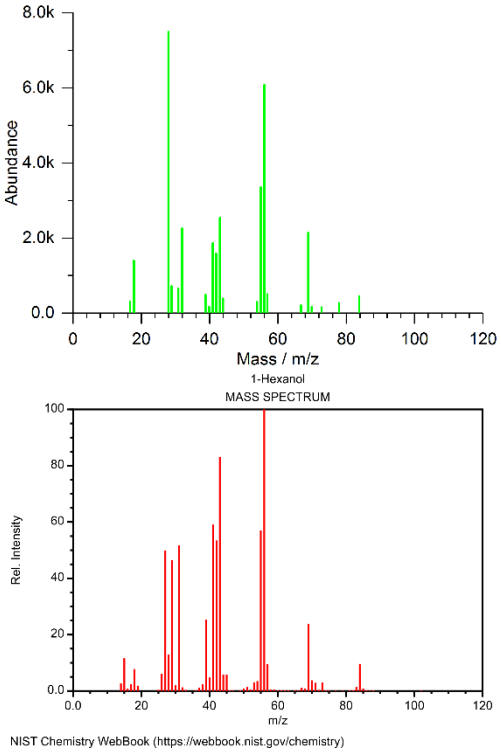

Figure S6.7. Mass spectrum of mPE-S-ox at 6.68 min, and a comparative spectrum of 1-hexanol from the NIST database.[1]

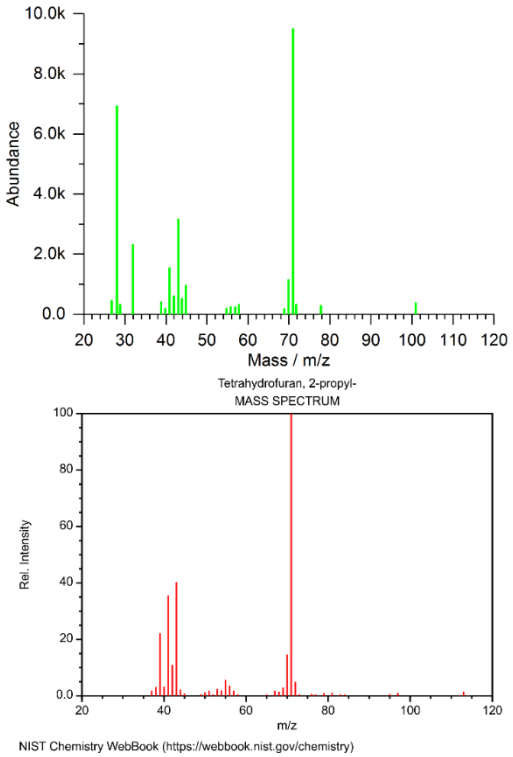

Figure S6.8. Mass spectrum of mPE-S-ox at 7.75 min, and a comparative spectrum of 2-propyl tetrahydrofuran from the NIST database.[1]

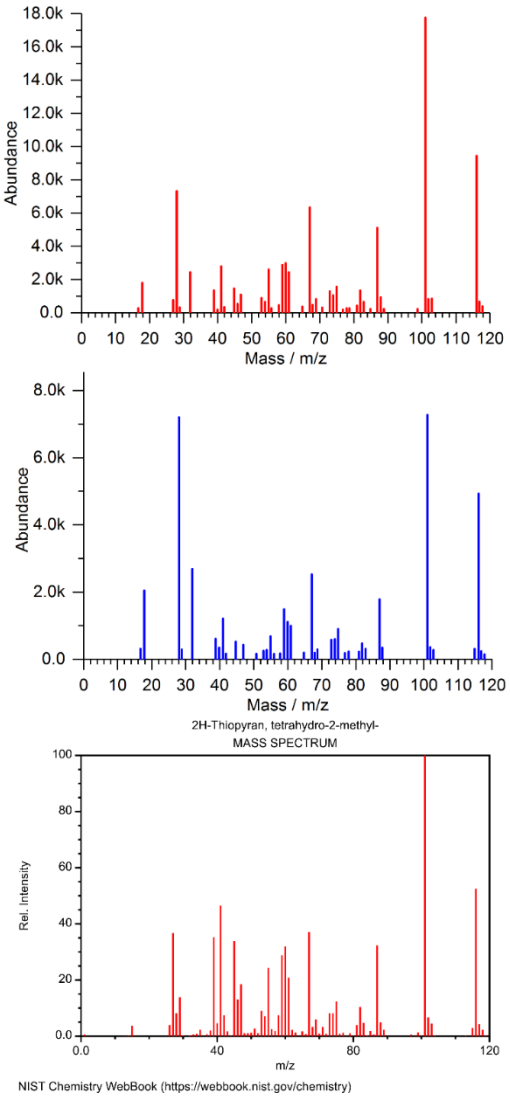

Figure S6.9. Mass spectra of mPE-S and hbPPE at 7.79 min, and a comparative spectrum of tetrahydro-2-methyl 2H-thiopyran from the NIST database.[1]

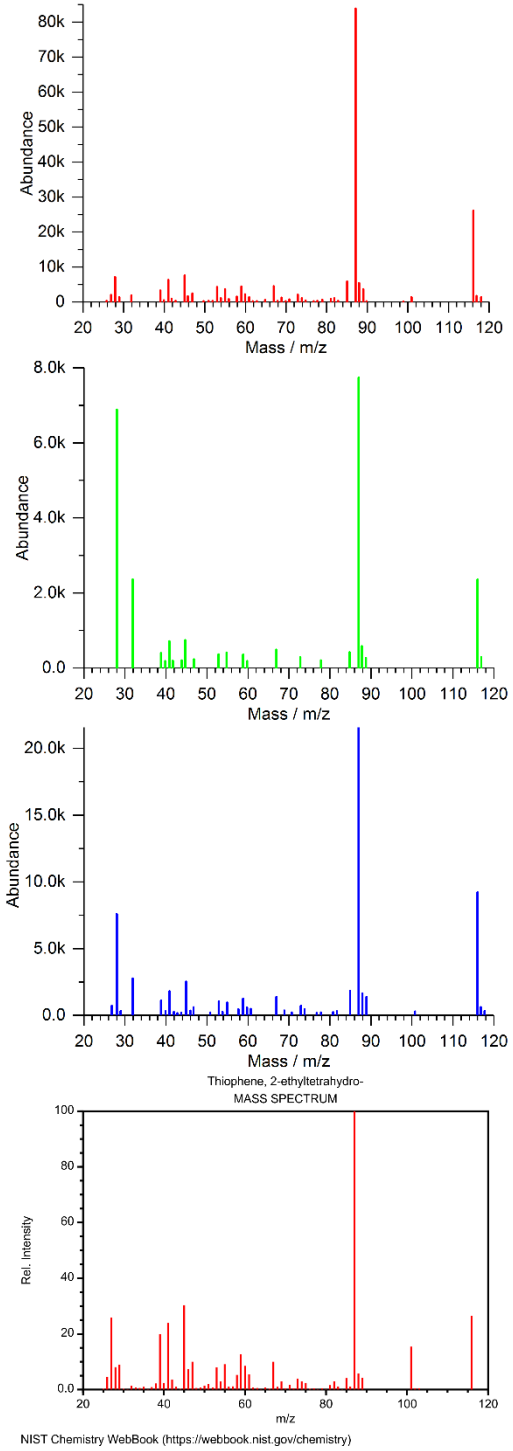

Figure S6.10. Mass spectra of mPE-S, mPE-S-ox, and hbPPE at 8.21 min, and a comparative spectrum of 2-ethyltetrahydro thiophene from the NIST database.[1]

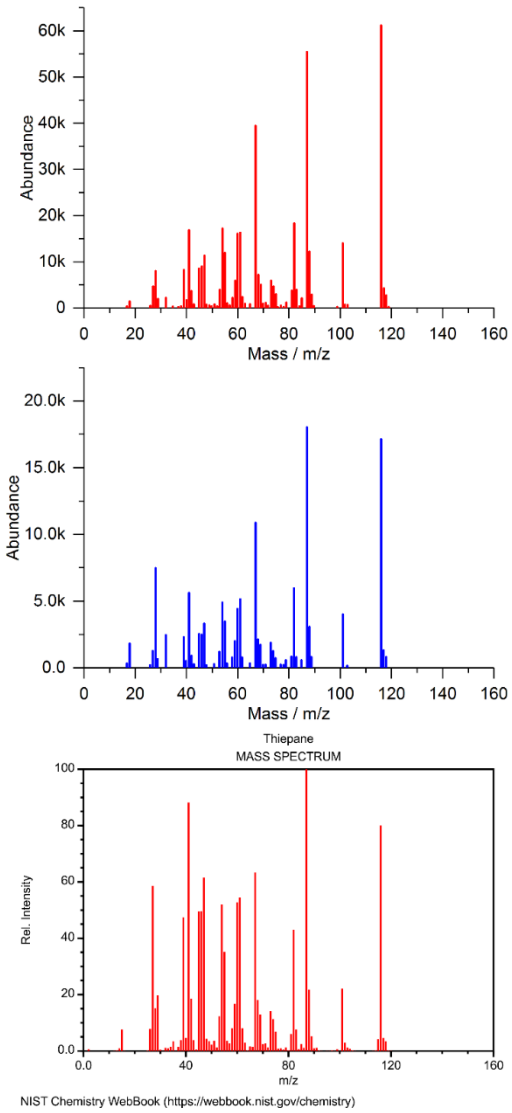

Figure S6.11. Mass spectrum of mPE-S and hbPPE at 9.29 min, and a comparative spectrum of thiopane from the NIST database.[1]

6.9.2 Thermogravimetric Analysis

Table S6.1. Results from thermogravimetric analysis (TGA) of EP and EP-FRs.

	$T_{5\%}$ / °C	T_1 / °C	ML_1 / wt.-%	T_{max} / °C	ML_{max} / wt.-%	T_2 / °C	ML_2 / wt.-%	Residue (700 °C) / wt.-%	Residue (calc) / wt.-%
EP	338 ±1	-	-	372 ±1	62.0 ±0.8	424 ±5	33.2 ±0.3	4.5 ±0.1	–
EP/BDP	304 ±1	-	-	357 ±1	74.6 ±0.2	423 ±1	16.1 ±0.3	8.2 ±0.1	4.2
EP/mPE	231 ±1	233 ±1	8.9 ±0.1	337 ±1	77.8 ±0.1	422 ±1	7.4 ±0.2	5.1 ±0.6	4.3
EP/mPE-S	286 ±1	294 ±1	9.8 ±0.2	358 ±1	73.0 ±0.1	434 ±1	8.8 ±0.1	6.3 ±0.2	4.7
EP/mPE-S-ox	289 ±2	286 ±1	10.2 ±0.2	356 ±0	73.1 ± 0.3	430 ±0	9.6 ±0.6	6.3 ±0.1	5.3
EP/hbPPE	289 ±1	-	-	351 ±1	54.6 ±0.1	424 ±6	23.2 ±0.7	7.7 ±0.1	5.2

Onset temperature ($T_{5\%}$); decomposition temperature of step prior to T_{max} (T_1); mass loss of decomposition step at T_1 (ML_1); temperature at maximum mass loss rate (T_{max}); mass loss of T_{max} (ML_{max}), decomposition temperature of step after T_{max} (T_2); mass loss of T_2 (ML_2).

6.9.3 Pyrolysis Combustion Flow Calorimetry

Table S6.2. Results from PCFC measurements.

	HRC / J g^{-1} K^{-1}	PHRR / W g^{-1}	THE / kJ g^{-1}	Residue / wt.-%	h_c^0 / kJ g^{-1}
EP	434 ±7	429 ±4	32.0 ±0.3	2.0 ±0.1	32.7 ±0.3
EP/BDP	413 ±1	381 ±3	30.1 ±0.4	6.2 ±0.1	32.1 ±0.4
EP/mPE	431 ±9	389 ±6	32.7 ±0.3	2.5 ±0.5	33.5 ±0.1
EP/mPE-S	396 ±13	353 ±4	30.4 ±0.1	4.9 ±0.6	31.9 ±0.3
EP/mPE-S-ox	349 ±7	340 ±7	30.0 ±0.2	4.9 ±0.1	31.5 ±0.2
EP/hbPPE	447 ±1	439 ±5	30.5 ±0.3	5.7 ±0.1	32.4 ±0.4

Heat release capacity (HRC); Peak of heat release rate (PHRR); Total heat evolved (THE); heat of complete combustion (h_c^0).

6.9.4 References SI Chapter 6

[1] Linstrom, P. J., Mallard, W.G., *NIST Standard Reference Database Number 69*. **2018**.

7. First phosphorus AB_2 monomer for flame-retardant hyperbranched polyphosphoesters: AB_2 vs A_2+B_3

Jens C. Markwart[a,b]+, Alexander Battig[c]+, Thomas Kuckhoff[a], Bernhard Schartel[c]*, Frederik R. Wurm[a]*

[a] *Physical Chemistry of Polymers - Max Planck Institute for Polymer Research, Ackermannweg 10, 55128 Mainz, Germany*

[b] *Technical Properties of Polymeric Materials - Bundesanstalt für Materialforschung und -prüfung (BAM), Unter den Eichen 87, 12205 Berlin, Germany*

[c] *Graduate School Materials Science in Mainz, Staudinger Weg 9, 55128 Mainz, Germany*

+ *These authors contributed equally to this work.*

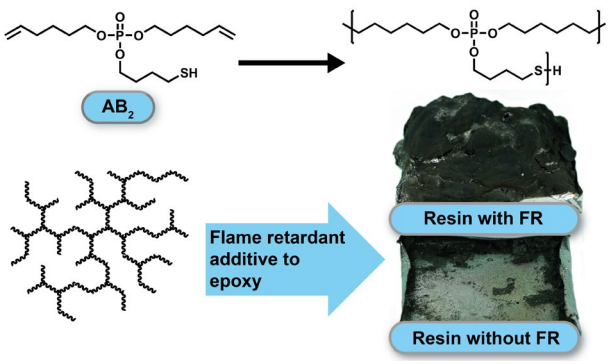

Keywords: phosphorus, flame-retardants, epoxy, hyperbranched polymers, polyphosphate

7.1 Notes

Alexander Battig performed the flame-retardancy measurements. Thomas Kuckhoff performed parts of the syntheses.

7.2 Abstract

Branched polymers are an important class of polymers with a high number of terminal groups, lower viscosity compared to their linear analogs and higher miscibility, which makes them especially interesting for flame retardant applications, where the flame retardants (FR) are blended with another polymer matrix. Hyperbranched polyphosphoesters (*hb*PPEs) are gaining more and more interest in the field of flame retardancy, as low molar mass FRs often have the disadvantage of blooming out or leaching, which is not desired in consumer products. Here, we present the first phosphorus-based AB_2 monomer for the synthesis of *hb*PPEs and assess its flame-retardant performance in an epoxy resin compared to a *hb*PPE synthesized by an A_2+B_3 approach. The *hb*PPE synthesized from an AB_2 monomer exhibited a slightly higher performance compared to a similar *hb*PPE, which was prepared by A_2 + B_3 polyaddition, probably due to its higher phosphorus content.

7.3 Introduction

Hyperbranched (*hb*) polymers, with their high number of terminal groups, lower viscosity, and higher matrix miscibility compared to their linear analogs, are especially interesting as flame-retardant additives, as effective blending with a polymer matrix is essential.[1-5] Moreover, flame retardants (FRs) with complex architectures have a decreased impact on the material properties of polymers.[6-7]

The synthesis of such dendritic polymers can be achieved by multi-step dendrimer syntheses, which is time-consuming, often needs several purification steps and therefore unattractive for large scale, flame-retardant applications.[1, 8] In contrast, *hb* polymers are readily available by one polymerization step, e.g. by polycondensation of commercially available A_2 + B_3 monomer mixtures. *hb* polymers do not exhibit an architecture as perfect as dendrimers, because the polymers are statistically branched with structural and molar mass dispersities. Despite these architectural differences, *hb* polymers still retain many of the particular properties of dendrimers.[1, 3]

Here we present, to the best of our knowledge, the first phosphorus-based AB_2 monomer for the synthesis of *hb* polyphosphoesters (*hb*PPEs), which are promising candidates as halogen-free flame-retardant additives.

To date, *hb*PPEs were synthesized by A_2 + B_3 approaches or by using AB* inimers, for which representative examples are given in **Scheme 7.1**. Penczek et al. prepared a family of oligomers with acidic end groups by an A_2 + B_3 approach by addition of H_3PO_4 to a bisphenol A based epoxy resins.[9] Liu et al. described a water-soluble *hb*PPE through a self-condensing ring-opening polymerization of an AB* inimer (2-(2-hydroxyethoxy)ethoxy-2-oxo-1,3,2-dioxaphospholane).[10] More recently, we used radical polyaddition of phosphorus-based B_3-monomers with dithiols to prepare *hb*PPEs, polyphosphoramidates, and -amides to elucidate their decomposition mechanism as flame-retardant additives in epoxy resins.[11]

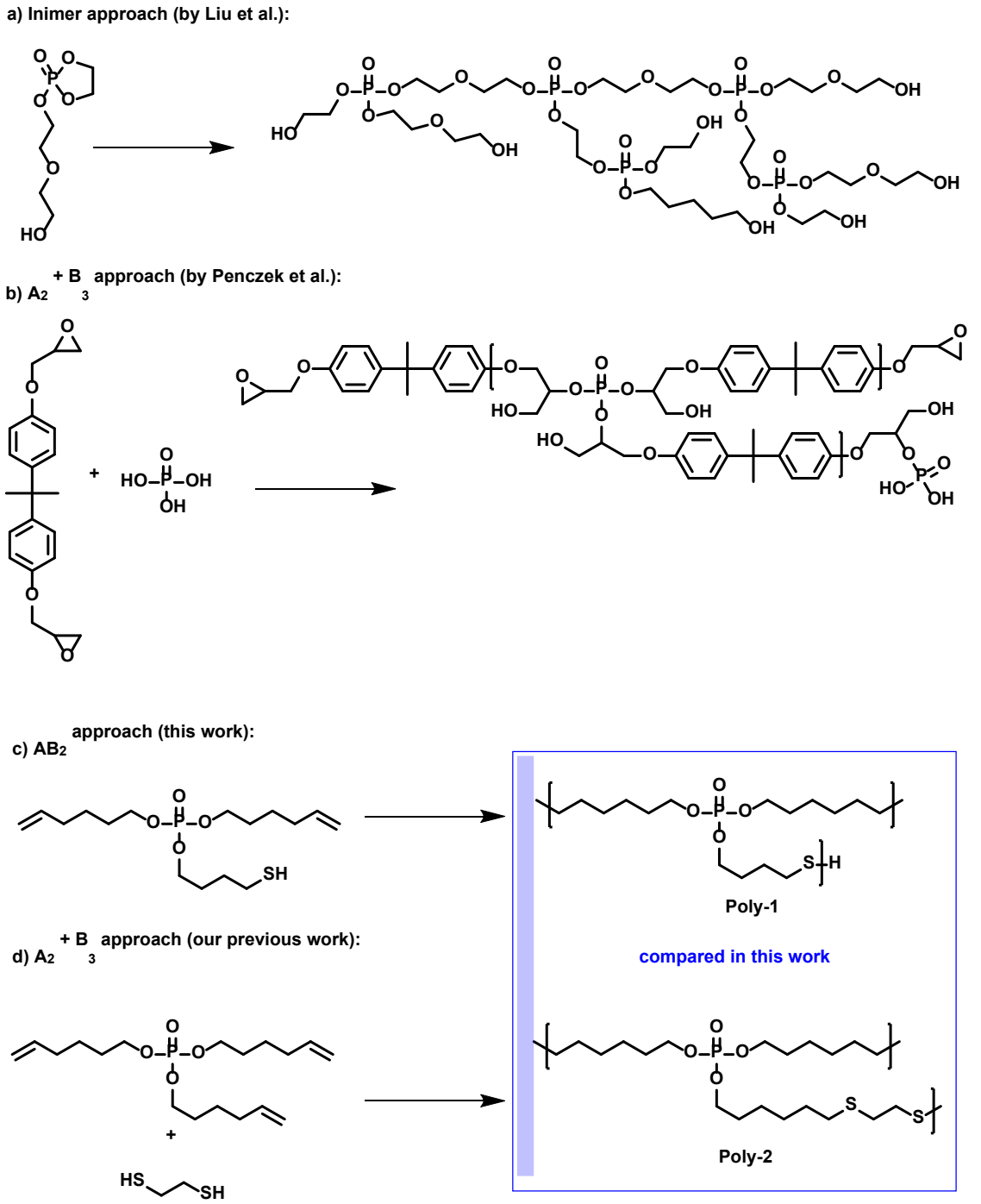

Scheme 7.1. . Examples of *hb*PPEs in literature: (**a**) *hb*PPEs via inimer approach by Yan et al.[10] (**b**) $A_2 + B_3$ approach by Penczek et al.[9] (**c**) this work: AB_2 monomer and (**d**) the comparison $A_2 + B_3$ approach by Battig et al.[11]

Previous studies used *hb*PPEs due to their biocompatibility and biodegradability for mostly biomedical[12-13] or optical applications[14]. With the ban of some halogenated FRs, phosphorus-based derivatives as effective alternatives are in growing demand in recent years.[15-18] Moreover, polymeric FRs are interesting as they exhibit less blooming out or leaching compared to low molar mass FRs, which is not desired in consumer products.[19] In addition, the thermal stability of low

molar mass FRs is usually lower, thus limiting their processability. In comparison, oligomeric or polymeric FRs exhibit increased thermal stability and therefore higher effectiveness, which leads to improved chemical interaction during decomposition, yielding higher char yields and better overall flame retardancy.[11, 20-21] Furthermore, FRs with different architectures have been investigated, stressing the impact of complex chemical structure on the mechanical properties and glass-transition temperature (T_g) of the polymer matrix.

With the first example of an AB_2-type phosphate monomer for radical polycondensation, we present a straightforward approach to *hb*PPEs and thus avoid the chance of cross-linking during the synthesis. In addition, the versatile monomer design, which was exemplarily used for **1**, allows further tuning of the P-content or the hydrophilicity, i.e. matrix compatibility, by variation of the alkyl-spacers, which makes the herein presented approach also applicable for other polymer matrices.

7.4 Results and Discussion

For the synthesis of hyperbranched (*hb*) polymers, two common approaches exist: The AB_n and $A_n + B_m$ approach.[22] In the AB_n approach, first envisioned by Flory in 1952, only a single monomer with an AB_n ($n \geq 2$) structure is used.[23] When A and B groups react selectively with each other, a statistically branched polymer without cross-linking is generated.[24]

In the $A_n + B_m$ approach, two monomers are used for polymerization (A_n and B_m ($n, m \geq 2$)), with the most common method being the $A_2 + B_3$ approach, as several monomers are commercialized. However, to obtain soluble polymers, the polymerization needs to be terminated before the gel point, which requires adjustment of the reaction conditions, or adjustment of the monomer feed-ratio, etc. for each monomer set.[24Wurm, 2012 #574, 25-26]

For the synthesis of a *hb* polyphosphoester (*hb*PPE) via the AB_n approach, an AB_2 phosphoester with two different reactive groups (A and B) was prepared: di(hex-5-en-1-yl)(4-mercaptobutyl)phosphate (**1**) was synthesized in a four step reaction, starting from $POCl_3$ and 4-bromobutan-1-ol (**Scheme 7.2**). 4-Bromobutan-1-ol was obtained from refluxing THF with HBr for several hours, followed by neutralizing with $NaHCO_3$ and extraction with DCM, according to a literature protocol.[27] An excess $POCl_3$ was reacted with 4-bromobutan-1-ol. Removing the excessive amount of $POCl_3$ gives compound **1a**. **1a** was used in the next step without further purification and treated with 5-hexen-1-ol to give compound **1b**. The electrophilic alkyl bromide in **1b** renders it a versatile precursor for various modifications like the introduction of other

functional groups or as a monomer for ADMET itself. **1b** was mixed with potassium thioacetate and stirred overnight to obtain compound **1c**, which was purified by solvent extraction. The final AB_2-monomer **1** for radical polyaddition was obtained after treating **1c** with hydrazine, which cleaved the thioacetate group and released the free thiol. Monomer **1** is a liquid at room temperature and has a phosphorus content of 8.84 wt.%. It is soluble in most organic solvents (e.g. toluene, tetrahydrofuran, ethyl acetate, acetone, dichloromethane and chloroform), but insoluble in water. It is important to mention that the butyl spacer between thiol and phosphorus is essential for the monomer stability: a similar monomer structure with an ethyl spacer was recently used to prepare linear PPEs with pendant 2-acetylthioethyl side chains.[28] In this case, the pendant group acted as a protective group for the P-OH group after treatment with hydrazine, followed by a 3-exo-tet mechanism to release the P-OH group after cleavage of the phosphoester.

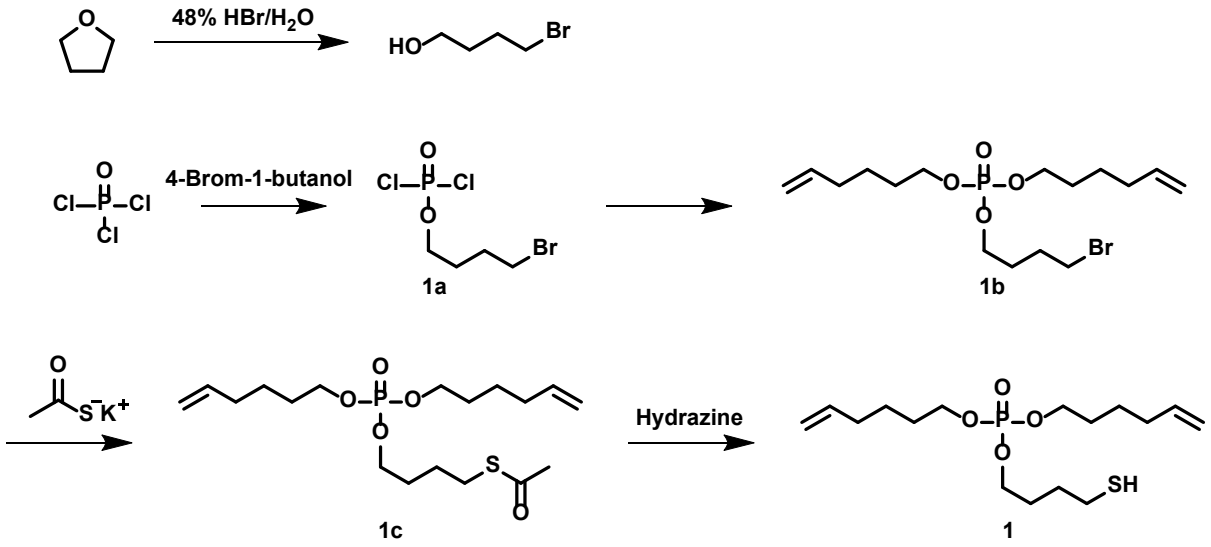

Scheme 7.2. Synthesis scheme of di(hex-5-en-1-yl)(4-mercaptobutyl)phosphate (**1**).

^{1}H NMR spectroscopy (**Figure 7.1a**) of **1** revealed two distinct resonances at 2.60 ppm (methylene group next to the thiol) and 1.36 ppm (SH). The olefinic signals were detected as multiplets in the region of 5.80 ppm and 5.00 ppm. The methylene group next to the double bond was found at 2.09 ppm and the methylene group next to the P-O group had a resonance at 4.05 ppm. The remaining signals of the methylene units were detected between 1.81 ppm and 1.45 ppm. The ^{31}P NMR spectrum shows a single signal at -0.68 ppm (**Figure 7.1c**).

Compound **1** was used as AB_2 monomer for the radical thiol-ene polyaddition to produce *hb* **poly-1** (**Scheme 7.3**). The statistically branched polymer with dendritic (D), linear (L), and terminal (T) units (cf. **Scheme 7.3**) was obtained as a viscous oil with a T_g of ca. -88 °C (**Figure 7.1i**). The ^{1}H NMR pattern of **poly-1** was very similar to that of **1** (**Figure 7.1b**); however, with increasing degree of

polymerization, the olefinic resonances, the methylene group next to the S-H group and the S-H signal decreased. Due to signal overlap, calculation of a degree of branching was not possible. The polymerization was followed by GPC and NMR by taking samples throughout the reaction and calculating the ratio between the methylene groups next to the P-O (n_{Ester}) and the double bond ($n_{Double\text{-}bond}$) $n_{Double\text{-}bond}/n_{Ester}$ (marked blue in **Figure 7.1f**). During polymerization, a new resonance appeared at 2.54 ppm representing the methylene groups next to the thioethers. Polymerization was conducted at different temperatures (50 °C, 70 °C, and 90 °C) with 0.03 eq. AIBN and additionally with different amounts of AIBN (0.03 eq., 0.06 eq. and 0.09 eq.) at 70 °C (e.g. **Figure 7.1h**). From the NMR data, only very slow reaction kinetics were detected at 50 °C, while at elevated temperatures (70 °C), no further reaction was observed after 7h (**Figure 7.1g**). With increasing initiator concentration, a slight increase in molar mass was observed (**Figure 7.1e**). The ^{31}P NMR resonance of **poly-1** remained relatively unchanged compared to the monomer with a single signal at -0.70 ppm (**Figure 7.1d**). As the degree of polymerization increased, $n_{Double\text{-}bond}/n_{Ester}$ became smaller.

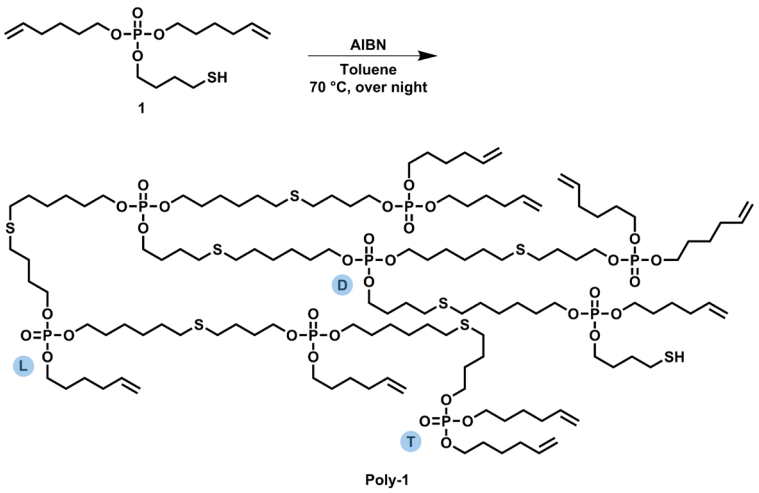

Scheme 7.3. Hyperbranching polymerization of monomer **1** to **poly-1** by radical thiol-ene polyaddition.

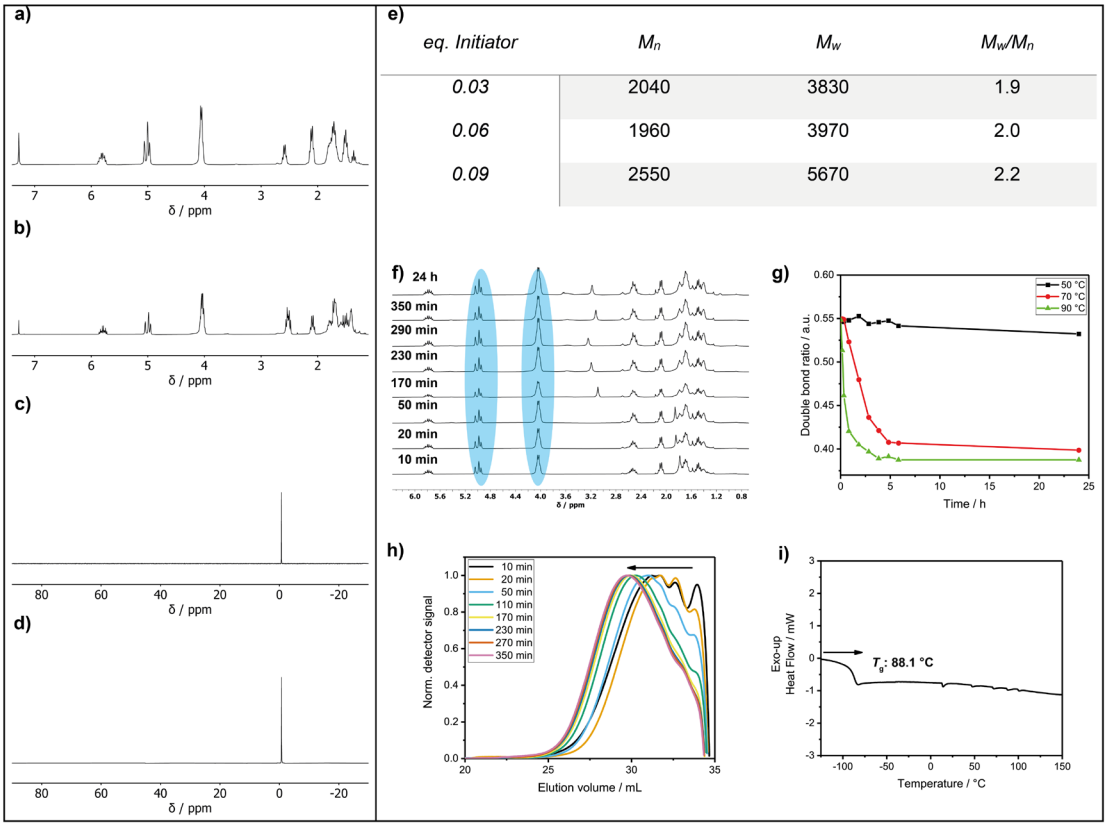

Figure 7.1. ^{1}H NMR spectra of **1** (**a**) and **poly-1** (**b**); ^{31}P NMR spectra of **1** (**c**) and the **poly-1** (**d**). **e)** Molar masses of the polymer at different initiator equivalents; (**f**) ^{1}H NMR kinetic of the polymerization of **1** at 90 °C and 0.03 eq. AIBN. **g)** Polymerization kinetics measured by NMR (change of $n_{\text{Double-bond}}/n_{\text{Ester}}$ over time) at different temperatures (50 °C, 70 °C and 90 °C). **h)** GPC kinetics of the polymerization of **1** with 0.09 eq. AIBN (measured in DMF). **i)** Differential scanning calorimetry (DSC) of **poly-1** with a T_g at 88.1 °C.

For the flame retardancy investigations, the resulting polymer had an M_w of 5,500 g/mol with an M_w/M_n of 2.39 (GPC in DMF). **Poly-1** was used as an additive flame retardant (FR) in epoxy resins, and the FR properties were compared to a similar *hb*PPE prepared by the $A_2 + B_3$ approach (**poly-2, Scheme 7.1**), M_w of 11,300 g/mol with an M_w/M_n of 3.29 (GPC in THF)[11], and a commercial phosphate-based FR, namely bisphenol A bis(diphenyl phosphate) (**BDP**), which was already used in epoxy resins like DGEBA/DMC.[19, 29] The ratio $n_{\text{Double-bond}}/n_{\text{Ester}}$, an indication of the amount of terminal double bonds, was identical for **poly-1** and **poly-2** (0.39). Looking at the phosphorus content, **poly-1** exhibits the same amount of P when compared to the monomer. In contrast, for **poly-2** the P content varied, depending on the monomer ratio and workup procedure. The theoretical phosphorus content deviated from the measured phosphorus content after precipitation. The theoretical phosphorus content of **poly-2** is 5.1 wt.-%, the measured phosphorus content by elemental analysis is 7.7 wt.-%.

7.4.1 Pyrolysis: Thermal decomposition of FRs via TGA

The pyrolytic decomposition of the FRs was investigated using thermogravimetric analysis (TGA) (**Figure 7.2**). During burning, the thermal decomposition of the material feeds volatile fuel into the flame zone, where exothermal combustion reactions, i.e. oxidation, occur. However, at the solid/gas interface, the reactions in the anaerobic pyrolysis zone determine the fire behavior. This model is accurate for polymeric materials in developing, which are simulated in the cone calorimeter, but also reaction-to-small-flame tests such as UL94 and LOI. Therefore, investigations into the pyrolytic reactions of FRs and FR-containing polymers via TGA in nitrogen atmosphere are an important analytical tool to understand the chemical mechanisms underlying the FR's modes of action.[30]

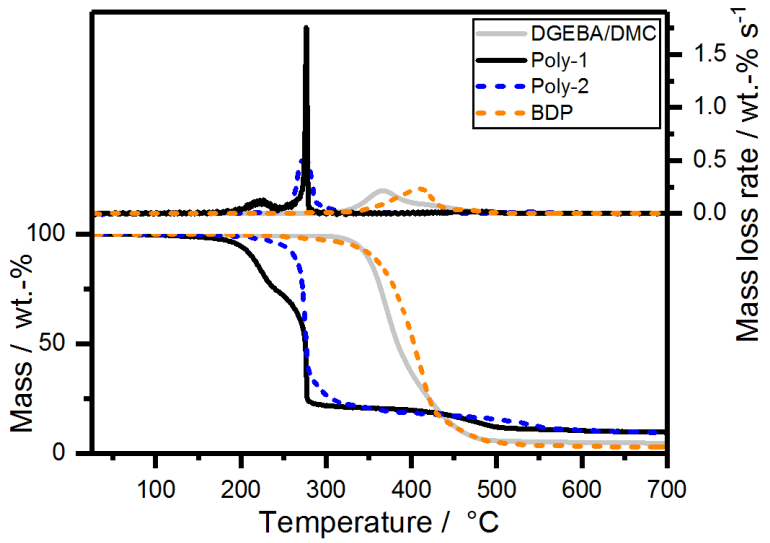

Figure 7.2. Mass loss (bottom) and mass loss rate (top) over *T* of **poly-1**, **poly-2**, bisphenol A bis(diphenyl phosphate) and neat epoxy resin from TGA measurements (10 K min^{-1}; N_2).

The mass loss curve of **poly-2** exhibited a main single decomposition step at 274 °C with a gradual decomposition thereafter (**Figure 7.2**). **Poly-1** exhibited an additional decomposition step at ca. 226 °C, followed by the second decomposition step at the same temperature as **poly-2**. The additional decomposition step might be rationalized with the cleavage of the terminal alkyl-SH group, similar to the mechanism described previously by Markwart et al.[28], which was confirmed by the presence of tetrahydrothiophene (from pyrolysis-(Py)-GC/MS measurements at 250 °C (**Figure S7.6** and **S7.8**) and TGA-FTIR measurements (**Figure S7.16**)). The amount of residue at 700 °C was very similar for both polymers (**poly-1**: 9.7 wt.-%, **poly-2**: 9.3 wt.-%).

7.4.2 Pyrolysis: Evolved gas analysis of FRs via TG-FTIR

Evolved gas analysis during pyrolysis of **poly-1** was performed via Py-GC/MS and TG-FTIR measurements. The analysis of epoxy resin (EP) and **poly-2** has been previously described in detail and will therefore not be discussed herein.[11, 31] For **poly-1**, two single-shot Py-GC/MS measurements at varied pyrolysis temperatures (250 °C and 500 °C) were conducted to isolate the decomposition products in the first decomposition step. The gas chromatogram at 250 °C (**Figure S7.6**) displays a single large signal at 5.62 min retention time, while at 500 °C (**Figure S7.7**), additional signals between 2.60 – 3.56 min were detected, as well as minor signals >5.62 min. The mass spectrum at 5.62 min was identified as tetrahydro thiophene (**Figure S7.8** and **S7.9**), thus confirming the cleavage of alkyl-SH groups of **poly-1** during the first decomposition step seen in TGA. The signals between 2.60 – 3.56 min corresponded to 1,5-hexadiene (**Figure S7.10** and **S7.11**) and its thermal rearrangement products. The rearrangement is proven by the presence of cyclohexane (**Figure S7.12** and **S7.13**) at 3.56 min, a product of cyclization of 1,5-hexadiene. At 6.57 min, the signal was identified as 5-hexen-1-ol (**Figure S7.14** and **S7.15**) resulting from hydrolysis of the phosphate-moiety.

7.4.3 Pyrolysis: EP-FR preparation and material properties

The FR-performances of **BDP**, **poly-1**, and **poly-2** were studied in an epoxy resin (**EP**) based on bisphenol A diglycidylether (DGEBA) and 2,2'-dimethyl-4,4'-methylene-bis-(cyclohexylamine) (DMC). All epoxy plates were prepared in the following manner: DGEBA was mixed with the respective FR (loading: 10 wt.-%) until homogenous. Then, DMC was added, and the mixture was poured into appropriately sized aluminum molds, followed by curing for 30 min at 90 °C, 30 min at 120 °C, and 1 h at 150 °C. Additive FRs can act as plasticizers in epoxy resins, thus reducing the glass transition temperature (T_g) of the resulting composite. Differential scanning calorimetry (DSC) measurements revealed that the flame retardant containing epoxy resins (**EP-FRs**) lowered T_g by an average of 24 °C: **Poly-1** had the strongest impact on the T_g of **EP**, lowering it by about 30 °C to 124 °C ($T_{g,\,EP}$ = 155 °C), while **poly-2** and **BDP** had a similar impact on the T_g of EP ($T_{g,\,EP\text{-}poly2}$ = 132 °C; $T_{g,\,EP\text{-}BDP}$ = 133 °C).The impact of FRs on the T_g of EP is presented in **Figure S7.20**, and the change of T_g relative to **EP** is noted.

7.4.4 Pyrolysis: Thermal decomposition and evolved gas analysis of EP-FRs via TGA and TG-FTIR

The decomposition behavior of **EP-FRs** was investigated by analyzing the mass loss and evolved gas during pyrolytic decomposition via TGA coupled with FTIR (**Table S7.2**). A significant change in decomposition behavior was observable for all **EP-FRs**, as the mass loss and mass loss rate curves (**Figure 7.3**) and the change in residue yields at 700 °C proved. The pure epoxy decomposed with an onset temperature ($T_{5\%}$) of 338 °C and reached the temperature of maximum mass loss rate (T_{max}) at 372 °C. EP decomposed in a single main step with a mass loss equal to 62 wt.-%. Following the main decomposition step, a shoulder beginning at 424 °C with a mass loss of 33 wt.-% was observed. At 700 °C, the residue yield was 4.5 wt.-%. The mass loss and evolved gas analysis of the epoxy resin (DGEBA/DMC) has been extensively investigated; therefore, it will not be discussed further.[32-33] When **BDP** was added to the resin (**EP-BDP**), the composite decomposed similarly to the pure **EP**, but $T_{5\%}$ was lowered by about 33 °C, and T_{max} was 15 °C lower than **EP**. This change is attributed to a reduction in cross-linking density of the **EP**-system when additives are present.[34] The plateau which started at 423 °C exhibited a lower decomposition rate compared to pure **EP**. An increase in mass loss at T_{max} to 75 wt.-% and a decrease to 16 wt.-% at the shoulder was observable. An explanation for this phenomenon is the interaction of the FR with the decomposing matrix.[35] More specifically, the phenol-derivates and cycloalkanes are bound; these exhibit a production rate maximum in this temperature range.[36] As a result, the residue yield of **EP-BDP** increased to 8.1 wt.-%, which is nearly twice that of pure EP.

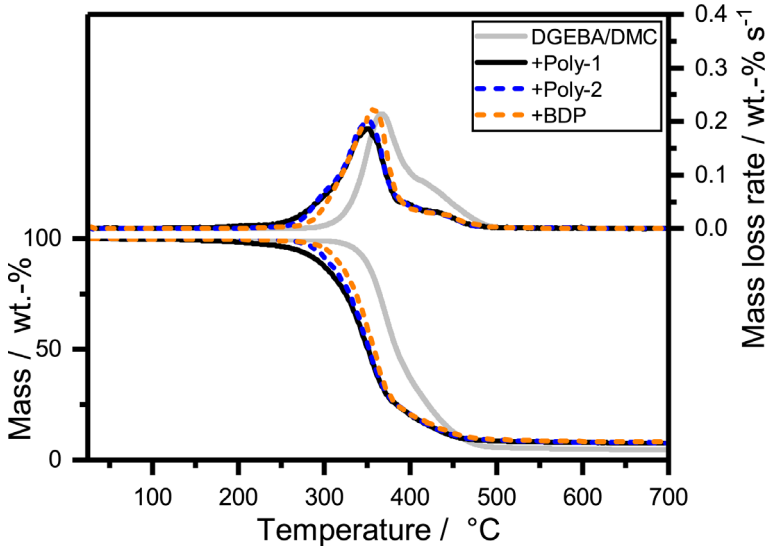

Figure 7.3. Mass loss (bottom) and mass loss rate (top) over *T* of EP-FRs from TGA measurements (10 K min^{-1}; N_2).

All *hb*-FR containing EPs (EP-*hb*-FRs) exhibited a decomposition behavior similar to **EP-BDP**. The $T_{5\%}$ of **EP** was lowered by 70 °C for **poly-1** and 47 °C for **poly-2**. T_{max} was also lowered when FRs were present, on average by approx. 16 °C. The lower $T_{5\%}$ of **EP-poly-1** compared to **EP-poly-2** is caused by the additional decomposition step in **poly-1**. All residue yields of **EP-FRs** were in a similar range, and all investigated FRs increased the residue of **EP** (7.9 and 7.7 wt.-% for **poly-1** and **poly-2**, respectively**,** and 8.1 wt.-% for **BDP**). The neat **EP** had a residue yield of only 4.6 wt.-%. This increase in residue indicates that the tested FRs interact with the decomposing matrix. As a result, thermally stable residues are formed.

From the evolved gas analysis of **EP-FRs** via TG-FTIR (**Figure S7.17**), two distinct decomposition products were visible for **EP-poly-1** and **EP-poly-2**, the first appearing in the range of about 290 °C and the second between 360 – 380 °C. At ca. 290 °C, the spectra of **EP-poly-1** and **EP-poly-2** exhibited the evolution of 5-hexen-1-ol, a product of either hydrolysis or transesterification. Its presence indicates that *hb*-FRs are active near $T_{5\%}$, forming either lower molecular phosphates (hydrolysis) which are active in the condensed phase, or phosphorylating the polymer matrix (transesterification), thus forming char precursors. The condensed phase mode of action is additionally proven by hot-stage FTIR (**Figure S7.19**). At 360 – 380 °C, all spectra are identical to EP, as the matrix decomposes in this temperature range.

7.4.5 Pyrolysis: Condensed phase analysis of EP-FRs via Hot-stage FTIR

The condensed phase mode of action of **poly-1** and **poly-2** in **EP** was proven by hot-stage FTIR measurements (**Figure S7.18** and **S7.19**). **Figure S7.18** displays the unique signals of **EP-poly-1** at 300 °C, namely 1146 and 1108 cm^{-1}, which are shifted to slightly lower wavenumbers and increase in intensity at 500 °C (**Figure S7.19**). These signals may correspond to ν(P=O) of R_2-(P=O)-OH resulting from the cleavage of terminal alkyl-SH groups which occurs more readily than cleavage of terminal hexene-moieties, as observed in Py-GC/MS (**Figure S7.8**) and TG-FTIR measurements (**Figure S7.16**) of **poly-1**. It is conceivable that **poly-1** is more reactive than **poly-2** in terms of phosphorylation of the epoxy resin matrix, especially given the increase in residue yields of fire testing and pyrolysis (**Table S7.1** and **S7.2**, respectively). At 600 °C, the hot-stage FTIR spectrum of **EP-poly-1** exhibits many bands that are also present in **EP-poly-2** and **EP-BDP**, which have already been previously described as phosphorus signals.[11] Moreover, additional bands at 1400, 1125, 1010, 974, and 585 cm^{-1} are present. Many types of compounds, including vinylene-moieties, cyclic aliphatic hydrocarbons, and secondary or tertiary alcohols, present signals at these wavenumbers. While the identification of specific compounds in hot-stage FTIR is not always

possible, it is certain that the spectrum of **EP-poly-1** presents clear signals that are distinct and different from EP, thereby proving a condensed-phase spectrum of **poly-1** in **EP**.

7.4.6 Fire testing: Forced flaming conditions

All **EP-*hb*-FRs** reduced the fire load (THE) of EP. **Poly-1** decreased the fire load of EP by 21%, whereas **poly-2** decreased the fire load by 17% and **BDP** by 19%. **Poly-1** reduced THE of **EP** more strongly than **poly-2** because it was able to retain more fuel in the condensed phase, as evidenced by its higher residue yield (**Figure 7.4d**). This fuel retention may be caused by the higher reactivity of **poly-1** compared to **poly-2**: as **poly-1** has a lower $T_{5\%}$, its decomposition products may interact earlier with the decomposing matrix than **poly-2**, therefore increasing char yield, i.e. fuel fixation, and thus lowering THE. The tested FRs lowered the peak of heat release rate (PHRR) of **EP** by ca. 30% for **BDP** and **poly-1,** and by 44% for **poly-2**. The HRR curves (**Figure 7.4a**) indicate that the formation of a protective char layer on the sample surface resulted in a plateau-like shape approx. 30 s after ignition, reducing PHRR by shielding the underlying material from irradiation. All FRs increased residue yields in the order **EP-poly-1** > **EP-poly-2** > **EP-BDP**. **EP-Poly-1** exhibited the highest residue amount (11.5 wt.-%) and **EP-BDP** showed the lowest (3.1 wt.-%). The residues after fire testing (**Figure 7.4d**) help visualize the differences in fire performance of **poly-1** and **poly-2** in EP: The residue of **EP-poly-2** was more voluminous than that of **EP-poly-1**, pointing to higher gas emission, similar to intumescent FR systems. This large char volume was effective in shielding some of the underlying material, acting as a protective layer and thereby reducing PHRR of EP.[37] However, **EP-poly-1** exhibited a lower THE and higher residue yield than **EP-poly-2**, because the thermal properties of its char were greater. As a result, **poly-1** was better able to bind fuel in the condensed phase in the form of char, which increased residue yields and thus reduced the fire load, i.e. THE. Although EHC of both materials were nearly identical, the change in char characteristics explains the difference in fire performance, as the residue morphology and its properties often determine effective flame retardancy.[35]

Additionally, the effective heat of combustion (EHC) was reduced by the release of P-containing volatiles. These P-containing volatiles acted in the gas phase as radical scavengers, i.e. by lowering the concentration of highly reactive radicals (H•, HO•, CO•, etc.) through P• or PO• radicals. The resulting flame inhibition led to less complete combustion; additionally, P enhanced charring thus stored fuel in the condensed phase, all of which resulted in a reduction of THE (**Figure 7.4b**).

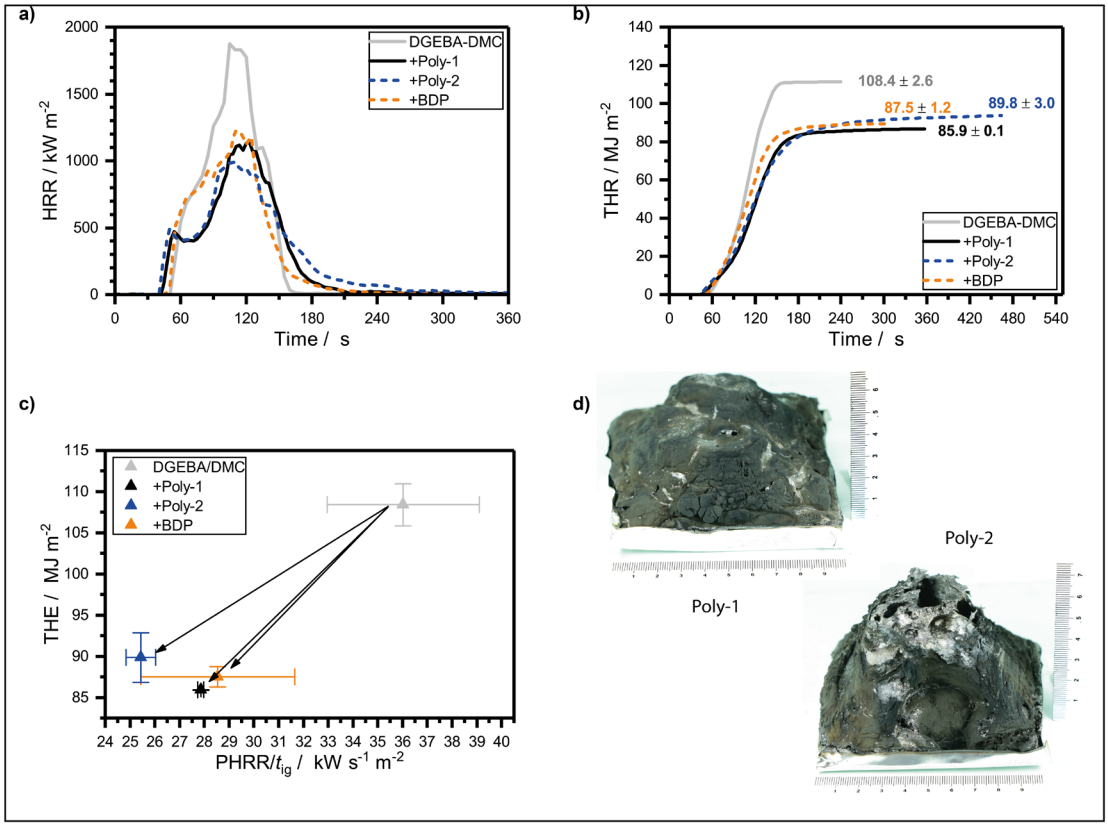

Figure 7.4. a) Heat release rate (HRR) of epoxy resin and epoxy resin with FRs. **b)** Total heat released (THR) of epoxy resin and epoxy resin with FRs. **c)** Petrella plot of the different epoxy resins with all FRs having a positive effect (lowering THE and PHRR/t_{ig}). **d)** Char residues of **EP-poly-1** and **EP-poly-2** after cone calorimeter test. Residue of EP-poly-2 is more voluminous than that of **EP-poly-1**, pointing to higher gas emission, similar to intumescent FR systems.

To further assess fire behavior and flame retardancy, the fire load (THE) is often plotted against the fire growth index (PHRR/t_{ig}, **Figure 7.4c**).[38], because THE describes heat release quantitatively, however it does not describe the release rate. PHRR/t_{ig} is a means of describing the time-dependent flashover potential or fire growth index, i.e. the severity of a fire, or peak heat release potential; however, it is not quantitative. The investigated FRs reduced both PHRR/t_{ig} and THE of **EP**, which had a PHRR/t_{ig} of 36 kW m^{-2} s^{-1} and a THE of 110 MJ m^{-2}. **EP-Poly-1** had a performance similar to **EP-BDP**: BDP reduced THE of **EP** by 19% to 88 MJ m^{-2} and **poly-1** reduced it by 21% to 86 MJ m^{-2}. The PHRR/t_{ig} was reduced by 21% to 29 kW s^{-1} m^{-2} and by 23% to 28 kW s^{-1} m^{-2} for **BDP** and **poly-1**, respectively. **Poly-2** exhibits a higher THE compared to **poly-1** and BDP but has a stronger reduction in PHRR/t_{ig}. The graph visualizes the overall good flame-retardancy potential of the *hb*-FRs: a shift to the lower-left corner of the coordinate system indicates a reduction of overall heat and fire growth. Both *hb*-FRs lower both values on a similar level to the benchmark material, proving their efficacy for this polymer resin system. Moreover, **poly-1** exhibited lower

fire loads than **poly-2** in **EP**; this implies that **poly-1** was more able to bind fuel in the condensed phase, as proven by the higher overall char yield. On the other hand, **poly-2** reduced the fire growth rate more strongly than **poly-1** in **EP**: this resulted from the better thermal barrier properties of **EP-poly-2**'s char, which lowered PHRR, as well as the higher thermal stability of **poly-2** which led to an increased t_{ig}.

7.5 Conclusion

Hyperbranched polymers, especially polyphosphoesters, are interesting candidates as polymeric flame retardants. *hb*PPEs were previously prepared by $A_n + B_m$ approaches, which might result in cross-linked PPEs, as adjustment of the monomer feed-ratio or termination before the gel point needs to be carefully conducted. Herein, we presented the first phosphorus-based AB_2 monomer (**1**), allowing the synthesis of *hb*PPEs in a single polyaddition step without the chance of undesired cross-linking.

In addition to the simplified polymerization procedure, **poly-1** exhibited a slightly higher performance compared to similar *hb*PPEs (**poly-2**), prepared by $A_2 + B_3$ polyaddition, probably due to its higher phosphorus content. This work further extends the possibilities for the preparation of branched polyphosphoesters, which might be used in biofriendly flame retardant applications or biomedical applications.

7.6 Experimental Section

7.6.1 Materials

All chemicals were purchased from commercial suppliers as reagent grade and used without further purification.

Samples for TGA-FTIR and hot-stage FTIR were milled prior to use. Powdered specimens were obtained using a RETSCH CryoMill under liquid nitrogen cooling.

7.6.2 DSC

For Differential Scanning Calorimetry (DSC), a Mettler Toledo DSC 823^e was used. With a heating and cooling rate of 10 K min^{-1}, three measurements of heating, cooling and heating were performed. The measurements were done in a nitrogen atmosphere with a flow rate of 30 mL min^{-1}.

EP-FRs were measured on a Netzsch 204 F1, type Pheonix. Two cooling and three heating runs were performed on 5 mg bulk material samples; the rate was 10 K min^{-1}, the temperature range was -80 to 180 °C, and the nitrogen flow rate was 30 mL min^{-1}. The second and third heating rate were used to determine T_g.

7.6.3 TGA

For the thermogravimetric analysis (TGA) of the neat flame retardants, a Mettler Toledo TGA/DSC 3+ in a nitrogen atmosphere was used. Using 10 mg of the sample, the measurements were performed in a range from 25 °C to 700 °C with a heating rate of 10 K min^{-1}.

7.6.4 TG-FTIR

Pyrolysis investigations into mass loss and evolved gas analysis were performed via thermogravimetric analysis (TGA) on a Netzsch TG 209, type Iris, which was coupled via transfer line to a Bruker Tensor 27 infrared spectrometer (FTIR). For TG-FTIR measurements of EP and EP-FRs, 10 mg powdered samples were used, while for pure *hb*-FRs, 5 mg samples were measured. Measurements were conducted from 30 – 900 °C (10 K min^{-1}) under a 30 ml min^{-1} nitrogen purge. Evolved gases passed through a transfer line heated to 270 °C into the FTIR gas cell which was also heated to 270 °C. The measuring range was 4000 – 400 cm^{-1} with a resolution of 1 cm^{-1}.

7.6.5 Hot Stage FTIR

Pyrolysis investigations of the condensed phase activity were performed on a Bruker Vertex 70 FTIR equipped with a Linkam FTIR600 hot stage cell. Powdered EP and EP-FR samples (ca. 5 mg) were mixed with 150 mg KBr in a mortar and pestle, then pressed into a platelet at 7 bar. Specimens were heated from 30 – 600 °C at a rate of 10 K min^{-1} under a nitrogen atmosphere. The measuring range was 4000 – 400 cm^{-1} with a resolution of 0.4 cm^{-1}.

7.6.6 Pyrolysis–Gas Chromatography-Mass Spectrometry (Py-GC/MS)

Pyrolytic evolved gas analysis was performed on a pyrolysis – gas chromatograph / mass spectrometer using a Frontier Lab PY3030iD micro-furnace single-shot pyrolyzer connected to an Agilent Technologies 7890B gas chromatograph via a split-/splitless inlet port. An Agilent Technologies 7890B mass selective detector was combined with the gas chromatograph; the

ionization energy (EI) was 70 eV and the scan range was 15–550 amu. 150 µg samples were pyrolyzed under helium atmosphere and inserted into the pyrolyzer via gravimetric fall; the temperature was 500 °C, except for measurements of **poly-1**, where the pyrolyzer temperature was set to 250 °C for an additional measurement. All evolved pyrolysis products were separated under a helium flow of 1 mL m^{-1} in an Ultra Allow +- 5 capillary column with a length of 30 m, inner diameter of 0.25 mm, and film thickness of 0.25 µm. First, the column was heated to 40 °C and held there for 2 min, then heated at a rate of 10 K min^{-1} up to 300 °C, where it was kept for 10 min. The GC injector was operated in a split mode of 1:300; the interface temperature was 300 °C. MS peak assignments were made using the NIST 14 MS library.

7.6.7 Cone Calorimeter

Fire testing was conducted on an FTT cone calorimeter operating at a heat flux of 50 kW m^{-2} according to ISO 5660, simulating a developing fire.[39] Samples sized 100 mm x 100 mm x 4 mm were conditioned at 23 °C and 50% RH for at least 48 h, then measured at a distance of 35 mm from the cone heater, as a distance of 25 mm was not suitable for the large residues of the materials.[40]

7.6.8 GPC

GPC measurements were performed in DMF (+LiBr 1 g L^{-1}) with a PSS SecCurity system (Agilent Technologies 1260 Infinity). Sample injection was performed by a 1260-ALS autosampler (Waters) at 60 °C. SDV columns (PSS) with dimensions of 300 × 80 mm, 10 µm particle size, and pore sizes of 10000, 1000, and 100 Å were employed. The IR 1260 RID detector and UV−vis 1260-VWD detector (Agilent) were used for detection. Calibration was achieved using poly(styrene) standards provided by Polymer Standards Service.

7.6.9 Elemental analysis

Elemental analysis was run on an Elementar Vario EL cube.

7.6.10 NMR

Nuclear magnetic resonance (NMR) analysis, ^{1}H, ^{31}P {H} and ^{13}C {H} NMR spectra were recorded with Bruker Avance spectrometers operating with 250, 300, 500 and 700 MHz frequencies in

deuterated chloroform, deuterated dimethyl sulfoxide or deuterated *N,N*-dimethylformamide as a solvent. The calibration of the spectra was done against the solvent signal. The spectra were analyzed using MestReNova 9 from Mestrelab Research S.L.

7.6.11 4-Bromobutan-1-ol

The synthesis was done according to a literature procedure.[27] In a 1 L flask, THF (270 mL, 3.33 mol) was added to hydrobromic acid (48%, 180 g, 1.06 mol). The mixture was refluxed for two hours, transferred into an Erlenmeyer flask, and the reaction was neutralized by the addition of $NaHCO_3$ under strong CO_2 development. The aqueous solution was extracted with dichloromethane and the organic layers were combined and dried with Na_2SO_4. The solvent was removed at reduced pressure, yielding the product (47.3 g, 29%), which was used without further purification.

^{1}H NMR (250 MHz, $CDCl_3$): δ [ppm] = 4.01 (s, 1H), 3.69 (t, J = 6.4 Hz, 2H), 3.44 (t, J = 6.6 Hz, 2H), 2.05 – 1.79 (dd, J = 8.0, 6.6 Hz, 2H), 1.79 – 1.62 (dd, J = 8.5, 6.4 Hz, 2H).

7.6.12 4-Bromobutyl phosphorodichloridate (1a)

To a dried three-necked, 500 mL round bottom flask equipped with two 100 mL dropping funnels, 0.522 mol phosphoryl chloride (80.00 g, 47.62 mL, 521.78 mmol, 5.0 eq) were added to ice-cooled, dry toluene (100 mL) under argon atmosphere. 4-bromobutan-1-ol (15.97 g, 9.51 mL, 104.36 mmol, 1.0 eq) dissolved in dry toluene (50 mL) and pyridine (8.25 g, 8.42 mL, 104.36 mmol, 1.0 eq) dissolved in dry toluene (50 mL) were added to the above flask dropwise, keeping the temperature at 0 °C. After stirring overnight at room temperature, pyridine hydrochloride was removed as a white solid by filtration. The filtrate containing the alkylene dichlorophosphate in toluene was concentrated at reduced pressure. 4-bromobutyl phosphoro-dichloridate was obtained as a colourless liquid (yield: 21.6 g, 77%).

^{1}H NMR (300 MHz, 298 K, $CDCl_3$, δ/ppm): 4.43-3.34 (m, 2H), 3.49-3.43 (t, *J* = 5.8 Hz, 2H), 2.07-1.95 (m, 4H).

^{31}P{H} NMR (202 MHz, 298 K, $CDCl_3$, δ/ppm): 7.21.

7.6.13 4-Bromobutyldi(hex-5-en-1-yl) phosphate (1b)

To a dry three-necked, 500 mL round bottom flask fitted with a 250 mL dropping funnel, 5-hexen-1-ol (17.61 g, 21.11 mL, 175.29 mmol, 2.1 eq) and pyridine (13.87 g, 14.15 mL, 175.29 mmol,

2.1 eq) were added to dry toluene (100 mL) under an argon atmosphere. **1** (22.53 g, 83.47 mmol, 1.0 eq) dissolved in dry toluene (100 mL) was added to the above flask dropwise at room temperature. After stirring overnight, pyridine hydrochloride was removed as a white solid by filtration. The organic solution was washed with sodium bicarbonate solution, 10% hydrochloric acid, and sodium chloride solution. The organic layer was dried over anhydrous sodium sulfate, filtered, and the solvent was removed at reduced pressure. 4-bromobutyldi(hex-5-en-1-yl) phosphate was obtained as a yellow liquid (yield: 30.2 g, 88%).

^{1}H NMR (300 MHz, 298 K, $CDCl_3$, δ/ppm): 5.90-5.68 (m, 2H), 5.06-4.92 (m, 4H), 4.40-3.92 (m, 6H), 3.69-3.61 (t, *J* = 6.3 Hz, 2H), 3.48-3.40 (t, *J* = 6.3 Hz,2H), 2.21-2.05 (m, 4H), 2.05-1.74 (m, 4H), 1.74-1.59 (m, 4H), 1.53-1.41 (m, 4H). ^{31}P{H} NMR (202 MHz, 298 K, $CDCl_3$, δ/ppm): -0.71.

7.6.14 Di(hex-5-en-1-yl) (4-acetylthiobutyl) phosphate (1c)

To a dry one-necked, 500 mL round bottom flask, **2** (29.05 g, 73.11 mmol, 1.0 eq) and potassium thioacetate (9.18 g, 80.42 mmol, 1.1 eq) were dissolved in acetone (100 mL). After stirring overnight at room temperature, potassium bromide was removed as a white solid by filtration. Acetone was removed at reduced pressure and the residue was dissolved in toluene (100 mL). The mixture was washed with sodium bicarbonate solution, 10% hydrochloric acid and sodium chloride solution. The organic layer was dried over anhydrous sodium sulfate, filtered and the solvent was removed at reduced pressure to isolate *S*-(4-((bis(hex-5-en-1-yloxy)phosphoryl)oxy)butyl)ethanethioate (yield: 27.7 g, 96%).

^{1}H NMR (300 MHz, 298 K, $CDCl_3$, δ/ppm): 5.87-5.70 (m, 2H), 5.06-4.92 (m, 4H), 4.23-3.94(m, 6H), 3.92-2.82 (m, 4H), 2.32 (s, 3H), 2.13-2.02 (m, 4H) 1.79-1.63 (m, 8H), 1.54-1.42 (m 4H).

^{31}P{H} NMR (202 MHz, 298 K, $CDCl_3$, δ/ppm): -0.55.

7.6.15 Di(hex-5-en-1-yl)(4-mercaptobutyl)phosphate (1)

1c (26.78 g, 68.24 mmol, 1.0 eq) was dissolved in dichloromethane (100 mL) in a dry one-necked, 500 mL round bottom flask. Then 1 M hydrazine in THF (102.36 mL, 102.36 mmol, 1.5 eq) was added dropwise. After stirring overnight at room temperature, the mixture was washed with sodium bicarbonate solution, 10% hydrochloric acid and sodium chloride solution. The organic layer was dried over anhydrous sodium sulfate, filtered and concentrated *in vacuo*. The remaining liquid was purified by column chromatography (3:7 ethyl acetate/petroleum ether) to obtain an off-white oil (yield: 5.8 g, 24%).

^{1}H NMR (300 Hz, 298 K, $CDCl_3$, δ/ppm): 5.88-5.70 (m, 2H), 5.06-4.92 (m, 4H), 4.10-3.98 (m, 6H), 2.62-2.50 (m, 2H), 2.14-2.02 (m, 4H), 1.88-1.58 (m, 8H), 1.54-1.41 (m, 4H), 1.34 (t, J = 7.9 Hz, 1H).
^{31}P{H} NMR (202 MHz, 298 K, $CDCl_3$, δ/ppm): -0.68.

7.6.16 Poly-1

Poly-1 was prepared by a radical thiol–ene polyaddition. 33 g (94.2 mmol; 1.0 eq.) of the previously synthesized monomer **1** were dissolved in 230 mL Toluene and added to a reactor fitted with a mechanical stirrer under an argon atmosphere. As a radical initiator, 1.4 g azobisisobutyronitrile (AIBN) (8.5 mmol; 0.1 eq.) was used. The solution was heated at 90 °C for 24 hours. The crude mixture was then concentrated and dried at reduced pressure until constant weight (yield: 32.5 g, 98.5%).
^{1}H NMR (300 Hz, 298 K, $CDCl_3$, δ/ppm): 5.88-5.70 (m, 2H), 5.06-4.92 (m, 4H), 4.10-3.98 (m, 6H), 2.62-2.50 (m, 4H), 2.14-2.02 (m, 4H), 1.88-1.58 (m, 8H), 1.54-1.41 (m, 4H).
^{31}P{H} NMR (202 MHz, 298 K, $CDCl_3$, δ/ppm): -0.70.

7.6.17 Poly-2

The synthesis was done according to a literature procedure.[11]

7.6.18 Poly-1 for kinetic studies:

In a 25 mL Schlenk tube, **1** (405 mg, 1.16 mmol) was dissolved in toluene (2.7 mL) under an argon atmosphere. AIBN (0.03, 0.06, or 0.09 eq.) was added to the Schlenk tube and the mixture was heated to 70 °C or 90 °C. After specific reaction times, samples (each 0.2 mL) were taken and terminated in air for the analysis of the polymerization kinetics. The crude product was dried *in vacuo* and analyzed by ^{1}H, ^{31}P NMR, and GPC.
^{1}H NMR (300 Hz, 298 K, $CDCl_3$, δ/ppm): 5.88-5.70 (m, 2H), 5.06-4.92 (m, 4H), 4.10-3.98 (m, 6H), 2.62-2.50 (m, 4H), 2.14-2.02 (m, 4H), 1.88-1.58 (m, 8H), 1.54-1.41 (m, 4H).
^{31}P{H} NMR (202 MHz, 298 K, $CDCl_3$, δ/ppm): -0.70.

7.6.19 Epoxy preparation

All epoxy resins were prepared using bisphenol A diglycidylether (DGEBA) (Araldite MY740, Bodo Möller Chemie GmbH, Offenbach am Main, Germany) as the epoxide agent and 2,2'-dimethyl-

4,4'-methylene-bis-(cyclohexylamine) (DMC) (Sigma Aldrich Co. LLC/ Merck KgaA, Darmstadt, Germany) as the amine hardener. The materials were mixed, poured into aluminum molds of desired dimensions, then hardened at 150 °C for 3h. The flame retarded epoxy resins were produced in the same manner, except 10 wt.-% of the mixture was replaced with the respective flame retardant.

7.7 Author Contributions

The manuscript was written through contributions of all authors. All authors have given approval to the final version of the manuscript. ‡These authors contributed equally.

7.8 Acknowledgments

The authors thank the Deutsche Forschungsgemeinschaft (DFG WU 750/ 8-1; SCHA 730/ 15-1) for funding. Jens C. Markwart is the recipient of a fellowship through funding of the Excellence Initiative (DFG/GSC 266) in the context of the graduate school of excellence "MAINZ" (Materials Science in Mainz). F.R. Wurm and Jens C. Markwart thank Prof. Dr. Katharina Landfester (MPI-P, Germany) for support. Alexander Battig thanks Dr. Katharina Kebelmann and Patrick Klack for their support with Py-GC/MS and the cone calorimeter.

7.9 References Chapter 7

[1] J. Liu, W. Huang, Y. Pang, D. Yan, *Chem. Soc. Rev.* **2015**, *44*, 3942-3953.

[2] M. D. Lechner, K. Gehrke, E. H. Nordmeier, *Makromolekulare Chemie: Ein Lehrbuch für Chemiker, Physiker, Materialwissenschaftler und Verfahrenstechniker*, Springer Berlin Heidelberg, **2014**.

[3] B. I. Voit, A. Lederer, *Chem. Rev.* **2009**, *109*, 5924-5973.

[4] B. Schartel, J. H. Wendorff, *Polymer Engineering & Science* **1999**, *39*, 128-151.

[5] K. Täuber, F. Marsico, F. R. Wurm, B. Schartel, *Polymer Chemistry* **2014**, *5*, 7042-7053.

[6] B. Perret, B. Schartel, K. Stöß, M. Ciesielski, J. Diederichs, M. Döring, J. Krämer, V. Altstädt, *Eur. Polym. J.* **2011**, *47*, 1081-1089.

[7] B. Perret, B. Schartel, K. Stöß, M. Ciesielski, J. Diederichs, M. Döring, J. Krämer, V. Altstädt, *Macromolecular Materials and Engineering* **2011**, *296*, 14-30.

[8] C. R. Yates, W. Hayes, *Eur. Polym. J.* **2004**, *40*, 1257-1281.

[9] S. Penczek, K. Kaluzynski, J. Pretula, *J. Appl. Polym. Sci.* **2007**, *105*, 246-254.

[10] J. Liu, W. Huang, Y. Pang, X. Zhu, Y. Zhou, D. Yan, *Biomacromolecules* **2010**, *11*, 1564-1570.

[11] A. Battig, J. C. Markwart, F. R. Wurm, B. Schartel, *Polymer Chemistry* **2019**, 10, 4346-4358.

[12] J. Khandare, M. Calderón, N. M. Dagia, R. Haag, *Chem. Soc. Rev.* **2012**, *41*, 2824-2848.

[13] Y. Zhou, W. Huang, J. Liu, X. Zhu, D. Yan, *Adv. Mater.* **2010**, *22*, 4567-4590.

[14] F. Marsico, A. Turshatov, R. Peköz, Y. Avlasevich, M. Wagner, K. Weber, D. Donadio, K. Landfester, S. Baluschev, F. R. Wurm, *J. Am. Chem. Soc.* **2014**, *136*, 11057-11064.

[15] M. M. Velencoso, A. Battig, J. C. Markwart, B. Schartel, F. R. Wurm, *Angew. Chem. Int. Ed. Engl.* **2018**, *57*, 10450-10467.

[16] P. Wen, X. Wang, W. Xing, X. Feng, B. Yu, Y. Shi, G. Tang, L. Song, Y. Hu, R. K. K. Yuen, *Industrial & Engineering Chemistry Research* **2013**, *52*, 17015-17022.

[17] J. Li, C. Ke, L. Xu, Y. Wang, *Polym. Degrad. Stab.* **2012**, *97*, 1107-1113.

[18] K.-C. Cheng, C.-C. Wang, J.-l. Ruan, C.-H. Wu, C.-W. Li, *Polym. Adv. Technol.* **2018**, *29*, 2529-2536.

[19] M. Rakotomalala, S. Wagner, M. Döring, *Materials* **2010**, *3*, 4300-4327.

[20] K. H. Pawlowski, B. Schartel, *Polym. Int.* **2007**, *56*, 1404-1414.

[21] B. Perret, K. H. Pawlowski, B. Schartel, *J. Therm. Anal. Calorim.* **2009**, *97*, 949-958.

[22] C. Gao, D. Yan, *Prog. Polym. Sci.* **2004**, *29*, 183-275.

[23] P. J. Flory, *J. Am. Chem. Soc.* **1952**, *74*, 2718-2723.

[24] D. Yan, C. Gao, H. Frey, *Hyperbranched Polymers: Synthesis, Properties, and Applications*, Wiley, **2011**.

[25] P. J. Flory, *J. Am. Chem. Soc.* **1941**, *63*, 3083-3090.

[26] C. Walling, *J. Am. Chem. Soc.* **1945**, *65*, 441-447.

[27] H. Tan, H. Liu, X. Chen, H. Chen, S. Qiu, *Organic & Biomolecular Chemistry* **2015**, *13*, 9977-9983.

[28] J. C. Markwart, F. R. Wurm, *Tetrahedron* **2018**, *74*, 7426-7430.

[29] M. Ciesielski, A. Schäfer, M. Döring, *Polym. Adv. Technol.* **2008**, *19*, 507-515.

[30] B. Schartel, C. A. Wilkie, G. Camino, *J. Fire Sci.* **2016**, *34*, 447-467.

[31] J. C. Markwart, A. Battig, L. Zimmermann, M. Wagner, J. Fischer, B. Schartel, F. R. Wurm, *ACS Applied Polymer Materials* **2019**, *1*, 1118-1128.

[32] L.-H. Lee, *Journal of Polymer Science Part A: General Papers* **1965**, *3*, 859-882.

[33] D. P. Bishop, D. A. Smith, *J. Appl. Polym. Sci.* **1970**, *14*, 205-223.

[34] M. Ciesielski, B. Burk, C. Heinzmann, M. Döring, in *Novel Fire Retardant Polymers and Composite Materials* (Ed.: D.-Y. Wang), Woodhead Publishing, **2017**, pp. 3-51.

[35] B. Schartel, B. Perret, B. Dittrich, M. Ciesielski, J. Krämer, P. Müller, V. Altstädt, L. Zang, M. Döring, *Macromolecular Materials and Engineering* **2016**, *301*, 9-35.

[36] B. Perret, K. Pawlowski, B. Schartel, *J. Therm. Anal. Calorim.* **2009**, *97*, 949-958.

[37] S. Brehme, B. Schartel, J. Goebbels, O. Fischer, D. Pospiech, Y. Bykov, M. Döring, *Polym. Degrad. Stab.* **2011**, *96*, 875-884.

[38] R. V. Petrella, *J. Fire Sci.* **1994**, *12*, 14-43.

[39] B. Schartel, T. R. Hull, *Fire and Materials* **2007**, *31*, 327-354.

[40] B. Schartel, M. Bartholmai, U. Knoll, *Polym. Degrad. Stab.* **2005**, *88*, 540-547.

7.10 Supporting Information

7.10.1 Additional data

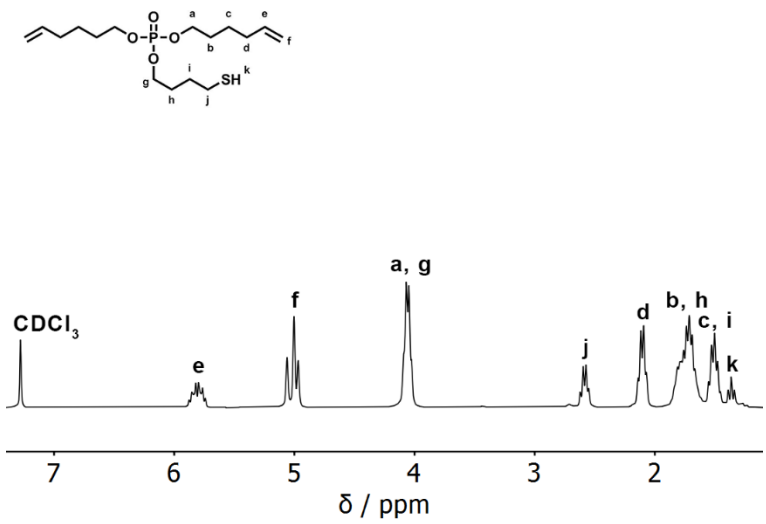

Figure S7.1. ^{1}H-NMR (300 MHz in $CDCl_3$ at 298 K) of **1**.

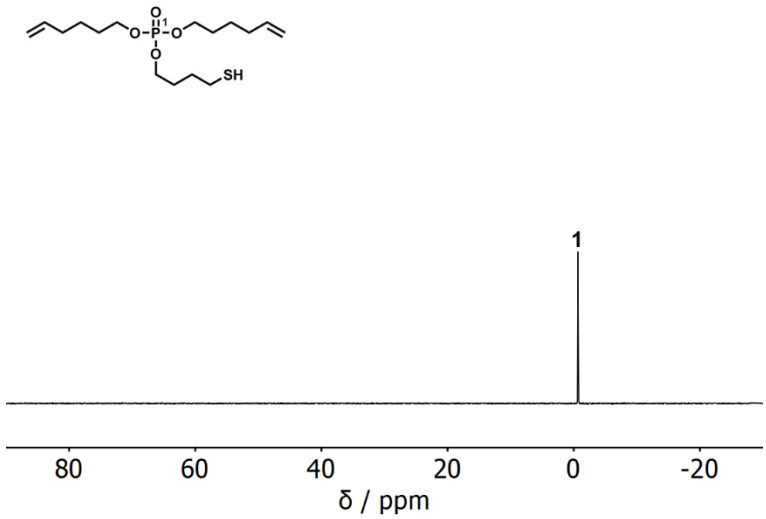

Figure S7.2. ^{31}P {H}-NMR (121 MHz in $CDCl_3$ at 298 K) of **1**.

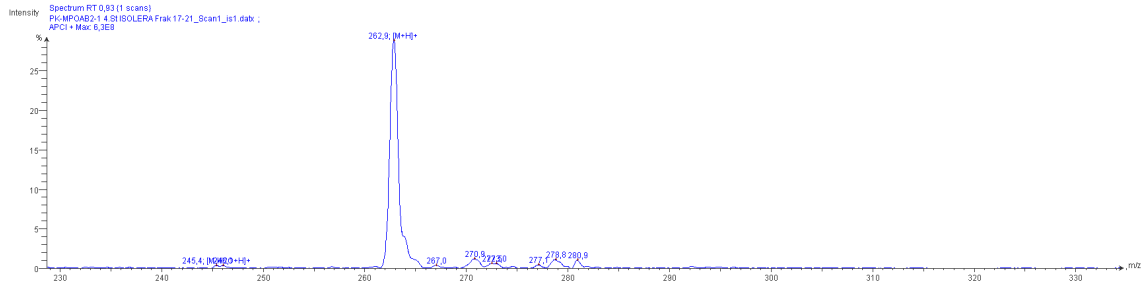

Figure S7.3. ASAP-MS of **1** $[M+H]^+$ 262.9 m/z.

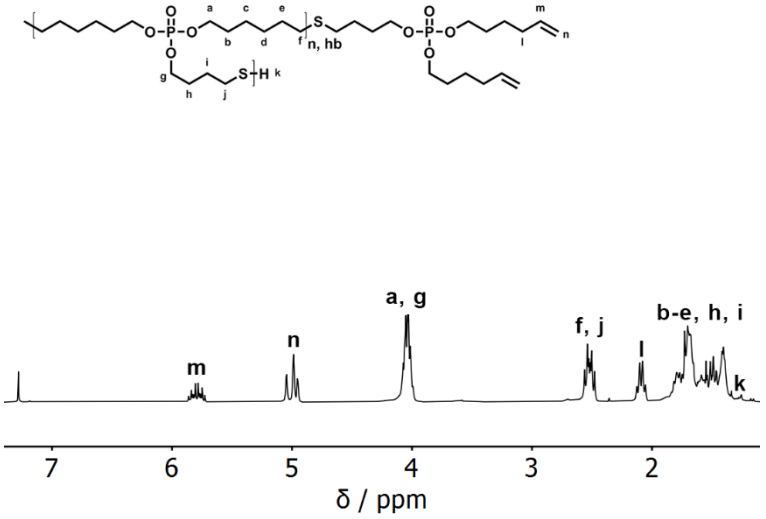

Figure S7.4. ^{1}H-NMR (300 MHz in $CDCl_3$ at 298 K) of **Poly-1**.

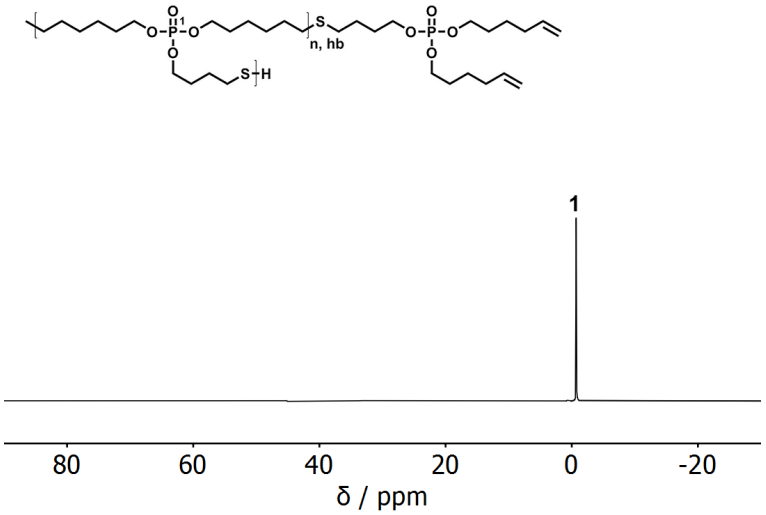

Figure S7.5. ^{31}P {H}-NMR (121 MHz in $CDCl_3$ at 298 K) of **Poly-1**.

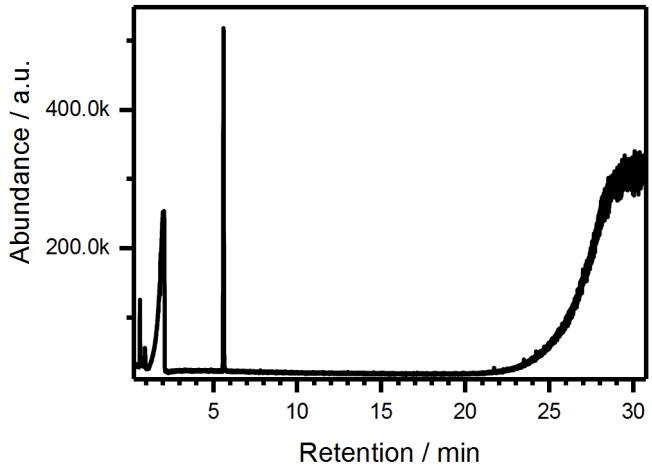

Figure S7.6. Total ion chromatogram of pyrolysis GC MS of **poly-1** measured at 250 °C (first decomposition step).

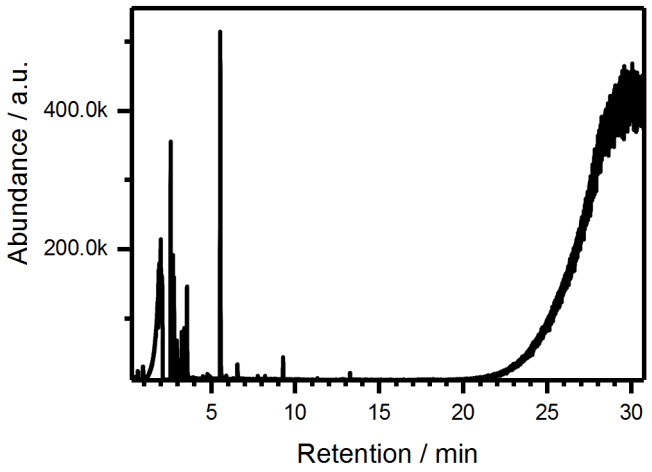

Figure S7.7. Total ion chromatogram of pyrolysis GC MS of **poly-1** measured at 500 °C (full decomposition).

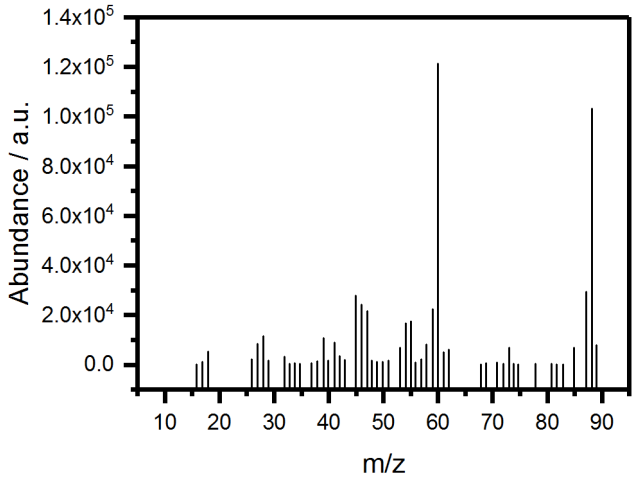

Figure S7.8. Mass spectrum at 5.62 min in the pyrolysis GC MS total ion chromatogram of **poly-1** at 250 °C, identified by NIST 14 library as tetrahydro thiophene.

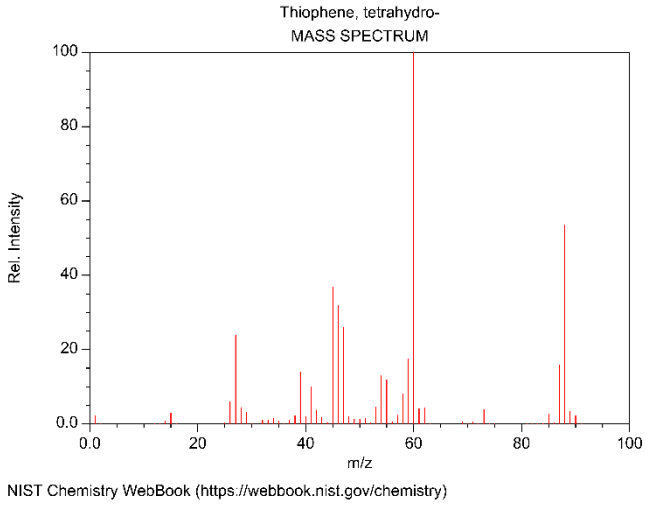

Figure S7.9. Comparative spectra of tetrahydro thiophene from NIST chemistry webbook.

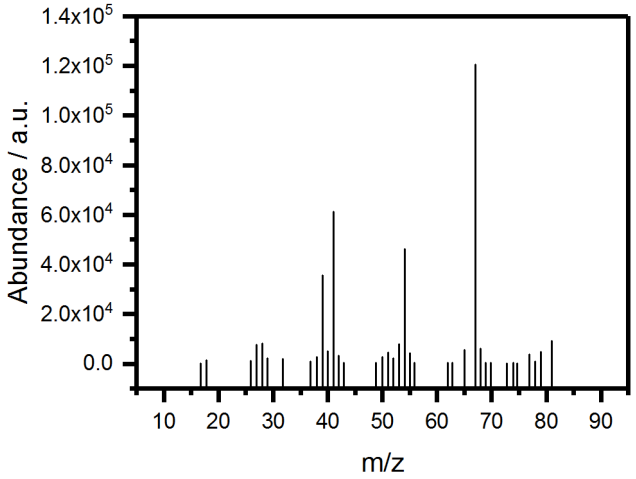

Figure S7.10. Mass spectrum at 2.60 min in the pyrolysis GC MS total ion chromatogram of **poly-1** at 500 °C, identified by NIST 14 library as 1,5-hexadiene.

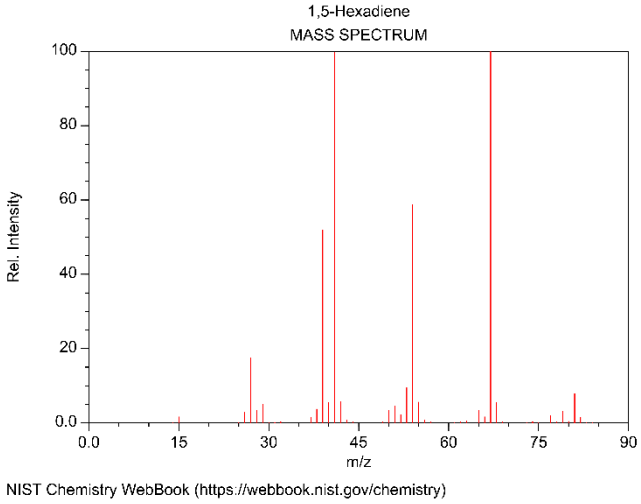

Figure S7.11. Comparative spectra of 1,5-hexadiene from NIST chemistry webbook.

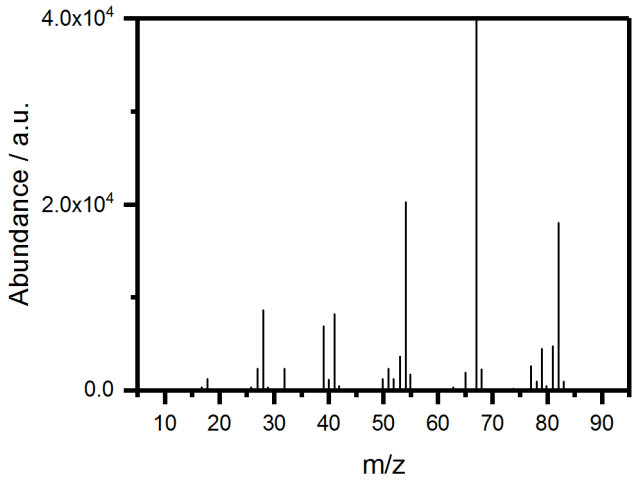

Figure S7.12. Mass spectrum at 3.56 min in the pyrolysis GC MS total ion chromatogram of **poly-1** at 550 °C, identified by NIST 14 library as cyclohexene.

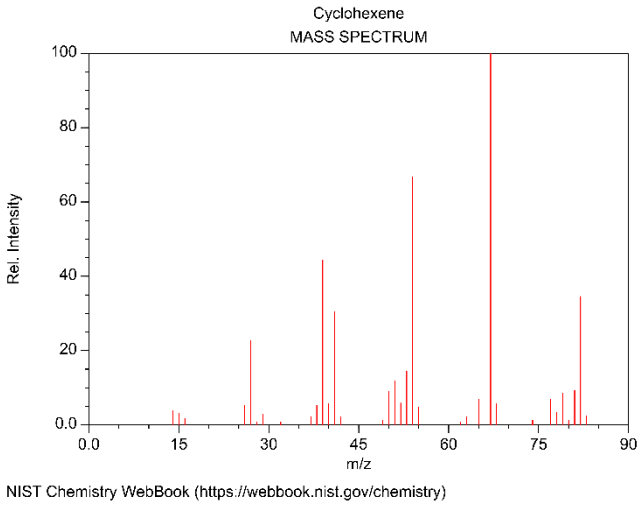

Figure S7.13. Comparative spectra of cyclohexene from NIST chemistry webbook.

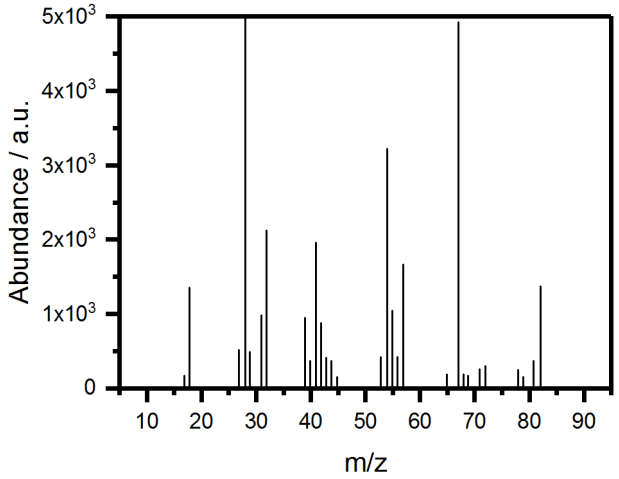

Figure S7.14. Mass spectrum at 6.57 min in the pyrolysis GC MS total ion chromatogram of **poly-1** at 500 °C, identified by NIST 14 library as 5-hexen-1-ol.

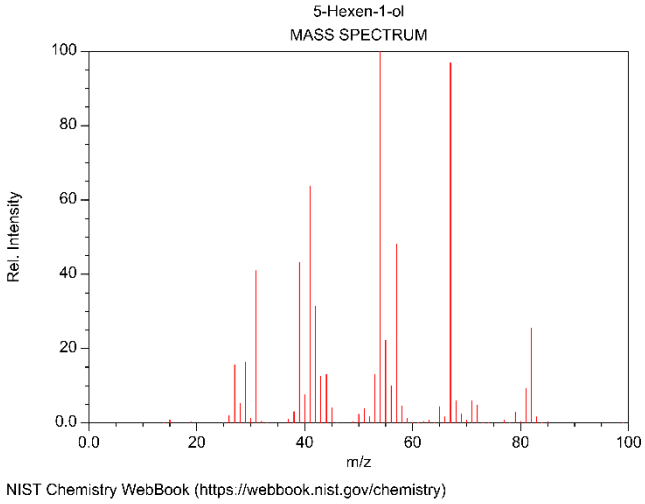

Figure S7.15. Comparative spectra of 5-hexen-1-ol from NIST chemistry webbook.

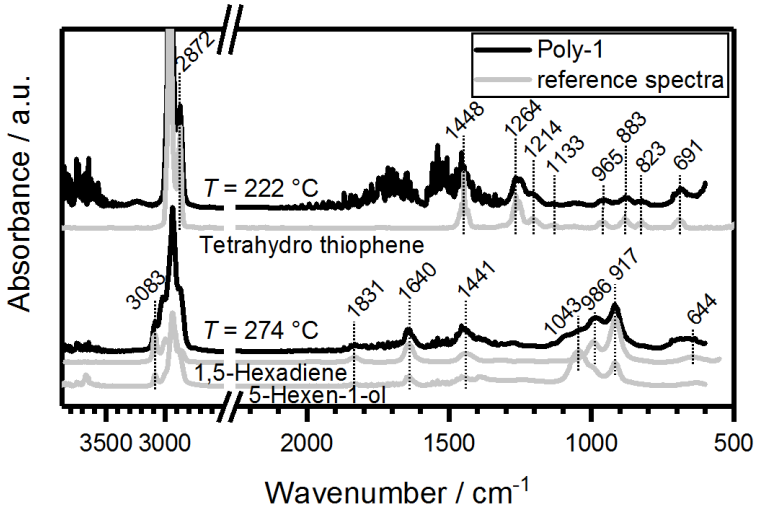

Figure S7.16. TGA-FTIR spectrum of **poly-1**, identifying the main decomposition products (tetrahydro thiophene; 1,5-hexadiene; 5-hexen-1-ol) at specific decomposition temperatures (222 °C, 274 °C) using references from NIST library.

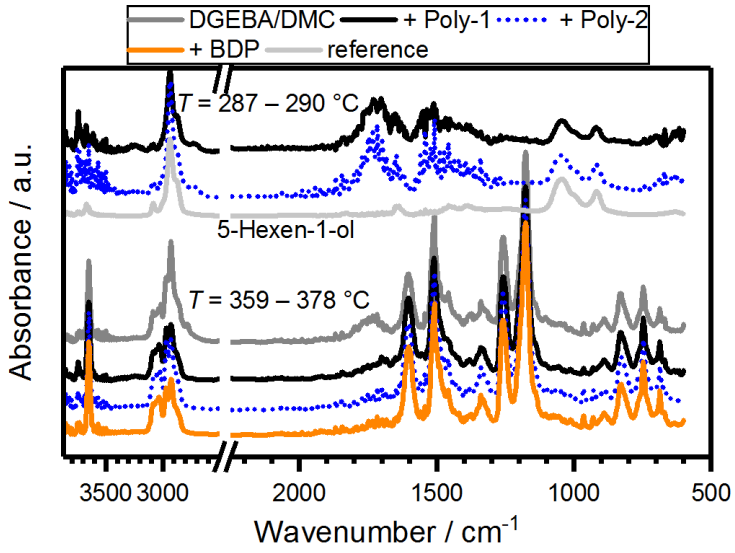

Figure S7.17. Evolved gas analysis of **EP-FRs** during pyrolysis via TGA coupled with FTIR (TG-FTIR), comparing the products at ca. 290 °C and ca. 360 – 380 °C.

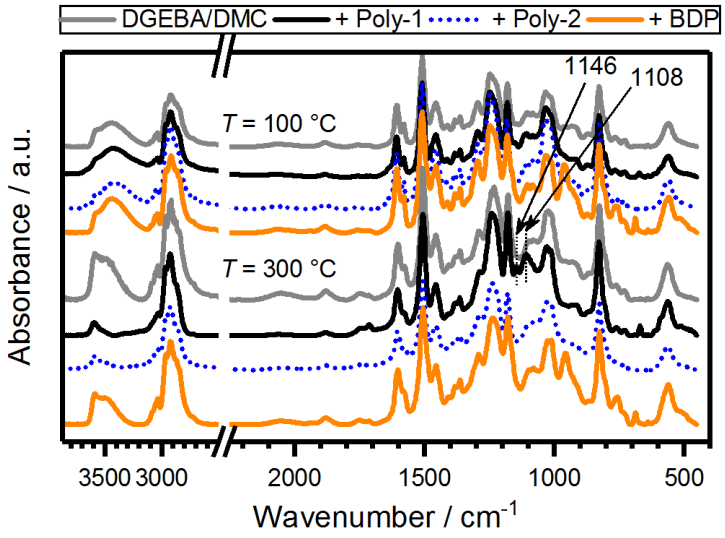

Figure S7.18. Results from hot-stage FTIR measurements, comparing the condensed phase spectra of **EP-FRs** at 100 °C and 300 °C.

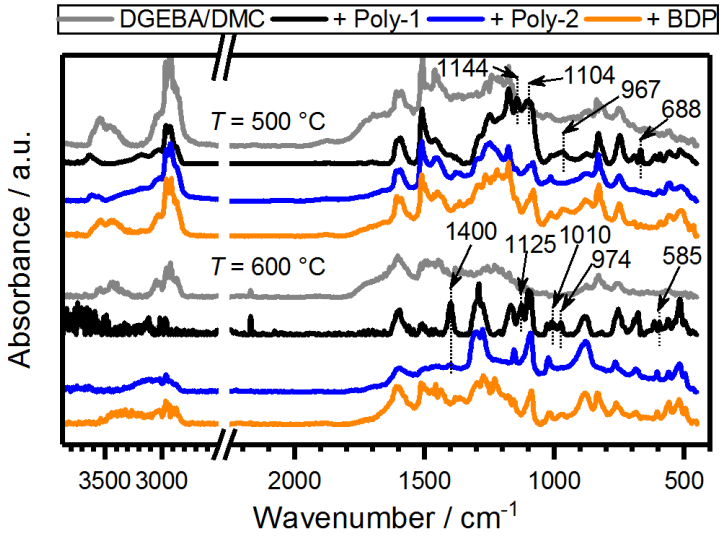

Figure S7.19. Results from hot-stage FTIR measurements, comparing the condensed phase spectra of **EP-FRs** at 500 °C and 600 °C.

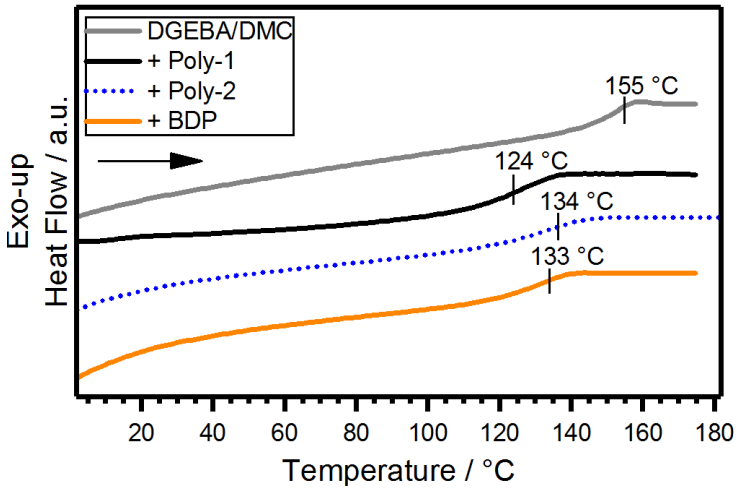

Figure S7.20. Results from DSC measurements, comparing glass-transition temperatures (T_g) of **EP** and EP-FRs.

Table S7.1. Results from cone calorimeter measurements of EP-FRs, comparing total heat evolved (THE; = total heat released at flame-out), peak of heat release rate (PHRR), time to ignition (t_{ig}), residue yield, and effective heat of combustion (EHC; = THE / total mass loss).

	EP	**EP-poly-1**	**EP-poly-2**	**EP-BDP**
THE / MJ m^{-2}	108.4 ± 2.6	85.9 ± 0.0	89.8 ± 3.0	87.4 ± 1.2
PHHR / kW m^{-2}	1696 ± 180	1170 ± 32	953 ± 41	1180 ± 41
t_{ig} / s	47 ± 1	39 ± 2	38 ± 3	42 ± 6
Residue / wt.-%	0.7 ± 0.1	11.5 ± 0.8	7.5 ± 0.6	3.1 ± 0.2
EHC / MJ kg^{-1}	26.9 ± 1.0	24.3 ± 0.2	24.3 ± 0.6	22.7 ± 0.2

Table S7.2. TGA results of **EP** and EP-FRs, comparing onset temperature ($T_{5\%}$), temperature of maximum mass loss rate (T_{max}), and residue at 700 °C.

	EP	**EP-poly-1**	**EP-poly-2**	**EP-BDP**
$T_{5\%}$ / °C	338 ± 1	268 ± 1	289 ± 1	304 ± 1
T_{max} / °C	372 ± 1	350 ± 0	351 ± 1	357 ± 0
Residue / wt.-%	4.5 ± 0.1	7.9 ± 0.3	7.7 ± 0.0	8.2 ± 0.1

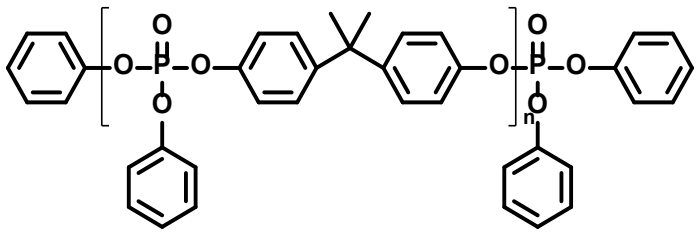

Scheme S7.1. Chemical structure of bisphenol A bis(diphenyl phosphate) (**BDP**).

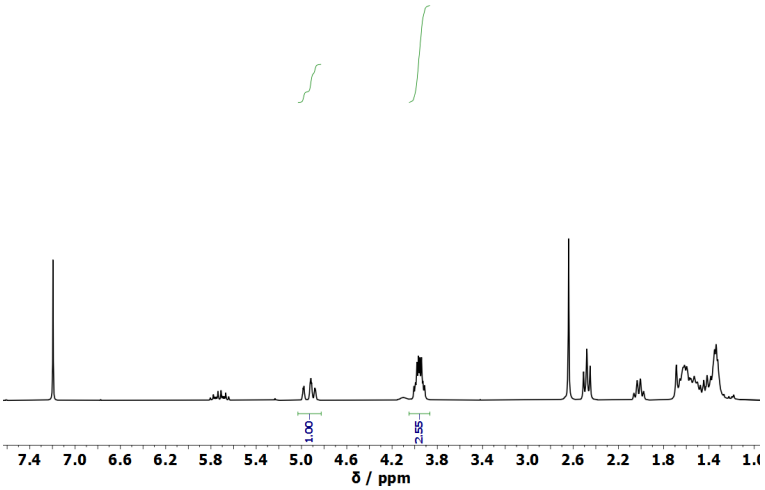

Figure S7.21 ^{1}H-NMR (300 MHz in $CDCl_3$ at 298 K) of **poly-2** showing a ratio of $n_{Double\text{-}bond}/n_{Ester}$ of 0.39.

Table S7.3. Elemental analysis of **poly-2**. %C, %H, %N and %S was measured, the other values were calculated as follows: %O&P = 100-(%C+%H+%N+%S); $\%P_{\%O\&P}$ = M(P)/(4*M(O) + M(P)) * 100%; %P = %O&P * $\%P_{\%O\&P}$ / 100%.

	%C	%H	%N	%S	%O&P	$\%P_{\%O\&P}$	%P
Poly-2	55.23	8.66	0	12.48	23.64	33	7.7

8. Intrinsic flame retardant vitrimers as a recyclable alternative for epoxy resins in composite materials

Jens C. Markwart,[a,b] Alexander Battig,[c] Hannes Schäfer,[d] Katharina Haag,[d] Katharina Koschek,[d] Bernhard Schartel,[b] Frederik R. Wurm[a]*

[a] *Physical Chemistry of Polymers - Max Planck Institute for Polymer Research, Ackermannweg 10, 55128 Mainz, Germany*

[b] *Graduate School Materials Science in Mainz, Staudinger Weg 9, 55128 Mainz, Germany*

[c] *Technical Properties of Polymeric Materials - Bundesanstalt für Materialforschung und -prüfung (BAM), Unter den Eichen 87, 12205 Berlin, Germany*

[d] *Fraunhofer Institute for Manufacturing Technology and Advanced Materials IFAM, Wiener Strasse 12, 28359 Bremen, Germany.*

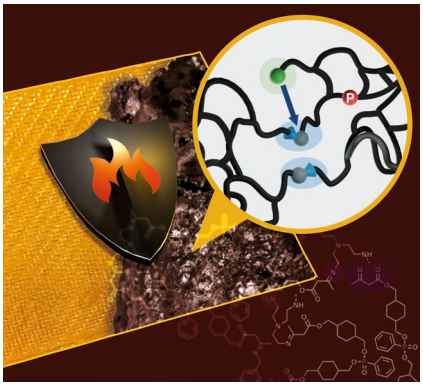

Keywords: Vitrimers, Phosphorus, Flame Retardant, Fiber-reinforced Polymer Composites, Recycling

8.1 Notes

To be submitted in this or altered form.

Alexander Battig performed the flame-retardancy measurements. Hannes Schäfer and Katharina Haag performed the mechanical test of the composites.

8.2 Abstract

Crosslinked-polymer composites currently on the market cannot be recycled. A promising alternative to reach recyclability is the development of dynamic covalent polymer networks. To date, however, additives such as flame retardants are still required for these materials if they are to follow safety regulations. Therefore, herein the first intrinsic flame-retardant dynamic polymer network based on vinylogous polyurethanes is presented and its flame retardant properties, as well as the application in composites, are assessed. In composites, vitrimers open the possibility of recycling, including reprocessing, repairing and separation of the fibers from the matrix. This is almost impossible for conventional fiber-reinforced polymer composites. In addition, the herein presented vitrimer has a similar glass transition temperature to commercially available epoxy resins and the determined values for the bending strength and bending modulus for the phosphorous-containing vitrimer lie within the range of permanently cross-linked epoxy resins reinforced with the same glass fibers.

8.3 Introduction

Cross-linked-polymer composites currently on the market cannot be recycled and often show high flammability. The development of dynamic covalent polymer networks gave access to the first composite materials with the potential for a circular economy.[1] To date, however, additives such as flame retardants are still required for these materials if they are to follow safety regulations. Herein, we present the first phosphonate-based and intrinsic flame-retardant dynamic polymer network based on vinylogous polyurethanes, eliminating the need for additional flame retardant additives. We show their recyclability, use in glass-fiber composites and study their flame retardancy and compare the data to the widely used epoxy resins.

Due to the high flammability of epoxy resins, flame retardant additives are required to fulfill current regulatory safety requirements.[2] However, the extensively used halogenated, mostly brominated, flame retardants are being phased out because of their potential negative environmental impacts.[3-6]

Therefore, halogenated flame retardants are often substituted by phosphorus-based flame retardants. Due to the chemical versatility of phosphorus chemistry and high effectiveness at already low loadings, phosphorus-containing flame retardants gained recently a lot of attention in science and industry.[6]

Most flame retardants are additive, i.e. not covalently connected to the polymer matrix. The physical blending, however, may alter the mechanical properties and can be prone to leaching from the matrix, which holds especially true for low molecular weight additives, making intrinsic flame-retardant polymeric materials more attractive.

Dynamic covalent polymer networks, which are often described as a new class of organic materials, were first reported by Leibler et al. in 2011, based on an epoxy resin.[7-8] The resin was cross-linked with di- and tri-carboxylic acids. The addition of mild Lewis acid catalyst (like zinc acetate) combined the classical mechanical properties of an epoxy resin with the ability to reprocess and reshape after full curing.[9] These so-called vitrimers have the unique characteristic that the cross-linking points exchange under thermal stimulation following an associative exchange mechanism, thus keeping the cross-linking density constant. The combination of mechanical properties and the insolubility of thermosets with a gradual change in viscosity like inorganic glasses enables processing similar to thermoplastic materials, e.g. extrusion.[10-12]

The first vitrimers were based on catalyzed transesterification. Since then, several different chemistries, such as olefin metathesis, [13-14] aromatic disulfide metathesis,[15] amine exchange of vinylogous urethanes,[11, 16] transalkylation of triazonium salts,[17] transesterification of boronic esters[18] and diboroxolan metathesis have been reported.[19]

Particularly in composites, which are mostly based on epoxy resins today, vitrimers could find a promising application. Composites, containing glass or carbon fibers, are gaining increased attention as lightweight and endurable alternatives to metals. These unique properties are especially interesting in structural applications like civil infrastructures or vehicles, where they are already used in Formula One or luxury cars, but it is expected that they find increased use in the automotive sector, e.g. for electric vehicles.[20]

However, for fiber composites, each component requires its own mold, which needs to be individually fabricated. This expensive process makes composites unsuitable for low production volumes. If it were possible to create a basic shape prepared from vitrimers, which then could be reshaped and formed to the final dimensions, a reduction in costs could be achieved.

Another challenge, which could be overcome by vitrimers, is that with the increasing size of the fabricated composite pieces, the risks of defects and challenges in manufacturing also increase. Thus, composites cannot always be prepared from a single part but engineers are forced to split larger parts into several smaller ones, which require later assembly and fixation strategies. For thermoplastic composites, several welding techniques[21-22] are known. In contrast, for thermoset composites, which mostly exhibit more desirable mechanical properties, welding is not an option, because a reprocessing is impossible after curing. Therefore, thermoset composites require mechanical jointing[23-24] of the different parts or the use of an additional adhesive[25-29]. Due the possibility for reshaping with temperature, vitrimers are a potential solution to this issue, as highlighted in previous work.[30] Furthermore, vitrimers open the possibility of repairing, recycling, including reprocessing, and separation of the fibers from the matrix, which is almost impossible for conventional fiber-reinforced polymer composites.[31]

8.4 Results and discussion

Vitrimers based on vinylogous urethanes were reported in a series of elegant papers by the Du Prez lab. They are an attractive pathway to catalyst-free vitrimers with similar mechanical properties to epoxy resins.[11, 16, 32] However, these materials are still highly flammable, making a phosphorus-containing vitrimer an attractive approach to intrinsic flame retardant vitrimers for composite applications.

A novel phosphonate-based monomer (1) for vinylogous polyurethanes was prepared by a two-step synthesis (**Figure 8.1a**). First, 1,4-cyclohexanedimethanol was transesterified with *tert*-butyl acetoacetate to 1a, which was coupled with dichlorophenylphosphine oxide to compound 1. 1 was obtained as a slightly yellow wax in 40% overall yield. To prevent a Knoevenagel condensation

as a side reaction, pyridine was chosen as base to neutralize the hydrochloric acid formed during synthesis, instead of the commonly used triethylamine. The aryl group was installed for two reasons: first, it sterically protects the phosphoester-linkages from transesterification and secondly, it can act as a char precursor to improve the flame-retardant properties.

Characterization of 1 by ^{1}H and ^{31}P NMR proved the successful synthesis (cf. **Figure 8.1** and Supp Info.); 1 exhibited a characteristic resonance at 18.95 ppm in the ^{31}P NMR.

Monomer 1 was copolymerized with m-xylylendiamine and tris(2-aminoethyl)amine to generate the vinylogoues polyurethanes. The polycondensation of the commercially available amines with the β-ketoester was conducted at room temperature in solution or elevated temperature in bulk to lower viscosity during the reaction (**Figures 8.1b** and **c**). The formulation was derived from a previous publication.[32] As phosphorus-free reference vitrimer, the vinylogous polyurethane previously published by Du Prez et al. was prepared (poly-2 in **Figure 8.1c**), of which for the first time, fire performance was investigated and compared to poly-1.[32]

During the spontaneous polycondensation, water is released, which needs to be removed. Therefore, the polymerized material was pressed to 1-2 mm thin plates at 90 °C by a hydraulic press to remove the generated water during the thermal curing in a convection oven. The oven was preheated to 90 °C and the temperature was increased to 150 °C after 24 h for an additional 1 h.

The ^{31}P MAS solid-state NMR of poly-1 revealed a single resonance at 16.77 ppm, showing no signs of degradation or transesterification (**Figure 8.1e**). Differential scanning calorimetry (DSC) with a heating rate of 10 K min^{-1} revealed a glass-transition temperature (T_g) of 70 °C, which is similar to a polyether-amine cured bisphenol A diglycidyl ether (DGEBA) (T_g of 88 °C), which is also used for composite materials.[33] The thermal stability of the resulting network was measured by thermogravimetric analysis in a nitrogen atmosphere and a heating rate at 10 K min^{-1}. The material was stable beyond 200 °C and showed a 5% onset degradation temperature of 285 °C. After heating to 700 °C, a char residue of ca. 22 wt.-% for the phosphorus-containing vitrimer was found, while the non-phosphorus-based vitrimer (poly-2) proved a lower char yield of ca. 14 wt.-%.

A key characteristic of vitrimers is their recyclability while sustaining material properties. Therefore, rheology was utilized to study the recycling of the phosphonate-based vitrimer (poly-1). The vinylogous polyurethane network was cut into small pieces and then loaded into a mold, where the pieces were compressed at 10 kN for 30 min at 150 °C. After cooling to room temperature while keeping the pressure constant, the samples were removed from the mold and measured by a rheometer. The recycled poly-1 exhibited a storage modulus (G') of 0.36 GPa at

50 °C, while the original material has a storage modulus of 2.4 GPa at 50 °C[32] and a DGEBA-based epoxy resin a storage modulus of 4.0-8.5 GPa at -25 °C[34]. Repeating the recycling a second and a third time, proved materials with similar properties as the as-prepared sample (**Figures 8.2b** and **c**). Furthermore, the storage modulus (*G'*) dominated the loss modulus (*G''*), which is typical for cross-linked networks. In addition, the rheology measurements confirmed the T_g of 70 °C obtained from DSC measurements.

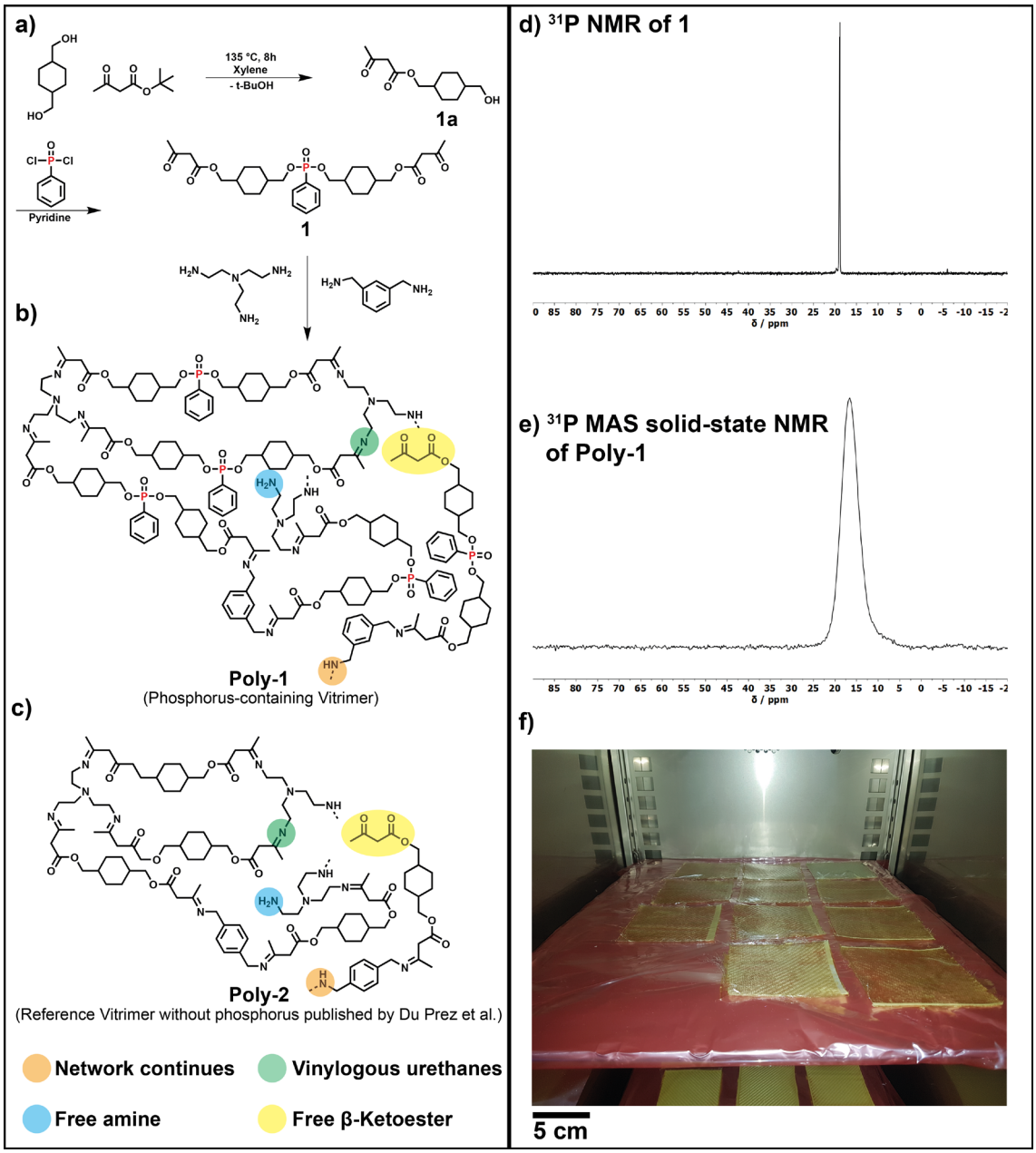

Figure 8.1. a) Synthesis of the β-ketoester-containing phosphonate monomer 1 and the formation of the vinylogous polyurethane network by polycondensation with amines (**b)** and **c)** (reference)). **d)** ^{31}P {H} NMR (121 MHz in $CDCl_3$ at 298 K) of 1. **e)** ^{31}P MAS solid-state NMR of poly-1, 20 kHz MAS, at 298 K and 121.5 MHz ^{31}P Lamor frequency. **f)** Curing of poly-1 glass fiber composites at 90 °C in a convection oven.

The intrinsic flame-retardant properties of poly-1 were investigated by forced flaming using the cone calorimeter, which is widely used for assessing the fire behavior of polymer materials.[35] The cone calorimeter provides information on the heat release rate (HRR), total heat released (THR), time to ignition (TTI), mass loss rate, smoke emission rate, and average CO and CO_2 emissions of a given sample, which represent the most important parameters to characterize fires.[36]

The heat release curve from cone calorimetry gives information about the thermal thickness of a material and its charring behavior.[37] The THR is the integral of HRR with respect to time. The THR at the end of the test is the total heat evolved (THE), which represents the fire load of a material.[37] The effective heat of combustion (EHC) is the total heat evolved divided by the total mass loss; it represents the heat available per unit of mass loss in the cone calorimeter. A reduction of EHC is indicative of the gas phase activity of an FR, i.e. flame dilution or flame inhibition.[38]

The specimen plates for cone calorimeter measurements were prepared by grinding the vinylogous urethane network to a powder using a kitchen blender. 50 g of the powder was transferred to a mold sized 12 x 12 cm^2 and compressed at 150 °C with 20 kN for 30 min and 50 kN for another 30 min to form the final plates as shown in **Figure 8.2a**. The mold was allowed to reach 50 °C while keeping the pressure of 50 kN before removing the sample. Of each material, three plates were prepared and cut to the final shape of 10 x 10 cm^2. The plates had a thickness of ca. 3 mm. The phosphonate-based vitrimer poly-1 exhibited a clear reduction in THE by 27% (from 89 MJ m^{-2} to 65 MJ m^{-2}) and PHRR by 33% (from 2346 kW m^{-2} to 1566 kW m^{-2}) compared to the vitrimer without phosphorus (poly-2). The reduction in THE and PHRR is explained by the increased residue from 10 wt.-% to 23 wt.-% in cone calorimetry, which is in agreement with TGA measurements, of the phosphonate-based vitrimer poly-1: The fixation of fuel in the char decreased the fire load, and the combination of increased residue yield and gas emission led to an intumescent behavior in fire, exhibiting an increased protective layer effect, which lowered the PHRR (**Figure 8.2f** and **g** show photos of the chars obtained after cone calorimetry). The protective layer effect is further evidenced by the plateau-like shape of the HRR curve resulting from the strong intumescent behavior. The intumescent behavior was supported by the phosphorus in poly-1 since it acted as an acid source, promoting the formation of a strong and voluminous multicellular char, which acted as a thermal insulator (**Figures 8.2f** and **g**).

In pyrolysis combustion flow calorimetry (PCFC) measurements, the heat release capacity (HRC) for both materials was determined to be similar (287 ± 2 and 284 ± 6 J g^{-1} K^{-1} for the reference poly-2 and the phosphonate-based vitrimer poly-1, respectively). As PCFC cannot detect flame poisoning, the nearly identical HRC values indicated a gas phase mechanism via flame-poisoning for the phosphonate-based vitrimer poly-1 as a major mode of action during the fire. This

assumption was further supported by a reduction of EHC by 14% as seen in the cone calorimetry data (from 28 MJ kg^{-1} to 24 MJ kg^{-1}). In addition, the THE-values measured by PCFC of 24.65 kJ g^{-1} for the reference poly-2 and 24.6 kJ g^{-1} for the phosphonate-based vitrimer poly-1, were very similar, which suggests no additional contribution to THE from the phosphorus species. Furthermore, we predicted UL-94 and LOI behavior from PCFC measurements following a literature approach:[39] from the PCFC data, a UL-94 rating of V-2 or V-1 and an LOI between 25 and 30 is expected for poly-1, which had a calculated phosphorus content of 4.7 wt.-%. In comparison, depending on the hardener epoxy resins normally contain 2-5 wt.-% phosphorus to achieve a V-1 or V-0 classification in UL-94.[40]

Epoxy resins are often used in fiber-reinforced composites. Therefore, a comparison of the flammability of epoxy resins with both vitrimers is interesting. According to our recent publication,[41] a DGEBA/2,2'-dimethyl-4,4'-methylene-bis-(cyclohexylamine)-based epoxy resin exhibited a THE of 108 MJ m^{-2} and a PHRR/t_{ig} of 36 kW m^{-2} s^{-1} (**Figure 8.2e**). The fire-load, which is indicated by the THE, was significantly reduced for both vitrimers compared to the epoxy resin. Adding 10 wt.-% BDP to the epoxy resin lowered the THE and PHRR significantly, but the THE with 87 MJ m^{-2} was on a similar level to the reference vitrimer poly-2 but still considerably higher than the phosphonate-based vitrimer poly-1. However, the fire growth index (PHRR/t_{ig}) was greater than 90 kW m^{-2} s^{-1} for both vitrimers as seen in **Figure 8.2e** and thus higher as the fire growth index of the neat epoxy (36 kW m^{-2} s^{-1}) and the epoxy loaded with 10 wt.-% BDP (29 kW m^{-2} s^{-1}). The above-mentioned data underlines the promising application of intrinsic flame-retardant vitrimers in composite materials. In composites today, often epoxides are used due to their good mechanical properties. Therefore, we also assessed the mechanical properties in composites of our material.

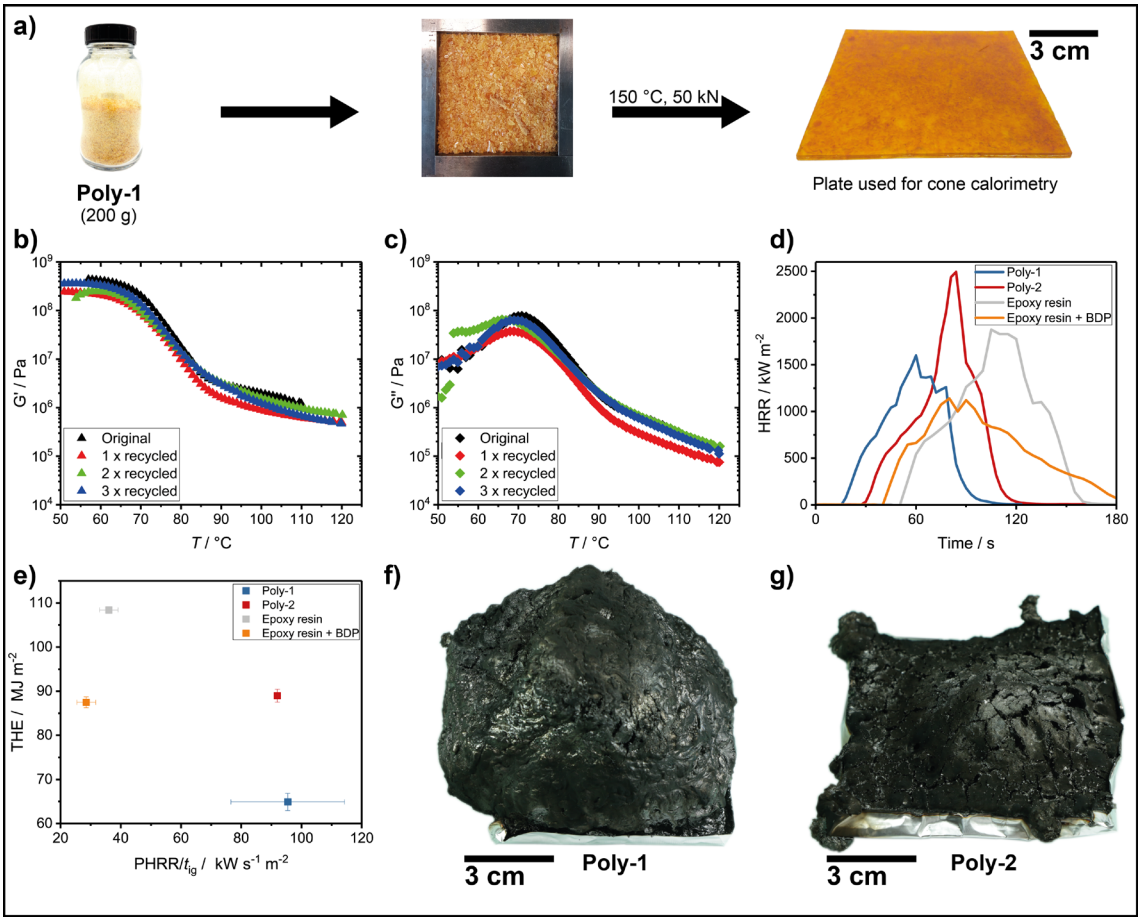

Figure 8.2. a) Preparation of the plates (poly-1) with a size of 12 x 12 cm^2, which are cut to 10 x 10 cm^2, and used for cone calorimetry. **b)** and **c)** Dynamical mechanical behaviour of poly-1, showing identical values after recycling. **d)** Heat release rate (HRR) over time of vitrimers poly-1 compared to the reference vitrimer (poly-2) and neat epoxy resin and epoxy resin loaded with BDP. **e)** Total heat evolved (THE) plotted against the ratio of peak heat release rate to the time of ignition (PHRR/t_{ig}) of both vitrimers compared to the epoxy resins ("Petrella plot"). **f)** and **g)** char residues of poly-1 and poly-2 after cone calorimeter test.

Poly-1 and poly-2 were used for the preparation of glass-fiber-reinforced composite materials: the pre-impregnated fibers ("prepregs") were prepared by polycondensation of the β-ketoester monomers of the reference or the phosphonate-based vitrimer (1) and the amines directly on the fiber mats. The monomers were dissolved separately in methanol and for each prepreg, 5 mL of the stock solutions were mixed quickly and ca. 7.5 mL was poured over twill weave glass fibers in a silicon mold. The mold with the prepreg was transferred to a preheated convection oven at 60 °C and the methanol was evaporated. The prepregs were cured for 24 h at 90 °C and 1 h at 150 °C. Optimum press parameters for manufacturing composites (GFRP) were determined in pre-tests using peeling experiments. With decreasing thickness of spacers (from 0.6 to 0.0 mm), the quality of the composited increases as indicated by higher peeling forces. The composites were manufactured by stacking six prepregs and consolidating them using a preheated hot press at

150 °C and 10 kN for 1 h. No polymer loss from the prepregs was observed during compaction and the glass-fibers were well impregnated (see **Figure 8.3c** and **e**). The fiber mass content of the composite was 62.2% for the herein presented vitrimer poly-1 and 58.6% for the reference system poly-2 as determined by TGA of the composites and the unreinforced polymers (**Tables S8.1-S8.3**). From the resulting composites, 5-6 specimens with the dimensions 10 x 70 mm were cut using guillotine shears (**Figure 8.3e**). The samples were conditioned in a desiccator with a dry atmosphere to exclude effects of humidity uptake until testing.

The mechanical properties of the composites determined by 3-point-bending tests according to DIN EN ISO 14125 in an acclimatized lab (23 °C, 50% RH) are shown in **Figures 8.3a** and **b**. The composites have mechanical properties, which proved the high potential of the vitrimers for composite applications: a bending strength of 387±16 MPa and a bending modulus of 20.7 ± 0.7 GPa for poly-1 composites were determined. These values for the phosphorous-containing system lie within the range of permanently cross-linked epoxy resins reinforced with the same glass fibers and processed via vacuum infusion.[42] The specimens showed fiber failure under tension at the bottom sides and without larger scale delamination of the layers (**Figure 8.3e**). This failure behavior indicates adequate load transfer from the polymer to the fibers and explains the high mechanical values.

While a more or less ductile stepwise failure can be observed for the reference poly-2 (higher strain at fracture compared to strain at maximum strength), the phosphorus-containing vitrimer poly-1 has a more brittle failure when reaching the bending strength (see **Figure 8.3a**).

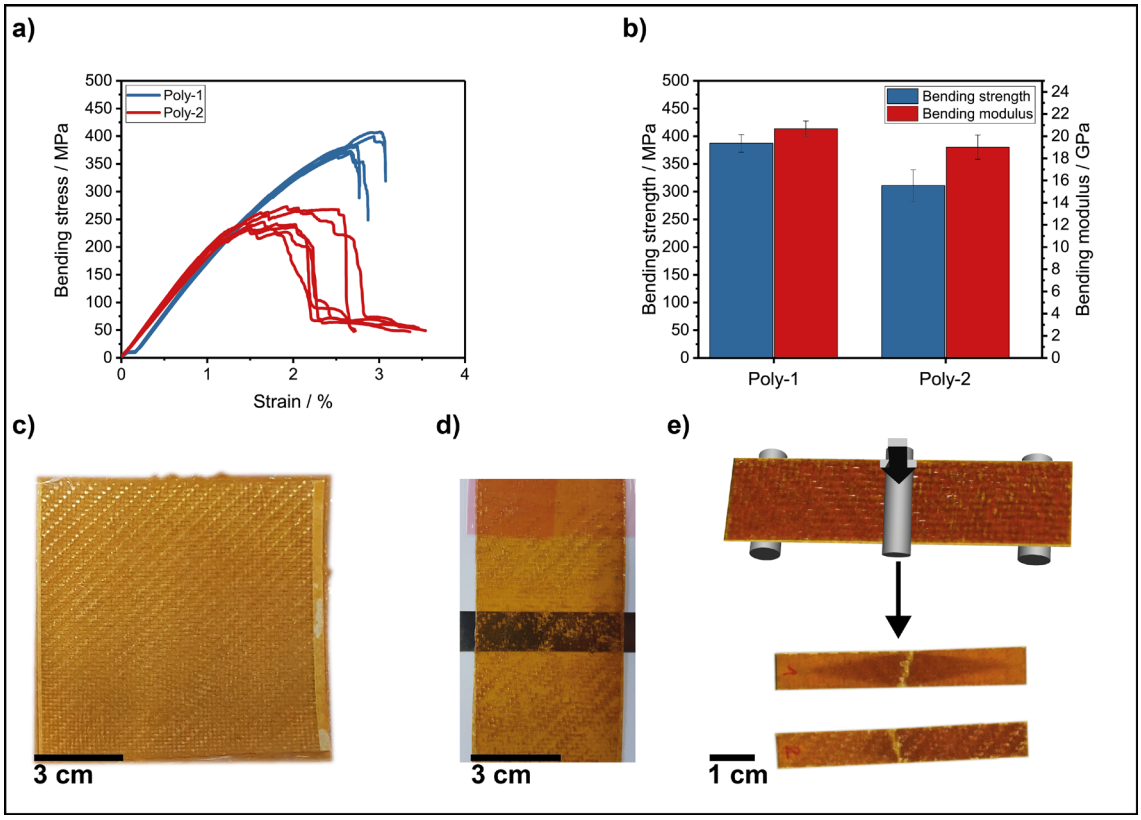

Figure 8.3. a) Stress-strain curves from the bending experiments. Blue curves correspond to the composites with poly-1, red curves to the reference poly-2. **b)** Bending strength and bending modulus of the composites with poly-1 and poly-2. **c)** Prepreg of poly-1 after curing. **d)** 2 prepregs were stacked and compression-molded with a separation layer on top for delamination experiments. **e)** From the composite, test specimens were cut and mechanical properties were determined in 3-point bending experiments.

8.5 Conclusion

In summary, we were able to prepare the first intrinsic flame-retardant vitrimer and investigated its applicability in glass fiber reinforced composite materials. A phosphonate-based vitrimer relying on the vinylogous polyurethane chemistry was prepared and its properties were compared to a phosphorus-free vinylogous polyurethane vitrimer and epoxy resins. The phosphorus-containing vitrimer (poly-1) exhibited a glass transition temperature of ca. 70 °C, which is similar to commercially available epoxy resins. Poly-1 was successfully recycled, which was proven by rheology experiments after compressing the blended flakes. In cone calorimeter tests, poly-1 exhibited a clear reduction of the THE by 27% and PHRR by 33% compared to the reference poly-2. The reduction in THE and PHRR can be explained by the increased residue from 10 wt.-% to 23 wt.-% (obtained by cone calorimetry) of the phosphonate-based vitrimer poly-1 and the, therefore, fixation of fuel in the char, which decreased the fire load. The combination of increased residue yield and gas emission led to an intumescent behavior in fire. In comparison to the neat

epoxy resin, the fire-load, which is indicated by the THE, was significantly reduced for both vitrimers. However, the fire growth index (PHRR/t_{ig}) was higher for the vitrimers compared to the neat and BDP-loaded epoxy resins.

Successful preparation of glass-fiber reinforced composites of poly-1 proved values for the bending strength and bending modulus for poly-1 similar to permanently cross-linked epoxy resins reinforced with the same glass fibers and processed via vacuum infusion.[42] The specimens showed fiber failure under tension at the bottom sides and without larger scale delamination of the layers. This failure behavior indicates adequate load transfer from the polymer to the fibers and explains the high mechanical values. Such materials could be sustainable and recyclable alternatives to currently used fiber-reinforced epoxies and broaden the scope of available vitrimers to polyphosphonates.

8.6 Conflicts of interest

There are no conflicts to declare.

8.7 Acknowledgements

The authors thank the Deutsche Forschungsgemeinschaft (DFG WU 750/ 8-1; SCHA 730/ 15-1) for funding. Jens C. Markwart is the recipient of a fellowship through funding of the Excellence Initiative (DFG/GSC 266) in the context of the graduate school of excellence “MAINZ” (Materials Science in Mainz). F.R. Wurm and Jens C. Markwart thank Prof. Dr. Katharina Landfester (MPI-P, Germany) for support. Jens C. Markwart thanks Dr. Kaloian Koynov and Andreas Hanewald for their support with rheology measurements.

8.8 References Chapter 8

[1] W. Denissen, J. M. Winne, F. E. Du Prez, *Chem Sci* **2016**, *7*, 30-38.

[2] B. Perret, B. Schartel, K. Stöß, M. Ciesielski, J. Diederichs, M. Döring, J. Krämer, V. Altstädt, *Eur. Polym. J.* **2011**, *47*, 1081-1089.

[3] S. V. Levchik, E. D. Weil, *J. Fire Sci.* **2006**, *24*, 345-364.

[4] S.-Y. Lu, I. Hamerton, *Prog. Polym. Sci.* **2002**, *27*, 1661-1712.

[5] S. D. Shaw, A. Blum, R. Weber, K. Kannan, D. Rich, D. Lucas, C. P. Koshland, D. Dobraca, S. Hanson, L. S. Birnbaum, *Reviews on environmental health* **2010**, *25*, 261-305.

[6] M. M. Velencoso, A. Battig, J. C. Markwart, B. Schartel, F. R. Wurm, *Angew. Chem. Int. Ed. Engl.* **2018**, *57*, 10450-10467.

[7] D. Montarnal, M. Capelot, F. Tournilhac, L. Leibler, *Science* **2011**, *334*, 965-968.

[8] M. Capelot, D. Montarnal, F. Tournilhac, L. Leibler, *J. Am. Chem. Soc.* **2012**, *134*, 7664-7667.

[9] M. Capelot, M. M. Unterlass, F. Tournilhac, L. Leibler, *ACS Macro Letters* **2012**, *1*, 789-792.

[10] C. N. Bowman, C. J. Kloxin, *Angew. Chem. Int. Ed.* **2012**, *51*, 4272-4274.

[11] W. Denissen, J. M. Winne, F. E. Du Prez, *Chemical Science* **2016**, *7*, 30-38.

[12] C. Taplan, M. Guerre, J. M. Winne, F. E. Du Prez, *Materials Horizons* **2019**.

[13] Y.-X. Lu, Z. Guan, *J. Am. Chem. Soc.* **2012**, *134*, 14226-14231.

[14] Y.-X. Lu, F. Tournilhac, L. Leibler, Z. Guan, *J. Am. Chem. Soc.* **2012**, *134*, 8424-8427.

[15] A. Rekondo, R. Martin, A. Ruiz de Luzuriaga, G. Cabañero, H. J. Grande, I. Odriozola, *Materials Horizons* **2014**, *1*, 237-240.

[16] W. Denissen, M. Droesbeke, R. Nicolay, L. Leibler, J. M. Winne, F. E. Du Prez, *Nat Commun* **2017**, *8*, 14857.

[17] M. M. Obadia, B. P. Mudraboyina, A. Serghei, D. Montarnal, E. Drockenmuller, *J. Am. Chem. Soc.* **2015**, *137*, 6078-6083.

[18] O. R. Cromwell, J. Chung, Z. Guan, *J. Am. Chem. Soc.* **2015**, *137*, 6492-6495.

[19] M. Röttger, T. Domenech, R. van der Weegen, A. Breuillac, R. Nicolaÿ, L. Leibler, *Science* **2017**, *356*, 62-65.

[20] L. Nicolais, M. Meo, E. Milella, *Composite Materials: A Vision for the Future*, Springer London, **2011**.

[21] C. Ageorges, L. Ye, M. Hou, *Composites Part A: Applied Science and Manufacturing* **2001**, *32*, 839-857.

[22] D. Stavrov, H. E. N. Bersee, *Composites Part A: Applied Science and Manufacturing* **2005**, *36*, 39-54.

[23] E. W. Godwin, F. L. Matthews, *Composites* **1980**, *11*, 155-160.

[24] M. J. Troughton, *Handbook of Plastics Joining: A Practical Guide*, Elsevier Science, **2008**.

[25] N. A. de Bruyne, *Aircraft Engineering and Aerospace Technology* **1944**, *16*, 115-118.

[26] F. L. Matthews, P. F. Kilty, E. W. Godwin, *Composites* **1982**, *13*, 29-37.

[27] J. R. J. Wingfield, *Int. J. Adhes. Adhes.* **1993**, *13*, 151-156.

[28] H. S. da Costa Mattos, E. M. Sampaio, A. H. Monteiro, *Int. J. Adhes. Adhes.* **2011**, *31*, 446-454.

[29] H. S. da Costa Mattos, A. H. Monteiro, R. Palazzetti, *Materials & Design* **2012**, *33*, 242-247.

[30] E. Chabert, J. Vial, J.-P. Cauchois, M. Mihaluta, F. Tournilhac, *Soft Matter* **2016**, *12*, 4838-4845.

[31] W. Denissen, I. De Baere, W. Van Paepegem, L. Leibler, J. Winne, F. E. Du Prez, *Macromolecules* **2018**, *51*, 2054-2064.

[32] W. Denissen, G. Rivero, R. Nicolaÿ, L. Leibler, J. M. Winne, F. E. Du Prez, *Adv. Funct. Mater.* **2015**, *25*, 2451-2457.

[33] T. H. Hsieh, A. J. Kinloch, K. Masania, A. C. Taylor, S. Sprenger, *Polymer* **2010**, *51*, 6284-6294.

[34] C. R. Amaral, R. J. S. Rodriguez, F. G. Garcia, L. P. B. Junior, E. A. Carvalho, *Polymer Engineering & Science* **2014**, *54*, 2132-2138.

[35] V. Babrauskas, *Fire and Materials* **1984**, *8*, 81-95.

[36] ISO, pub-ISO, **2015**, p. 55.

[37] B. Schartel, T. R. Hull, *Fire and Materials* **2007**, *31*, 327-354.

[38] B. Schartel, B. Perret, B. Dittrich, M. Ciesielski, J. Krämer, P. Müller, V. Altstädt, L. Zang, M. Döring, *Macromolecular Materials and Engineering* **2015**, *301*, 9-35.

[39] B. Schartel, K. H. Pawlowski, R. E. Lyon, *Thermochim. Acta* **2007**, *462*, 1-14.

[40] S. Levchik, A. Piotrowski, E. Weil, Q. Yao, *Polym. Degrad. Stab.* **2005**, *88*, 57-62.

[41] J. C. Markwart, A. Battig, L. Zimmermann, M. Wagner, J. Fischer, B. Schartel, F. R. Wurm, *ACS Applied Polymer Materials* **2019**, *1*, 1118-1128.

[42] K. Haag, J. Deitschun, D. Godlinski, V. Zoellmer, K. Koschek, in *ECCM18 – 18th European Conference on Composite Materials, Vol. 18*, Athens, Greece, **2018**.

8.9 Supporting Information

8.9.1 Experimental Procedures

8.9.1.1 Materials

All chemicals were purchased from commercial suppliers (Sigma Aldrich and Acros Organics) as reagent grade and used without further purification.

8.9.1.2 DSC

For Differential Scanning Calorimetry (DSC), a Mettler Toledo DSC 823^e was used. With a heating and cooling rate of 10 K min^{-1} three measurements of heating, cooling and heating were performed. The measurements were done in a nitrogen atmosphere with a flow rate of 30 mL min^{-1}.

8.9.1.3 TGA

For the thermogravimetric analysis (TGA) of the neat flame retardants, a Mettler Toledo TGA/DSC 3+ or a Q5000 from TA Instruments in a nitrogen or oxygen atmosphere was used. Using 10 mg of the sample, the measurements were performed in a range from 25 °C to 600 °C or 800 °C with a heating rate of 10 K min^{-1}.

8.9.1.4 Cone Calorimeter

All epoxy resin samples were subjected to bench-scale forced flaming combustion using a cone calorimeter (Fire Testing Technology Ltd., East Grinstead, UK) at a distance of 35 mm between specimen and cone heater and a heat flux of 50 kW m^{-2} and in accordance with ISO 5660. Specimens sized 100 x 100 x 4 mm^3 were conditioned at 23 °C and 50% relative humidity for at least 48 hours and then subjected to irradiation.

8.9.1.5 Atmospheric solids analysis probe mass spectra

Atmospheric solids analysis probe (ASAP) mass spectra were measured on an Advion expression compact mass spectrometer.

8.9.1.6 NMR

Nuclear magnetic resonance (NMR) analysis, ^{1}H, ^{31}P {H} and ^{13}C {H} NMR spectra were recorded with Bruker Avance spectrometers operating with 250, 300, 500 and 700 MHz frequencies in deuterated chloroform, deuterated dimethyl sulfoxide or deuterated *N,N*-dimethylformamide as a solvent. The calibration of the spectra was done against the solvent signal. The spectra were analyzed using MestReNova 9 from Mestrelab Research S.L.

8.9.1.7 Solid-state NMR

^{31}P MAS NMR measurements were performed with a standard 4 mm magic angle spinning MAS double resonance probe head at 298 K and 121.5 MHz Larmor frequency.

8.9.1.8 Dynamic mechanical analysis (DMA)

Dynamic mechanical analysis (DMA) was performed using an Advanced Rheometric Expansion System (ARES) equipped with a force-rebalanced transducer. Plate−plate geometry was used with plate diameters of 6 mm. The gap between plates was around 1 mm. Experiments were performed under a dry nitrogen atmosphere. The isochronal temperature dependencies of *G*' and *G*'' were determined for ω = 10 rad/s.

8.9.1.9 (4-(hydroxymethyl)cyclohexyl)methyl 3-oxobutanoate (1a)

1,4 cyclohexane dimethanol (200 g; 1.39 mol; 2 eq.) and *tert*-butyl acetoacetate (115 mL; 693.41 mmol; 1 eq.) were dissolved in 250 mL of xylene in a 1 L flask equipped with a still head and condenser. The mixture was heated for 8 h at 135 °C. The *tert*-butanol side-product was removed by distillation during the reaction and the temperature in the still head was typically between 75 and 90 °C. When the temperature dropped to 50 °C, the mixture was cooled and the solvent was removed *in vacuo*. The excessive 1,4 cyclohexane dimethanol was removed by distillation at 160 °C at reduced pressure. The crude product was purified by flash chromatography (ethyl acetate/petroleum ether 3:7) to give a clear oil (yield: 91.6 g, 58%).

^{1}H NMR (300 MHz, Chloroform-d, δ): 4.04 (d, 2H, c-cis), 3.94 (d, 2H, c-trans), 3.49 (d, 2H, h-cis), 3.43 (s, 2H, b), 3.42 (d, 2H, h-trans), 2.24 (s, 3H, a), 1.86-1.77 (m, 4H, d & g), 1.67-0.86 (m, 8H, e & f)

ASAP-MS: 229.2 [M+H]+, 457.5 [2M+H]+ (Calculated M+: 228.14).

8.9.1.10 Monomer 1

To a dried three-necked, 1 L round bottom flask equipped with a dropping funnel, 1a (51.61 g; 226.07 mmol; 2.03 eq.) and pyridine (18.3 mL; 226.07 mmol; 2.03 eq.) were added under an argon atmosphere and dissolved in dry dichloromethane (400 mL). Then, phenyl phosphonic dichloride (15.5 mL; 111.37 mmol; 1.0 eq.) dissolved in dry dichloromethane (100 mL) was added dropwise to the solution at room temperature. The reaction was allowed to stir overnight at room temperature and was then filtered. Afterward, the crude mixture was concentrated at reduced pressure, dissolved in toluene and then filtered to remove most of the ammonium salt byproduct. Then, the crude product was washed three times with water. The organic layer was dried over anhydrous magnesium sulfate, filtered, and dried *in vacuo*.

The crude product was purified by flash chromatography (ethyl acetate/petroleum ether 7:3) to give a clear, slight yellow oil (yield: 82.9 g, 69%).

^{1}H NMR (300 MHz, Chloroform-d, δ): 7.79 – 7.46 (m, 5H, i-k), 4.08 – 3.76 (m, 8H, c & h), 3.43 (s, 4H, b), 2.22 (s, 6H, a), 1.80 (m, 4H, d & g), 1.46 - 0.95 (m, 16H, e & f); ^{31}P {H} NMR (121 MHz, Dichloromethane-d_2, δ): 18.95 (d, 1P, 1)

ASAP-MS: 578.7 [M+H]+ (Calculated M+: 578.26).

8.9.1.11 1,4-Bis(hydroxymethyl)cyclohexane bis-acetoacetate

The synthesis was conducted as described elsewhere.[1]

8.9.1.12 Polymerizations

Poly-1

Monomer 1 (170 g; 0.29 mol; 1 eq.) was added to a glass reactor, equipped with a mechanical stirrer and heated to 70 °C. A mixture of *m*-xylylenediamine (19.2 g; 0.14 mol; 0.48 eq.) and tris(2-aminoethyl)amine (16.3 g; 0.11 mol; 0.38 eq.) were added quickly to the reactor, in which monomer 1 was kept stirring. After 2 min, the mixture turned opaque due to phase separation (water release of the condensation reaction). The mixture was kept stirring at 250 rpm until stalling of the mechanical stirrer. The resulting crude product was removed from the reactor and pressed into a film of 1-2 mm between two Teflon sheets using a preheated press at 110 °C at 30 kN. After 30 min, the film was dried for 24 h in a convection oven at 90 °C, followed by a short post-curing process of 1 h at 150 °C. The yield was quantitative.

Poly-2

1,4-Bis(hydroxymethyl)cyclohexane bis-acetoacetate (170 g; 0.54 mol; 1 eq.) was added to a glass reactor, equipped with a mechanical stirrer and heated to 70 °C. A mixture of *m*-xylylenediamine (35.6 g; 0.26 mol; 0.48 eq.) and tris(2-aminoethyl)amine (30.2 g; 0.21 mol; 0.38 eq.) were added quickly to the reactor, in which 1,4-Bis(hydroxymethyl)cyclohexane bis-acetoacetate was kept stirring. After 2 min, the mixture turned opaque due to phase separation (water release of the condensation reaction). The mixture was kept stirring at 250 rpm until stalling of the mechanical stirrer. The resulting crude product was removed from the reactor and pressed into a film of 1-2 mm between two Teflon sheets using a preheated press at 110 °C at 30 kN. After 30 min, the film was dried for 24 h in a convection oven at 90 °C, followed by a short post-curing process of 1 h at 150 °C. The yield was quantitative.

Prepreg preparations

For poly-1: Monomer 1 (19.2 g; 33.2 mmol; 1 eq.) and the mixture of m-xylylenediamine (2.2 g; 15.9 mmol; 0.48 eq) and tris(2-aminoethyl)amine (1.8 g; 12.6 mmol; 0.38 eq.) were weight into separate graduated cylinders and filled up to 55 mL with methanol to prepare separate stock solutions. For each prepreg, 5 mL of the two solutions were mixed quickly and 7.5 mL of this solution was then poured over twill weave glass fibres (Type 92125, Twill 2/2, 280 g/m2, P-D Interglass Technologies GmbH, Erbach, Germany) in a silicon mould. The mould with the prepreg was transferred to a preheated convection oven at 60 °C and the methanol was removed for 30 min. The prepregs were cured for 24 h at 90 °C and 1 h at 150 °C.

For poly-2: 1,4-bis(hydroxymethyl)cyclohexane bis-acetoacetate (17.3 g; 55.4 mmol; 1 eq.) and the mixture of m-xylylenediamine (3.6 g; 26.6 mmol; 0.48 eq.) and tris(2-aminoethyl)amine (3.1 g; 21.0 mmol; 0.38 eq.) were weight into separate graduated cylinders and filled up to 55 mL with methanol to prepare separate stock solutions. For each prepreg, 5 mL of the two solutions were mixed quickly and 7.5 mL of this solution were poured over twill weave glass fibres (Type 92125, Twill 2/2, 280 g/m2, P-D Interglass Technologies GmbH, Erbach, Germany) in a silicon mould. The mould with the prepreg was transferred to a preheated convection oven at 60 °C and the methanol was removed for 30 min. The prepregs were cured for 24 h at 90 °C and 1 h at 150 °C.

8.9.1.13 Plates for cone calorimetry

The vitrimer was shredded in a blender (Bestek BTBL1193). 50 g of the resulting granulate were weighed into a 12 cm x 12 cm steel form. The form with the vitrimer was heated to 150 °C in the

press without pressure to prevent deformation of the Teflo sheet. Afterwards, a sheet of Teflo was placed ontop of the vitrimer and the stamp of the form was inserted. The pressure was adjusted to 20 kN at 150 °C for 30 min and to 50 kN for another 30 min. The form was allowed to cool to room temperature, while keeping the pressure at 50 kN.

8.9.2 Additional Results

8.9.2.1 Calculation of fibre mass content (fmc)

Table S8.1. Equations used for the calculation of fibre mass content.

$w_{char,GFRP}$	in %	Char yield of the GFRP at 800 °C determined by TGA
$w_{combustible,GFRP} = 100 - w_{char,GFRP}$	in %	Combustible fraction of the GFRP
$w_{char,P}$	in %	Char yield of the neat polymer at 800 °C determined by TGA
$w_{non-combustible\ polymer,GFRP} = w_{char,GFRP} \cdot \left(\frac{w_{char,P}}{100 - w_{char,P}}\right)$	in %	Non-combustible fraction of the polymer in the GFRP
$w_{F,GFRP} = 100 - w_{combustible,GFRP} - w_{non-combustible\ polymer,GFRP}$	in %	Fibre mass fraction in the GFRP

Table S8.2. Char yield of the GFRP and the neat polymer determined by TGA at 800 °C in an oxygen atmosphere.

	$w_{char,GFRP}$ / %		$w_{char,P}$ / %	
	Average	Standard Deviation	Values	Average
Poly-1	71.3	0.5	24.1 24.2	24.2 ±0.1
Poly-2	66.1	3.6	19.3 17.0	18.2 ±1.2

Table S8.3. Fibre mass fraction in the GFRP.

	$w_{combustible,GFRP}$ / %	$w_{non-combusitble\ polymer,GFRP}$ / %	$w_{F,GFRP}$ / %
Poly-1	28.7	9.1	62.2
Poly-2	33.9	7.5	58.6

8.9.3 Additional Data

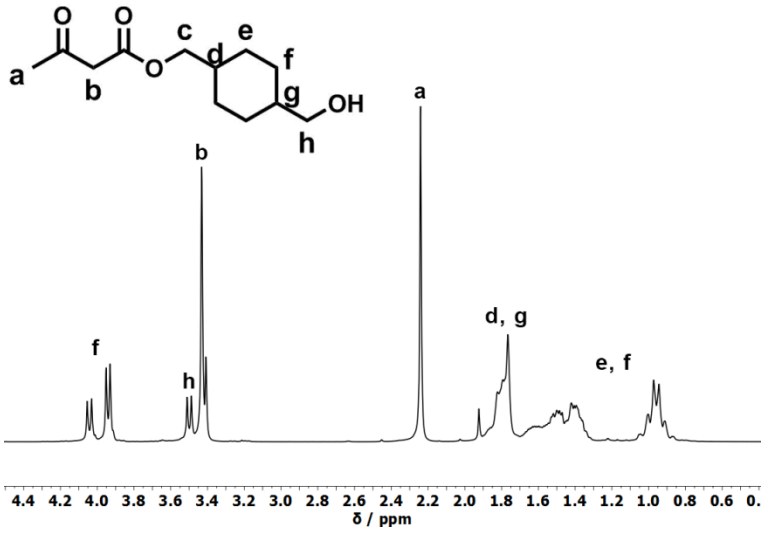

Figure S8.1. ^{1}H-NMR (300 MHz in $CDCl_3$ at 298 K) of 1a.

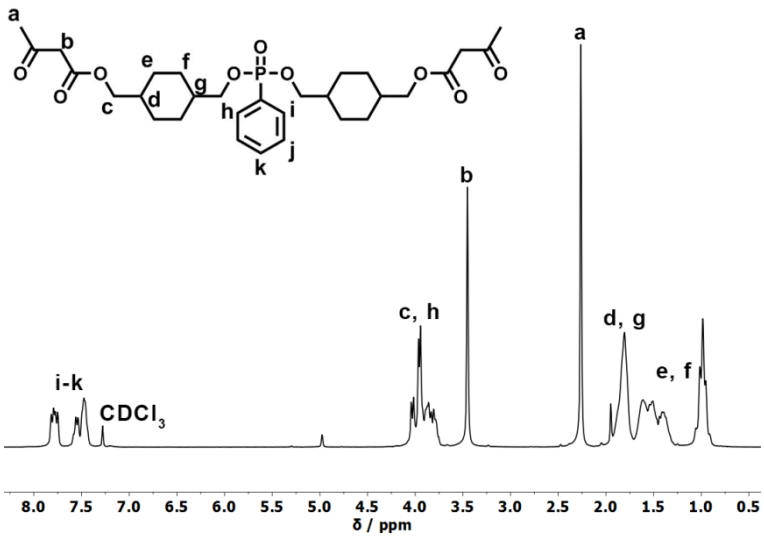

Figure S8.2. ^{1}H-NMR (300 MHz in $CDCl_3$ at 298 K) of 1.

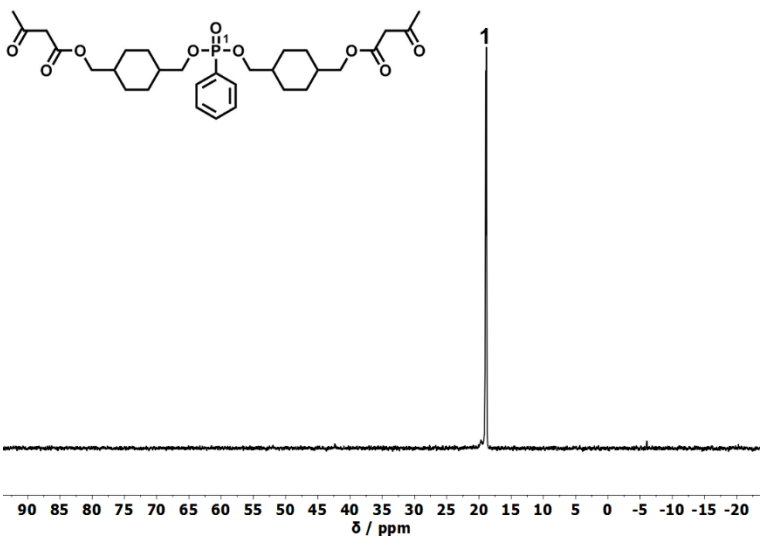

Figure S8.3. ^{31}P {H}-NMR (121 MHz in $CDCl_3$ at 298 K) of 1.

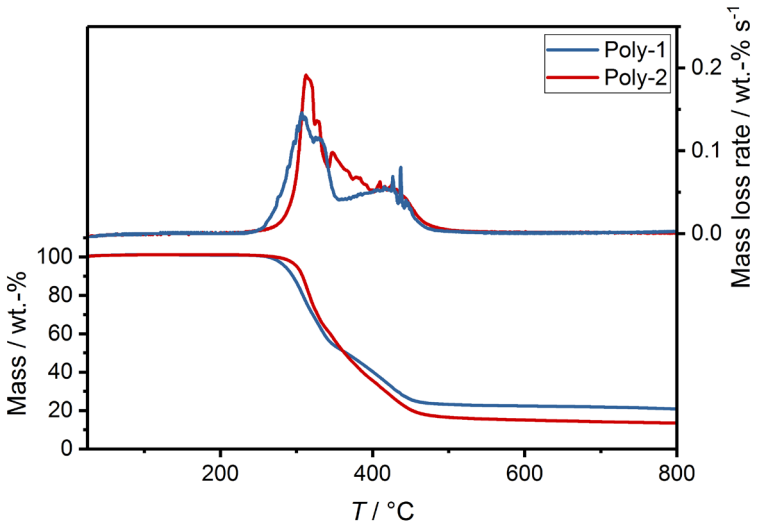

Figure S8.4. Mass loss (bottom) and mass loss rate (top) curves of vitrimers poly-1 and poly-2 in nitrogen via TGA. Heating rate: 10 K min^{-1}.

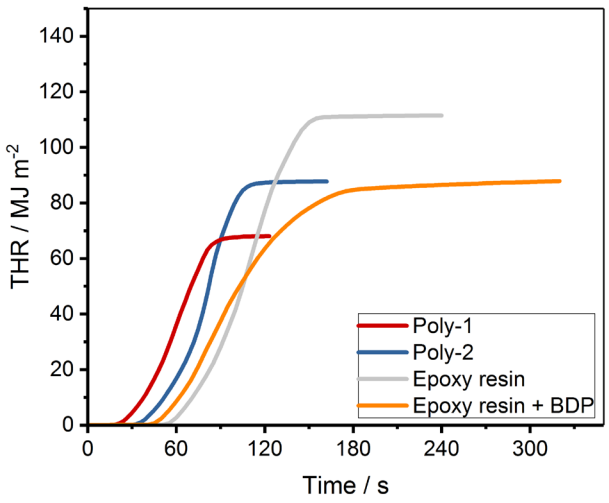

Figure S8.5. Total heat released (THR) measured by cone calorimetry.

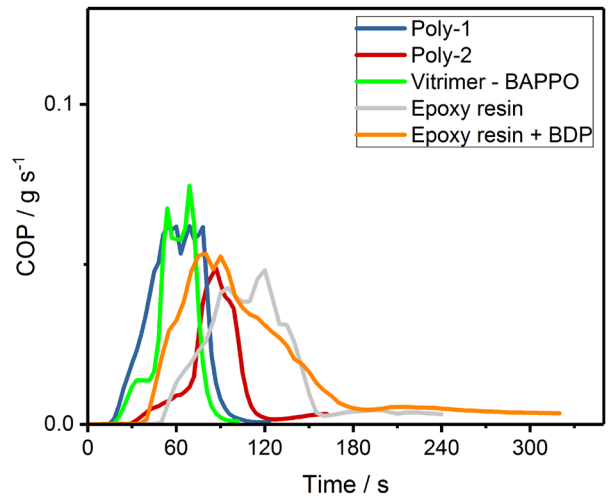

Figure S8.6. Carbon monoxide production (COP) from cone calorimetry.

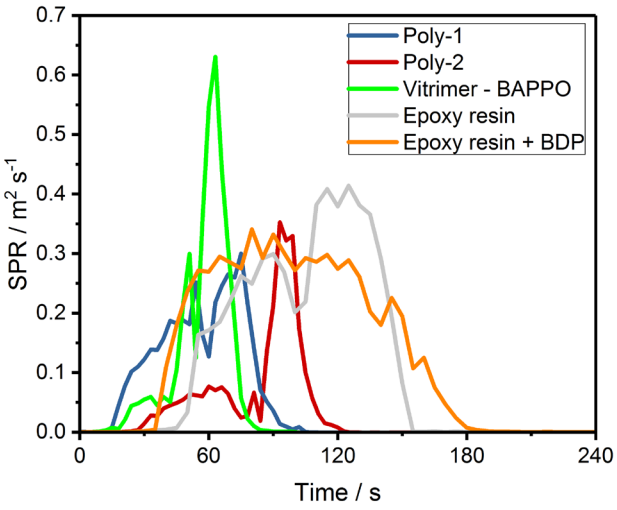

Figure S8.7. Amount of smoke release (SPR) during combustion processes measured by cone calorimetry.

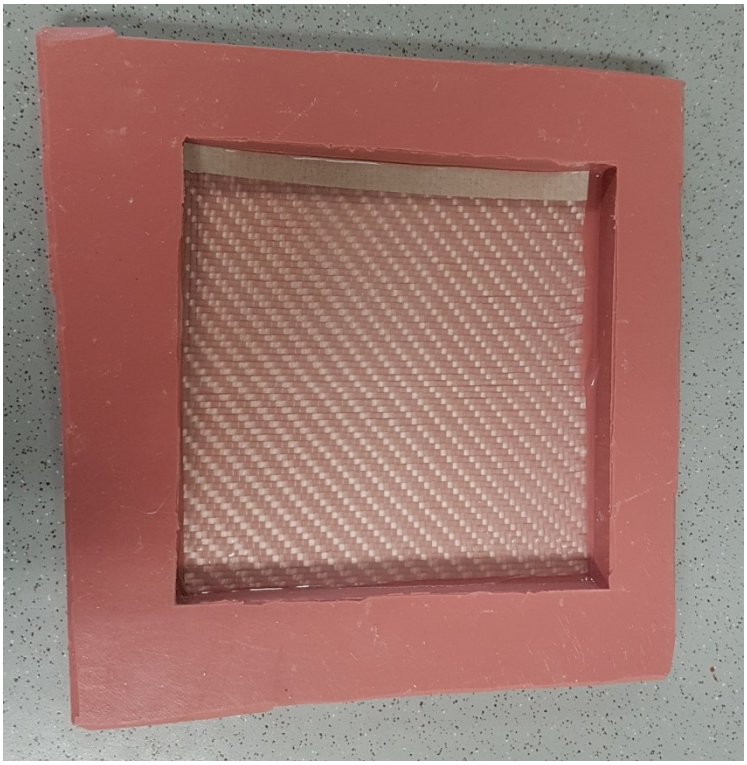

Figure S8.8. Silicone mold used for the preparation of the composites.

Figure S8.9. Prepregs after curing in the convection oven. Top: poly-1, Bottom: poly-2.

Figure S8.10. Preparation of a vitrimer in a heated glass-reacator.

Figure S8.11. Poly-1 after polycondensation and released from the glass-reactor.

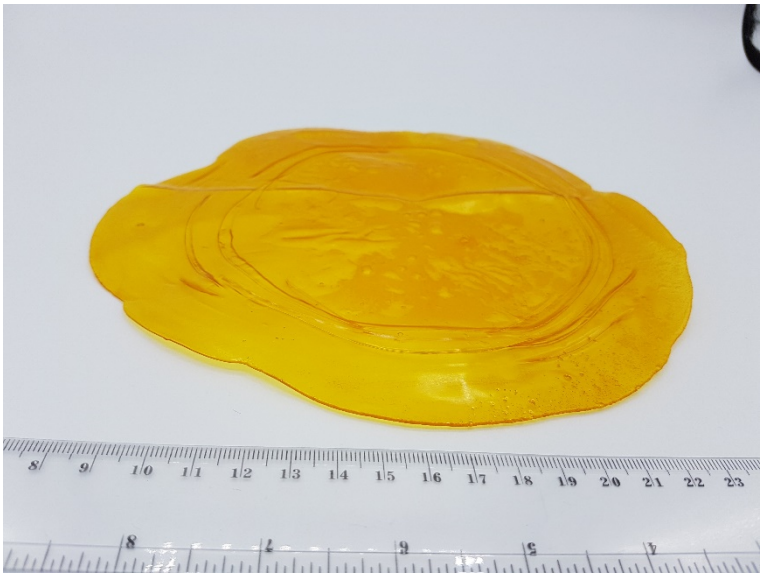

Figure S8.12. Poly-1 after Curing in a convertion oven.

Figure S8.13. Poly-1 after shredding with a blender (Bestek BTBL1193).

Figure S8.14. Preparation of 12 x 12 mm² cone plates: Poly-1 pouder in a steel mold.

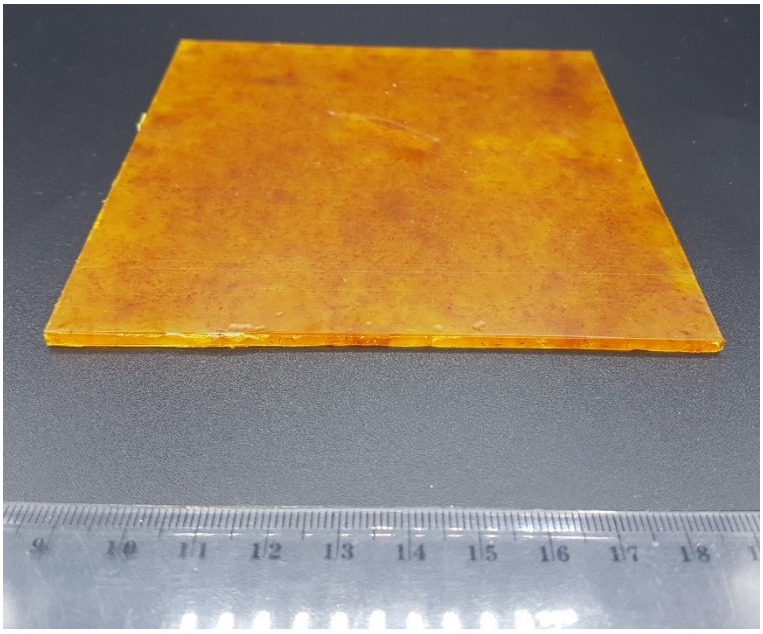

Figure S8.15. Preparation of 12 x 12 mm² cone plates: Poly-1 cone plate after releasing from the mold.

8.9.4 References SI Chapter 8

[1] W. Denissen, G. Rivero, R. Nicolaÿ, L. Leibler, J. M. Winne, F. E. Du Prez, *Adv. Funct. Mater.* **2015**, *25*, 2451-2457.

8.10 Appendix

Phosphinoxides are a promising material-class for vitrimers, due to the higher temperature and hydrolysis stability of the P-C bond in comparison to the P-O bond.[1] In addition, Braun et al. reported that phosphinoxides have a better flame-retradant effect in composite materials.[2]

Monomer 3 was prepared by a four-step synthesis as shown in **Figure A8.1a**. Starting from phenol and phenylphosphonic dichloride, compound 3a was synthesized, which was reacted in a Fries rearrangement to 3b. To yield compound 3c, 3b was reacted with 2- bromoethanol in a Williamson ether synthesis and in the last step, a transesterification with *tert*-butyl acetoacetate was conducted, yielding compound 3. Compound 3 was obtained as a white solid in 45% overall yield. The ^{31}P NMR of 3 exhibited two distinct signals at 23.74 ppm and 23.52 ppm, with the signal 23.74 ppm being the main signal. The second smaller signal at 23.52 ppm can be attributed to the keto-enol tautomer (**Figure A8.9**).

The vitrimer was prepared by spontaneous condensation of the amines m-xylylendiamine and tris(2-aminoethyl)amine with the β-ketoester monomer 3 analog to poly-1 and poly-2.

The ^{31}P MAS solid-state NMR of poly-3 exhibited a single resonance at 21.25 ppm, showing no signs of degradation (**Figure A8.1d**). Differential scanning calorimetry (DSC) with a heating rate of 10 K min^{-1} revealed a glass-transition temperature (T_g) of 94 °C, which is slightly higher than polyether-amine cured DGEBA (T_g of 88 °C). The thermal stability of the resulting network was measured by thermogravimetric analysis in a nitrogen atmosphere and a heating rate at 10 K min^{-1}. The material was stable past 200 °C and had the highest onset temperature ($T_{5\%}$)with 305 °C. The residue at 700 °C was 14 wt.-% and therefore similar to the non-phosphorus containing vitrimer poly-2. In comparison, poly-1 and poly-2 were stable past 200 °C as well, with a residue of 22 wt.-% and 14 wt.-% for poly-1 and poly-2, respectively. $T_{5\%}$ was 285 °C for poly-1 and 300 °C for poly-2.

The intrinsic flame-retardant properties of poly-3 were investigated by forced flaming using the cone calorimeter, which is widely used for assessing the fire behavior of polymer materials.[3] Poly-3 exhibited a clear reduction in THE by 46% (from 89 MJ m^{-2} to 48 MJ m^{-2}) compared to the vitrimer without phosphorus (poly-2) and a reduction in THE by 26% (from 65 MJ m^{-2} to 48 MJ m^{-2}) compared to the phosphonate-based vitrimer poly-1. However, a reduction in PHRR (2459 kW m^{-2} and 2346 kW m^{-2} for poly-3 and poly-2, respectively) was not observed. The reduction in THE is explained by the strong gas phase activity of phosphine oxides, leading to a

strong intumescent behavior, which finally extinguished the fire. The gas phase activity is also visible in pyrolysis combustion flow calorimetry (PCFC) measurements.

In PCFC measurements, the heat release capacity (HRC) for poly-3 was higher compared to the reference poly-2 (287 ± 2 and 349 ± 1 J g^{-1} K^{-1} for the reference poly-2 and poly-3, respectively). This correlates well with the observed higher PHRR in cone measurements. The high HRC is explaned by the increased production of volatile decomposition products compared to poly-2. As PCFC is blind to flame poisoning, the strong reduction in EHC from the cone calorimeter measurements by 43% (from 28 MJ kg^{-1} to 16 MJ kg^{-1} for poly-2 and poly-3, respectively) in spite of a strong increase of HRC in PCFC support the assumption of a strong gas-phase mechanism via flame-poisoning for poly-3. The THE in PCFC is reduced from 24.65 kJ g^{-1} for the reference poly-2 to 23.5 kJ g^{-1} for poly-3, which correlates well with cone measurements.

In conclusion, the fire load of poly-3 was significantly decreased compared to poly-1 and poly-2 due to its strong intumescent behavior and highest gas phase activity as evidenced by a strong reduction in EHC. However, the fire growth index (PHRR/t_{ig}) significantly increased, due to its early time of ignition and high PHRR. The epoxides, on the other hand, show a higher fire load as evidenced by the higher THE, but a reduced fire growth index, which might be explained by the reduced ability of depolymerization for the epoxides and therefore a reduced mass transfer from the condensed to the gas phase.

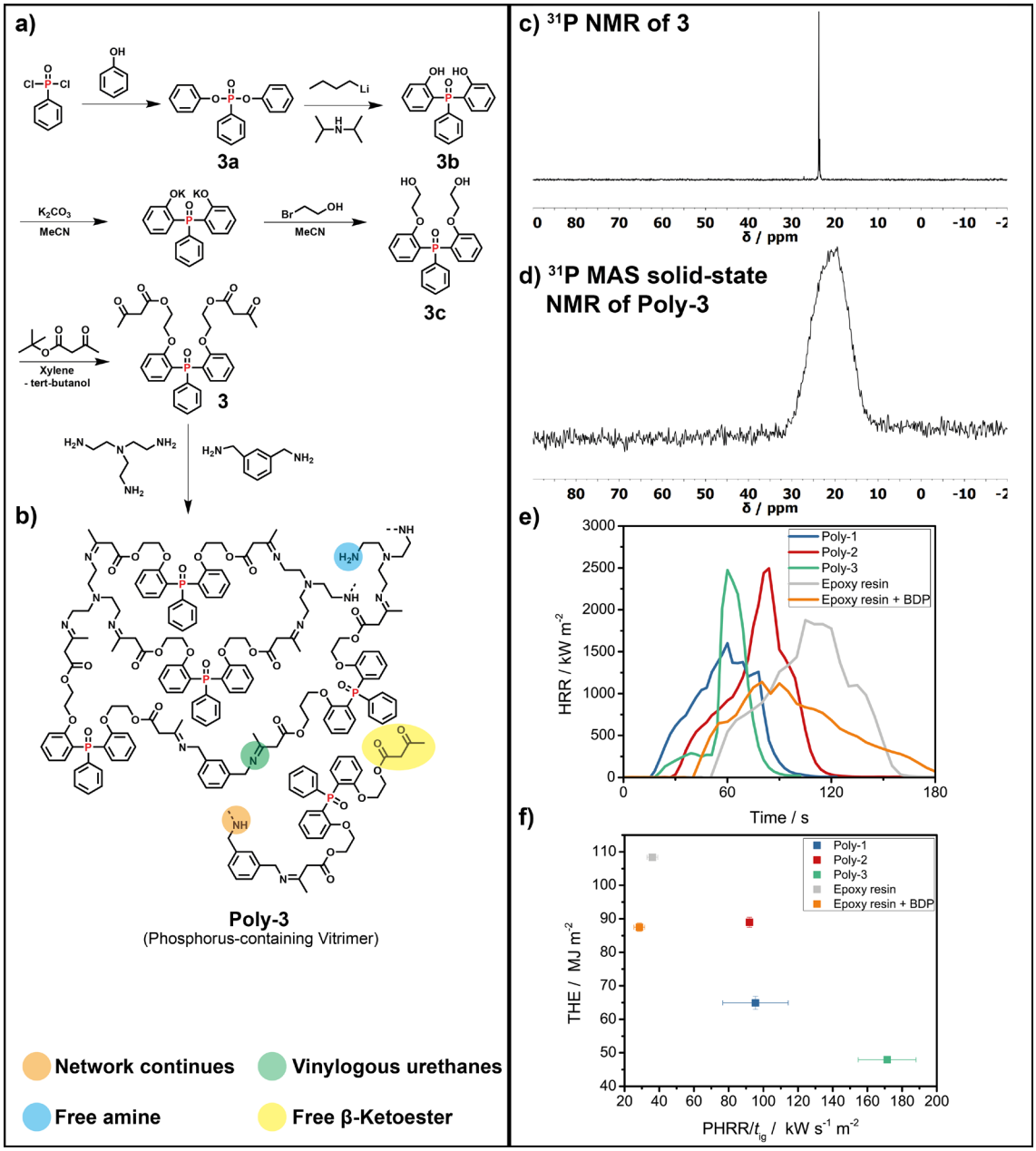

Figure A8.1. a) Synthesis of monomer 3 and **(b)** the formation of the vinylogous polyurethane network by spontaneous condensation of an amine with the β-ketoester group. **c)** ^{31}P {H} NMR (121 MHz in $CDCl_3$ at 298 K) of 3. **d)** ^{31}P MAS solid state NMR of poly-3, 20 kHz MAS, at 298 K and 121.5 MHz ^{31}P Lamor frequency. **e)** Heat release rate over time of vitrimers poly-1, poly-2, poly-3 and epoxy resins, with poly-2 and poly-3 presenting the highest peak heat release and the epoxy resin + BDP the lowest. **f)** Petrella plot of the vitrimers and epoxy resins with all phosphorus containing materials having a positive effect (lowering THE or PHRR/t_{ig}).

8.10.1 Experimental

8.10.1.1 3a

To a dried three-necked, 500 mL round bottom flask fitted with a dropping funnel, phenol (30.4 g; 323.11 mmol; 2.1 eq.) and triethyl amine (44.8 mL; 323.11 mmol; 2.1 eq.) were added under an argon atmosphere in dry dichloromethane (150 mL). Then phenylphosphonic dichloride (21.8 mL; 153.86 mmol; 1.0 eq.) dissolved in dry dichloromethane (60 mL) was added dropwise to the solution at room temperature. The reaction was allowed to stir overnight at room temperature and was then filtered. Afterwards, the crude mixture was concentrated at reduced pressure, dissolved in toluene and then filtered to remove most of the ammonium salt byproduct. Then, the crude product was washed three times with sodium bicarbonate solution, 10% hydrochloric acid and water. The organic layer was dried over anhydrous magnesium sulfate, filtered, and dried in vacuo. The yield was quantitative (47.7 g). The purity and chemical structure was determined by ^{1}H NMR and ^{31}P {H} NMR spectroscopy.

^{1}H NMR (300 MHz, Chloroform-d, δ): 7.98 – 7.79 (m, 2H), 7.55 (td, *J* = 7.4, 1.6 Hz, 1H), 7.44 (td, *J* = 7.5, 4.7 Hz, 2H), 7.23 (dd, *J* = 8.8, 7.0 Hz, 4H), 7.10 (d, *J* = 7.8 Hz, 6H); ^{31}P {H} NMR (121 MHz, Chloroform-d, δ): 11.71 (d, 1P, 1)

8.10.1.2 3b

To a dried three-necked, 1 L round bottom flask fitted with a dropping funnel, diisopropyl amine (37.7 g; 323.11 mmol; 2.1 eq.) and 2.5 M n-BuLi in THF (129.2 mL; 323.11 mmol; 2.1 eq.) were added under an argon atmosphere in dry THF (120 mL). Then 1a (47.7 g; 153.86 mmol; 1.0 eq.) dissolved in dry THF (200 mL) was added dropwise to the solution while cooling with a acetone/dry ice bath. After addition, the reaction was allowed to stir for 1 h at -80 °C and was then slowly warmed to room temperature. Afterwards, water (100 mL) and concentrated HCl (120 mL) was added. Then, to crude product DCM was added and washed three times with water. The organic layer was dried over anhydrous magnesium sulfate, filtered, and dried in vacuo. The yield was quantitative (95.5 g).

^{1}H NMR (300 MHz, Chloroform-d, δ): 7.74 – 7.58 (m, 3H), 7.58 – 7.42 (m, 4H), 7.13 – 6.98 (m, 4H), 6.91 (tdd, *J* = 7.5, 2.9, 1.1 Hz, 2H); ^{31}P {H} NMR (121 MHz, Chloroform-d, δ): 48.91 (d, 1P, 1)

8.10.1.3 3c

To a dried three-necked, 2 L round bottom flask fitted with a condenser, 1b (48.6 g; 156.72 mmol; 1.0 eq.) and potassium carbonate (216.6 g; 1.57 mol; 10.0 eq.) were added under an argon atmosphere in dry acetonitrile (1 L). The mixture was stirred for 20 min. Then 2-bromoethanol (111.1 mL; 1.57 mol; 10.0 eq.) was added and refluxed over night. Afterwards, the crude mixture was concentrated at reduced pressure, dissolved in DCM and then water was added. The aqueous phase was extracted five times with DCM. The organic layer was dried over anhydrous magnesium sulfate, filtered, and dried in vacuo.

The crude product was purified by recrystallization from ethanol. (Yield: 63.5 g; 52%).

^{1}H NMR (300 MHz, Chloroform-d, δ): 7.75 (dd, *J* = 12.7, 7.4 Hz, 2H), 7.54 (dtd, *J* = 67.1, 13.9, 10.2, 5.6 Hz, 5H), 7.36 – 7.15 (m, 2H), 7.03 (t, *J* = 6.9 Hz, 4H), 4.14 (t, *J* = 4.1 Hz, 4H), 3.79 – 3.49 (m, 4H); ^{31}P {H} NMR (121 MHz, Chloroform-d, δ): 30.62 (d, 1P, 1)

8.10.1.4 3

To a 1 L round bottom flask fitted with a condenser, 1c (57.5 g; 144.33 mmol; 1.0 eq.) and tert-butyl acetoacetate (48.0 g; 303.09 mmol; 2.1 eq.) were added in Xylene (450 mL) and heated at 135 °C until full conversion is reached. The tert-butanol was removed during the reaction. Afterwards, the crude mixture was concentrated at reduced pressure, dissolved in DCM and then precipitated in n-hexane four times to obtain the pure product (yield: 70.7 g; 86%).

^{1}H NMR (300 MHz, Chloroform-d, δ): 7.91 – 7.72 (m, 2H), 7.56 (ddd, *J* = 14.1, 7.5, 1.7 Hz, 2H), 7.50 – 7.28 (m, 5H), 7.08 – 6.91 (m, 2H), 6.81 (dd, *J* = 8.3, 5.2 Hz, 2H), 3.94 (ddd, *J* = 17.0, 8.7, 3.6 Hz, 6H), 3.84 – 3.63 (m, 2H), 3.28 (d, *J* = 5.5 Hz, 4H), 2.16 (s, 9H); ^{31}P {H} NMR (121 MHz, Chloroform-d, δ): 23.74 (d, 1P, 1). ASAP-MS *m*/*z*: 567.0 (M + H) (calculated: 566.17).

8.10.1.5 Poly-3

To a chemical reactor 3 (150 g; 0.26 mol; 1 eq.) dissolved in 15 mL methanol was added, heated to 80 °C and stirred with a mechanical stirrer. The amines m-xylylendiamine (17.3 g; 0.13 mol; 0.48 eq.) and tris(2-aminoethyl)amine (14.7 g; 0.10 mol; 0.38 eq.) were mixed in a beaker, dissolved in 10 mL methanol and added fast to the chemical reactor. After 2 min, the mixture turned white due to phase separation (water release of the condensation reaction). The resulting crude product was taken out and pressed into a film of 1-2 mm between two Teflon sheets using a preheated press at 100 °C at 30 kN. After 30 min, the film was dried for 24 h in a convection oven at 90 °C, followed by a short postcure process of 1 h at 150 °C in vacuo.

8.10.2 Supporting Data

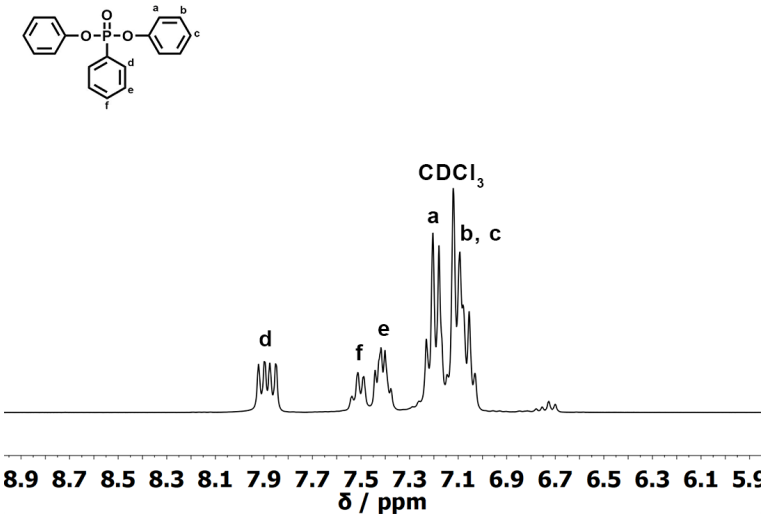

Figure A8.2. ^{1}H-NMR (300 MHz in $CDCl_3$ at 298 K) of 3a.

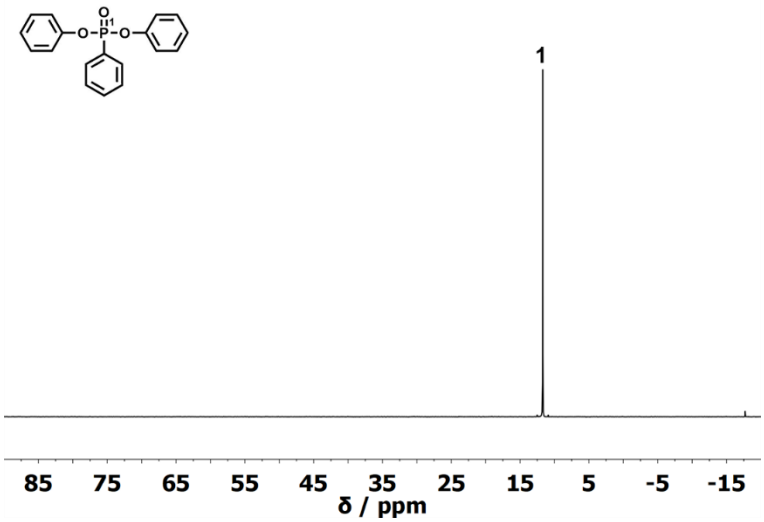

Figure A8.3. ^{31}P {H}-NMR (121 MHz in $CDCl_3$ at 298 K) of 3a.

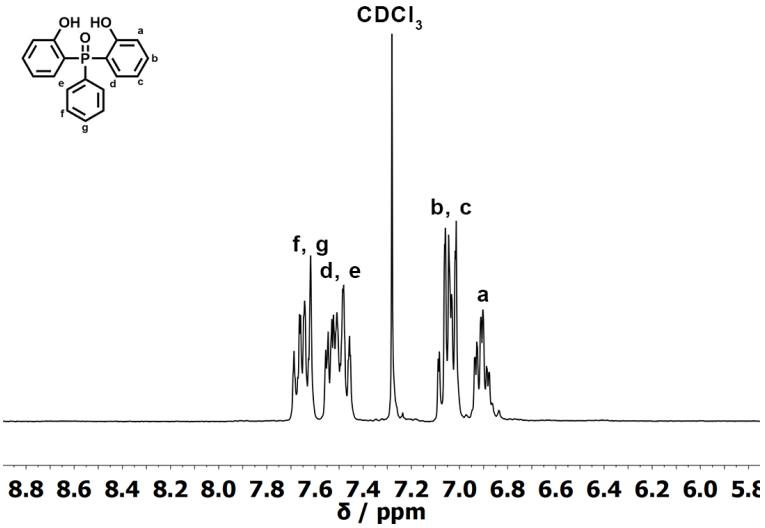

Figure A8.4. ^{1}H-NMR (300 MHz in $CDCl_3$ at 298 K) of 3b

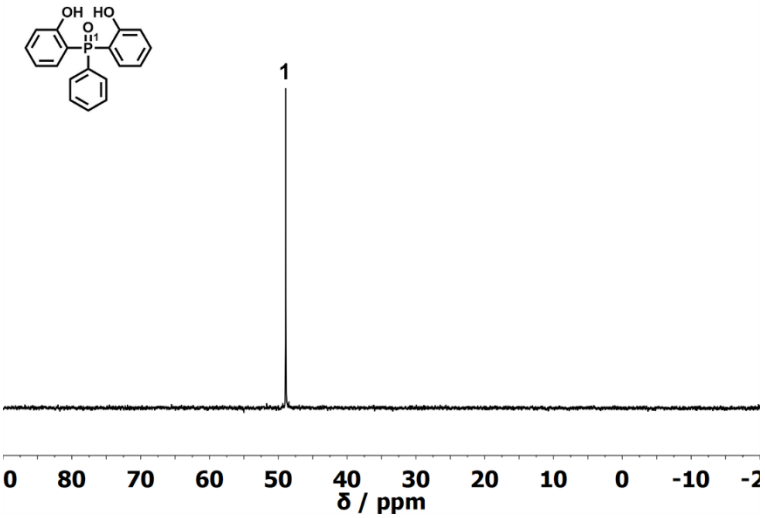

Figure A8.5. ^{31}P {H}-NMR (121 MHz in $CDCl_3$ at 298 K) of 3b.

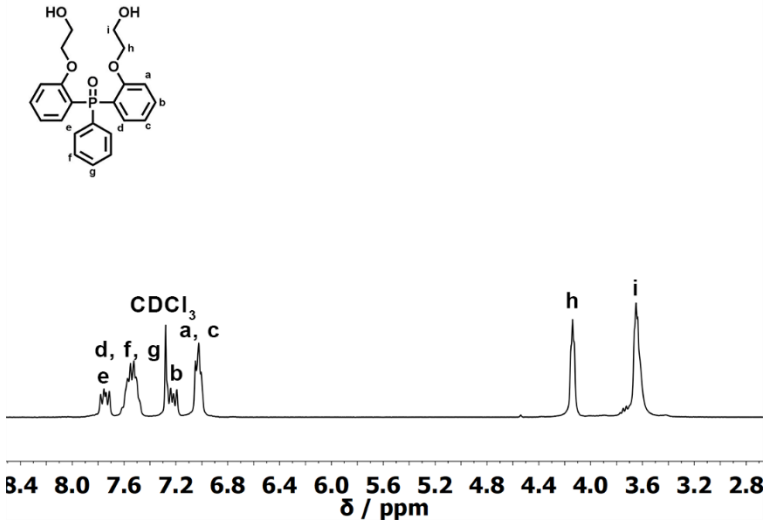

Figure A8.6. ^{1}H-NMR (300 MHz in $CDCl_3$ at 298 K) of 3c.

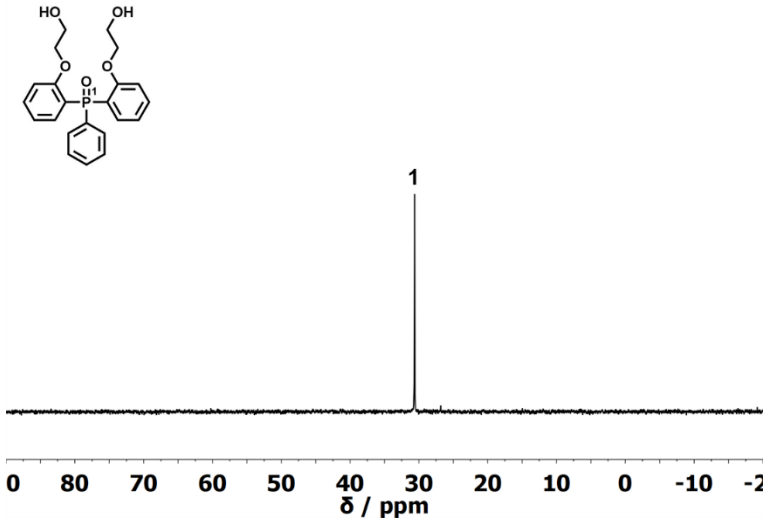

Figure A8.7. ^{31}P {H}-NMR (121 MHz in $CDCl_3$ at 298 K) of 3c.

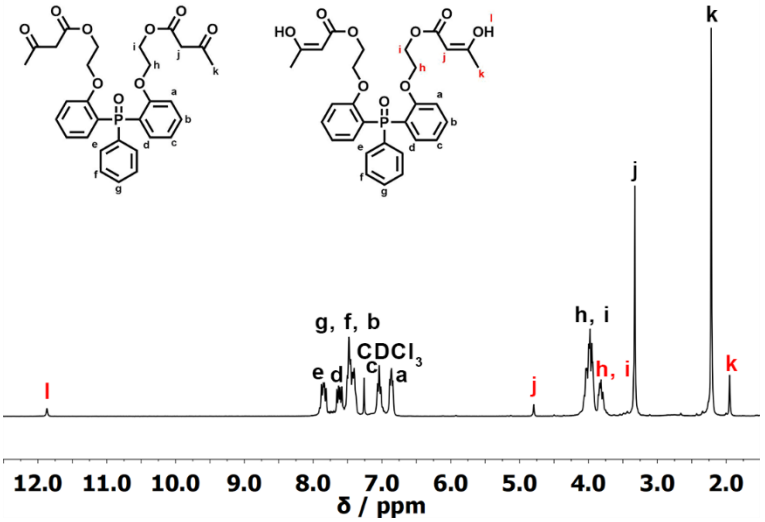

Figure A8.8. ^{1}H-NMR (300 MHz in $CDCl_3$ at 298 K) of 3.

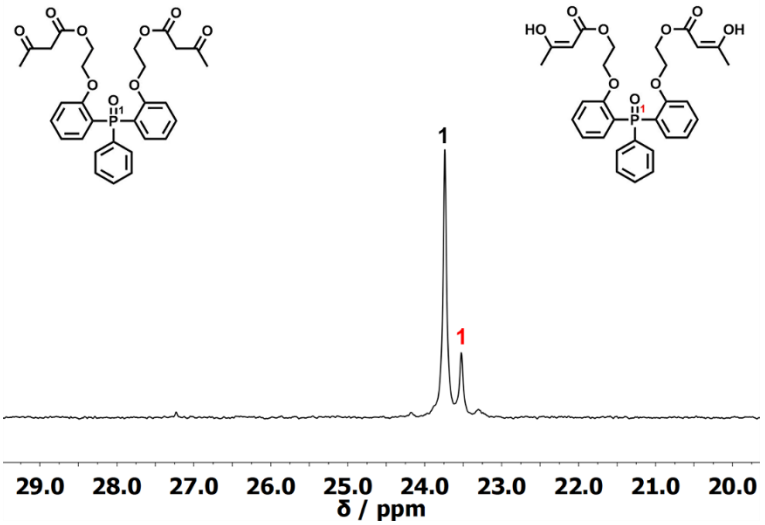

Figure A8.9. ^{31}P {H}-NMR (121 MHz in $CDCl_3$ at 298 K) of 3.

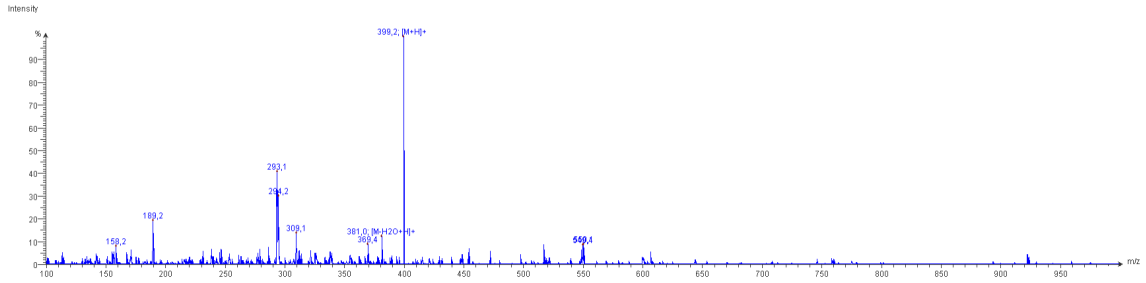

Figure A8.10. ASAP mass-spectrum of 3c, showing a signal at m/z 399.2.

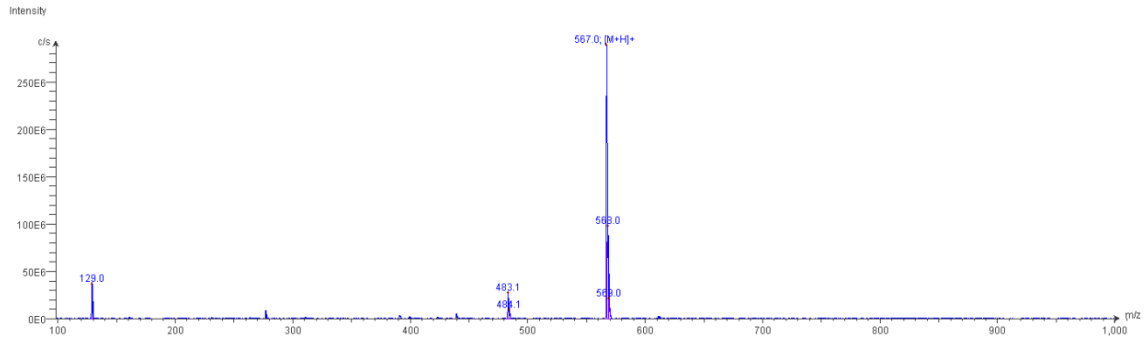

Figure A8.11. ASAP mass-spectrum of 3, showing a signal at m/z 567.0.

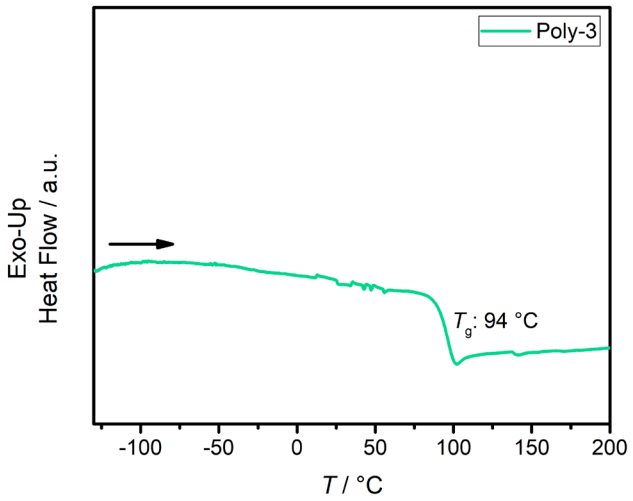

Figure A8.12. Results from DSC measurements (10 K min^{-1}) for Poly-3.

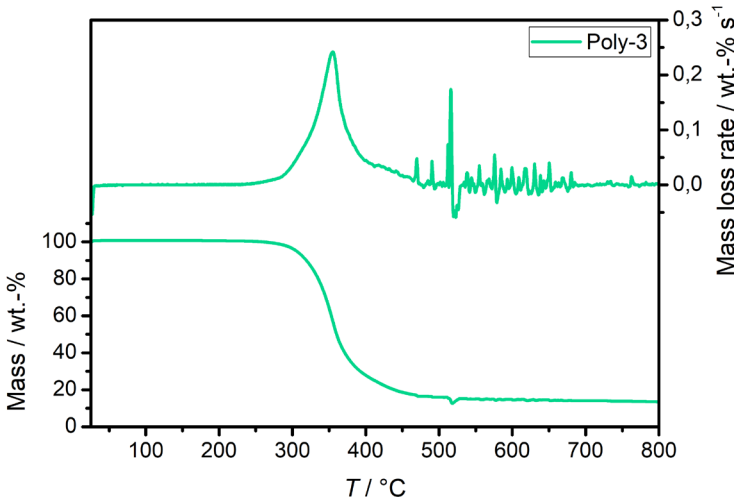

Figure A8.13. Mass loss (bottom) and mass loss rate (top) curves of poly-3 in N_2 via TGA. Heating rate: 10 K min^{-1}.

8.10.3 References Appendix Chapter 8

[1] Z. Tan, C. Wu, M. Zhang, W. Lv, J. Qiu, C. Liu, *RSC Advances* **2014**, *4*, 41705-41713.

[2] U. Braun, A. I. Balabanovich, B. Schartel, U. Knoll, J. Artner, M. Ciesielski, M. Döring, R. Perez, J. K. W. Sandler, V. Altstädt, T. Hoffmann, D. Pospiech, *Polymer* **2006**, *47*, 8495-8508.

[3] V. Babrauskas, *Fire and Materials* **1984**, *8*, 81-95.

9. The 2-acetylthioethyl ester group: A versatile protective group for P-OH-groups

Jens C. Markwart[a,b], Frederik R. Wurm[a]*

[a] *Physical Chemistry of Polymers - Max Planck Institute for Polymer Research, Ackermannweg 10, 55128 Mainz, Germany*

[b] *Graduate School Materials Science in Mainz, Staudinger Weg 9, 55128 Mainz, Germany*

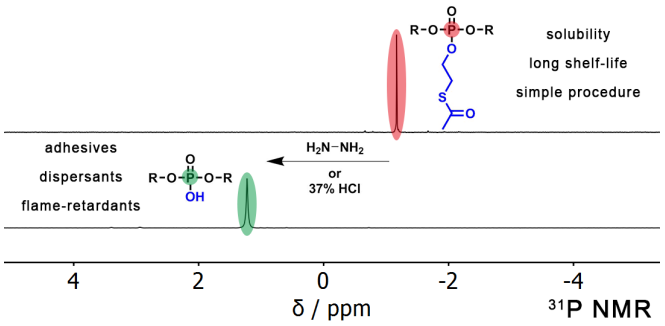

Keywords: Polyphosphoester, Protective group, ADMET, Adhesive, Phosphorus

9.1 Notes

9.2 Abstract

Phosphodiesters are bridging elements in nucleic acids. In nature and synthesis, their negative charge protects them from hydrolysis and controls their solubility profile. RNA is a promising material for gene technology but cellular uptake is low due to negative charges. Synthetic oligonucleotides were delivered into cells by a prodrug approach relying on the enzymatic release of the polyphosphodiester oligonucleotides. In synthetic chemistry, a protective group for the P-OH functionality is often necessary, e.g. due to solubility or chemical incompatibility. Several methods for P-OH protection were proposed, but often with low selectivity or harsh conditions. Here, we present the 2-acetylthioethyl group as a versatile protective group for low molecular weight or polymeric phosphodiesters, which can be cleaved under acidic conditions in water or by hydrazine in THF to release the P-OH-functionality, but olefins remain intact. This straightforward use allows designing various synthetic polyphosphodiesters, e.g. for flame-retardant or dispersants.

9.3 Introduction

Phosphodiesters build the backbone of DNA or RNA. Their negative charge protects DNA from hydrolytic degradation.[2,3] In modern medicine, oligonucleotides are promising gene therapeutics, but due to the negative charge are only poorly internalized by cells.[1] To increase cellular uptake, prodrug approaches were developed.[1] One method used a 2-acetylthioethyl group, which masks the negative charge of the phosphate by creating a neutral phosphotriester. Those neutral oligonucleotides could be internalized by cells, but the thioacetate is cleaved enzymatically by intracellular carboxyesterases to release the free thiol-group, which then forms the phosphodiester under the release of thiirane.[1]

Besides biomedical applications, polyphosphodiesters are also interesting for synthetic chemistry, e.g. for the generation of potentially biocompatible and biodegradable materials[4-7] or to increase polymer hydrophilicity. However, the direct preparation of polyphosphodiesters is not possible. Polycondensation with phosphoryl chloride results in ill-defined branched or cross-linked structures or acyclic diene metathesis polymerization (ADMET) only produced oligomeric PPEs.[8] Also, the ring-opening polymerization of cyclic phospholanes does not tolerate free P—OH-groups and makes protective groups inevitable.[9] We recently used a diene monomer containing a P-Cl bond for ADMET, followed by hydrolysis to the respective polyphosphodiester.[8,10] However, the high electrophilicity of the P—Cl makes handling difficult and working under strictly dry conditions is essential to prevent short shelf life and cross-linking reactions during polymerization. Other protective groups could be removed by hydrogenation, e.g. benzylesters.[9] This method however, would also remove olefins in the desired polymers.[9] Other reports used dealkylation of an alkoxy sidechain by treating the phosphate with a strong nucleophilic reagent, which however is plagued by backbone degradation.[11-13] The third method utilized the different pH-stability of phosphoramidates and phosphates, in which the acid-labile phosphoramidate bond was cleaved under relatively mild acidic conditions.[14,15] Other routes rely on the oxidation of H-phosphonates with N_2O_4 [16] or thermolysis of tert-butyl esters.[17]

We propose the 2-acetylthioethyl ester group as a protective group for the P—OH functionality in low molecular weight phosphates as well as polyphosphates. In contrast to the above-mentioned strategies, the protected materials are accessible by straightforward chemistry and possess long shelf lives with fast purifications. The cleavage was possible both in organic solvents as well as in water and did not interfere with olefins. All these factors render the 2-acetylthioethyl phosphoester an attractive protective group for synthetic (poly)phosphodiesters.

9.4 Results and discussion

Phosphoryl chloride was first reacted with 2-bromoethanol followed by a reaction with hex-5-en-1-ol to yield 2-bromoethyl di (hex-5-en-1-yl)phosphate (**2**), which was then reacted with potassium thioacetate to give 2-acetylthioethyl di(hex-5-en-1-yl)phosphate (**3**, Fig. 9.1). This compound was used as an unsaturated model compound for the cleavage of the 2-acetylthioethyl phosphoester to di(hex-5-en-1-yl) hydrogen phosphate (**4**).

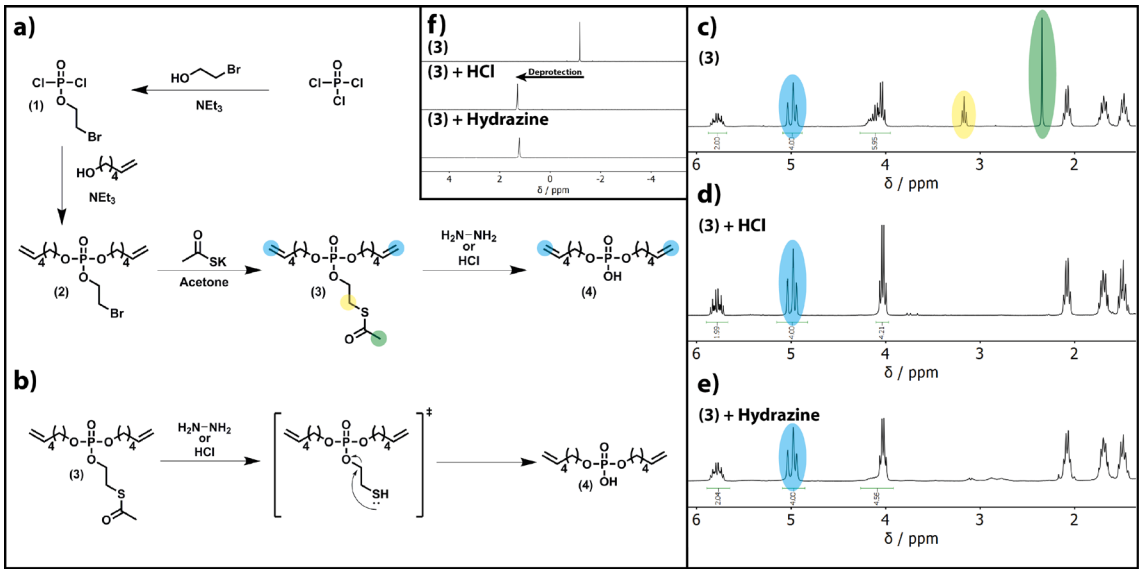

Figure 9.1. a) Synthesis of 2-acetylthioethyl ester–protected unsaturated phosphate 3 and removal of the protective group to 4 according to b) the proposed mechanism.1 c) ^{1}H NMR spectrum (300 MHz, $CDCl_3$, T = 298 K) of 3. d, e) ^{1}H NMR (300 MHz, $CDCl_3$, T = 298 K) of reaction of 3 with HCl (d) and hydrazine (e). f) ^{31}P NMR spectra (121 MHz, $CDCl_3$, T = 298 K) of the 2-acetylthioethyl ester–protected compound (3) and the reaction product (4) after treatment with HCl or hydrazine.

Thioesters are often used as a protective group for the highly nucleophilic thiols, which can be cleaved under acidic or basic conditions.[18-20] However, if a 2-acetylthioethyl group is linked via a phosphoester, the hydrolysis of the thioester to the thiol will be followed by a complete removal of the alkyl chain from the phosphate and releases a phosphodiester.[1,21] This strategy was extensively used in solid-phase oligonucleotide synthesis, followed by enzymatic cleavage of the thioester.[1,21] We used either hydrazine (method a (Experimental)) or hydrochloric acid (method b (Experimental)) to successfully release the $PO(OR)_2OH$ (compounds **4** or **Poly-4**). The successful formation of the P-OH group was proven by ^{31}P{H} and ^{1}H NMR spectroscopy and mass spectrometry. The first indication for a successful removal of the 2-acetylthioethyl ester was the down-field shift in the ^{31}P NMR from −1.17 ppm in compound **3** to 1.30 ppm in compound **4** (Fig. 9.1 f). The release of the P-OH-group was further supported by the integral of the methylene

groups next to the phosphoesters at ca. 4 ppm in the ^{1}H NMR spectra, which corresponded to four instead of six (Fig. 9.1 c – e). This indicates that there are only two alkyl chains attached to the phosphate. Furthermore, the resonances for the methylene groups next to the thioester at 3.15 ppm vanished and no new resonances for a free thiol group are detected (Fig. 9.1 d, e). When we used K_2CO_3 in methanol to remove the 2-acetylthioethyl group (another typical procedure for the cleavage of thioesters[20]), we found partial formation of **4**, but also the formation of the methyl ester via transesterification with methanol. The ^{1}H NMR spectrum of the crude reaction mixture showed a typical doublet with a J = 11.1 Hz for a methyl-ester ("P-O-CH_3") due to the coupling with phosphorus (Fig. S9.8).

The mechanism for the enzymatic removal of the 2-acetylthioethyl ester in synthetic oligonucleotides was reported to release the phosphodiesters.[1,21] After hydrolysis of the thioester to the thiol, a nucleophilic attack by the thiol on the methylene group next to the ester group was postulated to release the phosphodiester and thiirane, which probably will be hydrolyzed to mercaptoethanol or react with the nucleophilic hydrazine.[1,21] We propose the same mechanism on the synthetic phosphates as shown in Fig. 9.1 b, which retains the olefins in the molecule for further functionalization. Mass spectrometry analysis of the crude reaction from **3** to **4** proves the formation of the product **4** and the cleaved side chain with further adducts with hydrazine (cf. Supp. Info.). The reaction was also monitored by real-time ^{1}H NMR spectroscopy as the disappearance of the thioacetate resonance gives a direct insight to the reaction kinetics (cf. Supp. Info. for further details). The successful formation of **4** was proven by the reaction with trimethylsilyldiazomethane to convert the hydroxyl group to a methyl ester. The typical doublet for the methyl ester due to coupling with phosphorus can be appreciated in the ^{1}H NMR spectrum (J = 11.1 Hz, Fig. S9.1).

After the successful preparation of low molecular weight phosphodiesters, we studied the synthesis of polyphosphodiesters by the 2-acetylthioethyl ester protective group. The synthesis of polyphosphodiesters with a hydrophobic backbone is often plagued by the low solubility of oligomers or polymers in common organic solvents.[8] Thus, a solubilizing protective group is a desirable intermediate. We used monomer **2** to prepare a polyphosphate by ADMET polymerization (**Poly-2**, Mn = 5100 g mol-1 D = 1.68) according to a modified literature procedure.[10] After the polymerization, the alkyl bromide in the pendant chains was reacted with potassium thioacetate (in acetone, r.t., 12 h) to produce the 2-acetylthioethyl ester protected PPE (**Poly-3**). The product shows two characteristic resonances in the ^{1}H NMR spectrum at 2.28 ppm, which were attributed to the methyl group of the thioacetate, and the methylene group at 3.10 ppm next to the thioester. The polymer (**Poly-3**) was bench-stable at room temperature for

at least several weeks. In the final step, the polymer was treated with hydrazine in THF at r.t. to release the polyphosphodiester (**Poly-4**). During the reaction, the polymer precipitated from solution. The crude product **Poly-4** was soluble in $CDCl_3$/MeOD and the removal of the 2-acetylthioethyl ester was proven as the resonance of the methylene group next to the thioester at 3.17 ppm vanished and the signal of the leaving group shifts to 1.73 ppm. In addition a down-field shift in the ^{31}P NMR from −1.16 ppm to 0.55 ppm was observed, which is indicative for the cleavage of the pendant ester. Purification of **Poly-4** was achieved by precipitation into diethyl ether and obtained as an off-white viscous liquid in 84% yield. The ^{1}H DOSY-NMR spectrum additionally proves the formation of **Poly-4** (Fig. 9.2 e).

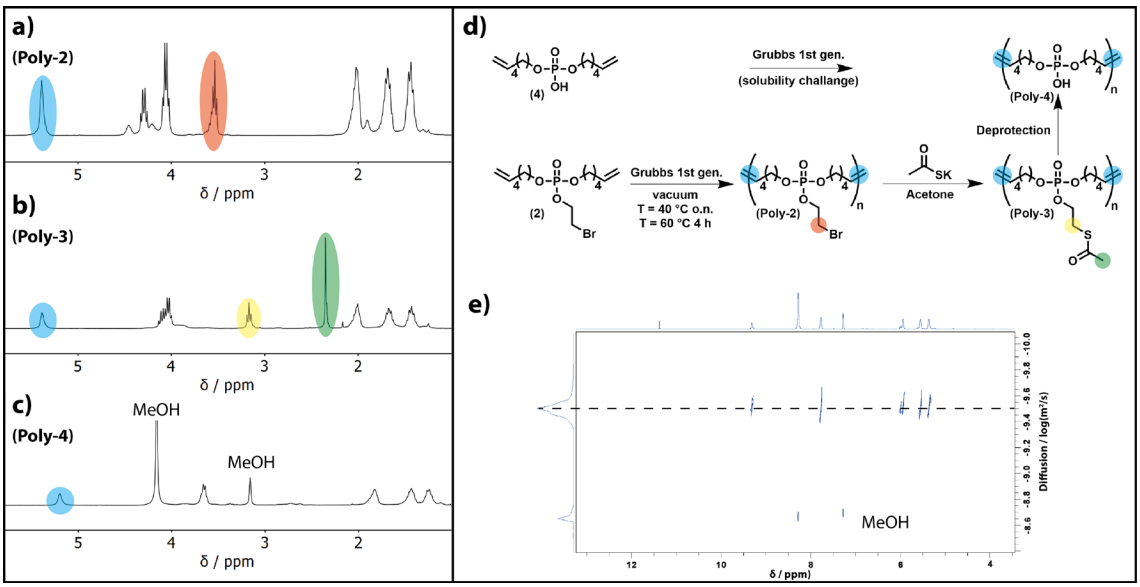

Figure 9.2. Polymer Examples: a-c) ^{1}H NMRs (300 MHz, $CDCl_3$, T = 298 K) of the polymers a) poly-2, b) poly-3 after introducing the thioacetate group, and c) of the polyphosphodiester (poly-4, measured at 300 MHz, in $CDCl_3$:MeOD 7:3, T = 298 K). d) Reaction scheme. e) ^{1}H DOSY (700 MHz, $CDCl_3$:MeOD 7:3, T = 298 K) spectrum of poly-4 underlining the successful removal of the pendant chains.

9.5 Conclusion

We demonstrated the use of the 2-acetylthioethyl ester group for the protection of (poly)phosphodiesters. The protective group guarantees solubility in common organic solvents and the compounds show high shelf-lives. The 2-acetylthioethyl ester was successfully removed either by hydrazine (in THF) or hydrochloric acid (in water) and additional double bonds in the (macro)molecule remained untouched during the procedure. The 2-acetylthioethyl ester can be used as a soluble precursor for P-OH-containing polymers which are appealing for adhesives, dispersants, or flame-retardants.

9.6 Experimental

All chemicals were purchased from commercial suppliers as reagent grade and used without further purification. ^{1}H and ^{31}P nuclear magnetic resonance (NMR) spectra were recorded on Bruker AV 300 at 300 MHz (^{1}H) and 121.50 MHz (^{31}P) or Bruker AV 700 spectrometers at 700 MHz (^{1}H). The temperature of measurement is indicated in the corresponding figure captions. Chemical shifts are reported in ppm using the residual non-deuterated solvent signals as an internal reference.

9.6.1 2-Bromoethyl phosphorodichloridate (1)

To a dried three-necked, 250 mL round-bottomed flask fitted with a dropping funnel, 61.35 mL of phosphoryl chloride (672.19 mmol; 7.0 eq.) were added under an argon atmosphere in 300 mL of dry toluene. Then 13.31 mL of triethylamine (96.03 mmol; 1.0 eq.) and 12 g of 2-bromoethanol (96.03 mmol; 1.0 eq.) dissolved in 50 mL of dry toluene were added dropwise to the above-mentioned flask at 0 °C. The reaction was allowed to stir overnight at room temperature. Afterward, the crude mixture was filtered to remove the triethylammonium chloride and concentrated at reduced pressure. Then, all by-products and starting material were removed at reduced pressure (R.T., $5 * 10^{-2}$ mbar). The product was used without further purification. 87% (20.2 g) yield.

9.6.2 2-Bromoethyl di (hex-5-en-1-yl)phosphate (2)

To a dried three-necked, 250 mL round-bottomed flask fitted with a dropping funnel, 7.00 g of 2-bromoethyl phosphorodichloridate (28.95 mmol; 1.0 eq.) were added under an argon atmosphere in 40 mL of dry toluene. Then 7.30 mL of hex-5-en-1-ol (60.79 mmol; 2.1 eq.) and 8.43 mL of triethylamine (60.79 mmol; 2.1 eq.) were dissolved in 20 mL of dry toluene and added dropwise to the mixture at 0 °C. The reaction was allowed to warm up to room temperature, stirred for an additional 12 h and filtered. The toluene was removed on the rotary-evaporator and the crude product was dissolved in toluene to wash it with 10% aqueous hydrochloric acid solution, a saturated solution of calcium carbonate and brine. The organic layer was dried over anhydrous magnesium sulfate, filtered, and dried at reduced pressure. 82% (8.6 g) yield.

^{1}H NMR (300 MHz, 298 K, chloroform-*d*): δ [ppm] = 5.81–5.68 (m, 2H); 4.98–4.89 (m, 4H); 4.29–4.22 (q, 2H); 4.06–4.00 (q, 4H); 4.49 (t, 2H); 2.08–2.01 (td, 4H); 1.71–1.62 (tt, 4H); 1.50–1.40 (tt, 4H).

^{31}P {H} NMR (121 MHz, 298 K, chloroform-*d*): δ [ppm] = −1.23 (s, 1P).

9.6.3 2-Acetylthioethyl di (hex-5-en-1-yl)phosphate (3)

The synthesis of 2-acetylthioethyl di (hex-5-en-1-yl)phosphate was carried out adopting a procedure previously described by Liras et al.[22]

To a 100 mL round bottom flask 500 mg of 2-Bromoethyl di (hex-5-en-1-yl)phosphate (1.35 mmol; 1.0 eq.) and 170.11 mg of potassium thioacetate (1.49 mmol; 1.1 eq.) were added under argon atmosphere in 5 mL of acetone and stirred for 20 h at room temperature.

Then, the mixture was filtered through Celite 501 to remove the salt. The acetone was removed by rotary evaporation. The crude mixture was dissolved in diethyl ether and washed three times with brine. The organic layer was dried over anhydrous sodium sulfate, filtered, and concentrated on the rotary evaporator. The purified product was recovered as a viscous oil (yield: 0.4 g, 82%). The purity and chemical structure were determined by ^{1}H NMR and ^{31}P {H} NMR spectroscopy.

^{1}H NMR (300 MHz, 298 K, chloroform-*d*): δ [ppm] = 5.81–5.68 (m, 2H); 5.02–4.93 (m, 4H); 4.16–3.99 (m, 6H); 3.15 (t, 2H); 2.33 (s, 3H); 2.08–2.01 (td, 4H); 1.71–1.62 (tt, 4H); 1.50–1.40 (tt, 4H).

^{31}P {H} NMR (121 MHz, 298 K, chloroform-*d*): δ [ppm] = −1.17 (s, 1P).

9.6.4 Di(hex-5-en-1-yl) hydrogen phosphate (4)

a) **3** (1 g), 5 mL of 1 M hydrazine solution in THF were mixed and 10 mL dichloromethane and stirred overnight at r.t. in an argon atmosphere. The solvent was removed at reduced pressure and the crude product redissolved in dichloromethane and the organic phase was washed with 10% HCl, saturated $NaHCO_3$ and again 10% HCl. The organic phase was dried over $MgSO_4$ and the solvent removed at reduced pressure to yield the product (yield: 736 mg, 83%).

b) **3** (200 mg) was dissolved in 0.66 mL methanol. Then 0.5 mL (10 eq.) of 37% HCl was added and the solution was stirred at 65 °C overnight. The solvent was removed at reduced pressure and the crude product was dissolved in diethyl ether and washed two times with brine. The organic phase was dried over $MgSO_4$ to yield the pure product (yield: 0.2 g, 87%).

^{1}H NMR (300 MHz, 298 K, chloroform-*d*): δ [ppm] = 5.85–5.71 (m, 2H; 5.04–4.95 (m, 4H, f); 4.06–4.00 (q, 4H); 2.12–2.05 (td, 4H); 1.74–1.65 (tt, 4H); 1.54–1.44 (tt, 4H).

^{31}P {H} NMR (121 MHz, 298 K, chloroform-*d*): δ [ppm] = 1.30 (s, 1P).

9.6.5 Poly-2

In a Schlenk tube equipped with a stir bar, 500 mg of **2** with 10 mg (0.6 mol%) of Grubbs I catalyst were added. The reaction was allowed to procede at reduced pressure over night at 40 °C, then the temperature was increased to 60 °C for another 4 h to give the product in quantitative yield (439 mg).

^{1}H NMR (300 MHz, 298 K, chloroform-*d*): δ [ppm] = 5.39 (m, 2H); 4.28 (q, 2H); 4.05 (q, 4H); 3.53 (m, 2H); 2.02 (m, 4H); 1.68 (m, 4H); 1.43 (m, 4H).

^{31}P {H} NMR (121 MHz, 298 K, chloroform-*d*): δ [ppm] = −1.26 (s, 1P).

9.6.6 Poly-3

Poly-2 (150 mg), 51.03 mg of potassium thioacetate (0.447 mmol; 1.1 eq.) and 2 mL of acetone were stirred overnight at r.t. under an argon atmosphere. The solution was filtered through a syringe filter and the solvent was removed under reduced pressure to give the product in quantitative yield (148 mg)

^{1}H NMR (300 MHz, 298 K, chloroform-*d*): δ [ppm] = 5.39 (m, 2H); 4.09 (q, 2H); 4.02 (q, 4H); 3.17 (m, 2H); 2.35 (s, 3H); 2.00 (m, 4H); 1.67 (m, 4H); 1.43 (m, 4H).

^{31}P {H} NMR (121 MHz, 298 K, chloroform-*d*): δ [ppm] = −1.16 (s, 1P).

9.6.7 Poly-4

Poly-3 (150 mg), 0.6 mL 1 M hydrazine solution in THF and 2.5 mL DCM were stirred overnight at room temperature under an argon atmosphere. The polymer precipitated during the reaction and the solvent was removed at reduced pressure. The polymer could be redissolved in chloroform:methanol 7:3. It was then precipitated into diethyl ether for purification. 84% (90.7 mg) yield.

^{1}H NMR (300 MHz, 298 K, chloroform-*d:* methanol-d_4 7:3): δ [ppm] = 5.20 (m, 2H); 3.66 (m, 4H); 1.83 (m, 4H); 1.43 (m, 4H); 1.24 (m, 4H).

^{31}P {H} NMR (121 MHz, 298 K, chloroform-*d:* methanol-d_4 7:3): δ [ppm] = 0.55 (s, 1P).

9.7 Acknowledgments

The authors thank Prof. Dr. Katharina Landfester (MPIP) for her support. J.M. is recipients of a fellowship through funding of the Excellence Initiative (DFG/GSC 266) in the context of the graduate school of excellence “MAINZ” (Material Sciences in Mainz). J.M. and F.R.W. thank the Deutsche Forschungsgemeinschaft (DFG WU 750/8-1) for support.

9.8 References Chapter 9

[1] F. Debart, C. Dupouy, J.-J. Vasseur, *Beilstein Journal of Organic Chemistry* **2018**, *14*, 436-469.

[2] Z. Zhao, J. Wang, H.-Q. Mao, K. W. Leong, *Advanced Drug Delivery Reviews* **2003**, *55*, 483-499.

[3] F. Marks, U. Klingmüller, K. Müller-Decker, *Cellular Signal Processing: An Introduction to the Molecular Mechanisms of Signal Transduction*, CRC Press, **2017**.

[4] Z. E. Yilmaz, C. Jérôme, *Macromolecular Bioscience* **2016**, *16*, 1745-1761.

[5] Y.-C. Wang, Y.-Y. Yuan, J.-Z. Du, X.-Z. Yang, J. Wang, *Macromolecular Bioscience* **2009**, *9*, 1154-1164.

[6] T. Steinbach, F. R. Wurm, *Angew. Chem. Int. Ed.* **2015**, *54*, 6098-6108.

[7] K. N. Bauer, H. T. Tee, M. M. Velencoso, F. R. Wurm, *Prog. Polym. Sci.* **2017**, 73, 61-122.

[8] G. Becker, L.-M. Ackermann, E. Schechtel, M. Klapper, W. Tremel, F. R. Wurm, *Biomacromolecules* **2017**, *18*, 767-777.

[9] I. Yasuhiko, K. Takashi, Y. Shin-ichi, *Chem. Lett.* **2009**, *38*, 1054-1055.

[10] M. Steinmann, J. Markwart, F. R. Wurm, *Macromolecules* **2014**, *47*, 8506-8513.

[11] E. Y. Zeynep, D. Antoine, C. Brice, B. Frank, J. Christine, *Journal of Materials Chemistry B* **2015**, *3*, 7227-7236.

[12] A. C. A. Wan, H.-Q. Mao, S. Wang, S. H. Phua, G. P. Lee, J. Pan, S. Lu, J. Wang, K. W. Leong, *Journal of Biomedical Materials Research Part B: Applied Biomaterials* **2004**, *70B*, 91-102.

[13] Y. Hirano, Y. Iwasaki, *Colloids and Surfaces B: Biointerfaces* **2017**, *153*, 104-110.

[14] S. Zhang, H. Wang, Y. Shen, F. Zhang, K. Seetho, J. Zou, J.-S. A. Taylor, A. P. Dove, K. L. Wooley, *Macromolecules* **2013**, *46*, 5141-5149.

[15] A. Cankaya, M. Steinmann, Y. Bulbul, I. Lieberwirth, F. R. Wurm, *Polymer Chemistry* **2016**, *7*, 5004-5010.

[16] T. Biela, S. Penczek, S. Slomkowski, O. Vogl, *Die Makromolekulare Chemie, Rapid Communications* **1982**, *3*, 667-671.

[17] H. Yasuda, M. Sumitani, A. Nakamura, *Macromolecules* **1981**, *14*, 458-460.

[18] J. Kang, D. Miyajima, Y. Itoh, T. Mori, H. Tanaka, M. Yamauchi, Y. Inoue, S. Harada, T. Aida, *J. Am. Chem. Soc.* **2014**, *136*, 10640-10644.

[19] D. Toulemon, B. P. Pichon, C. Leuvrey, S. Zafeiratos, V. Papaefthimiou, X. Cattoën, S. Bégin-Colin, *Chem. Mater.* **2013**, *25*, 2849-2854.

[20] J.-P. R. Chauvin, M. Griesser, D. A. Pratt, *J. Am. Chem. Soc.* **2017**, *139*, 6484-6493.

[21] G. Tosquellas, K. Alvarez, C. Dell'Aquila, F. Morvan, J.-J. Vasseur, J.-L. Imbach, B. Rayner, *Nucleic Acids Res.* **1998**, *26*, 2069-2074.

[22] M. Liras, O. Garcia, N. Guarrotxena, M. Palacios-Cuesta, I. Quijada-Garrido, *Polymer Chemistry* **2013**, *4*, 5751-5759.

9.9 Supporting Information

9.9.1 Materials and Methods

9.9.1.1 Chemicals

All chemicals were purchased from commercial suppliers as reagent grade and used without further purification.

9.9.1.2 Methods

^{1}H and ^{31}P nuclear magnetic resonance (NMR) spectra were recorded on Bruker AV 300 at 300 MHz (^{1}H) and 121.50 MHz (^{31}P) or Bruker AV 700 spectrometers at 700 MHz (^{1}H). The temperature of measurement is indicated in the corresponding figure captions. Chemical shifts are reported in ppm using the residual non-deuterated solvent signals as an internal reference. For SEC measurements in dimethylformamide (DMF) (containing 1.0 g/L of lithium bromide as an additive) an Agilent 1100 Series was used as an integrated instrument, including a GRAM (PSS) column (1000/1000/100 A), a UV detector (270 nm), and a RI detector at a flow rate of 1 mL/min at 60 °C. Calibration was carried out using PS standards provided by Polymer Standards Service. Atmospheric solids analysis probe (ASAP) mass spectra were measured on an Advion expression compact mass spectrometer.

9.9.2 General procedure for the methylation of di(hex-5-en-1-yl) hydrogen phosphate

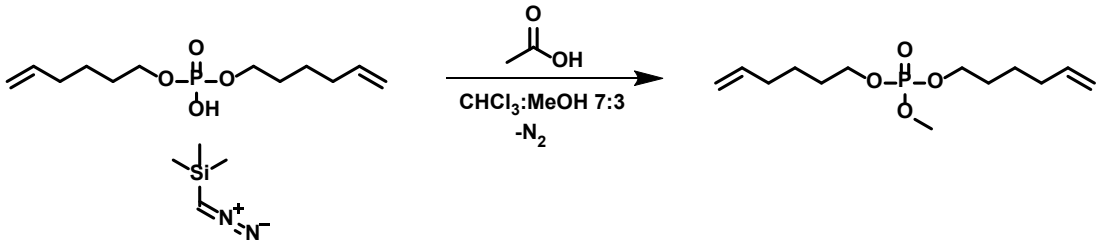

360 mg of di(hex-5-en-1-yl) hydrogen phosphate were dissolved in 10 mL chloroform:methanol 7:3 in an argon atmosphere. Then trimethylsilyldiazomethane was slowly added to the solution. After stirring for 15 min 4 mL of acetic acid were added. After another 5 min the solution was concentrated at reduced pressure to give the product in quantitative yield.

^{1}H NMR (300 MHz, 298K, chloroform-*d*): δ [ppm] = 5.76 – 5.62 (m, 2H); 4.94 – 4.85 (m, 4H); 3.99 – 3.92 (q, 4H); 3.68 – 3.65 (d, 3H); 2.02 – 1.93 (td, 4H); 1.65 – 1.55 (tt, 4H); 1.44 – 1.33 (tt, 4H).
^{31}P {H} NMR (121 MHz, 298K, chloroform-*d*): δ [ppm] = 0.16 (s).

9.9.3 Removal of the protective group with K_2CO_3

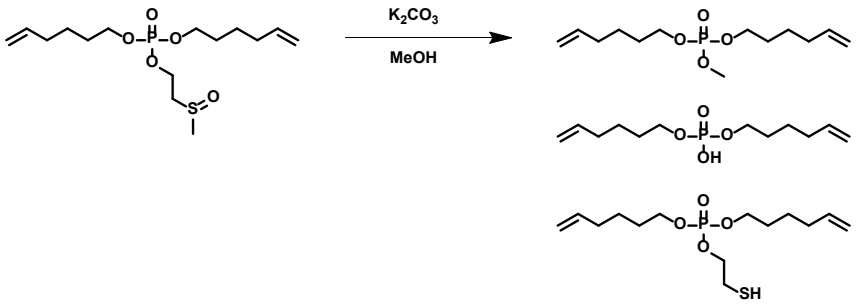

In a schlenktube 200 mg of 2-acetylthioethyl di (hex-5-en-1-yl)phosphate was dissolved in 3 mL methanol and 77.4 mg (1.1 eq.) of potassium carbonate were added. After 45 min the crude mixture was dissolved in diethylether and washed with 10% HCl and brine before drying over Na_2SO_4.

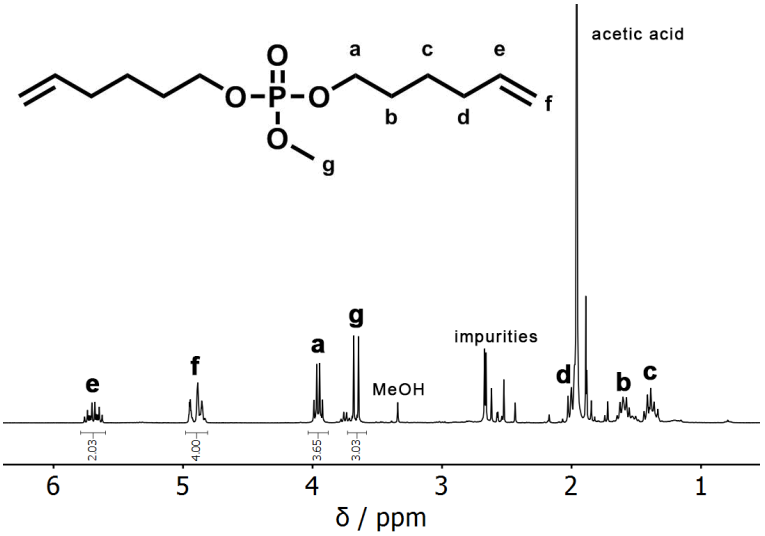

Figure S9.1. ^{1}H NMR of di(hex-5-en-1-yl) hydrogen phosphate treated with trimethylsilyldiazomethane, the methylester is noticeable by its characteristic doublet signal (300 MHz, chloroform-*d, T* = 298K).

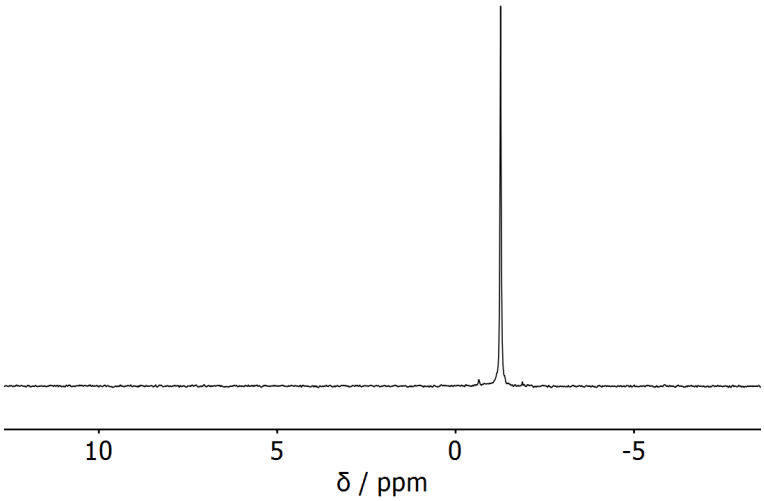

Figure S9.2. ^{31}P NMR of poly-2 (121.50 MHz, chloroform-*d, T* = 298K).

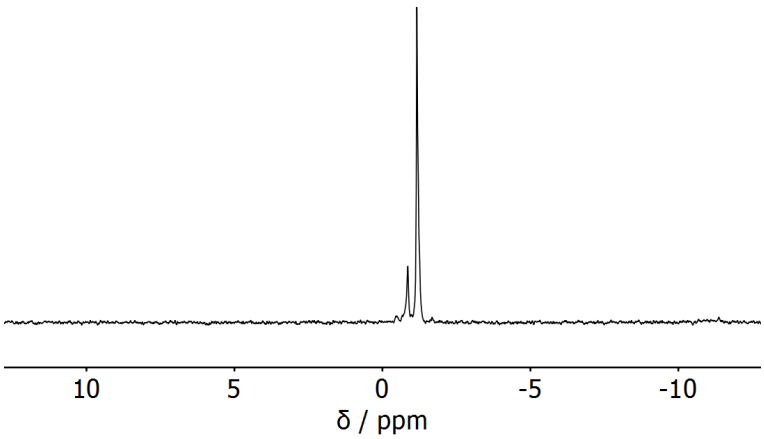

Figure S9.3. ^{31}P NMR of poly-3 (121.50 MHz, chloroform-*d, T* = 298K).

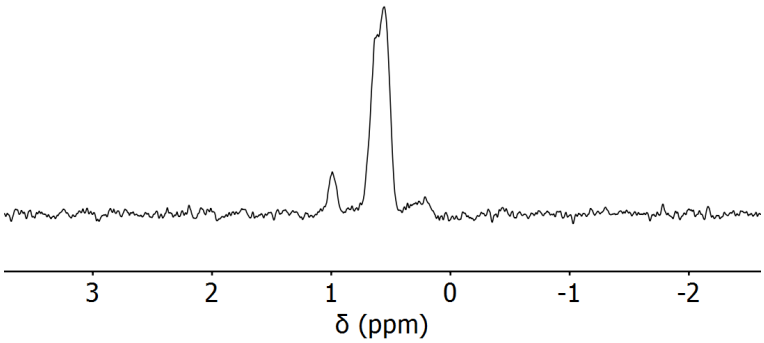

Figure S9.4. ^{31}P NMR of poly-4 (121.50 MHz, chloroform-*d, T* = 298K).

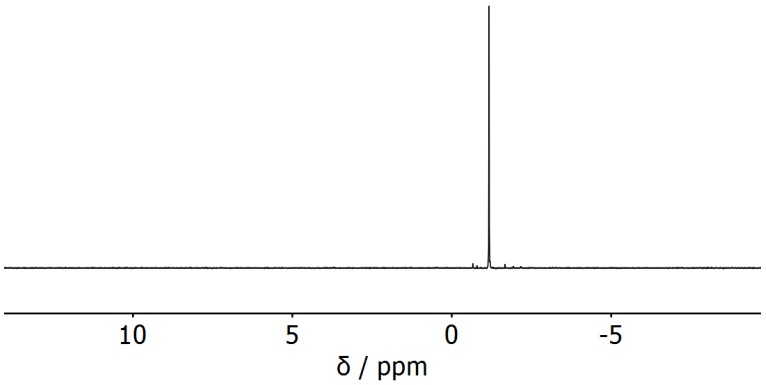

Figure S9.5. ^{31}P NMR of 2-acetylthioethyl di (hex-5-en-1-yl)phosphate (121.50 MHz, chloroform-*d, T* = 298K).

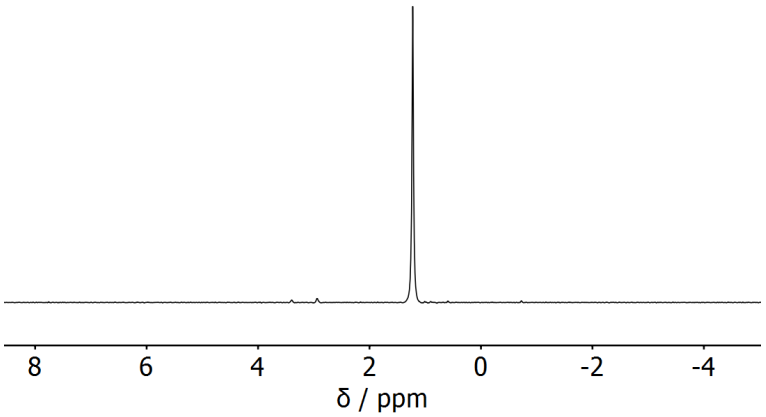

Figure S9.6. ^{31}P NMR of di(hex-5-en-1-yl) hydrogen phosphate by hydrazine (121.50 MHz, chloroform-*d, T* = 298K).

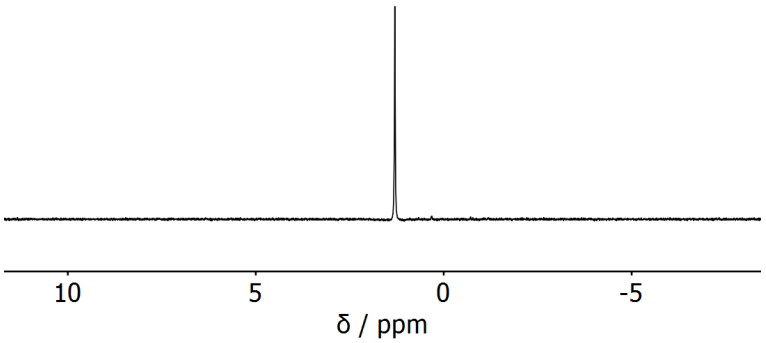

Figure S9.7. ^{31}P NMR of di(hex-5-en-1-yl) hydrogen phosphate by HCl (121.50 MHz, chloroform-*d, T* = 298K).

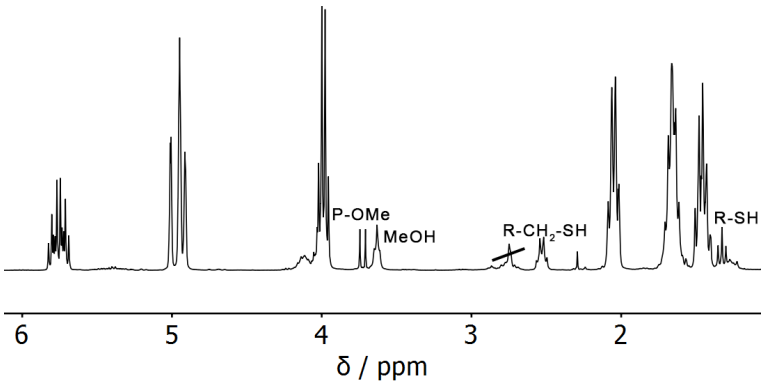

Figure S9.8. ^{1}H NMR of the product mixture after deprotection with K_2CO_3 (300 MHz, chloroform-*d, T* = 298K).

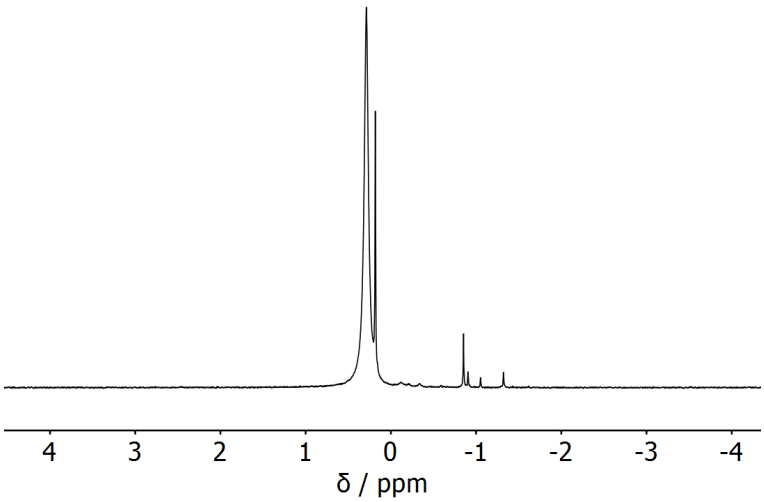

Figure S9.9. ^{31}P NMR of di(hex-5-en-1-yl) hydrogen phosphate by K_2CO_3 (121.50 MHz, chloroform-*d, T* = 298K).

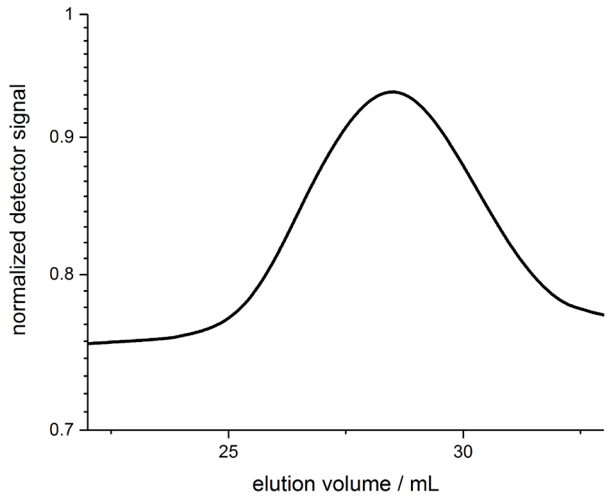

Figure S9.10. GPC elugram of poly-2 (vs. PS standard: M_n: 5100 g/mol, M_w: 8500 g/mol, $Đ$: 1.68).

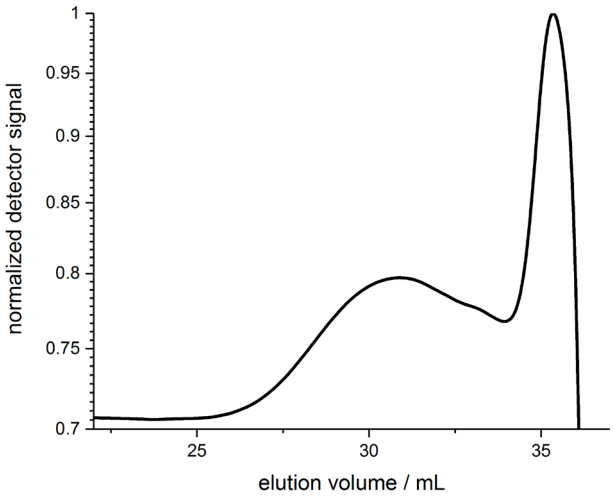

Figure S9.11. GPC elugram of poly-3.

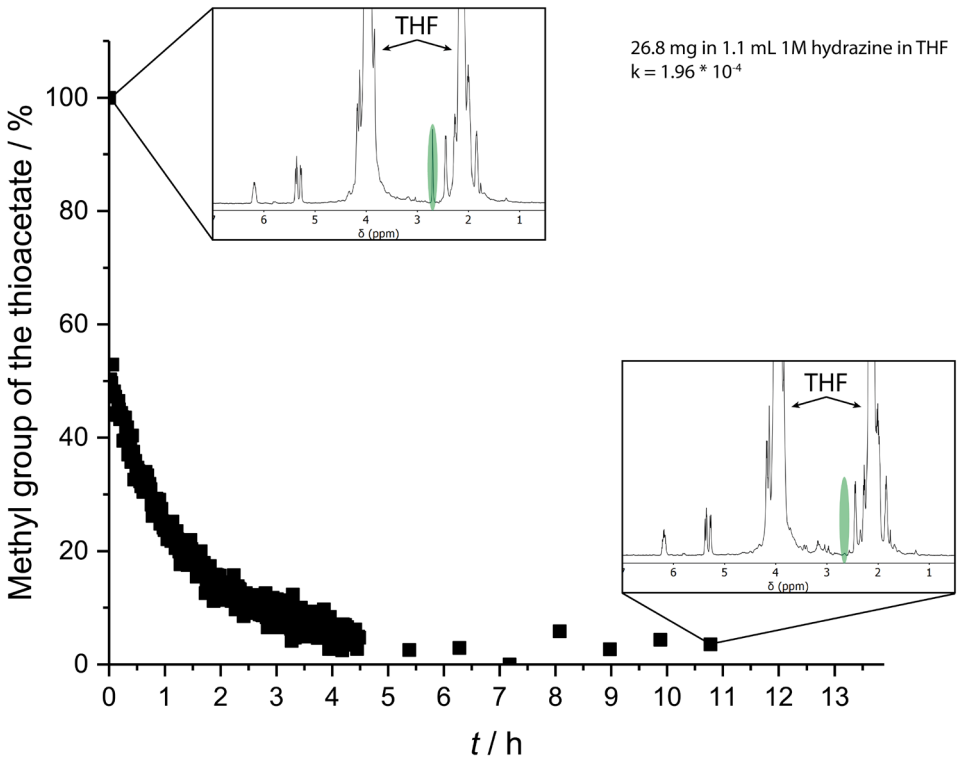

Figure S9.12. ^{1}H real-time kinetics (500 MHz, *T* = 298K) of the release of P-OH by reacting 3 with hydrazine in THF (monitored is the resonance of the methyl group of the thioacetate group at ca. 2.8 ppm, highlighted in green in the insets).

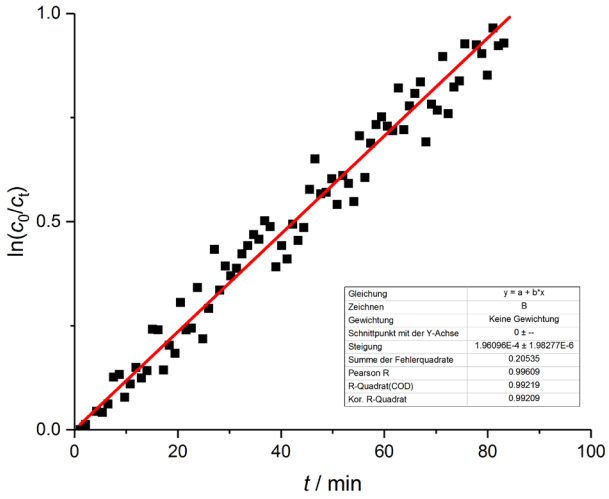

Figure S9.13. Plot of the ^{1}H real-time kinetics of 3 reacted with 1M hydrazine as $\ln(c_0/c_t)$ vs. time for the calculation of the rate constant under these conditions: k=1.96 * 10^{-4}.

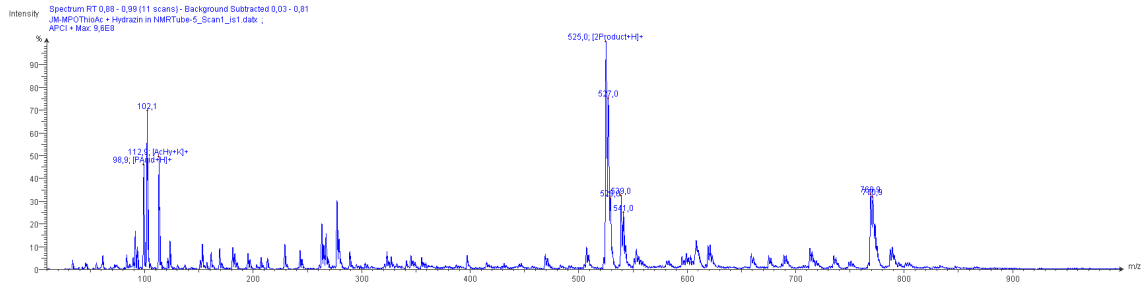

Figure S9.14. Overview of ASAP mass-spectrum after reacting 3 with 1M hydrazine in THF.

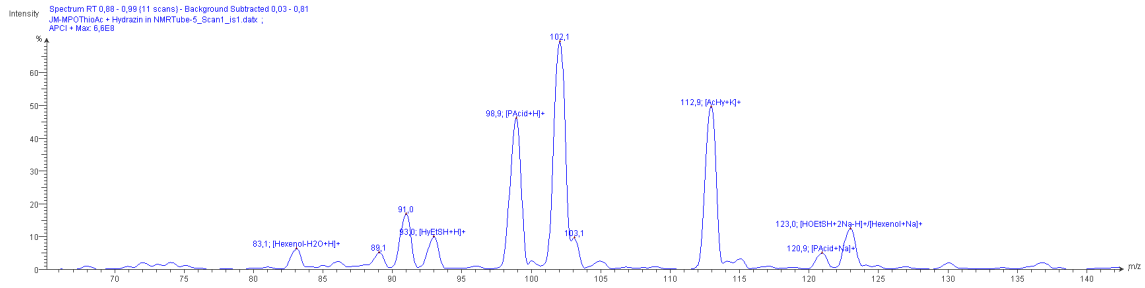

Figure S9.15. Low molecular weight region of ASAP mass-spectrum after reacting 3 with 1M hydrazine in THF.

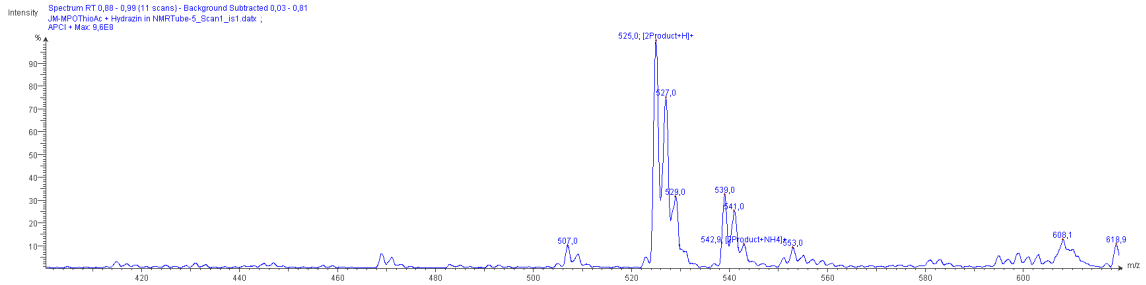

Figure S9.16: High molecular weight region of ASAP mass-spectrum after reacting 3 with 1M hydrazine in THF.

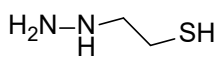

Chemical Formula: $C_2H_8N_2S$
Exact Mass: 92,04

HyEtSH

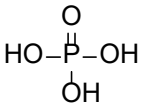

Chemical Formula: H_3O_4P
Exact Mass: 97,98

PAcid

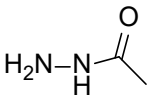

Chemical Formula: $C_2H_6N_2O$
Exact Mass: 74,05

AcHy

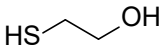

Chemical Formula: C_2H_6OS
Exact Mass: 78,01

HOEtSH

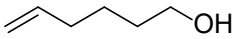

Chemical Formula: $C_6H_{12}O$
Exact Mass: 100,09

Hexenol

Figure S9.17. Fragments assigned in the ASAP mass-spectrum after reacting 3 with 1 M hydrazine in THF.

10. Defect engineering of precision polymers: size control and surface chemistry of anisotropic polymer platelets after solution crystallization

Jens C. Markwart[a b], Oksana Suraeva[a], Ingo Lieberwirth[a], Tobias Haider[a], Robert Graf[a], Frederik R. Wurm[a]**

[a] *Physical Chemistry of Polymers - Max Planck Institute for Polymer Research, Ackermannweg 10, 55128 Mainz, Germany*

[b] *Graduate School Materials Science in Mainz, Staudinger Weg 9, 55128 Mainz, Germany*

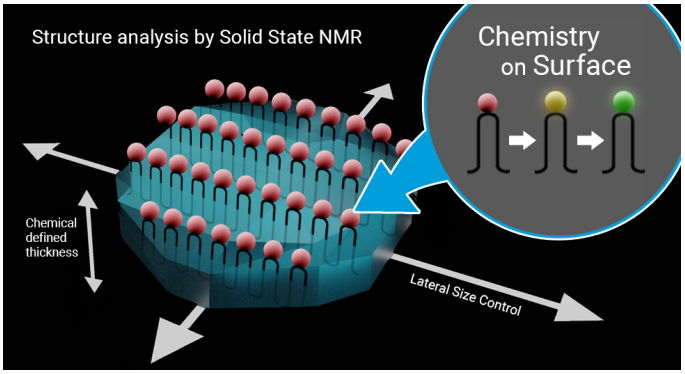

Keywords: Defect engineering, polyphosphoester, acyclic diene metathesis, polyethylene, single crystal

10.1 Notes

To be submitted in this or altered form.

Oksana Suraeva and Ingo Lieberwirth performed the TEM measurements. Tobias Haider performed parts of the polymerization. Rober Graf performed the solid-state NMR measurements.

10.2 Abstract

Anisotropic materials with very high aspect ratios (“2D materials”), such as platelets are an interesting material class due to their unique properties based on their unilamellar geometry. We utilized phosphorus chemistry and simple polycondensation to introduce precisely spaced defects in polyethylene like polymers. The relatively large size and flexibility of the phosphate groups allows the control of the chain-folding during crystallization. We investigated this behavior by solid state NMR and TEM imaging. Furthermore, we showed that we are able to do chemistry “on surface”. The pendant ester group at the phosphate gives the possibility for the introduction of functional groups which are accessible for further chemical modification on the crystal surface, which was proven by the introduction of the 2-acetylthioethyl ester group and a later cleavage of the 2-acetylthioethyl ester group to P-OH. In addition we were able to control the lateral crystal size by different temperature profiles.

10.3 Introduction

Due to the pioneering work of Karl Ziegler and Giulio Natta the catalyzed synthesis of polyethylene and propylene at mild temperatures and pressure got possible, which has led to more than hundred million tons of polyethylene (PE) and polypropylene (PP) produced per year.[1-3] The application of these polymers is determined by their bulk properties like melting or glass transition temperature. Today, PE and PP are known as high performance and commodity material with applications in fields like foils or applications which need high abrasion resistance.[4-7]

In contrast to these bulk materials, planar 2D materials with very high aspect ratios, such as platelets, are an interesting material class due to their unique properties based on their unilamellar geometry, allowing anisotropic material properties. Examples for these 2D materials are graphene or inorganic platelets, which are often used to reinforce bulk polymers.[8] To date, no 2D-polymers based on commodity plastics like polyethylene were reported. However, solution crystallization of PE was already reported in the 1950s.[9]

We utilized phosphorus chemistry and simple polycondensation to introduce precisely spaced defects in polyethylene-like polyphosphoesters (PPEs).[10] From the viewpoint of polymer crystallization, the phosphates act as defects for crystallizing in a polyethylene-like fashion as they are too large to be incorporated inside of a lamellar crystal. This led to a layered morphology of crystallites in the bulk.[10-11] In addition, the phosphate units also confine the thickness of the polymer lamellae, which resulted in the formation of anisotropic polymer platelets, when crystallized from dilute solution.[11] The relatively large size and flexibility of the phosphate groups allow controlling the chain-folding during polymer crystallization. In addition, the pendant ester group at the phosphate gives the possibility for the introduction of functional groups which are accessible for further chemical modification on the crystal surface after crystallization from solution. Polymers have been intensively studied with respect to their crystallization behavior.[10] Ramakrishnan's group followed a related concept for the preparation of liquid crystals from bulk by preparing polyethylene-like polyesters, carrying long-chain alkylene segments along the backbone and poly(ethylene glycol) (PEG) or fluorinated pendant groups at precisely placed positions.[12]

An example for post modification could be the grafting from the crystal surface resulting in architectures which are of particular interest due to their ability to undergo hierarchical self-assembly[13-15], and have a number of potential applications, including drug delivery[16-17], as stabilizers[18-19], hybrid materials[20-21], and in catalysis[22] and optoelectronics[23].

The crystallization of PE from dilute solution was used already in the 1960s to prepare PE-single crystals.[24] The conditions for crystallization from solution of polymers influence the crystal

properties and can be controlled for example by the rate of cooling[25-27], concentration[28] or techniques like self-seeding[24, 29]. However, with all techniques it is challenging to adjust the lateral size and thickness of the materials at the same time. Precisely control over the chain folding by defect engineering allows eliminating the variable of varying thickness and focusing on lateral size control during crystallization from dilute solution.

Lateral size control can be achieved by limiting self-nucleation and thus the resultant randomly sized assemblies.[30] This can be achieved by a seed-growth approach like self-seeding. In self-seeding a suspension is heated within its dissolving temperatures, leading to a melting of less crystalline regions and remaining of more crystalline regions. These surviving crystals serving as seeds for the free polymer in solution, leading to a suspension of crystals uniform in size.[29]

10.4 Results and Discussion

Acyclic diene metathesis polymerization (ADMET) is a versatile technique to prepare a broad range of linear aliphatic functional polymers and was used by our group extensively for the preparation of phosphate-containing polymers.[11, 31-36] The remaining double bonds can be used to add further functionalities[37] or hydrogenated to get polyethylene like polymers. For the synthesis of linear polyethylene like PPEs via acyclic diene metathesis (ADMET) polymerization, a phosphoester monomer with two long-chain olefins is mandatory. In this study, four different monomers were synthesized equipped with two C_{11} unsaturated alkyl chains starting from $POCl_3$. **M1** is a phosphotriester carrying a phenoxy side group, **M2** is a phosphodiester with a P−OH side group and **M3** is a phosphodiester with an ethoxy side group (Scheme 10.1). The synthesis of these three monomers was previously described by Tee et al.[38-39] In addition, **M4** was prepared by the reaction of 10 equivalent phosphorus oxychloride with 1 equivalent of 2-bromoethanol and in a second step with 2 equivalents of 10-undecen-1-ol, in order to install the alkyl-bromide functionality as side chain. The excessive 10-undecen-1-ol was removed by flash chromatography over AlOx. The resulting monomer is a liquid at room temperature and is soluble in aromatic and halogenated solvents (e.g. toluene, dichloromethane, chloroform) and insoluble in water. The alkyl-bromide in the pendant chain acts as versatile electrophilic functionality, as it can be functionalized by various nucleophilic substitutions after the synthesis or after polymerization.

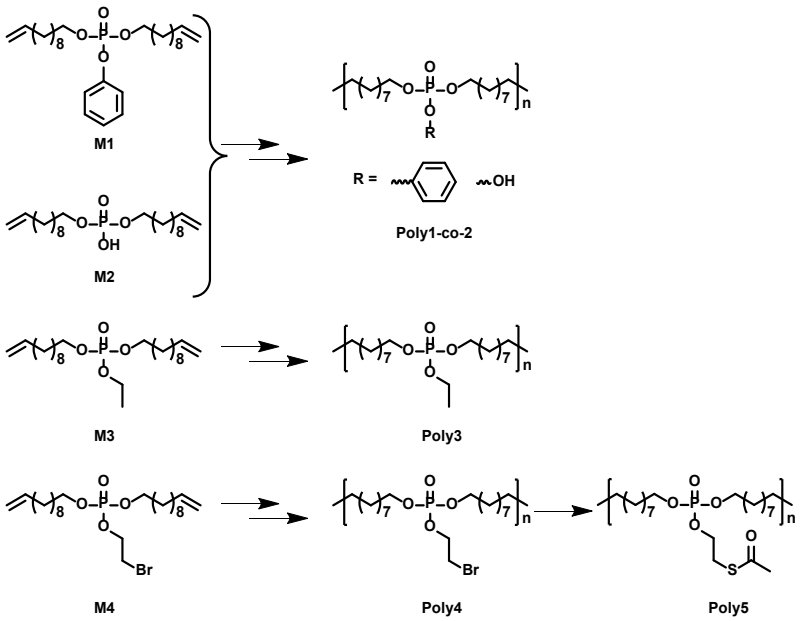

Scheme 10.1. The different monomers used to synthesize the studied polymers.

The phosphate groups in the polymer chain are precisely spaced after the ADMET polymerization. The aliphatic methylene spacer between them was adjusted to 20 units (-$(CH_2)_{20}$-) to guarantee their ability to crystallize. If crystallized from dilute solution, this resulted in anisotropic crystals with the phosphate groups on two opposing sides. With the possibility of installing chemical functionality in the phosphate unit, this strategy gives access to polymer platelets bearing functional groups on their surface which are accessible for further surface chemistry (Scheme 10.2).

To prove that the phosphate groups are expelled from the crystal and arranged in a single plain **poly3** was synthesized from **M3** according to literature[39] and analyzed by transmission electron microscopy (TEM). From the diffraction pattern in Figure 10.1 a the lattice distance d_{hkl} amounts to 4.1 Å. All reflexions appear at nearly the same angle and hence we can assume that (110) ≈ (200). When presuming an orthorhombic lattice, this yields lattice constants of a = 8.2 Å and b = 4.7 Å, where a becomes nearly equal to $b\sqrt{3}$ and hence the unit cell becomes pseudo-hexagonal.[40]. Using the unit cell parameters obtained by transmission electron microscopy studies, different models for the local planar arrangement of the ^{31}P sites relative to the orthorhombic/pseudo-hexagonal lattice of the aliphatic chains can be derived (Figure 10.2 top) and compared to structural information gathered by solid state NMR.

Commonly used solid state NMR methods like ^{31}P magic angle spinning (MAS) NMR or ^{31}P{^{1}H} CP-MAS NMR may probe the local chemical environment of the ^{31}P sites in the solid state, however, they will not provide any information on spatial proximities of the chemically isolated ^{31}P sites in

poly3. Utilizing double-quantum (DQ) MAS-NMR methods, it is possible to probe molecular proximities in the range of 0.5 nm and thus gaining information regarding conformations and packing.[41] In addition to ^{31}P DQ-SQ correlation experiments, probing directly spatial proximities between chemically distanced ^{31}P sites, this method can probe as well ^{31}P-^{31}P DQ dipolar coupling between chemically equivalent ^{31}P sites based on measurements of build-up curves. These build-up curves (Figure 10.1 c) are sensitive to P-P inter-nuclear distances, as the nuclear dipolar coupling constant $D_{ij} = \frac{\mu_0 \hbar^2 \gamma_i \gamma_j}{4\pi^2 r_{ij}^3}$ between two spins *i* and *j* is proportional to the inverse cube of the inter-nuclear distance r_{ij}, and the strongest ^{31}P dipolar coupling, thus the closest spatial proximity, determines predominantly the initial t^2-proportional rising of the double quantum build-up curve. Moreover, the long term behavior of DQ build up curves provides qualitative information on the distribution of the ^{31}P dipolar couplings and spatial proximities. In crystalline arrangements with well-defined distinct distances between neighboring ^{31}P sites, an oscillatory behavior of the DQ build up curves is observed (see Figure 10.6b, in publication by Saalwächter et al.[42]). For very long excitation times, these oscillations vanish in powder samples due to the orientation dependence of the DQ excitation efficiency. In less controlled assemblies with broad distributions of distances and thus dipolar couplings, the oscillatory behavior of the DQ build-up curve vanishes due to destructive interferences of the different oscillation frequencies of discrete dipolar coupling values. In these cases, a second moment description of the dipolar coupling assuming a dipolar interaction of a single site with continuously distributed surrounding ^{31}P sites is more appropriate and provides a better description of the DQ build-up behavior. The smooth DQ build-up curve with its quadratic initial behavior obtained for the local packing of the ^{31}P sites in crystallized **poly3** samples shown in Figure 10.1 indicates that the second moment analysis of the local packing should be appropriate. Please note, that the fluctuations occurring in the DQ build-up curve for longer DQ excitation times result from increasing relative experimental uncertainties with increasing DQ excitation times and thus do not indicate the presence of discrete dipolar coupling values resulting from a crystalline lattice (which should vanish for long DQ excitation times) like the oscillations mentioned above.

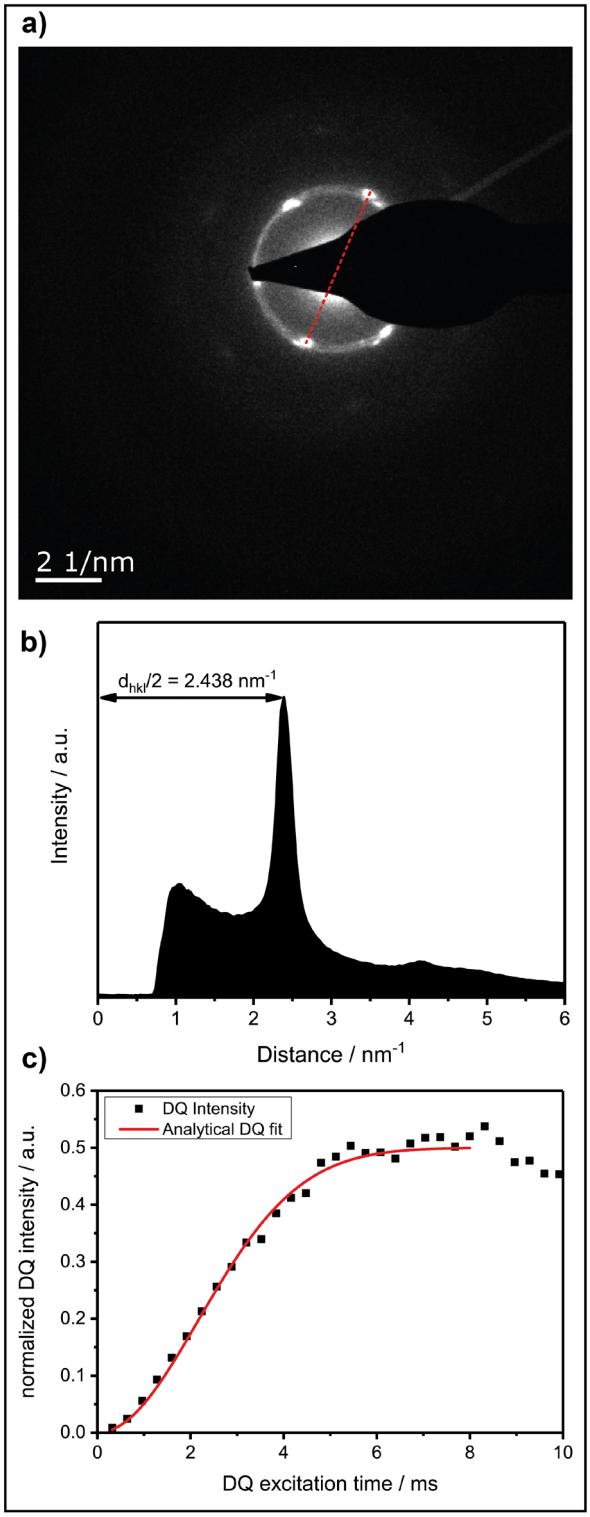

Figure 10.1. a) Diffraction pattern of a single crystal **poly3** showing the (110) and (200) plane. **b)** Radial intensity profile of the diffraction pattern. c) Double quantum build-up curve of solution crystallized **poly3**, recorded at 25 kHz MAS, *T*=25 °C and 202 MHz ^{31}P Lamor frequency.

In Figure 10.2, we have drawn three possibilities, how the polymer chains may propagate along the unit cell of the crystallites from our TEM studies, with the phosphate groups positioned between the lattice positions of the alkyl chain in an alternating pattern as illustrated in Figure 10.2. For clarity, only the phosphorus atoms of the top surface are shown. In Model 1 (Figure 10.2 a) the polymer chain propagates diagonal to the unit cell along the (110) direction of the crystal. In Model 2 (Figure 10.2 b), the polymer chain propagates along the *b* axis of the unit cell, but the neighboring polymer chain is shifted by *b*/2. In Model 3 (Figure 10.2 c), the polymer chains propagate along the b axis, but the shift alternates between + and – *b*/2.

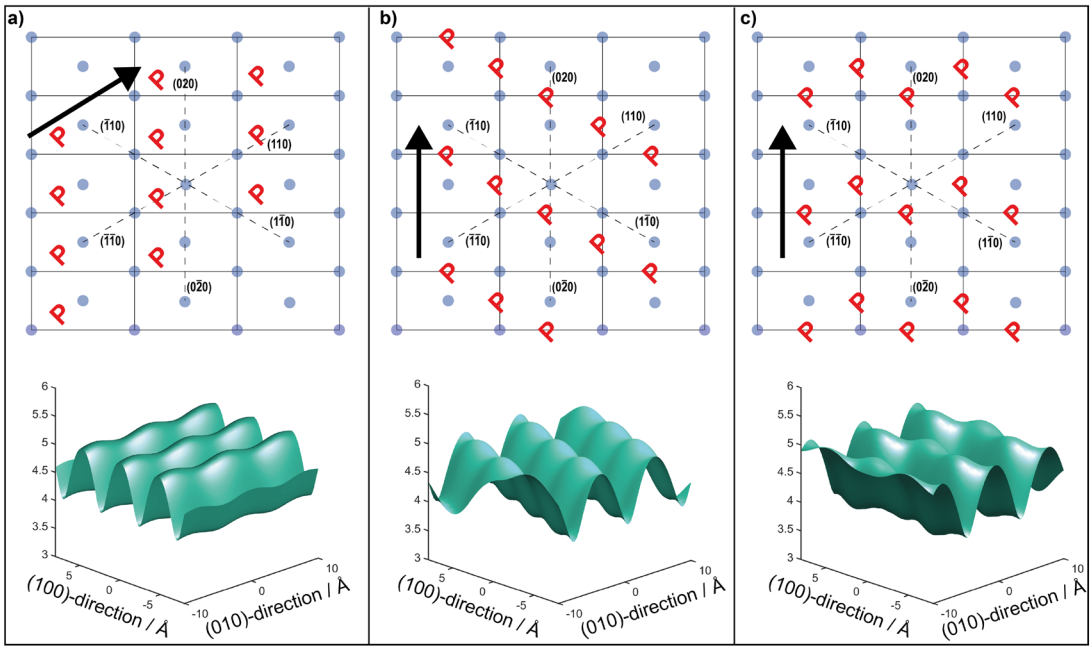

Figure 10.2. a) Polymer chain propagating diagonal to the crystal lattice (Model 1). **b)** Polymer chain propagating along the b axis of the crystal shifted by b/2 (Model 2). **c)** Polymer chain propagating along the b axis of the crystal shifted by b/2 alternating (Model 3). (**bottom**) Plane on which M_2 equals the experimentally obtained value of 0.197 kHz².

From the different models, the distance r_{ij} between two phosphate groups in close spatial proximity is known and thus can be used to calculate the ^{31}P dipolar second moment (M_2) ($M_2 = \frac{3}{5}\gamma^4\hbar^2 I(I+1)\sum_j r_{ij}^{-6}$)[43] and compare it to the M_2 obtained by the experimental DQ build-up curves of 0.197 kHz² (for details on data acquisition, processing and analysis see Solid State NMR experimental section). For the calculation of M_2 five units cells in each direction (-a, a, -b and b) were taken into account. Note that the integral contribution more remote ^{31}P sites to the value of M_2 is less than 0.1%, as their contribution to the second moment decreases with the 6th power of the distance. For all 3 models, the calculation yields a M_2 of ~0.14 kHz² with only minor variations, which is significantly lower than the M_2 value obtained from the experimental DQ build-up curves.

However, the crystals were measured in a dry state, so that stacking of multiple crystalline layers is possible. Considering the adjacent-reentry model, the phosphate groups are located on the crystal surface and the interactions of phosphate groups in the *c* direction with neighboring crystalline layers have also to be taken into account. It should be noted that the interaction between the two phosphate planes within a single platelet can safely be neglected, because the distance between them is by far too large. Shifting the surfaces of the two single crystals in x, y, and z direction to each other gives a plane on which M_2 equals the experimentally obtained value 0.197 kHz^2 (Figure 10.2 bottom). These planes predict distances of 4.0 – 5.2 Å between the phosphorus atoms in z direction, which is in a reasonable range.

For these predicted distances, the phosphorous attached ethoxy chains between the crystal surfaces have a density between 1012 and 1320 kg m^{-3}, which compares very well to the density of PEG (~ 1128 kg m^{-3}). It should be pointed out, that the lowest density value of 1012 kg m^{-3} results from an unfavorable geometry, where the ^{31}P atoms of neighboring layers would sit directly on top of each other, causing maximum steric interaction and is therefore energetically not favored.

10.4.1 Surface modification of polymer platelets

The chemical accessibility of the pendant chains in the phosphate units at the surface of the polymer platelets was studied by a multi-step reaction, which was conducted "on surface" (Scheme 10.2). The first reaction step was the reaction of the polymer platelets of **poly4** to **poly5**. The polymer platelets were prepared by solution crystallization of **poly4**, which was prepared as followed. **M4** was polymerized via ADMET (**poly4a**, M_n=20500 g/mol, M_w/M_n=2.07), the purified polymer was then hydrogenated using a Pd/C catalyst in the presence of 50 bar hydrogen gas to give **poly4** (M_n=15900, M_w/M_n=1.67). To prepare the dispersion of the polymer platelets of **poly4**, the polymer was dissolved in hot ethyl acetate (at 60 °C) at a concentration of 1 mg mL^{-1}. Then the solution was cooled in a temperature bath, which was set to 20 °C. A part of the cooled solution was transferred to a separate vial as reference for later TEM images. To the remaining solution potassium thioacetate was added and stirred overnight at 20 °C. Afterwards, a small sample was taken and the solvent was removed quickly at reduced pressure. The dried polymer platelets were dissolved in deuterated chloroform and a ^1H NMR was measured immediately. The ^1H NMR shows the characteristic resonances at 3.17 ppm and 2.35 ppm for **poly5** (Figure S10.11) proofing a successful modification. The TEM images in Figure S10.12 and S10.13 show the polymer platelets of **poly4** and **poly5** with a similar size.

The second reaction step was the cleavage of the 2-acetylthioethyl protective group, which was conducted "on surface" as well. The 2-acetylthioethyl ester group is a protective group for phosphoric acid (P-OH-groups) and can be cleaved under acidic or basic conditions to release P-OH functionality, which should alter the surface properties of the polymer platelets.[44]

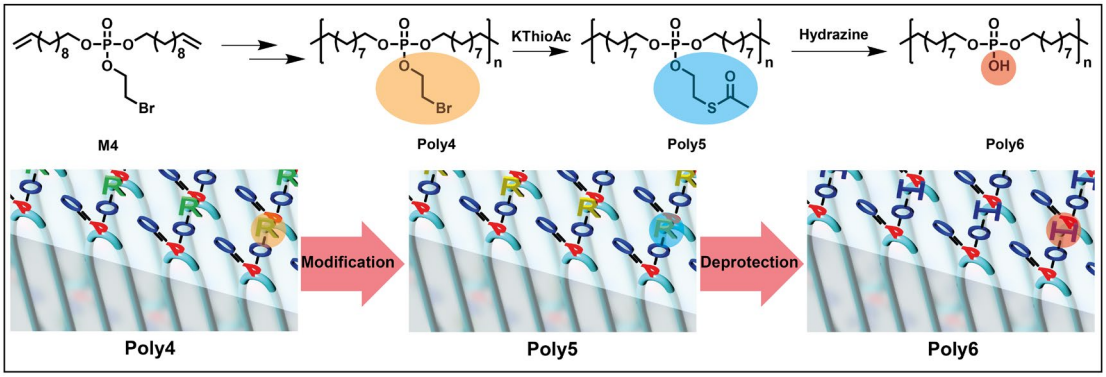

Scheme 10.2. Schematic representation of the multi-step reaction, which was conducted "on surface" of the polymer platelets: 1) Modification of the Br-group to a thio acetate-group. 2) Cleavage of the 2-acetylthioethyl protective group.

The cleavage with hydrazine was conducted with the above polymer platelet solution by adding 2 equivalent hydrazine at 20 °C and with freshly crystallized polymer platelets of **poly5**. The polymer platelets were prepared by solution crystallization of **poly5**, which was prepared as followed. **Poly4** was reacted with potassium thioacetate to substitute the alkyl-bromides and to prepare **poly5** with 2-acetylthioethyl ester groups as pendant chains. ^{1}H NMR spectroscopy (Figure S10.9) of **poly5** revealed three characteristic resonances at 4.10 ppm (methylene group next to the P-O of the 2-acetylthioethyl ester group), 3.17 ppm (methylene group next to the thio acetate group) and 2.35 ppm (methyl group of the thio acetate group). The ^{31}P NMR spectrum shows a single signal at -1.13 ppm (Figure S10.10) confirming only one phosphorus species present.

In DSC measurements **poly5** shows a T_g of -49 °C and a T_m of 58 °C (Figure 10.3). To prepare the dispersion of the polymer platelets of **poly5**, the polymer was dissolved in hot ethyl acetate (at 60 °C) at a concentration of 1 mg mL^{-1}. Then, the solution was allowed to cool to room temperature for 4 to 5 h to crystalize the polymer into unilamellar PE like polymer platelets.

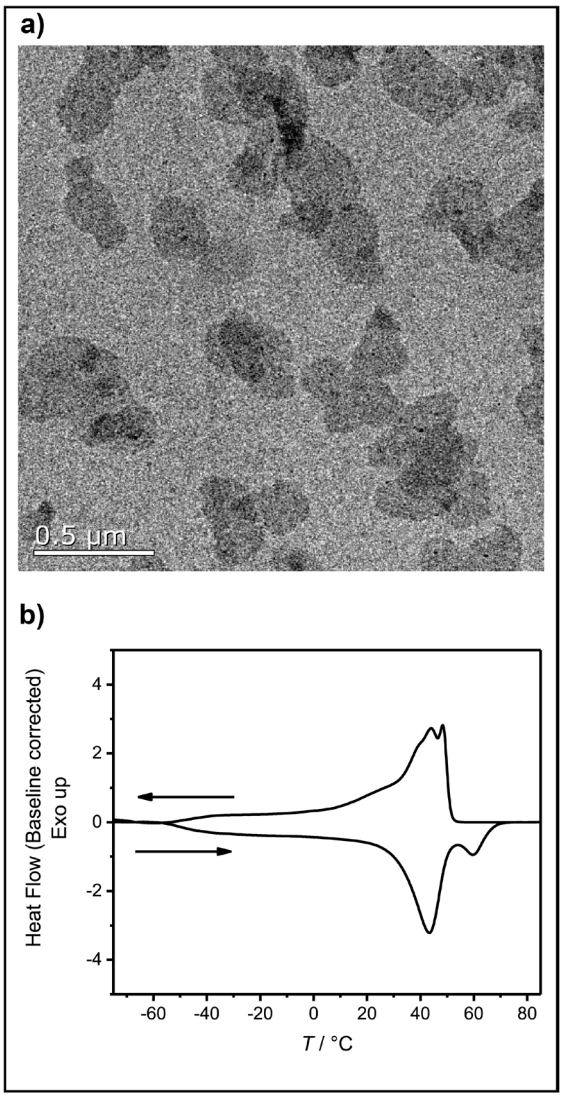

Figure 10.3. a) Transmission Electron Microscope image of the single **poly5** crystals (0.1 mg mL^{-1}). **b)** Differential Scanning Calorimetry (baseline corrected) of **poly5** showing the second heating and cooling curve with a T_g at -49 °C and T_m at 58 °C determined in the second heating curve.

Afterwards, the dispersion was cooled to 0 °C for 15 minutes before starting stirring and adding the hydrazine in ethanol. After ca. 45 minutes, aggregation of the crystals was visible. The solvent was removed by blowing nitrogen over night while keeping the temperature at 0 °C. The product (**poly6**) was not soluble in any solvent, as expected for a polyphosphodiester.[38]

Figure 10.4 shows the TEM images of the crystal dispersion before (**poly5**) (Figure 10.4 a and b) the addition of hydrazine and after (**poly6**) (Figure 10.4 c and d) the addition of hydrazine. Before the treatment, the crystals have a size of around 128 ± 40 nm and are crystalline as it is apparent from the diffraction pattern. After the addition of the hydrazine, the crystal size remained at around 132 ± 46 nm and the diffraction pattern still proves their crystallinity. The P-OH groups on

the crystal surface induced hydrogen bonds, which lead to a stacking of the crystals, with P-OH as a H-bond donor and P=O as an H-bond acceptor.[38]. Figure 10.4 c shows a TEM image of the crystals stacking on top of each other.

IR spectroscopy proved the successful cleavage of the thioacetyl-protective group and the formation of the P-OH groups as shown in Figure 10.5. The C=O stretching frequency at 1694 cm^{-1} and the C(O)-S stretching frequency at 625 cm^{-1}, which are characteristic for thio acetates[45], vanished and a new resonance at 1200 cm^{-1} appeared, which is characteristic for P=O stretching in acid phosphates.[46]

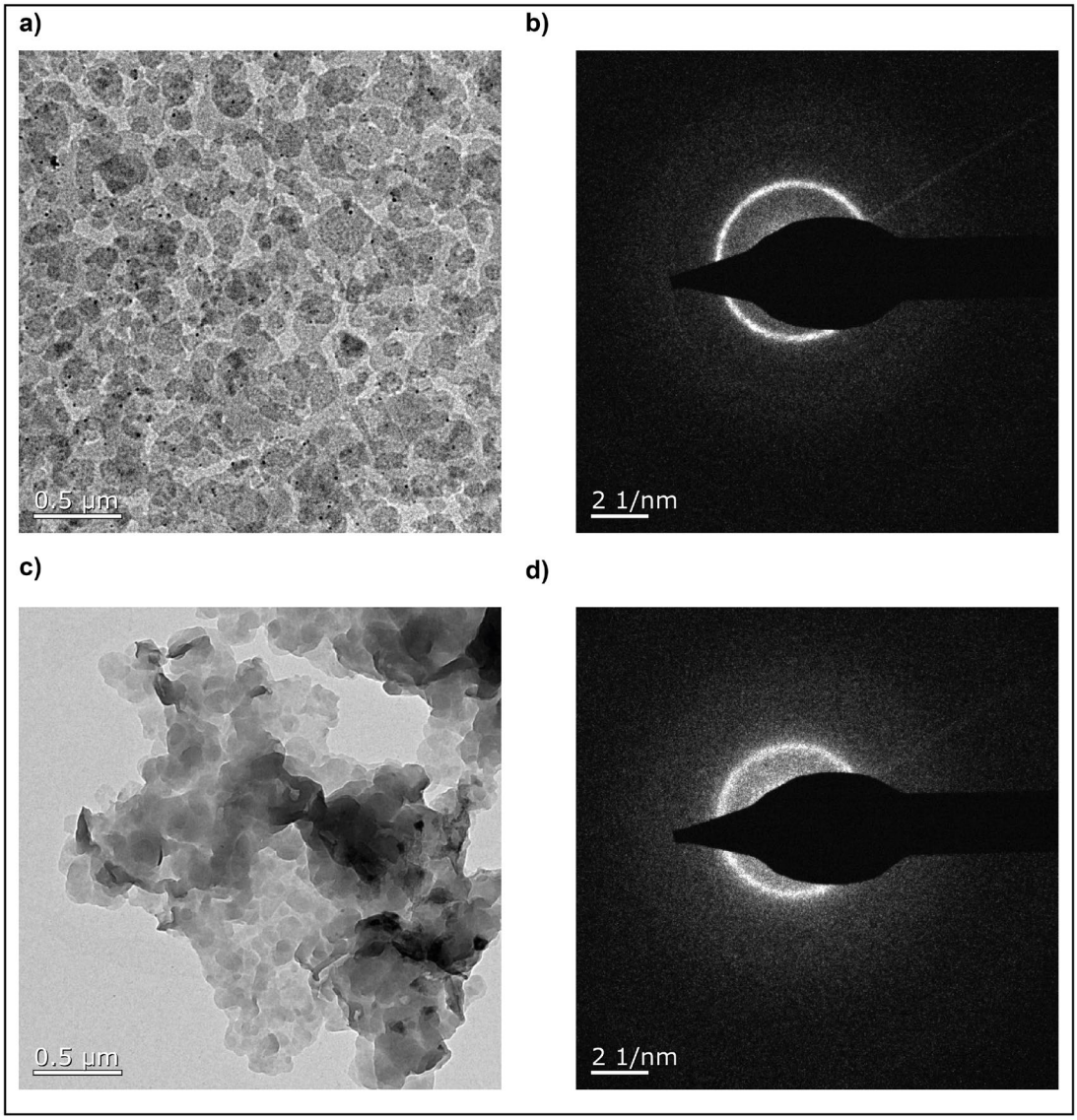

Figure 10.4. a) Transmission electron microscopy image of 1 mg mL^{-1} **poly5**. b) Transmission electron microscopy diffraction pattern of 1 mg mL^{-1} **poly5**. c) Transmission electron microscopy image of 1 mg mL^{-1} **poly5**. b) Transmission electron microscopy diffraction pattern of 1 mg mL^{-1} **poly6**.

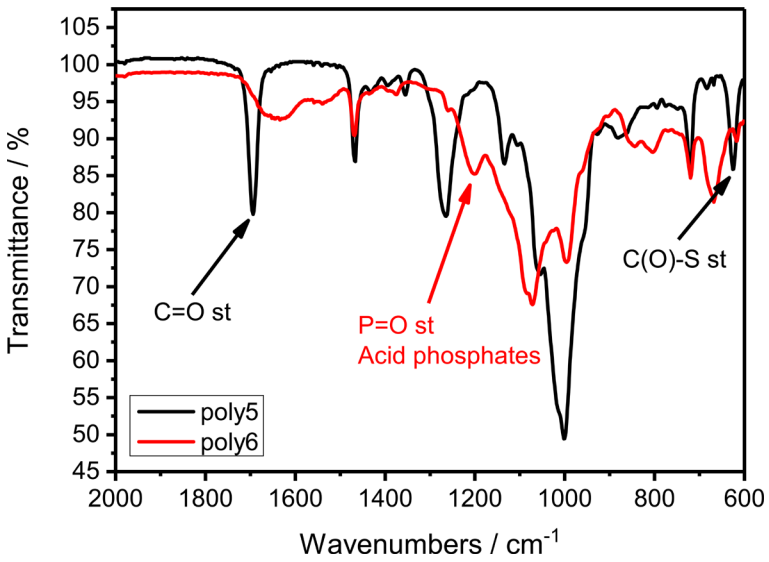

Figure 10.5. FTIR spectrum of **poly5** and **poly6** (after two step reaction) highlighting the important frequencies.

10.4.2 Size control

The precisely placed phosphate units confine the thickness of the platelets during the crystallization. The chain folding by such a "defect engineering"[47-48] eliminates the variable thickness of the platelets and allows only focusing on lateral size control. Herein, we achieved the lateral size control for the first time for such defect PEs by controlled crystallization kinetics.

We first determined the temperature, at which the crystals form in solution by dynamic light scattering (DLS). At room temperature, the platelet dispersion of **poly1-co-2** in ethyl acetate proved a high intensity of scattered light, due to the presence of the particles. When the dispersion was heated to 60 °C, the scattering intensity quickly vanished, as the crystals melt and the polymer chains dissolve. When this solution was cooled at 3 °C min^{-1} while measuring the count rate, the polymer chains crystallized again, underlining the reversible and dynamic behavior of the formation of such polymer platelets. The count rate increased upon cooling, proving the crystallization temperature of ca. 27 °C (Figure 10.6).

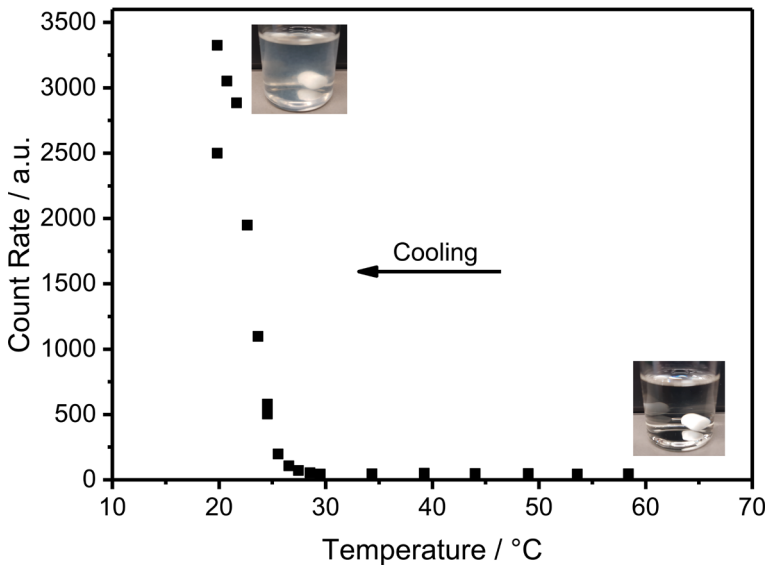

Figure 10.6. Dynamic light scattering countrate at different temperatures indicating crystallization at ca. 27 °C.

In a first experiment, the clear solution was cooled from 60 °C to 27 °C (Figure S10.17) within one hour and left at this temperature for another two hours after which the formed crystals were characterized by TEM. The TEM images showed a high polydispersity of crystals ranging from < 100 nm to > 1 µm (Figure S10.17 and Table S10.3). After the samples were taken the same solution was rapidly cooled to 0 °C within 30 min (Figure S10.18) and kept at this temperature for another two hours after which a sample was taken for TEM measurements. The smaller crystals disappeared and only large crystallites of > 1.5 µm were visible (Fig S10.18 and Table S10.4).

To control the lateral size of the polymer platelets, we utilized a well-established technique called self-seeding.[24, 29] In a self-seeding experiment, a suspension is heated within its dissolving temperatures, leading to a melting of less crystalline regions and remaining of more crystalline regions. These surviving crystals serve as seeds for the dissolved polymer chains in solution, leading to a suspension of crystals with a more uniform size distribution.[29] The seeds were grown by cooling the clear crystal solution from 60 °C to 15 °C within two hours and keeping the dispersion at this temperature for another 30 min. The less crystalline crystals were molten by heating the dispersion to 35 °C within 60 min and holding this temperature for 30 min. The crystals were now grown by cooling the dispersion from 35 °C to 28 °C within 7 hours and holding the temperature for another 24 hours before taking a sample for TEM (Figure S10.16). The resulting crystals have a size of around 500 nm and are almost monodisperse (Fig S10.16 and Table S10.5).

10.5 Conclusion

We utilized phosphorus chemistry and simple polycondensation to introduce precisely spaced defects in polyethylene like polymers. We could demonstrate, that the relatively large size and flexibility of the phosphate groups allows the control of the chain-folding during crystallization. The crystal structure was studied by TEM and solid state NMR, which proven a pseudo hexagonal crystal structure with the phosphate groups on two opposing surfaces of the crystal. In addition, we could prove that the pendant ester group at the phosphate gives the possibility for the introduction of functional groups which are accessible for further chemical modification on the crystal surface. This was proven by the cleavage of a 2-acetylthioethyl ester group to P-OH. Furthermore, we were also able to control the lateral crystal size without influencing the thickness by various cooling profiles.

10.6 Experimental Section

10.6.1 2-bromoethyl di(undec-10-en-1-yl) phosphate (M4)

A threenecked round bottom flask, equipped with a dropping funnel, was charged with 2-bromoethyl phosphorodichloridate (11.87 g, 40.1 mmol, 1 eq.), dissolved in dry toluene (100 mL) under an argon atmosphere. The solution was cooled with a water bath. Triethyl amine (14.3 mL, 103.1 mmol, 2.1 eq.), and 10-undecen-1-ol (20.7 mL, 103.1 mmol, 2.1 eq.) were dissolved in dry toluene (60 mL) and added slowly via the dropping funnel. After the addition the reaction was stirred overnight at room temperature. The crude mixture was concentrated at reduced pressure, dissolved in diethyl ether, and filtered. The organic phase was washed with $NaHCO_3$ solution, with 10% aqueous hydrochloric acid solution and with brine. The organic layer was dried over magnesium sulfate, filtered, concentrated at reduced pressure, and purified by flash chromatography over neutral alumina using dichloromethane as eluent to give a clear yellowish liquid.

^{1}H NMR (300 MHz, Chloroform-*d,* δ) 5.82 (ddt, *J* = 17.0, 10.3, 6.7 Hz, 2H), 4.97 (dd, *J* = 18.3, 13.6 Hz, 4H), 4.31 (q, *J* = 6.8 Hz, 2H), 4.06 (p, *J* = 6.4, 6.0 Hz, 4H), 3.55 (t, *J* = 6.3 Hz, 2H), 2.05 (q, *J* = 7.0 Hz, 4H), 1.70 (p, *J* = 6.7 Hz, 4H), 1.30 (s, 24H).

^{31}P {H} NMR (121 MHz, Chloroform-*d,* δ) -1.25 (s, 1P).

10.6.2 Poly4a

M4 (500 mg, 0,98 mmol) was placed in a 25 mL Schlenk tube equipped with a stir bar and the system was degassed by three consecutive Argon/vacuum cycles. 8 mg of Grubbs catalyst 1st generation (0.1 mol%) were added and polymerization was carried out at 40 °C at reduced pressure (0.1 mbar). An increasing viscosity of the solution indicated ongoing polymerization. After 18 h, a second portion of Grubbs catalyst 1st generation was added and the polymerization was continued for additional 24 h. The solution was allowed to cool down to room temperature, then 2 mL CH_2Cl_2 were added to dissolve the polymer and 200 µL ethyl vinyl ether were added to quench the catalyst. The mixture was kept stirring for 2 h while its color changed from purple to orange. Further CH_2Cl_2 was added to dilute the solution and the polymer was precipitated from methanol. After centrifugation, the product was isolated and dried under vacuum to yield a dark yellow, honey-like polymer (67% yield).

SEC (PS standard, THF as the eluent): M_n = 20,500 g mol^{-1}, M_w = 42,500 g mol^{-1}, M_w/M_n = 2.07

^{1}H NMR (300 MHz, $CDCl_3$): δ = 5.36 (b, 2H, -CH_2-C<u>H</u>=), 4.29 (q, *J* = 6.9 Hz, 2H, -O-C<u>H_2</u>-CH_2-Br), 4.05 (q, *J* = 6.8 Hz, 4H, -OPO_3-C<u>H_2</u>-), 3.53 (t, *J* = 6.3 Hz, 2H, -O-CH_2-C<u>H_2</u>-Br), 1.98 (m, 4H, -C<u>H_2</u>-CH=), 1.68 (m, 4H, -OPO_3-CH_2-C<u>H_2</u> 1.41 – 1.24 (m, 24H, alkyl).

^{13}C NMR (75 MHz, $CDCl_3$) δ = 130.32, 68.15 (d, *J* = 6.2 Hz), 66.47 (d, *J* = 5.3 Hz), 32.62, 30.26 (d, *J* = 6.8 Hz), 29.78 - 29.16 (m), 27.23, 25.42.

^{31}P NMR (121 MHz, $CDCl_3$) δ = -1.24.

10.6.3 Poly4

Poly4a (260 mg, 0.54 mmol) was dissolved in 10 mL dry toluene in a glass vessel equipped with a stirring bar. Argon was bubbled through the solution for 10 min to remove Oxygen. 52 mg of 10 wt% Pd/C was added, and the glass vessel was charged in a 250 mL ROTH autoclave. Hydrogenation was performed at 50 °C and 50 bar of H_2 for 19 h. Pd/C was removed by filtration and the polymer was obtained after solvent evaporation as an off-white, hard material (quantitative yield).

SEC (PS standard, THF as the eluent): M_n = 15,900 g mol^{-1}, M_w = 26,500 g mol^{-1}, M_w/M_n = 1.67

^{1}H NMR (300 MHz, $CDCl_3$): δ 4.29 (q, *J* = 8.4, 6.3 Hz, 2H, -O-C$\underline{H_2}$-CH_2-Br), 4.04 (q, *J* = 6.4 Hz, 4H, -OPO_3-C$\underline{H_2}$-), 3.53 (t, *J* = 6.3 Hz, 2H, -O-CH_2-C$\underline{H_2}$-Br), 1.68 (p, *J* = 6.7 Hz, 4H, -OPO_3-CH_2-C$\underline{H_2}$), 1.25 (s, 32H, alkyl), 0.87.

^{13}C NMR (75 MHz, $CDCl_3$) δ = 68.16 (d, *J* = 6.2 Hz), 66.47 (d, *J* = 5.3 Hz), 30.26 (d, *J* = 6.8 Hz), 29.76 – 29.44 (m), 29.15, 25.43.

^{31}P NMR (121 MHz, $CDCl_3$) δ = -1.25.

10.6.4 Poly5

A Schlenk tube was charged with **poly4b** (48.1 mg, 93.7 µmol, 1 eq.) and potassium thioacetate (12.8 mg, 112.4 µmol, 1.2 eq.), dissolved in dry THF (3 mL) under an argon atmosphere. The reaction was stirred overnight at 40 °C. The crude mixture was filtered, concentrated at reduced pressure and dissolved in dichloro methane. The organic phase was washed with distilled water. The organic layer was dried over magnesium sulfate, filtered and concentrated at reduced pressure to give a yellowish powder.

^{1}H NMR (250 MHz, Chloroform-*d,* δ) 4.07 (m, 6H), 3.17 (t, *J* = 6.5 Hz, 2H), 2.35 (s, 3H), 1.67 (t, *J* = 7.0 Hz, 4H), 1.25 (m, 32H).

^{31}P {H} NMR (202 MHz, Chloroform-*d,* δ) -1.13 (s, 1P).

10.6.5 Poly6

A vial was charged with **poly5** (30 mg, 59.0 µmol, 1 eq.) and ethyl acetate (30 mL). The dispersion was heated to 60 °C and allowed to cooled to R.T. for 4-5 h. Then the crystal dispersion was cooled to 0 °C and hold at this temperature for 15 min. The stirring was turned on and 1 M hydrazine solution in ethanol (2 mL, 2 mmol, 40 eq.) was added while keeping the temperature at 0 °C. After

24 h the solvent was evaporated with a flow of nitrogen while still keeping the temperature at 0 °C.

10.6.6 Transmission Electron Microscopy (TEM)

Crystallization behavior of these polymers was studied by drop-cast TEM measurement. TEM micrograph of solution-grown of polymers were prepared from a 1 mg mL^{-1} or 0.1 mg mL^{-1} solution in ethyl acetate. The solution was heated and cooled according to the different temperature profiles. One drop of each dispersion was applied to a carbon coated TEM grid, excess liquid was blotted off with a filter paper and the specimen was allowed to dry under ambient conditions.

10.6.7 Solid State NMR

The solid state NMR measurements have been performed on a Bruker Avance III console operating at 500.2 MHz ^{1}H Larmor frequency using a commercial double resonance MAS NMR probe supporting zirconia rotors with 2.5mm outer diameter at 25 kHz MAS spinning frequency and 100 kHz rf nutation frequency on the variable x-channel of the probe tuned to the ^{31}P Larmor frequency of 202 MHz. The BABA-xy16 sequence[42] has been applied for DQ excitation and reconversion. For data analysis the normalization and fitting procedures described for static ^{1}H DQ applications by Saalwächter in detail [49] have been applied to our ^{31}P DQ data, acquired under fast MAS conditions. Combining the analytical expression for DQ build-up depending on the dipolar second moment M_2 (Saalwächter et al.[49], eqn. 15) and the DQ excitation efficiency of the BABA-xy16 pulse sequence (Saalwächter et al.[42], eqn. 11) we get

$$I_{DQ}(\tau_{DQ}) = \frac{1}{2}\left(1 - exp\left\{\frac{16}{3\pi^2}M_2\tau_{DQ}^2\right\}\right)$$

for the analytical description of the ^{31}P DQ build-up, where τ_{DQ} is the experimental DQ excitation time and the second Moment M_2 the only free parameter.[42]

10.7 Author Contributions

The manuscript was written through contributions of all authors. All authors have given approval to the final version of the manuscript.

10.8 Acknowledgments

The authors thank the Deutsche Forschungsgemeinschaft (DFG WU 750/ 8-1) for funding. Jens C. Markwart is the recipient of a fellowship through funding of the Excellence Initiative (DFG/GSC 266) in the context of the graduate school of excellence "MAINZ" (Materials Science in Mainz). F.R. Wurm and Jens C. Markwart thank Christine Rosenauer for the DLS measurements. F.R. Wurm and Jens C. Markwart thank Prof. Dr. Katharina Landfester (MPI-P, Germany) for support.

10.9 References Chapter 10

[1] R. Geyer, J. R. Jambeck, K. L. Law, *Science Advances* **2017**, *3*, e1700782.

[2] T. E. Nowlin, *Business and Technology of the Global Polyethylene Industry: An In-depth Look at the History, Technology, Catalysts, and Modern Commercial Manufacture of Polyethylene and Its Products*, Wiley, **2014**.

[3] T. M. Karlsson, L. Arneborg, G. Broström, B. C. Almroth, L. Gipperth, M. Hassellöv, *Marine Pollution Bulletin* **2018**, *129*, 52-60.

[4] J. M. Kelly, *Journal of Macromolecular Science, Part C* **2002**, *42*, 355-371.

[5] S. Hambir, J. P. Jog, *Bull. Mater. Sci.* **2000**, *23*, 221-226.

[6] B. M. Sole, A. Ball, *Tribology International* **1996**, *29*, 457-465.

[7] G. Liu, Y. Chen, H. Li, *Wear* **2004**, *256*, 1088-1094.

[8] L. A. Goettler, K. Y. Lee, H. Thakkar, *Polymer Reviews* **2007**, *47*, 291-317.

[9] P. H. Till Jr., *Journal of Polymer Science* **1957**, *24*, 301-306.

[10] Y.-R. Zheng, H. T. Tee, Y. Wei, X.-L. Wu, M. Mezger, S. Yan, K. Landfester, K. Wagener, F. R. Wurm, I. Lieberwirth, *Macromolecules* **2016**, *49*, 1321-1330.

[11] T. Haider, O. Shyshov, O. Suraeva, I. Lieberwirth, M. von Delius, F. R. Wurm, *Macromolecules* **2019**, *52*, 2411-2420.

[12] J. Mandal, S. Krishna Prasad, D. S. S. Rao, S. Ramakrishnan, *J. Am. Chem. Soc.* **2014**, *136*, 2538-2545.

[13] A. H. Groschel, A. Walther, T. I. Lobling, F. H. Schacher, H. Schmalz, A. H. Muller, *Nature* **2013**, 503, 247-251.

[14] D. J. Lunn, O. E. C. Gould, G. R. Whittell, D. P. Armstrong, K. P. Mineart, M. A. Winnik, R. J. Spontak, P. G. Pringle, I. Manners, *Nature Communications* **2016**, *7*, 12371.

[15] H. Qiu, Y. Gao, C. E. Boott, O. E. C. Gould, R. L. Harniman, M. J. Miles, S. E. D. Webb, M. A. Winnik, I. Manners, *Science* **2016**, *352*, 697-701.

[16] R. K. O'Reilly, C. J. Hawker, K. L. Wooley, *Chem. Soc. Rev.* **2006**, *35*, 1068-1083.

[17] Z. Ge, S. Liu, *Chem. Soc. Rev.* **2013**, *42*, 7289-7325.

[18] R. Bahrami, T. I. Löbling, H. Schmalz, A. H. E. Müller, V. Altstädt, *Polymer* **2015**, *80*, 52-63.

[19] R. Bahrami, T. I. Löbling, A. H. Gröschel, H. Schmalz, A. H. E. Müller, V. Altstädt, *ACS Nano* **2014**, *8*, 10048-10056.

[20] T. Gegenhuber, M. Krekhova, J. Schöbel, A. H. Gröschel, H. Schmalz, *ACS Macro Letters* **2016**, *5*, 306-310.

[21] A. H. Gröschel, A. H. E. Müller, *Nanoscale* **2015**, *7*, 11841-11876.

[22] J. Schöbel, M. Burgard, C. Hils, R. Dersch, M. Dulle, K. Volk, M. Karg, A. Greiner, H. Schmalz, *Angew. Chem. Int. Ed.* **2017**, *56*, 405-408.

[23] J. Wang, W. Li, J. Zhu, *Polymer* **2014**, *55*, 1079-1096.

[24] D. J. Blundell, A. Keller, A. J. Kovacs, *Journal of Polymer Science Part B: Polymer Letters* **1966**, *4*, 481-486.

[25] S. A. E. Boyer, J. M. Haudin, *Polym. Test.* **2010**, *29*, 445-452.

[26] T. Miyata, T. Masuko, *Polymer* **1998**, *39*, 5515-5521.

[27] N. Bosq, N. Guigo, E. Zhuravlev, N. Sbirrazzuoli, *The Journal of Physical Chemistry B* **2013**, *117*, 3407-3415.

[28] L. Mandelkern, *J. Appl. Phys.* **1955**, *26*, 443-451.

[29] G. Guerin, G. Molev, D. Pichugin, P. A. Rupar, F. Qi, M. Cruz, I. Manners, M. A. Winnik, *Macromolecules* **2019**, *52*, 208-216.

[30] B. Jin, K. Sano, S. Aya, Y. Ishida, N. Gianneschi, Y. Luo, X. Li, *Nature Communications* **2019**, *10*, 2397.

[31] F. Marsico, M. Wagner, K. Landfester, F. R. Wurm, *Macromolecules* **2012**, *45*, 8511-8518.

[32] T. Steinbach, E. M. Alexandrino, C. Wahlen, K. Landfester, F. R. Wurm, *Macromolecules* **2014**, *47*, 4884-4893.

[33] T. Steinbach, E. M. Alexandrino, F. R. Wurm, *Polymer Chemistry* **2013**, *4*, 3800-3806.

[34] M. Steinmann, J. Markwart, F. R. Wurm, *Macromolecules* **2014**, *47*, 8506-8513.

[35] H. Mutlu, L. M. de Espinosa, M. A. R. Meier, *Chem. Soc. Rev.* **2011**, *40*, 1404-1445.

[36] H. Li, L. Caire da Silva, M. D. Schulz, G. Rojas, K. B. Wagener, *Polym. Int.* **2017**, *66*, 7-12.

[37] G. Becker, L. Vlaminck, M. M. Velencoso, F. E. Du Prez, F. R. Wurm, *Polymer Chemistry* **2017**, *8*, 4074-4078.

[38] H. T. Tee, K. Koynov, T. Reichel, F. R. Wurm, *ACS Omega* **2019**, *4*, 9324-9332.

[39] K. N. Bauer, H. T. Tee, I. Lieberwirth, F. R. Wurm, *Macromolecules* **2016**, *49*, 3761-3768.

[40] O. Ruiz de Ballesteros, F. Auriemma, G. Guerra, P. Corradini, *Macromolecules* **1996**, *29*, 7141-7148.

[41] K. Saalwächter, in *Modern Magnetic Resonance* (Ed.: G. A. Webb), Springer International Publishing, Cham, **2018**, pp. 755-781.

[42] K. Saalwächter, F. Lange, K. Matyjaszewski, C.-F. Huang, R. Graf, *Journal of Magnetic Resonance* **2011**, *212*, 204-215.

[43] P. A. Abragam, A. Abragam, *The Principles of Nuclear Magnetism*, Clarendon Press, **1961**.

[44] J. C. Markwart, F. R. Wurm, *Tetrahedron* **2018**, *74*, 7426-7430.

[45] A. M. M. El-Assar, C. P. Nash, L. L. Ingraham, *Biochemistry* **1982**, *21*, 1972-1976.

[46] G. Socrates, *Infrared and Raman Characteristic Group Frequencies: Tables and Charts*, Wiley, **2004**.

[47] Z. Liang, A. Nardes, D. Wang, J. J. Berry, B. A. Gregg, *Chem. Mater.* **2009**, *21*, 4914-4919.

[48] L. D. Carr, M. T. Lusk, *Nature Nanotechnology* **2010**, *5*, 316-317.

[49] K. Saalwächter, *Prog. Nucl. Magn. Reson. Spectrosc.* **2007**, *51*, 1-35.

10.10 Supporting Information

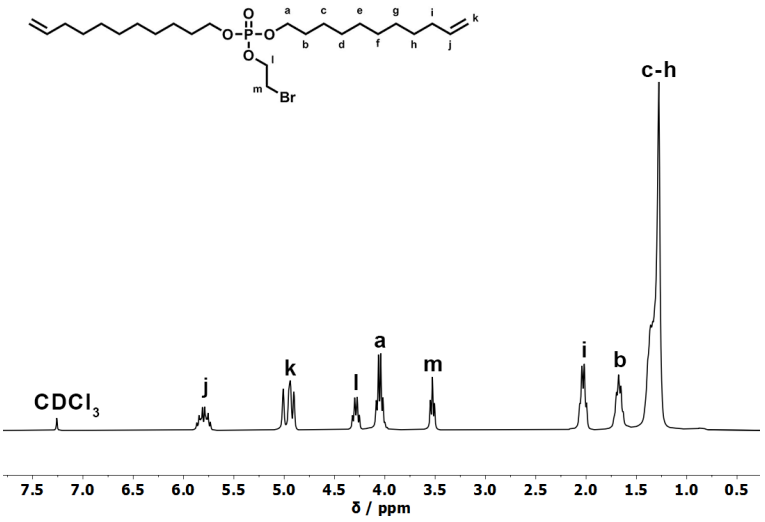

Figure S10.1. ^{1}H-NMR (300 MHz in $CDCl_3$ at 298 K) of **M4**.

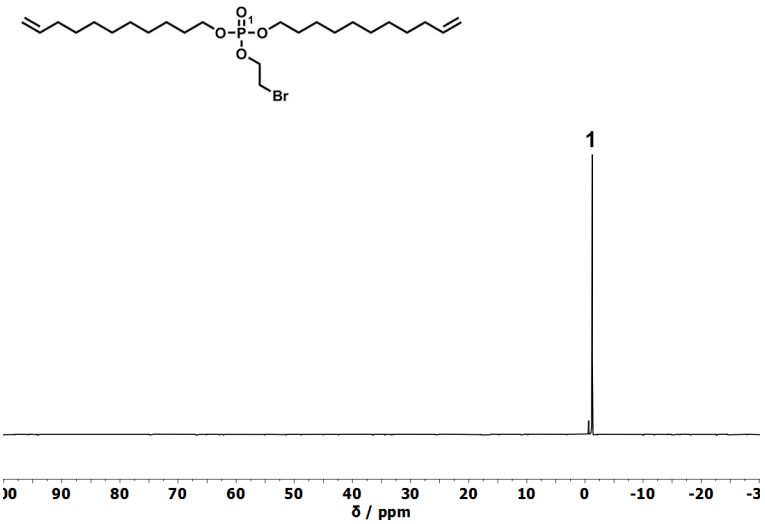

Figure S10.2. ^{31}P {H}-NMR (121 MHz in $CDCl_3$ at 298 K) of **M4**.

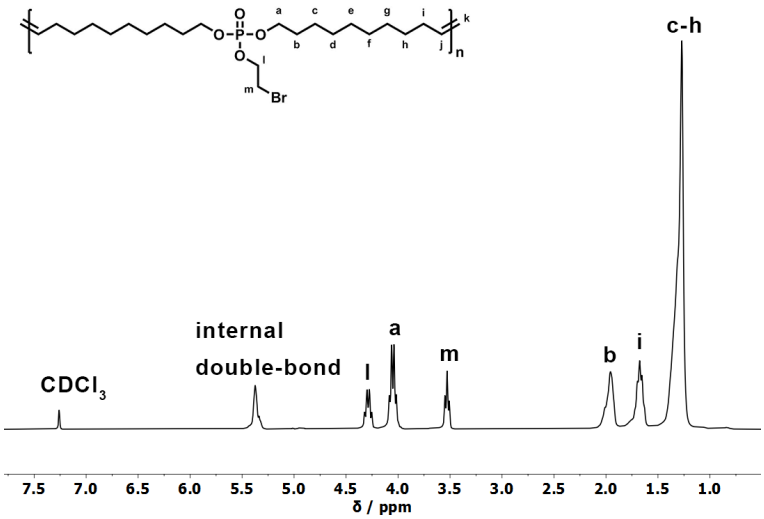

Figure S10.3. ^{1}H-NMR (300 MHz in $CDCl_3$ at 298 K) of **poly4a**.

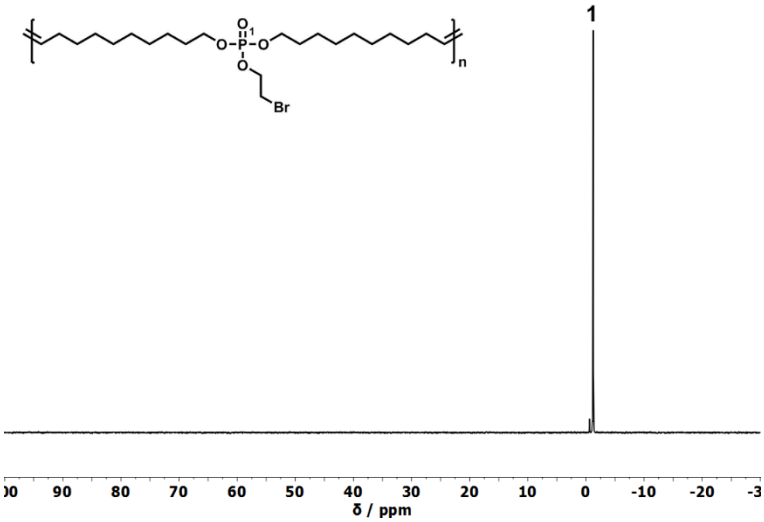

Figure S10.4. ^{31}P {H}-NMR (121 MHz in $CDCl_3$ at 298 K) of **poly4a**.

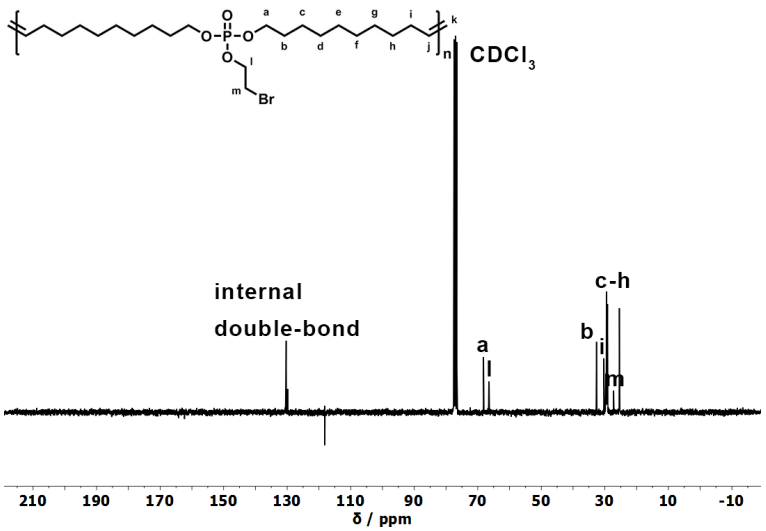

Figure S10.5. ^{13}C-NMR (75 MHz in $CDCl_3$ at 298 K) of **poly4a**.

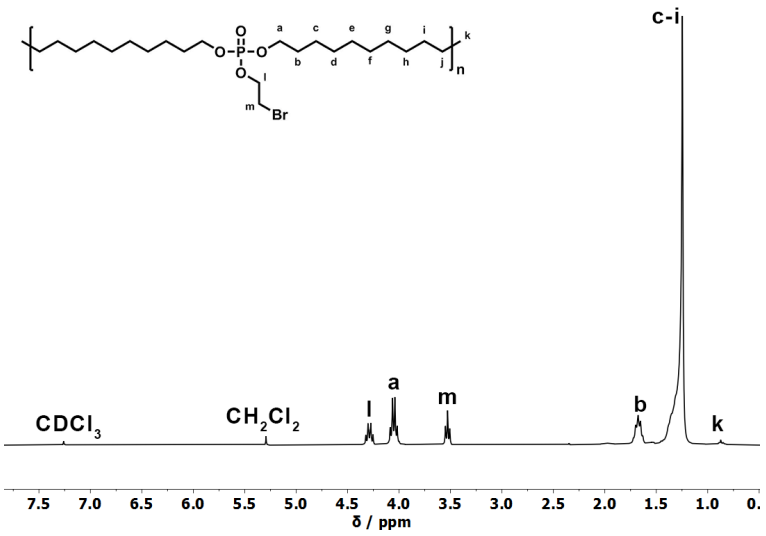

Figure S10.6. ^{1}H-NMR (300 MHz in $CDCl_3$ at 298 K) of **poly4**.

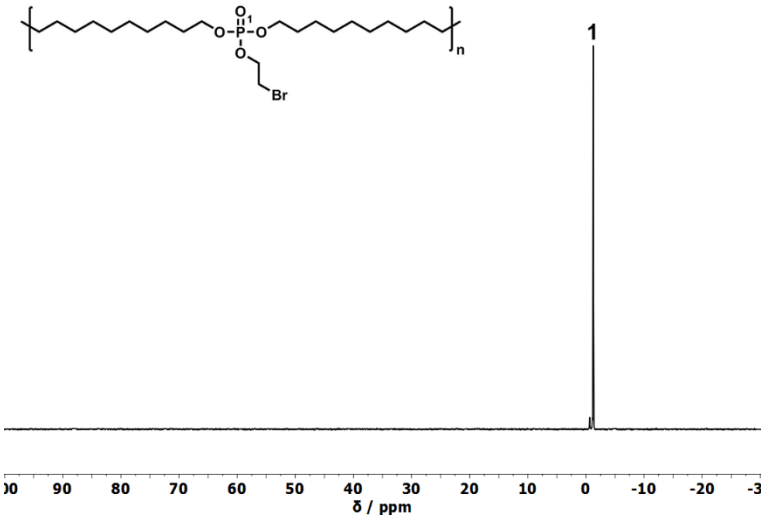

Figure S10.7. ^{31}P {H}-NMR (121 MHz in $CDCl_3$ at 298 K) of **poly4**.

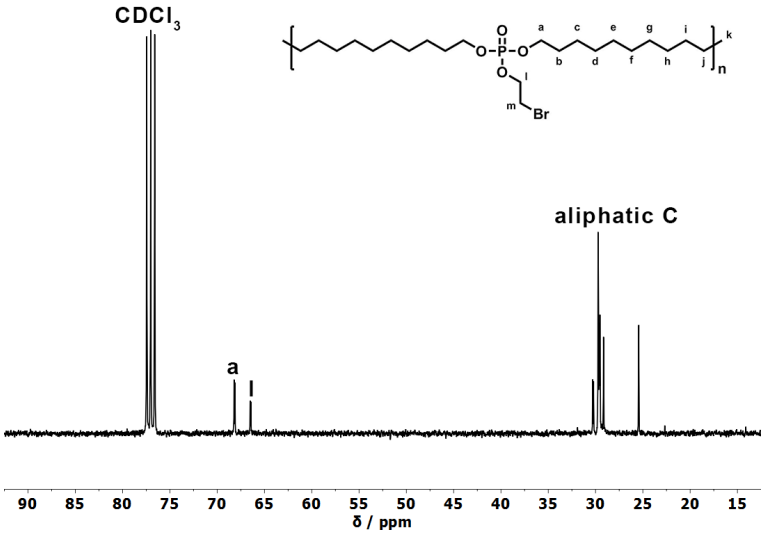

Figure S10.8. ^{13}C-NMR (75 MHz in $CDCl_3$ at 298 K) of **poly4**.

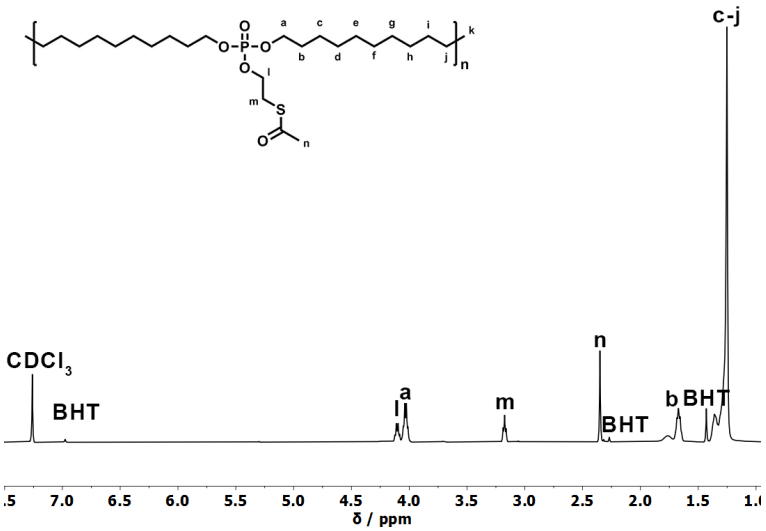

Figure S10.9. ^{1}H-NMR (300 MHz in $CDCl_3$ at 298 K) of **poly5**.

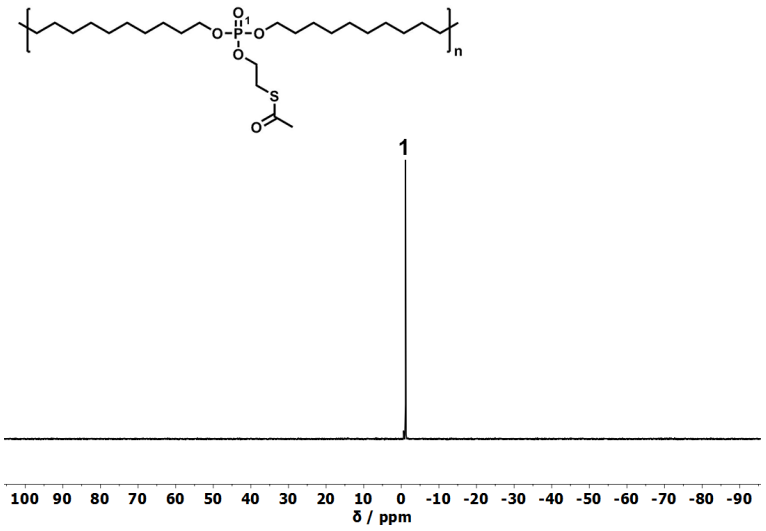

Figure S10.10. ^{31}P {H}-NMR (121 MHz in $CDCl_3$ at 298 K) of **poly5**.

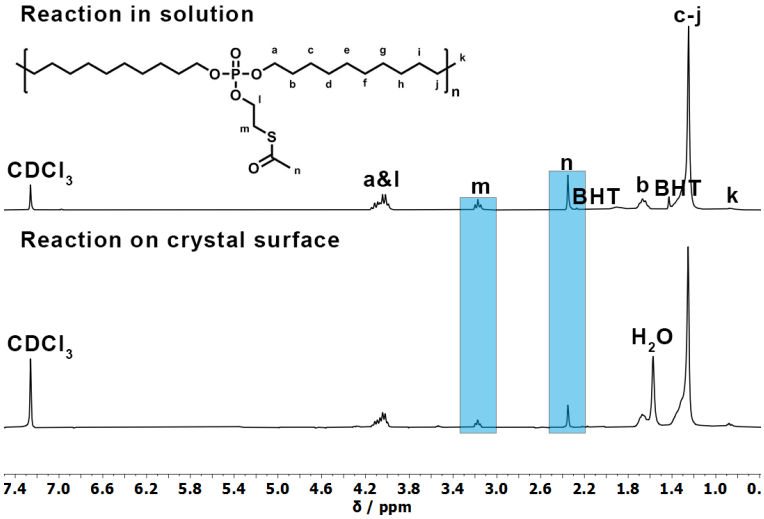

Figure S10.11. ^{1}H-NMR (300 MHz in $CDCl_3$ at 298 K) of **poly5** synthesized in solution and in dispersion. Both spectra are identical and show the characteristic resonances at 3.17 ppm and 2.35 ppm (blue).

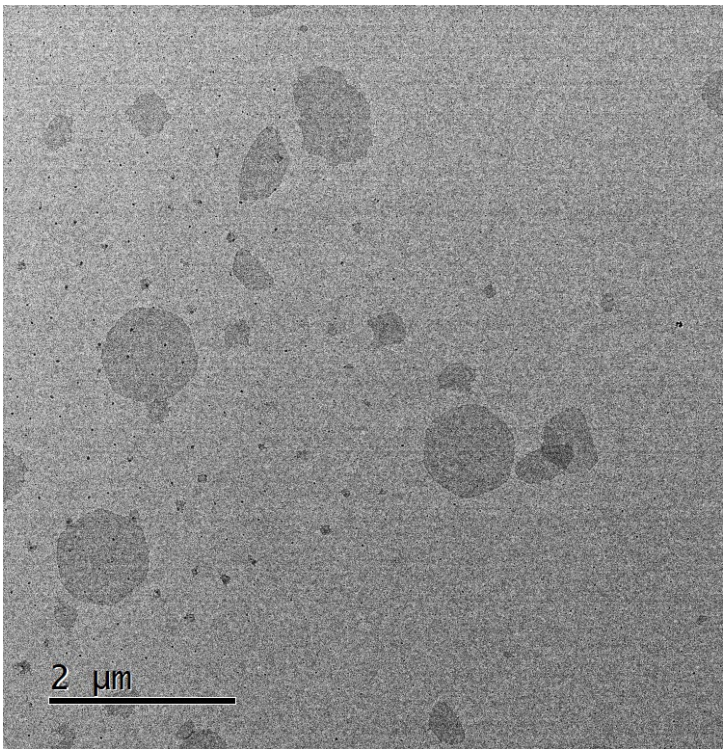

Figure S10.12. TEM image of the polymer platelets of **poly4** (diluted before measurement).

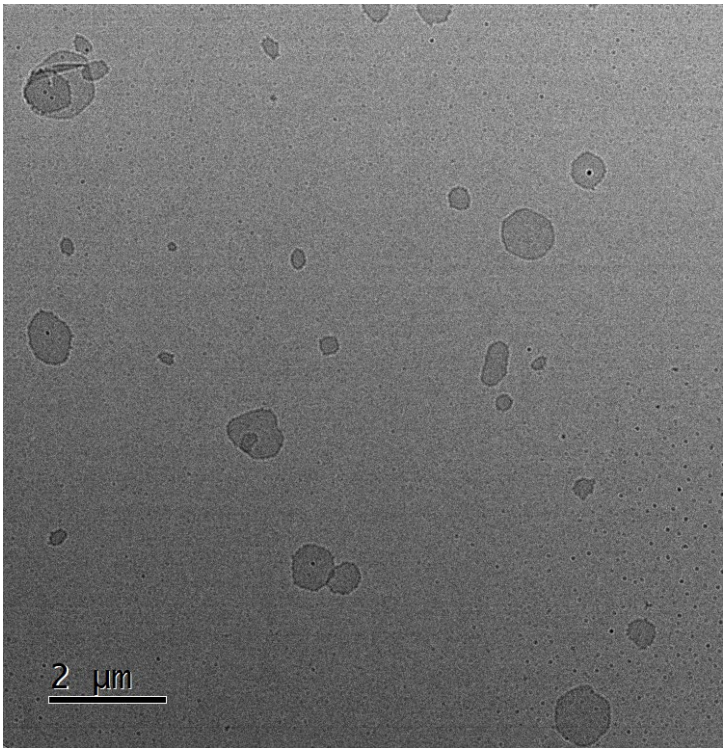

Figure S10.13. TEM image of the polymer platelets of **poly5** (diluted before measurement).

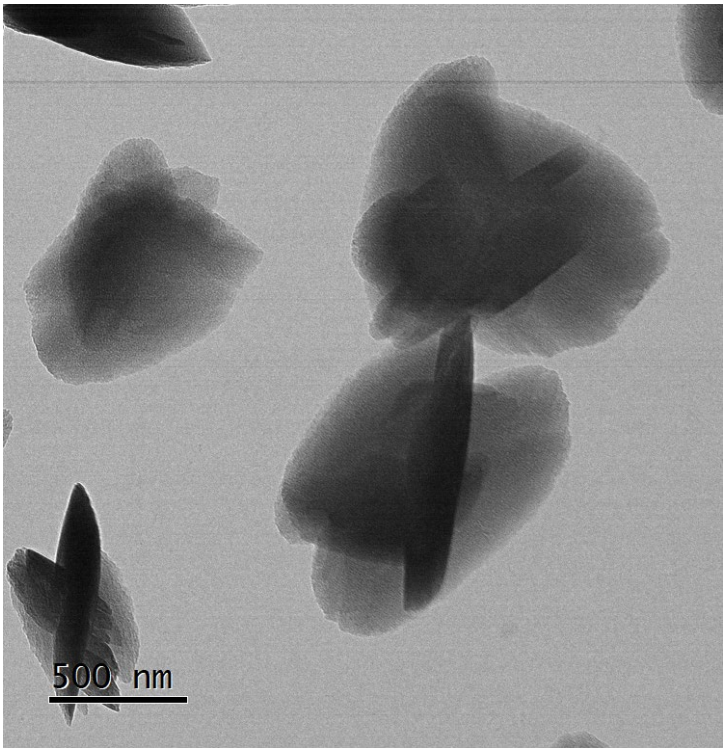

Figure S10.14. TEM image of the polymer platelets of **poly6** (diluted before measurement).

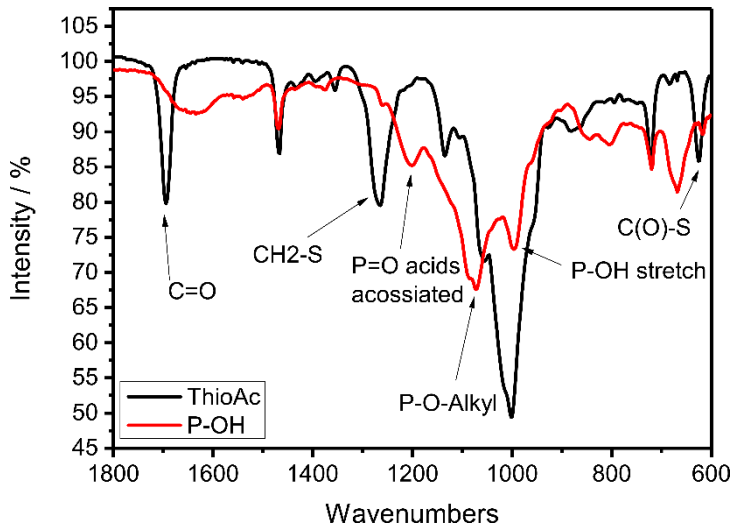

Figure S10.15. FTIR spectrum of **poly5** and **poly6** (after two step reaction) highlighting the important frequencies.

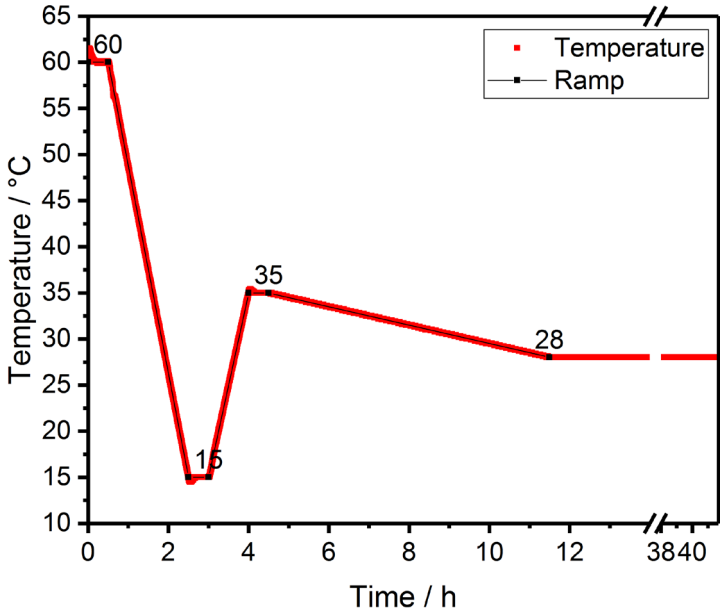

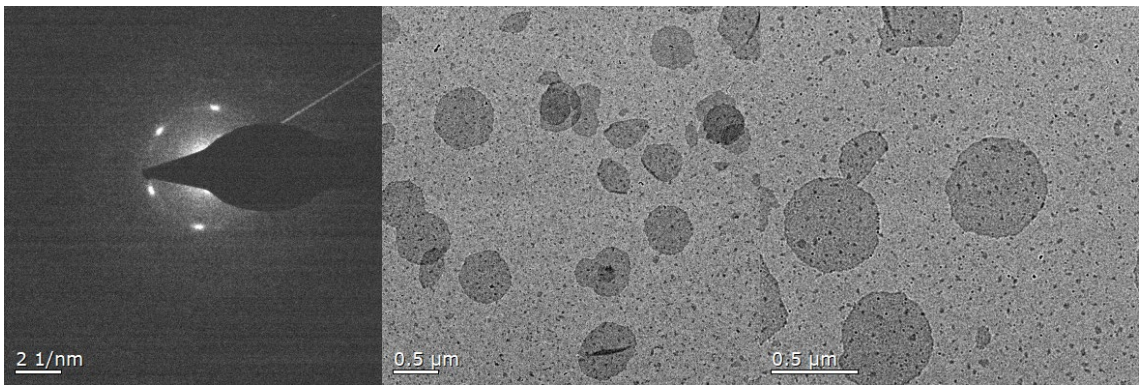

Figure S10.16. Temperature ramp of the self-seeding experiment with the corresponding TEM images of the polymer platelets of **poly1-co-2** (0.1 mg mL^{-1}) at the end of the ramp.

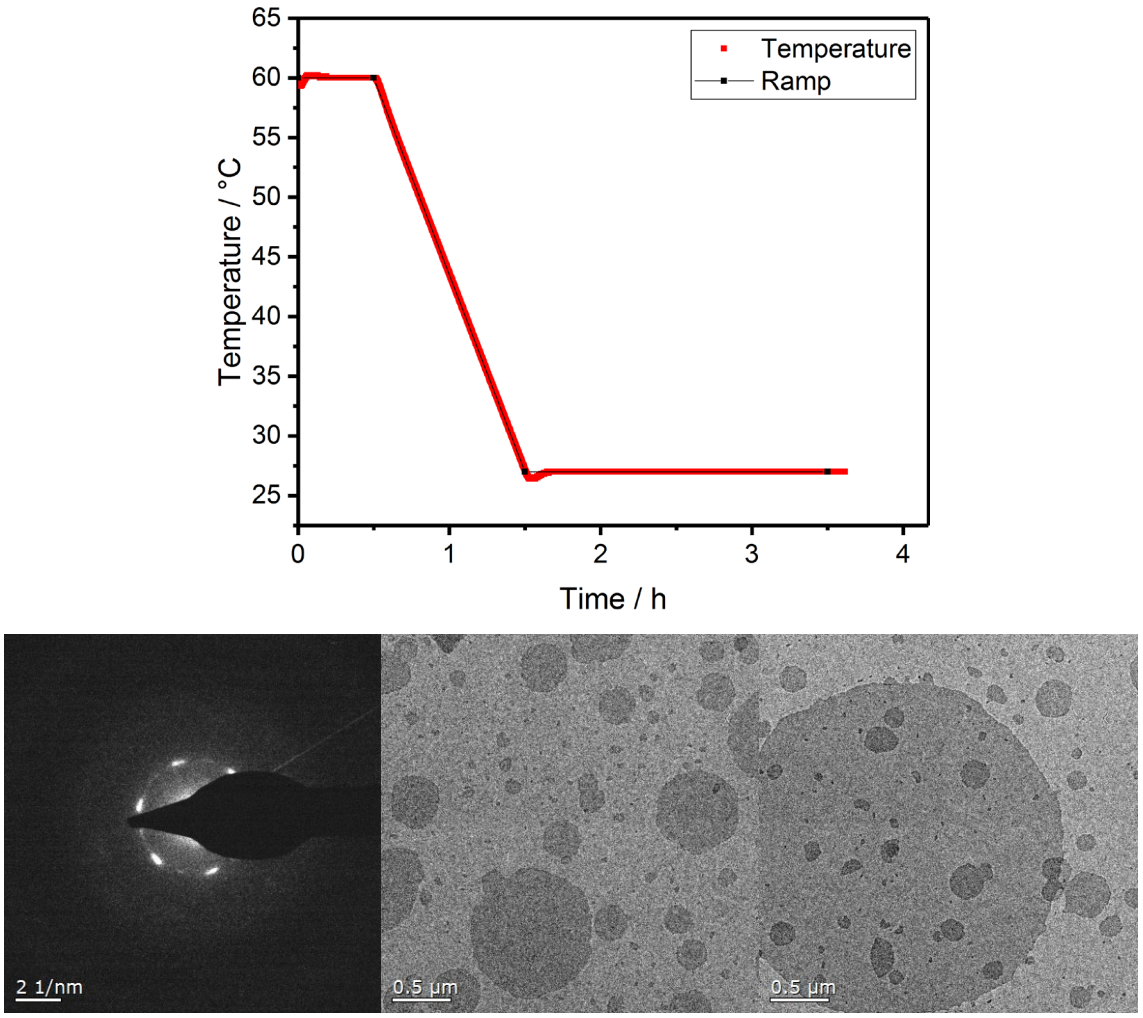

Figure S10.17. Temperature ramp from 60 °C to 27 °C with the corresponding TEM images of the polymer platelets of **poly1-co-2** (0.1 mg mL^{-1}) at the end of the ramp.

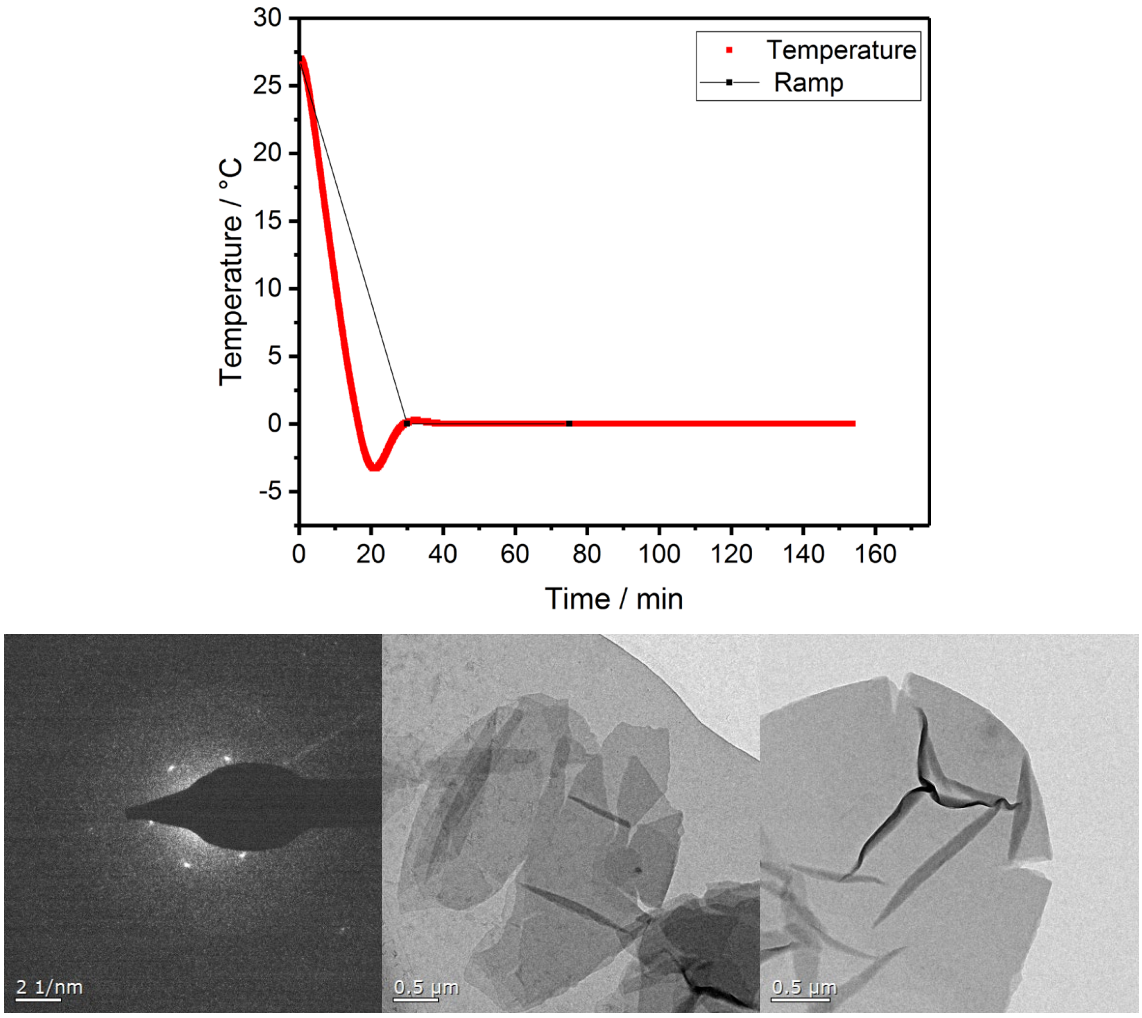

Figure S10.18. Temperature ramp from 27 °C to 0 °C with the corresponding TEM images of the polymer platelets of **poly1-co-2** (0.1 mg mL^{-1}) at the end of the ramp.

Table S10.1. Size distribution of the polymer platelets of **poly5** before the treatment with Hydrazine.

Index	Diameter / µm	Index	Diameter / µm	Index	Diameter / µm
1	0.166	36	0.076	71	0.099
2	0.221	37	0.088	72	0.149
3	0.102	38	0.101	73	0.173
4	0.159	39	0.117	74	0.115
5	0.145	40	0.115	75	0.137
6	0.121	41	0.162	76	0.128
7	0.181	42	0.131	77	0.091
8	0.099	43	0.161	78	0.125
9	0.071	44	0.117	79	0.195
10	0.163	45	0.183	80	0.131
11	0.1	46	0.091	81	0.136
12	0.176	47	0.087	82	0.094
13	0.091	48	0.094	83	0.176
14	0.071	49	0.092	84	0.098
15	0.09	50	0.134	85	0.133
16	0.172	51	0.08	86	0.105
17	0.255	52	0.058	87	0.14
18	0.11	53	0.178	88	0.152
19	0.276	54	0.123	89	0.13
20	0.169	55	0.08	90	0.136
21	0.095	56	0.099	91	0.124
22	0.125	57	0.072	92	0.148
23	0.141	58	0.133	93	0.164
24	0.089	59	0.113	94	0.142
25	0.11	60	0.091	95	0.159
26	0.101	61	0.101	96	0.175
27	0.208	62	0.06	97	0.106
28	0.14	63	0.124	98	0.104
29	0.152	64	0.154	99	0.145
30	0.168	65	0.14	100	0.149
31	0.17	66	0.112	101	0.063
32	0.132	67	0.21	102	0.078
33	0.085	68	0.151	103	0.112
34	0.095	69	0.114		
35	0.109	70	0.095		

Table S10.2. Size distribution of the polymer platelets of **poly6** after the treatment with Hydrazine.

Index	Diameter / µm	Index	Diameter / µm	Index	Diameter / µm
1	0.351	18	0.106	35	0.152
2	0.128	19	0.152	36	0.136
3	0.128	20	0.121	37	0.18
4	0.068	21	0.121	38	0.095
5	0.147	22	0.067	39	0.14
6	0.085	23	0.084	40	0.177
7	0.15	24	0.108	41	0.19
8	0.105	25	0.065	42	0.108
9	0.108	26	0.169	43	0.129
10	0.095	27	0.087	44	0.148
11	0.123	28	0.139	45	0.091
12	0.155	29	0.152	46	0.148
13	0.183	30	0.133	47	0.135
14	0.116	31	0.129	48	0.096
15	0.128	32	0.092	49	0.082
16	0.208	33	0.106	50	0.118
17	0.173	34	0.185		

Table S10.3. Size distribution of the polymer platelets of **poly1-co-2** cooling from 60 °C to 27 °C.

Index	Diameter / µm	Index	Diameter / µm	Index	Diameter / µm
1	1.938	96	0.146	193	0.245
2	1.875	97	0.173	194	0.059
1	0.075	98	0.329	195	0.042
2	0.065	99	0.168	196	0.102
3	0.035	100	0.147	197	0.204
4	0.06	101	0.102	198	0.373
5	0.061	102	0.078	199	0.095
6	0.246	103	0.064	200	0.129
7	0.208	104	0.084	201	0.093
8	0.071	105	0.077	202	0.084
9	0.106	106	0.119	203	0.049
10	0.108	107	0.064	204	0.102
11	0.157	108	0.065	205	0.203
12	0.064	109	0.226	206	0.136
13	0.228	110	0.096	207	0.102
14	0.136	111	0.197	208	0.394
15	0.064	112	0.227	209	0.137
16	0.14	113	0.238	210	0.106
17	0.252	114	0.156	211	0.112
18	0.152	115	0.065	212	0.057
19	0.06	116	0.075	213	0.074
20	0.071	117	0.093	214	0.17

21	0.251	118	0.135	215	0.085
22	0.05	119	0.093	216	0.09
23	0.045	120	0.184	217	0.05
24	0.102	121	0.086	218	0.275
25	0.093	122	0.192	219	0.067
26	0.102	123	0.093	220	0.168
27	0.107	124	0.083	221	0.161
28	0.042	125	0.728	222	0.253
29	0.032	126	0.112	223	0.138
30	0.035	127	0.061	224	0.099
31	0.181	128	0.113	225	0.073
32	0.311	129	0.159	226	0.061
33	0.204	130	0.288	227	0.157
34	0.301	131	0.057	228	0.075
35	0.08	132	0.068	229	1.224
36	0.313	133	0.099	230	0.165
37	0.079	134	0.353	231	0.247
38	0.077	135	0.307	232	0.106
39	0.199	136	0.074	233	0.133
40	0.047	137	0.114	234	0.119
41	0.118	138	0.061	235	0.244
42	0.036	139	0.072	236	0.116
43	0.033	140	0.054	237	0.098
44	0.212	141	0.14	238	0.105
45	0.118	142	0.456	239	0.047
46	0.197	143	0.181	240	0.128
47	0.134	144	0.339	241	0.109
48	0.066	145	0.09	242	0.075
49	0.288	146	0.151	243	0.218
50	0.052	147	0.111	244	0.14
51	0.094	148	0.071	245	0.058
52	0.052	149	0.123	246	0.405
53	0.053	150	0.106	247	0.251
54	0.048	151	0.109	248	0.192
55	0.119	152	0.403	249	0.174
56	0.126	153	0.534	250	0.212
57	0.476	154	0.218	251	0.091
58	0.155	155	0.103	252	0.083
59	0.038	156	0.175	253	0.195
60	0.077	157	0.06	254	0.309
61	0.052	158	0.058	255	0.075
62	0.107	159	0.126	256	0.058
63	0.077	160	0.322	257	0.122
64	0.12	161	0.302	258	0.184
65	0.057	162	0.099	259	0.085
66	0.055	163	0.107	260	0.092

67	0.086	164	0.127	261	0.151
68	0.057	165	0.159	262	0.179
69	0.056	166	0.122	263	0.384
70	0.075	167	0.424	264	0.177
71	0.215	168	1.091	265	0.184
72	0.199	169	0.678	266	0.199
73	0.135	170	0.231	267	0.045
74	0.115	171	0.276	268	0.165
75	0.122	172	0.298	269	0.204
76	0.048	173	0.427	270	0.292
77	0.111	174	0.135	271	0.13
78	0.149	175	0.354	272	0.088
79	0.083	176	0.2	273	0.089
80	0.08	177	0.185	274	0.088
81	0.144	178	0.087	275	0.116
82	0.161	179	0.146	276	0.115
83	0.2	180	0.12	277	0.287
84	0.071	181	0.061	278	0.117
85	0.109	182	0.133	279	0.084
86	0.038	183	0.138	280	0.084
87	0.075	184	0.12	281	0.1
88	0.277	185	0.194	282	0.081
89	0.675	186	0.176	283	0.1
90	0.062	187	0.088	284	0.235
91	0.07	188	0.12	285	2.87
92	0.075	189	0.069	286	0.193
93	0.11	190	0.056	287	0.061
94	0.096	191	0.168		
95	0.107	192	0.072		

Table S10.4. Size distribution of the polymer platelets of **poly1-co-2** cooling from 27 °C to 0 °C.

Index	Diameter / µm
1	2.654
2	3.976
1	2.89
2	3.379
1	2.23
2	3.103
1	1.41
2	0.857
3	1.349
1	3.254

Table S10.5. Size distribution of the polymer platelets of **poly1-co-2** after self-seeding.

Index	Diameter / µm	Index	Diameter / µm	Index	Diameter / µm
1	0.535	32	0.529	63	0.275
2	0.274	33	0.355	64	0.348
3	0.585	34	0.572	65	0.701
4	0.449	35	0.515	66	0.518
5	0.213	36	0.536	67	0.5
6	0.256	37	0.462	68	0.395
7	0.529	38	0.451	69	0.574
8	0.42	39	0.575	70	0.322
9	0.517	40	0.645	71	0.688
10	0.52	41	0.537	72	0.308
11	0.476	42	0.227	73	0.657
12	0.54	43	0.244	74	0.386
13	0.414	44	0.274	75	0.689
14	0.444	45	0.494	76	0.669
15	0.504	46	0.466	77	0.546
16	0.501	47	0.527	78	0.531
17	0.646	48	0.293	79	0.408
18	0.504	49	0.537	80	0.73
19	0.276	50	0.611	81	0.374
20	0.303	51	0.628	82	0.411
21	0.279	52	0.66	83	0.591
22	0.338	53	0.513	84	0.68
23	0.455	54	0.65	85	0.577
24	0.394	55	0.611	86	0.731
25	0.319	56	0.355	87	0.524
26	0.406	57	0.532	88	0.561
27	0.53	58	0.246	89	0.501
28	0.456	59	0.521	90	0.72
29	0.52	60	0.693	91	0.523
30	0.561	61	0.592	92	0.266
31	0.592	62	0.603		

11. Appendix

11.1 Cooperation Projects

During my PhD thesis a number of cooperation project have been developed. Already published papers are presented in the following. Ongoing projects will not be presented herein.

1. Copolymerization of Cyclic Phosphonate and Lactide: Synthetic Strategies toward Control of Amphiphilic Microstructure

11.1.1 Copolymerization of Cyclic Phosphonate and Lactide: Synthetic Strategies toward Control of Amphiphilic Microstructure

Macromolecules

Article

Cite This: Macromolecules 2019, 52, 1220−1226

pubs.acs.org/Macromolecules

Copolymerization of Cyclic Phosphonate and Lactide: Synthetic Strategies toward Control of Amphiphilic Microstructure

James Beament,[§] Thomas Wolf,[‡] Jens C. Markwart,[‡] Frederik R. Wurm,*[,‡] Matthew D. Jones,*[,§] and Antoine Buchard*[,§]

[§]Department of Chemistry, University of Bath, Claverton Down, Bath BA2 7AY, U. K

[‡]Max Planck Institute for Polymer Research, Ackermannweg 10, D-55128 Mainz, Germany

Supporting Information

ABSTRACT: Controlling the microstructure of polymers through chemical reactivity is key to control the material properties of synthetic polymers. Herein we investigate the ring-opening copolymerization of a mixture of lactide and 2-ethyl-2-oxo-1,3,2-dioxaphospholane, promoted by an aluminum pyrrolidine monophenolate complex or 1,8-diazabicyclo[5.4.0]undec-7-ene (DBU). This monomer mixture provides fast access to amphiphilic copolymers. The reaction conditions control the copolymer microstructure, which has been determined via a combination of ^{1}H and ^{31}P NMR spectroscopy. The choice of initiator has a profound impact: both initiators produce tapered block copolymers but with reverse monomer selectivity. While the aluminum initiator favors the cyclic phosphonate monomer, DBU favors lactide polymerization. Moreover, a sequential control of temperature facilitates the preparation of block copolymers in one pot. Thermal properties measured by TGA and DSC correlate to copolymer architectures. This methodology is the first report of copolymerization between cyclic phosphonates and lactide and opens the possibility to tune the thermal properties, solubility, and degradation rates of the resulting materials.

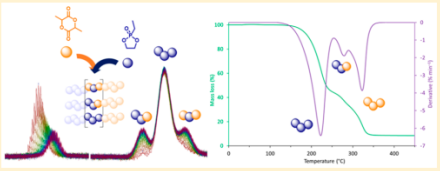

INTRODUCTION

Poly(lactic acid) (PLA) is arguably one of the most promising commodity plastics derived from renewable feedstocks and industrially compostable, which has penetrated a highly unsustainable market of nondegradable polymers based around crude-oil feedstocks.[1−3] The production of PLA was close to 220 000 tonnes in 2017 and is predicted to increase by 50% by 2022.[4] Much research has been directed toward improving the thermal properties of PLA, in particular through the development of stereoselective ring-opening polymerization (ROP) catalysts for lactide.[5] In parallel, increasing efforts have focused on improving the biodegradability of PLA and its composites in natural and landfill environments.[6−8] Notable strategies have included the development of PLA-based polymer blends,[9−14] as well as copolymerization methods to incorporate more degradable linkages into the PLA polyester backbone.[15,16]

In that regard, phosphorus(V)-based monomers, such as phosphoesters {P(=O)(OR)$_2$OR′}, phostones, or phosphonates {P(=O)(OR)$_2$R′}, are of interest due to their low toxicity and facile hydrolysis. Furthermore, while they have been polymerized via step-growth esterification and acyclic diene metathesis,[17,18] cyclic phosphoesters, phostones, and phosphonates are also amenable to ROP,[19,20] which allows copolymerization with lactide.

Penczek and co-workers first investigated polyphosphoesters (−[P(=O)(OR′)ORO]$_n$−) in 1976, as precursors for polyelectrolytes.[21] Since then, these polymers and related polyphosphates have been widely studied for biomedical applications and as flame retardants.[20,22−24] Catalytic ROP of five-membered cyclic phosphoesters has been demonstrated to produce well-defined polyphosphoesters,[25,26] with recent catalyst development (e.g., the combination of thioureas (TUs) and 1,8-diazabicyclo[5.4.0]undec-7-ene (DBU))[27−30] overcoming the broad molecular weight distributions from initial studies.[31−36] Block copolymers of cyclic phosphoesters and lactide synthesized via sequential addition have been studied and applied for tissue engineering and drug delivery,[37−40] these systems showing high rates of enzymatic degradation under physiological conditions.[37]

Polyphosphonates (−[P(=O)R′ORO]$_n$−) are another class of phosphorus(V)-based polymers which differ from polyphosphates in their alkyl side arm (R′), which alters polymerization kinetics and degradation rates compared to phosphates analogues.[41−43] Wurm and co-workers have thus recently synthesized copolymers of phosphonates (PPn) with hydrophilic and hydrophobic segments, which have both lower and upper critical solution temperatures, yielding a route to self-assembled and degradable polymersomes.[44] Compared to polyphosphates, polyphosphonates are less susceptible to transesterification, so that simple ROP initiating systems

Received: November 7, 2018
Revised: January 11, 2019
Published: January 30, 2019

DOI: 10.1021/acs.macromol.8b02385
Macromolecules 2019, 52, 1220−1226

such as DBU/alcohol can be used in a controlled manner with cyclic phosphonates. A few metal catalytic systems have also been reported, with comparable control and rates faster than those of organocatalysts.[36,45] As polyphosphonates give fast access to hydrophilic and low-T_g polymers with a low tendency toward transesterification, copolymerization with lactide would be a straightforward way to amphiphilic PLA derivatives with adjustable thermal properties. The variety of catalytic strategies that have been developed for lactide ROP could further enable the control of the comonomer reactivity and the production of polyesters with defined sequence and enhanced, tailored degradability. However, to date, copolymers of cyclic phosphonates and lactide have not been investigated.

Herein we have explored the formation of copolymers of rac-LA and L-LA with 2-ethyl-2-oxo-1,3,2-dioxaphospholane (EtPPn) using a pyrrolidine salan Al complex or DBU (see Figure 1). We have investigated the influence of the catalyst on

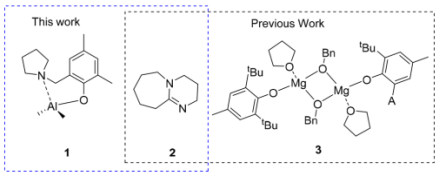

Figure 1. Initiators for the ROP of EtPPn.

the copolymerization kinetics and copolymer microstructure. We also report how a temperature switch can be exploited in combination with the Al system to control comonomer reactivity and prepare, in one pot, PLA-EtPPn block copolymers. We have investigated how the different initiators and polymerization conditions affect the thermal properties (in particular the T_g) of the resulting copolymer.

RESULTS AND DISCUSSION

Homopolymerization of EtPPn. To date, EtPPn has only been polymerized with a few catalytic systems (Figure 1 and Table 1, entries 7 and 8). We first tested its polymerization with Al pyrrolidine complex **1** in the presence of benzyl alcohol (BnOH) as co-initiator, a system that we have recently reported for the ROP of lactide.[46] Initiator **1** was active at both 25 °C and 80 °C for the ROP of EtPPn. Under solvent free conditions, at 25 °C, and a $[EtPPn]_0$:$[\mathbf{1}]_0$:$[BnOH]_0$ feed ratio of 50:1:1 ($[\mathbf{1}]_0$ = 0.86 mol L^{-1}), 90% monomer conversion was observed within 5 min, with excellent control of the molecular weight (Table 1, entry 1). Reactions under dilute conditions ($[EtPPn]_0$ = 0.35 mol L^{-1}), in either CH_2Cl_2 or toluene, maintained good conversion (89−96%), albeit after longer reaction times (Table 1, entries 2 and 3). Furthermore, increasing initial monomer concentration from 0.35 to 0.7 mol L^{-1} increased conversion (Table 1, entries 3−6).

Sequential Polymerization of EtPPn and Lactide. Copolymerization of L-lactide (L-LA) and EtPPn was next investigated using **1** in toluene with a total monomer concentration of 0.7 mol L^{-1}. Initially, sequential addition of monomers was investigated to produce block copolymers. Complete conversion of L-LA (96%) with **1** was found to require 24 h at 80 °C (for $[LA]_0$ = 0.35 mol L^{-1} and $[LA]_0$:$[I]_0$:$[BnOH]_0$ = 50:1:1). Cooling the active solution to 25 °C followed by addition of 50 equiv of EtPPn (0.35 mol L^{-1}) yielded high conversions of EtPPn after 1 h (88%). Conversions of both monomers were determined by relative integration of polymer signals in the ^{1}H NMR spectra of the crude reaction mixture (following quenching). Relative integration of the ^{31}P NMR spectra further confirmed EtPPn conversions.

^{1}H and ^{31}P DOSY NMR experiments indicated only one diffusing polymer species (Figures S8 and S16), supporting the formation of a copolymer. Size-exclusion chromatography (SEC) also revealed a unimodal trace, with molecular weights in good agreement with expected values (M_n^{theo} = 13.0 kg mol^{-1}, M_n^{SEC} = 10.5 kg mol^{-1}). Insight into the poly(phosphonate-*b*-lactide) chain microstructure was determined via ^{31}P NMR spectroscopy, which revealed two phosphorus environments. On the basis of previous experiments, the main broad signal between 34.3 and 35.2 ppm was attributed to a polyphosphonate sequence.[47] A much smaller signal (~2% relative intensity) was also apparent between 35.2 and 36.0 ppm, evidence of the enchainment between a lactide and a phosphonate unit. This was later confirmed by the analysis of more random poly(phosphonate-*co*-lactide) copolymers (vide infra).

Triblock poly(phosphonate-*b*-lactide-*b*-phosphonate) copolymers could be synthesized in a similar way by using a

Table 1. Ring-Opening Polymerization of EtPPn[a]

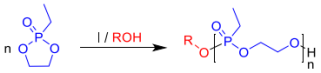

entry	I	T (°C)	solvent	time (h)	$[EtPPn]$ (mol L^{-1})	conv (%)[c]	M_n^{theo} (kg mol^{-1})[d]	M_n^{SEC} (kg mol^{-1}) [$Đ$][e]
1	**1**	25	N/A	0.08	bulk	90	6.2	4.3 [1.11]
2	**1**	25	DCM	3	0.35	96	6.6	5.3 [1.14]
3	**1**	25	Tol	24	0.35	89	6.2	4.9 [1.32]
4	**1**	80	Tol	4	0.35	55	3.8	3.1 [1.20]
5	**1**	25	Tol	24	0.7	99	6.8	4.8 [1.38]
6	**1**	80	Tol	4	0.7	90	6.2	5.3 [1.21]
7	**2**[41]	25	DCM	16	4	90	6.2	5.4 [1.07]
8[b]	**3**	−20	THF	1	2	89	12.2	14.2 [1.46]

[a]I: Initiator, $[EtPPn]_0$:$[I]_0$:$[BnOH]_0$ = 50:1:1. [b]$[EtPPn]_0$:$[\mathbf{3}]_0$ = 100:1, **3** = $[(BHT)Mg(OBn)(THF)]_2$.[36] [c]Conversion calculated from ^{1}H NMR by relative integration of the CH_2 signals in the polymer (1.74−1.85 ppm) and in the monomer (1.93−2.03 ppm). [d][((Conversion [M]/100 × $[M]_0$:$[I]_0$) × 136.03) + 108]. [e]Determined by SEC in DMF at 60 °C.

DOI: 10.1021/acs.macromol.8b02385
Macromolecules 2019, 52, 1220−1226

Table 2. Copolymerization of EtPPn with LA to Produce Copolymers with Adjustable Microstructure

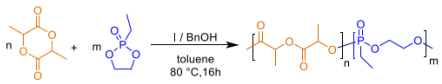

entry	I	feed ratio [LA]:[EtPPn]:[I]:[BnOH]	conv of LA/EtPPn (%)[f]	EtPPn content in polymer (%)[g]	M_n^{SEC} (kg mol^{-1}) [$Đ$][h]	M_n^{NMR} (kg mol^{-1})[i]	M_n^{theo} (kg mol^{-1})[k]	T_g (°C)	P triads ratios PPL:PPP:LPL
1[a]	**1**	50:50:1:1	75/100	57	15.6 [1.06]	13.3	12.3	−9.7	22:51:27
2[a]	**1**	100:50:1:1	77/98	39	12.5 [1.02]	8.6	18.0	−3.1	28:59:13
3[a]	**1**	100:20.1:1	83/100	19	16.2 [1.27]	16.6	14.8	19.6	28:45:27
4[a]	**1**	100:10.1:1	95/100	10	12.9 [1.23]	11.7	15.2	27.4	44:15:41
5[b]	**1**	50:50.1:1	73/100	58	21.0 [1.12]	9.5	12.2	18.7	21:62:17
6[b]	**1**	100:50:1:1	75/100	40	20.6 [1.06]	20.1	17.6	23.3	29:38:33
7[c]	**1**	50:50:1:1	30/96	76	6.1 [1.31][j]	7.7	8.8	−35.8	8:87:5
8[b]	**2**	50:50:1:1	85/67	45	4.3 [1.10]	8.6	10.5	2.9	30:45:25
9[d]	**2**	50:50:1:1	81/46	35	4.8 [1.18]	8.6	9.4	7.9	32:35:34
10[e]	**2**	50:50:1:1	91/18	17	3.2 [1.10]	7.2	7.9	18.1	40:14:46

[a]$[\text{rac-LA}]_0$ = 0.7 mol L^{-1}, $[\text{EtPPn}]_0$ varies. [b]$[\text{L-LA}]_0$ = 0.7 mol L^{-1}, $[\text{EtPPn}]_0$ varies. [c]$[\text{L-LA}]_0 = [\text{EtPPn}]_0$ = 0.35 mol L^{-1}, at 25 °C for 120 h. [d]$[\text{L-LA}]_0 = [\text{EtPPn}]_0$ = 0.35 mol L^{-1}. [e]$[\text{L-LA}]_0 = [\text{EtPPn}]_0$ = 0.35 mol L^{-1}, in CH_2Cl_2 at 25 °C for 16 h. [f]Conversions calculated from ^{1}H NMR by relative integration of the side chain CH_2 signals corresponding to EtPPn and poly(EtPPN), and of the methine region of LA and PLA. [g]Calculated from the ratio of polymer units in the crude product. [h]Determined by SEC, carried out in THF at 35 °C. [i]Determined by SEC, carried out in DMF at 60 °C. [j]Calculated from the integration of polymer signals against the BnO end group. [k]Calculated from conversion of each monomer (M) multiplied by $[\text{M}]_0/[\text{I}]_0$.

bifunctional initiator, 1,4-benzenedimethanol, at feed ratios of 100:100:2:1 ($[\text{EtPPn}]_0$:$[\text{LA}]_0$:$[\mathbf{1}]_0$:$[C_6H_4(CH_2OH)_2]_0$). In this case, a more intense resonance corresponding to lactide−phosphonate enchainment was observed in the ^{31}P NMR spectrum, as expected from a monomer switch on both sides of the centrally growing polymer (Figure S12).

One-Pot Copolymerization of EtPPn and Lactide. Copolymerization was then performed in one pot, from a monomer mixture of rac-LA and EtPPn ($[\text{rac-LA}]_0 = [\text{EtPPn}]_0$ = 0.7 mol L^{-1}), in toluene at 80 °C. Using **1**, complete conversion of EtPPn and high conversion of LA were achieved after 16 h (Table 2, entry 1). The formation of a true copolymer was confirmed by DOSY and unimodal SEC traces ($Đ$ < 1.27). It was possible to vary the percentage of EtPPn incorporated into the copolymer (Table 2, entries 1−4) with a good fit to that of the initial feeds. Molecular weights obtained via SEC (most copolymers were soluble in THF) and ^{1}H NMR showed good agreement with expected values (calculated based on monomers conversions). The copolymer microstructure was further probed via ^{31}P NMR spectroscopy, which revealed three phosphorus environments, consistent with the three possible sequence triads involving a central phosphonate linkage: P-**P**-L (or L-**P**-P), P-**P**-P, and L-**P**-L (Figure 2). On the basis of the polyphosphonate and poly(lactide-*b*-phosphonate) polymers prepared previously, the P-P-P and P-P-L triads were identified as the signals at 34.3−35.2 and 35.2−36.0 ppm, respectively. The additional resonance between 33.0 and 34.3 ppm was therefore assigned to L-P-L triad. The ^{31}P NMR for the polymer obtained from Table 2 entry 1 indicated that the P-P-P triad was the dominant resonance, albeit with significant P-P-L and L-P-L signals, indicative of a copolymer of a blocky nature. By increasing the LA:EtPPn ratio, the amount of lactide-containing triads increased compared to the P-P-P triad, yet without removing it completely, supporting further the blocky nature of the phosphonate linkages in the synthesized copolymers (Table 2, entry 4).

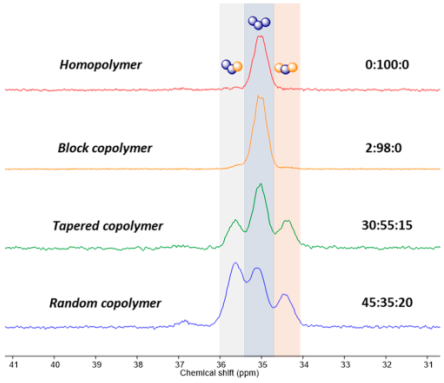

Figure 2. Stacked ^{31}P NMR spectra for copolymers of LA-EtPPn. Triad sequences shown identified as PPL, PPP, and LPL (left to right).

To gain further insight, copolymerization kinetics were monitored in situ in toluene-d_8 at 80 °C, and the microstructure of the copolymer was evaluated as a function of time, using ^{1}H and ^{31}P NMR spectroscopy (Figure 3a). In these experiments, temperature equilibration, lactide dissolution in toluene, and data acquisition delay means that the first 10 min of the reaction cannot be reliably quantified. However, within this period, 70% of EtPPn and 17% of lactide has polymerized, so that a copolymer with a high proportion of P-P-P linkages (66%) is already present at the start of the monitoring. Next, EtPPn continues to be incorporated preferentially into the copolymer: the conversion of individual monomers can be successfully modeled using a pseudo-first-order kinetics approach,[46] but EtPPn reacts twice as fast compared to L-LA

DOI: 10.1021/acs.macromol.8b02385
Macromolecules 2019, 52, 1220−1226

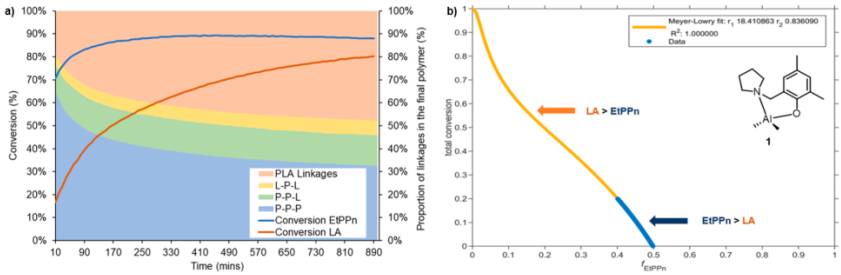

Figure 3. NMR-monitored copolymerization of EtPPn and L-LA in toluene-d_8, $[\text{L-LA}]_0 = [\text{EtPPn}]_0 = 0.35$ mol L^{-1}, $[\text{L-LA}]_0$:$[\text{EtPPn}]_0$:$[\mathbf{1}]_0$:$[\text{BnOH}]_0 = 50{:}50{:}1{:}1$, 80 °C, 16 h: (a) conversion and microstructure composition calculated from ^{31}P NMR vs time; (b) calculation of EtPPn and L-LA reactivity ratios using Meyer−Lowry fits.

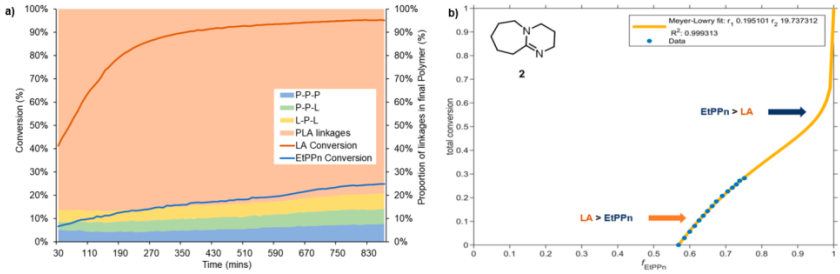

Figure 4. NMR-monitored copolymerization of EtPPn and L-LA in toluene-d_8, $[\text{L-LA}]_0 = [\text{EtPPn}]_0 = 0.35$ mol L^{-1}, $[\text{L-LA}]_0$:$[\text{EtPPn}]_0$:$[\mathbf{2}]_0$:$[\text{BnOH}]_0 = 50{:}50{:}1{:}1$, 80 °C, 16 h: (a) conversion and microstructure composition calculated from ^{31}P NMR vs time; (b) calculation of EtPPn and L-LA reactivity ratios using Meyer−Lowry fits.

($k_{\text{obs(EtPPn)}} = 9.0 \times 10^{-3}$ min^{-1} and $k_{\text{obs(LA)}} = 4.4 \times 10^{-3}$ min^{-1} (Figure S40)). As the conversion of EtPPn plateaus, at 88%, and [EtPPn] decreases, the proportion of PLA linkages in the copolymer increases and lactide polymerization becomes dominant. This results in a gradient copolymer with poly(EtPPn) as the first block, followed by a tapered segment of LA and EtPPn, and finally a PLA homopolymer block.

DBU (**2**) was also trialed for the one-pot copolymerization of EtPPn and L-LA. Compared to when using **1**, a stark difference was observed in the reactivity of the comonomers and in the microstructure of the resulting copolymers, with lower EtPPn incorporation and more random phosphorus-containing linkages obtained (Table 2, entries 8−10). Under the conditions used previously, initial rate kinetic analysis showed a much faster propagation rate for L-LA ($k_{\text{obs}} = 6.5 \times 10^{-3}$ min^{-1}) than for EtPPn ($k_{\text{obs}} = 6.3 \times 10^{-4}$ min^{-1}) (Figure 4a and Figure S30). With low EtPPn conversion (around 25% after 14 h) is it likely that this system features a dispersion of EtPPn throughout the PLLA chain, with an increase in tapering as [EtPPn] exceeds [L-LA]. This yields a polymer with thermal properties closer to that of PLLA with a glass transition temperature T_g = 18.1 °C, while distributing the more biodegradable units throughout.

The reactivity ratios of each monomer (EtPPn = r_1, L-LA = r_2) was calculated from kinetic data and supports the formation of tapered block copolymers with both **1** and **2** ($r_1 \gg 1 \gg r_2$ and $r_1 \ll 1 \ll r_2$, respectively). Using **1**, the high speed of reaction limited the recording of data at low monomer conversions, so that a data fit was applied to the experimental results (Figures S46 and S47). From Meyer−Lowry methodologies, values of $r_1 = 18.41$ and $r_2 = 0.83$ are obtained for **1**, while reverse reactivity is seen when **2** is the initiator ($r_1 = 0.19$, $r_2 = 19.74$) (Figures 3b and 4b).[48] Meyer−Lowry log, Jaacks, and Direct Numerical Integration methods agree with these trends, albeit some variations on r values are observed (Figures S50−S57, Tables S4 and S5).[48−51] This analysis further confirms that initiator choice has a profound impact on the microstructure of the copolymer.

Temperature Sequence for the Preparation of Block Copolymers from a Mixture of EtPPn and Lactide. The gradient strength of one-pot copolymers was further increased by a sequential temperature protocol. As LA is poorly soluble but EtPPn undergoes rapid ROP in toluene at room temperature, the selectivity for EtPPn should be increased under such copolymerization conditions. A temperature sequence was therefore applied to a copolymerization experiment in toluene-d_8 ($[\text{EtPPn}]_0$:$[\text{L-LA}]_0$:$[\text{BnOH}]_0$:$[\mathbf{1}]_0 = 50{:}50{:}1{:}1$): 2 h at 25 °C, then 16 h at 80 °C. The reaction was monitored in situ by ^{1}H and ^{31}P NMR spectroscopy. During the first phase of this protocol, 66% of EtPPn and less than 5% of L-LA conversion reacted, yielding a polymer with almost exclusively (>99%) P-P-P linkages, i.e., an almost pure polyphosphonate first block (Figure 5). When the temperature was increased to 80 °C, simultaneous conversion of both

DOI: 10.1021/acs.macromol.8b02385
Macromolecules 2019, 52, 1220−1226

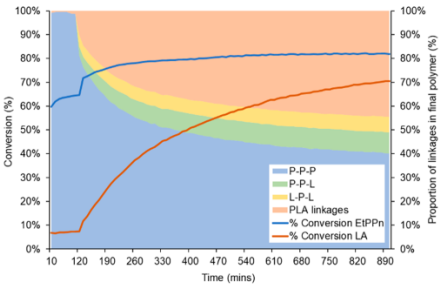

Figure 5. NMR-monitored copolymerization of EtPPn and L-LA in toluene-d_8 ($[L\text{-}LA]_0$ = $[EtPPn]_0$ = 0.35 mol L^{-1}, $[L\text{-}LA]_0$:$[EtPPn]_0$:$[\mathbf{1}]_0$:$[BnOH]_0$ = 50:50:1:1), using the temperature sequence: (1) 25 °C, 2 h, (2) 80 °C, 14 h. Final copolymer: P triad composition P-P-L:P-P-P:L-P-L = 12:73:15; M_n^{SEC} = 11750 g mol^{-1}, D = 1.09.

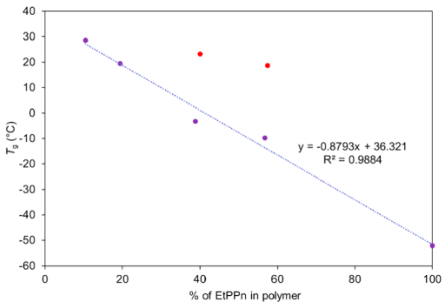

Figure 6. T_g of poly(phosphonate-*co*-lactide) tapered block copolymers depending on EtPPn content (type of lactide unit: rac-LA, blue; L-LA, red).

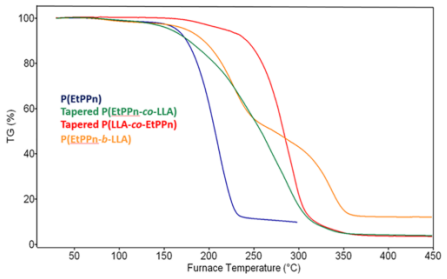

Figure 7. TGA analysis of poly(phosphonate-co-lactide) copolymers of various microstructure. Tapered P(EtPPn-co-LLA) (green) was made using **1**, tapered P(LLA-co-EtPPn) (red) was made using **2**, see details in ESI (Figures S61–68). The y-axis is weight loss as determined by TGA.

monomers was seen, with all possible linkages observed, indicative of statistical copolymerization. As in previous examples, once the conversion of EtPPn reached a plateau, polymerization of L-LA occurred with the formation of a pure PLLA block, without further incorporation or EtPPn. Increasing the time of the initial 25 °C phase did not increase the conversion of EtPPn or L-LA, whether the reaction was monitored in situ or via sampling from a stirred solution (Figures S43 and S44).

While pure blocks are not accessible yet with this methodology, a significant reduction in the statistical enchainment of monomers (P triads ratios P-P-L:P-P-P:L-P-L = 12:73:15 in comparison to 21:61:17 (Table 2, entry 5)) shows the potential of temperature sequencing to exacerbate differences in reactivity ratios and lead to clean block poly(phosphonate-*co*-lactide) copolymers in one pot. Through the same temperature sequencing, but at higher monomer concentrations of 3.4 mol L^{-1}, a further reduction in tapering was achieved (P triads ratios P-P-L:P-P-P:L-P-L = 9:84:7), while also granting a significant increase in polymerization rate (entry 10, Table S3).

Thermal Analysis. DSC analysis of poly(phosphonate-*co*-lactide) copolymers synthesized with **1** showed a negative correlation between the molar fraction of EtPPn incorporated and the glass transition temperature. The Al initiator thus gives access to copolymers with a range of glass transitions between that of the homopolymers (Figure 6). This behavior is expected for random copolymer systems as expressed in the Fox equation.[52] A similar trend has been observed with the copolymerization of ^{cy}HexPPn and ^{i}PrPPn.[43] Copolymers produced by temperature sequencing also yielded copolymers with only one transition (Figures S61 and S62). Only copolymers from sequential addition exhibited two distinct thermal transitions at 63.9 °C and −48.0 °C, indicating that monomer misinsertion is then low enough to form polymer blocks capable of phase separation.

Thermal gravimetric analysis (TGA) showed poly(phosphonate-*co*-lactide) copolymers to degrade within a wide temperature range (130–350 °C), with degradation profiles alluding to their microstructure (Figures 7 and S61–68). Tapered block copolymers thus showed only one degradation step, closer to that of pure P(EtPPn) or PLA, depending on the use of initiator **1** or **2**, respectively. Block polymers synthesized from sequential addition displayed two distinct degradation steps, with derivative maxima at 227 °C and 336 °C, indicative of P(EtPPn) and PLLA blocks, respectively, with an initial onset at 138 °C (Figure S65). Triblock poly(phosphonate-*b*-lactide-*b*-phosphonate) copolymer showed similar features but proved more stable, with degradation derivative maxima at 269 °C (corresponding to 63% mass loss) and 352 °C (further 37% mass loss) (Figure S68). This is likely a result of the greater degree of polymerization in this system. For block copolymers, peak deconvolution also yielded an associated % mass loss for each degradation step (e.g., 63% and 37% mass loss in the case of the triblock), which could be linked to the content of each monomer in the copolymer (60% of EtPPn units and 39% of L-LA units). This aligned well with polymer ratios (EtPPn:L-LA = 58:42) calculated through NMR spectroscopic analysis of the purified sample, providing an additional method for the analysis of block copolymers.

■ CONCLUSION

Copolymers of a cyclic phosphonate (2-ethyl-2-oxo-1,3,2-dioxaphospholane) and lactide have been prepared for the first

DOI: 10.1021/acs.macromol.8b02385
Macromolecules 2019, 52, 1220−1226

time. We were able to control the microstructure of the copolymer (determined by ^{1}H and ^{31}P NMR spectroscopy), via judicious choice of initiator (Al complex (**1**) or DBU (**2**), in combination with benzyl alcohol) and via the polymerization conditions (sequential addition or one-pot copolymerization, concentration, temperature). Block copolymers were obtained by sequential monomer addition, and tapered block copolymers were obtained by one-pot copolymerization. Interestingly, the choice of the catalyst inverted the reactivity ratios of the comonomers. The degree of tapering could also be reduced using a temperature sequence protocol, providing a route to one-pot block copolymer synthesis and an additional handle to tune the properties of the resulting poly(phosphonate-*co*-esters). Such amphiphilic copolymers with adjustable thermal properties are interesting candidates for future applications in drug delivery or materials science, because they are likely to also exhibit tunable degradation patterns. Future work will focus on investigating the hydrolytic degradation profiles of the copolymers.

■ ASSOCIATED CONTENT

Supporting Information

The Supporting Information is available free of charge on the ACS Publications website at DOI: 10.1021/acs.macromol.8b02385.

Experimental details; NMR, SEC, TGA, DSC, and MALDI-ToF data for copolymers; kinetic data for copolymerization experiments and reactivity ratios calculations (PDF)

■ AUTHOR INFORMATION

Corresponding Authors

*E-mail: a.buchard@bath.ac.uk.
*E-mail: mj205@bath.ac.uk.
*E-mail: wurm@mpip-mainz.mpg.de.

ORCID

Frederik R. Wurm: 0000-0002-6955-8489
Matthew D. Jones: 0000-0001-5991-5617
Antoine Buchard: 0000-0003-3417-5194

Author Contributions

The manuscript was written through contributions of all authors. All authors have given approval to the final version of the manuscript.

Notes

The authors declare no competing financial interest.

■ ACKNOWLEDGMENTS

Analytical facilities were provided through the Chemical Characterization and Analysis Facility (CCAF) at the University of Bath and the Max Planck Institute for Polymer Research. We thank the EPSRC and University of Bath for funding a studentship for J.B. A.B. acknowledges Roger and Sue Whorrod (fellowship) and the Royal Society (UF/160021 fellowship).

■ REFERENCES

(1) Nguyen, H. T. H.; Qi, P.; Rostagno, M.; Feteha, A.; Miller, S. A. The Quest for High Glass Transition Temperature Bioplastics. *J. Mater. Chem. A* **2018**, *6*, 9298−9331.

(2) Sin, L. T.; Rahmat, A.; Rahman, W. A. *Polylactic Acid: PLA Biopolymer Technology and Applications*; William Andrew, 2012.

(3) Yu, S.; Xiang, H.; Zhou, J.; Zhu, M. Preparation and Characterization of Fire Resistant PLA Fibers with Phosphorus Flame Retardant. *Fibers Polym.* **2017**, *18* (6), 1098−1105.

(4) *Bioplastics Market Data 2017*; European Bioplastics, Institute for Bioplastics and Biocomposites: Berlin, 2017.

(5) Dijkstra, P. J.; Du, H.; Feijen, J. Single Site Catalysts for Stereoselective Ring-Opening Polymerization of Lactides. *Polym. Chem.* **2011**, *2* (3), 520−527.

(6) Rudeekit, Y.; Numnoi, J.; Tajan, M.; Chaiwutthinan, P.; Leejarkpai, T. Determining Biodegradability of Polylactic Acid under Different Environments. *J. Met. Mater. Miner.* **2008**, *18* (2), 83−87.

(7) Haider, T.; Völker, C.; Kramm, J.; Landfester, K.; Wurm, F. R. Plastics of the Future? The Impact of Biodegradable Polymers on the Environment and on Society. *Angew. Chem., Int. Ed.* **2019**, *58*, 50−62.

(8) Rocca-Smith, J. R.; Whyte, O.; Brachais, C. H.; Champion, D.; Piasente, F.; Marcuzzo, E.; Sensidoni, A.; Debeaufort, F.; Karbowiak, T. Beyond Biodegradability of Poly(lactic acid): Physical and Chemical Stability in Humid Environments. *ACS Sustainable Chem. Eng.* **2017**, *5* (3), 2751−2762.

(9) Muller, J.; González-Martínez, C.; Chiralt, A. Combination Of Poly(Lactic) Acid and Starch for Biodegradable Food Packaging. *Materials* **2017**, *10* (8), 952.

(10) Yemisci, F.; Aytac, A. Compatibilization of Poly(Lactic Acid)/Polycarbonate Blends by Different Coupling Agents. *Fibers Polym.* **2017**, *18* (8), 1445−1451.

(11) Pepper, K. J.; Masson, T.; De Focatiis, D.; Howdle, S. M. Can. a Combination of Poly(Ethylene Glycol) and Dense Phase Carbon Dioxide Improve Processing of Polylactide? A High Pressure Rheology Investigation. *J. Supercrit. Fluids* **2018**, *133*, 343−348.

(12) Han, W.; Ren, J.; Xuan, H.; Ge, L. Controllable Degradation Rates, Antibacterial, Free-Standing and Highly Transparent Films Based on Polylactic Acid and Chitosan. *Colloids Surf., A* **2018**, *541*, 128−136.

(13) Chaiwutthinan, P.; Pimpan, V.; Chuayjuljit, S.; Leejarkpai, T. Biodegradable Plastics Prepared from Poly(Lactic Acid), Poly(Butylene Succinate) and Microcrystalline Cellulose Extracted from Waste-Cotton Fabric with a Chain Extender. *J. Polym. Environ.* **2015**, *23* (1), 114−125.

(14) Suthapakti, K.; Molloy, R.; Punyodom, W.; Nalampang, K.; Leejarkpai, T.; Topham, P. D.; Tighe, B. J. Biodegradable Compatibilized Poly(l-Lactide)/Thermoplastic Polyurethane Blends: Design, Preparation and Property Testing. *J. Polym. Environ.* **2018**, *26* (5), 1818.

(15) Martin, R. T.; Camargo, L. P.; Miller, S. A. Marine-Degradable Polylactic Acid. *Green Chem.* **2014**, *16* (4), 1768−1773.

(16) Nguyen, H. T. H.; Short, G. N.; Qi, P.; Miller, S. A. Copolymerization of Lactones and Bioaromatics via Concurrent Ring-Opening Polymerization/Polycondensation. *Green Chem.* **2017**, *19* (8), 1877−1888.

(17) Marsico, F.; Wagner, M.; Landfester, K.; Wurm, F. R. Unsaturated Polyphosphoesters via Acyclic Diene Metathesis Polymerization. *Macromolecules* **2012**, *45* (21), 8511−8518.

(18) Steinbach, T.; Alexandrino, E. M.; Wurm, F. R. Unsaturated Poly(Phosphoester)s via Ring-Opening Metathesis Polymerization. *Polym. Chem.* **2013**, *4* (13), 3800−3806.

(19) Bauer, K. N.; Liu, L.; Andrienko, D.; Wagner, M.; Macdonald, E. K.; Shaver, M. P.; Wurm, F. R. Polymerizing Phostones: A Fast Way to In-Chain Poly(Phosphonate)s with Adjustable Hydrophilicity. *Macromolecules* **2018**, *51* (4), 1272−1279.

(20) Bauer, K. N.; Tee, H. T.; Velencoso, M. M.; Wurm, F. R. Main-Chain Poly(Phosphoester)s: History, Syntheses, Degradation, Bio- and Flame-Retardant Applications. *Prog. Polym. Sci.* **2017**, *73*, 61−122.

(21) Kałużyński, K.; Libiszowski, J.; Penczek, S. A New Class of Synthetic Polyelectrolytes. Acidic Polyesters of Phosphoric Acid (Poly(Hydroxyalkylene Phosphates)). *Macromolecules* **1976**, *9* (2), 365−367.

DOI: 10.1021/acs.macromol.8b02385
Macromolecules 2019, 52, 1220−1226

(22) Klosiński, P.; Penczek, S. Synthesis of Models of Teichoic Acids by Ring-Opening Polymerization. *Macromolecules* **1983**, *16* (2), 316−320.
(23) *Novel Fire Retardant Polymers and Composite Materials*; Wang, D. Y., Ed.; Elsevier Science, 2016.
(24) Velencoso, M. M.; Battig, A.; Markwart, J. C.; Schartel, B.; Wurm, F. R. Molecular Firefighting - How Modern Phosphorus Chemistry Can Help Solve the Flame Retardancy Task. *Angew. Chem., Int. Ed.* **2018**, *57*, 10450−10467.
(25) Tsao, Y. Y. T.; Wooley, K. L. Synthetic, Functional Thymidine-Derived Polydeoxyribonucleotide Analogues from a Six-Membered Cyclic Phosphoester. *J. Am. Chem. Soc.* **2017**, *139* (15), 5467−5473.
(26) Tsao, Y. Y. T.; Smith, T. H.; Wooley, K. L. Regioisomeric Preference in Ring-Opening Polymerization of 3′,5′-Cyclic Phosphoesters of Functional Thymidine DNA Analogues. *ACS Macro Lett.* **2018**, *7* (2), 153−158.
(27) Pratt, R. C.; Lohmeijer, B. G. G.; Long, D. A.; Lundberg, P. N. P.; Dove, A. P.; Li, H.; Wade, C. G.; Waymouth, R. M.; Hedrick, J. L. Exploration, Optimization, and Application of Supramolecular Thiourea-Amine Catalysts for the Synthesis of Lactide (Co)Polymers. *Macromolecules* **2006**, *39* (23), 7863−7871.
(28) Lohmeijer, B. G. G.; Pratt, R. C.; Leibfarth, F.; Logan, J. W.; Long, D. A.; Dove, A. P.; Nederberg, F.; Choi, J.; Wade, C.; Waymouth, R. M.; et al. Guanidine and Amidine Organocatalysts for Ring-Opening Polymerization of Cyclic Esters. *Macromolecules* **2006**, *39* (25), 8574−8583.
(29) Kiesewetter, M. K.; Shin, E. J.; Hedrick, J. L.; Waymouth, R. M. Organocatalysis: Opportunities and Challenges for Polymer Synthesis. *Macromolecules* **2010**, *43* (5), 2093−2107.
(30) Clément, B.; Grignard, B.; Koole, L.; Jérome, C.; Lecomte, P. Metal-Free Strategies for the Synthesis of Functional and Well-Defined Polyphosphoesters. *Macromolecules* **2012**, *45* (11), 4476−4486.
(31) Darensbourg, D. J.; Choi, W.; Ganguly, P.; Richers, C. P. Biometal Derivatives as Catalysts for the Ring-Opening Polymerization of Trimethylene Carbonate. Optimization of the Ca(II) Salen Catalyst System. *Macromolecules* **2006**, *39* (13), 4374−4379.
(32) Yasuda, H.; Sumitani, M.; Nakamura, A. Novel Synthesis of Acidic Polyesters of Phosphoric Acid by Thermal Elimination of Isobutylene from Poly(Alkylene Tert-Butyl Phosphates). *Macromolecules* **1981**, *14* (2), 458−460.
(33) Xiao, C. S.; Wang, Y. C.; Du, J. Z.; Chen, X. S.; Wang, J. Kinetics and Mechanism of 2-Ethoxy-2-Oxo-1,3,2-Dioxaphospholane Polymerization Initiated by Stannous Octoate. *Macromolecules* **2006**, *39* (20), 6825−6831.
(34) Iwasaki, Y.; Yamaguchi, E. Synthesis of Well-Defined Thermoresponsive Polyphosphoester Macroinitiators Using Organocatalysts. *Macromolecules* **2010**, *43* (6), 2664−2666.
(35) Stukenbroeker, T. S.; Solis-Ibarra, D.; Waymouth, R. M. Synthesis and Topological Trapping of Cyclic Poly(Alkylene Phosphates). *Macromolecules* **2014**, *47* (23), 8224−8230.
(36) Nifant'ev, I. E.; Shlyakhtin, A. V.; Bagrov, V. V.; Komarov, P. D.; Kosarev, M. A.; Tavtorkin, A. N.; Minyaev, M. E.; Roznyatovsky, V. A.; Ivchenko, P. V. Controlled Ring-Opening Polymerisation of Cyclic Phosphates, Phosphonates and Phosphoramidates Catalysed by Heteroleptic BHT-Alkoxy Magnesium Complexes. *Polym. Chem.* **2017**, *8* (44), 6806−6816.
(37) Lim, Y. H.; Tiemann, K. M.; Heo, G. S.; Wagers, P. O.; Rezenom, Y. H.; Zhang, S.; Zhang, F.; Youngs, W. J.; Hunstad, D. A.; Wooley, K. L. Preparation and in Vitro Antimicrobial Activity of Silver-Bearing Degradable Polymeric Nanoparticles of Polyphosphoester-Block-Poly(l-Lactide). *ACS Nano* **2015**, *9* (2), 1995−2008.
(38) Yang, X.-Z.; Sun, T.-M.; Dou, S.; Wu, J.; Wang, Y.-C.; Wang, J. Block Copolymer of Polyphosphoester and Poly(l-Lactic Acid) Modified Surface for Enhancing Osteoblast Adhesion, Proliferation, and Function. *Biomacromolecules* **2009**, *10* (8), 2213−2220.
(39) Lim, Y. H.; Heo, G. S.; Cho, S.; Wooley, K. L. Construction of a Reactive Diblock Copolymer, Polyphosphoester- Block -Poly(l-Lactide), as a Versatile Framework for Functional Materials That Are Capable of Full Degradation and Nanoscopic Assembly Formation. *ACS Macro Lett.* **2013**, *2* (9), 785−789.
(40) Borguet, Y. P.; Khan, S.; Noel, A.; Gunsten, S. P.; Brody, S. L.; Elsabahy, M.; Wooley, K. L. Development of Fully Degradable Phosphonium-Functionalized Amphiphilic Diblock Copolymers for Nucleic Acids Delivery. *Biomacromolecules* **2018**, *19* (4), 1212−1222.
(41) Wolf, T.; Steinbach, T.; Wurm, F. R. A Library of Well-Defined and Water-Soluble Poly(Alkyl Phosphonate)s with Adjustable Hydrolysis. *Macromolecules* **2015**, *48* (12), 3853−3863.
(42) Wolf, T.; Rheinberger, T.; Wurm, F. R. Thermoresponsive Coacervate Formation of Random Poly(Phosphonate) Terpolymers. *Eur. Polym. J.* **2017**, *95*, 756−765.
(43) Wolf, T.; Naß, J.; Wurm, F. R. Cyclohexyl-Substituted Poly(Phosphonate)-Copolymers with Adjustable Glass Transition Temperatures. *Polym. Chem.* **2016**, *7* (17), 2934−2937.
(44) Wolf, T.; Rheinberger, T.; Simon, J.; Wurm, F. R. Reversible Self-Assembly of Degradable Polymersomes with Upper Critical Solution Temperature in Water. *J. Am. Chem. Soc.* **2017**, *139* (32), 11064−11072.
(45) Macdonald, E. K.; Shaver, M. P. An Expanded Range of Catalysts for Synthesising Biodegradable Polyphosphonates. *Green Mater.* **2016**, *4*, 81−88.
(46) Beament, J.; Mahon, M. F.; Buchard, A.; Jones, M. D. Aluminum Complexes of Monopyrrolidine Ligands for the Controlled Ring-Opening Polymerization of Lactide. *Organometallics* **2018**, *37*, 1719−1724.
(47) Steinbach, T.; Ritz, S.; Wurm, F. R. Water-Soluble Poly(Phosphonate)s via Living Ring-Opening Polymerization. *ACS Macro Lett.* **2014**, *3* (3), 244−248.
(48) Patino-Leal, H.; Reilly, P. M.; O'Driscoll, K. F. On the Estimation of Reactivity Ratios. *J. Polym. Sci., Polym. Lett. Ed.* **1980**, *18* (3), 219−227.
(49) Kazemi, N.; Duever, T. A.; Penlidis, A. Reactivity Ratio Estimation from Cumulative Copolymer Composition Data. *Macromol. React. Eng.* **2011**, *5* (9−10), 385−403.
(50) Hauch, E.; Zhou, X.; Duever, T. A.; Penlidis, A. Estimating Reactivity Ratios from Triad Fraction Data. *Macromol. Symp.* **2008**, *271* (1), 48−63.
(51) Jaacks, V. A Novel Method of Determination of Reactivity Ratios in Binary and Ternary Copolymerizations. *Makromol. Chem.* **1972**, *161* (1), 161−172.
(52) Brostow, W.; Chiu, R.; Kalogeras, I. M.; Vassilikou-Dova, A. Prediction of Glass Transition Temperatures: Binary Blends and Copolymers. *Mater. Lett.* **2008**, *62* (17−18), 3152−3155.

DOI: 10.1021/acs.macromol.8b02385
Macromolecules 2019, 52, 1220−1226

11.2 List of Publications

First author and shared first author

Battig, A.; **Markwart, J. C.**; Wurm, F. R.; Schartel, B., Matrix Matters: Hyperbranched Flame Retardants in Aliphatic and Aromatic Epoxy Resins. *Polymer Degradation and Stability* **2019**.

Markwart, J. C.; Battig, A.; Kuckhoff, T.; Schartel, B.; Wurm, F. R., First phosphorus AB_2 monomer for flame-retardant hyperbranched polyphosphoesters: AB_2 vs A_2+B_3. *Polymer Chemistry* **2019**.

Battig, A.; **Markwart, J. C.**; Wurm, F. R.; Schartel, B., Hyperbranched phosphorus flame retardants: multifunctional additives for epoxy resins. *Polymer Chemistry* **2019,** *10* (31), 4346-4358.

Markwart, J. C.; Battig, A.; Zimmermann, L.; Wagner, M.; Fischer, J.; Schartel, B.; Wurm, F. R., Systematically Controlled Decomposition Mechanism in Phosphorus Flame Retardants by Precise Molecular Architecture: P–O vs P–N. *ACS Applied Polymer Materials* **2019,** *1* (5), 1118-1128.

Markwart, J. C.; Wurm, F. R., The 2-acetylthioethyl ester group: A versatile protective group for P-OH-groups. *Tetrahedron* **2018,** *74* (52), 7426-7430.

Velencoso, M. M.; Battig, A.; **Markwart, J. C.**; Schartel, B.; Wurm, F. R., Molecular Firefighting-How Modern Phosphorus Chemistry Can Help Solve the Challenge of Flame Retardancy. *Angew. Chem. Int. Ed. Engl.* **2018,** *57* (33), 10450-10467.

Markwart, J. C.; Battig, A.; Velencoso, M. M., Pollok, D., Schartel, B.; Wurm, F. R., Comparison of novel aromatic and aliphatic hyperbranched poly(phosphoester)s as flame retardants in epoxy resins. *Submitted* **2019**.

Battig, A.; **Markwart, J. C.**; Wurm, F. R.; Schartel, B., Sulfur's Role in the Flame Retardancy of Thio-Ether–linked Hyperbranched Poly(phosphoesters) in Epoxy Resins. *Submitted* **2019**.

Markwart, J. C.; Suraeva, O.; Lieberwirth, I.; Haider, T.; Graf, R.; Wurm, F. R., Defect engineering of precision polymers: size control and surface chemistry of anisotropic polymer platelets after solution crystallization. *Submitted* **2019**.

Markwart, J. C.; Schäfer, H.; Battig, A.; Koschek, K.; Schartel, B.; Wurm, F. R., Intrinsic flame retardant vitrimers as a recyclable alternative for epoxy resins in composite materials. *Submitted* **2019**.

Co-authorship

Beament, J.; Wolf, T.; **Markwart, J. C.**; Wurm, F. R.; Jones, M. D.; Buchard, A., Copolymerization of Cyclic Phosphonate and Lactide: Synthetic Strategies toward Control of Amphiphilic Microstructure. *Macromolecules* **2019**, 52 (3), 1220-1226.

Huang, W.; **Markwart, J. C.**; Briseno, A. L.; Hayward, R. C., Orthogonal Ambipolar Semiconductor Nanostructures for Complementary Logic Gates. *ACS Nano* **2016**, 10 (9), 8610-8619.

Steinmann, M.; **Markwart, J.**; Wurm, F. R., Poly(alkylidene chlorophosphate)s via Acyclic Diene Metathesis Polymerization: A General Platform for the Postpolymerization Modification of Poly(phosphoester)s. *Macromolecules* **2014**, 47 (24), 8506-8513.

Gleede, T.; **Markwart, J. C.**; Huber, N.; Rieger, E.; Wurm, F. R., Competitive Copolymerization: Access to Aziridine Copolymers with Adjustable Gradient Strengths. *Submitted* **2019**.

Yasir, M.; Liu, P.; **Markwart, J. C.**; Wurm, F. R.; Smart, J.; Lattuada, M.; Kilbinger, A. F. M., Conversion of Fischer Carbene to Schrock Carbene and Its Application in Compositional Analysis of One-Step Living Ring Opening Metathesis Block Copolymer. *Submitted* **2019**.